# Transactions of the ASME®

# Journal of Fluids Engineering

Published Quarterly by The American Society of Mechanical Engineers

VOLUME 122 • NUMBER 3 • SEPTEMBER 2000

## TECHNICAL PAPERS

(Contents continued on inside back cover)

This journal is printed on acid-free paper, which exceeds the ANSI Z39.48-1992 specification for permanence of paper and library materials. ∞™
♲ 85% recycled content, including 10% post-consumer fibers.

**FLUIDS ENGINEERING DIVISION**
Technical Editor
**JOSEPH KATZ (2005)**
Editorial Assistant
**LAUREL MURPHY (2005)**

Associate Technical Editors
**P. W. BEARMAN (2001)**
**P. BRADSHAW (2000)**
**J. BRIDGES (2002)**
**U. GHIA (2001)**
**M. HAJJ (2001)**
**G. KARNIADAKIS (2002)**
**J. LASHERAS (2002)**
**Y. MATSUMOTO (2002)**
**C. L. MERKLE (2000)**
**L. MONDY (2002)**
**P. RADD (2001)**
**B. SCHIAVELLO (2002)**
**Y. TSUJIMOTO (2002)**
**F. K. WASDEN (2000)**
**D. R. WILLIAMS (2000)**
**K. ZAMAN (2001)**

**BOARD ON COMMUNICATIONS**
Chairman and Vice-President
**R. K. SHAH**

**OFFICERS OF THE ASME**
President, **JOHN R. PARKER**
Exec. Director
**D. L. BELDEN**
Treasurer
**J. A. MASON**

**PUBLISHING STAFF**
Managing Director, Engineering
**CHARLES W. BEARDSLEY**
Director, Technical Publishing
**PHILIP DI VIETRO**
Managing Editor, Technical Publishing
**CYNTHIA B. CLARK**
Managing Editor, Transactions
**CORNELIA MONAHAN**
Production Assistant
**MARISOL ANDINO**

**Transactions of the ASME, Journal of Fluids Engineering** (ISSN 0098-2202) is published quarterly (Mar., June, Sept., Dec.) by The American Society of Mechanical Engineers, Three Park Avenue, New York, NY 10016. Periodicals postage paid at New York, NY and additional mailing offices. POSTMASTER: Send address changes to Transactions of the ASME, Journal of Fluids Engineering, c/o THE AMERICAN SOCIETY OF MECHANICAL ENGINEERS, 22 Law Drive, Box 2300, Fairfield, NJ 07007-2300. **CHANGES OF ADDRESS** must be received at Society headquarters seven weeks before they are to be effective. Please send old label and new address. **STATEMENT from By-Laws.** The Society shall not be responsible for statements or opinions advanced in papers or ... printed in its publications (B7.1, Par. 3).

**COPYRIGHT © 2000** by the American Society of Mechanical Engineers. Authorization to photocopy material for internal or personal use under those circumstances not falling within the fair use provisions of the Copyright Act, contact the Copyright Clearance Center (CCC), 222 Rosewood Drive, Danvers, MA 01923, tel: 978-750-8400, www.copyright.com. Request for special permission or bulk copying should be addressed to Reprints/Permission Department.

**INDEXED** by Applied Mechanics Reviews and Engineering Information, Inc. Canadian Goods & Services Tax Registration #126148048.

Downloaded 03 Jun 2010 to 171.66.16.159. Redistribution subject to ASME license or copyright; see http://www.asme.org/terms/Terms_Use.cfm

(**Contents continued**)

**Journal of Fluids Engineering** **Volume 122, Number 3** **SEPTEMBER 2000**

## TECHNICAL BRIEFS

## ANNOUNCEMENTS

# The Use of Cavitating Jets to Oxidize Organic Compounds in Water

**K. M. Kalumuck**
Principal Research Scientist

**G. L. Chahine**
President

DYNAFLOW, Inc.,
7210 Pindeil School Rd.,
Fulton, MD 20759
e-mail: info@dynaflow-inc.com

*Exposure to ultrasonic acoustic waves can greatly enhance various chemical reactions. Ultrasonic acoustic irradiation of organic compounds in aqueous solution results in oxidation of these compounds. The mechanism producing this behavior is the inducement of the growth and collapse of cavitation bubbles driven by the high frequency acoustic pressure fluctuations. Cavitation bubble collapse produces extremely high local pressures and temperatures. Such conditions are believed to produce hydroxyl radicals which are strong oxidizing agents. We have applied hydrodynamic cavitation to contaminated water by the use of submerged cavitating liquid jets to trigger widespread cavitation and induce oxidation in the bulk solution. Experiments were conducted in recirculating flow loops using a variety of cavitating jet configurations and operating conditions with dilute aqueous solutions of p-nitrophenol (PNP) of known concentration. Temperature, pH, ambient and jet pressures, and flow rates were controlled and systematically varied. Samples of the liquid were taken and the concentration of PNP measured with a spectrophotometer. Experiments were conducted in parallel with an ultrasonic horn for comparison. Submerged cavitating liquid jets were found to generate a two order of magnitude increase in energy efficiency compared to the ultrasonic means.* [S0098-2202(00)00303-5]

## Introduction

Ultrasonic cavitation is known (Brown and Goodman [1]) to produce sonochemically activated reactions in water resulting in the formation of highly effective oxidizing hydroxyl radicals. Usually this is achieved using ultrasonic horns that send a high intensity acoustic beam into the solution and excite microcavities. Such systems have been found to promote a wide range of chemical reactions (Suslick [2]) and to be capable of oxidizing dilute aqueous mixtures of organic compounds. However, such devices essentially self limit the efficiency of the process by achieving cavitation only in a thin layer near the surface of the sonifer. In addition, the efficiency of the transfer of electric power into ultrasonic waves into the liquid is known to be quite low—of the order of 15–20 percent.

We employ a mechanism for generating cavitation in a wide body of the liquid by an array of submerged cavitating jets. This process can be made very efficient and benefits in addition from the fact that pumps are quite efficient (of the order of 75 percent) at converting electric (or other) power into hydraulic power. A system based on this technology would be relatively inexpensive, and could be designed into a low-energy technology that will perform at an optimum level creating fast degradation of toxic substances without generating carcinogenic materials such as can occur with chlorination.

## Dissociation of Water and Release of Oxidizing Radicals

Exposure to ultrasonic waves can drive many chemical reactions through the generation, growth, and subsequent collapse of cavitation bubbles (e.g., Brown and Goodman [1], Suslick [2]). It is universally accepted that this cavitation with its accompanying local high pressures and temperatures drives these reactions rather than the acoustic waves themselves. The acoustic waves provide a means for transferring the energy of the acoustic driver to cavitation nuclei whose subsequent behavior converts this energy to pressure, heat, erosion, chemical reaction, etc.

When subjected to cavitation, water undergoes dissolution according to the following chemical reaction (e.g., Suslick [3], Neppiras [4])

$$H_2O \rightarrow H^{\cdot} + OH^{\cdot}. \tag{1}$$

The free hydroxyl radical $OH^{\cdot}$ is one of the most powerful oxidizing agents and is an excellent initiator of chain reactions. Oxidation of organic compounds results in various intermediate and end products depending on the compound. These include water vapor, carbon dioxide, inorganic ions and short chain inorganic acids (e.g., see Suslick [2]; Hua et al. [5]; Skov et al. [6]). Often the intermediate products also undergo subsequent oxidation. Modeling of radical production due to cavitation bubble collapse has recently been performed by Gong and Hart [7].

Under the oscillating pressure field of an ultrasonic horn or due to large fluctuating pressure forces in the shear layer of a cavitating and resonating jet, pre-existing microscopic bubble nuclei in the liquid grow and collapse. There are several competing theories for the predominant phenomena that triggers the anomalous chemistry present during the bubble collapse. According to one, the generation of a ''hot spot'' upon bubble collapse (local high temperature and pressure region) is responsible for the phenomena (Neppiras [4]; Suslick et al. [8]; Suslick et al. [9]). Others suggest that the reactions are due to shock waves or electric discharges generated at the collapse and the fragmentation (Margulis [10]) or to the plasma like state generated in the collapsing bubble (LePoint and Mullie [11]).

Recently, a number of researchers have looked into using ultrasound to degrade organic contaminants. The list is too extensive to review here. However, a sample of relevant work includes that of Hua et al. [5,12], Kotronarou et al. [13,14], Cheung et al. [15], and Hua and Hoffman [16]. Such work has been performed in both batch and continuous flow modes using ultrasonic horns and plates. Also recently, a commercial scale process has been employed utilizing a venturi type cavitation flow loop often in combination with UV irradiation and hydrogen peroxide addition (U.S. Environmental Protection Agency [17]; Skov et al. [6]).

**Cavitation Bubble Dynamics.** In a pressure field, a bubble works as an oscillator with the gaseous contents acting as a spring

---

Contributed by the Fluids Engineering Division for publication in the JOURNAL OF FLUIDS ENGINEERING. Manuscript received by the Fluids Engineering Division October 14, 1999; revised manuscript received May 3, 2000. Associate Technical Editor: J. Katz.

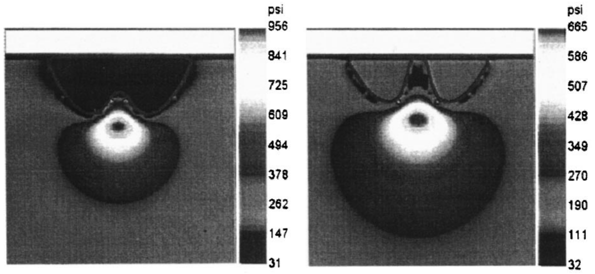

**Fig. 1 Pressure field associated with nonspherical bubble collapse. Taken from Chahine and Duraiswami [19]**

and the inertia being provided by the motion of the surrounding liquid. Under external pressure forcing, the bubble undergoes volume and shape oscillations. As the bubble compresses the inside pressure grows.

For a collapsing spherical cavity in a liquid of density $\rho$ under external steady pressure $P_{\mathrm{amb}}$, and with gas inside the bubble having a specific heat ratio $k$, Neppiras [4] has shown that as the bubble collapses, a very high pressure region is generated near the bubble wall in the liquid with a maximum pressure $P_{\max}$ given by

$$p_{\max}=p_{g0}\left[\frac{P_{\mathrm{amb}}(k-1)}{p_{g0}}\right]^{k/(k-1)}, \tag{2}$$

where $p_{g0}$ is the initial gas pressure in the bubble. For a value of $k=4/3$ he obtained the corresponding temperature

$$T_{\max}=T_0\left(\frac{P_{\mathrm{amb}}}{3p_{g0}}\right). \tag{3}$$

With $P_{\mathrm{amb}}=1$ atm, and $p_{g0}=0.01$ atm, *the maximum pressure may be as high as* $1.2\times10^4$ *atm, and the temperature could be as high as 10,000°K (Young [18]). Thus extremely high values of temperature and pressure are generated in a small region of space where the bubble collapse occurs.* Such physical conditions could explain the enhancement by cavitation of the chemical dissociation of the aqueous medium releasing hydroxyl radicals.

However, cavitation bubbles rarely behave spherically. Typically, *due to initial or boundary condition asymmetries and to bubble interacting,* the bubble, upon collapse, forms a *high speed reentering jet* (Young [18]; Chahine and Duraiswami [19]). Figure 1 presents a calculation we have performed for a bubble collapsing near a solid wall and forming a high speed jet which impacts the wall. Visible in the figure are the very high pressures in the liquid near the jet (Chahine and Duraiswami [19]). Such computations show the potential for extremely high pressures not only in the gas inside the bubble but also in a focused area of the liquid. In practice, bubbles often occur in ''clouds'' in which bubble/bubble interaction and bubble deformation effects occur (Chahine [20]; Chahine and Duraiswami [21]). In cavitating jets, elongated, rotating, and ring shaped bubble cavities form which have also been found to collapse with the formation of reentering jets (Chahine and Johnson [22]; Chahine and Genoux [23]).

**Cavitating Water Jets.** *Cavitating water jet technology* represents one successful attempt to harness and utilize the destructive power of cavitation. Various means and nozzle designs can be used to induce the explosive growth of microscopic cavities or bubbles within a liquid jet. Moving away from the orifice region, these bubbles encounter higher pressures and collapse. For example, by inserting a solid surface in front of the nozzle at an appropriate distance, nozzle generated cavities can be induced to collapse violently on that surface in the high-pressure stagnation region of the jet so created (Johnson et al. [24]; Chahine and Johnson [22]; Chahine et al. [25]).

Cavitating jets have the following advantages over ultrasonic devices.

1 The cavitation can be made to be much more intense and aggressive.
2 The location of the cavitation ''center'' can be more easily controlled, and multiple centers in a small volume can be easily provided.
3 From a practical standpoint, a jet based process is simpler, more flexible, easily scaled up and able to process larger industrial level quantities of liquid for a given power input.
4 As demonstrated in this paper, the jets are significantly more efficient.

The dimensionless parameter characterizing cavitation is the cavitation number, $\sigma$,

$$\sigma=\frac{P_{\mathrm{amb}}-p_v}{1/2\rho V^{*2}}\approx\frac{P_{\mathrm{amb}}-p_v}{\Delta P}, \tag{4}$$

where $\rho$ is the liquid density, $V^*$ is the characteristic flow velocity, and $\Delta P$ is the presence drop across the nozzle. The particular value at which cavitation is incipient $\sigma_i$ is termed the cavitation inception number. Thus if the operating conditions for a submerged jet are such that $\sigma/\sigma_i<1$, cavitation will occur, and as $\sigma/\sigma_i$ continues to decrease below unity the amount of cavitation will increase.

## Experimental Setup

Experiments were conducted in several jet flow loops and in an ultrasonic system. Preliminary investigations were conducted in a cavitation reaction chamber constructed of plexiglass to enable viewing of the cavitation and flow. Due to the potential for many organic compounds to attack plexiglass this cell was not used for actual oxidation tests. Instead, jet cavitation reactors constructed of stainless steel were utilized.

One loop was driven by a triplex positive displacement pump which produced a flow of 4.5 gpm at pressures up to 1000 psi. The flow from the pump was sent to a multi-stage cavitation reaction chamber. Each stage included a jet orifice plate with multiple orifices and a stagnation plate located downstream of the orifice plate and designed to stagnate the jet flows thereby inducing strong bubble collapse. A second was driven by a centrifugal pump capable of 56 gpm at up to 75 psi and is shown in the sketch of Fig. 2. The loop was fabricated of steel piping. Upon exiting the pump, the liquid flowed into a pipe manifold into which a large number of orifices had been machined. The total fluid volume of this loop was 6.5 liters. Reservoir temperature was maintained at the desired value by use of a cooling loop inside the reservoir and immersion of the reservoir in a large tank filled with water and containing a refrigeration coil.

**Ultrasonic Setup.** A sketch of the ultrasonic device is provided in Fig. 3. The device is driven by magnetostrictive oscillations produced in a nickel stack surrounded by electromagnetic

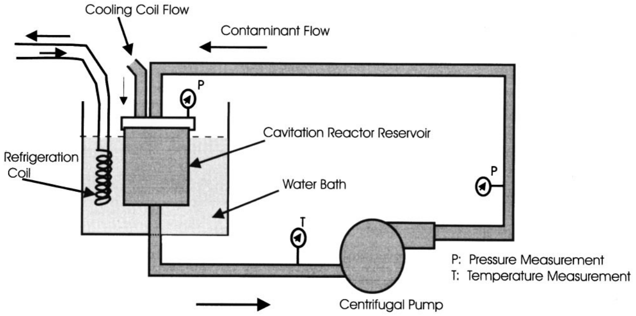

**Fig. 2 Sketch of jet loop capable of 56 gpm at 60 psi**

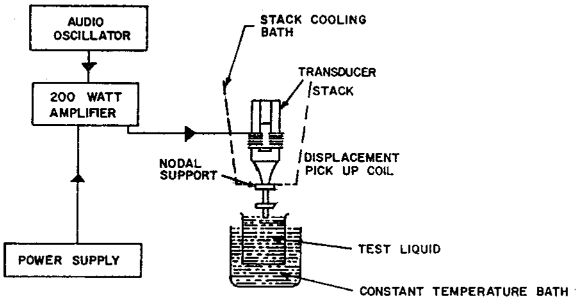

**Fig. 3 Sketch of ultrasonic experimental setup**

coils. The oscillations are amplified by a tapered titanium horn tuned to resonate at 15.7 kHz. The waveform is produced by a frequency generator and amplified before being fed to the coils. A 3/8 in. diameter titanium "button" or "tip" was attached to the end of the horn. The amplitude of oscillation of the tip was initially calibrated using a bifilar microscope. Its amplitude was monitored during testing by a sensor whose voltage output is proportional to displacements. The tip displacement amplitude was set to 0.0026 in. peak to peak.

The horn tip was submerged 0.125 in. in a 150 ml glass beaker filled with 25 ml of test sample liquid. Initially, the submergence was varied, and the value of 0.125 in. was selected because it produced the greatest amount of cavitation. The top of the beaker was covered with a plastic sheet through which the horn was inserted. The sample beaker was surrounded with a cooling bath to maintain a constant temperature.

**Measurement Techniques and Procedures.** Reagent grade p-Nitrophenol—"PNP"—(Aldrich, 99 percent), phosphoric acid (Aldrich, 85 percent), and sodium hydroxide (VWR Scientific, 1.0 N) were used. The PNP was in crystalline form and was mixed with distilled water.

PNP concentrations were measured using a UV-Vis spectrophotometer following the procedures of Kotronarou et al. [13] and Hua et al. [12]. The spectrophotometer was calibrated against known concentrations of PNP in distilled water at a wavelength of 400 nm after shifting the sample pH to 11 by the addition of NaOH to enable measurement employing the absorption band at 400 nm.

During testing, 3 ml samples were drawn from the test reservoir. Following the addition of NaOH, the sample was drawn through a Gelman 0.2 micron PFTE syringe filter to remove any particulate contaminants such as titanium erosion particles from the ultrasonic tests. The filtered sample was then placed in the spectrophotometer and its transmittance measured.

**Uncertainty Estimates.** The estimated uncertainty in measured quantities are: flow rate, ±5 percent; pressure, ±1 psi; concentration, ±0.2 ppm; pH, ±0.2; temperature, ±1°F. The oxidation efficiency (defined in Eq. (5)) and the nondimensional concentration, $C/C_0$ are derived quantities. Their estimated uncertainties are: oxidation efficiency, ±10 percent; $C/C_0$, ±4 percent.

## Results and Discussion

**Performance Evaluation: Oxidation Efficiency.** A key measure of the performance of the oxidation process is the energy required to remove a unit mass of a given compound. For overall performance, this can be expressed as the cumulative mass of contaminant removed per unit energy expended. When plotted against time, this represents a running value of the efficiency. We define this to be the *oxidation efficiency* given by

$$m^*(t)=\frac{(C_0-C(t))*\mathcal{V}}{t*\mathcal{P}}. \tag{5}$$

**Table 1 Comparison of power densities for PNP oxidation experiments**

| | watts/ml | Type |
|---|---|---|
| Ultrasonic | 0.36 | Batch |
| Cavitating Jets | 0.18-12 | Continuous flow |

Here, $C_0$ is the initial concentration, $C(t)$ the concentration at time $t$, $\mathcal{V}$ the liquid volume, and $\mathcal{P}$ the power expended. The peak value in the curve of $m^*(t)$ can be used to characterize the peak performance of each system.

The power used in this efficiency calculation is that which is imparted to the liquid. For the jet process, it is simply based on the hydraulic power imparted by the pump. For the ultrasonic horn, it is the acoustic energy dissipated in the liquid which was determined with a calorimetric test by measuring the heat generated. This enables use of the "*oxidation efficiency*" as a measure of the efficiency of the particular configuration for the cavitation phenomenon and removes variations in power consumption due to varying pump, motor, or horn configurations. The actual amount of energy that must be supplied to a system employing either the ultrasonic or jet induced cavitation is therefore larger due to these conversion inefficiencies. The ranges of the power input to the liquid per unit volume (power density) we utilized are shown in Table 1.

**Ultrasonic Tests.** Sample results of ultrasonic tests of the oxidation of PNP are presented in Fig. 4. Figure 4 presents the measured concentrations as a function of time for several cases run at a pH of 3.5 and initial concentrations of 8 and 25 ppm for comparison with the jet oxidation studies. We did not seek to

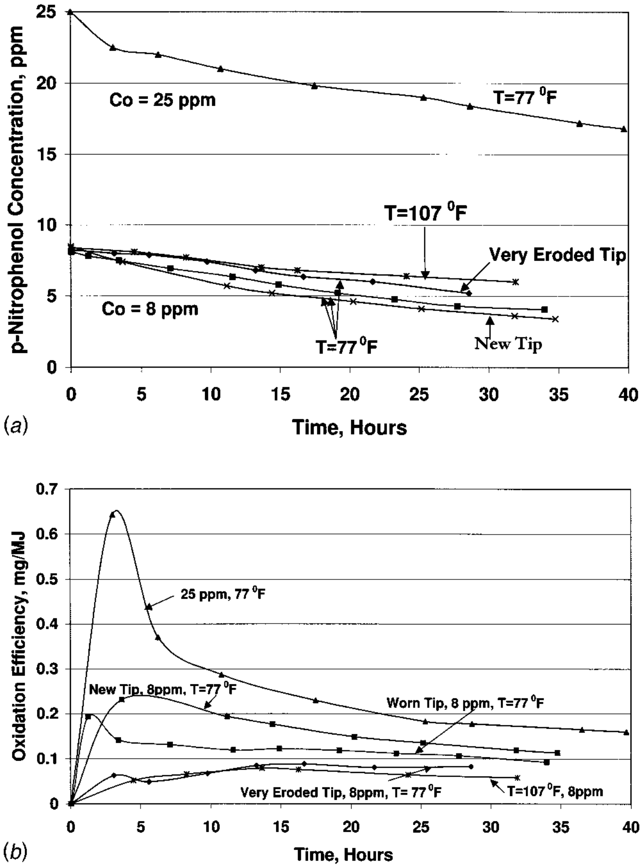

**Fig. 4 Ultrasonic sonication of PNP at pH=3.5. Top: concentration versus time. Bottom: oxidation efficiency.**

optimize the conditions for the ultrasonic horn since this has been experimentally investigated for aqueous solutions of PNP by others (Kotronarou et al. [13], Hua et al. [5,12]). We selected conditions from the literature which were near optimal. These tests were run at 77°F and 107°F with the rate of oxidation lower at 107°F than at 77°F—consistent with the general behavior of sonochemical reaction rates as described in Suslick [2]. Direct comparison of these results with those in the literature can be done using oxidation rates normalized with applied power. Normalization of results with the applied power shows that our results are comparable to those in the literature; e.g., the oxidation rate of Kotronarou et al. [13] is 0.89 mg/MJ. Calorimetric measurements showed that approximately 18 percent of the electric power input to the horn was converted to acoustic power and dissipated as heat in the liquid.

**Cavitating Jet Results.** Figure 5 presents sample results of the oxidation of PNP with submerged cavitating jets conducted in the flow loop of Fig. 2. The operating temperature was 107°F which, as described below, was found to produce the best performance. The pH was comparable to that of the ultrasonic tests of Fig. 4, and the initial concentration, 8 ppm, was used in the majority of the cases in Fig. 4. We can compare the oxidation efficiencies in Figs. 4 and 5 for achieving a given decrease in PNP concentration. For example, a 50 percent reduction (from 8 ppm to 4 ppm) is achieved by the jet system in 1.5 hrs. while the ultrasonic horn requires approximately 30 hrs. The corresponding oxidation efficiency for the cavitating jets (3 mg/MJ) is about 25 times larger than that of the ultrasonic device (0.12 mg/MJ). While the investigations conducted have not as yet been of sufficient scope to state that either the jet or ultrasonic devices are operating at their optima, a range of parameters have been investigated in the current study for the jets and in the literature for the ultrasonic device. The conditions of Figs. 4 and 5 are near the best known for each device. If the differences in conversion efficiency of input power to power into the liquid (e.g., 18 percent for ultrasonic, approximately 75 percent for a motor/pump) were used, an additional factor of 4 would need to be applied, and the cavitating jet results would exhibit overall energy efficiencies 100 times higher than the ultrasonic device. This suggests strong promise for application of jet cavitation to oxidation.

**Temperature Effect.** The results of the experiments of jet oxidation of PNP indicated the existence of an optimal temperature or temperature range for oxidation efficiency. Figure 6 shows the influence of temperature on the oxidation efficiency at three times during the oxidation process. Performance is seen to be best at the intermediate temperature range near 42°C (107°F). Such behavior is consistent with cavitation erosion intensity which is known to achieve a maximum value that is temperature and liquid dependent. For water at atmospheric pressure, this peak is at approximately 50°C (122°F) (Brown and Goodman [1]). Above this temperature the bubble dynamics becoming increasingly thermally controlled rather than inertially controlled which leads to an increase in vapor pressure and cushioning of the bubble collapse.

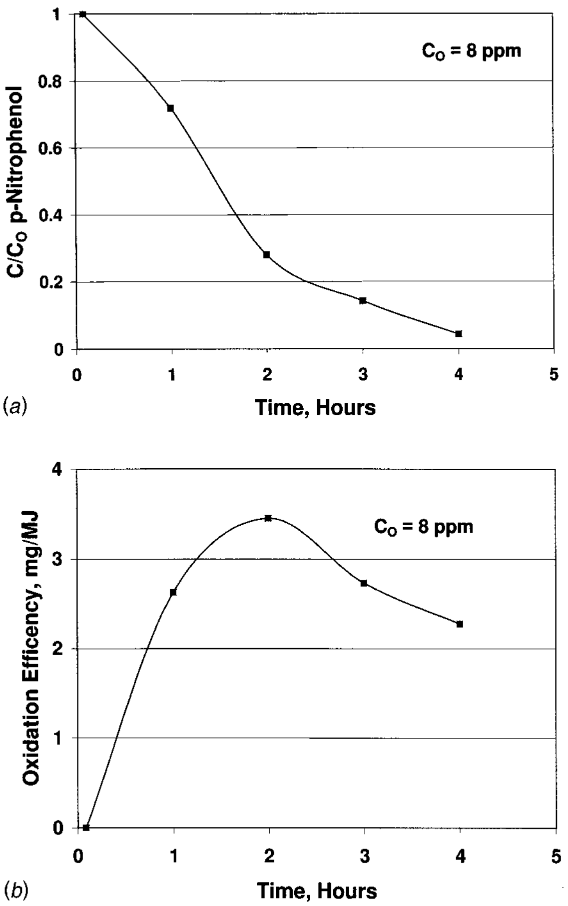

**Fig. 5 Cavitating jet oxidation of PNP: pH=3.8, T=107°F, ambient pressure=20 psia, pressure entering nozzles =75 psia, flow rate=57 gpm, $C_0$=8 ppm. Top: time variation of the ratio of PNP concentration to its initial value. Bottom: oxidation efficiency.**

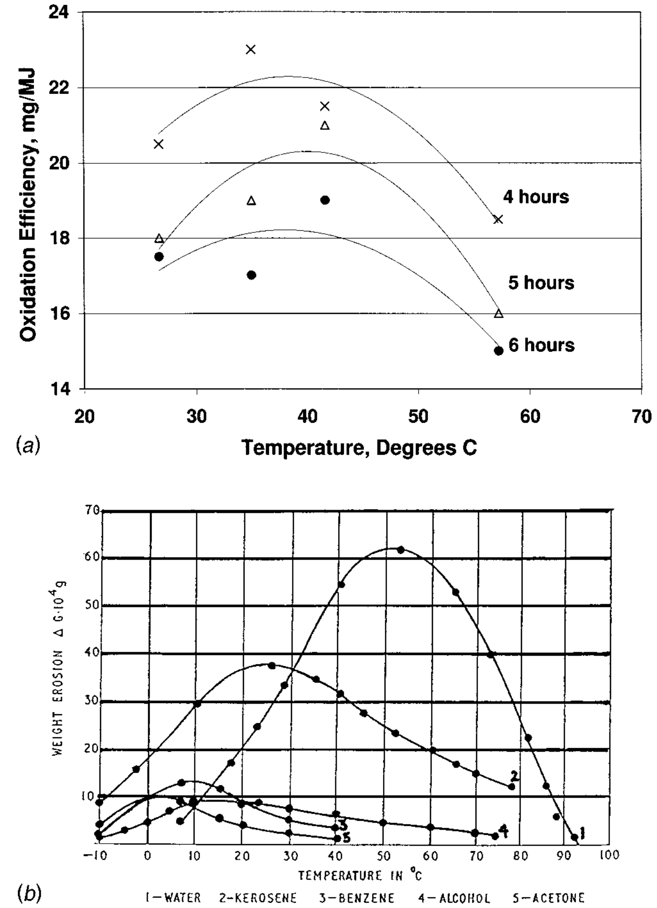

**Fig. 6 Influence of temperature on cavitation effects exhibiting a region of maximum influence. (a) Jet oxidation efficiency of PNP at 4, 5, and 6 hours of operation; pH=3.8, ambient pressure=21 psia, pressure entering nozzles=70 psi. (b) Erosion of aluminum as a function of temperature for various liquids; taken from Brown and Goodman [1].**

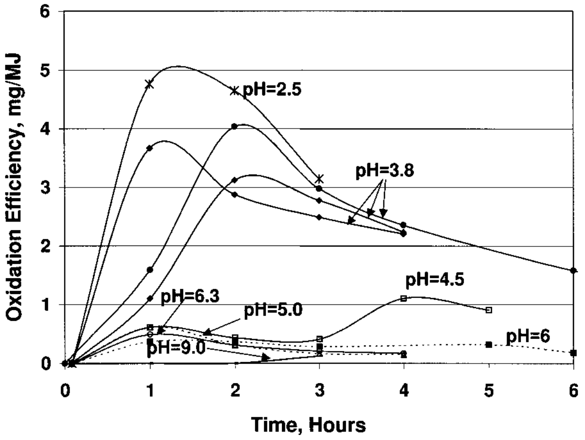

**Fig. 7 Influence of pH on jet oxidation efficiency of PNP: T=107°F, ambient pressure=20 psia, pressure entering nozzles=75 psia**

**pH Effect.** The values of pH in the flow loops were adjusted periodically to their set point values by the addition of phosphoric acid or sodium hydroxide. The pH was typically maintained within ±0.3. Figure 7 provides the results of operation at varying pH. The oxidation efficiencies are seen to strongly depend on pH in a nonlinear fashion with little influence for pH above about 4. As the pH decreases below 4, the rate is found to increase, initially at long times and then at shorter times for decreasing pH. The data of Kotronarou et al. [13] with PNP using an ultrasonic device showed similar behavior.

*To assure that our increased efficiencies with decreased pH was indeed due to the cavitation oxidation and not solely to pH, a sample of the PNP solution was adjusted to a pH of 2.5 and left to sit for 4 days. Measurement of the PNP concentration after 4 days showed no change from the initial measurement.*

**Influence of Cavitation Number.** The effects of cavitation number were studied by changing the ambient pressure while maintaining the pressure drop across the nozzle constant. The results are presented in Fig. 8 for two values of the cavitation number. The lower cavitation number shows a significant increase in degradation rate which can be explained by the creation of a larger volume of cavitation created with lower power.

**Ring Vortex Cavities.** A simple analysis based on jet cavitation occurring in vortical structures is now presented. A cavitating and structured jet can be considered as being formed of a succession of vortex bubble rings of diameter equal to the orifice diameter $D_0$. The cavitation intensity per unit time, $I_{\mathrm{cav}}$, can be expressed as the product of the number of cavitation events per unit time, $N$, and the collapse energy of each cavitation event, $E_{\mathrm{bub}}$,

$$I_{\mathrm{cav}}=NE_{\mathrm{bub}}. \qquad (6)$$

The cavity potential energy $E_{\mathrm{bub}}$ can be expressed as the product of its maximum volume and the pressure difference between the surrounding liquid and the cavity contents which we will approximate as the ambient pressure, $P_{\mathrm{amb}}$. For ring cavities, with a maximum cross-section radius $R_{\mathrm{max}}$,

$$E_{\mathrm{bub}}=\pi^2 D_0 R_{\mathrm{max}}^2 P_{\mathrm{amb}}. \qquad (7)$$

For a ring emission frequency, $f$, for each of $n$ nozzles, $I_{\mathrm{cav}}$, is given by

$$I_{\mathrm{cav}}=fnE_{\mathrm{bub}}. \qquad (8)$$

Using the product of the pressure and flow for hydraulic power, the energy conversion efficiency, $\eta$, can be taken as:

$$\eta=\frac{fnE_{\mathrm{bub}}}{1/2\rho V_{\mathrm{jet}}^2 Q}=\epsilon^2 2\pi\frac{S_d P_{\mathrm{amb}}}{\rho V_{\mathrm{jet}}^2}=\epsilon^2 2\pi S_d\sigma\sim\epsilon^2, \qquad (9)$$

where $\epsilon$ and the jet Strouhal number $S_d$ are defined as:

$$\epsilon=\frac{2R_{\mathrm{max}}}{D_0}, \quad S_d=\frac{fD_0}{V_{\mathrm{jet}}}\cong 0.3. \qquad (10)$$

The volume fraction of liquid cavitated, $\alpha$, is the ratio of the volume of all ring cavities at their maximum size created during a unit time, $\mathcal{V}_{\mathrm{cav}}$, and the flow rate $Q$:

$$\alpha=\frac{\mathcal{V}_{\mathrm{cav}}}{Q}=\frac{4\pi R_{\mathrm{max}}^2 f}{D_0 V_{\mathrm{jet}}}=\pi S_d\epsilon^2\sim\epsilon^2. \qquad (11)$$

*We see that the parameters $\alpha$ and $\eta$ both increase strongly with $\epsilon$.* This is illustrated by the results of Kalumuck et al. [26], which showed, based on numerical simulations using a vortex ring cavity dynamics model (Chahine and Genoux [23]; Genoux and Chahine [27]), that $\epsilon$ increases with lower ambient pressures thus increasing both the volume fraction of fluid cavitated and the efficiency of conversion of hydraulic energy to cavity collapse energy.

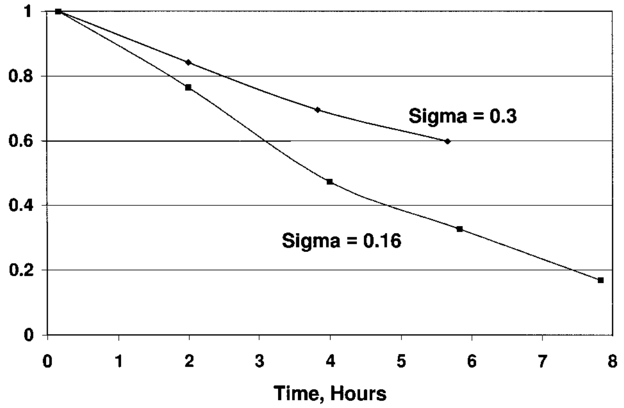

**Fig. 8 Influence of cavitation number, sigma, on jet oxidation of PNP: pH=3.8, T=107°F**

## Conclusions

Experiments to establish the feasibility of utilizing cavitating jets for oxidation of organic compounds in dilute aqueous solutions were carried out in recirculating flow loops. Baseline tests were conducted with an ultrasonic device for comparison. Results were consistent with those of the literature. Cavitating jet oxidation of p-nitrophenol was found to exhibit a two order of magnitude increase in energy efficiency compared to ultrasonic means. The data indicate an inverse relation of efficiency with cavitation number which is consistent with the results of a simple jet cavitation model. An optimal temperature for cavitating jet oxidation may be that for peak erosion rates due to cavitation. As with ultrasonic results of the literature, cavitating jet oxidation rates improved with decreasing pH.

These results suggest a great potential for the use of jet cavitation in full scale waste treatment and remediation systems.

## Acknowledgments

The authors wish to thank Gary Frederick and Patrick Aley of DYNAFLOW for conducting the experiments and Dr. Nail Gumerov of DYNAFLOW for discussions and modeling efforts. The authors also wish to thank Drs. Lawrence Principe of the Johns Hopkins University, Inez Hua of Purdue University, Alan Brause of ACSC, and Andrew Alpert of PolyLC for a number of helpful discussions and consultations. This work was sponsored in part by NSF under SBIR award No. DMI-9661572.

## References

[1] Brown, B., and Goodman, J. E., 1965, *High Intensity Ultrasonics*, Van Nostrand, Inc., Princeton, NJ.

[2] Suslick, K. S., ed., 1988, *Ultrasound, Its Chemical, Physical, and Biological Effects*, VCH, New York.

[3] Suslick, K. S., 1989, ''Sonochemistry,'' Science, **247**, pp. 1439–1445.

[4] Neppiras, E. A., 1980, ''Acoustic Cavitation,'' Phys. Rep., **61**, pp. 159–251.

[5] Hua, I., Hochemer, R., and Hoffman, M., 1995, ''Sonochemical Degradation of p-Nitrophenol in a Parallel Plate Near Field Acoustic Processor,'' Environ. Sci. Technol., **29**, pp. 2790–2796.

[6] Skov, E., Pisani, J., and Beale, S., 1997, ''Cavitation Induced Hydroxyl Radical Formation,'' American Institute of Chemical Engineering National Meeting, Houston, TX.

[7] Gong, C., and Hart, D. P., 1998, ''Ultrasound Induced Cavitation and Sonochemical Yields,'' J. Acoust. Soc. Am., **104**, No. 4, pp. 2675–2682.

[8] Suslick, K. S., Cline, Jr., R. E., and Hammerton, D. A., 1986, ''The Sonochemical Hot Spot,'' J. Am. Chem. Soc., **108**, p. 5641.

[9] Suslick, K. S., Doktycz, S. J., and Flint, E. B., 1990, ''On the Origin of Sonoluminescence and Sonochemistry,'' Ultrasonics, **28**, pp. 280–290.

[10] Margulis, M. A., 1990, ''The Nature of Sonochemical Reactions and Sonoluminescence,'' Adv. Sonochem., **1**, pp. 39–81.

[11] LePoint, T., and Mullie, F., 1994, ''What Exactly is Cavitation Chemistry?'' Ultrason. Sonochem., **1**, pp. 13–22.

[12] Hua, I., Hochemer, R., and Hoffman, M., 1995, ''Sonolytic Hydrolysis of p-Nitrophenyl Acetate: The Role of Supercritical Water,'' J. Phys. Chem., **99**, pp. 2335–2342.

[13] Kotronarou, A., Mills, G., and Hoffman, M., 1991, ''Ultrasonic Irradiation of p-Nitrophenol in Aqueous Solution,'' J. Phys. Chem., **95**, pp. 3630–3638.

[14] Kotronarou, A., Mills, G., and Hoffman, M., 1992, ''Decomposition of Parathion in Aqueous Solution by Ultrasonic Irradiation,'' Environ. Sci. Technol., **26**, pp. 1460–1462.

[15] Cheung, H. M., Bhatnagar, A., and Jansen, G., 1991, ''Sonochemical Destruction of Chlorinated Hydrocarbons in Dilute Aqueous Solution,'' Environ. Sci. Technol., **25**, p. 1510.

[16] Hua, I., and Hoffman, M., 1996, ''Kinetics and Mechanism of the Sonolytic Degradation of $CCl_4$: Intermediates and Byproducts,'' Environ. Sci. Technol., **30**, pp. 864–871.

[17] U. S. Environmental Protection Agency, 1994, ''CAV-OX Cavitation Oxidation Process Magnum Water Technology, Inc. Applications Analysis Report,'' U.S. Environmental Protection Agency Report EPA/540/AR-93/520.

[18] Young, F. R., 1989, *Cavitation*, McGraw-Hill, London.

[19] Chahine, G. L., and Duraiswami, R., 1994, ''Boundary Element Method for Calculating 2D and 3D Underwater Explosion Bubble Behavior in Free Water and Near Structures,'' U. S. Naval Surface Warfare Center Technical Report NSWCDD/TR-93/44.

[20] Chahine, G. L., 1991, ''Dynamics of the Interaction of Non-Spherical Cavities,'' *Mathematical Approaches in Hydrodynamics*, Miloh, T., ed., SIAM, Philadelphia.

[21] Chahine, G. L. and Duraiswami, R., 1992, ''Dynamical Interactions in a Bubble Cloud,'' ASME J. Fluids Eng., **114**, No. 4, pp. 680–686.

[22] Chahine, G. L., and Johnson, V. E., Jr., 1985, ''Mechanics and Applications of Self-Resonating Cavitating Jets,'' *International Symposium on Jets and Cavities*, ASME, WAM, Miami, FL.

[23] Chahine, G. L., and Genoux, Ph., 1983, ''Collapse of a Cavitating Vortex Ring,'' ASME J. Fluids Eng., **105**, pp. 400–405.

[24] Johnson, V. E., Kohn, R. E., Tiruvengadam, A., and Conn, A. F., 1972, ''Tunneling, Fracturing, Drilling, and Mining with High Speed Water Jets Utilizing Cavitation Damage,'' *Proceedings, 1st International Symposium on Jet Cutting Technology*, Coventry, U.K.

[25] Chahine, G. L., Kalumuck, K. M., and Frederick, G. S., 1995, ''Cavitating Water Jets for Deep Hole Drilling in Hard Rock,'' *Proceedings, 8th American Water Jet Conference*, Houston, TX, Vol. 2, pp. 765–778.

[26] Kalumuck, K. M., Chahine, G. L., Frederick, G. S., Aley, P. D., Brittain, W. L., and Gumerov, N. A., 1997, ''Oxidation of Organic Compounds in Water with Cavitating Jets,'' DYNAFLOW, INC. Technical Report 97002-1nsf.

[27] Genoux, Ph. and Chahine, G. L., 1984, ''Simulation of the Pressure Field Due to a Submerged Oscillating Jet Impacting on a Solid Wall,'' ASME J. Fluids Eng., **106**, 491–496.

# On the Stability of Parallel Bubbly Cavitating Flows

**Luca d'Agostino**
Professor

**Fabio Burzagli**
M.S. Student

Dipartimento di Ingegneria Aerospaziale,
Università degli Studi di Pisa, 2 Via Diotisalvi,
56126, Pisa, Italy
e-mail: luca.dagostino@ing.unipi.it

*This paper illustrates the effects of the dynamics of bubbles with arbitrary vapor-gas contents on the inviscid and viscous stability of two-dimensional parallel bubbly flows of low void fraction. The linear perturbation equations derived for the stability analysis include the effects of bubble compressibility, inertia, and energy dissipation due to the viscosity of the liquid and the transfer of heat and mass as a consequence of compression/expansion of the noncondensable gas and evaporation/condensation of the vapor contained in the bubbles. Numerical solution of the spatial stability problem for two-dimensional inviscid shear layers and Blasius boundary layers confirms that the presence of the dispersed phase is generally in favor of stability. Significant deviations from the classical results for compressible and incompressible single phase fluids are observed, especially when the occurrence of large compliant and/or resonant oscillations of the bubbles greatly enhances their dynamic coupling with the perturbation field. More importantly, the present analysis points out some major differences in the stability of parallel flows with noncondensable gas bubbles with respect to cavitating flows containing bubbles with a dominant content of vapor. Unconditional stability is predicted in the travelling bubble cavitation limit for low pressures and high vapor mass fraction of the bubble contents. Results are shown to illustrate these effects for some representative flow configurations and conditions.* [S0098-2202(00)00603-9]

## Introduction

The crucial role of cavitation in limiting the performance of hydraulic machinery has long been recognized in the literature (Brennen [1], Knapp et al. [2]). Its adverse effects (efficiency degradation, vibrations, fluid dynamic instabilities, erosion, etc.) are common to a wide range of technical applications, but become especially manifest in turbopumps of cryogenic liquid rocket propellants, which operate near the saturation conditions at extremely high specific power levels in the presence of extensive cavitation. From the physical point of view, cavitation involves complex dynamic and thermal interactions of the liquid and gaseous phases in the presence of nucleating agents and can develop in a number of different forms depending on the specific flow conditions. For a detailed review of cavitation phenomena and their relations with cavity dynamics and turbomachinery flows the reader is referred to the excellent monographs by Brennen [1,3].

Of special interest because of its frequent occurrence in technical applications is the analysis of unsteady bubbly cavitating flows when bubble dynamics effects are explicitly considered. Earlier analyses in several configurations of engineering relevance clearly showed that even at moderate void fractions the compliant, dissipative and inertial behavior of noncondensable gas bubbles significantly modifies the dynamic properties of the flow, which becomes dispersive and no longer behaves as a barotropic mixture (d'Agostino and Brennen [4–6], d'Agostino et al. [7], d'Auria [8,9], d'Agostino and d'Auria [10]). This is especially the case when the naturally unstable frequencies of the flow approach the resonant frequency of oscillation of individual bubbles, thus providing an efficient mechanism of energy extraction from the perturbation field to sustain the bubble oscillations. This kind of coupling is relatively weak in bubbly flows at room pressures, but can actually become quite significant in low-pressure cavitating flows essentially containing pure vapor bubbles, which are characterized by large compliance and important irreversible effects associated with the evaporation/condensation phenomena at the phase interface. In this case the dynamic response of cavitation bubbles can greatly interfere with the development of the perturbation field, and therefore with the stability of the flow.

Travelling bubble cavitation frequently occurs in quasi-parallel flows that spontaneously develop unstable oscillations (Betchov and Criminale [11], Drazin and Reid [12]). In these flows the observed dependence of turbulent transition, bubble response and low-frequency noise on the Euler number indicate that bubble dynamic effects may play an important role in the flow stability (Marboe et al. [13], Arakeri and Shanmuganathan [14], Ceccio and Brennen [15]). Recently, this hypothesis has also been confirmed on theoretical grounds by linear stability analyses of parallel bubbly flows (d'Agostino et al. [16]; d'Auria et al. [17], d'Agostino et al. [18]). These analyses were limited to inviscid flows containing small noncondensable gas bubbles and generalize for dispersive and dissipative bubbly mixtures the classical linear stability theories of barotropic fluids. The aim of the present article is to illustrate the extensions of the linear stability theory to viscous case and to parallel flows containing cavitation bubbles with arbitrary compositions of vapor and non-condensable gas.

According to the original development of our work on this subject (Burzagli [19], d'Auria et al. [20], Burzagli and d'Agostino [21]), this paper specifically focuses on the linear stability of parallel two-dimensional bubbly cavitating inviscid shear layers and (viscous) Blasius boundary layers surrounded by a single-phase incompressible liquid. Following Rayleigh's and Orr-Sommerfeld's classical approaches, the linearized perturbation equations for a bubbly mixture are derived and the numerical solutions of the resulting eigenvalue problems are obtained by means of a shooting method combined, in the viscous case, with Davey's [22] orthogonalization method, in order to overcome the convergence problems associated with the mathematical stiffness of the stability equations at higher Reynolds numbers. Nondimensional quantities are introduced to deal in a synthetic and systematic way with the various parameters involved.

## Bubbly Cavitating Flow Model

The bubbly cavitating mixture is visualized as an equivalent homogeneous fluid where the bubbles are treated as isolated source-sink singularities uniformly distributed in a force-free liq-

---

Contributed by the Fluids Engineering Division for publication in the JOURNAL OF FLUIDS ENGINEERING. Manuscript received by the Fluids Engineering Division March 28, 1999; revised manuscript received April 25, 2000. Associate Technical Editor: J. Katz.

uid with constant properties and low void fraction, $\alpha \ll 1$. Neglecting local flow perturbations (Rietema and van den Akker [23]), the bubble mass, and the effects of coalescence, dissolution and relative motion, the flow is governed by the continuity, momentum and Rayleigh-Plesset equations

$$\nabla \cdot \mathbf{u} = \frac{3\alpha}{R_o}\frac{DR}{Dt}$$

$$\rho_L(1-\alpha)\frac{D\mathbf{u}}{Dt} = -\nabla p + \mu_L \nabla \cdot [\nabla \mathbf{u} + (\nabla \mathbf{u})^T]$$

$$R\frac{D^2R}{Dt^2} + \frac{3}{2}\left(\frac{DR}{Dt}\right)^2 + 4\frac{\nu_L}{R}\frac{DR}{Dt} = \frac{p_B - p}{\rho_L} - \frac{2S}{\rho_L R}$$

The dynamics of bubbles containing both vapor and noncondensable gas is described as proposed by Nigmatulin [24,25], Nigmatulin and Khabeev [26,27], Nagiev and Khabeev [28], Nigmatulin et al. [29]. In addition to the effects of bubble compressibility, inertia, and energy dissipation due to the liquid viscosity and thermal exchanges with the bubble contents, their model explicitly accounts for the occurrence of evaporation/condensation phenomena at the interface and for the presence of the temperature and concentration gradients necessary to support the associated transfers of heat and mass between and within the two phases.

If harmonic excitation at frequency $\omega_L$ is assumed, the steady-state linear oscillations of vapor-gas bubbles are described by the equation

$$(-\omega_L^2 - i\omega_L 2\lambda + \omega_B^2)\hat{R} = -\frac{\hat{p}}{\rho_L R_o}$$

where $\hat{R}$ and $\hat{p}$ are the complex amplitudes of the radius and pressure perturbations $\hat{R}e^{-i\omega_L t}$ and $\hat{p}e^{-i\omega_L t}$ about their undisturbed values $R_o$ and $p_o$. The damping coefficient $\lambda$ and the natural frequency $\omega_B$ of the bubbles are given by:

$$2\lambda(\omega_L) = \frac{3p_{Bo}}{\rho_L \omega_L R_o^2}\operatorname{Im}\left\{\frac{\gamma_{VG}}{E(\omega_L)}\right\} + 4\frac{\nu_L}{R_o^2}$$

$$\omega_B^2(\omega_L) = \frac{3p_{Bo}}{\rho_L R_o^2}\operatorname{Re}\left\{\frac{\gamma_{VG}}{E(\omega_L)}\right\} - \frac{2S}{\rho_L R_o^3}$$

in terms of the function $E(\omega_L)$ (whose expression is reported in the Appendix) and generalize to arbitrary vapor-gas composition of the bubble content the formally similar expressions obtained by Chapman and Plesset [30] and Prosperetti [31,32] for bubbles of noncondensable gas. The partial pressure $p_{Go}$ of the gas in a bubble of mean radius $R_o$ at equilibrium with a liquid of unperturbed pressure $p_o$, temperature $T_o$ and surface tension $S$ is obtained from $p_o = p_{Bo} - 2S/R_o$, where $p_{Bo} = p_{Go} + p_{Vo}$ is the bubble internal pressure and the vapor pressure $p_{Vo}$ is equal to the saturation value $p_S(T_o)$. The mass fractions of the vapor, $Y_V = \rho_{Vo}/\rho_{Bo}$, and the noncondensable gas in the bubble, $Y_G = 1 - Y_V$, are then readily determined as functions of $T_o$, $p_o$ and $R_o$ using the perfect gas equation $p = \rho \mathcal{R} T$.

The typical behavior of a vapor-gas bubble is shown in Fig. 1 as a function of the excitation frequency $\omega_L$. The high frequency peak is the classic Minneartian resonance (the only one present in the case of bubbles containing noncondensable gas), while the low frequency peak is the so-called "second resonance" (Finch and Neppiras [33]; Wang [34]) introduced by the presence of the vapor. Below this resonance the natural frequency $\omega_B(\omega_L)$ of the bubble becomes imaginary and consequently the motion is unstable (Fanelli et al. [35,36], Prosperetti [31]). For the bubble to be quasi-statically stable (Daily and Johnson [37]), and therefore also dynamically stable at all frequencies, it is sufficient that the isothermal (low-frequency) bubble natural frequency $\omega_{B0}^2 = \omega_B^2(0) > 0$, which implies (Nagiev and Khabeev [28]):

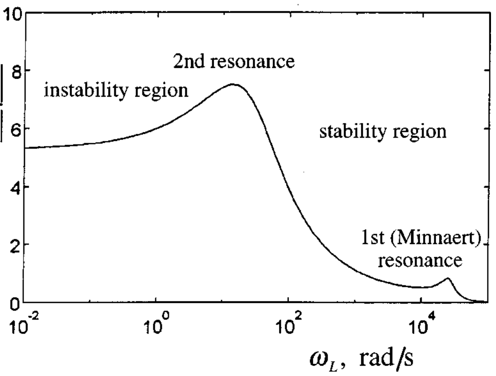

**Fig. 1 Normalized amplitude of radius oscillations of a bubble with high vapor mass fraction ($Y_V = 0.995$) in water ($T_o = 308$ K, $p_o = 5$ kPa and $R_o = 0.15$ mm)**

$$Y_V < Y_V^* = \frac{(3+2\mathrm{We})\mathcal{R}_G}{(3+2\mathrm{We})\mathcal{R}_G + \mathrm{We}\mathcal{R}_V}$$

where $\mathrm{We} = 2S/R_o p_o$ is the Weber number of the bubble. Figure 2 shows the stability region for a typical 1 mm radius air-vapor bubble in water with the external pressure as a parameter. Notice that the pressure of water bubbles with a dominant content of vapor increases rapidly with the temperature. Following the traditional classification of "cold" (or inertial) and "warm" (or thermal) cavitation at lower pressures one may then speak of cold vapor-gas bubbles as opposed to warm vapor-gas bubbles corresponding to higher values of $p_o$.

The different spectral responses of cold and warm vapor-gas bubbles are illustrated in Figs. 3 and 4 for several values of the vapor mass fraction. In general, for increasing excitation frequencies it is possible to identify four regimes dominated by different physical phenomena:

- *compressible*, at low frequencies, characterized by a relatively flat quasi-static response of the gas, with negligible thermal, diffusive and inertial effects;
- *thermal*, at intermediate frequencies, characterized by the gradual decline of the bubble response under the effect of the increasing dissipation associated with the phase changes at the interface;
- *resonant*, near the Minnaert frequency, characterized by the response peak corresponding to the dynamic balance of bubble compressibility and inertial effects;
- *super-resonant*, beyond the Minnaert frequency, characterized by a rapid approach to the incompressible limit under the dominant effect of the inertia of the liquid surrounding the bubble.

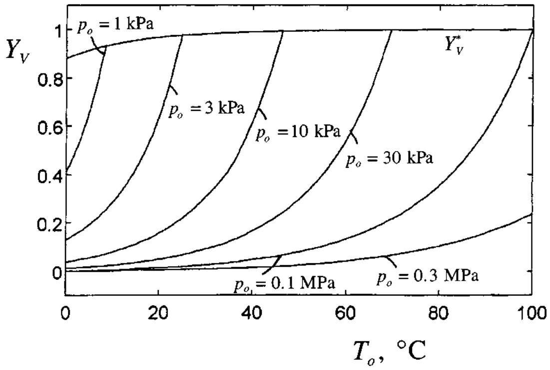

**Fig. 2 Vapor mass fraction $Y_V$ as a function of the temperature $T_o$, for several values of the liquid pressure $p_o$**

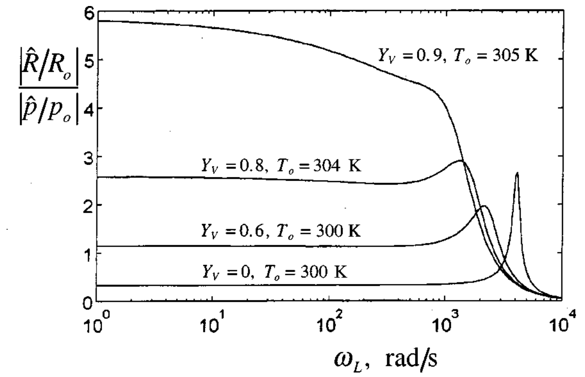

**Fig. 3 Normalized amplitude of radius oscillations of a "cold" bubble in water as a function of the excitation frequency $\omega_L$ for several values of the vapor mass fraction $Y_V$ for $R_o = 1$ mm and $p_o = 5$ kPa**

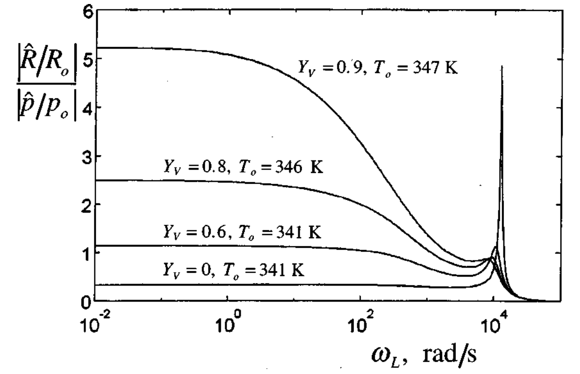

**Fig. 4 Normalized amplitude of radius oscillations of a "warm" bubble in water as a function of the excitation frequency $\omega_L$ for several values of the vapor mass fraction $Y_V$ for $R_o = 1$ mm and $p_o = 40$ kPa**

The thermal regime is absent in pure gas bubbles ($Y_V = 0$) because of the modest dissipation introduced by the compression/expansion of the noncondensable gas, and is always present in warm vapor-gas bubbles. On the other hand, it is practically absent in cold vapor-gas bubbles, where phase transitions effectively damp the resonance peak but are dominated by the inertial effects, which are responsible for the rapid decline of the bubble response toward the incompressible limit at super-resonant frequencies. Also notice in Figs. 3 and 4 the rapid increase of the bubble response with the vapor mass fraction $Y_V$. Since the relation $\Delta R/R_o \propto \Delta p/p_o$ approximately holds throughout the frequency spectrum, the absolute compliance $\Delta R$ of the bubbles increases with their radius and inversely with the flow pressure. Hence, in particular, cold cavitation bubbles, which are characterized by a dominant content of vapor and very low values of $p_o$, are much more compliant than warm cavitation bubbles of equal vapor mass fraction.

## Stability of Parallel Bubbly Flows

The flow equations for a parallel viscous layer containing vapor-gas bubbles (see Fig. 5) are linearized for small perturbations around the mean (undisturbed) flow properties $U(y)$, $p_o$ and $R_o$:

$$u = \mathrm{Re}\{U(y) + \hat{u}(y) e^{i(kx-\omega t)}\}; \quad v = \mathrm{Re}\{\hat{v}(y) e^{i(kx-\omega t)}\}$$

$$p = \mathrm{Re}\{p_o + \hat{p}(y) e^{i(kx-\omega t)}\}; \quad R = \mathrm{Re}\{R_o + \hat{R}(y) e^{i(kx-\omega t)}\}$$

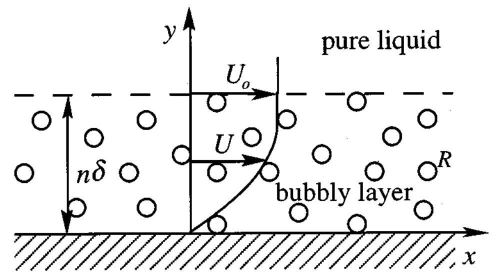

**Fig. 5 Schematic of the flow configuration**

Here $\omega$ and $k$ are the perturbation frequency and the wave number, $x$ and $u$ are the coordinate and velocity in the streamwise direction, and $y$ and $v$ are perpendicular to $x$ and $u$. The following system in the complex amplitudes of the perturbations $\hat{p}$, $\hat{u}$, $\hat{v}$, and $\hat{R}$ is obtained:

$$ik\hat{u} + \hat{v}' = -i\omega_L \frac{3\alpha}{R_o} \hat{R}$$

$$\rho_L(1-\alpha)(-i\omega_L \hat{u} + U'\hat{v}) = -ik\hat{p} + \mu_L(-k^2\hat{u} + \hat{u}'')$$

$$-i\omega_L \rho_L (1-\alpha)\hat{v} = -\hat{p}' + \mu_L(-k^2\hat{v} + \hat{v}'')$$

$$(-\omega_L^2 - i\omega_L 2\lambda + \omega_B^2)\hat{R} = -\frac{\hat{p}}{\rho_L R_o}$$

where $\omega_L = \omega - kU$ represents the Lagrangian frequency experienced by the bubbles in their motion with the mean flow and primes indicate differentiation with respect to the independent variable $y$.

In order to reduce the above equations in normal form and avoid the complexities associated with the differentiation of bubble dynamic terms, the problem has been reformulated in terms of the flow divergence, $\hat{s} = ik\hat{u} + \hat{v}'$, and vorticity, $\hat{r} = \hat{u}' - ik\hat{v}$. Upon nondimensionalization of the flow variables with respect to the reference velocity $U_o$, a typical thickness $\delta$ of the layer, and the liquid pressure $p_o$, the following system in $\tilde{u}$, $\tilde{v}$, and $\tilde{r}$ is obtained:

$$\tilde{u}' = \tilde{r} + i\tilde{k}\tilde{v}$$

$$\tilde{v}' = -i\tilde{k}\tilde{u} + \left( i\tilde{\omega}_L \tilde{u} - \tilde{v}\tilde{U}' + \frac{1}{\mathrm{Re}}\tilde{r}' \right) M^2 \frac{\tilde{\omega}_L}{\tilde{k}} \left( 1 - i\tilde{\omega}_L \frac{M^2}{\mathrm{Re}} \right)^{-1}$$

$$\begin{aligned} \tilde{r}'' = {} & (\tilde{k}^2 - i\tilde{\omega}_L \,\mathrm{Re})\tilde{r} + \tilde{U}''\tilde{v}\,\mathrm{Re} \\ & + [\tilde{U}'\tilde{r}' + (i\tilde{U}'\tilde{u} - \tilde{U}'^2\tilde{v})\mathrm{Re}] M^2 \frac{\tilde{\omega}_L}{\tilde{k}} \left( 1 - i\tilde{\omega}_L \frac{M^2}{\mathrm{Re}} \right)^{-1} \end{aligned}$$

where tildes indicate nondimensional quantities, $\mathrm{Re} = U_o\delta/\nu_L$ is the flow Reynolds number and $M^2(\omega_L) = U_o^2/c_M^2$ is the (squared) flow Mach number based on the free-space speed of sound in the bubbly mixture when excited at frequency $\omega_L$

$$c_M^2(\omega_L) = \frac{-\omega_L^2 - i\omega_L 2\lambda + \omega_B^2}{3\alpha(1-\alpha)/R_o^2}$$

In the present formulation the influence of viscosity, surface tension, layer thickness, pressure, bubble interactions and vapor concentration on the stability of viscous layers in bubbly liquids has been expressed in terms of the following non-dimensional parameters: $\mathrm{Re} = U_o\delta/\nu_L$, $\mathrm{We} = 2S/R_o p_o$, $\pi_R = \delta/R_o$, $\pi_P = \delta^2\sqrt{p_o/\rho_L}/R_o\nu_L$, $\pi_B = 3\alpha(1-\alpha)\delta^2/R_o^2$, and $\pi_Y = Y_V/Y_V^*$, respectively. The parameter $\pi_B$ has been previously identified and commented by d'Agostino and Brennen [4–6] and its importance in connection with bubble dynamic interaction phenomena has been confirmed by earlier analyses (d'Agostino, et al. [16,18]; d'Auria et al. [17]; d'Auria et al. [20]; Wang [38]). In terms of the above nondimensional parameters, the isothermal bubble natural frequency and Mach number in the two-phase mixture are expressed by:

$$\tilde{\omega}_{B0}^2=\tilde{\omega}_B^2(0)=\frac{\delta^2}{R_o^2}\frac{p_o}{\rho_L U_o^2}\left(3+\frac{2S}{R_o p_o}\right)=\frac{\pi_P^2}{\mathrm{Re}^2}(3+\mathrm{We})$$

$$M_o^2=M^2(0)=\frac{U_o^2}{c_M^2}=\frac{\pi_B \mathrm{Re}^2}{\pi_P^2(3+\mathrm{We})}$$

For simplicity, in this paper we consider the classical case of a Blasius boundary layer with displacement thickness $\delta$. The relevant boundary conditions require no-slip at the wall ($\hat{u}=0$, $\hat{v}=0$ at $y=0$) and smooth matching with the far-field converging solution outside the boundary layer ($y=n\delta$ with $n\gg 1$). Assuming a stratified flow where the bubbles are present only inside the boundary layer ($0<y<n\delta$) as shown in Fig. 5, the latter condition writes (Burzagli [19])

$$\tilde{r}=-\tilde{k}(1+\tilde{\beta})\tilde{u}-i\tilde{k}(1+\tilde{\beta})\tilde{v}$$

$$\tilde{r}'=\tilde{k}^2\tilde{\beta}(1+\tilde{\beta})\tilde{u}+i\tilde{k}\tilde{\beta}(1+\tilde{\beta})\tilde{v}$$

where $\tilde{\beta}=\sqrt{1-i\tilde{\omega}_L\,\mathrm{Re}/\tilde{k}^2}$ and $\mathrm{Re}\{\tilde{\beta}\}\geqslant 0$.

The stability equations for inviscid parallel bubbly flows are readily obtained as a special case for $\mu_L=0$. Then, elimination of the pressure from the linearized perturbation equations leads to the following system in normal from (d'Agostino et al. [16], d'Auria et al. [9], d'Agostino et al. [18]):

$$\hat{u}'=ik\hat{v}-i\frac{U''}{\omega_L}\hat{v}-i\frac{U'}{kc_M^2}(i\omega_L\hat{u}-U'\hat{v})$$

$$\hat{v}'=-ik\hat{u}+\frac{\omega_L}{kc_M^2}(i\omega_L\hat{u}-U'\hat{v})$$

The classical Rayleigh stability formulations for single phase incompressible or compressible fluids are readily recovered as special cases by eliminating $\hat{u}$ and setting $\alpha\to 0$ ($c_M\to\infty$) or $\omega_L\to 0$ ($c_M\to c_{Mo}\equiv\text{constant}$), respectively.

In the following we consider the simple case of two-dimensional free shear layers of unperturbed velocity profile:

$$U(y)=\frac{U_1+U_2}{2}+\frac{U_1-U_2}{2}\tanh\frac{y}{\delta}$$

The relevant boundary conditions require smooth matching with the upper/lower unperturbed far field solutions (subscripts 1 and 2):

$$\hat{u}=\pm A_{1,2}\frac{ik}{\sqrt{k^2-\omega_L^2/c_{M1,2}^2}}e^{\pm y\sqrt{k^2-\omega_L^2/c_{M1,2}^2}}$$

$$\hat{v}=A_{1,2}e^{\pm y\sqrt{k^2-\omega_L^2/c_{M1,2}^2}}$$

where $A_{1,2}$ are arbitrary complex constants (the principal branch of the square root is implied) and the appropriate sign is determined by requiring that the solution does not diverge as $y\to\pm\infty$. All quantities are expressed in nondimensional form (denoted by an asterisk in the inviscid case) using the typical width of the flow $\delta$ and the shear layer velocity difference $\Delta U=U_1-U_2$ as reference length and velocity. The nondimensional parameters used in the inviscid stability analysis are the quasi-static natural frequency of the gas bubbles $\omega_{B0_G}^*=\omega_{B0_G}\delta/\Delta U$, the bubble radius $R^*=R/\delta$, the vapor content of the bubble $Y_V$, and the void fraction $\alpha$.

When supplemented with the relevant boundary conditions in the new formulation, the above perturbation equations represent a linear eigenvalue problem for the free parameters $\omega$ or $k$. As in the single phase case, the set of the admissible (generally complex) values of $\omega$ or $k$ (the eigenvalues) is uniquely determined by the condition that the corresponding nontrivial solutions (the eigenfunctions) satisfy the boundary conditions. Any two free parameters can be specified; the remaining one is then determined. Spatially growing oscillations are studied by assigning a real frequency $\omega$ and solving for the complex wave number $k=k_r+ik_i$. On the other hand, temporally growing oscillations are studied by assigning a real value to $k$ and solving for the complex $\omega=\omega_r+i\omega_i$. The two cases become identical at neutral stability, when both $\omega$ and $k$ are real. The present analyses focus on spatially growing oscillations, where $k_i$ is the spatial attenuation rate of the flow perturbations and $2\pi/k_r$ is their wavelength. With current notations a negative value of $k_i$ therefore implies amplification of the flow disturbances in the positive streamwise direction.

## Results and Discussion

**Inviscid Shear Layer.** Expanding on our earlier work on the stability of parallel flows containing gas bubbles (d'Agostino, et al. [18]), for illustrative purposes we first consider the spatial stability of hyperbolic tangent free shear layers containing bubbles with different mass fractions of vapor and air. The relevant boundary value problem has been solved numerically by means of a multiple shooting method (Stoer and Burlish [39]). The integration has been carried out using a fourth-order Runge-Kutta routine (extrapolated to the fifth order) with self-adaptive step size (Press et al. [40]) and the eigenvalues have been evaluated iteratively by means of a modified multidimensional Newton-Raphson method (Stoer [41]). The code has been validated against the single-phase incompressible results by Betchov and Criminale [11] and Michalke [42].

Figure 6 shows the spatial attenuation rate $k_i^*$ as a function of the excitation frequency $\omega^*$ for a free shear layer with void fraction $\alpha=0.01$ and containing 1 mm radius ''cold'' vapor-air bubbles of different mass fractions $Y_V$ at an external pressure of 5 kPa and temperatures ranging from 286 K to 295 K. The results for pure air bubbles and the single-phase incompressible solution are also shown for comparison. Since value of $\omega^*$ is always significantly smaller than the bubble natural frequency $\omega_B^*\approx\omega_{B0_G}^*$, the bubble response is dominated by compressibility effects, while energy dissipation and inertia play a relatively minor role. In single-phase inviscid and viscous fluids the compressibility of the medium is known to promote the stability of parallel flows because part of the energy of the perturbation field has to develop work against the compliance forces of the medium and cannot be

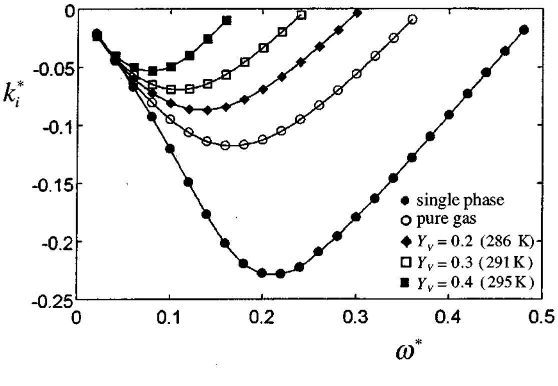

**Fig. 6 Spatial attenuation rate $k_i^*$ of a shear layer with ''cold'' bubbles in the compressibility regime as a function of the excitation frequency $\omega^*$ for several values of the bubble vapor mass fraction $Y_V$. In all cases: $\omega_{B0_G}^*=12.85$, $\alpha=0.01$, $R_o^*=0.01$, $p_o=5$ kPa and $R_o=1$ mm. The incompressible flow solution ($\alpha=0$) is also shown for comparison.**

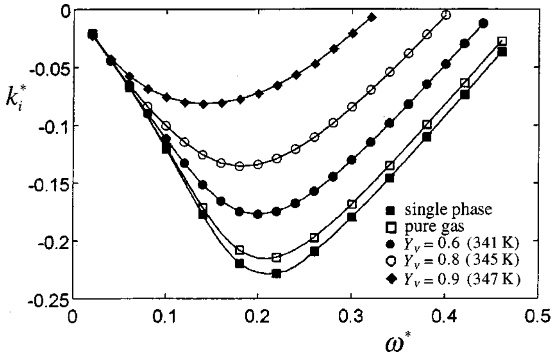

**Fig. 7 Spatial attenuation rate $k_i^*$ of a shear layer with "warm" bubbles in the compressibility regime as a function of the excitation frequency $\omega^*$ for several values of the bubble vapor mass fraction $Y_V$. In all cases: $\omega_{B0_G}^*=36.5$, $\alpha=0.01$, $R_o^*=0.01$, $p_o=40$ kPa and $R_o=1$ mm. The incompressible flow solution $(\alpha=0)$ is also shown for comparison.**

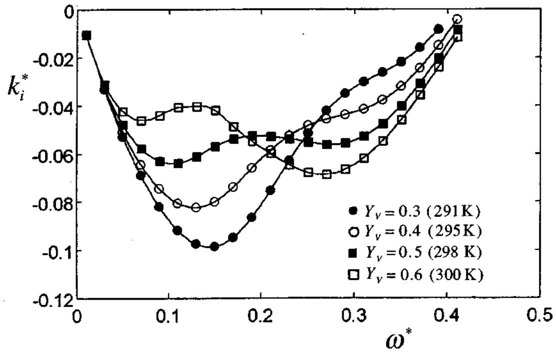

**Fig. 8 Spatial attenuation rate $k_i^*$ of a shear layer with "cold" bubbles in the resonant regime as a function of the excitation frequency $\omega^*$ for several values of the bubble vapor mass fraction $Y_V$. In all cases: $\omega_{B0_G}^*=0.39$, $\alpha=0.00075$, $p_o=6$ kPa and $R_o^*=0.1$.**

used to sustain fluid dynamic instabilities. Earlier analyses by d'Agostino et al. [18] generalized this finding to parallel inviscid flows containing noncondensable gas bubbles. Hence, the previous discussion of the dynamic behavior of vapor-gas bubbles suggests that their presence in the flow should have a significant stabilizing effect, and that this effect should increase with the compliance of the two-phase mixture at lower pressures and higher bubble vapor contents $Y_V$ and flow void fractions $\alpha$. The results of Fig. 6 confirm these conclusions and are qualitatively consistent with those obtained by Drazin [43], Blumen [44], Blumen et al. [45], and Drazin and Davey [46] in the temporal stability analysis of symmetric inviscid compressible shear layers. As a consequence of the small value of the pressure, the absolute compliance of the flow is high and even a relatively modest increase of the vapor mass fraction in the bubbles from zero (pure air) to 40 percent reduces the streamwise spatial amplification rate of the flow disturbances and the range of unstable frequencies to less than one half their original values. Figure 6 also shows that the most unstable frequency (corresponding to the minimum of the attenuation rate $k_i^*$) decreases markedly with $Y_V$, thus indicating that the presence of cavitating bubbles not only modifies the amplitude of the flow instabilities but is also likely to modify their spectral distribution by inducing a significant shift towards lower frequencies.

Figure 7 illustrates the results of similar computations for the same flow ($\alpha=0.01$, $R_o=1$ mm) with warm bubbles of different mass fractions $Y_V$ at temperatures ranging from 341 K to 347 K. At these higher temperatures the flow pressure $p_o$ has raised to 40 kPa as a consequence of the increase of the saturation pressure. Compressibility effects are still the dominant phenomenon in the dynamics of the bubbles and the general features of the solution are essentially unchanged. However, the absolute compliance of the flow has dropped inversely with $p_o$ and comparison with Fig. 6 shows that the magnitude of the stabilizing effects is greatly reduced. The solution for pure air bubbles is close to the one for incompressible fluids, while the maximum amplification rate and the range of unstable frequencies are only moderately reduced even for bubble vapor contents as high as 90 percent.

Next we examine the resonant case where the bubble natural frequency $\omega_B^* \approx \omega_{B0_G}^*$ is internal to the range of unstable frequencies $\omega^*$ of the flow. As an example, consider the curves plotted in Fig. 8 relative to an inviscid shear layer with void fraction $\alpha=0.00075$ and containing 1 mm radius cold vapor-air bubbles with $\omega_{B0_G}^*=0.39$ and different mass fractions $Y_V$ at a pressure of 6 kPa and temperatures ranging from 291 K to 300 K. The behavior of the attenuation rate $k_i^*$ is quite different near resonance conditions, where the greater power necessary to sustain damped large-amplitude resonant oscillations of the bubbles effectively contributes to stabilize the flow. The amplification rate is relatively small and, even if the stability limits do not vary much with $Y_V$, the curves for different values of the vapor mass fraction intersect each others when the natural frequency moves to lower values as $Y_V$ is increased. Therefore flows with higher values of $Y_V$ are, on some limited portions of the frequency spectrum, less stable than flows with lower vapor mass fraction, and the most unstable frequency undergoes a sudden change (mode jumping) for $Y_V \cong 0.5 \div 0.6$, indicating that the occurrence of resonance can significantly modify the spectrum of the flow instabilities.

Finally, in Fig. 9 we illustrate the influence of the void fraction $\alpha$ (or, equivalently, of the bubble interaction parameter $\pi_B=3\alpha(1-\alpha)\delta^2/R_o^2$) with reference to the behavior of a resonant shear layer containing 1 mm radius "warm" vapor-air bubbles with $\omega_{B0_G}^*=0.28$ and $Y_V=0.4$ at a pressure of 35 kPa and temperature of 331 K. The results clearly show that the general features of the flow stabilization near bubble resonance conditions remain essentially unchanged also at higher temperatures and that an increase of the void fraction $\alpha$ results in a substantial reduction of the spatial amplification rate of the flow perturbations, with just minor modifications of the instability region in the frequency spectrum. This finding agrees well with the results for pure air bubbles and with the physical interpretation of the parameter

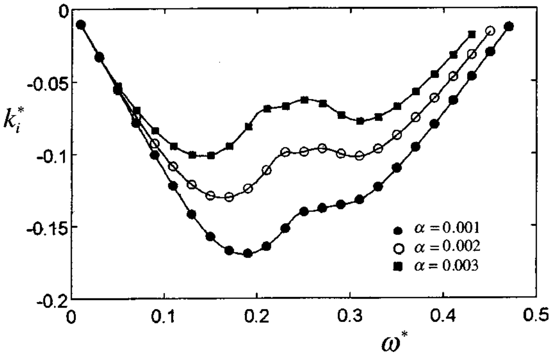

**Fig. 9 Spatial attenuation rate $k_i^*$ of a shear layer with "warm" bubbles in the resonant regime as a function of the excitation frequency $\omega^*$ for several values of the void fraction $\alpha$. In all cases: $\omega_{B0_G}^*=0.28$, $p_o=35$ kPa, $Y_V=0.4$ $(T_o=331$ K$)$, and $R_o^*=0.1$.**

$\pi_B=3\alpha(1-\alpha)\delta^2/R_o^2$ as an indicator of the importance of bubble dynamic interactions (d'Agostino and Brennen [4–6], d'Agostino et al. [16,18], d'Auria et al. [17], d'Auria et al. [20]). Since the sound speed $c_M^2$ is inversely proportional to $\alpha$, the stabilizing effect of higher void fractions is also fully consistent with the well-known behavior of parallel compressible flows at increasing Mach numbers.

**Blasius Boundary Layer.** We next consider the spatial stability of a Blasius boundary layer in water containing either air or air-vapor bubbles. The orthogonalization method by O'Drury [47] and Davey [22] has been used, together with the shooting procedure previously developed for the inviscid case, to deal with the diverging and stiff nature of viscous stability problems at high Reynolds numbers. The code has been validated against the single-phase incompressible results by Jordinson [48] and Ng and Reid [49] for both the spatially and temporally growing oscillations. As for the inviscid case, the presence of vapor-air bubbles is expected to contribute to the flow stabilization through the effect of compressibility and the increase of energy dissipation (both thermal and viscous) associated with the bubble dynamic response, especially near resonance conditions where the amplitude of the bubble oscillations is large.

We first illustrate the effects of the presence of air bubbles in the flow. As an example, Fig. 10 reports the spatial attenuation rate $\tilde{k}_i$ as a function of the excitation frequency $\tilde{\omega}$ for a Blasius boundary layer with Reynolds number Re=50,000, void fraction $\alpha=0.01$, at several pressures ranging from 1 to 20 kPa and containing 1 mm radius air bubbles in the compressible region of the response spectrum. The general features of the viscous solution are qualitatively similar to the inviscid case. As expected, comparison with the single-phase incompressible solution confirms that the compressibility of air bubbles promotes the stability of the flow. The results also indicate that the stabilizing effect is quite moderate except for pressures on the order of 1 kPa, when the bubble compliance has raised enough for the pressure perturbations to be able to excite a significant response of the bubbles. The influence of bubble compressibility on the same boundary layer flow at different pressure levels is well illustrated in nondimensional form by the marginal stability diagrams of Fig. 11 for several values of the pressure parameter $\pi_P=\delta^2\sqrt{p_o/\rho_L}/R_o\nu_L$. Appreciable stabilization only takes place for Re>$10^4$ and small values of $\pi_P$, both of which promote the interaction of the perturbation flow with the bubble response by increasing the pressure disturbances and the bubble compliance, respectively.

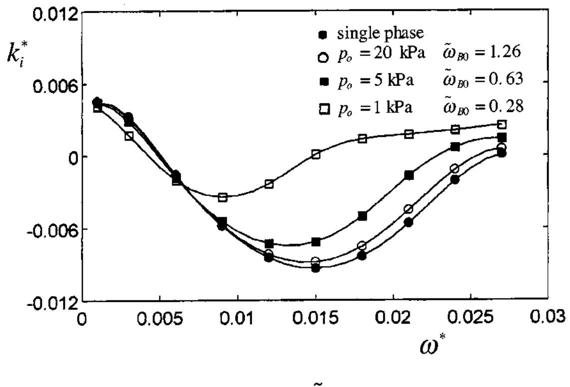

Fig. 10 Spatial attenuation rate $\tilde{k}_i$ as a function of the excitation frequency $\tilde{\omega}$ for a Blasius layer in water containing air bubbles in the compressibility regime ($\tilde{\omega}\ll\tilde{\omega}_{B0}$) at several values of the pressure $p_o$=1, 5 and 10 kPa. In all cases: $\alpha$=0.01 and $R_o$=1 mm. The single-phase incompressible flow solution ($\alpha$=0) is also shown for comparison.

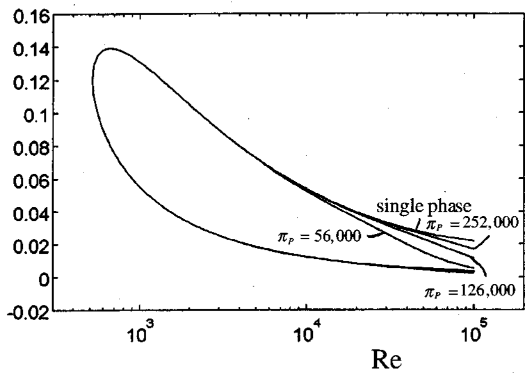

Fig. 11 Neutral stability curves of the Blasius layer of Fig. 10 for $\pi_R$=7.5, $\pi_B$=1.67 and several values of $\pi_P$=56,000, 126,000, and 252,000. The single-phase incompressible flow solution ($\alpha$=0) is also shown for comparison.

Next we examine the influence of bubble resonance phenomena on the flow stability. From the expression of the quasi-static natural frequency of a gas bubble in terms of the pressure $p_o$

$$\omega_{B0}=\sqrt{\frac{3p_o}{\rho_L R_o^2}+\frac{4S}{\rho_L R_o^3}}$$

it follows that discrimination of resonance effects in flows of water with air bubbles is practically impossible even at the lowest pressures because the surface tension $S$ shifts the bubble natural frequency in the region of Re>$10^6$, where the resonant behavior of the bubbles is effectively masked by the dominant influence of compressibility. However, bubble resonance effects become readily apparent if the surface tension is neglected ($S=0$), a situation not realistic for water-air systems, but nevertheless quite useful to illustrate the potential impact of bubble resonance on the fluid dynamic stability of parallel bubbly flows of nonpolar liquids (like most cryogenic rocket propellants), which are characterized by low surface tension.

An example of the effect of bubble resonance on the neutral stability of Blasius layers in water containing air bubbles with zero surface tension (We=0) is shown in Fig. 12. All points of the two-phase flow solution correspond to weakly super-resonant excitation frequencies according to the above equation, whose trace on the diagram would be represented by a negative exponential curve just below the instability region. The higher damping associated with resonant bubble oscillations manifests its usual tendency to stabilize the flow by inducing a moderate reduction of the region of instability at all frequencies and Reynolds numbers, especially in the lower part of the diagram near the curve corresponding to bubble resonance conditions. For the same reason, the critical Reynolds number increases beyond its incompressible flow value, delaying the threshold for the onset of spontaneous

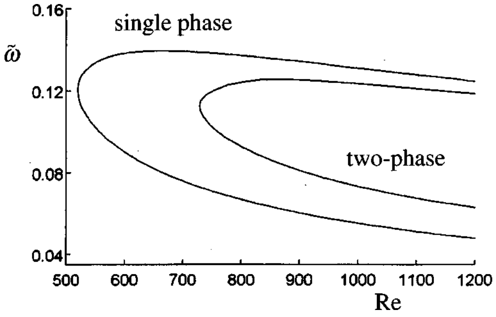

Fig. 12 Neutral stability curves of single phase and two-phase Blasius layers containing pure air bubbles in water for $\pi_P$ =400, $\pi_B$=0.034, $\pi_R$=7.5 and We=0

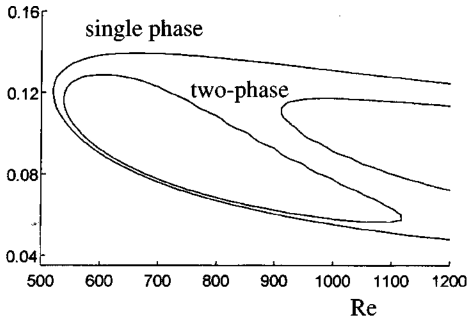

**Fig. 13 Neutral stability curves of single phase and two-phase Blasius layers containing pure air bubbles in water for $\pi_P = 620$, $\pi_B = 0.034$, $\pi_R = 7.5$ and We=0**

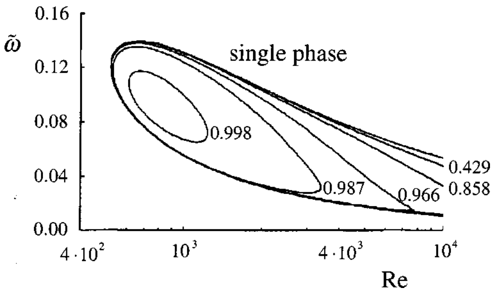

**Fig. 15 Neutral stability curves of single phase and two-phase Blasius layers containing air-vapor bubbles in water for $\pi_B = 1.67$, $\pi_R = 7.5$, $\pi_P = 56000$ and several values of $\pi_Y$**

self-sustained oscillations of the boundary layer. As the pressure parameter $\pi_P$ is increased, the bubble resonance curve crosses the central portion of the instability region and, for an appropriate choice of $\pi_P$ and $\pi_B$, divides it in two separate lobes (Fig. 13). In this case, the presence of two overlapping regions of instability indicates the existence of two competing most unstable modes, and therefore the possible occurrence of sudden transitions (mode jumping) as the Reynolds number varies across the coexistence region. Therefore, the presence of resonant air bubbles can substantially modify the spectral behavior of the unstable perturbations, but the magnitude of its impact on the neutral stability of the flow remains relatively modest.

On the other hand, the flow stabilization is much larger in the presence of vapor-air bubbles, in accordance with the results obtained in the inviscid analyses. Typical examples of the marginal stability curves for Blasius layers with vapor-air bubbles in water are plotted in Fig. 14 for a fixed value of the composition parameter $\pi_Y = Y_V / Y_V^*$ and several values of the pressure parameter $\pi_P$. It appears that also in the viscous flow case cold bubbles (corresponding to lower values of $\pi_P$) are more stabilizing than warm bubbles. This result confirms the different dynamic behavior of bubbly cavitating flows in the presence of significant thermal effects. Similar stabilization of the flow is also manifest when the vapor concentration in the bubbles is increased toward its critical value at constant pressure ($\pi_Y \to 1$), as illustrated in Fig. 15. In both cases the marginal stability curves close at high Reynolds numbers and the unstable region becomes progressively smaller. Notice, however, that the changes of the critical Reynolds number and of the corresponding unstable frequency are relatively modest. Hence, the presence of vapor-gas bubbles in the boundary layer is expected to effectively damp unstable perturbations without significantly affecting their frequency. More importantly, notice that the instability region eventually disappears for low external pressures and when the vapor mass fraction approaches the critical value for the quasi-static stability of the bubbles. These conditions approximately correspond to travelling bubble cavitation. Hence, the present theory predicts that the occurrence of this form of cavitation should tend to make Blasius boundary layers unconditionally stable at all Reynolds numbers and frequencies. This result is at least not qualitatively inconsistent with the appearance of travelling bubble cavitating boundary layers on lifting surfaces, where the occurrence of transition to fully developed turbulence is usually delayed to the bubble collapse region of the flow.

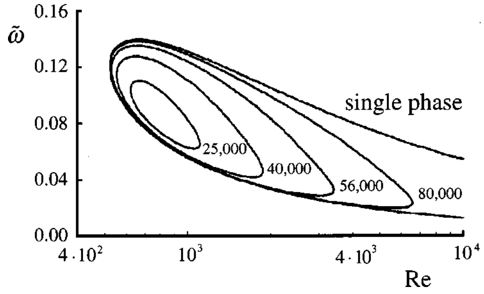

**Fig. 14 Neutral stability curves of single phase and two-phase Blasius layers containing air-vapor bubbles in water for $\pi_B = 1.67$, $\pi_R = 7.5$, $\pi_Y = 0.987$ and several values of $\pi_P$**

## Limitations

We now briefly examine the restrictions imposed to the previous theory by the various simplifying assumptions that have been made. Specifically we shall discuss the limitations due to the introduction of the continuum model of the flow, to the applicability of the parallel flow assumption to the stability analysis of travelling bubble cavitating flows, to the use of the linear perturbation approach in deriving the solution, to the neglect of the relative motion between the phases and of the local pressure perturbations in the neighborhood of each individual bubble.

For the continuum approach to be valid the two phases must be minutely dispersed with respect to the shortest characteristic length of the flow, here either the layer thickness $\delta$ or the wave length $\lambda \approx 1/k_r$ of the perturbations in the streamwise direction. Hence the unperturbed bubble radius $R_o$ is required to satisfy the most restrictive of the two conditions: $R_o/\delta \ll 1$ and $k_r R_o \ll 1$. Together with the assumption of a bubble population with uniform equilibrium radius, this is probably one of the most stringent limitations of the present analysis.

The parallel flow assumption implies that the layer thickness and the unperturbed bubble radius can be approximated as constant for the purpose of assessing the flow stability. Although none of these conditions is rigorously met in most bubbly cavitating flows, the first one has been found to yield results in good agreement with the experiments in barotropic fluids and is usually accepted in the stability analysis of quasi-parallel flows. On the other hand, the assumption of constant bubble radius implies the invariance of the flow pressure and is approximately verified in bubbly cavitating flows with small curvature, like free shear layers, jets and wakes, but also in more complex boundary layer flows on lifting surfaces, where the cavitating portion of the suction side is often designed for nearly constant pressure coefficient.

The perturbation approach simply requires that $|\hat{R}/R_o| \ll 1$, a condition that can safely be assumed in the analysis of incipient instabilities of laminar flows.

In order to estimate the error associated with the neglect of local pressure effects due to the dynamic response of each individual bubble, we consider the pressure perturbation experienced by one bubble as a consequence of the growth or collapse of a neighbor

$$\Delta p=\rho_L\left\{\frac{R}{s}\left[R\,\frac{D^2R}{Dt^2}+2\left(\frac{DR}{Dt}\right)^2\right]-\frac{R^4}{2s^4}\left(\frac{DR}{Dt}\right)^2\right\}$$

where $R=\mathrm{Re}\{R_o+\hat{R}(y)e^{i(kx-\omega t)}\}$ is given by the solution of the stability problem. To the same order of approximation used to develop the present analysis, comparison with the global pressure change:

$$\hat{p}=-\rho_L R_o(-\omega_L^2-i\omega_L 2\lambda+\omega_B^2)\hat{R}$$

then shows that the local pressure perturbations are unimportant if:

$$\left|\frac{\Delta\hat{p}}{\hat{p}}\right|\approx\alpha^{1/3}\left|\frac{\omega_L^2}{-\omega_L^2-i\omega_L 2\lambda+\omega_B^2}\right|\leqslant\alpha^{1/3}\frac{\omega_B}{2\lambda}\ll 1$$

Since the nondimensional damping coefficient $\xi=\lambda/\omega_B$ of resonant bubbles is on the order of 10 percent or higher in most practical situations, this condition is generally satisfied in flows with void fraction $\alpha<0.01$.

Finally, in order to address the error introduced by the neglect of the relative velocity between the two phases, let us consider the equation of motion for a bubble of negligible mass (Voinov [50]) with Stokes' viscous drag:

$$\frac{D\mathbf{u}}{Dt}-\frac{1}{3}\,\frac{D\mathbf{u}_B}{Dt}+\frac{1}{R}\,\frac{DR}{Dt}(\mathbf{u}-\mathbf{u}_B)=\frac{2\nu_L}{R^2}(\mathbf{u}-\mathbf{u}_B)$$

where $\mathbf{u}_B$ is the velocity of the bubble. Linearizing as before and assuming also for $\mathbf{u}_B$ a perturbation solution of the form $\mathbf{u}_B=\mathrm{Re}\{\mathbf{U}+\hat{\mathbf{u}}_B e^{i(kx-\omega t)}\}$, one obtains:

$$\left|\frac{\hat{\mathbf{u}}-\hat{\mathbf{u}}_B}{\hat{\mathbf{u}}}\right|=\frac{2}{\sqrt{1+(6\nu_L/\omega_L R_o^2)^2}}\ll 1$$

Hence, relative motion effects are unimportant when $\omega_L\ll\nu_L/R_o^2$, a condition that is typically verified even by resonant bubbles, especially in low pressure cavitating flows.

## Summary and Conclusions

As anticipated in the introduction and confirmed by the present theory, the dynamics of vapor-gas bubbles is strongly coupled through the pressure and velocity fields with the overall dynamics of parallel bubbly flows, both viscous and inviscid, and under suitable conditions dramatically increases their fluid dynamic stability. The bubble response to the periodic perturbations of transitioning flows introduces compliance, dissipative and inertial phenomena, and leads to the identification of four different excitation regimes, here designated as compressible, thermal, resonant and super-resonant.

Compressibility effects play a significant role at all frequencies except for super-resonant excitation, and become dominant in the low frequency limit. They act in favor of the flow stability by absorbing part of the perturbation energy and by generating the deformations necessary for final dissipation by irreversible phenomena. Their importance increases with the bubble compliance, and therefore at low pressures and high vapor concentrations. In vapor bubbles the pressure is strongly related to the temperature through the saturation conditions and significant differences arise between the stability of parallel flows with cold and warm cavitation bubbles.

Resonance effects originate from the dynamic balance between the compliant elastic response of the bubble contents and the inertia of the surrounding liquid. They are typical of bubbles with significant amount of noncondensable gas and become important when the excitation frequency of the bubbles is comparable with their natural frequency of oscillation. For this to happen relatively low values of the flow pressure and the surface tension are in general necessary. The occurrence of resonance amplifies the dynamic response of the bubbles increasing the energy dissipation, and therefore has a stabilizing effect the flow.

Thermal effects are generated by the compression/expansion of the noncondensable gas in the bubbles and, more so, by the evaporation/condensation of the vapor at the interface. They involve irreversible transfers of heat in the presence of finite temperature gradients and represent the major source of energy dissipation, especially in bubbles with high vapor mass fractions. Therefore, they also efficiently promote the flow stability, in particular when combined with large bubble compliance or resonance effects.

The linear stability of two-dimensional parallel inviscid free shear layers and (viscous) Blasius boundary layers containing vapor-gas bubbles has been examined and a suitable sets of nondimensional parameters have been proposed to account for the effects of the various physical parameters of the two-phase mixture. As expected, it has been observed that bubbly flows are always more stable than single-phase ones. Computations show that the presence of pure air bubbles in water has a moderate influence on the behavior of the flow stability and that such an influence is mostly due to the greater compressibility of the flow caused by the presence of the finely dispersed gaseous cavities. In flow configurations of practical relevance, the resonant coupling with the inertial dynamics of bubbles containing only noncondensable gas is prevented by the presence of the surface tension. When the latter is neglected and the flow pressure is sufficiently low, it is possible for the natural frequency of the bubbles to approach the excitation frequency of the flow perturbations. This occurrence is responsible for strong spectral deviations of the flow stability from both the compressible and incompressible solutions, but the overall magnitude of its effects on the marginal stability limits of the flow is relatively modest.

When the presence of vapor in the bubbles is explicitly considered, the effects on the flow stability increase dramatically, especially at low pressures and high vapor concentrations. The results of the stability analysis clearly indicate that bubbles with high vapor mass fractions are far more effective in dissipating the energy subtracted from the perturbation field because of their greater compliance and the higher damping introduced by phase changes at the bubble interface. These mechanisms are enhanced by the reduction of the bubble pressure—and consequently the temperature—and are responsible for significant differences in the linear stability of parallel flows with cold (inertial) and warm (thermal) vapor-gas bubbles. Unconditional stability is predicted in the travelling bubble cavitation limit for low external pressures and vapor mass fractions approaching the critical value for the quasi-static stability.

The present theory has been derived under fairly restrictive simplifying assumptions and therefore it is not expected to provide an accurate description of the stability of real parallel bubbly flows. However, the results of this investigation identify the fundamental physical mechanisms responsible for the interaction of the perturbation field with the dynamics of the bubbles and reveal a number of effects which may be of importance in real bubbly and cavitating flows. Even the very simple geometry of the flows considered here can nevertheless provide an introduction to the study of flows of great technical interest. Bubbly cavitating flows of similar geometry occur in many fields of applied hydrodynamics such as the study of pump blades, propellers, lifting surfaces, valves, etc. In these flows the present theory might contribute to shed some light on the influence of the presence of the bubbles on the fluid dynamic stability, on turbulent transition and other related boundary-viscous effects, on the most appropriate ways for controlling the flow development, and on the possible choice of more suitable parameters and laws for efficient scaling of unsteady bubbly and cavitating flows.

## Acknowledgments

This research has been supported by the Ministero dell'Università e della Ricerca Scientifica e Tecnologica, by the Agenzia Spaziale Italiana, and by internal funds of Centrospazio, Pisa, Italy. The authors would like to gratefully acknowledge the help of Dr. Fabrizio d'Auria in developing and implementing the numerical codes, as well as the constant encouragement of Profs. Mariano Andrenucci, Director of Centrospazio, and Renzo Lazzeretti of the Aerospace Engineering Department, University of Pisa, Pisa, Italy.

## Appendix

The quantity $E(\omega_L)$ in the expressions of the damping coefficient and the natural frequency of the bubbles is given by:

$$E = 1 + \frac{3\gamma}{z_{VG}} \psi_{VG} \left( 1 - \frac{1}{\gamma} - \frac{\mathcal{R}_V T_o}{Q_V} \right) - \gamma E_1 E_2$$

$$E_1 = \frac{Y_{Vo}}{z_D} \left[ 1 + \frac{\mathcal{R}_V - \mathcal{R}_G}{\mathcal{R}_{VG}\gamma} (1 - Y_{Vo}) \right] + 3\psi_{VG} \frac{a_1}{z_{VG}} + \frac{a_2(1-Y_{Vo})Y_{Vo}}{z_{VG}(1-\mathrm{Le}_{VG})} \left( \frac{\psi_{VG}}{\psi_D} - 1 \right)$$

$$E_2 = \frac{(1+\sqrt{z_L}) \dfrac{k_L}{k_{VG}} \dfrac{\mathcal{R}_V T_o}{Q_V} + \psi_{VG} \left( \dfrac{\mathcal{R}_V T_o}{Q_V} + \dfrac{1}{\gamma} - 1 \right)}{\dfrac{a_2(1-Y_{Vo})Y_{Vo}}{3(1-\mathrm{Le}_{VG})} \left( 1 - \dfrac{\psi_{VG}}{\psi_L} \right) - a_1 \left( \psi_{VG} - \dfrac{1+\sqrt{z_L}}{k_L/k_{VG}} \right) - \dfrac{Y_{Vo}}{a_3}}$$

$$z_D = \frac{i\omega_L R_o^2}{D_{VG}}, \quad z_L = \frac{i\omega_L R_o^2}{\chi_L}, \quad z_{VG} = \frac{i\omega_L R_o^2}{\chi_{VG}}, \quad \mathrm{Le}_{VG} = \frac{\chi_{VG}}{D_{VG}}$$

$$\psi_D = \sqrt{z_D} \coth \sqrt{z_D} - 1, \quad \psi_{VG} = \sqrt{z_{VG}} \coth \sqrt{z_{VG}} - 1$$

$$a_1 = \left[ 1 + \frac{a_1 \zeta (1-Y_{Vo}) \mathcal{R}_G}{\mathcal{R}_{VG} \psi_D} \frac{\mathcal{R}_V T_o}{Q_V} \right] \frac{1}{3 a_4 \zeta}, \quad a_2 = \frac{\mathcal{R}_V - \mathcal{R}_G}{c_{pVG}}$$

$$a_3 = \frac{3 c_{pVG} T_o \mathrm{Le}_{VG}}{Q_V}, \quad a_4 = \frac{R_o Q_V}{D_{VG} \sqrt{2\pi \mathcal{R}_V T_o}}$$

where $\zeta$ is the evaporation/condensation coefficient defined as the fraction of the vapor molecules impinging the bubble interface that condense on the liquid.

## Nomenclature

$c$ = sound speed
$c_p$ = constant pressure specific heat
$D_{VG}$ = binary diffusion coefficient
$i$ = imaginary unit
$k$ = wave number
$\mathrm{Le} = \chi/D$ = Lewis number
$p$ = pressure
$Q_V$ = latent heat of vaporization
$R$ = bubble radius
$\mathcal{R}$ = gas constant
$S$ = surface tension
$t$ = time
$T$ = temperature
$\mathbf{u}$ = flow velocity vector
$u$ = $x$-velocity component
$U$ = laminar flow velocity
$v$ = $y$-velocity component
$x$ = streamwise coordinate
$y$ = transversal coordinate
$Y$ = mass fraction
$\alpha$ = void fraction
$\delta$ = layer thickness
$\gamma$ = specific heat ratio
$\lambda$ = damping coefficient
$\mu$ = viscosity
$\nu$ = kinematic viscosity
$\xi$ = nondimensional bubble damping coefficient
$\rho$ = density
$\chi$ = thermal diffusivity
$\zeta$ = evaporation/condensation coefficient
$\omega$ = angular frequency

### Subscripts

$B$ = bubble
$G$ = gas
$VG$ = vapor-gas
$i$ = imaginary
$L$ = liquid, Lagrangian
$M$ = mixture
$o$ = unperturbed
$r$ = real
$S$ = saturation
$V$ = vapor

## References

[1] Brennen, C. E., 1994, *Hydrodynamics of Pumps*, Oxford University Press, NY.
[2] Knapp, R. T., Daily, J. W., and Hammitt, F. G., 1970, *Cavitation*, McGraw-Hill, NY.
[3] Brennen, C. E., 1995, *Cavitation and Bubble Dynamics*, Oxford University Press, NY.
[4] d'Agostino, L., and Brennen, C. E., 1983, ''On the Acoustical Dynamics of Bubble Clouds,'' *ASME Cavitation and Multiphase Flow Forum*, Houston, TX, USA, pp. 72–75.
[5] d'Agostino, L., and Brennen, C. E., 1988, ''Acoustical Absorption and Scattering Cross Sections of Spherical Bubble Clouds,'' J. Acoust. Soc. Am., **84**, pp. 2126–2134.
[6] d'Agostino, L., and Brennen, C. E., 1989, ''Linearized Dynamics of Spherical Bubble Clouds,'' J. Fluid Mech., **199**, pp. 155–176.
[7] d'Agostino, L., Brennen, C. E., and Acosta, A. J., 1988, ''Linearized Dynamics of Two-Dimensional Bubbly and Cavitating Flows over Slender Surfaces,'' J. Fluid Mech., **192**, pp. 485–509.
[8] d'Auria, F., d'Agostino, L., and Brennen, C. E., 1994, ''Linearized Dynamics of Bubbly and Cavitating Flows in Cylindrical Ducts,'' FED Vol. 194, *1994 ASME Fluids Engineering Summer Meeting*, Incline Village, NV, June 19–23, pp. 59–66.
[9] d'Auria F., d'Agostino, L., and Brennen, C. E., 1995, ''Bubble Dynamics on the Rotordynamic Forces in Cavitating Inducers,'' FED Vol. 201, pp. 47–54, *1995 ASME Fluids Engineering Summer Meeting*, Hilton Island, SC, USA, August 13–18.
[10] d'Agostino, L., and d'Auria, F., 1997, ''Three-Dimensional Analysis of Rotordynamic Forces on Whirling and Cavitating Inducers,'' *1997 ASME Fluids Engineering Division Summer Meeting*, Vancouver, BC, Canada, June 22–26.
[11] Betchov R., and Criminale, W. O., Jr., 1967, *Stability of Parallel Flows*, Academic, NY.
[12] Drazin, P. G., and Reid, W. H., 1981, *Hydrodynamic Stability*, Cambridge University Press.
[13] Marboe, R. C., Billet, M. L., and Thomson, D. E., 1986, ''Some Aspects of Traveling Bubble Cavitation and Noise,'' *International Symposium on Cavitation and Multiphase Flow Noise*, Anaheim, CA.
[14] Arakeri, V. H., and Shanmuganathan, V., 1985, ''On the Evidence for the Effect of Bubble Interference on Cavitation Noise,'' J. Fluid Mech., **159**, pp. 131–150.
[15] Ceccio, S. L., and Brennen, C. E., 1990, ''Observations of the Dynamics and Acoustics of Attached Cavities,'' *ASME Cavitation and Multiphase Flow Forum*, Toronto, Ontario, Canada, pp. 79–84.
[16] d'Agostino, L., d'Auria, F., and Brennen, C. E., 1995, ''Stability of Parallel Bubbly and Cavitating Flows,'' *International Symposium on Cavitation*, Deauville, France, May 12–15.
[17] d'Auria, F., d'Agostino, L., and Brennen, C. E., 1995, ''Inviscid Stability of Bubbly Jets,'' AIAA Paper 95-2377, *31st AIAA/ASME/SAE/ASEE Joint Prop. Conf.*, San Diego, CA, July 10–12.
[18] d'Agostino, L., d'Auria, F., and Brennen, C. E., 1997, ''On the Inviscid Stability of Parallel Bubbly Flows,'' J. Fluid Mech., **339**, pp. 261–274.
[19] Burzagli, F., 1997, ''Stabilità di Flussi Paralleli Liquido-Aeriforme Contenenti Bolle,'' Laurea thesis, Aerospace Engineering Dept., Pisa University, Pisa, Italy.
[20] d'Auria, F., d'Agostino, L., and Burzagli, F., 1997, ''Linear Stability of Parallel Shear Layers Containing Vapor-Gas Bubbles,'' 1997 *ASME Fluids Engineering Division Summer Meeting*, Vancouver, BC, Canada, June 22–26.
[21] Burzagli, F., and d'Agostino, L., 1998, ''Linear Stability of Blasius Boundary Layers Containing Gas-Vapor Bubbles,'' *Proc. 3rd International Symposium on Cavitation*, Vol. 1, pp. 99–105, Grenoble, France, April 7–10.
[22] Davey, A., 1983, ''An Automatic Orthonormalization Method for Solving Stiff Boundary-Value Problems,'' J. Comput. Phys., **51**, pp. 343–356.
[23] Rietema, K., and van den Akker, H. E. A., 1983, ''On the Momentum Equations in Dispersed Two-Phase Systems,'' Int. J. Multiphase Flow, **9**, pp. 21–36.
[24] Nigmatulin, R. I., 1970, ''Methods of Mechanics of a Continuum Medium for

the Description of Multiphase Mixtures,'' J. Appl. Math. Mech., **34**, pp. 1033–1049.

[25] Nigmatulin, R. I., 1971, ''Small-Scale Effects and Surface Effects in the Hydrodynamics of Multiphase Media,'' J. Appl. Math. Mech., **35**, pp. 409–420.

[26] Nigmatulin, R. I., and Khabeev, N. S., 1976, ''Dynamics of Vapor-Gas Bubbles,'' translated from Izv. Akad. Nauk. SSSR, Mekh. Zhid. Gaza, No. 3, pp. 867–871.

[27] Nigmatulin, R. I., and Khabeev, N. S., 1977, ''Dynamics of Vapor-Gas Bubbles,'' Fluid Dyn., **12**, pp. 59–67.

[28] Nagiev, F. B., and Khabeev, N. S., 1979, ''Heat Transfer and Phase Transition Effects Associated with Oscillations of Vapor-Gas Bubbles,'' Sov. Phys. Acoust., **25**, pp. 148–152.

[29] Nigmatulin, R. I., Khabeev, N. S., and Nagiev, F. B., 1981, ''Dynamics, Heat and Mass Transfer of Vapor-Gas Bubble in a Liquid,'' Int. J. Heat Mass Transf., **24**, pp. 1033–1044.

[30] Chapman, R. B., and Plesset, M. S., 1971, ''Thermal Effects in the Free Oscillation of Gas Bubbles,'' ASME J. Basic Eng., **93**, pp. 373–376.

[31] Prosperetti, A., 1984, ''Bubble Phenomena in Sound Fields: Part One,'' Ultrasonics, **22**, pp. 69–77.

[32] Prosperetti, A., 1991, ''The Thermal Behaviour of Oscillating Gas Bubbles,'' J. Fluid Mech., **222**, pp. 587–616.

[33] Finch, R. D., and Neppiras, E. A., 1973, ''Vapour Bubble Dynamics,'' J. Acoust. Soc. Am., **53**, pp. 1402–1410.

[34] Wang, T., 1974, ''Effects of Evaporation and diffusion on an Oscillating Bubble,'' Phys. Fluids, **17**, pp. 1121–1126.

[35] Fanelli, M., Prosperetti, A., and Reali, M., 1981, ''Radial Oscillations of Gas-Vapor Bubbles in Liquids: Part I: Mathematical Formulation,'' Acustica, **47**, No. 4, pp. 253–265.

[36] Fanelli, M., Prosperetti, A., and Reali, M., 1981, ''Radial Oscillations of Gas-Vapor Bubbles in Liquids: Part II: Numerical Examples,'' Acustica, **49**, pp. 98–109.

[37] Daily, J. W., and Johnson, V. E., Jr., 1958, ''Turbulence and Boundary Layer Effects on Cavitation Inception from Gas Nuclei,'' Trans. ASME, **78**, pp. 1695–1706.

[38] Wang, Yi-Chun, 1998, ''Effects of Nuclei Size Distribution on the Dynamics of a Spherical Cloud of Cavitation Bubbles,'' *ASME FED Summer Meeting*, FEDSM'98, June 21–25.

[39] Stoer, J., and Burlish, R., 1980, *Introduction to Numerical Analysis*, Springer.

[40] Press, W., Teulkowsky, S., Vetterling, W., and Flannery, B., 1992, *Numerical Recipes in FORTRAN*, 2nd ed., Cambridge University Press.

[41] Stoer, J., 1974, ''Introduzione all' Analisi Numerica 1,'' Zanichelli, ed. S.p.A., Bologna, Italy.

[42] Michalke, A., 1965, ''On Spatially Growing Disturbances in an Inviscid Shear Layer,'' J. Fluid Mech., **23**, pp. 521–544.

[43] Drazin, P. G., 1958, ''The Stability of a Shear Layer in an Unbounded Heterogeneous Inviscid Fluid,'' J. Fluid Mech., **4**, pp. 214–224.

[44] Blumen, W., 1970, ''Shear Layer Instability of an Inviscid Compressible Fluid,'' J. Fluid Mech., **40**, pp. 769–781.

[45] Blumen, W., Drazin, P. G., and Billing, D. F., 1975, ''Shear Layer Instability of an Inviscid Compressible Fluid. Part 2,'' J. Fluid Mech., **71**, pp. 305–316.

[46] Drazin, P. G., and Davey, A., 1977, ''Shear Layer Instability of an Inviscid Compressible Fluid. Part 3,'' J. Fluid Mech., **82**, pp. 255–260.

[47] O'Drury, L. C., 1980, J. Comput. Phys., **37**, p. 133.

[48] Jordinson, R., 1970, ''The Flat Plate Boundary Layer. Part 1. Numerical Integration of the Orr-Sommerfeld Equation,'' J. Fluid Mech., **43**, pp. 801–811.

[49] Ng, B. S., and Reid, W. H., 1980, ''On the Numerical Solution of the Orr-Sommerfeld Problem: Asymptotic Initial Conditions for Shooting Methods,'' J. Comput. Phys., **38**, pp. 275–293.

[50] Voinov, O. V., 1973, ''Force Acting on a Sphere in an Inhomogeneous Flow of an Ideal Incompressible Fluid,'' Plenum (Transl. from Z. Prikl. Mekh. i Tekh. Fiz., **4**, pp. 182–184, July–August 1973).

[51] Blake, 1986, *Mechanics of Flow-Induced Sound and Vibration*, Academic, NY.

[52] Herbolzeimer, E., 1983, ''Stability of the Flow During Sedimentation in Inclined Channels,'' Phys. Fluids, **26**, pp. 2043–2054.

[53] Shaqfeh, E. S. G., and Acrivos, A., 1986, ''The Effect of Inertia on the Stability of the Convective Flow in Inclined Particle Settlers,'' J. Physiol. (Paris), **30**, pp. 960–973.

[54] Yang, Y., Chung, J. N., Troutt, T. R., and Crowe, C. T., 1990, ''The Influence of Particles on the Spatial Stability of Two-Phase Mixing Layers,'' Phys. Fluids A, **2**, pp. 1839–1845.

**Morten Kjeldsen**
Associate Professor,
Norwegian University of Science and Technology
(NTNU),
Dept. of Thermal Energy and Hydropower,
Alfred Getz v.4, N7034 Trondheim,
Norway
e-mail: Morten.Kjeldsen@tev.ntnu.no

**Roger E. A. Arndt**
Professor
e-mail: arndt001@tc.umn.edu

**Mark Effertz**
Undergraduate Student
e-mail: Mark.J.Effertz-1@tc.umn.edu

St. Anthony Falls Laboratory,
University of Minnesota,
Mississippi River at 3rd Avenue S.E.,
Minneapolis, MN 55414

# Spectral Characteristics of Sheet/Cloud Cavitation

*Cavitation observations were made using a highly instrumented 2D NACA 0015 hydrofoil mounted in a specially designed water tunnel. It was found that the dynamic characteristics of the cavitation vary considerably with various combinations of angle of attack and cavitation number, $\sigma$. At higher angles of attack, two types of flow unsteadiness are observed. At low $\sigma$, a low frequency shedding of cloud cavitation results in a strong oscillation in lift and $\Delta p$ at a Strouhal number, based on chord length, fc/U, of about 0.15. This frequency is relatively insensitive to changes in $\sigma$. As $\sigma$ is raised, the harmonic content of the oscillations changes significantly. A spectral peak at much higher frequency is noted that increases in frequency almost linearly with cavitation number. Similar behavior is noted in the lift fluctuations.* [S0098-2202(00)02503-7]

## Motivation

Although sheet cavitation has been the object of intense studies over the years, several aspects have not fully been investigated. Examples are the nonstationary load due to cavitation, and the influence of the test facility on such studies.

From a design point-of-view the minimum use of structural thickness in order to reduce blockage effects gives reason for concerns about nonstationary loading and subsequent fatigue problems. Another topic is the linkage between shedding physics and other deleterious cavitation phenomena like noise and erosion. For rotating machinery a substantial number of harmonics can be naturally present as pressure pulsations. These pulsations can be coupled with sheet cavitation/cloud shedding phenomena, resulting in strong vibrations.

An example of such phenomena has been found in the six-bladed high pressure fuel turbopump (HPFTP) used in the space shuttle. Vibration was noted at side band frequencies of $6\Omega \pm \beta$, where $\beta$ is in the range $0.1\Omega$ to $0.3\Omega$ ($\Omega$ being the rotational speed). This phenomenon is apparently due to the modulation of a lower frequency oscillation at the blade passing frequency. The data of Yamamoto [1] suggest that $\beta/\Omega$ is given by

$$\frac{\beta}{\Omega} = 0.3\sqrt{\sigma} \quad \text{(pumps)} \tag{1}$$

suggesting that cavitation dependent oscillation phenomena are occurring in the flow passages.

Although the rotational speeds are very different, the specific speed of Francis turbines are comparable to that of the HPFTP. Hence the cited phenomena are important in the operation of hydroturbines as well. As the power market is being deregulated in both the U.S. and Europe, the power plant owners will probably be more inclined to run their turbines in cavitating regimes. This operation will be justified by the fact that repair costs will be relatively less compared to the high prices achieved in high power demand periods over the year.

There is, however, an economic limit to operation in the cavitating regime. Major damage can occur, such that the success of such an operation is dependent on a monitoring system that can sense the intense sheet/cloud cavitation. The construction of such a monitoring system is dependent on detailed knowledge of the impact of sheet/cloud cavitation on the structure and especially with regard to nonstationary blade loading. The study presented in this paper examines the consequence of this type of cavitation, suggesting dimensionless parameters as a design tool. The experimental results also provide generic knowledge on how to improve cavitation monitoring systems.

## Relation to Erosion Research

Many researchers have recognized that the basic physics of erosion in pumps and turbines can be simulated by experiments with partially cavitating hydrofoils in a water tunnel (Avellan et al. [2] Bourdon et al. [3], Avellan and Dupont [4], Abbot et al. [5], Le et al. [6,7]). These studies indicate that maximum erosion occurs at the trailing edge of a cavity. The cavitation cloud at the trailing edge contains complex vortical structures that are highly erosive. Several investigators have noted that the erosion process is modulated at a frequency that depends on the cavity length, i.e., $fl/U \sim 0.3$. This modulation will be easily detected with the detection schemes used in this study.

Kato et al. [8] performed a series of tests using two different sized foils having an NACA-0015 cross section. Using soft indium inserts mounted on the suction side of the hydrofoil, they were able to quantify the erosion rate using the pit counting technique. They also found that they could simulate either bubble cavitation or sheet cavitation by simply changing the angle of attack. The so-called ductile probe technique was developed by Hackworth and Arndt [9] for application to measuring cavitation erosion on full scale ship propellers (Hackworth [10]). A comparison between weight loss and pit counting techniques was studied by Simoneau et al. [11] who have also used hydrofoil tests to develop a unique electrochemical technique for monitoring cavitation erosion. This technique is suitable for monitoring erosion in both turbine models and full scale turbines. This work was extended by Bourdon et al. [3] who demonstrated through laboratory tests and field experience that hydrofoil cavitation provides a good simulation of hydroturbine cavitation. They used both the electrochemical detection method and the vibratory monitoring technique originally developed by Abbot [12] and Abbot et al.

---

Contributed by the Fluids Engineering Division for publication in the JOURNAL OF FLUIDS ENGINEERING. Manuscript received by the Fluids Engineering Division June 15, 1999; revised manuscript received March 9, 2000. Associate Technical Editor: J. Katz.

[13]. Thus, there is ample evidence that cavitation erosion in hydroturbines can be simulated using cavitation hydrofoil tests in a water tunnel.

## Experimental Methods

All the experiments were carried out in the St. Anthony Falls Laboratory (SAFL) high speed water tunnel. This tunnel (described in Arndt et al. [14]) has several unique features, including the ability to remove as much as 4 percent by volume of injected air. This feature was useful in a previous study of the favorable effects of minimizing cloud cavitation erosion with air injection (Arndt et al. [15]). This feature also permits rapid change of dissolved gas content. Gas content can be changed in the range 2 ppm–15 ppm in about four hours. The test section is separated into two parts by a thin plexiglass sheet. The lower section is 190 mm square and 1250 mm in length and handles flows up to 30 m $s^{-1}$ in velocity. The upper tank contains stagnant water in which an array of hydrophones is mounted. This barrier between the flow and the hydrophones is approximately acoustically transparent.

The hydrofoil designed for this project is similar in overall configuration to hydrofoils being used for other cavitation studies (Arndt et al. [14]). It is approximately 2D, spanning the test section in the vertical direction with an NACA-0015 cross section. It is mounted in the test section on a circular plug allowing for a setting at any desired angle of attack. A force balance can also be fitted at this position. The overall dimensions are 190 mm in span with an 81 mm chord. Both instrumented and plain foils can be inserted in the test section (Fig. 1).

The instrumented foil, shown in Fig. 2, is fitted with a row of 11 static pressure ports. At another spanwise position the foil is fitted with interchangeable instrumented inserts. One type of insert consists of an array of conductivity probes for void fraction measurements. This instrumentation can be replaced by a second insert consisting of an array of piezoelectric film transducers as described in Arndt et al. [16]. Finally, a third insert can be used in the same position that is machined of commercially pure aluminum for pitting studies. In addition to this pressure instrumentation, two Entran EPX transducers are flush mounted in the circular plug in which the foil is mounted. They are positioned symmetrically with the chord-line at mid position and are 65 mm (0.8 c) apart.

As shown in Fig. 1, the basic instrumentation used in this study consisted of hydrophones, accelerometers, flush mounted piezoelectric transducers, and video recording. Two hydrophones were mounted in the water tank above the test section. The acoustic path between the foil and the hydrophones was one of constant acoustic impedance. An array of 19 flush-mounted piezoelectric pressure transducers was incorporated into a removable section of the suction side of the foil. These were not used in the study described herein, but will be used in subsequent investigations.

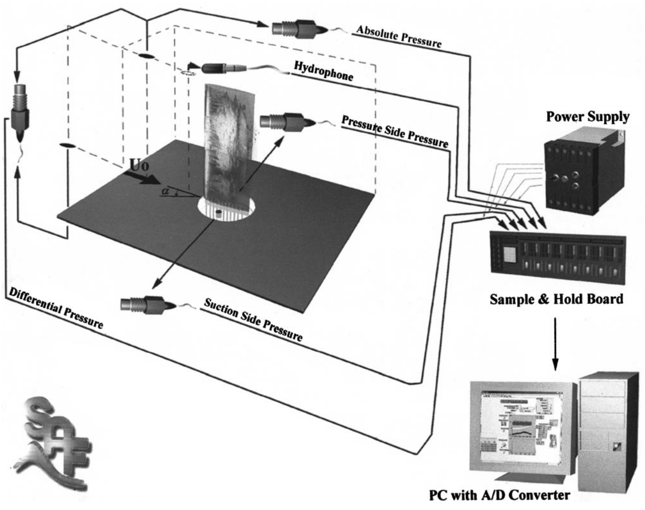

Fig. 1 Test setup

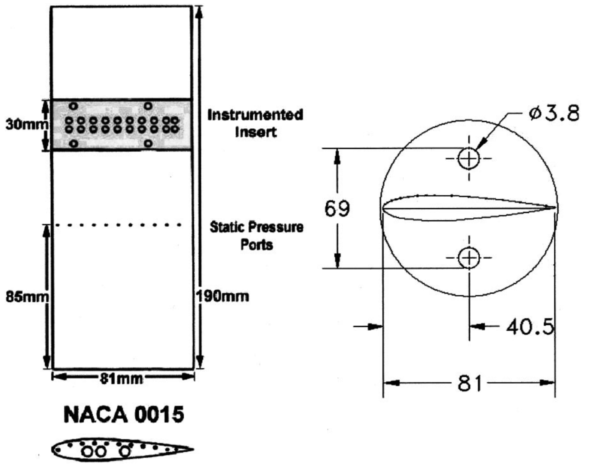

Fig. 2 View of instrumented foil (left) and mounting plug with transducer positions shown (right)

Velocity measurements were made using a TSI Color Burst LDA/LDV system with a beam splitter and an IFA Processor in the backscatter mode.

## Experimental Results

**Static Pressure Distribution.** A comparison between the measured pressure distribution and the computed pressure distribution, $Cp$ versus $x/c$, is shown in Fig. 3. In making this comparison, a bias error in the reading of the angle of attack was discovered for one of two mounting plugs. It was found that the best fit between the experimental and theoretical data sets was achieved when a bias error of −2 deg was applied to the angle of attack readings. This bias correction, presumably due to a protrac-

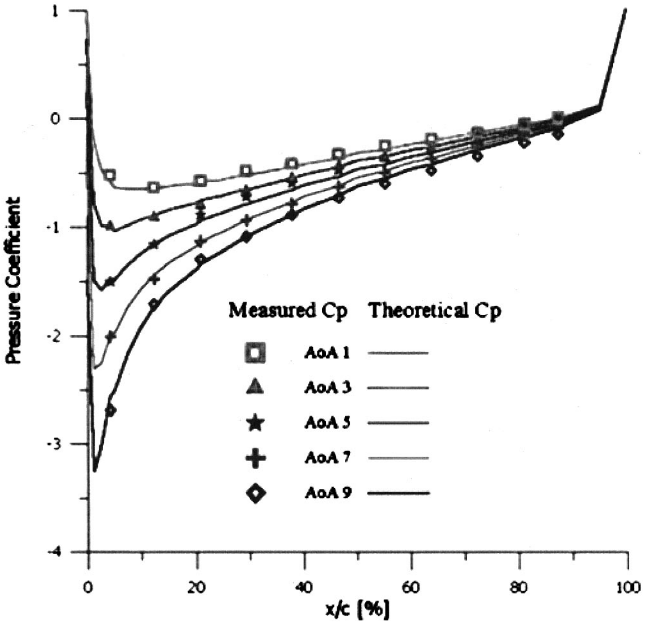

Fig. 3 Comparison of measured and theoretical pressure distribution on a NACA 0015 foil

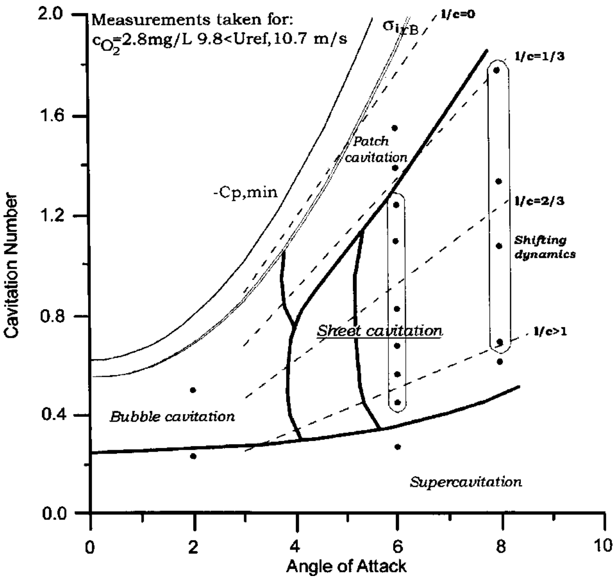

**Fig. 4 Mapping of cavitation regimes. The lines $l/c$=constant are obtained from a linear fit to the cavity length data in Fig. 5.**

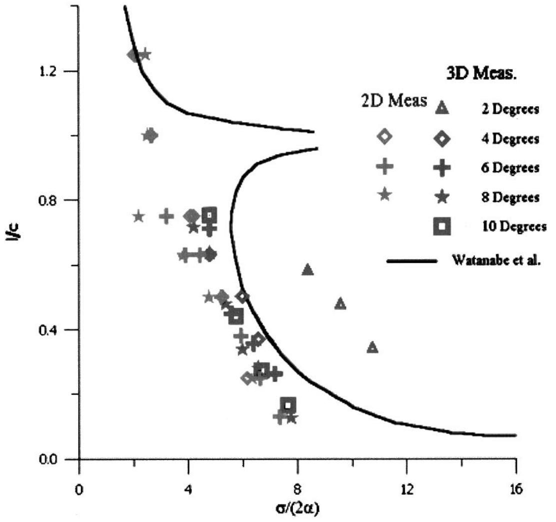

**Fig. 5 Cavity length**

tor mounting error, has been made in all subsequent plots in the paper. In general, the agreement between experiment and theory is good, placing additional confidence on the accuracy of the machining process.

**Cavitation Mapping.** Figure 4 contains a pictorial display of the various types of cavitating flow that were observed at various combinations of angle of attack, $\alpha$, and cavitation number, $\sigma$. These observations were made on a carefully polished and anodized foil. It is important to note that several different cavitating regimes occur depending on the combination of $\sigma$ and $\alpha$. The demarcation between ''inception''and $-C_{pm}$ (computed) varies such that $\sigma_i$ is always less than $-C_{pm}$, as expected. At low angle of attack, say less than 4 deg, only bubble cavitation occurred. At intermediate angles of attack, cavitation inception is in the form of patchy cavitation. Further lowering of cavitation number results in sheet cavitation that is dominated by relatively low oscillations, $fc/U=0.2$. At higher angles of attack, $\alpha \geqslant 6$ deg, a more complex sequence of events occurs. The flow is still dominated by sheet cavitation. However, the characteristic frequencies of oscillation increase with increasing $\sigma$, as will be shown in subsequent plots. Sheet cavitation with large scale break-off of cavitation clouds is also observed. A significant variation in the dynamics with variations in $\sigma$ was noted at $\alpha=8$ deg.

**Cavity Length.** The measured cavity length at various angles of attack is presented in Fig. 5 in the form of $l/c$ versus $\sigma/2\alpha$. These data are compared with previously collected data for an NACA 0015 hydrofoil with an elliptic planform of aspect ratio 3 by Arndt et al. [15]. The comparison is made by adjusting $\sigma/2\alpha$ for the 3D data to equivalent 2D values, using standard lift line theory. For an elliptic planform with an aspect ratio of 3, the correction is

$$\left[\frac{\sigma}{2\alpha}\right]_{2D}=0.6\left[\frac{\sigma}{2\alpha}\right]_{3D} \tag{2}$$

Also plotted is the partial and super-cavitation theory of Watanabe et al. [17].[1] All the data agree except for the 2 deg data. The discrepancy at 2 deg is not unexpected since careful inspection indicates that bubble cavitation occurs at this angle of attack. Considering the assumptions made in the theory, the agreement with experiment is quite good. It is also noted that agreement between the 2D foil and the elliptic planform foil is quite satisfactory, suggesting that a quasi-2D theory might be good estimate for cavity length for elliptically loaded foils.

The data in Fig. 5 can be fitted by a straight line and extrapolated to $l/c=0$. From this extrapolation, a simple prediction for the inception of sheet cavitation is obtained

$$\sigma_i \simeq 17\,\alpha \quad (\alpha \ \text{in radians}) \tag{3}$$

This relation appears to fit the observations reasonably well in the range (2 deg$\leqslant \alpha \leqslant$8 deg).

**Spectral Characteristics.** Large variations in the spectral characteristics of the flow are noted at a fixed angle of attack as the cavitation index is varied. This is seen in Fig. 6. This presentation utilizes the Joint Time-Frequency Analysis (JTFA) of *ramping tests*. These specific experiments were made keeping the flow at a constant rate while allowing the system pressure to vary linearly over time. The measured data are the suction side pressure obtained with the Entran transducer. The JTFA used can be

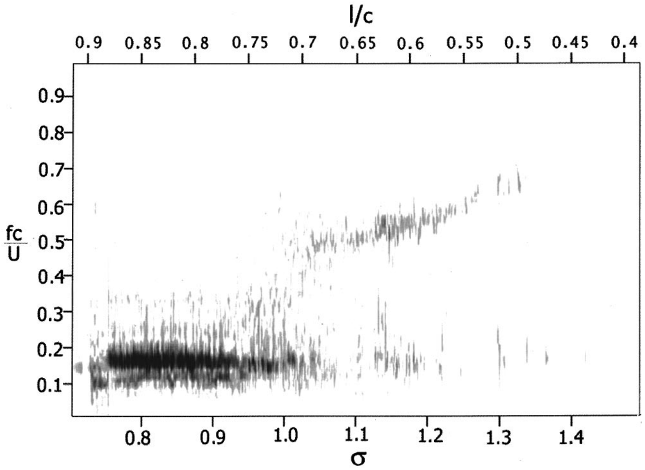

**Fig. 6 JFTA of suction side pressure transducer at 7 degrees angle of attack. The intensity of the color denotes the amplitude. St≡fc/U.**

---

[1] Courtesy of Professor Watanabe who applied his cavitating flat plate theory to our test setup. The effects of blockage are apparently minimal since the theory agrees well with the theory of Acosta [18] for an unconfined flat plate.

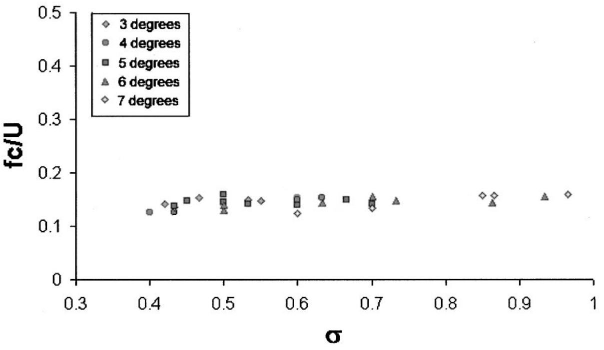

**Fig. 7 Composite plot of type I peak frequency obtained at various angles of attack**

considered as a Short Time Fourier Transform, described by the following inner product equation (Qian and Chen [19])

$$STFT(t,\omega)=\int s(\tau)\gamma(\tau-t)e^{-j\omega\tau}d\tau \qquad (4)$$

where $y$ can be considered a window function centered at $t_i$ and $s$ is the measured signal. If the ramping rate is sufficiently small, the results are equivalent to the usual FFT.

Figure 6 clearly visualizes the characteristic change in the frequency domain. It is also important to note that Fig. 6 is a composite JTFA plot, containing data collected over different values of velocity. This indicates that Strouhal scaling is appropriate. In the cited examples, it was found that there was a good correspondence between the frequency characteristics in the ramping experiments and those measured under steady state conditions but over a range of cavitation numbers.

At cavitation number less than about 1 ($l/c \geqslant 0.73$, Type I mode) a strong spectral peak exists (indicated by a bright red orange color) at a Strouhal number, $fc/U$ of about 0.15 that is independent of cavitation number. It was also noted that the low frequency peak appears to be independent of angle of attack as well as cavitation number. This is illustrated in Fig. 7 that is a composite plot of Strouhal number for the low frequency peak as a function of cavitation number for various values of angle of attack.

At values of cavitation index greater than about 1 ($l/c \leqslant 0.73$, Type II mode), a higher frequency, albeit weaker spectral peak dominates. The Strouhal frequency of the weaker tone is almost a linear function of cavitation number. If cavity length scaling is used, the data indicate that this weaker peak corresponds to a constant Strouhal number, *based on cavity length*, of about 0.3. Note the transition occurs at an $l/c$ of about 0.73. This behavior is predicted by Watanabe et al. [17]. They refer to type II modes as $l/c < 0.78$ and type I modes for $l/c > 0.78$. The instability of the type I modes is caused by negative cavitation compliance. Both types of spectral characteristics are more evident at $\alpha \geqslant 6$ deg. These observations are also in agreement with numerical simulations that are being carried out in a companion study by Professor Song and his colleagues.

**Lift Fluctuations.** Recent numerical simulations by Song and He,[2] in a companion study, indicate that pressure side cavitation will occur at positive angle of attack. This was found to be true. Periodic pressure side cavitation is observed to occur under certain conditions. It is conjectured that this is due to lift fluctuations associated with the periodic shedding of cavitation clouds that are large vortical structures. A negative lift fluctuation is associated with each shed structure. Lift fluctuations were observed as predicted.

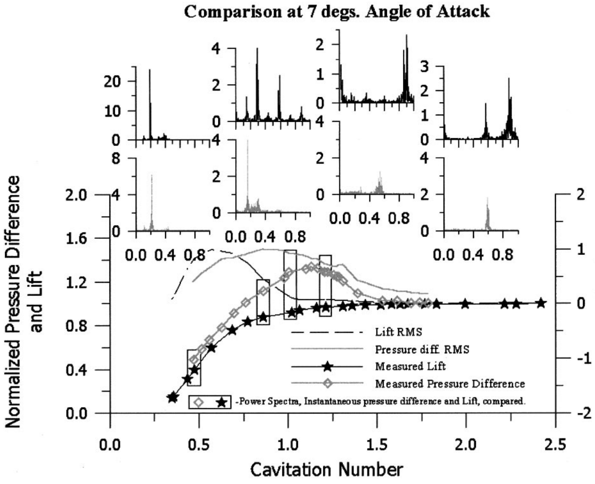

**Fig. 8 Average and dynamic characteristics of lift and pressure difference have been found to correlate well with each other. The abscissa of the power spectra is in Strouhal number, fc/U.**

Further studies were made using the two flush mounted Entran EPX transducers at the base of the foil to measure instantaneous values of the pressure difference between the suction and pressure sides of the foil. The main intention for using this transducer configuration is to have an independent metric for fluctuating lift, since the frequency response of the lift/drag balance may not be high enough to properly resolve the lift dynamics over the frequency range of interest.

In order to verify the use of this transducer configuration as a metric for lift, several tests have been performed. The pressure difference measured by the two transducers under noncavitating conditions were compared with the theoretical lift coefficient. It was found that $\Delta p$ is proportional to $C_l$ as expected. For the dynamic verification, the $\Delta p$ measurements have been correlated with an Entran EGAX accelerometer mounted inside the hydrofoil. The specifics of this verification will not be reported here, but the dynamics in the $\Delta p$ frequency domain did correspond to the *demodulated* accelerometer response in the lift-direction.

In comparing the measured lift with $\Delta p$ as a function of cavitation number, Fig. 8, we can see fundamental differences. At every angle of attack studied, the lift monotonically decreases with decreasing cavitation index, while $\Delta p$ peaks at a certain value of the cavitation index before a sudden breakdown occurs. The increase of $\Delta p$ just before breakdown is due to a more rapid decrease in suction side pressure than the corresponding pressure side pressure. At lower cavitation numbers, the opposite trend occurs, now the pressure side experiences a higher rate in pressure drop as the cavitation index is decreasing. This trend is probably related to the placement of the two pressure transducers. However, the average and dynamic characteristics of lift and pressure difference have been found to correlate well with each other.

Although the exact physics behind the $\Delta p$ measurements has not been completely resolved, $\Delta p$ does appear to be a good indicator of the variation in the cavitation dynamics with $\sigma$. At relatively high values of cavitation number, a relatively high frequency signature is noted, with frequency following an almost linear dependence on cavitation number. At low values of the cavitation number, a strong tone is dominant at a relatively low frequency that is almost independent of cavitation number. This dynamical feature was noted over a range of angle of attack. Measurements to date indicate that the peak in $\Delta p$ occurs at a value of $l/c$ where transition from Type I to Type II modes is predicted by Watanabe (see Fig. 5). It is also interesting to note that the additional spectral content noted in the lift fluctuations at higher values of $\sigma$ is also predicted in the numerical analysis.

---

[2] Unpublished work I.

**Wake Characteristics.** An important consideration is the wake characteristics behind a cavitating hydrofoil. During the current study, LDV measurements were made in the wake of the foil in cavitating and noncavitating conditions. Velocity profiles were obtained at several cross-sections downstream of the trailing edge of the foil. Mean velocity data were obtained and analyzed for a variety of conditions ($\sigma$ and $\alpha$). To date, two different types of analysis have been performed. These analyses provide insight into the problem of predicting bubbly wakes due to cavitation. The basic idea for both methods is an observed increase in measured data rate when bubbles are passing through the LDV measurement volume. This increase is, in general, greater than 10 times that for noncavitating conditions.

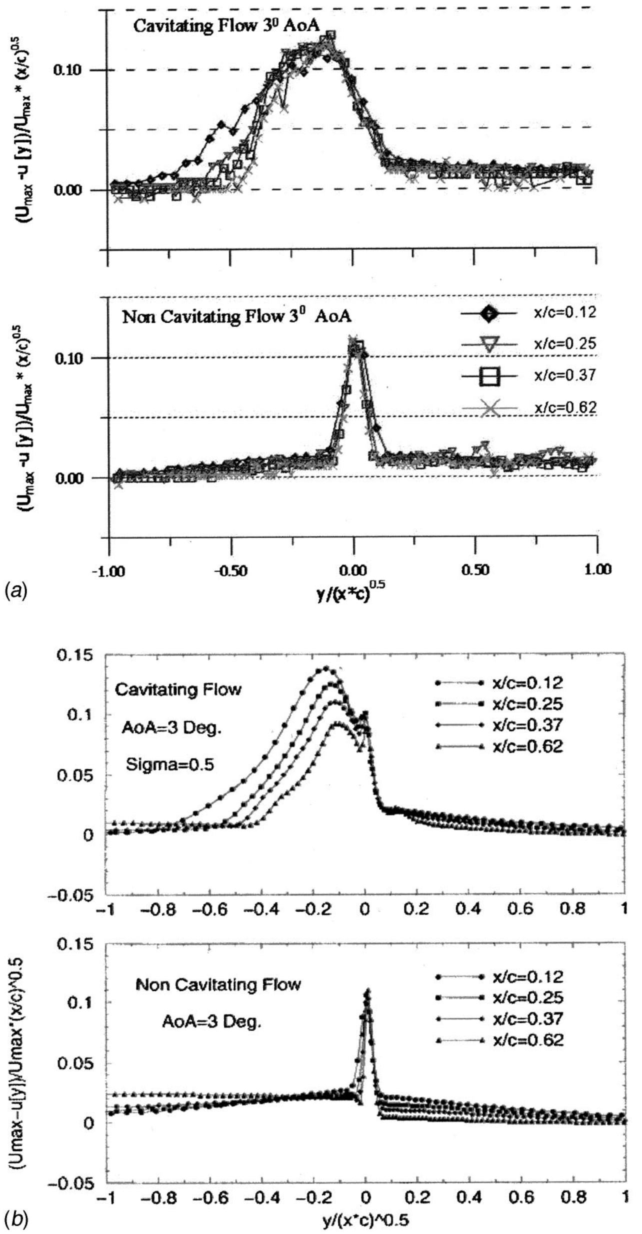

**Fig. 9 Mean velocity comparison with and without cavitation. $y=0$ is taken to be that of maximum velocity deficit for the noncavitating case. (*a*) Measured data. (*b*) Numerical simulations of Song and He.**

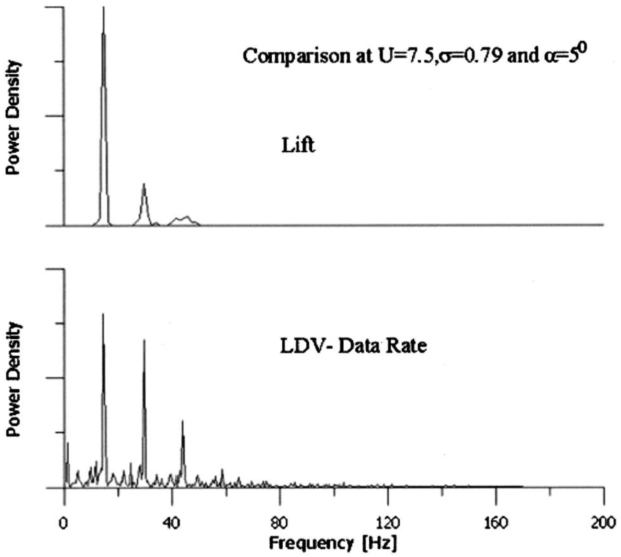

**Fig. 10 Comparison of lift dynamics with the FFT of data rate in a cavitating flow. The fundamental frequency corresponds to a Strouhal number, fc/U=0.15.**

*Wake Velocity Measurements.* Mean velocity profiles for cavitating and non-cavitating conditions are presented in Fig. 9(*a*). The data are presented in a form suggested by the similitude of turbulent wakes

$$\frac{(U_{\text{ref}}-u(y))}{U_{\text{ref}}}\sqrt{\frac{x}{c}}=f\left[\frac{y}{\sqrt{xc}}\right] \qquad (5)$$

where $x$ is distance from the trailing edge, $y$ is the distance normal to the flow measured from the center of the wake, $c$ is the chord length and $U_{\text{ref}}$ is the velocity at the edge of the wake. It is clearly evident that the rate of spreading of the wake is significantly larger under cavitating flow conditions. This effect has been also reported by other workers in the field (Kubota et al. [20]). This is consistent with visual observations. When cloud cavitation is present, large vortical structures containing numerous bubbles are shed into the wake. These clouds of bubbles extend much further in the cross stream direction than the viscous wake associated with noncavitating flow.

Much of the important physics in the process are obscured by the averaging process. While the noncavitating LDV signal resembles a typical turbulence signature, the cavitating signal is skewed towards lower velocity. The strong negative fluctuations in velocity are due to the imprint left by the periodic passage of vortical clouds of bubbles. This imprint of the ''debris'' from the cavitation process extends much further from the wake centerline than a typical viscous wake. This is graphically illustrated in the numerical simulations of Song and He shown in Fig. 11. It should also be pointed out that averaged numerical data also agree very well with data shown in Fig. 9(*a*), for *both cavitating and non-cavitating flow*. This is shown in Fig. 9(*b*). In the case of cavitating flow, it is important to note that the numerical simulations fit the data close to the trailing edge, but deviate from the measurements further downstream. It is conjectured that this is an effect of dissolved gas that has come out of solution. The numerical model considers only vapor that will condense downstream, while gas bubbles will persist in the wake.

It is also natural to conclude that the gas content in the wake will show a cyclic behavior. By also considering the fact that bubbles are counted more efficiently than naturally occurring LDV seeds in the flow, the average velocity will contain more weight from the shed bubbles. This has an effect on the LDV measurements that still needs to be resolved. However, the observation that the wake spreading is significantly more pronounced with cavitation is still qualitatively correct.

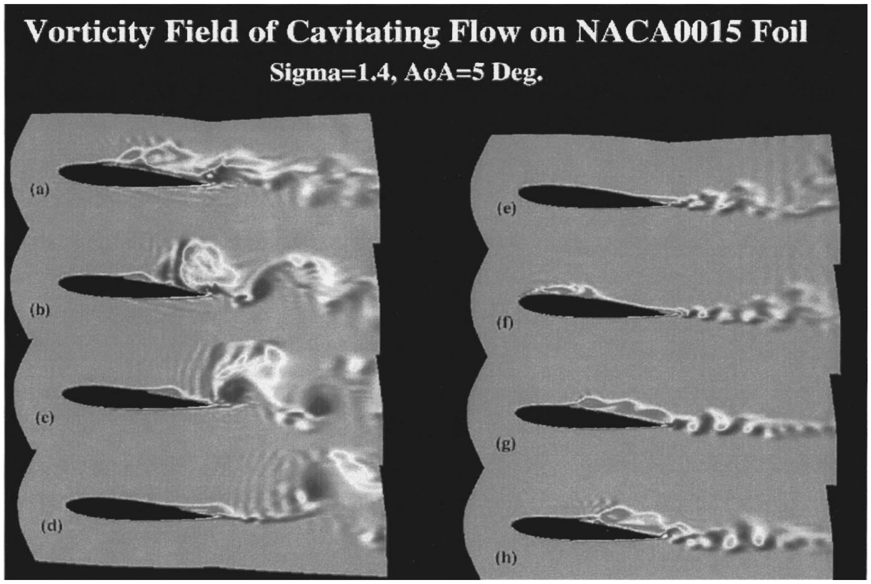

**Fig. 11 Numerical simulations of cavitating flow. Shown is the variation over one cycle of oscillation. Shading denotes vorticity, with dark black being positive.**

*Dynamics of Cavitation Based on LDV Measurements.* The observed cyclical increase in the data rate can be exploited. It was found that a plot of data rate versus time could give additional information regarding cavitation dynamics. The data rate is defined as the time elapsed between two acquired valid samples by the LDV system. In order to process data automatically the described data set is smoothed by creating a curve for the date rate versus time that is uniformly spaced in the time-domain. This was accomplished by using interpolation functions in MatLab. The smoothed set is then processed in a regular FFT algorithm. In comparing the LDV frequency domain fingerprint with the corresponding lift, similarities are found. This is shown in Fig. 10.

When analyzing these data we must keep in mind that the results from the LDV are based on a point measurement. The existence of higher harmonics as seen clearly in the lift spectrum, can be interpreted as an uneven and 180 deg out phase shedding in the spanwise direction of the foil. However, when the same tendency shows up in the data rate spectrum it is reasonable to believe that the super-harmonics are based on a locally occurring cavitation shedding phenomenon. At higher cavitation numbers, the cavitation regimes start to consist of, as visually observed, shedding of apparently independent and smaller swirling cavitating structures. It is very important to note that these features appear to be captured by the numerical simulations. By comparing numerical and experimental data, an approach toward calculating the bubbly wakes behind cavitating hydrofoils is emerging.

## Summary

Cavitation observations were made using a 2D NACA 0015 hydrofoil. It was found that the dynamic characteristics of the cavitation vary considerably with $\alpha$ and $\sigma$. At higher angles of attack, two types of flow unsteadiness are observed. At low $\sigma$, $l/c \geqslant 0.78$, a low frequency shedding of cloud cavitation results in a strong oscillation in lift and $\Delta p$ at a Strouhal number, $fc/U$, of about 0.15. This frequency is relatively insensitive to changes in $\sigma$. As $\sigma$ is raised, $l/c \leqslant 0.78$, the harmonic content of the oscillations changes significantly. A spectral peak at much higher frequency is noted and frequency varies almost linearly with cavitation number. This corresponds to a constant Strouhal number based on cavity length of about 0.3.

Similar behavior is noted in the lift fluctuations. It is significant to note that the harmonic content of the lift fluctuations is more complex, since more harmonics are noted over a range of sigma corresponding to well below cavitation breakdown to slightly lower than cavitation dessinence. At relatively high values of $\sigma$, two frequency peaks in lift are noted that are both higher in frequency than the strong peak noted at low values of $\sigma$. A typical range of sigma over which the marked change in dynamic behavior is noted is $0.5 \leqslant \sigma \leqslant 1.25$. *These observations are in very good agreement with numerical simulations, providing encouragement that even complex cavitation behavior can eventually be simulated*.

Observations in the wake of the cavitating hydrofoil indicate a significant effect of the shedding of clouds of bubbles into the flow. This effect is so strong that fluctuations in the data rate of the LDV measurements can be used to measure the frequency of shedding. Numerical simulations appear to capture much of the fundamental physics, *leading to the conclusion that a model for calculating the bubbly wake behind a cavitating hydrofoil can be developed*.

## Acknowledgments

This work is supported by both the National Science Foundation and the Office of Naval Research. Dr. John Foss is the program manager for NSF, while Dr. Edwin Rood serves as the contract monitor for ONR. Dr. Kjeldsen acknowledges the receipt of a NATO Science Fellowship that partially supported his stay at the St. Anthony Falls Laboratory. The authors would also like to acknowledge the help of Professor S. Watanabe, who generously made the theoretical calculations of cavity length for our test configuration utilizing his computer code.

## References

[1] Yamamoto, K., 1991, ''Instability in a Cavitating Centrifugal Pump,'' JSME Int. J. Ser. II, **34**, pp. 9–17.
[2] Avellan, F., Dupont, P., and Farhat, M., 1991, ''Cavitation Erosion Power,'' *Proc. ASME-JSME Cavitation* '91 Symp., FED-Vol. 116.
[3] Bourdon, P., Simoneau, R., and Lavigne, P., 1989, ''A Vibratory Approach to the Detection of Erosive Cavitation,'' *Proc. ASME Intl. Symp. on Cavitation Noise and Erosion in Fluid Systems*, Arndt, R. E. A., Billet, M. L., and Blake, W. K., eds., FED-Vol. 88.
[4] Avellan, F., Dupont, P., and Ryhming, I., 1988, ''Generation Mechanism and Dynamics of Cavitation Vortices Downstream of a Fixed Leading Edge Cavity,'' *Proc. 17th ONR Symp. on Naval Hydrodynamics*, The Hague, The Netherlands.
[5] Abbot, P. A., Arndt, R. E. A., and Shanahan, T. B., 1993, ''Modulation Noise

Analysis of Cavitation Hydrofoils,'' *Proc. ASME Intl. Symp. on Bubble Noise and Cavitation Erosion in Fluid System*, Winter Annual Meeting, Dec.

[6] Le, Q., Franc, J. P., and Michel, J. M., 1993, ''Partial Cavities: Global Behavior and Mean Pressure Distribution,'' ASME J. Fluids Eng., **115**, No. 2, June.

[7] Le, Q., Franc, J. P., and Michel, J. M., 1993, ''Partial Cavities: Pressure Pulse Distribution around Cavity Closure,'' ASME J. Fluids Eng., **115**, No. 2, June.

[8] Kato, H., Ye, Y. P., and Maeda, M., 1989, ''Cavitation Erosion and Noise Study on a Foil Section,'' *Proc. ASME Intl. Symp. on Cavitation Noise and Erosion in Fluid Systems*, Arndt, R. E. A., Billet, M. L., and Blake, W. K., eds., FED-Vol. 88.

[9] Hackworth, J. V., and Arndt, R. E. A., 1974, ''Preliminary Investigation of the Scale Effects of Cavitation Erosion in a Flowing Media,'' *Cavitation and Polyphase Flow Forum*, ASME.

[10] Hackworth, J. V., 1979, ''Predicting Cavitation Erosion of Ship Propellers from the Results of Model Experiments,'' *Proc. 5th Intl. Conf. on Erosion by Solid and Liquid Impact*, Cambridge, U.K.

[11] Simoneau, R., Avellan, F., and Kuhn de Chizelle, Y., 1989, ''On Line Measurement of Cavitation Erosion Rate on a 2-D NACA Profile,'' *Proc. ASME Intl. Symp. on Cavitation Noise and Erosion in Fluid Systems*, Arndt, R. E. A., Billet, M. L., and Blake, W. K., eds., FED-Vol. 88.

[12] Abbot, P. A., 1989, ''Cavitation Detection Measurements on Francis and Kaplan Hydroturbines,'' *Proc. ASME Intl. Symp. on Cavitation Noise and Erosion in Fluid Systems*, Arndt, R. E. A., Billet, M. L., and Blake, W. K., eds., FED-Vol. 88.

[13] Abbot, P. A., Welsh, J., and Halas, R., 1991, ''Cavitation Noise Investigation of a Pump Turbine,'' *Proc. Intl. Conf. on Waterpower*, Denver, CO, July.

[14] Arndt, R. E. A., Arakeri, V. H., and Higuchi, H., 1991, ''Some Observations of Tip Vortex Cavitation,'' J. Fluid Mech., **229**, pp. 269–289.

[15] Arndt, R. E. A., Ellis, C. R., and Paul, S., 1995, ''Preliminary Investigation of the Use of Air Injection to Mitigate Cavitation Erosion,'' ASME J. Fluids Eng., **117**, Sept. See also *Proc. Symp. on Bubble Noise and Cavitation Erosion in Fluid Systems,* ASME FED Vol. 176, 1993.

[16] Arndt, R. E. A., Ellis, C. R., and Paul, S., 1997, ''The Use of Piezoelectric Film in Cavitation Research,'' J. Hydraulic Eng., **123**, No. 6, pp. 539–548.

[17] Watanabe, S., Tsujimoto, Y., Franc, J. P., and Michel, J. M., 1998, ''Linear Analyses of Cavitation Instabilities,'' *Proceedings of Third International Symposium on Cavitation*, Grenoble, France, Apr.

[18] Acosta, A. J., 1955, ''A Note on Partial Cavitation of Flat Plate Hydrofoils,'' Calif. Inst. of Tech. Hydro Lab Rep.E-19.9.

[19] Qian, S., and Chen, D., 1996, *Joint Time-Frequency Analysis*, Prentice-Hall, NJ.

[20] Kubota, A., Kato, H., Yamaguchi, H., and Maeda, M., 1989, ''Unsteady Structure Measurement of Cloud Cavitation on a Foil Section Using Conditional Sampling Technique,'' ASME J. Fluids Eng., **111**, No. 2, June, pp. 204–210.

**Roger E. A. Arndt**
St. Anthony Falls Laboratory,
University of Minnesota,
Mississippi River at 3rd Avenue S.E.
Minneapolis, MN 55414

**Brant H. Maines**
Lockheed-Martin Aeronautics Company
Fort Worth, TX 76101

# Nucleation and Bubble Dynamics In Vortical Flows

*The cavitation inception process in trailing vortices has been studied for several years. One of the important findings from these studies is the strong sensitivity to nuclei size and number as well as significant viscous effects. In order to understand the nucleation and bubble growth process in more detail, a photographic study was conducted with the aim of developing high quality visualizations of the dynamical growth of bubbles.* [S0098-2202(00)00403-X]

## 1 Introduction

Tip vortex cavitation has been extensively studied in order to reduce or limit its occurrence. McCormick [1] conducted one of the first systematic studies of tip vortex cavitation inception. He developed a semi-empirical relation by assuming that the radius of the vortex core is proportional to the boundary layer thickness on the pressure side. His hypothesis resulted in the relation

$$\sigma_i = (\alpha - \alpha_0)^n \, \mathrm{Re}^m \tag{1}$$

where $\alpha$ is the angle of attack and Re is the Reynolds number. Recent studies carried out over the past decade have refined this relationship

$$\sigma_i = K C_l^2 \, \mathrm{Re}^m - \frac{T}{\frac{1}{2}\rho U^2} \tag{2}$$

where the effects of flow unsteadiness have been suppressed (see Arndt [2] for a review).

McCormick found that $n=1.4$ and $m=0.4$ in Eq. (1). Maines and Arndt [3] found that $0.059 \leqslant K \leqslant 0.073$, depending on the foil cross section, and $m=0.4$ in Eq. (2). This is reasonable agreement with other studies, e.g., Fruman [4]. Arndt and Keller [5] suggest that the discrepancy between the exponent of 1.4 in Eq. (1) and the exponent of 2 in Eq. (2) is due to tension effects that were not considered in McCormick's study.

The dependence of cavitation inception on liquid tension is primarily an effect of nuclei distribution. It is well known that tip vortex flow is very sensitive to the size and number of nuclei in the on-coming flow. Lingeul and Latorre [6,7] indicate that spherical bubbles in the free stream are attracted to the tip vortex with the rate of attraction related to vortex strength, initial bubble size and distance from the core centerline. In a more recent study, Chahine [8] numerically examined bubble growth characteristics during vortex capture and cavitation inception for varying liquid tension. He found significant differences in bubble growth behavior when comparing the capture of bubbles with large growth rates and low surface tension to bubble capture with small growth rates and surface tension. Since nuclei typically range in size from a few microns to several hundred microns in diameter a significant level of tension, $T$, can result before inception occurs (Arndt and Keller [5], Arndt and Maines [9]).

The focus of this paper is to develop a model of bubble growth during cavitation inception within a wing tip vortex for varying water quality. This work summarizes a portion of a larger program on the study of tip vortex cavitation inception. Complementary investigations performed include topics on the viscous effects on cavitation inception (Maines and Arndt [3]), the singing of a fully cavitating vortex (Maines and Arndt [10]), and computational studies to detail the tip vortex flow field (Song and Chen [11]) and bubble dynamics at inception (Wang [12]).

## 2 Experimental Method

Two hydrofoils of elliptic planform with aspect ratio 3 but different cross sections were used for this study. The hydrofoil sections chosen were a NACA $66_2$-415$a=0.8$, and a modified NACA 4215 (designated herein as NACA 4215M). This variation in cross-section results in dramatically different boundary layer characteristics at equal lift coefficients (Maines and Arndt [3]). Two sets of each foil were constructed. The smaller set had a root chord c, of 81 mm and a half span, b, of 95 mm while for the larger set $c=129.4$ mm and $b=152.4$ mm. Both sets of hydrofoils were used for observation of the bubble dynamics and lift and drag measurements. A companion study on ''vortex singing'' associated with fully developed cavitation also used the same setup (Maines and Arndt [10]).

Testing was conducted at three water tunnel facilities, two at the Saint Anthony Falls Laboratory (SAFL) each having a 190 mm square cross section (Arndt et al. [13]) and the other at the Versuchsanstalt für Wasserbau in Obernach, Germany (VFW) with a 300 mm square cross section (Arndt and Keller [5]). Several methods were used to study the bubble dynamics within the tip vortex. These included high speed movies, high speed video, and a newly developed still photographic technique. Noise produced by inception was recorded simultaneously with both the high speed video and still photographic techniques.

Observations of the bubble dynamics were performed for several values of velocity, vortex strength, and water quality. At SAFL, high speed movies were filmed with a Fastax camera at framing rates up to 6000/s (Maines and Arndt [14]). The flow was saturated with air to provide a sufficient cavitation event rate so that each film could record numerous events. Data were collected using the NACA $66_2$-415 at a velocity of approximately 10.3 m/s and at an angle of attack of $(\alpha - \alpha_0) \approx 9$ deg. High speed video were recorded using a Kodak Ektapro 1000 Motion Analyzer and Imager for the NACA 4215M at two different lift coefficients over a range of velocities. Two recording sessions were performed. The test schedule was first conducted in weak water (high air content) and then repeated in strong water after degassing. Data were obtained by fixing the velocity and lowering the pressure until inception occurred. In weak water, inception was anticipated to occur close to the tip, thus a close-up lens was used to increase magnification of the early stages of inception. A standard 50 mm lens was used for recording cavitation in strong water. The lens configuration and lighting restrictions limited framing rates in weak water to 4000 fps. Framing rates in strong water were 6000 fps.

An improved method to examine the bubble dynamics was also developed to complement the high speed movies utilizing a still photographic technique based on the ideas of Keller [15] and Cec-

---

Contributed by the Fluids Engineering Division for publication in the JOURNAL OF FLUIDS ENGINEERING. Manuscript received by the Fluids Engineering Division March 23, 1999; revised manuscript received May 15, 2000. Associate Technical Editor: J. Katz.

cio and Brennen [16]. The high speed movie camera imposed several limitations such as low resolution (16 mm format), a limited maximum framing rate (6000 fps) and a variable elapsed time between each successive frame. Since the duration of each roll of film was only one second, the random nature of cavitation at inception made data collection expensive. This new system however, is based on 35 mm format film to provide high quality images and is activated by individual cavitation events. Equivalent framing rates of 40,000/s have been obtained in practice. Photographs of bubble dynamics for both the NACA 4215M and $66_2$-415 were obtained at two lift coefficients and velocities.

The new system consists of a laser beam ''trip wire,'' a threshold/delay circuit, strobe lighting, and a standard 35 mm camera with extension bellows. As a nucleus or bubble enters the vortex core and cavitates, it passes through the laser beam, scattering light which triggers the delay circuit. At the end of the delay, the strobe lights are flashed. Test section pressure and velocity are recorded simultaneously with the flash of the strobe light using pressure transducers. Approximately 12 pictures were taken for each delay time so bubble characteristics could be ensemble averaged. Several delay times at each test condition then provided a history of the bubble trajectory, and growth behavior during inception. Photographs were obtained using bulb exposure and high speed film. Thus, relatively high cavitation event rates were necessary to reduce the length of time the shutter was open. Great care was taken to reduce reflected laser light or ambient light from over exposing the film. The same laser trip wire technique was used at Obernach where observations were made with the aid of a Kodak 4540 high speed video camera using framing rates as high as 18,000 fps.

Analysis of all photographic data, both video and still, was performed by digitizing each image and subsequently measuring the bubble length, diameter, and location. Still photographs were digitized using a Nikon LS-3510AF 35 mm film scanner at a resolution of 0.012 mm/pixel to 0.022 mm/pixel corresponding to the magnification of the original photo. High speed video images were digitized using a MIROVideo-D1 frame grabber with resolutions of 0.098 mm/pixel for weak water and 0.161 mm/pixel for strong water. A complete uncertainty analysis was performed with details given in Maines [17]. Approximately 500 different cavitation events were studied in total.

## 3 General Observations of Bubble Growth and Capture

The first stage of cavitation inception is capture of a nucleus of critical size by the vortex. The primary source of nuclei is the free stream. However, Arndt et al. [13] have observed that under certain conditions separation bubbles can become supersaturated and provide additional nuclei to the flow. This is important since separation bubbles have been observed to interact with the tip vortex flow as discussed in Maines and Arndt [3].

Upon capture, the shape of a bubble during growth is highly dependent on the surrounding pressure field. During the growth phase, the bubble in a vortex experiences large radial pressure gradients but only small pressure gradients in the axial direction. Thus one can expect bubble growth in a tip vortex to be non-spherical. Maines and Arndt [14] described tip vortex cavitation in terms of four different phases. A spherical nucleus is first drawn into the vortex core, apparently from the free stream, and then grows as a spheroidal bubble. As the bubble travels downstream, growth in the radial direction (perpendicular to the vortex axis) is arrested while the bubble continues to grow at an almost constant rate of change in its length as shown in Fig. 1.

Growth in the axial direction is somewhat analogous to radial growth of a spherical bubble in a constant pressure field. As time increases, the bubble travels downstream while the elongation rate decreases. This behavior is consistent with an adverse axial pressure gradient very close to the tip as observed experimentally by Fruman et al. [4] and in the numerical simulations of Song and Chen [11]. The numerical simulations predict large axial variations in pressure while the experimental data show smaller axial changes. However, both experiment and simulation indicate that the minimum pressure occurs very close to the tip.

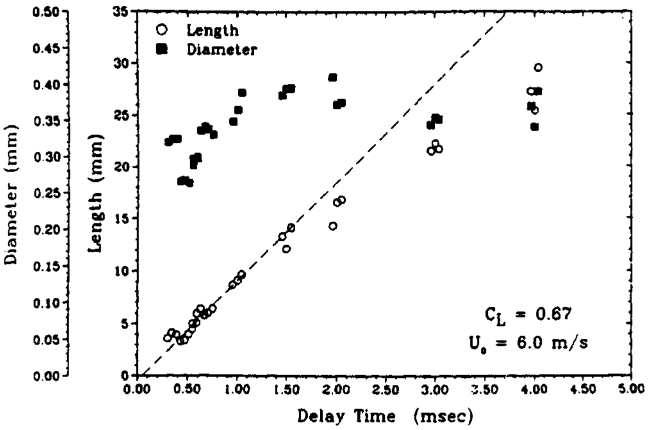

Fig. 1 Typical observed bubble growth, $\sigma=4.7$

Direct experimental observation of capture is extremely difficult due the small size of the nuclei and their velocity. Thus numerical studies have been used primarily to study nuclei capture (Lingeul and Latorre [6,7], Chahine [8] and Song and Chen [11]). Simulations by Lingeul and Latorre indicate that spherical bubbles in the free stream are attracted to the tip vortex with the rate of attraction related to vortex strength, initial bubble size and distance from the core centerline. Capture distance downstream from the wing tip decreases with increasing bubble size and vortex strength and with decreasing initial radial distance from the core. Thus capture near the wing tip requires a flow field with a high nuclei population of large initial radii. This type of nuclei distribution is referred to as weak water.

Chahine's numerical studies extended Lingeul and Latorre's work by using a three-dimensional model which allowed the bubble to deform while being captured. He examined capture of bubbles with large growth rates and low surface tension (herein referred to as Case I), and those with both small growth rates and surface tension (Case II). In Case I, bubbles were observed to spiral around the vortex while being drawn toward the center. During growth, large deformations were observed with a reentrant jet forming directed toward the centerline. The presence of the re-entrant jet indicates that bubble collapse or splitting may occur before elongation as a cylindrical bubble. A possible example of Case I behavior was observed while filming with the high speed movie camera. Figure 2 shows a brief sequence of a large bubble being captured from the pressure side of the foil. The bubble grows spherically outside the vortex core in the first three frames to a large diameter and then dramatically deforms in the last frame. Although no re-entrant jet is observed, a large change in bubble shape occurs once the bubble moves toward the centerline of vortex core.

In Case II of Chahine's numerical study, large nuclei with low growth rates may experience extreme elongation, wrapping around the viscous core region while spiraling inward. Figure 3 is the trajectory of such a case obtained with the high speed video camera. One must imagine the three-dimensional trajectory this plot represents. The bubble enters the frame from the pressure side and rotates about the core centerline twice before being ingested into the center. Video images indicated that growth was slow and became mildly elongated before reaching the vortex centerline.

However, most cavitation events in this study were observed initially along the centerline of the core as a spheroidal or cylindrical bubble which then elongated along the vortex axis. Once on the core centerline, no helical motion was observed in the high

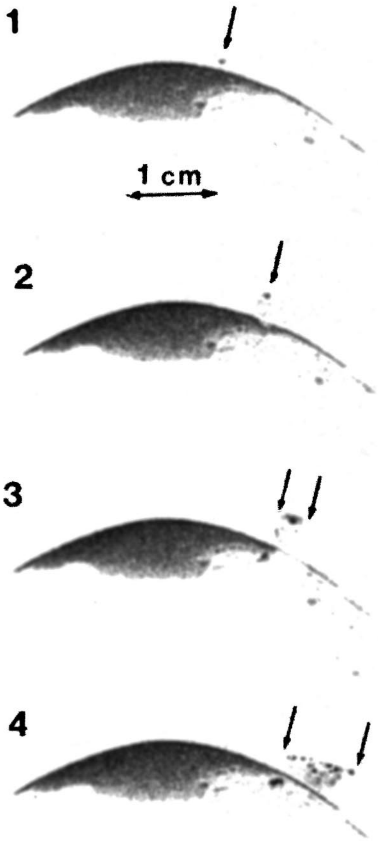

**Fig. 2 Capture of a large nucleus**

speed videos and movies. An example of the latter stages of inception depicted with a series of photographs is shown in Fig. 4. This series was obtained using the laser trip wire technique and clearly shows the cylindrical bubble growth. Each photograph depicts the bubble which best describes the average at that particular time. These photographs provide excellent detail not possible with the high speed video or movie camera. Close examination reveals surface irregularities and two different types of end caps. The bubble tail, downstream end, may either appear somewhat spherical or have a pointed tip. In general, the bubble nose appears somewhat spherical. In addition, these photographs suggest that bubble splitting and bubble coalescence may occur throughout the inception process.

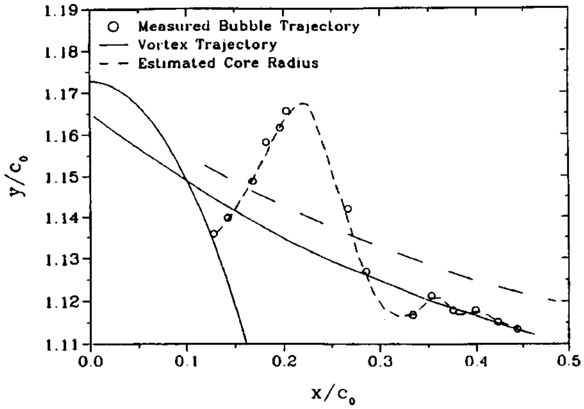

**Fig. 3 Typical nucleus trajectory. (Uncertainty in position ±1 percent)**

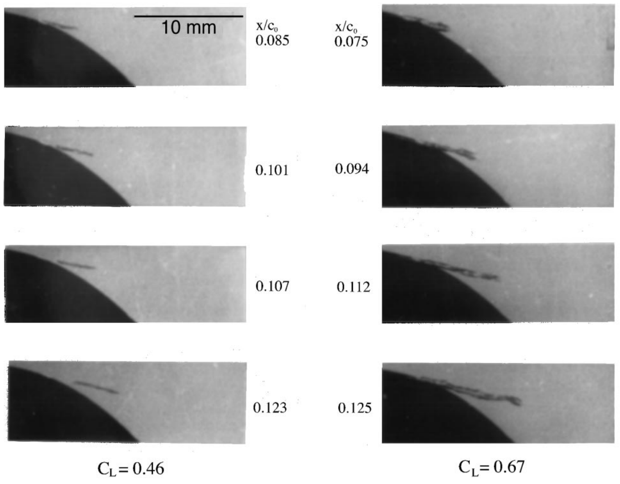

**Fig. 4 Cylindrical bubble growth with different values of $C_l$ (NACA $66_2$-415, U=6 m/s; Uncertainty: $x/c_0$±1 percent, $C_l$±1.5 percent)**

Bubble elongation rates have been observed to vary from 1 to almost 5 times the free stream velocity. At low elongation rates, the bubble slowly elongates while traveling downstream. As the elongation rate increases, the bubble nose is observed to remain stationary or at the largest elongation rates, travel upstream against the flow. Naturally, the tail then travels downstream at velocities much higher than the free stream. Little is known about the modification of the flow field by the presence of the bubble. However, simulations of the single phase flow suggest that significant pressure field variations exist along the bubble. As the bubble extends downstream and enters a higher pressure zone, elongation rates decrease as shown in Fig. 1. This characteristic of bubble growth becomes more pronounced as lift coefficient increases. At this final growth stage, the high speed video images show that a short segment of the bubble tail is likely to split from the main bubble. The split segment is then observed to travel downstream at a rate greater than the main bubble. Small segments continue to break off until a significant portion of the bubble has moved into the high pressure region. At this point, the remainder of the bubble collapses and then rebounds.

Water quality was varied from very weak to quite strong where tension of the order of one atmosphere is sustained before inception occurs. The highest bubble growth rates occurred in strong water. Figures 5 and 6 are samples of 179 plots that were prepared

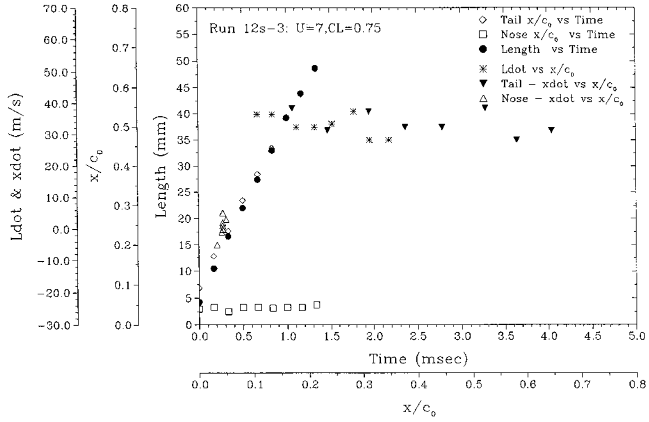

**Fig. 5 Typical bubble growth data obtained in strong water with the high speed video. (Uncertainty Estimates: $x/c_0<\pm 1$ percent, for L=10 mm±3.5 percent, for $\dot{L}$=40 m/s±2.5 percent)**

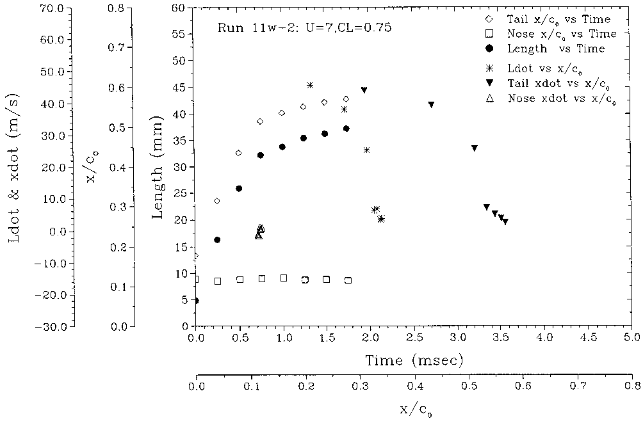

**Fig. 6 Typical bubble growth data obtained in weak water with the high speed video. (Uncertainty Estimates: $x/c_0 < \pm 1$ percent, for $L = 5$ mm±4 percent, for $\dot{L} = 20$m/s±2.0 percent)**

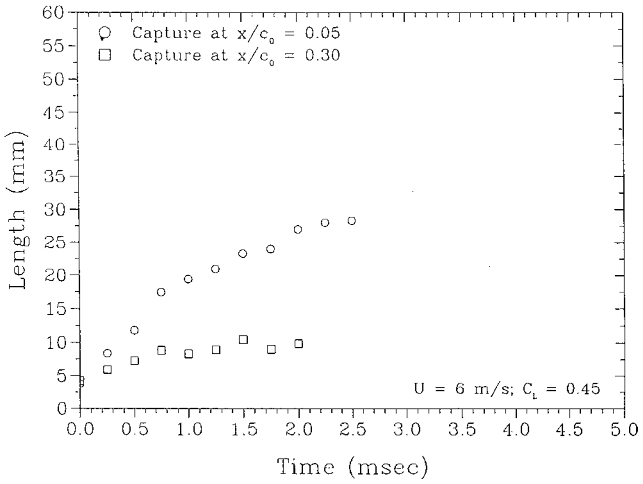

**Fig. 7 Effect of capture location on elongation rates. (Uncertainty Estimates: $x/c_0 < \pm 1$ percent, for $L = 5$ mm±4 percent)**

from the high speed video sequences obtained in one of the SAFL tunnels. The differences in bubble growth in weak and strong water are evident. Note also that the leading edge of the bubble remains relatively fixed in place while the tail of the bubble continues to expand downstream. In addition, bubble growth is influenced by the position of capture. This is illustrated in Fig. 7. Not only is the bubble growth significantly different in weak or strong water, but it is also observed that, in the case of strong water, capture and inception can occur a significant distance downstream. In this case the leading edge of the bubble is observed to move upstream to finally stabilize at the same position observed with weak water.

## 4 Bubble Growth Rates

During the course of these experiments cavitation was generally observed only in the later stages of inception after the captured nucleus began growing as a cylindrical bubble. Each photograph or video frame was digitized, and length, diameter, and position were measured subject to the uncertainty discussed previously. For all conditions and events, once the bubble began rapidly elongating lengthwise no helical motion was observed indicating that the bubble was stabilized. Only lengthwise growth rates will be discussed.

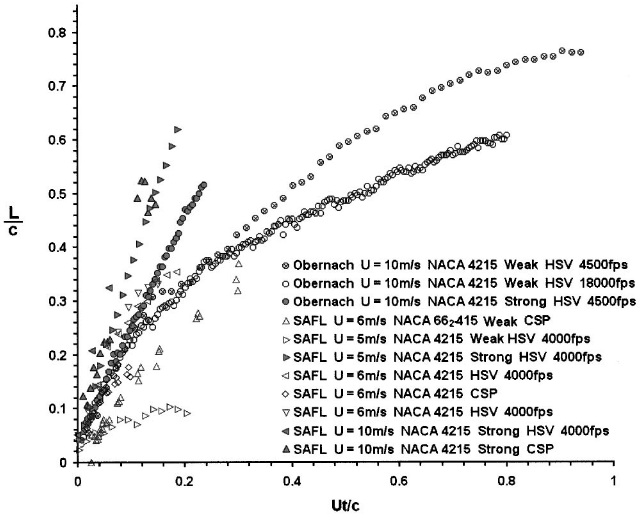

**Fig. 8 Bubble growth data obtained in different facilities with different water quality and different observational techniques. HSV=High Speed Video, CSP=Conditionally Sampled Photos. (Uncertainty Estimates: U=6 m/s±0.75 percent, CSP: L=10 mm ±0.5 percent, HSV Strong: L=10 mm±3.5 percent, Weak: L=10 mm±2 percent)**

There are many factors that enter into bubble growth rate. Figure 8 is a compilation of bubble growth data obtained in different facilities with different water quality and different observational techniques. As already stated, water quality, lift coefficient, and position of capture are important variables. However, there are certain features of the growth process that are generic. It was observed that the bubble radius reaches an equilibrium value while the length changes at a constant rate. This is due to the strong radial pressure gradient that quickly arrests radial growth. Centrifugal forces and surface tension are thus balanced by the internal pressure. The end caps, however, see a pressure differential and thus continue to expand. A simple model was derived in a manner analogous to the derivation of the Rayleigh-Plesset equation utilizing work-energy principles.

As in the case of spherical bubble growth, the kinetic energy was simply related to the wall velocity of the bubble, or simply

$$KE = \frac{1}{2} M v^2 \tag{3}$$

where it is assumed that $M$ is the mass of the fluid displaced by the bubble, and $v$ is equal to the bubble wall velocity. For our case, the bubble expands in the axial direction.

A control surface analysis for the simple case of a bubble elongating in a uniform stream does indicate that for low elongation rates, Eq. (3) may be a reasonable estimate of the kinetic energy in the fluid. Details of this analysis are given in Maines [17]. Thus rate of change of kinetic energy becomes

$$\frac{dKE}{dt} = \frac{1}{2} \dot{M} \dot{L}^2 + M \dot{L} \ddot{L} \tag{4}$$

where $L$ is the bubble length. It is now left to determine the added mass of the cylindrical bubble. For the spherical case, the added mass is easily found. As in the spherical case, the cylindrical bubble is a constant pressure surface, however the radius of curvature varies along the surface. Unfortunately, the location of this surface is in general unknown. Simple representations such as a Rankine body or half body which are not constant pressure surfaces are thus poor models for the cylindrical bubble. To circumvent this problem, we assume that the added mass of the cylindrical bubble is simply related to volume as $M \sim c_m \pi \rho r_b^2 L$. Note, however, that the bubble shape ratio $(L/r_b)$, does not remain constant as is the case for a spherical bubble. This expression for added mass can not be expected to be valid for very long bubbles. As mentioned before, the work done in elongating the bubble occurs only at the spherical end caps, thus

$$Rate\ \ of\ \ Work = 4\pi r_b^2 \Delta p \dot{L}$$

$$where\ \ \Delta p = p_i - p_\infty \tag{5}$$

and $p_i$ and $p_\infty$ are the internal and external pressure respectively. Combining Eqs. (4) and (5) yields

$$c_m \ddot{L} L + \frac{c_m}{2} \dot{L}^2 = \frac{4\Delta p}{\rho} \tag{6}$$

which is very similar in form to the Rayleigh-Plesset equation for spherical bubbles.

In a Rankine vortex, the pressure in the axial direction is constant. Equation (6) is therefore analogous to the Rayleigh-Plesset equation for a constant pressure differential. Thus the elongation rate is[1]

$$\frac{\dot{L}}{U} = \sqrt{\frac{4\Delta p}{c_m \frac{1}{2} \rho U^2}} \tag{7}$$

The added mass coefficient, $c_m$, can be easily estimated from typical experimental values for $\dot{L}$ and $\Delta p$. Numerical simulations and experimental data suggest that $c_m$ is the order of 1. The maximum tension at inception can be determined from the difference between the values of $\sigma$ at inception of strong and weak water. However, this estimate did not always work well particularly in weak water where bubble growth was often observed at values of $\sigma \geqslant \sigma_i$. This is not clearly understood at this time. However, an alternate form of $\Delta p$ can be determined that takes into account to some degree the influence of the bubble on the pressure field in the core of the vortex. Since observations indicate that the bubble radii are always less than the viscous core radius, solid body rotation can be assumed in the region of the bubble. The rate of rotation, $\Omega$ is proportional to the circulation, $\Gamma$. Hence an estimate of the tension is given by

$$\Delta p \simeq \rho \left( \frac{\Gamma}{a^2} \right)^2 r_b^2 \ \ \text{where} \ \ \Gamma = \frac{1}{2} C_L U c_o \tag{8}$$

Substitution of Eq. (8) into Eq. (7) yields

$$\frac{\dot{L}}{U} \sim C_L \frac{r_b}{c_o} \left( \frac{c_o}{a} \right)^2 \tag{9}$$

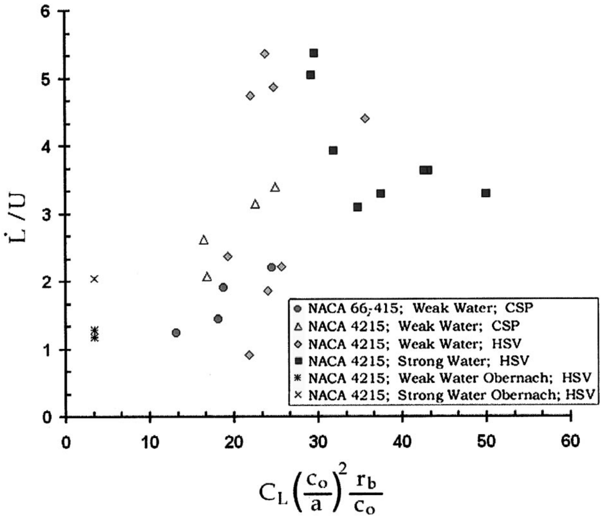

**Fig. 9 Correlation of bubble growth rate with theoretical tension in the vortex. (Uncertainty Estimates in $\dot{L}$/U are driven by the uncertainty in the measurement of bubble radius. CSP $\dot{L}$/U Uncertainty <10 percent, HSV $\dot{L}$/U Uncertainty ∼30 percent)**

As illustrated in Fig. 9, Eq. (9) is used to compare the data shown in Fig. 8. Although there is a general collapse of the data, the scatter is considerable and is disappointing. However, this is not unexpected in light of all the environmental factors that enter into the bubble growth rate. Although the simplicity of Eq. (7) has appeal, it does not describe how much tension can be sustained before inception occurs. Clearly this factor depends on water quality (nuclei content). Arndt and Keller [5] and Maines [17] have observed that, for a given water quality, the sustainable tension increases with increasing lift coefficient. This is illustrated in Fig. 4, where bubble growth is compared at two different lift coefficients, but at the same velocity. Comparison is made at each instant when the cavitation bubble is at the same relative position in the vortex. Both cavity length and bubble radius are larger at the same relative position. This infers that the tension is greater at the higher lift coefficient as suggested by Eq. (9). Measurements of tension over a range of lift coefficient by Arndt and Maines [18] also confirm this observation. They found that tension, normalized to measured tension determined with a cavitation susceptibility device, varied almost linearly with lift coefficient. It is interesting to note that the tension sustained during inception in strong water is only comparable to tension measured with the cavitation susceptibility meter at high lift coefficient.

Only approximate agreement with experiment, using these simple models, is obtained. This suggests that a more complex approach is necessary. As Chahine [8] points out, numerical methods offer the best hope of solution. The main complication of the analytical models arises from the requirement that the bubble is a constant pressure surface with nonspherical end caps. This suggests a surface integral approach or boundary element method.

## 5 Conclusions

A simple, but effective, photographic technique has been developed to obtain high quality images of the growth process at equivalent framing rates as high as 40,000 fps. Bubble growth rates obtained in this manner agreed favorably with those obtained with high speed video. This new still photographic technique provides not only accurate growth information but also provides an excellent library of high quality images of bubble shape during the inception process. This technique circumvents some of the uncertainties encountered with high speed video because of its relatively poor spatial resolution.

With a sufficiently large supply of nuclei, inception is observed to occur close to the tip of the hydrofoil. Bubble growth in the radial direction is rapidly stabilized at a radius that is somewhat smaller than the viscous core. Bubble growth continues in the axial direction at a rate proportional to the free-stream velocity and the square root of the tension sustained before inception.

When the size and number of nuclei are suppressed, relatively large values of tension can be sustained, and the observed location for inception becomes intermittent, with the inception location being equally likely at $0.05 \leqslant x/c \leqslant 1.0$. Numerical calculations (unpublished) confirm this trend.

## Acknowledgments

The authors would especially like to thank Dr. Andreas Keller of the Versuchsanstalt für Wasserbau, Obernach, Germany and Christian Dugue formerly of the Ecole Nationale Superieure de Technique Avancees, Paris, France for their extensive contributions to this project. Mr. Mark Effertz assisted in the analysis of the Obernach high speed video data. This study was supported by

---

[1] Note that for spherical growth, where $\dot{L} = 2\dot{r}_b$ and $c_m = 3$, Eq. (7) reduces to the well-known result obtained with the Rayleigh-Plesset equation.

the Office of Naval Research. Dr. Edwin Rood is the contract monitor. Professor Arndt would also like to acknowledge the support of the Alexander von Humboldt Foundation that made the collaboration with the VFW possible.

## Nomenclature

$a$ = vortex core radius, m
$c$ = chord length, m
$c_m$ = added mass coefficient
$C_l$ = lift coefficient, $C_l = 2l/\rho U^2 c$
$l$ = lift per unit span, N/m
$L$ = bubble length, m
$m$ = exponent for Re
$M$ = added mass, kg
$n$ = McCormick exponent for $\alpha$
$p_v$ = vapor pressure, Pa
$p_\infty$ = pressure at infinity, Pa
$r_b$ = bubble radius, m
Re = Reynolds number, $Uc/v$
$T$ = liquid tension, Pa
$U$ = flow velocity, m/s
$\alpha$ = angle of attack
$\alpha_0$ = angle of zero lift
$\sigma$ = cavitation number, $\sigma = 2(p_\infty - p_v)/\rho U^2$
$v$ = kinematic viscosity, $m^2/s$
$\rho$ = liquid density, $kg/m^3$

## References

[1] McCormick, B. W., 1962, ''On Cavitation Produced by a Vortex Trailing from a Lifting Surface,'' ASME J. Basic Eng., **84** pp. 369–379.

[2] Arndt, R. E. A., 1995, Vortex Cavitation, Chap. 16, *Fluid Vortices*, Green, S., ed., Kluwer, Dordrecht.

[3] Maines, B. H., and Arndt, R. E. A., 1997, ''Tip Vortex Formation and Cavitation,'' ASME J. Fluids Eng., **119**, June.

[4] Fruman, D. H., 1994, ''Recent Progress in the Understanding and Prediction of Tip Vortex Cavitation,'' *2nd Intl. Symp. on Cavitation*, Tokyo, Apr.

[5] Arndt, R. E. A., and Keller, A. P., 1992, ''Water Quality Effects on Cavitation Inception in a Trailing Vortex,'' ASME J. Fluids Eng., **114**, No. 3, pp. 430–438.

[6] Lingeul, P., and Latorre, R., 1989, ''Study on the Capture and Noise of Spherical Nuclei in the Presence of the Tip Vortex of Hydrofoils and Propellers,'' Acustica, **68**, pp. 1–14.

[7] Lingeul, P., and Latorre, R., 1993, ''Study of Nuclei Distribution and Vortex Diffusion Influence on Nuclei Capture by a Tip Vortex and Nuclei Capture Noise,'' ASME J. Fluids Eng., **115**, pp. 504–507. Sept.

[8] Chahine, G. L., 1995, ''Bubble Interaction with Vortices,'' *Fluid Vortices*, Chapter 19, Green, S., ed., Kluwer, Dordrecht.

[9] Arndt, R. E. A., and Maines, B. H., 1994, ''Further Studies of Tip Vortex Cavitation,'' *2nd Intl. Symposium on Cavitation*, Tokyo, Japan.

[10] Maines, B. H., and Arndt, R. E. A., 1997, ''The Case of the Singing Vortex,'' ASME J. Fluids Eng., **119**, June, pp. 271–276.

[11] Song, C. C. S., and Chen, C., 1993, ''Numerical Simulation of Turbulent Flows Around a Hydrofoil,'' *Proc. Sixth Intl. Conf. on Num. Ship Hydrodynamics*, Iowa City, IA, Aug. 2–5.

[12] Wang, Q., 1995, ''Numerical Simulation of Compressibility Effects on Bubble Dynamics,'' Ph.D. dissertation, University of Minnesota.

[13] Arndt, R. E. A., Arakeri, V. H., and Higuchi, H., 1991, ''Some Observations of Tip-vortex Cavitation,'' J. Fluid Mech., **229**, pp. 269–289.

[14] Maines, B. H., and Arndt, R. E. A., 1993, ''Bubble Dynamics of Cavitation Inception in a Wing Tip Vortex,'' *Proc. Cav. and Multiphase Flow Forum*. ASME, NY, June.

[15] Keller, A. P., 1972, ''The Influence of the Cavitation Nucleus Spectrum on Cavitation Inception, Investigated with a Scattered Light Counting Method,'' ASME J. Basic Eng., **94**, pp. 917–925.

[16] Ceccio, S. L., and Brennen, C. E., 1991, ''Observations of the Dynamics and Acoustics of Traveling Bubble Cavitation,'' J. Fluid Mech., **233**, pp. 633–660.

[17] Maines, B. H., 1995, ''Tip Vortex Formation and Cavitation,'' Ph.D. dissertation, University of Minnesota.

[18] Arndt, R. E. A., and Maines, B. H., 1994, ''Vortex Cavitation: A Progress Report,'' Proc. Cavitation and Gas-Liquid Flow in Fluid Machinery and Devices, ASME FED Vol. 190.

# Cavitation Nuclei and Bubble Formation—A Dynamic Liquid-Solid Interface Problem

**Knud A. Mørch**
Associate Professor,
Department of Physics,
Technical University of Denmark,
DK-2800 Kgs. Lyngby,
Denmark

*A model of the formation of cavitation nuclei is developed assuming local detachment of the liquid at locations of concave solid surface topography. The detachment is attributed to diffusion of gas molecules into the interfacial liquid, where the liquid-solid bonds are strained due to interfacial tension in the liquid. Calculations indicate that attached interfacial voids may grow into stabilized cavitation nuclei as a consequence of broad-band resonance, excited by external sources of noise or vibration in the whole range of frequencies up to the MHz regime. The gas content in the liquid and the amplitude and frequency of the sound field determine a balance between rectified diffusion of gas into the void and diffusion out of it due to the excess pressure in the void. In strong acoustic fields and in supersaturated liquids the voids may grow into bubbles that detach and form free gas bubbles.* [S0098-2202(00)01503-0]

## 1 Introduction

Cavitation nuclei were suggested by Harvey et al. [1] to be gas pockets stabilized in conical cracks and crevices of submerged, hydrophobic solid surfaces. The model explains several features characteristic of cavitation inception, but most solid surfaces are not observed to be hydrophobic, and generally they exhibit a wavy surface structure rather than conical cracks and crevices. Further, e.g., the dependence of inception on temperature is not explained by the Harvey model.

In a revised model (Mørch [2]) it is suggested that at locations of *concave* solid surface topography, interfacial liquid tension sets up tensile strain in the bonds between the interfacial liquid and the solid, and that here diffusion of gas molecules from the bulk of the liquid into the orderly structured layer of interfacial liquid causes the strained bonds to break one by one, i.e., locally the interface develops a hydrophobic character. At locations of *convex* topography, interfacial liquid tension supports the liquid-solid contact. Further, the convex topography is expected to weaken the orderly structure outside the first layer of interfacial liquid so that gas molecules have reduced probability of being caught at the interface. This supports a hydrophilic interface character at convex locations. Investigations by force spectroscopy of water-stainless steel interfaces have indicated that interfacial voids occur (Mortensen et al. [3]), but their relation to the topography of the solid is not yet established experimentally.

Diffusion of gas into a void formed by detachment of the liquid from a concave solid surface might explain that at the pressure at which the liquid is saturated with gas, a planar liquid-gas interface developed. Normally, however, such an interface would not satisfy the angle of attachment at the locus of solid-liquid-gas contact, and it would contract to form a convex gas-liquid interface. At static conditions this interface would shrink by preferential diffusion of gas from the void to the liquid. However, as sound and vibrations are present in most flow systems it is appropriate to consider the dynamics of an attached void. The present paper shows that an attached void may be at resonance, or close to resonance at arbitrary frequencies up to the MHz-regime when its radius of contact, the contact angle of the gas-liquid interface and the total void volume are suitably related. In such cases, rectified diffusion may ensure a diffusion balance as required to maintain the void as a stable spherical segment. The calculations reveal that at locations of concave solid surface topography small, almost planar attached voids with a very small sub-volume below the plane of attachment may grow by resonance vibrations into much larger voids shaped as segments of spheres, attached at appropriate contact angles.

The model of cavity nucleation presented in this paper applies to solid-liquid interfaces in general, i.e., it applies to the nuclei at solid surfaces normally termed ''surface nuclei'' and to those ''free stream nuclei'' (Brennen [4]) which develop at solid particles embedded in liquid flows. Often such particles are of diameter up to 25 $\mu$m (Crum [5]), and they may develop cavitation nuclei which cover concave parts of the particle surfaces. It is characteristic that when solid particles are filtered out from the liquid its tensile strength increases greatly (Greenspan and Tschiegg [6]). The model is not relevant to other sorts of free-stream nuclei.

## 2 Interfacial Liquid

Water between surfaces of mica and silica exhibits effects of an orderly structure (Israelachvili and Pashley [7]), and computer simulations of water at Pt(100) and Pt(111) surfaces show that around 300 K the interfacial layer of water molecules has an essentially solid-like structure, while the next layer is relatively orderly and biased toward hexagonal ice-1, though essentially liquid-like. The third layer is only weakly biased toward hexagonal ice-1 (Xia et al. [8]). This supports the theory that water exhibits a more or less ice-like structure also when adjacent to normal solid surfaces. The more orderly the structure, the smaller its coordination number, and it favors the migration of gas molecules into such domains. At concave surface elements, the convergence of the surface normals strains the structure of the interfacial liquid right at the solid surface so that the molecular bonds are weakened. Therefore gas molecules present in the structure tend to break the bonds. Thus, it is expected that at locations of high concave curvature, solid surfaces tend to be hydrophobic and that here an appreciable interfacial liquid tension occurs. At locations of convex curvature, where the surface normals diverge, the orderly character of the structure is reduced already beyond the first interfacial layer of water. This supports hydrophilicity, but inevitably hydrophilicity also depends on the molecular structure of the solid surface itself. These considerations explain why dissolved gas in combination with particles in the liquid (Greenspan and Tschiegg [6]) or bounding solid walls is important for the tensile strength of the liquid.

---

Contributed by the Fluids Engineering Division for publication in the JOURNAL OF FLUIDS ENGINEERING. Manuscript received by the Fluids Engineering Division January 17, 2000; revised manuscript received May 2, 2000. Associate Technical Editor: J. Katz.

## 3 Resonance of an Attached Void

Let us consider an axisymmetric, concave solid surface from which the liquid has detached locally so that a gas filled void has developed, the detached liquid-gas interface being a segment of a sphere of radius $S_o$ and centered at $O$ as shown in Fig. 1. It is attached to the solid along a circle of radius $R_o$, at an angle $\theta_o$ (the segment angle) with the horizontal plane. The void volume consists of the volume of the spherical segment and the subvolume $V_s$ below its plane of attachment. The conditions of resonance for this void will be investigated. The vibrating interface itself and the motion of the liquid outside the interface can be modeled by the volume flow from a dipole as

$$q_d \cdot l = M_o \sin \omega t \tag{1}$$

and superposed by a monopole given as

$$q_m = -\frac{2 \cos \theta_o}{S_o} M_o \sin \omega t \tag{2}$$

which cancels the disturbance from the dipole at $\theta = \theta_o$. Both are located at $O$ and considered for radii $r \geqslant S = S_o + \delta S(\theta,t)$, where $\delta S(\theta,t) = \delta S(\theta,t)_d + \delta S(\theta,t)_m$ is the local liquid-gas interface displacement from equilibrium and the subscripts $d$ and $m$ indicate the components related to the dipole and the monopole, respectively. The local displacement of the liquid-gas interface of the void becomes

$$\delta S(\theta,t) = \delta S(0,t)_d (\cos \theta - \cos \theta_o). \tag{3}$$

The velocity field in the liquid space is given by a radial component as

$$u_r = u(0,t)_d \left[ \cos \theta \left( \frac{S(0,t)_d}{r} \right)^3 - \cos \theta_o \left( \frac{S(0,t)_d}{r} \right)^2 \right] \tag{4}$$

and a tangential component as

$$u_\theta = u(0,t)_d \frac{\sin \theta}{2} \left( \frac{S(0,t)_d}{r} \right)^3. \tag{5}$$

The locus of $u_r = 0$ divides the liquid space into two domains, one having the void-liquid interface $r = S$, $0 \leqslant \theta \leqslant \theta_o$ as its inner boundary. This domain carries the kinetic energy of the liquid corresponding to that of the real liquid in the half-space bounded by the real solid surface. The other domain is the one related to the dipole drain placed in $O$ instead of being a drain at infinity and to the non-relevant part of the monopole field. Actually, the solid surface shifts the tangential velocity into a radial flow, but it does not change the kinetic energy of the liquid field.

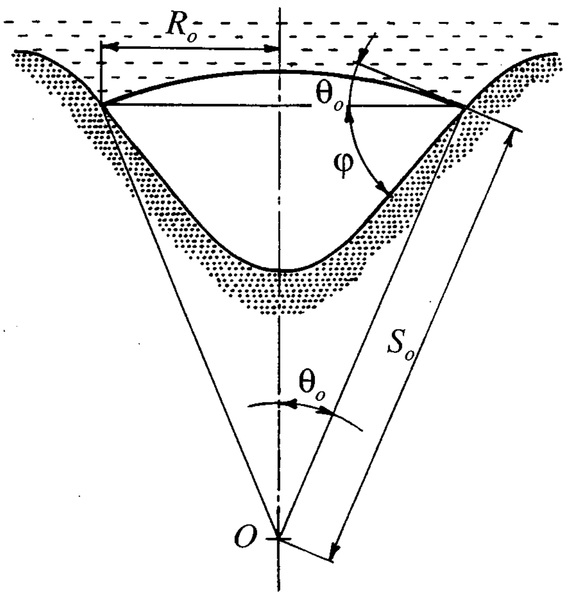

**Fig. 1 Concave solid surface with attached void. The liquid-gas interface is modeled by a dipole superposed by a related monopole in *O*.**

During resonance vibrations of the void an energy balance is maintained between the potential energy of the gas-filled void, its surface energy, and the kinetic energy of the liquid, so that

$$\frac{\partial}{\partial t} \left[ \int_{\Omega_v} E_{\text{pot}} \, d\Omega_v + \int_{A_{\text{surf}}} E_{\text{surf}} \, dA_{\text{surf}} + \int_{\Omega_l} E_{\text{kin}} \, d\Omega_l \right] = 0. \tag{6}$$

The fluctuations of the void volume are given as

$$\begin{aligned} \delta\Omega_v &= \int_{\delta S(\theta,t)=0}^{\delta S(\theta,t)} \int_{\theta=0}^{\theta_o} 2\pi S^2(\theta,t) \sin \theta d\theta d(\delta S(\theta,t)) \\ &= \left( (1-\cos \theta_o)^2 \delta S(0,t)_d + \frac{2}{3} \frac{\delta S(0,t)_d^2}{S_o} (1-\cos \theta_o)^3 \right) \pi S_o^2 \end{aligned} \tag{7}$$

and the changes of the potential energy of the void by

$$\begin{aligned} \int_{\Omega_v} E_{\text{pot}} d\Omega_v &= \int (p_\infty - p_g) d(\delta\Omega_v) \\ &= (p_\infty - p_{g,0}) \pi S_o^2 \left[ (1-\cos \theta_o)^2 \delta S(0,t)_d + \frac{2}{3} (1-\cos \theta_o)^3 \frac{\delta S(0,t)_d^2}{S_o} \right] \\ &\quad + \frac{\kappa p_{g,0}}{\left( \frac{\pi}{3} \right) S_o^3 (2 - \cos \theta_o (1+\cos^2 \theta_o)) + V_s} \cdot \frac{1}{2} \left( \pi S_o^2 \left[ (1-\cos \theta_o)^2 \delta S(0,t)_d + \frac{2}{3} (1-\cos \theta_o)^3 \frac{\delta S(0,t)_d^2}{S_o} \right] \right)^2. \end{aligned} \tag{8}$$

It is assumed that the gas pressure is expressed as $p_g = p_{g,0} (\Omega_{v,0}/\Omega_v)^\kappa$.

The change of the surface energy of the void due to its vibration is determined from

$$\begin{aligned} \int_{\delta S(0,t)_d=0}^{\delta S(0,t)_d} E_{\text{surf}} \, dA_{\text{surf}} &= \int_{\delta S(0,t)_d=0}^{\delta S(0,t)_d} \sigma \frac{d}{d(\delta S(0,t)_d)} \left( \int_{\theta=0}^{\theta_o} S^2 \sin \theta 2\pi d\theta \right) d(\delta S(0,t)_d) \\ &\simeq 2\pi\sigma S_o^2 \left( (1-\cos \theta_o)^2 \frac{\delta S(0,t)_d}{S_o} + \frac{(1-\cos \theta_o)^3}{3} \left( \frac{\delta S(0,t)_d}{S_o} \right)^2 \right). \end{aligned} \tag{9}$$

Finally, the kinetic energy within the volume $\Omega_l$ bounded by the void surface $r=S$, $0\leqslant\theta\leqslant\theta_o$ and by $u_r=0$, which by Eq. (4) implies $\cos\theta=r\cdot\cos\theta_o/S(0,t)_d$, is

$$\int_{\Omega_l} E_{\text{kin}}d\Omega_l=\int_{\theta=0}^{\theta_o}\frac{1}{2}\rho\int_{r=S(0,t)_d}^{S(0,t)_d\cos\theta/\cos\theta_o}(u_r^2+u_\theta^2)2\pi r^2\sin\theta dr$$

$$=G(\theta_o)\pi\rho u(0,t)_d^2 S(0,t)_d^3 \tag{10}$$

for $\theta_o\leqslant 90$ deg, and where

$$G(\theta_o)\simeq\frac{1}{6}-\frac{5}{8}\cos\theta_o+\cos^2\theta_o+\cos^3\theta_o\left(-\frac{13}{24}+\frac{1}{4}\ln\cos\theta_o\right). \tag{11}$$

Inserting Eqs. (8)–(10) into Eq. (6) and using $p_\infty-p_{g,0}=-2\sigma/S_o$ we find

$$\frac{d^2\delta S(0,t)_d}{dt^2}=-H(\theta_o)\cdot K(V_s^*,\theta_o,S_o)\delta S(0,t)_d \tag{12}$$

where $V_s^*=3V_s/(2\pi S_o^3)$ and in which

$$H(\theta_o)\simeq\frac{(1-\cos\theta_o)^4}{1-\frac{15}{4}\cos\theta_o+6\cos^2\theta_o+\cos^3\theta_o\left(\frac{3}{2}\ln\cos\theta_o-\frac{13}{4}\right)}. \tag{13}$$

$H(\theta_o)$ comes from the kinetic energy term and is positive for all $\theta_o$ while

$$K(V_s^*,\theta_o,S_o)$$

$$=\frac{9\kappa p_\infty}{2\rho S_o^2\left(1-\frac{\cos\theta_o}{2}(1+\cos^2\theta_o)+V_s^*\right)}+\frac{\sigma}{\rho S_o^3}$$

$$\times\left(\frac{9\kappa}{1-\frac{\cos\theta_o}{2}(1+\cos^2\theta_o)+V_s^*}+4-\frac{8}{1-\cos\theta_o}\right) \tag{14}$$

may be positive as well as negative in dependence of the void parameters. The resonance frequency $f_o$ of the attached void is expressed as

$$f_o=\frac{1}{2\pi}(H(\theta_o)\cdot K(V_s^*,\theta_o,S_o))^{1/2} \tag{15}$$

and approaches zero at certain conditions. In such cases the normally high resonance frequency degenerates and the void becomes sensitive to the whole spectrum of low frequency pressure fluctuations characteristic of general noise and vibrations. A broad-band resonance occurs.

## 4 Discussion

We consider a hemispherical void, $\theta_o=90$ deg, and introduce its radius of attachment expressed as

$$R_o=S_o\sin\theta_o. \tag{16}$$

Eq. (15) now becomes

$$f_o=\frac{1}{2\pi}\left[\frac{9\kappa p_\infty}{2\rho R_o^2(1+V_s^*)}-\frac{\sigma}{\rho R_o^3}\left(4-\frac{9\kappa}{1+V_s^*}\right)\right]^{1/2}, \tag{17}$$

which for the case of water-solid interfaces at atmospheric pressure and room temperature and on the assumption of $\kappa=1$ is shown in Fig. 2 at selected segment sub-volumes $V_s^*$. It appears that for $V_s^*>1.25$ broad-band resonance occurs. Close to this limiting value broad-band resonance is connected to voids with very small contact radii $R_o$. As $V_s^*$ is increased $R_o$ increases. When $V_s^*<1.25$ the resonance frequencies are very nearly those of free spherical gas bubbles of radius $R_o$ (Minnaert [9]), shown as the curve ''Minnaert.''

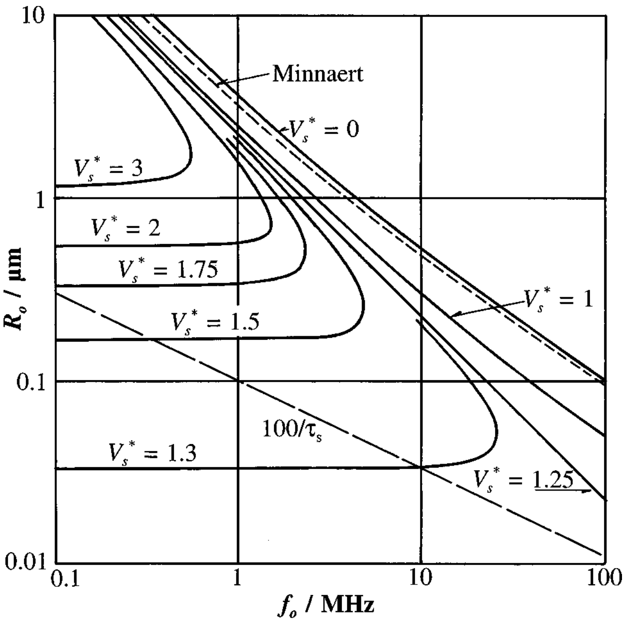

**Fig. 2 Resonance map for hemispherical voids in water at concave solid surface elements. $p_\infty=1\cdot10^5$ Pa, $\sigma=0.075$ N/m, $\kappa=1$.**

At static conditions a free (spherical) gas bubble shrinks and it dissolves in a time $\tau_s$ (Epstein and Plesset [10]), but at oscillating pressures of frequency high compared to $\tau_s^{-1}$ rectified diffusion of gas into the bubble may balance its shrinking. Likewise, an attached hemispherical void will shrink at static conditions essentially as the free bubble does, but in cases of resonance vibrations the shrinking may be balanced by rectified diffusion. A correct estimate of the conditions for achieving a balance depends on the resonance conditions and the gas content in the liquid. In Fig. 2 the curve $100/\tau_s$ is shown to indicate a tentative frequency limit above which the voids may grow into stabilized cavitation nuclei, while below such a limit they shrink.

Now, the hemispherical void represents the limit of a self-stabilizing void. At liquid detachment from a solid the hydrophobic interface conditions implicate a small contact angle $\theta_o$. Therefore, also small values of $\theta_o$ are most important in the study of the growth and shrinking of interfacial voids.

Considering Eq. (15) for lower values of $\theta_o$ we find qualitatively similar resonance curves, exemplified by Fig. 3 in which $\theta_o=5$ deg and Fig. 4 in which $\theta_o=45$ deg. Here broad-band resonance occurs even for vanishing $V_s^*$. A physically flat solid surface does not give rise to detachment, but at solid surfaces with roughness initial detachment may arise locally at the bottom of concave surface elements. When gas molecules enter the interfacial liquid and locally make it hydrophobic so that initial liquid detachment occurs, $V_s^*$ is inevitably small, but from Fig. 3 we see that even then the liquid-gas interface may be stabilized by broad-band resonance at small $\theta_o$ corresponding to the local degree of hydrophobicity. With a large content of dissolved gas in the liquid, the rectified diffusion is strong and the voids may grow and stabilize at large $R_o$ and $\theta_o$ as apparent from Figs. 4 and 5.

Figure 5 presents curves of broad-band resonance of attached cavities relating $\theta_o$ and $R_o$ for selected $V_s^*$. We see that by the influence of sound and vibrations, essentially planar attached voids, developed by detachment of the liquid from hydrophobic concave solid surface structures, and initially with a very small radius $R_o$, may develop into significantly larger voids of consid-

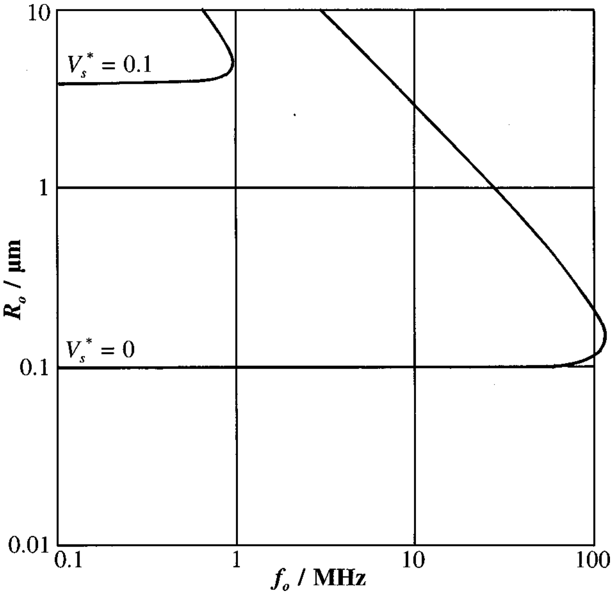

**Fig. 3 Resonance map for spherical segment of angle $\theta_o$=5 deg**

erable void curvature if the solid surface topography leads to an increased sub-volume $V_s^*$ and the voids are attached at large contact angle. We notice that the actual liquid-gas-solid contact angle is the sum of $\theta_o$ and the local angle of the solid surface with the plane of void attachment $\varphi$. Such voids may be in balance at the locus of attachment if the strength of the liquid-solid bonding changes with the interface curvature from hydrophobic contact at concave locations to hydrophilic contact at convex locations as argued in the above considerations of gas diffusion into the interfacial liquid.

We also notice that if an existing void shrinks, e.g., due to a reduced noise level, it does not necessarily dissolve, but it may survive as a smaller void of reduced sub-volume, still with a significant angle of attachment.

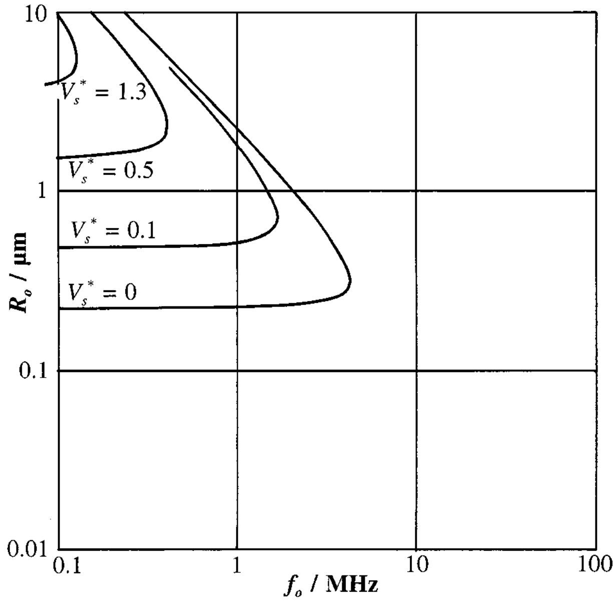

**Fig. 4 Resonance map for spherical segment of angle $\theta_o$=45 deg**

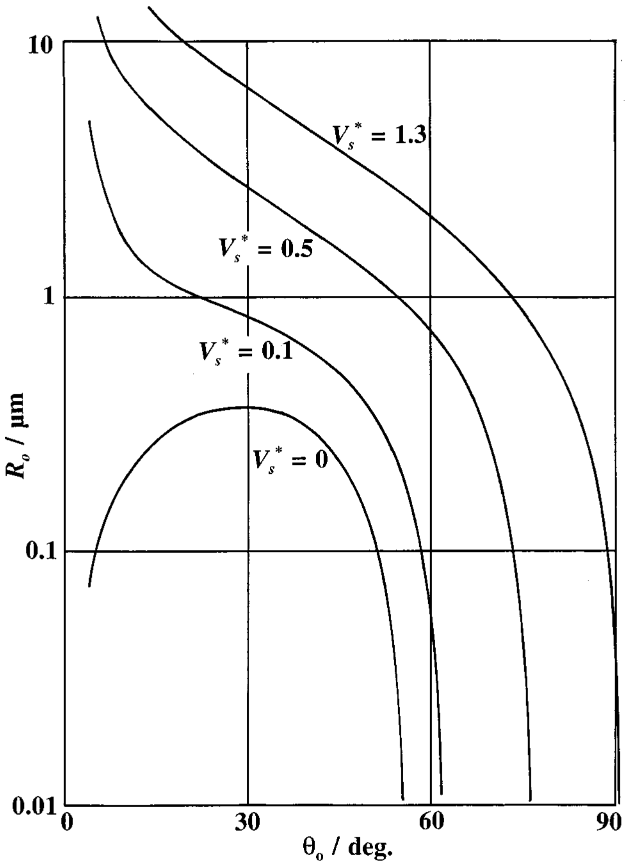

**Fig. 5 Graph of broad-band resonance conditions in water, relating void attachment radius $R_o$ to segment angle $\theta_o$ and segment sub-volume $V_s^*$**

The sound level is decisive for the diffusion balance, but even a small attached void may have a relatively large radius of curvature of its water-gas interface, so that only a small excess pressure has to be maintained in the void, and at broad-band resonance a threshold of rectified diffusion (Safar [11]) may vanish. Stabilized voids act as cavitation nuclei which at exposure to a sufficient tensile stress in the liquid explode into large vapor cavities. We see that these voids are dependent on numerous parameters related to the solid surfaces and to the liquid as well as to the dynamic conditions present in the system considered. At normal conditions of operation most of these parameters are highly statistical, and it explains that the tensile strength of water—and of liquids in general—is a highly statistical quantity. In flow systems, such as water tunnels, the noise level may be quite low, and then shrinking of the interfacial voids could be expected to result in a high tensile strength of the water within a fairly short period of time, i.e., at sufficient distance from the propeller. This is not observed and it might be conjectured that a void, already grown to a large size on a solid-liquid interface of multiple large and fine scale roughnesses may be prevented from shrinking due to local pinning at the fine scale roughnesses along its contour of attachment.

In ultrasonic cleaning facilities it is observed that large, e.g., millimeter sized bubbles form on the container walls at specific locations. These locations are interpreted to be corrugations that supply a significant sub-volume below relatively large, attached voids which have not reached diffusion balance when they have grown to a hemispherical form at the moderate frequencies applied, usually in the 20–40 kHz range. Therefore they grow further and develop into bubbles attached to the solid surfaces. Small voids do not reach hemispherical form at these relatively low frequencies, and therefore they do not develop into regular bubbles.

When intensive, high frequency sound is applied, e.g., 1 MHz, large numbers of small bubbles are generated throughout the liquid. These bubbles are supposed to develop from sites on the numerous micrometer and sub-micrometer size particles normally present in a liquid. The initial voids formed here must be notably smaller than the particles themselves. It requires high frequencies for such voids to develop beyond a hemispherical form and expand into small free bubbles as actually observed in the bulk of water.

It is apparent from the above analysis that attached voids developed at solid surfaces are closely related to the gas content of the liquid and to the roughness of the surfaces. This agrees well with experimental observations of the influence of these parameters on the tensile strength of water and on cavitation inception (Briggs [12], Keller [13,14]). A remarkable influence of temperature on the tensile strength of water is also observed (Briggs [12], Keller [13]). A maximum value is found at about 10°C in highly filtered water as well as in technically cleaned water, though the absolute values of maximum tensile strength in the two cases are very different. The strength decreases sharply toward very low values as the freezing point is approached, but only slowly at increase of the temperature. The present model of void formation offers an explanation based on the molecular bonding in the interfacial liquid at locations of convex solid surface topography. Here the number of liquid layers showing bias toward hexagonal ice-1 structure is expected to increase when the temperature approaches the freezing point. Therefore, at locations of concave structure, the liquid layers closest to the solid surface are increasingly strained, and the molecular bonds break and allow void formation already when the liquid is exposed to a low tensile stress. The effect of an increased straining in the interfacial liquid structure set up by reduction of the temperature below 10°C is much stronger than that obtained by increasing the temperature correspondingly, because an increase of temperature affects only the kinetic energy of the molecular vibrations, not the number of orderly structured liquid layers.

## Acknowledgment

The author thanks Dr. A. P. Keller for valuable discussions on the tensile strength of liquids and Mr. A. Northeved for discussions on cavitation in high frequency sound fields.

## Nomenclature

$A_{\text{surf}}$ = surface area
$E_{\text{kin}}$ = kinetic energy per unit volume
$E_{\text{pot}}$ = potential energy per unit volume
$E_{\text{surf}}$ = energy per unit surface area
$f_o$ = resonance frequency
$p_g, p_{g,o}$ = gas pressure in void, mean pressure
$p_\infty$ = far field pressure
$R_o$ = contact radius of void
$r$ = radial coordinate
$S, S_o$ = radius of curvature of liquid-gas interface, mean radius
$t$ = time
$u_r$ = radial velocity
$u_\theta$ = tangential velocity
$u(0,t)_d$ = velocity of liquid-gas void interface induced by dipole for $\theta=0$
$V_s$ = void volume below plane of attachment (subvolume of spherical segment)
$V_s^*$ = $V_s$ normalized by the volume of a hemisphere of radius $S_o$
$\delta S(\theta,t)$ = displacement of liquid-gas void interface
$\delta S(\theta,t)_d$ = displacement of liquid-gas void interface by dipole
$\delta S(\theta,t)_m$ = displacement of liquid-gas void interface by monopole
$\theta$ = angular coordinate
$\theta_o$ = angle of liquid-gas interface at contact point =angle of spherical segment
$\kappa$ = polytropic exponent of the gas in the void
$\rho$ = density of the liquid
$\sigma$ = surface tension constant of the liquid
$\tau_s$ = time for a spherical cavity to go into solution
$\varphi$ = local inclination of solid surface relative to plane of void attachment
$\Omega_l$ = liquid space (volume)
$\Omega_v$ = void space (volume)
$\omega$ = angular frequency

## References

[1] Harvey, E. N., Barnes, D. K., McElroy, W. D., Peace, D. C., and Cooper, K. W., 1944, ''Bubble Formation in Animals. I. Physical Factors,'' J. Cell. Comp. Physiol., **24**, pp. 1–22.
[2] Mørch, K. A., 1992, ''A Molecular Approach to Cavitation Inception,'' 2éme Journees Cavitation. Societe Hydrotechnique de France, Comite Technique—Colloque d'Hydrotechnique, Session No. 144, Paper 1, 18.3.1992.
[3] Mortensen, N. A., Kühle, A., and Mørch, K. A., 1998, ''Interfacial Tension in Water at Solid Surfaces,'' Proceedings 3rd International Symposium on Cavitation, Michel, J. M., and Kato, H., eds., Grenoble, France, Vol. 1, pp. 87–91.
[4] Brennen, C. E., 1995, *Cavitation and Bubble Dynamics*, Oxford University Press, Oxford, U.K. and New York.
[5] Crum, L. A., 1980, ''Acoustic Cavitation Thresholds in Water,'' *Cavitation and Inhomogeneities in Underwater Acoustics*, Lauterborn, W., ed., Springer Series in Electrophysics, Vol. 4, pp. 84–89, Springer-Verlag, Berlin.
[6] Greenspan, M., and Tschiegg, C. E., 1967, ''Radiation-Induced Acoustic Cavitation: Apparatus and Some Results,'' J. Res. Natl. Bur. Stand., Sect. C, **71C**, pp. 299–312.
[7] Israelachvili, J. N., and Pashley, R. M., 1983, ''Molecular Layering of Water at Surfaces and Origin of Repulsive Hydration Forces,'' Nature (London), **306**, pp. 249–250.
[8] Xia, X., Perera, L., Essmann, U., and Berkowitz, M. L., 1995, ''The Structure of Water at Platinum/Water Interfaces, Molecular Dynamics Computer Simulations,'' Surf. Sci., **335**, pp. 401–415.
[9] Minnaert, M., 1933, ''On Musical Air-Bubbles and the Sound of Running Water,'' Philos. Mag., **16**, pp. 235–248.
[10] Epstein, P. S., and Plesset, M. S., 1950, ''On the Stability of Gas Bubbles in Liquid-Gas Solutions,'' J. Chem. Phys., **18**, pp. 1505–1509.
[11] Safar, M. H., 1968, ''Comment on Papers Concerning Rectified Diffusion of Cavitation Bubbles,'' J. Acoust. Soc. Am., **43**, pp. 1188–1189.
[12] Briggs, L. J., 1950, ''Limiting Negative Pressure of Water,'' J. Appl. Phys., **21**, pp. 721–722.
[13] Keller, A. P., 1982, Schlussbericht über das Forschungsvorhaben ''Beginnende Kavitation, Zugspannungen in Flüssigkeiten,'' 2. Teil, Versuchsanstalt für Wasserbau und Wassermengenwirtschaft, der Technischen Universität, München/Obernach, Germany.
[14] Keller, A. P., 1988, ''Cavitation Scale Effects,'' AGARD Report 827, High Speed Body Motion in Water, NATO.

# Effects of Air Entrainment on the Ability of Air Vessels in the Pressure Surge Suppressions

**T. S. Lee**
Associate Professor,
Mechanical and Production
Engineering Department,
National University of Singapore,
Singapore 119260
e-mail: mpeleets@nus.edu.sg

*This paper describes a new and efficient model for the study of air entrainment effects on the responses of a typical horizontal air vessel. The effects of air entrainment on the pressure surges for unsteady flow in a pipeline system were investigated. Studies showed that entrained, entrapped, or released gases in the transient fluid system tend to amplify the first pressure peak, increase surge damping, and produce asymmetric pressure surges with respect to the static head. The pressure surges showed longer periods of down-surge and shorter periods of upsurge. The upsurge was considerably amplified and down-surge was marginally reduced when compared with the gas-free case. With the horizontal air vessel installed, studies showed that the effects of air entrainment on the maximum transient pressure can be considerably reduced with an appropriately configured air vessel.* [S0098-2202(00)00203-0]

## Introduction

When an air vessel is installed in a pumping system, it is usually used as an extreme pressure surge protection device for the unsteady flow conditions (Clarke [1]). For the present study, the air vessel has the shape of a horizontal cylinder and it is placed immediately downstream of the pumps and the check valves. It is designed to turn high frequency, high pressure transients into low frequency, low pressure oscillations in the fluid system. The horizontal air vessel has a number of advantages over both the open top surge tank and the valve type surge suppressor. The air vessel can be built smaller than the open surge tank with greater damping effect introduced by the compressibility of the enclosed air. Environmental problems associated with ambient pollution and debris in the open surge tank are avoided and less space is generally required. And, in addition, for concealment in flat terrain, the horizontal air vessel may prove more attractive as the required height clearance is much lower than that of the vertical air vessel. When pumps trip, fluid is drawn from the vessel into the pipeline and the volume of air within the vessel expands, causing the air pressure in the air vessel to drop. The rate at which the pressure in the air vessel drops is dependent on the initial air volume, the thermodynamic process which the air goes through, and the rate at which the liquid is being drawn out of the vessel. The ESDU data and Graze and Horlacher [2] charts provide an estimate of the initial air volume, $\mathrm{Vol.}_{\mathrm{ref}}$ required by the air vessel. This initial estimated volume of the air vessel is usually very much over estimated and will require computer simulations to optimize its size and configuration (Martin [3]). Charts (Fok [4]) can also be used for the preliminary sizing of an air vessel needed for a pipeline system. These charts can be used to determine the size of an air vessel for a pipeline to keep the maximum and minimum pressures within designed limits (Evans and Crawford [5]). The air vessel volume is obtained by giving an allowance factor to the initial air volume. This allowance is typically in the range of up to 25 percent. Throttling is usually not included in the above selection of the air vessel size. Graze and Horlacher [2] showed that air chambers are under utilized if optimum bypass throttling is not included with the air chamber installation. However, throttling is usually done on inflow as throttling on outflow into the pipeline might cause column separation.

## Effects of Air Entrainment on Air Vessel Responses

For the air vessel installed on the pipeline at a point B in Fig. 1 the general governing equations can be obtained from Fox [6] and Wylie et al. [7]. However, at any instant of time, the effects of air entrainment on the air vessel performances is newly modeled here through its continuity equation as

$$A_P V_{i-1}^{k+1} = A_t(h_t)\,\frac{dh_t}{dt} + A_P V_{i+1}^{k+1} + K_t \varepsilon_i^{k+1} A_p (V_{i-1}^{k+1} - V_{i+1}^{k+1}) \tag{1}$$

where $K_t \varepsilon_i^{k+1} A_p (V_{i-1}^{k+1} - V_{i+1}^{k+1})$ is due to the effects of air entrainment. The value of $Kt$ is of the order of 1.4 obtained through field measurements (Lee and Cheong [8]).

For the air column inside the air vessel, the general Gas Law governing the compression and expansion of the volume of air in the tank is given by (Fox [6])

$$P_a^{k+1}[V_a^{k+1}]^n = P_a^k [V_a^k]^n \tag{2}$$

In estimating the gas expansion characteristics within the air vessel, an appropriate value of the polytropic coefficient of expansion must be selected. Values in the range 1.0 to 1.4 are normally utilized for $n$. Thorley and Lastowiecki [9] recommended a value of 1.3 to 1.4 if little or no heat transfer is expected and values closer to 1.0 if significant heat transfer occurs, effectively rendering the process isothermal. To restrict the inflow into or outflow from the air chamber, an orifice is usually provided between the

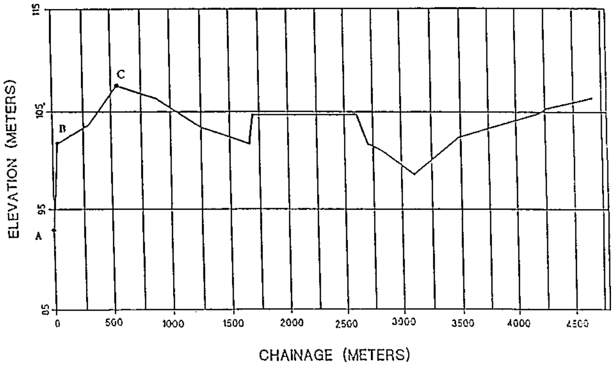

Fig. 1 Pipeline profile

---

Contributed by the Fluids Engineering Division for publication in the JOURNAL OF FLUIDS ENGINEERING. Manuscript received by the Fluids Engineering Division April 8, 1999; revised manuscript received March 10, 2000. Associate Technical Editor: J. Katz.

chamber and pipeline. A ratio of 2.5:1 between the orifice losses for the small inflow and outflow is commonly used. Allievi [10], Angus [11], and Evans and Crawford [5] are some of the historical works on the use of air chambers in pumping stations to control transients generated by power failure to the pumps. Equation (2) is valid only over a very short interval of time specified by a $\Delta t$ value. The value of $n=1.0$ (isothermal) is used for ''slow'' processes while $n=1.4$ (adiabatic) is assumed for ''fast'' transient systems. The difference in the extreme transient pressure response of a fluid system can be of the order of 20 percent (Graze and Horlacher [2]) for different values of *n* used.

The wave speed for the fluid system with air entrainment is given through a newly modified model of Lee and Pejovic [12]

$$a_i^k=\left[\rho_w(1-\varepsilon_i^k)\cdot\left(\frac{1}{K}+\frac{\varepsilon_i^k}{np_i^k}+\frac{cD}{eE}\right)\right]^{-1/2} \tag{3}$$

The transient computation of the above fraction of air content in Eq. (3) along the pipeline depends on the local pressure and local air volume and is given by

$$\varepsilon_T^{k+1}=\left(\frac{p_i^k}{p_i^{k+1}}\right)^{1/n}\varepsilon_i^k \quad \text{and} \quad \varepsilon_0^{k+1}=\left(\frac{p_0}{p_i^{k+1}}\right)^{1/n}\varepsilon_0; \tag{4}$$

(a) for $p_i^{k+1}\geqslant p_g$ and $\varepsilon_T^{k+1}\leqslant\varepsilon_0^{k+1}+\alpha_{gr}\varepsilon_g$: $\quad \varepsilon_i^{k+1}=\varepsilon_T^{k+1}$ (4*a*)

(b) for $p_i^{k+1}\geqslant p_g$ and $\varepsilon_T^{k+1}>\varepsilon_0^{k+1}+\alpha_{gr}\varepsilon_g$ with a time delay of $Ka\Delta t$:

$$\varepsilon_i^{k+1}=\left(\frac{p_i^k}{p_i^{k+1}}\right)^{1/n}(\varepsilon_i^k-\alpha_{ga}\varepsilon_g) \tag{4b}$$

(c) for $p_i^{k+1}<p_g$ and at a time delay of $Ke\Delta t$:

$$\varepsilon_i^{k+1}=\left(\frac{p_i^k}{p_g}\right)^{1/n}(\varepsilon_i^k+\alpha_{ga}\varepsilon_g). \tag{4c}$$

The present study set the absorption of free gases and the evolution of dissolved gases with a time delay of $Ka\Delta t$ and $Ke\Delta t$, respectively, and an instant cavitation at vapor pressure under transient conditions. Typical values used for $Ka$ and $Ke$ are 1.000. These $Ka$ and $Ke$ values are currently under fine tuning for the better prediction of the pressure transients. However, there is proof in our study to show that both $Ka$ and $Ke$ are slightly larger than 1.000 and that $Ka>Ke$. For water saturated at atmospheric pressure the gas release pressure head ($Pg$) approaches that of the vapor pressure (i.e., 2.4 m water absolute). A typical free air content in sewage at atmospheric pressure is about 0.1 percent; the free gas content evolved at the gas release head is about 2.0 percent at atmospheric pressure head. The fraction of gas absorption is $\alpha_{ga}\approx 0.3$ and the fraction of gas release is $\alpha_{gr}\approx 0.6$ (Pearsall [13], Kranenburg [14], Provoost [15]). For the comparative study of constant wave speed cases, the present study assumed $\varepsilon=0.000$ in the fluid system even when the transient pressure falls below the gas release pressure ($P<Pg$ at any point), i.e., the system is assumed completely free from the influence of entrapped air. The above model expressions in Eqs. (1) and (2) are very significantly different from that obtained by Pearsall [13], Fox [6], Chaudhry et al. [16], and Wylie et al. [7].

When reversed flow is encountered in the pump, the check valve is assumed closed. Downstream of each of the above profiles is assumed a constant head reservoir. The method of characteristics applied to the above pressure transient problem with variable wave speed ($ai$) and any grid point ($i$) along the pipe can be obtained from Chaudhry et al. [16] or Fox [6]. They will not be repeated here. The results obtained in this work are for a computation with mesh points $N=1001$. Grid independence studies have been done previously (Lee and Cheong [12]) and will not be repeated here.

## Results and Discussion

The effects of air entrainment on pressure transients generated by the simultaneous pump trip of all pumps operating in a pumping station with the undulating pipeline contour as shown in Fig. 1 were investigated with the horizontal air vessel (Figs. 2 and 3) installed at point B. The pumping station uses three parallel centrifugal pumps to supply 1.08 m/s of water to a tank 19.7 m above the sump level, through a 0.985 m diameter main of 4720 m length. The pumpset moment of inertia (including the flywheel) is 33.30 kgm$^2$ for each of the operating pumps. The air volumetric void fraction $\varepsilon$ studied was in the range of 0.000 to 0.030.

Figure 4 shows the typical effects of air entrainment on the pressure transients at a point A (immediately downstream of the check valves) and at a point C (at the peak) of the pipeline contour for six (6) different air entrainment ($\varepsilon$) values. Several distinct pressure transient characteristics can be observed from the numerous numerical experiments performed: (i) The pressure peak varies with the $\varepsilon$ and it is above that predicted by the constant wave speed model ($\varepsilon=0.000$) with the transient time that occurs differ. The frequencies of the pressure transient are noted to decrease as $\varepsilon$ increases. (ii) The transient peak pressure increases as $\varepsilon$ increases from 0.000. However, the increment stops when the air entrainment value reaches the range of above 0.010, after which the transient peak pressure began to dip. The initial increase of the

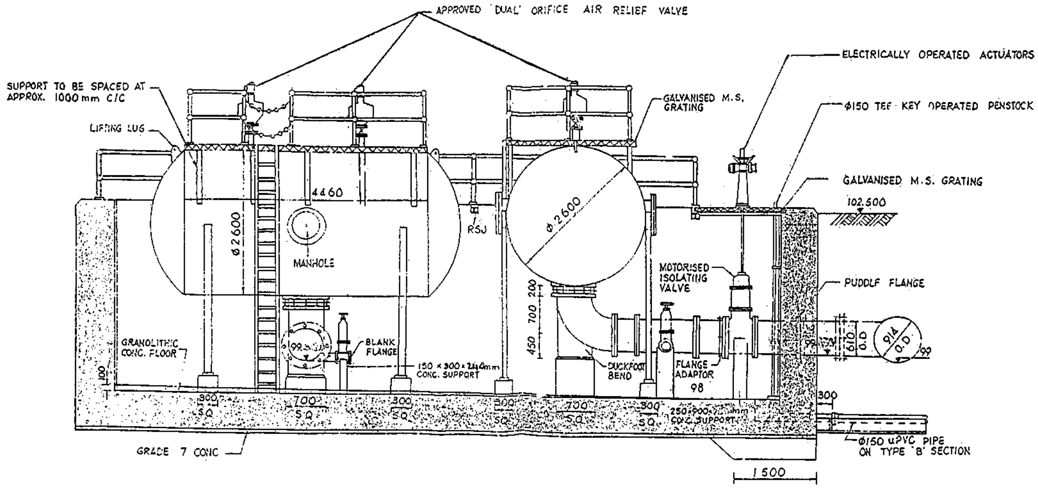

Fig. 2 Horizontal air vessel at location B

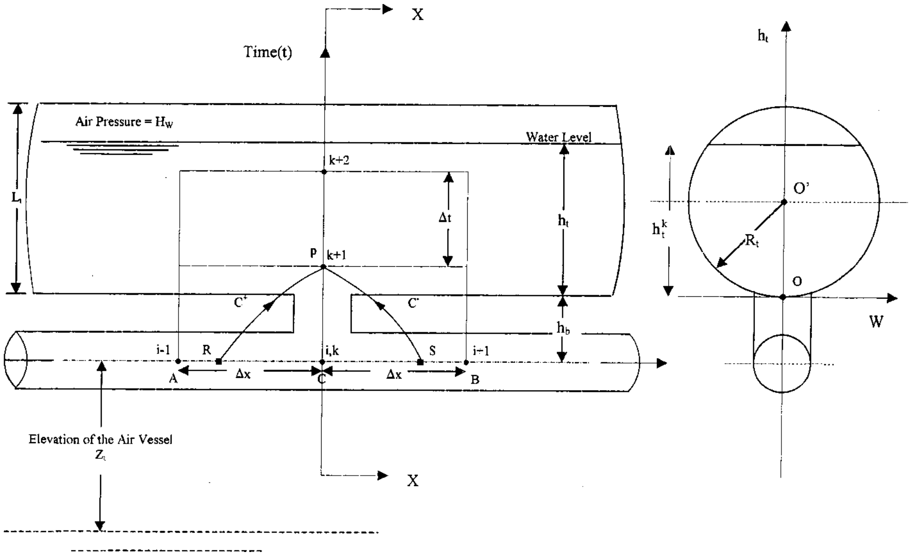

**Fig. 3 Schematic model and computational characteristic grid of horizontal air vessel at location B**

maximum transient pressure, as explained by Lee and Pejovic [12], is due to the fact that the lower average wave speed delays the wave reflection at the reservoir. This delayed reflection would therefore allow a more complex variation in pressure interaction to occur in the system, culminating in a peak at a specific transient interval. (iii) When air was entrained into the system, the pressure transient showed long periods of down surge and short periods of upsurge when compared with the gas-free constant wave speed case. From past experiences, surge measurements (Jonsson [17], Lee and Cheong [8]) indicate that the damping is faster in reality indicating that more energy dissipating mechanisms than the ordinary friction are at hand. (iv) The degree of amplification of the first pressure peak is dependent upon the rate of deceleration of the flow after the pump trip. Further investigations show that, for a given pumpset inertia, the maximum pressure peaks need not necessarily occur at the minimum or maximum air entrainment levels (0.000 and 0.030 respectively in the present study). It can occur at an intermediate critical range of air entrainment value. This range of critical air entrainment value can only be obtained through numerical experimentation for a given pumping system.

Figure 5 shows the effects of air entrainment on the local variation of the wave speed with respect to the transient pressure and time. If there are evolution and subsequent absorption of the gas in the liquid along the pipeline, the initial increase of the local

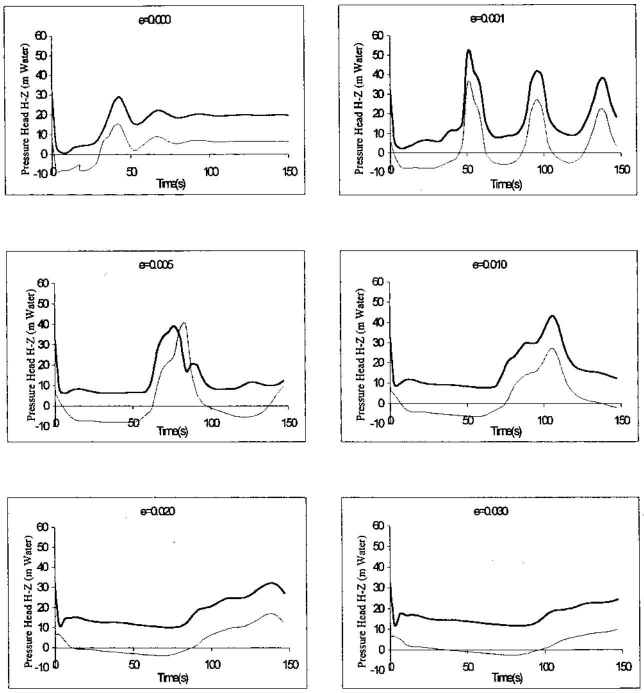

**Fig. 4 Effects of air entrainment on pressure transients. Immediate downstream of check valve (A): ▬▬. At the peak location of pipeline profile (C):——.**

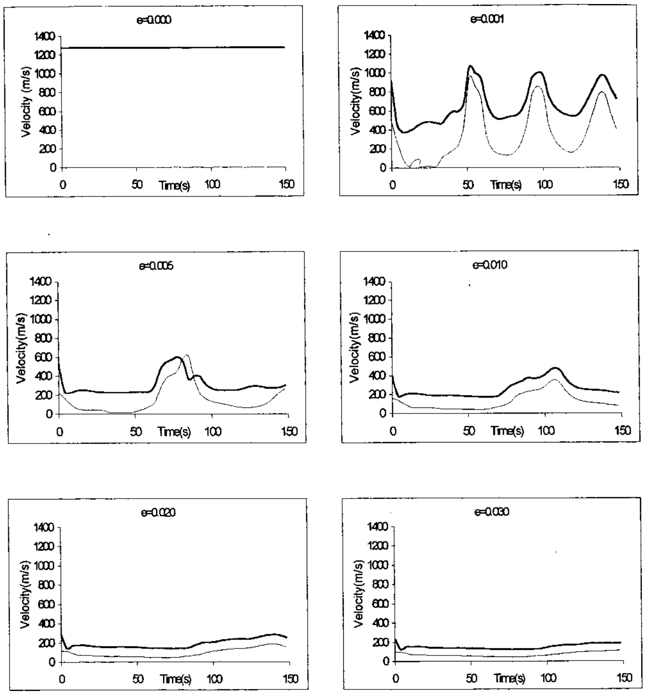

**Fig. 5 Effects of air entrainment on local wave speeds. Immediate downstream of check valve (A): ▬▬. At the peak location of pipeline profile (C):——.**

wave speed caused by the higher transient pressures at the pumping station may be small but it is very often followed by a delayed substantial local wave speed and pressure upsurge as shown in Fig. 5 for various $\varepsilon$ values. This delayed substantial local wave speed increase following the pressure upsurge due to gas release at the gas release head along the pipeline was also observed by Clarke [1]. The arrival of the substantial pressure upsurge at the pumping station generates a positive pressure transient with the resulting increase in local wave speed that travels upstream toward the reservoir. This positive pressure transient raises the wave speed along the pipeline and the increased positive pressure causes the free gas present in the flow to dissolve, so increasing the effective bulk modulus and thus the wave speed (as shown in Fig. 5). This positive pressure wave was then reflected off the downstream reservoir as a negative pressure wave. Due to the higher pressure upstream of the reservoir, this negative pressure wave travels rapidly and arrests the high pressure upsurge at the pumping station. Hence, the substantial pressure upsurge was present for a short duration. As the surge damping due to losses and the presence of air content sets in, the pressure down-surge along the pipeline usually does not subsequently fall below the gas release head, and a regular oscillating pressure surge with the resulting wave speed periodic variation will then be observed. Hence, the entrainment of free air and the release of gas at the gas release head reduces the local wave speed considerably and produces a complicated phenomena of reflection of pressure waves off these ''cavities.'' The lower local wave speed also increases the duration of the pressure down-surge as compared with the duration of the pressure upsurge. The above characteristics were also observed experimentally by Whiteman and Pearsall [18,19], Dawson and Fox [20], and Jonsson [17]. There are several reasons given in the literatures for the increase in the peak pressure and local wave speed during the pressure transient with air entrainment. Jonsson attributed the increase in peak pressure and local wave speed to the compression of ''an isolated air pocket'' in the flow field after the valve closure. Dawson and Fox attributed the increase in peak pressure and local wave speed to the ''cumulative effect of minor flow changes during the transient.'' Through the numerous numerical experiments performed on the variable wave speed model, the authors observed that the greater peak pressure obtained for the variable wave speed model is due to the fact that lower average wave speed delays the wave reflection at the reservoir and thus allows a greater complex variation in pressure interaction to occur in the system cumulating with a peak at a specific transient interval. Falconer et al. [21] also showed through computer studies that it is possible for a low wave speed to increase the pressure peak, even though a lower wave speed also implies a reduced change in pressure head for a given velocity change.

Figure 6 analyzes the corresponding effects of the air entrainment on the maximum and minimum volume of resident water in the air vessel under extreme pressure transient conditions. During the pressure down surge with $\varepsilon=0.000$, when the transient water volume in the air vessel reaches zero for about 20 seconds, the air vessel is able to recover from the return positive pressure surge with water re-introduced into the air vessel. Subsequently, there is no further complete draining of the water inside the vessel. When the air content is increased to $\varepsilon=0.001$, the duration of the water draining down below zero level is considerably reduced to about 10 seconds. For $\varepsilon\geqslant0.005$, the down draining of the water below zero level diminished. It should be noted here that down draining of the resident water in the vessel should be kept to a minimum whenever possible. If excessive amount of air from the air vessel gets into the pipeline system, this may caused ''air lock'' and column separation problems. Thus, although adequate amount of air in the air vessel is required to control the maximum magnitude of the positive pressure surges, there must also be sufficient volume of water in the air vessel to prevent the resident water from draining dry during down-surge. Thus, the optimum size and configuration of the air vessel will have to be obtained through numerical simulations at different air entrainment values for the various extreme pump operations. Numerical experiments also showed that air vessel is an effective surge suppressor only if the complementary pumpset inertia is of sufficient magnitude (not necessary large). For low pumpset inertia, the rate of decrease of the pump head was often so rapid that it prevented the air vessel from having sufficient time to respond in order to minimize the extreme pressure surges.

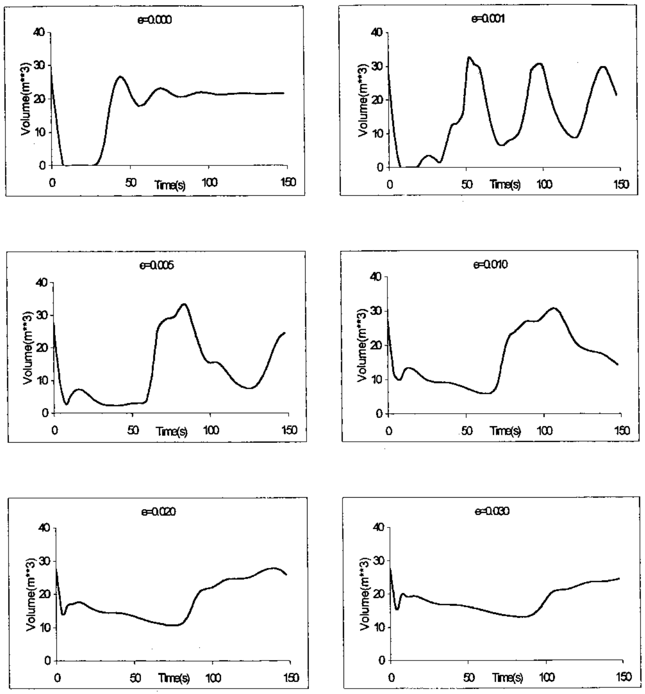

**Fig. 6 Effects of air entrainment on resident water volume in the tank. Immediate downstream of check valve (A): ▬. At the peak location of pipeline profile (C):—.**

## Comparison With Field Measurements

Field measurements (Lee and Cheong [8]) were carried for a simulated case mentioned in this study in order to verify the validity of the simulations. Monitoring of the transient pressures was conducted at location A (immediate downstream of the check valve of the pump) within the pumping station for the pumping main as shown in Fig. 1. The transducers used are piezoresistive absolute pressure transducers with the capability of measuring subatmospheric pressures. Measurements were carried out with simultaneous three pumps trip with the air vessel isolated. The air vessel is installed along the pumping system at B as shown in Fig. 1. This air vessel can be temporarily deactivated (i.e., shut-off) during the field measurements. The corresponding transient pressure at a location A of the pumping main obtained through the surge analysis above are reproduced for comparison in Fig. 7 without the air vessel. The computed results with a specified $\varepsilon=0.001$ value compared very well with the corresponding field measurements. There are proper phasing of the computed pressure surges when compared with the field measurements. The magnitudes of the computed and measured pressure surges are in good agreement. The air entrainment level is estimated to be of the order of $\varepsilon\approx0.001$. This air entrainment value was obtained through the analysis of the resulting acoustic signatures of the flow through the electromagnetic flow meter with respect to the precalibrated acoustic signatures of the flow through the electromagnetic flow meter with a known amount of air introduced into the system. The known amount of air introduced was through an air compressor and an air flow meter. The air flow volume was

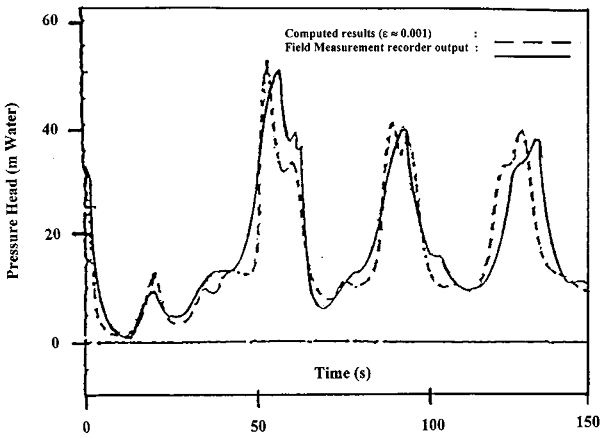

**Fig. 7 Comparison with field measurements (air vessel isolated)**

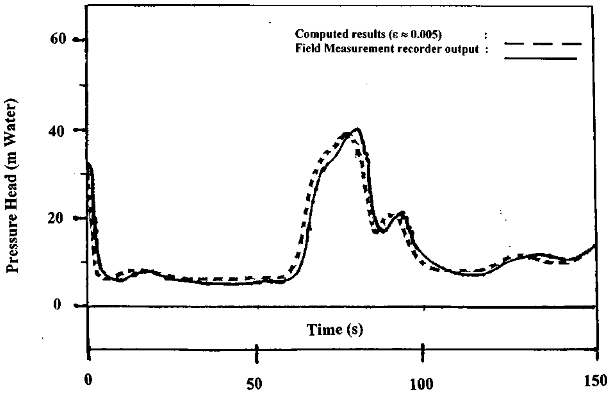

**Fig. 8 Comparison with field measurements (air vessel activated)**

converted to air volume at standard conditions of one atmospheric pressure and at 20°C. During the estimations of the air entrainment fraction, extreme care must be taken during the experiment to minimize the surrounding electromagnetic interference of the overhead high power electrical appliances during the power shut-off and turn-on. With the air vessel activated, the field measurement recorder output is shown in Fig. 8. The corresponding transient pressure at location A of the pumping main obtained through the surge analysis is superimposed for comparison in Fig. 8. The air entrainment value of $\varepsilon$ obtained through the analysis of the acoustic signature of the flow through the electromagnetic flow meter is estimated to be approximately 0.005. The computed results with $\varepsilon=0.005$ value matches very well with the corresponding field measurements. There are also proper phasing of the computed pressure surges when compared with the field measurements.

## Conclusions

The effects of air entrainment in the fluid system with a horizontal air vessel were studied through a new model. Free and dissolved gases in the transported fluid, and cavitation at vapor pressure are included in the air vessel model equations. Numerical experiments show that the maximum transient pressure can be considerably reduced if an appropriately sized horizontal air vessel is chosen. The results obtained are in quantitative agreement with observations from field measurements.

## Acknowledgments

The author gratefully acknowledges the assistance of K. L. Ngoh in this investigation. The support of a National University of Singapore research grant (No. RP3792715) is also gratefully acknowledged.

## Nomenclature

$a$ = wave speed
$A_p$ = cross-sectional area of the pipe
$A_t(h_t)$ = cross-sectional area of the tank
$c$ = parameter of pipe constraint
$D$ = mean diameter of pipe
$E$ = modulus of elasticity of water
$e$ = local pipe-wall thickness
$g$ = gravitational acceleration
$h_t$ = height of water in the tank
$H$ = gauge piezometric pressure head
$H_g$ = gas release pressure head
$i$ = node point at $xi=(i-1)\Delta x$
$K$ = bulk modulus of elasticity of pipe
$P_a$ = absolute pressure of the air in the air vessel
$P_g$ = gas release pressure
$t$ = instantaneous time in transient flow
$V$ = flow velocity
$V_a$ = volume of air in the air vessel
$\alpha_{ga}$ = fraction of gas absorption
$\alpha_{gr}$ = fraction of gas release
$\varepsilon$ = fraction of air in liquid
$\varepsilon_0$ = fraction of free gas in liquid at atmospheric pressure
$\varepsilon_g$ = fraction of dissolved gas in liquid
$\rho_w$ = density of liquid

## References

[1] Clarke, D. S., 1985, ''Surge Suppression—A Warning,'' Proceedings of the International Conference on the Hydraulics of Pumping Stations, Manchester, England, 17-19 Sept., pp. 39–54.
[2] Graze, H. R., and Horlacher, H. B., 1986, ''Design Charts for Throttle (By-Pass) Air Chamber,'' 5th Int. Conference on Pressure Surges, Hannover, Germany, 22–24 Sept., pp. 309–322.
[3] Martin, C. S., 1972, ''Method of Characteristics Applied to Calculation of Surge Tank Oscillations,'' Proceedings of the International Conference on Pressure Surges, University of Kent, Canterbury, England, 6–8 Sept., pp. E1-1 to E1-12.
[4] Fok, A. T. K., 1978, ''Design Charts for Air Chamber on Pump Pipe Lines,'' J. Hydraul. Div., Am. Soc. Civ. Eng., **HY9**, Sept., pp. 1289–1302.
[5] Evans, W. E., and Crawford, C. C., 1954, ''Design Charts for Air Chambers and Pump Lines,'' Trans. Am. Soc. Civ. Eng., **119**, pp. 1025–1045.
[6] Fox, J. A., 1984, *Hydraulic Analysis of Unsteady Flow In Pipe Network*, Macmillan Press, London.
[7] Wylie, E. B., Streeter, V. L., and Suo, L., 1993, *Fluid Transients in Systems*, McGraw-Hill, New York.
[8] Lee, T. S., and Cheong, H. F., 1998, ''Tanjong Rhu Pumping Station—Site Measurement and Analysis of Surge in Pumping Main,'' Ebara Engineering Singapore Pte Ltd., Singapore, July.
[9] Thorley, A. R. D., and Lastowiecki, P., 1985, ''Air Vessel Design for Rising Mains,'' Proceedings of the International Conference on the Hydraulics of Pumping Stations, Manchester, England, 17–19 Sept., pp. 89–98.
[10] Allievi, L., 1937, ''Air Chamber for Discharge Lines,'' Trans. ASME, **59**, pp. 651–659.
[11] Angus, R. W., 1937, ''Air Chambers and Air Valves in Relation to Water Hammer,'' Trans. ASME, **59**, pp. 661–668.
[12] Lee, T. S., and Pejovic, S., 1996, ''Air influence on similarity of hydraulic transients and vibrations,'' ASME J. Fluids Eng., **118**, pp. 706–709.
[13] Pearsall, I. S., 1965/66, ''The Velocity of Water Hammer Waves,'' Symposium on Surges in Pipelines, Proc. Inst. Mech. Eng., Vol. 180, Part 3E, pp. 12–20.
[14] Kranenburg, C., 1974, ''Gas release during transient cavitation in pipes,'' J. Hydraul. Div., Am. Soc. Civ. Eng., **100**, pp. 1383–1398.
[15] Provoost, G. A., 1976, ''Investigation into Cavitation in a Prototype Pipeline caused by Waterhammer,'' Proc. Second Int. Conf. on Pressure Surges, Bedford, England, BHRA, Sept., pp. 35–43.
[16] Chaudhry, M. H., Bhallamudi, S. M., Martin, C. S., and Naghash, M., 1990, ''Analysis of Transient Pressures in Bubbly, Homogeneous, Gas-Liquid Mixtures,'' ASME J. Fluids Eng., **112**, pp. 225–231.
[17] Jonsson, L., 1985, ''Maximum Transient Pressures in a Conduit with Check

Valve and Air Entrainment,'' International Conference on the Hydraulics of Pumping Stations, The University of Manchester Institute of Science and Technology (UMIST) & BHRA—The Fluid Engineering Centre, England. 17–19 Sept., pp. 55–76.

[18] Whiteman, K. J., and Pearsall, I. S., 1959, ''Reflux Valve and Surge Tests at Kingston Pumping Station,'' Brit. Hydromech. Res. Assoc./National Engineering Laboratory Joint Report No. 1, Apr.

[19] Whiteman, K. J., and Pearsall, I. S., 1962, ''Reflux Valve and Surge Tests at a Station,'' Fluid Handling, **XIII**, Sept. and Oct., pp. 248–250 and 282–286.

[20] Dawson,, P. A., and Fox, J. A., 1983, ''Surge Analysis and Suppression Techniques for a Water Supply Scheme—A Case Study,'' Trans. Inst. M. C., **5**, No.4, pp. 134–142.

[21] Falconer, R. H., Banks, W., and Ellis, J., 1983, ''Surge Pressures at Riding Mill Pumping Station: Actual Values and Theoretical Predictions,'' *4th International Conference on Pressure Surges*, University of Bath, England. Sept. 21–23, pp. 427–445.

# A Turbulent Model for Gas-Particle Jets

**J. García**
Professor

**A. Crespo**
Professor
e-mail: crespo@enerflu.etsii.upm.es

Departamento de Ingeniería Energética
y Fluidomecánica,
Universidad Politécnica de Madrid,
C/José Gutiérrez Abascal, 2
28006 Madrid, Spain

*This work is concerned with turbulent diffusion in gas-particle flows. The cases studied correspond to dilute flows and small Stokes number, this implies that the mean velocity of the particles is very similar to that of the fluid element. The classical $k$-$\varepsilon$ method is used to model the gas-phase, modified with additional terms for the k and $\varepsilon$ equations, that takes into account the effect of particles on the carrier phase. The additional dissipation term included in the equation for k is due to the slip between phases at an intermediate scale, far from both the Kolmogorov and the integral scales. This term has a proportionality constant equal to 3/2 of Kolmogorov constant, $C_0$. In this paper, a value of 3.0 has been used for this constant as suggested by Du et al., 1995, ''Estimation of the Kolmogorov Constant $C_0$ for the Langarian Structure Using a Second-Order Lagrangian Model of Grid Turbulence,'' Phys. Fluids* ***7****, (12), pp. 3083–3090. The additional source term for the $\varepsilon$ equation is taken as proportional to $\varepsilon/k$, as is usually done. In all experiments analyzed the particles increased the dissipation of turbulent kinetic energy. A comparison is made between the results obtained with the model proposed in this work and the experiments of Shuen et al., 1985, ''Structure of Particle-Laden Jets: Measurements and Predictions,'' AIAA Journal,* ***23****, No. 3, and Hishida et al., 1992, ''Experiments on Particle Dispersion in a Turbulent Mixing Layer,'' ASME Journal of Fluids Engineering,* ***119****, pp. 181–194.* [S0098-2202(00)02103-9]

## Introduction

Turbulent dispersion of dilute concentrations of discrete particles is present in many industrial applications such as, pulverized-coal reactors, spray combustor, cyclone separators, and pneumatic transport of particulate material. Even, in some cases droplet flows can be studied with the same models that previous flows. In fact, the model proposed in this article was first applied to the case of propane stored at its vapor pressure, so that its release from below the liquid level, produces a two-phase flashing jet, García and Crespo [1].

The majority of numerical models used for engineering analysis are based on the solution of the Reynolds-averaged Navier-Stokes equations for the carrier phase. The most common model used for turbulent flows is the classical $k$-$\varepsilon$ model. When the particle mass concentration is small enough, it is not necessary to modify the $k$-$\varepsilon$ model. Otherwise, the turbulence model for the continuum phase has to be modified in order to retain the effect of particles on the turbulence. The general approach is to modify the single-phase flow equations for conservation of turbulence intensity and dissipation. In the present work, an additional term is included in each equation.

A compilation of experimental data by Gore and Crowe [2] indicated that large particles generate turbulence. The data suggested that the transition occurs when the particle size is about 1/10 of the integral length scale. In our case the particle diameters are smaller than 1/10 of the turbulent scale and dissipation dominates. For the cases of this work the volumetric fractions are in the range $10^{-3}$ to $10^{-6}$ and the Stokes numbers are below one; then, according to Elgobashi and Truesdell [3], the particles should produce an additional dissipation of $k$. Squires and Eaton [4], using data from direct numerical simulation of particle-laden isotropic turbulent flows, evaluate the particle influence on the production and dissipation of $k$, and find that the classical constant, $C_{\varepsilon 2}$, can either increase or decrease with mass loading depending on the Stokes number. They also find an additional sink term in the equation for $k$, and either a sink or a source term in the equation for $\varepsilon$, depending on the value of the Stokes number. In this work, we do not change the classical coefficients of the $k$-$\varepsilon$ model, and we only introduce two additional sink terms, due to the particles in the equations for $k$ and $\varepsilon$. Yuan and Michaelides [5] calculate the dissipation of turbulent energy due to the particles as the drag of the particles multiplied by their relative velocity, integrated over the minimum of the eddy lifetime or the time that it takes the particle to cross the eddy, and compare it to the production of $k$ due to the vortex shedding and the disturbance of the flow by the wake. They conclude that, for small particles, such that the Stokes number is smaller than one, as it happens in the cases considered in this work, dissipation dominates. Yarin and Hestroni [6] study the interaction of particles, of arbitrary sizes and a turbulent fluid element, taking into account that for coarse particles the wake may be turbulent; their model considers both enhancement due to coarse particles and suppression due to small ones. They apply their results to several configurations, however, for a turbulent jet, they consider only coarse particles. Shuen et al. [7] studied turbulent particle-laden jets injected into a still environment. They proposed a modified $k$-$\varepsilon$ model, but the $C_{\varepsilon 3}$ constant varies in a wide range (0,1–5) depending on the experiments used to calibrate it.

None of the previous authors give a specific functional dependence of the dissipation term due to the particles with the average flow variables, allowing the problem closure. A method proposed by Levich [8] has been used here to estimate the distribution, for different turbulence scales, of relative turbulent velocities between particles and gas, and from those to estimate the additional dissipation as the product of drag and relative particle velocity. It turns out that, for the practical cases considered, the most significant slip velocities between phases occur at an intermediate scale, far from both the Kolmogorov and the integral scales, whose order of magnitude is determined. The dissipation term $\varepsilon_p$, turns out to be proportional to the mass concentration of particles and to $\varepsilon$ and contains Kolmogorov's constant that has been assumed to be $C_0 = 3$ from Du et al. [9]. The dissipation term in the equation for $\varepsilon$ has been assumed to be of the form $C_{\varepsilon 3}(\varepsilon/k)\varepsilon_p$, as it is usually done in the literature (Berlemont et al. [10], Squires and Eaton [4]). The value of $C_{\varepsilon 3}$ has been taken equal to 0,9 by fitting with experimental results of Shuen et al. [7]. Further comparisons have been made with experiments of Hishida et al. [11]. This value of $C_{\varepsilon 3}$ is within the usual range found in the literature.

Fessler and Eaton [12] obtain for a large Stokes number a

---

Contributed by the Fluids Engineering Division for publication in the JOURNAL OF FLUIDS ENGINEERING. Manuscript received by the Fluids Engineering Division December 5, 1997; revised manuscript received April 4, 2000. Associate Technical Editor: J. Eaton.

simple expression for the extra dissipation, $\varepsilon_p$, that is inversely proportional to the particle time constant, but they recognize that the experimental data contradicts this result. The expression found in this article is, however, independent of the particle time constant, and applies for small Stokes numbers.

The system of equations is solved numerically using the SIMPLER procedure and a finite volume discretization, with a code developed by the authors for axisymmetric jets.

## Diffusion Model

The averaged turbulent flow equations for a homogeneous mixture have been used, together with those for $k$ and $\varepsilon$, needed to calculate the turbulence transport terms.

$$\frac{\partial}{\partial x_j}(\rho v_j)=0 \tag{1}$$

$$\frac{\partial}{\partial x_j}(\rho v_j v_i)=\frac{\partial}{\partial x_j}\left[\mu_t\left(\frac{\partial v_i}{\partial x_j}+\frac{\partial v_j}{\partial x_i}\right)-\frac{2}{3}\delta_{ij}k\right]-\frac{\partial p}{\partial x_i}+\rho g_i \tag{2}$$

$$\frac{\partial}{\partial x_j}(\rho v_j k)=\frac{\partial}{\partial x_j}\left(\frac{\mu_t}{\sigma_k}\frac{\partial k}{\partial x_j}\right)+P-\rho\varepsilon-\rho\varepsilon_p \tag{3}$$

$$\frac{\partial}{\partial x_j}(\rho v_j \varepsilon)=\frac{\partial}{\partial x_j}\left(\frac{\mu_t}{\sigma_\varepsilon}\frac{\partial \varepsilon}{\partial x_j}\right)+(C_{\varepsilon 1}P-C_{\varepsilon 2}\rho\varepsilon)\frac{\varepsilon}{k}-S_\varepsilon \tag{4}$$

The additional terms ($\rho\varepsilon_p$) and $S_\varepsilon$ in the equations for $k$ and $\varepsilon$, respectively, account for the dissipation due to the particles, and will be evaluated later. $P$ is the production term of $k$, and $\mu_t$ is the turbulent viscosity

$$P=\mu_t\frac{\partial v_i}{\partial x_j}\left(\frac{\partial v_i}{\partial x_j}+\frac{\partial v_j}{\partial x_i}\right) \qquad \mu_t=C_\mu\rho\frac{k^2}{\varepsilon} \tag{5}$$

The classical constants of the $k$-$\varepsilon$ model have been used

$$\begin{gathered} C_\mu=0.09, \quad C_{\varepsilon 1}=1.44, \quad C_{\varepsilon 2}=1.92 \\ \sigma_k=1.0, \quad \sigma_\varepsilon=1.3 \end{gathered} \tag{6}$$

A conservation equation for the mass fraction of particles, is also needed

$$\frac{\partial}{\partial x_j}(\rho v_j Y_p)=\frac{\partial}{\partial x_j}\left(\frac{\mu_t}{\sigma_Y}\frac{\partial Y_p}{\partial x_j}\right), \quad \text{where} \quad \sigma_Y=0.7 \tag{7}$$

Gravity has been neglected in this work, this is in accordance with the experiments used for comparison. Stationary flow is assumed. The density depends on particle concentration as $\rho\approx\rho_g/(1-Y_p)$, if $\rho_p\gg\rho_g$ and $Y_p$ is not close to one.

## Dissipation Term Due to the Particles

The following assumptions have been made:

- The density of the particles is much larger than the gas density, and Basset forces and virtual mass can be neglected.
- The volume fraction is small enough, so that particle-particle interaction can be neglected.
- Froude number is large enough so that gravity can be neglected compared to inertia.

The equation of motion can be written in terms of the relative velocity $\mathbf{u}=\mathbf{v}_g-\mathbf{v}_p$ as

$$\rho_p V\frac{d\mathbf{u}}{dt}=\rho_p V\frac{d\mathbf{v}_g}{dt}-\frac{1}{2}C_D\rho_g S u\mathbf{u} \tag{8}$$

From this equation, using an order of magnitude analysis proposed by Levich [8], it has been estimated how the relative velocity $\mathbf{u}$ depends on the turbulent scale, and it has been found to what scale corresponds the maximum value of $u$. In this work, we will assume that turbulent dissipation is determined by this maximum value of $u$. For the different turbulent scales, $\lambda$, larger than the Kolmogorov scale and smaller than the integral scale, $L>\lambda>\lambda_0$, we have:

- For the gas phase the characteristic time will be: $T_{g\lambda}\approx\lambda/v_{g\lambda}\approx\lambda^{2/3}/\varepsilon^{1/3}$, and the acceleration,

$$\frac{dv_g}{dt}\approx\frac{v_{g\lambda}}{T_{g\lambda}}\approx\frac{\lambda}{T_{g\lambda}^2}\approx\frac{\varepsilon^{2/3}}{\lambda^{1/3}} \tag{9}$$

- For the particles the characteristic time of interaction will be the time it takes them to cross the eddy, $T_{p\lambda}\approx\lambda/u_\lambda$, so that the acceleration will be,

$$\frac{du}{dt}\approx\frac{u_\lambda}{T_{p\lambda}}\approx\frac{u_\lambda}{\lambda/u_\lambda}\approx\frac{u_\lambda^2}{\lambda} \tag{10}$$

Introducing the accelerations calculated in Eqs. (9) and (10) into Eq. (8), we obtain for the relative velocity

$$u_\lambda\approx A(\rho_p V)^{1/2}\frac{\varepsilon^{1/3}\lambda^{1/3}}{\left(B\rho_p V+\frac{1}{2}C_D\rho_g S\lambda\right)^{1/2}} \tag{11}$$

where $A$ and $B$ are constants that cannot be determined with the order of magnitude analysis. From this expression it can be seen that $u_\lambda$ should have a maximum for a certain intermediate value of $\lambda$. For small $\lambda$ the last term in (8) is negligible, and the relative velocity of the particle is like the gas velocity and tends to zero like $(\varepsilon\lambda)^{1/3}$; on the other hand, for large $\lambda$ the first term of the right side of (8) is negligible and the particle tends to follow the gas flow (it has been assumed in this work that the Stokes number is small). The maximum value of $u_\lambda$ is given by

$$\frac{\partial u_\lambda}{\partial\lambda}=0\Rightarrow\lambda|_{u\,\max}=\lambda^*\approx\frac{1}{C_D}\frac{\rho_p}{\rho_g}\frac{V}{S} \tag{12}$$

$$u_{\max}=u^*\approx(d)^{1/3}(\varepsilon)^{1/3}\left(\frac{\rho_p}{\rho_g}\right)^{1/3}\left(\frac{1}{C_D}\right)^{1/3} \tag{13}$$

The value of $\lambda^*$ is much larger than the particle size $d\approx V/S$, and increases linearly with it if $C_D$ is constant. It is assumed that the most important contribution to turbulence dissipation due to the particles occurs at the scale $\lambda^*$. The value of $\varepsilon_p$ will be obtained by multiplying the dissipation produced by each particle by the number of particles per unit mass

$$\varepsilon_p\approx F_{\text{Drag}}u^*\frac{Y_p}{\rho_p d^3}\approx C_D\left(\frac{\rho_g}{\rho_p}\right)\frac{u^{*3}}{d}Y_p \tag{14}$$

introducing $u^*$ from Eq. (13) it is obtained

$$\varepsilon_p=C\varepsilon Y_p \tag{15}$$

where all magnitudes have canceled except $\varepsilon$ and $Y_p$. It includes a constant $C$ that in a previous work by García and Crespo [1] was determined by comparison with experiments from a flashing jet.

For the Stokesian case and spherical particles the value of $C$ can be more precisely inferred from theoretical considerations. If we rewrite Eq. (14) averaging over all the turbulence scales, we can write it in an exact form

$$\varepsilon_p=\langle F_{\text{Drag}}u\rangle\frac{Y_p}{\rho_p\frac{\pi}{6}d^3}=\frac{Y_p}{\tau_p}\langle u^2\rangle \tag{16}$$

where in the Stokes limit, $F_{\text{Drag}}=3\pi\mu u d$ and $\tau_p=\rho_p d^2/18\mu$. In order to estimate $\langle u^2\rangle$, the Fourier transform of Eq. (8), that in the Stokesian limit is

$$\frac{d\mathbf{u}}{dt}=\frac{d\mathbf{v}_g}{dt}-\frac{\mathbf{u}}{\tau_p} \tag{17}$$

is made, and it is obtained the following relationship between the modulus of the transform vector of the gas velocity and relative velocity

$$\tilde{u}^2 = \frac{\tilde{v}_g^2}{1+\dfrac{1}{\omega^2\tau_p^2}} \tag{18}$$

Then, assuming that at these small scales, turbulence is quasi-homogeneous and isotropic, the relationship between the spectra of gas velocity and relative velocity is

$$S_u(\omega) = S_g(\omega)\,\frac{1}{1+\dfrac{1}{\omega^2\tau_p^2}} \tag{19}$$

This equation can be found also in Hinze [13]. Since we have assumed that the scales of interest are in the inertial subrange ($\tau_L^{-1} \ll \omega \ll \tau_{\lambda 0}^{-1}$), and the presence of particles does not affect in a first approximation the carrier fluid, the Lagrangian time spectrum of the gas can be written, in first approximation, in the form $S_g(\omega) = (3C_0/\pi)\varepsilon\omega^{-2}$, where $C_0$ is an universal constant (Kolmogorov's constant) appearing in the Lagrangian velocity structure function ($D_L = C_0\varepsilon\tau$, where $\tau$ is the time difference in the correlated velocities). The value of the average of the square relative velocity will be given by

$$\langle u^2\rangle = \frac{3}{\pi}\int_0^\infty \frac{C_0\varepsilon\omega^{-2}}{\dfrac{1}{\omega^2\tau_p^2}+1}\,d\omega = \frac{3}{2}C_0\varepsilon\tau_p \tag{20}$$

and substituting Eq. (20) into Eq. (16) an expression for the additional dissipation is obtained

$$\varepsilon_p = \frac{3}{2}C_0\varepsilon Y_p \tag{21}$$

which is similar to the one obtained by Graham [14] if the derivative of the Lagrangian autocorrelation $R_L'(0)$ is $3C_0\varepsilon/4k$, which seems to be the case as shown by Pope [15].

Pope [15] gives for $C_0$ a very wide range of values, from 5.0–6.5. Other authors referred in the review paper by Pope give values going from 2.1 to 5.9. A more recent work, Du et al. [9], gives a value of 3.0±0.5 for the Kolmogorov constant using a second-order Lagrangian model of grid turbulence. In this paper, the value $C_0 = 3$, suggested by Du et al., has been used.

In the equation for the dissipation of turbulent kinetic energy an additional source term has been introduced, that takes into account the effect of particles. The form of this source term (sink) is similar to the expressions used in the majority of the $k$-$\varepsilon$ models for particle flows

$$S_\varepsilon = C_{\varepsilon 3}\frac{\varepsilon}{k}\varepsilon_p \tag{22}$$

The constant $C_{\varepsilon 3}$ is calibrated from the experimental values reported in the experiments of Shuen et al. [7]. The value obtained by a least square fitting is $C_{\varepsilon 3} = 0{,}9$. Berlemont et al. [10] propose that $C_{\varepsilon 3} = 1{,}9$, and Squires and Eaton [4] give a value that depends on $Y_p$, and for small values of $Y_p$ tends to $C_{\varepsilon 3} = 1{,}2$.

For smaller particles such that $\tau_p \ll \tau_{\lambda 0}$, the following analysis, also of Levich [8], applies. In this limit it can be seen that in Eq. (17) the term on the left-hand side representing relative acceleration, of order of $u/\tau_{\lambda 0}$, is negligible compared to $u/\tau_p$, and the balance of the other two terms can be expressed by the following expression

$$u \approx \tau_p\frac{v_{g\lambda 0}}{\tau_{\lambda 0}} \tag{23}$$

Introducing the characteristic time of the particle, $\tau_p = \rho_p d^2/(18\mu)$, the characteristic velocity in the Kolmogorov scale, $v_{g\lambda 0} = (\varepsilon\lambda_0)^{1/3}$, the characteristic time of the Kolmogorov scale, $\tau_{\lambda 0} = \lambda_0/v_{g\lambda 0}$, and the Kolmogorov scale, $\lambda_0 \approx (\mu/\rho_g)^{3/4}/\varepsilon^{1/4}$, the following expression for the slip velocity is obtained

$$u \approx \left(\frac{\rho_p}{\rho_g}\right)\frac{\varepsilon^{3/4}}{(\mu/\rho_g)^{5/4}}d^2 \tag{24}$$

Then, using Eq. (16), the source term for the turbulent kinetic energy will be given by

$$\varepsilon_p \approx \left(\frac{\rho_p}{\rho_g}\right)\left(\frac{\varepsilon}{(\mu/\rho_g)}\right)^{3/2}d^2 Y_p \tag{25}$$

$\varepsilon_p$ is now proportional to $d^2$ and will vanish for light particles. Expression (25) is only valid for very small particles, such that, $\tau_p \ll \tau_{\lambda 0}$, that are particles much smaller than those appearing in the experiments described below, consequently only Eq. (21) will be used in the following. For very small particles, the value of $\varepsilon_p$ can be negligible, even for finite values of $Y_p$ (see also Graham [14]).

## Numerical Model

The system of Eqs. (1)–(7) is solved numerically, using a code developed by the authors, based on a finite volume discretization. The SIMPLER procedure was used to treat the coupling between continuity and momentum equations through pressure. The equations are assumed to behave in a parabolic way in the streamwise direction, neglecting the diffusion in that direction. This allows a marching method to solve the system of equations. In the simulation of the jet the axisymmetric condition is applied, so that the fluxes at the axis are assumed to be zero, and boundary conditions are applied at infinity. In the mixing layer the flow is assumed two-dimensional, and, in order to reproduce the experiments of Hishida et al. [11], boundary conditions were applied at the confining walls limiting the flow. In both cases a constant pressure condition was fixed at the exit. At the entrance the flow conditions are fixed for velocity and turbulent kinetic energy, according to the experimental conditions. Nonuniform Cartesian grids are used, that are more refined at the axis of the jet and at the entrance. For the mixing layer case, the grid is more refined in the center, on the confining walls, and also at the entrance. In order to check the grid independence, different grid sizes were tested, up to 300×100 cells, and it was found that a grid of 100×40 cells was appropriate for both cases (jet and mixing layer).

## Results and Comparison With Experiments

A comparison is made between the numerical results obtained with the model proposed, and the experimental results from Shuen et al. [7] (Figs. 1–4) for a particle jet, and Hishida et al. [11], (Figs. 5–8) for a turbulent mixing layer. The experimental conditions are given in Tables 1 and 2, respectively. The same value for the $C_{\varepsilon 3}$ constant ($C_{\varepsilon 3} = 0.9$) is used in all cases. This value has been obtained by comparison with the first set of experiments of Shuen et al. [7].

**Table 1 Experimental conditions of Shuen et al. [7] experiments**

| | Case 1 | Case 2 |
|---|---|---|
| Particle properties: | | |
| Sauter mean diameter, $\mu$m | 79 | 119 |
| Loading ratio | 0,2 | 0,2 |
| Jet exit velocity, m/s | 24,1 | 24,2 |
| Jet exit mass flux, kg/m$^2$s | 6,06 | 6,50 |
| Air velocity, *Uo*, m/s | 26,1 | 29,9 |

**Table 2 Experimental conditions of Hishida et al. [11] experiments**

| | Case 1 |
|---|---|
| Particle properties: | |
| Mean diameter, $\mu$m | 42 |
| Mass flow rate, g/s | 7.5 |
| Density, kg/m$^3$ | 2590 |
| Air velocity, m/s | |
| $U_1$ | 13 |
| $U_2$ | 4 |

**(a) Comparison With Shuen et al. Experiments.** Figures 1 and 2 correspond to cases 1 and 2, respectively, of Shuen experiments, and show the distribution of axial mean gas-phase velocity. The numerical results exhibit a good agreement with experiments. In Figs. 3 and 4 is represented the axial variation of the centerline turbulent kinetic energy of the gas-phase, made nondimensional with the square of the exit velocity. The values predicted by the model are lower than experimental ones. The reason for this may be that our model uses an isotropic turbulence model ($k$-$\varepsilon$ model), and that the turbulent properties are calculated as in a homogeneous flow. The turbulent kinetic energy calculated is an averaged value of the streamwise (high values in experiments) and radial distribution (low values in experiments). It may also be that our model assumes small Stokes numbers, and consequently from Eqs. (11) or (19) the contribution to $k$ for large $\lambda$ or small $\omega$ will be neglected, whereas in reality it may be a significant value. In Figs. 1–4, are also presented the model results for nonparticle situations. It can be seen that the model proposed here substantially improves the agreement with experiments. The particle dissipation increases the velocity and decreases the turbulent kinetic energy, particularly in the region of high particle concentration near the exit, and upstream the self-similar region.

**(b) Comparison With Hishida et al. Experiments.** In Figs. 5 and 6 are shown the results obtained for turbulent fluctuations in a mixing layer, made nondimensional with the velocity

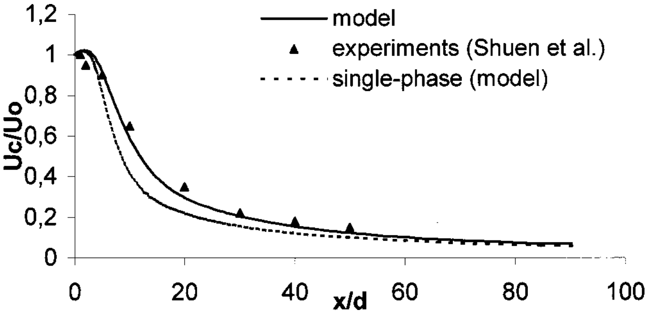

**Fig. 1 Axial variation of centerline mean gas-phase velocity for a jet (case 1)**

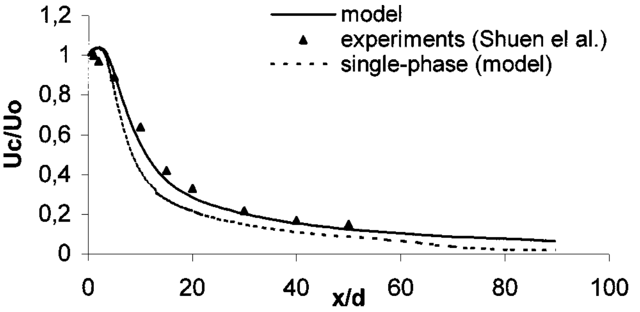

**Fig. 2 Axial variation of centerline mean gas-phase velocity for a jet (case 2)**

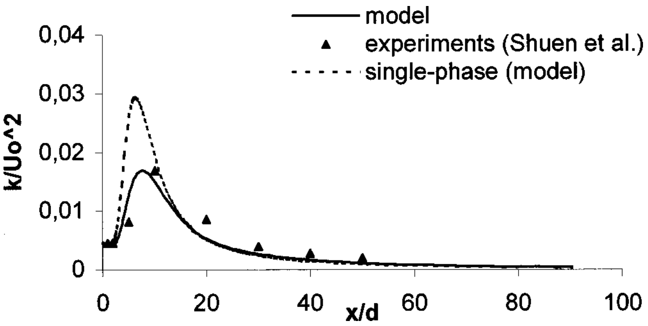

**Fig. 3 Axial variation of centerline gas-phase turbulent kinetic energy for a jet (case 1)**

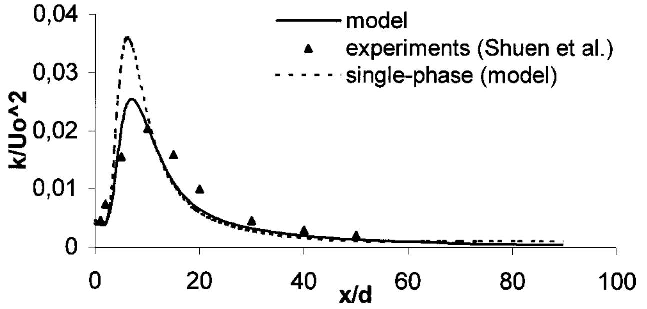

**Fig. 4 Axial variation of centerline gas-phase turbulent kinetic energy for a jet (case 2)**

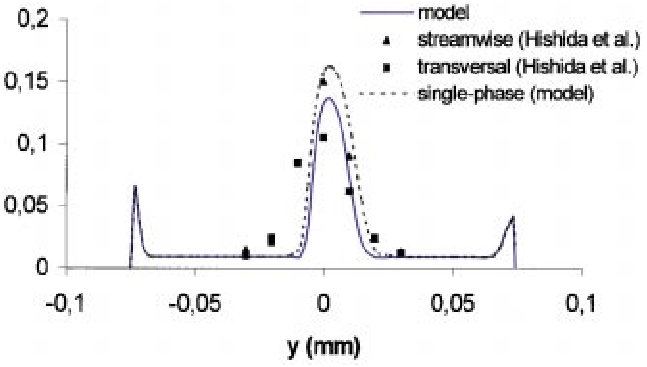

**Fig. 5 Transversal distribution of velocity fluctuations at $x = 200$ mm downstream for a mixing layer. —— Model $(2k/3)^{1/2}/(U_1-U_2)$; ▲ $v'_x/(U_1-U_2)$, ■ $v'_y/(U_1-U_2)$ Hishida et al. [11].**

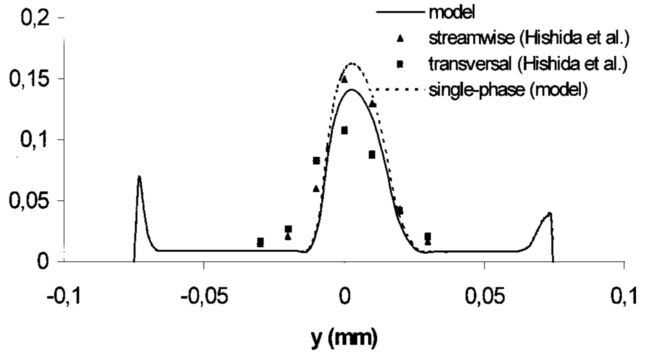

**Fig. 6 Transversal distribution of velocity fluctuations at $x = 250$ mm downstream for a mixing layer. —— Model $(2k/3)^{1/2}/(U_1-U_2)$; ▲ $v'_x/(U_1-U_2)$, ■ $v'_y/(U_1-U_2)$ Hishida et al. [11].**

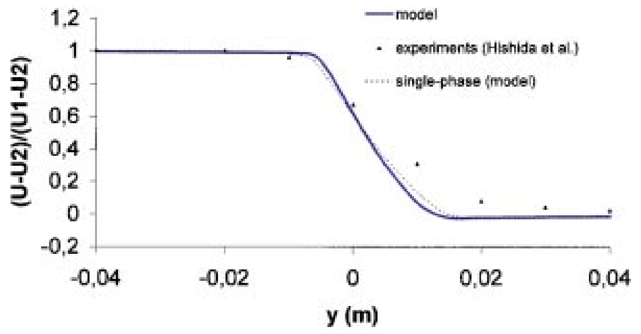

**Fig. 7 Transversal distribution of fluid mean velocity at $x=200$ mm downstream for a mixing layer**

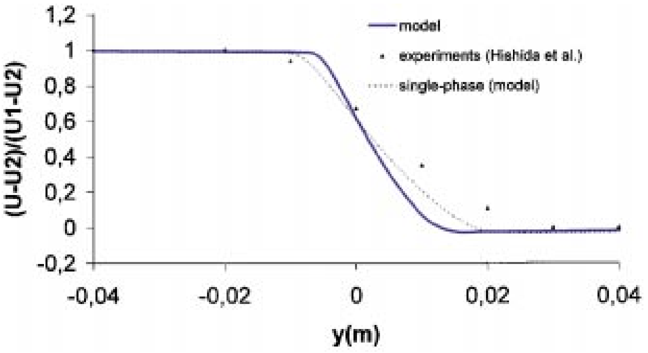

**Fig. 8 Transversal distribution of fluid mean velocity at $x=250$ mm downstream for a mixing layer**

difference $U_1-U_2$. Our model is compared with the experimental data obtained by Hishida et al. [11]. In the experiments, turbulence is not isotropic, and the transverse, $v_y'$, and streamwise, $v_x'$, turbulent fluctuations are actually different; we have compared them with the calculated value of $(2k/3)^{1/2}$. In spite of that, the agreement seems to be quite acceptable. It should be also noted that the calculated value corresponding to the turbulent kinetic energy is between the values corresponding to streamwise and radial turbulent velocities. The peaks observed at the sides correspond to the turbulent kinetic energy produced at the confining walls simulating the experimental conditions. In Figs. 7 and 8 are shown the calculated values of the mean velocity variation through the mixing layer and its comparison with Hishida et al. [11] experiments. In Figs. 5–8, are also presented the model results for nonparticle situations. As should be expected, the particle dissipation reduces the spreading rate of velocity in the shear layer, and decreases the peak values of turbulent kinetic energy. However, the agreement with experimental results is not so clearly improved by using the proposed model for the effect of particles as in the jet case, particularly in Figs. 7 and 8 for velocity profiles. This may be due to the fact that the constant $C_{\varepsilon 3}$ was chosen by comparison with the jet experiments

## Conclusions

A fairly simple model, with a theoretical basis, has been proposed to take into account the extra dissipation due to small particles in turbulent flow for small Stokes numbers. Although the agreement with experimental results is encouraging, it is necessary to make more comparisons to check the validity of this procedure in more general situations.

## Acknowledgments

This work has been carried out under the E.U. contract ''An Experimental and Modeling Study of Two Phase Flashing Jets'' (EV5V-CT94-0431) of the Environment Program.

## Nomenclature

$C$ = constant in Eq. (15)
$C_D$ = drag coefficient
$C_0$ = Kolmogorov's constant
$C_{\varepsilon 1}$, $C_{\varepsilon 2}$, $C_\mu$ = constants of $k$-$\varepsilon$ model
$d$ = particle diameter
$F_{\mathrm{Drag}}$ = drag
$g$ = gravity
$k$ = turbulent kinetic energy
$L$ = integral scale
$p$ = pressure
$P$ = production term of $k$
$S$ = transverse particle area
$S_\varepsilon$ = source term for $\varepsilon$
$T$ = characteristic time
$\mathbf{u}$ = relative velocity
$\mathbf{v}$ = velocity
$v_x'$ = axial velocity fluctuation
$v_y'$ = transverse velocity fluctuation
$V$ = particle volume
$Y$ = mass fraction of particles

### Greek

$\delta_{ij}$ = Kronecker delta function
$\varepsilon$ = dissipation rate of $k$
$\lambda$ = turbulence scale
$\lambda_0$ = Kolmogorov scale
$\mu$ = viscosity
$\mu_t$ = turbulent viscosity
$\rho$ = density
$\sigma_k$, $\sigma_\varepsilon$, $\sigma_Y$ = Prandtl numbers

### Subscripts

$a$ = air
$g$ = gas
$p$ = particle
$\lambda$ = length scale

## References

[1] García, J., and Crespo, A., 1997, ''A Model of Turbulent Two-Phase Flashing Jets,'' FEDSM97-3584, *Proceedings of the ASME Fluids Engineering Division Summer Meeting*, June, Vancouver, Canada.
[2] Gore, R. A., and Crowe, C. T., 1989, ''Effect of Particle Size on Modulating Turbulence Intensity,'' Int. J. Multiphase Flow, **15**, pp. 279–285.
[3] Elghobashi, S. E., and Truesdell, G. C., 1992, ''Direct Simulation of Particle Dispersion in Decaying Isotropic Turbulence,'' J. Fluid Mech., **242**, pp. 655–700.
[4] Squires, K. D., and Eaton, J. K., 1994, ''Effect of Selective Modification of Turbulence on Two-Equation Models for Particle-Laden Turbulent Flows,'' ASME J. Fluids Eng., **116**, pp. 778–784.
[5] Yuan, Z., and Michaelides, E. E., 1992, ''Turbulence Modulation in Particulate Flows—A Theoretical Approach,'' Int. J. Multiphase Flow, **18**, No. 5, pp. 779–785.
[6] Yarin, L. P., and Hetsroni, G., 1994, ''Turbulence Intensity in Dilute Two-Phase Flows—1,2,3,'' Int. J. Multiphase Flow, **20**, No. 1, pp. 1–44.
[7] Shuen, J-S. et al., 1985, ''Structure of Particle-Laden Jets: Measurements and Predictions,'' AIAA J., **23**, No. 3, pp. 396–404.
[8] Levich, V. G., 1962, *Physicochemical Hydrodynamics*, Prentice-Hall, NY.
[9] Du, S., et al., 1995, ''Estimation of the Kolmogorov Constant ($C_0$) for the Lagrangian Structure, Using a Second-Order Lagrangian Model of Grid Turbulence,'' Phys. Fluids, **7**, No. 12, pp. 3083–3090.
[10] Berlemont, A., et al., 1990, ''Particle Lagrangian Simulation in Turbulent Flows,'' Int. J. Multiphase Flow, **16**, No. 1, pp. 19–34.
[11] Hishida, K., Ando, A., and Maeda, M., 1992, ''Experiments on Particle Dispersion in a Turbulent Mixing Layer,'' Int. J. Multiphase Flow, **18**, No. 2, pp. 181–194.
[12] Fessler, J. R., and Eaton, J. K., 1999, ''Turbulence Modification by Particles in a Backward-Facing Step Flow,'' J. Fluid Mech., **394**, pp. 97–117.
[13] Hinze, J. O., 1975, *Turbulence*, McGraw-Hill, New York.
[14] Graham, D. I., 1997, ''Turbulence Modification in the Limiting Cases of Heavy- and Tracer-Particles,'' ASME J. Fluids Eng., **119**, pp. 458–460.
[15] Pope, S. B., 1994, ''Lagrangian PDF Methods for Turbulent Flows,'' Annu. Rev. Fluid Mech., **26**, pp. 23–63.

**T. Sato**
Associate Professor
e-mail: sato@triton.naoe.t.u-tokyo.ac.jp

**R.-T. Jung**
Ph.D. Student
e-mail: rtjung@triton.naoe.t.u-tokyo.ac.jp

**S. Abe**[1]
Master-Course Student

Department of Environmental
and Ocean Engineering,
University of Tokyo
7-3-1 Hongo, Bunkyo-ku,
Tokyo 113-8656, Japan

# Direct Simulation of Droplet Flow With Mass Transfer at Interface

*A direct simulation code has been developed to solve two-phase flow with mass transfer at the interface. The position of the interface is determined by solving a transport equation of the maker density function, one of front-capturing methods. The present method performs the dissolution of mass of a dispersed phase into a continuous phase as a notable feature. Moreover, transfer of the dissolved mass is solved in the continuous phase. At the interface, mass diffusion flux is calculated both for the boundary condition of mass transfer and for the shrinkage of a droplet. For the validation of the present method, three case studies are successfully demonstrated: rise of single droplet, dissolution from a rigid sphere, and dissolution from a rising droplet.* [S0098-2202(00)01303-1]

## 1 Introduction

The injection of liquid CO2 (LCO2) at the depth of 1000–2000 m in the ocean is one of the feasible and economical options for the mitigation of so-called greenhouse effects (e.g., Herzog et al. [1], Ohsumi [2], Nakashiki et al. [3], and Ozaki [4]). Emitted LCO2 at the depth of 1000–2000 m in the deep ocean is believed to form a plume of rising droplets, which entrains surrounding seawater. The LCO2 droplets are dissolved out during the rise and water of large concentration of CO2 is expected to peel out of the rising plume, to sink as a density current and to intrude into the surrounding stratified ocean, the density of which is equal to that of the CO2 rich water. From an environmental point of view, it is important to know how fast CO2 is diluted for making biological impacts insignificant. Therefore, slow dissolution in laminar droplet flow is preferred to rapid one of turbulent spray in order to avoid locally low pH region and to enlarge the dissolution distance in the vertical direction.

The purpose of this article is to develop a CFD code for two-phase flows with unidirectional dissolution from a dispersed phase into a continuous phase. Direct CFD codes of front-capturing type for bubble/droplet flows have been developed by a number of researchers, such as Kanai and Miyata [5], Tomiyama et al. [6], Gueyffier and Zaleski [7], and Bidoae and Raad [8]. The interface is expressed by a variety of scalar-function methods, e.g., volume of fluid (VOF), marker-density function (MDF), VOF in micro-cells, or the level-set methods. On the other hand, Matsumoto et al. [9] applied a front-tracking method using the boundary-fitted coordinates to single-bubble flows. Although it seems that the front-tracking type gives more accurate representation of the interface shape than the front-capturing type because it tracks the interface in the geometrically direct way, grid skew may cause numerical inaccuracy when the deformation of the interface becomes large. Tryggvason et al. [10] developed an explicit front-tracking mesh for bubble/droplet flows, in which the interface is expressed by the moving mesh in the orthogonal grids which never move. This seems to confirm the grid skew problem.

Here we have selected the MDF method because the front-capturing method with volume fraction has more flexibility in coping with large curvature, coalescence, pinch-off, etc., than the front-tracking type. In the numerical procedure of the MDF, steep shock surfaces are transferred, so that the present method adopts the total variation-diminishing (TVD) scheme to suppress artificial oscillations.

Since it is still not cheap to treat a number of droplets by direct simulations with current computing facilities, we only focus on the movement of a single droplet. For the same reason, the thickness of mass boundary layer is assumed to have the same order of magnitude as that of momentum boundary layer in this study. Accordingly, high Schmidt number problems such as the LCO2-seawater systems, Sc which is about 1000, are left for the future challenge. Moreover, the formation of CO2 clathrate hydrate is ignored.

The problems we tackle in this study are: (1) the movement of the interface between a droplet and a liquid continuous phase; (2) the dissolution of mass from the droplet to the continuous phase through the interface; (3) the shrink of the droplet because of the dissolution; and (4) the transfer of dissolved mass in the continuous phase for low Sc problems. This article explains the present CFD method in detail and case studies done for its validation.

## 2 Numerical Method

**2.1 Governing Equations for Two-Phase Flow.** Since we are interested in liquid-liquid two-phase systems, in which the densities and viscosities of both phases do not differ very much compared with gas-liquid systems, a one-fluid model is adopted and, therefore, both phases are treated just like one kind of fluid where the density and viscosity vary depending on the fluid on the spot. The governing equations of three-dimensional, transient, and isothermal two-phase flows are the conservation laws of mass and momentum

$$\frac{\partial \rho}{\partial t} + \nabla \cdot (\rho \mathbf{u}) = 0 \tag{1}$$

$$\frac{\partial}{\partial t}(\rho \mathbf{u}) + \nabla \cdot (\rho \mathbf{u}\mathbf{u}) = -\nabla p + \frac{\rho}{\mathrm{Fn}^2}\mathbf{g} + \frac{1}{\mathrm{Re}}\nabla \cdot [\mu(\nabla \mathbf{u} + (\nabla \mathbf{u})^T)] + \mathbf{f} \tag{2}$$

where **f** will be given in Section 2.3. In the cells including the interface, the density and viscosity are volume-averaged in each cell using MDF $\boldsymbol{\Phi}_A$ ($\boldsymbol{\Phi}_B = 1 - \boldsymbol{\Phi}_A, 0 \leqslant \boldsymbol{\Phi}_A \leqslant 1$) as follows

$$\rho = \boldsymbol{\Phi}_B + \boldsymbol{\Phi}_A \rho_A / \rho_B \tag{3}$$

$$\mu = \boldsymbol{\Phi}_B + \boldsymbol{\Phi}_A \mu_A / \mu_B \tag{4}$$

The MDF has a value of 1 and 0 in the dispersed and the continuous phases, respectively. In the interface cells, the MDF is regarded as the volume fraction of the dispersed phase. For simplic-

---

[1] Currently, Chief Officer, Maritime Technology and Safety Bureau, Ministry of Transport, 2-1-3 Kasumigaseki, Chiyuda-ku, Tokyo 100-8989, Japan.

Contributed by the Fluids Engineering Division for publication in the JOURNAL OF FLUIDS ENGINEERING. Manuscript received by the Fluids Engineering Division April 1, 1999; revised manuscript received March 31, 2000. Associate Technical Editor: M. Sommerfeld.

ity, densities, $\rho_A$ and $\rho_B$, and viscosities, $\mu_A$ and $\mu_B$, are constants in this study, even though the dispersed phase is dissolved into the continuous phase.

**2.2 Movement of Interface.** The movement of the interfaces is computed by a front-capturing method using the MDF, following a series of successful simulations about free surface flows (e.g., Kanai and Miyata [11]). The transport equation of the MDF, which is solved to move the position of the interface, is given by putting Eq. (3) into Eq. (1) and dividing Eq. (1) into each phase.

$$\frac{\partial(\rho_A \mathbf{\Phi}_A)}{\partial t} + \nabla \cdot (\rho_A \mathbf{\Phi}_A \mathbf{u}) = -\Gamma \tag{5}$$

$$\frac{\partial(\rho_B \mathbf{\Phi}_B)}{\partial t} + \nabla \cdot (\rho_B \mathbf{\Phi}_B \mathbf{u}) = \Gamma \tag{6}$$

where $\Gamma$ will be given in Section 2.5. Here

$$\mathbf{u} = \mathbf{u}_A = \mathbf{u}_B \tag{7}$$

is assumed in the interface cells since the density difference between the two liquid phases is small compared with that of gas-liquid systems. This also means that the mass-averaged velocity is the same as volume-averaged velocity, $\mathbf{\Phi}_A \mathbf{u}_A + \mathbf{\Phi}_B \mathbf{u}_B$, which satisfies the solenoidal condition if the dissolved volume of the dispersed phase is simply added to the continuous phase

$$\nabla \cdot \mathbf{u} = 0 \tag{8}$$

To determine the position of the interface, Eq. (5) is solved by using a third-order TVD scheme utilizing the Minmod limiter for the advection term. Equation (8) is used for obtaining the Poisson equation for pressure.

**2.3 Surface Tension.** Surface tension is treated as a body force in the NS equation only at the interface cells.

$$\mathbf{f} = \frac{1}{We} \kappa \mathbf{n} S/V \tag{9}$$

where

$$\kappa = \nabla \cdot \mathbf{n} \tag{10}$$

$$\mathbf{n} = \frac{\nabla \mathbf{\Phi}_A}{|\nabla \mathbf{\Phi}_A|} \tag{11}$$

Here $\mathbf{\Phi}_A$ is smoothed by using the averaged values at vertices and, otherwise, $\mathbf{n}$ looses the cell-wise continuity.

**2.4 Mass Transfer in Continuous Phase.** There is no liquid-gas phase change and the concentration of dissolved mass is small, so that the Stefan flow is ignored. It is also known that CO2 easily dissolves into water under the wide range of temperature and pressure, but not vice-versa (e.g., Wiebe et al. [12]). Therefore, the dissolution of the dispersed-phase is regarded as unidirectional diffusion from the dispersed phase at the interface. An advection-diffusion equation for the dissolved mass concentration $C$ is solved in the continuous phase after obtaining flow field at each time step.

$$\frac{\partial C}{\partial t} + \nabla \cdot (\mathbf{u} C) = \frac{1}{\mathrm{Re}\,\mathrm{Sc}} \nabla^2 C \tag{12}$$

In the interface cells, mass transfer is also taken into account only in the continuous phase (the hatched part in Fig. 1), where the solenoidal condition in each phase is satisfied considering the velocity of the interface movement.

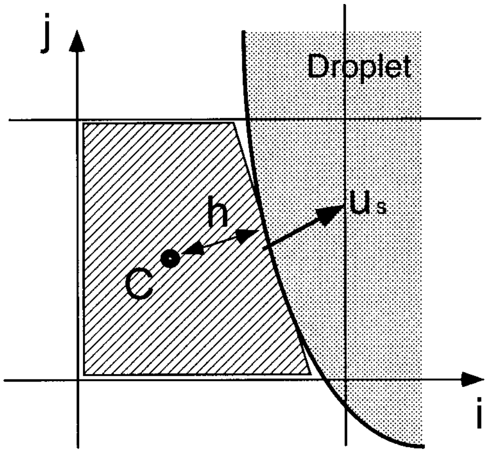

**Fig. 1 Schematic of interface cell**

**2.5 Boundary Conditions.** If not mentioned in each case study, zero-gradient condition is imposed on outer boundaries, such as side, top, and bottom boundaries, for velocity, pressure, and concentration. For rising-droplet simulations, the top boundary is inflow, and, therefore, the standard pressure is given, velocities are given as the negative value of rise velocity, and the concentration of CO2 is set to be 0. Since Eq. (12) is solved only in the continuous phase, the dissolution flux $\nabla C/\mathrm{Re}\,\mathrm{Sc}$ is given at the interface as a boundary condition. This flux also gives the rate at which the droplet shrinks

$$\Gamma = \frac{S}{V} \frac{\nabla C}{\mathrm{Re}\,\mathrm{Sc}} \tag{13}$$

As shown in Fig. 1, the gradient of concentration is calculated by

$$\nabla C = \frac{C_S - C}{h} \tag{14}$$

The concentration of the dispersed-phase mass at the interface on the continuous-phase side is set to be that of saturation. Because Eq. (14) is a linear approximation, there must be some errors. Equation (12) in steady state without flow in the spherical coordinates is

$$\frac{d^2 C}{dr^2} + \frac{2}{r} \frac{dC}{dr} = 0 \tag{15}$$

The analytical solution under the boundary conditions, $C = C_S$ at $r = R_0$ and $C = 0$ as $r \to \infty$, is

$$C = \frac{R_0 C_S}{r}, \quad \frac{dC}{dr} = -\frac{R_0 C_S}{r^2} \tag{16}$$

At $r = R_0$ the error of the first derivative can be estimated that

$$E = \left| \frac{C(r=h) - C_S}{h} - \frac{C_S}{R_0} \right| \bigg/ \frac{C_S}{R_0} \tag{17}$$

As shown in Fig. 1, the maximum $h$ is a half of the cell size. When the diameter of the spherical droplet is as long as $N$ times of the cell size, the error is at most

$$E_{\text{upper}} = \frac{1}{N+1} \tag{18}$$

If $N = 28$, the estimated error is at most 3.4 percent.

**2.6 NS Solver.** The NS solver used in this study is based on the WISDAM code that has been developed by our group of the University of Tokyo for more than a decade (e.g., Miyata et al.

[13], Miyata et al. [14], and Sato et al. [15]). The WISDAM adopts a finite-volume formulation and an explicit MAC-type algorithm

$$\mathbf{u}^{n+1}=\mathbf{u}^{*}-\frac{\Delta t}{\rho}\nabla p^{n+1} \tag{19}$$

$$\mathbf{u}^{*}=\mathbf{u}+\Delta t\left[-\mathbf{u}\cdot\nabla\mathbf{u}+\frac{1}{\mathrm{Re}}\frac{1}{\rho}\nabla\cdot[\mu(\nabla\mathbf{u}+(\nabla\mathbf{u})^{T})]+\frac{1}{\mathrm{Fn}^{2}}\mathbf{g}+\mathbf{f}\right] \tag{20}$$

where the Poisson equation for pressure is solved to attain incompressibility

$$\nabla\left(\frac{1}{\rho}\nabla p^{n+1}\right)=\frac{1}{\Delta t}\nabla\cdot\mathbf{u}^{*} \tag{21}$$

The variables with upper suffix $n+1$ indicate the values at $(n+1)$ time step and the others are the ones at $n$ time step. Pressure and Cartesian components of velocity are allocated in a staggered way. For the convection term in the NS equation, a fifth-order upwinding is used while a third-order upwinding with a TVD scheme is applied to the advection terms in Eqs. (5) and (12), the variables of which are defined at cell center.

**2.7 Computation Procedure.** First of all, grids of constant size are provided in the computational domain, where local grid refinement is not adopted. After setting the initial conditions, i.e., the rest state, Eq. (5) is solved to determine the position of the interface at each time step of evolutionary explicit algorithm, where $\rho_A$ is constant and, consequently, differentiated out. The MDF is reset to be 0 or 1 at each time step, so that only interface cells have nondigit values and the interface is kept within one-cell size. Any numerical errors during the transport of the MDF lead to the erroneous change of the volume of a droplet. This must deteriorate the accuracy of physical shrinkage of the droplet. Therefore, it is necessary to calculate the dissolution rate and the volumes of the droplet before and after the transport, respectively, and to recover the erroneous volume at each time step.

Using this MDF, the density and viscosity are calculated by Eqs. (3) and (4), and the NS equation is solved by the above-mentioned NS solver. In rising droplet simulations, to keep the droplet at the middle of the computational domain, the negative value of acceleration at its gravity center is added to the momentum equation as inertia. Once velocity field is obtained, Eq. (12) is solved in the continuous phase to transfer dissolved CO2. This process is iterated in a time-marching way, where time increment is determined by setting both the Courant and diffusion numbers to be 0.2, the latter of which is based not only on kinematic viscosity but diffusion coefficient of mass transfer.

## 3 Case Studies

**3.1 Rise of Single Droplet.** The present method is first applied to three-dimensional simulations of rising droplets. Mass transfer at the interface is not considered in this case. Table 1 indicates the conditions of the simulations. The reference velocity, $U$, is set to be 0.1 m/s, considering that the order of magnitude of rise velocity of a droplet, the diameter of which has the order of magnitude of 0.01 m. At this Reynolds number, flow is laminar, so that no turbulent model is taken into account.

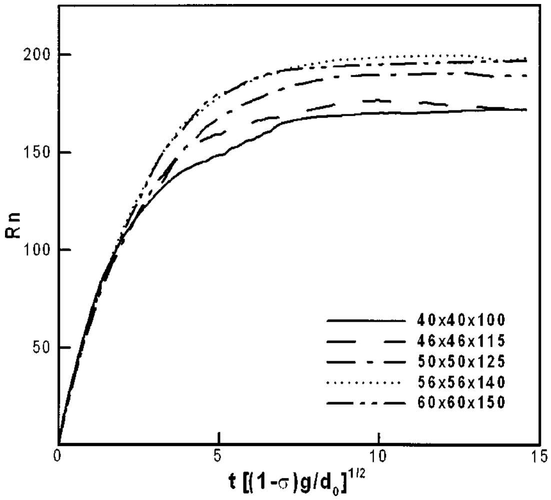

**Fig. 2 Time history of rise velocity of droplet depending on grid size for Case 1-2**

In order to examine the grid dependency of the method, rise

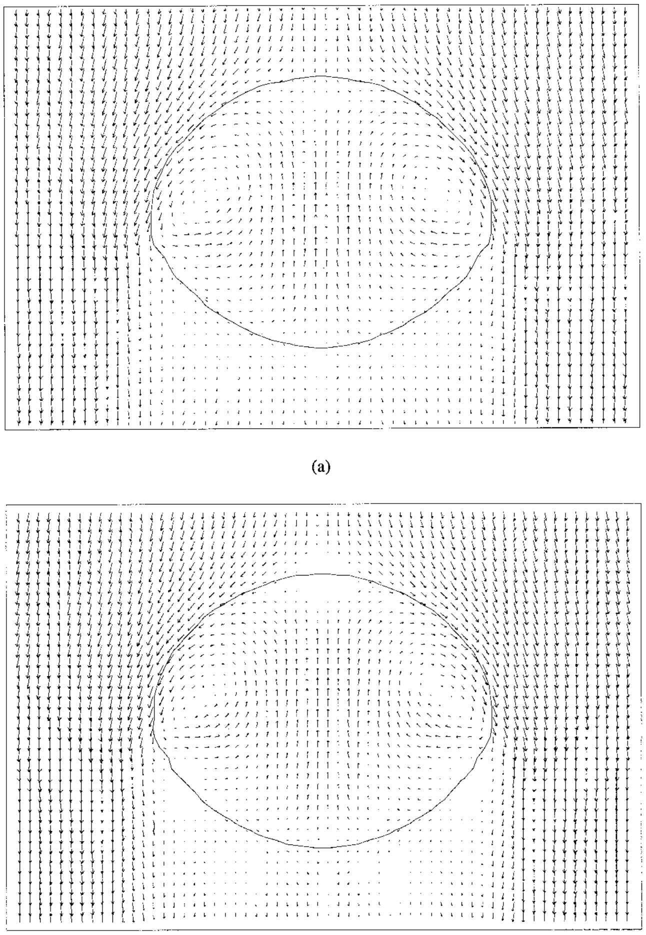
(a)

(b)

**Fig. 3 Velocity vectors around droplet and contour line of MDF (0.5) for Case 1-2. Numbers of grids are (*a*) 56×56×140 and (*b*) 60×60×150, respectively**

**Table 1 Conditions of simulation for rising droplets**

| parameters | Case 1-1 | | Case 1-2 | Case 1-3 |
|---|---|---|---|---|
| | Domain 1-B | Domain 1-A | | |
| Size of Computation Domain | 4.0 x 4.0 x 5.0 | 2.0 x 2.0 x 5.0 | | |
| Number of Grid Points | 112 x 112 x 140 | 56 x 56 x 140 | 40 x 40 x 100<br>46 x 46 x 115<br>50 x 50 x 125<br>56 x 56 x 140<br>60 x 60 x 150 | 56 x 56 x 140 |
| Density Ratio ( $\rho_1/\rho_0$ ) | 0.988 | | | |
| Viscosity Ratio ( $\mu_1/\mu_0$ ) | 0.644 | | | |
| Weber Number ( $We$ ) | 2.53 | | 7.58 | |
| Reynolds Number ( $Re$ ) | 500 | | | 1500 |
| Froude Number ( $Fn$ ) | 0.447 | | | 0.258 |

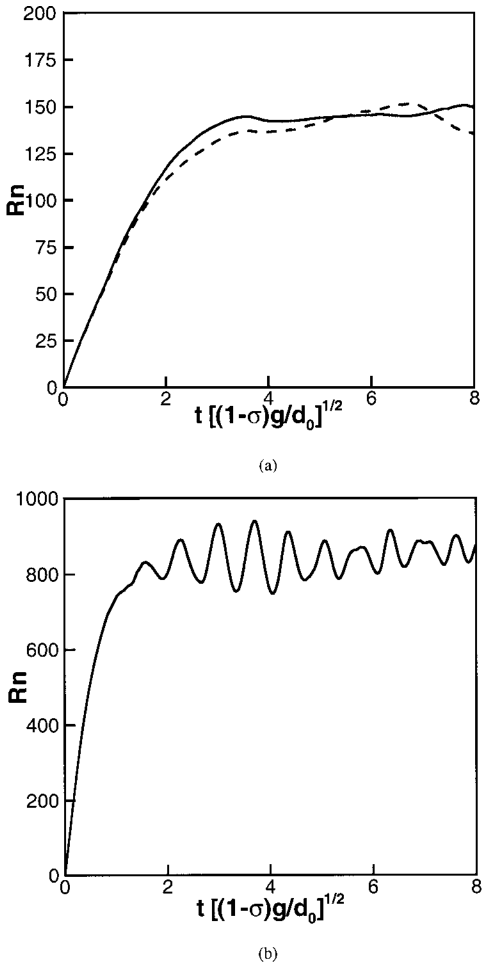

**Fig. 4 Time history of rise velocity of rising droplet. (*a*) Case 1-1. Solid line and broken lines denote results in Domains 1-A and 1-B, respectively. (*b*) Case 1-3.**

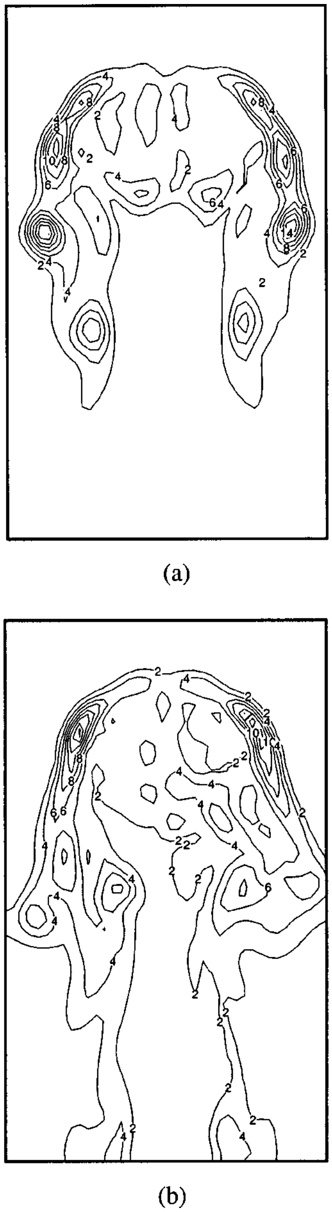

**Fig. 5 Contour map of vorticity for Case 1-3. (*a*) $t=7.2$. (*b*) $t=8.7$**

velocities of a droplet for various grid sizes with time are shown in Fig. 2. Grid convergence is seen to be attained when the grid size becomes as small as $0.0357d_0$ (56 cells in the horizontal direction, in other words, 28 cells for the diameter of the initial spherical droplet). Figure 3 denotes velocity vectors around the droplet and a contour line of the MDF of 0.5, which actually indicates the interface, in two grid systems, 56×56×140 and 60 ×60×150, respectively. It is observed that the shape of the droplet and the velocity field, such as circulations in the droplet, are almost identical.

Figures 4(*a*) and (*b*) indicate the time histories of rise velocity for Cases 1-1 and 1-3, respectively. Physically, these cases correspond to different droplet-diameters for the same liquid-liquid system. Grid size was chosen to be $0.0357d_0$. For Case 1-1, simulations were done in two different computational domains. The resultant rise velocities seem to oscillate with time and have a phase difference between each other. Although unsteadiness is thought to be physical, numerical artifacts, such as computational domain sizes, may cause its ignition. It is also considered that, in terms of time-averaged values, Fig. 4(*a*) suggests small domain-size dependency.

Figure 4(*b*) shows a distinct oscillatory tendency with time in rise velocity. To investigate this, the contour lines of vorticity on a vertical plane slicing the droplet center at $t=7.2$ and at $t=8.7$ are shown in Fig. 5. These timings correspond to a hollow and a hump, respectively, of the time history of rise velocity shown in Fig. 4(*b*). A strong vortex ring is attached to the droplet when the rise velocity is small at $t=7.2$, while the ring moves away from the droplet when the velocity is large at $t=8.7$. This fact may be associated with the oscillatory movement of rise velocity.

### 3.2 Dissolution From a Spherical Droplet without Flow.

To verify the present dissolution algorithm, a simple problem with an analytical solution is solved, that is, mass transfer from a rigid sphere with infinite sink around it. In this case, there is no flow. Table 2 states the conditions of this simulation.

**Table 2 Conditions of simulation for dissolution from a rigid sphere**

| parameters | |
|---|---|
| Size of Computation Domain | 2.0 x 2.0 x 2.0 |
| Number of Grid Points | 56 x 56 x 56 |
| Reynolds Number ( $Re$ ) | 525 |
| Schmidt Number ( $Sc$ ) | 1.0 |

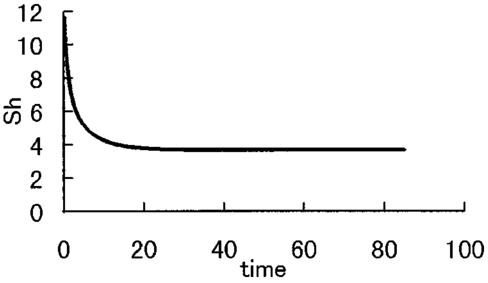

**Fig. 6 Time history of Sherwood number for dissolution from rigid sphere without flow**

An analytical solution of this problem follows. The diffusion flux at the surface of the sphere is solved under the boundary conditions: $C=C_S$ at $r=R_0$ and $C=C_\infty$ at $r=2R_0$

$$q=-4\pi r^2\frac{1}{\mathrm{Sc\,Re}}\frac{dC}{dr}=8\pi R_0\frac{C_S-C_\infty}{\mathrm{Sc\,Re}} \tag{22}$$

On the other hand, mass transfer coefficient at the interface $k$ is defined as

$$q=4\pi R_0^2k'(C_S-C_\infty) \tag{23}$$

Equations (22) and (23) give

$$k'\,\mathrm{Sc\,Re}=\frac{2}{R_0} \tag{24}$$

From the definition of the Sherwood number, we obtain

$$\mathrm{Sh}\equiv 2R_0k'\,\mathrm{Sc\,Re}=4 \tag{25}$$

The time history of the Sherwood number resulting from this simulation is shown in Fig. 6. It is almost identical to the analytical solution and its error is about 3 percent from the solution of Eq. (25) when the steady state is attained. This error is inevitable and reasonable because of the present method described in Section 2.5.

**3.3 Dissolution From a Rising Droplet.** Finally, we applied the present method to a rising droplet flow with mass transfer at the interface. Conditions of this simulation are stated in Table 3. The nondimensional numbers are based on the LCO2-seawater system except for Sc, which is set 1.0 here and it is lower than that of reality. Again, velocities are nondimensionalized by 0.1 m/s.

Figure 7 denotes the time histories of rise velocity and diameter of the droplet, the latter of which is calculated assuming that the droplet is spherical. The results of using two grid systems are almost identical until the nondimensional time of about 7.0, when the grid size of Grid 3-I comes to be about 0.0385$d$. This may mean that 26-cell disposition for the droplet diameter is sufficient to make grid dependency insignificant. In this context, for the finer grids (Grid 3-II), computational results can be reliable until the shrinking diameter becomes as long as 26 cells. Accordingly, the computation was stopped at such timing, the nondimensional time of 12.0.

**Table 3 Conditions of simulation for dissolution from a rising droplet**

| parameters | Grid 3-I | Grid 3-II |
|---|---|---|
| Size of Computation Domain | 2.0 x 2.0 x 4.0 | |
| Number of Grid Points | 60 x 60 x 120 | 70 x 70 x 140 |
| Density Ratio ( $\rho_1/\rho_0$ ) | 0.90 | |
| Viscosity Ratio ( $\mu_1/\mu_0$ ) | 0.10 | |
| Weber Number ( $We$ ) | 1.17 | |
| Reynolds Number ( $Re$ ) | 525 | |
| Froude Number ( $Fn$ ) | 0.451 | |
| Schmidt Number ( $Sc$ ) | 1.0 | |
| Saturated Concentration ( $C_S$ ) | 0.14 $Kg/m^3$ | |

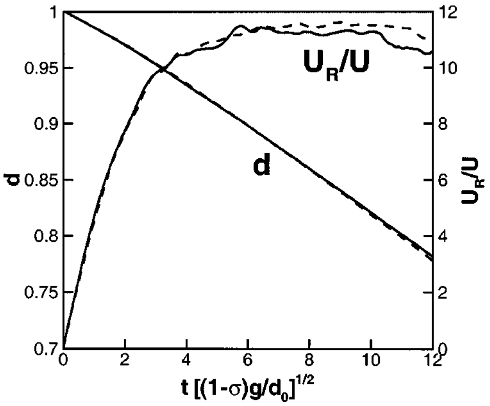

**Fig. 7 Time histories of rise velocity and diameter of rising droplet with mass transfer at interface. Solid and broken lines denote results for Grid 4-I and 4-II, respectively.**

Figure 8 denotes the time histories of resultant Reynolds and Sherwood numbers based on the rise velocity and the diminishing diameter of the droplet for Grid 3-II. Also shown is the time history of the Sherwood number calculated by the Ranz-Marshall's equation

$$\mathrm{Sh_{RM}}=2.0+0.60Rn^{1/2}\mathrm{Sc}^{1/3} \tag{26}$$

This equation was obtained for a rigid sphere in uniform flows. It is not necessarily expected that the both Sherwood numbers match because the droplet is deformed and flow around it is unsteady. Textbooks suggest some modifications for droplet flows, such as

$$\mathrm{Sh_{MRM}}/\mathrm{Sh_{RM}}=\mathrm{Sc}^{\alpha/6}\sqrt{1+1.9\alpha} \tag{27}$$

where

$$\alpha=U_I/U_R \tag{28}$$

In this simulation, simulated $U_I/U_R$ is about 0.97 and, therefore, $\mathrm{Sh_{MRM}}/\mathrm{Sh_{RM}}\approx 1.7$. The Sherwood number, Sh, resulted from the simulation is in moderately good agreement with $\mathrm{Sh_{MRM}}$ obtained

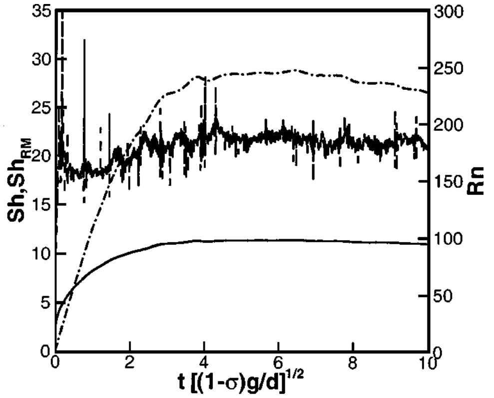

**Fig. 8 Time histories of Reynolds number and Sherwood number of rising droplet with mass transfer at interface for Grid 4-2. Solution of Ranz-Marshall's equation for rigid sphere is superimposed.**

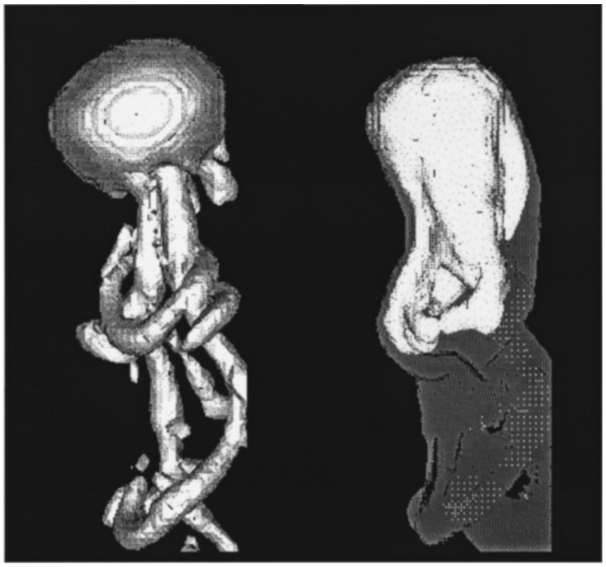

(a) (b)

**Fig. 9 3D shaded images of rising droplet with mass transfer at interface. (*a*) Iso-surface (20.0) of Laplacian of pressure. (*b*) Iso-surfaces ($0.05\ C_S, 0.13\ C_S$) of mass concentration.**

by Eq. (27), though it is still necessary to compare it with experiments to assure the validity of the present method.

Figure 9(*a*) shows an iso-surface of the Laplacian of pressure, which denotes the position and the shape of vortices. The droplet seems to be deformed to an elliptic shape. Ring-type and horseshoe-type vortices are clearly visualized in the wake of the deformed droplet, as is generally seen in the wake of a sphere about this Reynolds number. Figure 9(*b*) shows two iso-surfaces of $C$. It is observed that the dissolved mass attaches the fringe of the vortices in the wake.

## 4 Conclusions

A numerical simulation method has been developed for solving two-phase flow with mass transfer through the interface. The interface is determined by a front-capturing method solving the transport equation of marker density function. Surface tension is treated as a body force in the NS equation. From the interface, mass of the dispersed phase dissolves into the continuous phase and diminishes at the rate of dissolution. Transfer of the dissolved mass is obtained by solving an advection-diffusion equation for its concentration in the continuous phase.

Three case studies were carried out to validate the present method. Rise of a droplet was simulated and verified by confirming grid convergence. Simulated Sherwood number of a rigid sphere without flow was in good agreement with an analytical solution. Finally, dissolution from a rising droplet was simulated successfully. It was visualized that horseshoe-type vortices are attached by dissolved mass in the wake of the deformed droplet. The simulated Sherwood number was compared moderately well with the solution of an empirical equation.

## Acknowledgments

This work is supported by the Research Institute of Innovative Technology for Earth (RITE), which is entrusted by the New Energy and Industrial Technology Development Organisation (NEDO).

## Nomenclature

$C$ = mass concentration, Kg/m$^3$
$C_S$ = saturated concentration, Kg/m$^3$
$C_\infty$ = concentration at infinite distance, Kg/m$^3$
$d$ = nondimensional diameter of droplet
$d_0$ = reference length: initial diameter of droplet, m
$D$ = diffusion coefficient of dispersed-phase mass in continuous phase, m$^2$/s
$\mathbf{f}$ = nondimensional body force vector
Fn = $U/\sqrt{gd_0}$ Froude number
$g$ = gravity acceleration, m/s$^2$
$\mathbf{g}$ = unit gravity vector
$h$ = distance between interface and volume-center of interface cell
$k$ = mass transfer coefficient at interface, m/s
$k'$ = $k/U$ nondimensional mass transfer coefficient at interface
$\mathbf{n}$ = unit normal vector to interface
$p$ = nondimensional pressure
$q$ = nondimensional mass diffusion flux at interface
$r$ = nondimensional coordinate component in radial direction of a droplet
$R$ = $\sqrt[3]{3V_d/4\pi}$ nondimensional radius of a droplet assuming that its shape is sphere
$R_0$ = 0.5 nondimensional radius of initial droplet
Re = $\rho_0 d_0 U/\mu_0$ Reynolds number
Rn = $U_R$ Re Reynolds number based on rise velocity
$S$ = nondimensional area of interface in an interface cell
Sc = $\mu_0/(\rho_0 D)$ Schmidt number
Sh = $d_0 k/D = k'$ Sc Re Sherwood number
Sh$_{\mathrm{RM}}$ = Sherwood number given by the empirical Ranz-Marshall's equation
Sh$_{\mathrm{MRM}}$ = modified Ranz-Marshall's Sherwood number for droplets
$\mathbf{u}$ = $(\rho_A \mathbf{\Phi}_A \mathbf{u}_A + \rho_B \mathbf{\Phi}_B \mathbf{u}_B)/(\rho_A \mathbf{\Phi}_A + \rho_B \mathbf{\Phi}_B)$ mass-averaged velocity vector
$\mathbf{u}_A$ = velocity vector of dispersed phase
$\mathbf{u}_B$ = velocity vector of continuous phase
$U$ = reference velocity, 0.1 m/s
$U_I$ = nondimensional interfacial velocity
$U_R$ = nondimensional rise velocity
$V$ = nondimensional volume of an interface cell
$V_d$ = nondimensional volume of droplet
We = $\rho_0 d_0 U^2/\sigma$ Weber number
$\Gamma$ = mass flux of dispersed phase at interface by dissolution
$\mathbf{\Phi}_A$ = volume fraction of dispersed phase or, in other words, marker density function
$\mathbf{\Phi}_B$ = $1 - \mathbf{\Phi}_A$, volume fraction of continuous phase
$\kappa$ = nondimensional curvature of interface
$\mu$ = nondimensional viscosity
$\mu_A$ = viscosity of dispersed phase, Kg/(ms)
$\mu_B$ = viscosity of continuous phase, Kg/(ms)
$\rho$ = nondimensional density
$\rho_A$ = density of dispersed phase, Kg/m$^3$
$\rho_B$ = density of continuous phase, Kg/m$^3$
$\sigma$ = interface tension, Kg/s$^2$

## References

[1] Herzog, H., Adams, E., Auerbach, D., and Caulfield, J., 1996, ''Environmental Impact of Ocean Disposal of CO2,'' Energy Convers. Manage., **37**, Nos. 6–8, pp. 999–1005.
[2] Ohsumi, T., 1997, ''CO2 Storage Options in the Deep Ocean,'' Mar. Technol. Soc. J., **29**, No. 3, pp. 58–66.
[3] Nakashiki, N., Ohsumi, T., and Katano, N., 1995, ''Technical View on CO2 Transportation onto the Deep Ocean Floor and Dispersion at Intermediate Depths,'' Handa, N., and Ohsumi, T. eds., *Direct Ocean Disposal of Carbon Dioxide*, pp. 183–193.

[4] Ozaki, M., 1997, ‘‘CO2 Injection and Dispersion in Mid-Ocean Depth by Moving Ship,’’ Waste Management, **17**, No. 5/6, pp. 369–373.

[5] Kanai, A., and Miyata, H., 1998, ‘‘Numerical Simulation of Bubbles in a Boundary Layer by Maker-Density-Function,’’ *Proceedings of 3rd International Conference on Multiphase Flow*, ICMF’98, Lyon, France.

[6] Tomiyama, A., Makino, Y., Zun, I., and Sakaguchi, T., 1998, ‘‘Bubble Shape Modelling for a 3D Two-Way Bubble Tracking Method,’’ *Proceedings of 3rd International Conference on Multiphase Flow*, ICMF’98, Lyon, France.

[7] Gueyffier, D., and Zaleski, S., 1998, ‘‘Full Navier-Stokes Simulations of Droplet Impact on Thin Liquid Films,’’ *Proceedings of 3rd International Conference on Multiphase Flow*, ICMF’98, Lyon, France.

[8] Bidoae, R., and Raad, P. E., 1998, ‘‘Mitigation of Large Wave Damage on Shoreline Structure,’’ *Proceedings of ASME Fluids Engineering Division Summer Meeting*, FEDSM98-5222, pp. 1–6.

[9] Matsumoto, Y., and Takagi, S., 1998, ‘‘Multiscale Analysis of Bubbly Flow,’’ *Proceedings of ASME Fluids Engineering Division Summer Meeting*, FEDSM98-5311, pp. 1–2.

[10] Tryggvason, G., Bunner, B., Esmaeeli, A., and Mortazavi, S., 1998, ‘‘Direct Numerical Simulations of Dispersed Flows,’’ *Proceedings of 3rd International Conference on Multiphase Flow*, ICMF’98, Lyon, France.

[11] Kanai, A., and Miyata, H., 1996, ‘‘Numerical Analysis of Structure of Free-Surface Shock Wave About a Wedge Model,’’ J. Ship Res., **40**, No. 4, pp. 278–287.

[12] Wiebe, R., and Gaddy, V. L., 1941, ‘‘Vapor Phase Composition of Carbon Dioxide-Water Mixtures at Various Temperatures and at Pressures to 700 Atmospheres,’’ J. Am. Chem. Soc., **63**, pp. 475–477.

[13] Miyata, H., Sato, T., and Baba, N., 1987, ‘‘Difference Solution of a Viscous Flow with Free-Surface Wave,’’ J. Comput. Phys., **72**, No. 2, pp. 393–421.

[14] Miyata, H., Zhu, M., and Watanabe, O., 1992, ‘‘Numerical Study on a Viscous Flow with Free-Surface Waves about a Ship in Steady Straight Course by a Finite-Volume Method,’’ J. Ship Res., **36**, No. 4, pp. 332–345.

[15] Sato, T., Izumi, K., and Miyata, H., 1998, ‘‘Numerical Simulation of Manoeuvering Motion,’’ *Proceeding of 22nd Symposium on Naval Hydrodynamics* (in press).

**N. A. Patankar**
Research Associate,
Department of Aerospace Engineering
and Mechanics,
University of Minnesota,
Minneapolis, MN 55455
e-mail: patankar@aem.umn.edu

**H. H. Hu**
Associate Professor,
Department of Mechanical Engineering
and Applied Mechanics,
University of Pennsylvania,
Philadelphia, PA 19104-6315

# A Numerical Investigation of the Detachment of the Trailing Particle From a Chain Sedimenting in Newtonian and Viscoelastic Fluids

*Particles sedimenting in a viscoelastic fluid form chains. It has been observed in experiments that, sometimes, the last particle in the chain gets detached. In this paper, we investigate this phenomenon. It is known that a long chain falls faster than a single particle in fluids. This long body effect tends to detach the last particle from the chain. The wake effect and the normal stress effect are the mechanisms that work against the long body effect. The last particle is not detached if the inertial wake effects are strong enough to cause substantial drag reduction on it. The detachment is also restricted by the elastic normal stress of the viscoelastic fluid.* [S0098-2202(00)01003-8]

## 1 Introduction

Many researchers have studied the interaction between spheres settling in Newtonian and viscoelastic fluids. Goldman et al. [1] have obtained exact numerical values, in the creeping flow limit, of the terminal velocities of two identical, arbitrarily oriented spheres settling in a Newtonian fluid. Their results and experimental data show that two spheres settling slowly along their line of centers fall with a common terminal velocity. Riddle et al. [2] presented an experimental investigation in which the distance between two identical spheres falling along their line of centers in a viscoelastic fluid was determined as a function of time. They found that, for all five fluids used in the experiment, the spheres attract for small initial separations and separate if they are not close (Fig. 1). This led to the definition of critical initial separation. The Reynolds number in their study was less than 0.05. It is, therefore, fair to say that the phenomenon they observed was due to the elastic effects of the fluid rather than the inertial effects.

Theoretical investigation has been attempted to explain the above phenomenon. Highly successful perturbation theories have been developed, based on the second-order fluid model (Leal [3] and Brunn [4]). Brunn [5] applied these schemes to the interaction of two sedimenting spheres. His analysis shows that the spheres always attract, in apparent disagreement with the observation of Riddle et al. [2]. Using the second-order fluid model, Joseph [6] attributed the tendency of attraction to the normal stress effects. He also mentioned that shear thinning, which is generally observed in most viscoelastic fluids, would enhance the attraction between the spheres. Feng et al. [7] performed two-dimensional numerical simulation of the interaction of particles (circular) in an Oldroyd-B fluid. They carried out two kinds of simulations of particles settling along their line of centers at low Reynolds number, viz. static and dynamic. They calculated the drag on the top and bottom particles in their static simulations. Their static simulation results were in qualitative agreement with the experimental observations of Riddle et al. [2]. The repulsive force between the two particles, which they obtained from their static simulations, was very weak and was easily drowned out in their dynamic simulations. As a result the separation of two particles released one far above the other was not realized in their dynamic simulations. Bird et al. [8] suggest that the critical distance of separation for end-to-end settling may be associated with a negative wake. The issue of separation of particles falling, very slowly, one above the other is still an unresolved one.

At higher Reynolds numbers two particles falling one behind the other in Newtonian fluids exhibit a tendency to draft, kiss, and tumble (Joseph [6]). Drafting and kissing are seen because of the wake effect and tumbling is related to the stability of long bodies falling in a fluid. A trailing sphere caught in the wake of a leading one experiences a reduced drag and thus falls faster than the leading sphere. This is drafting. The increased speed of fall impels the trailing sphere into kissing contact with the leading sphere. In addition to the inertial effect, the normal stress effects cause two particles to attract, in a viscoelastic fluid, if their separation is not very large.

A chain of spheres falling behind a single sphere in Newtonian or viscoelastic fluids, at very low Reynolds number, converges with the leading sphere to form a longer chain (Fig. 2). The long chain of spheres behaves like a long object and tends to fall faster than a single sphere. The weight of a long body increases in proportion to its length but the drag exerted by the fluid on it does not increase in the same proportion. This causes a kissing contact between the chain and the leading sphere. Due to the inertial

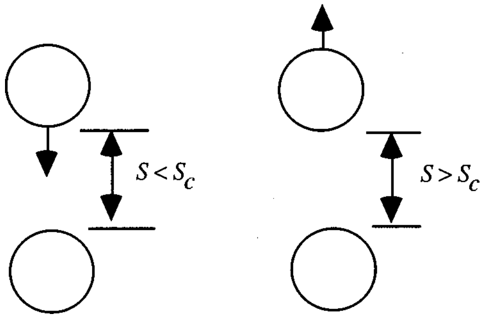

**Fig. 1 Phenomenon of critical distance with two spheres settling in a viscoelastic fluid. The mechanism of attraction is explained by compressive normal stresses (Joseph [6]). The mechanism of separation is yet unresolved.**

---

Contributed by the Fluids Engineering Division for publication in the JOURNAL OF FLUIDS ENGINEERING. Manuscript received by the Fluids Engineering Division October 20, 1999; revised manuscript received April 18, 2000. Associate Technical Editor: M. Dhaubhadel.

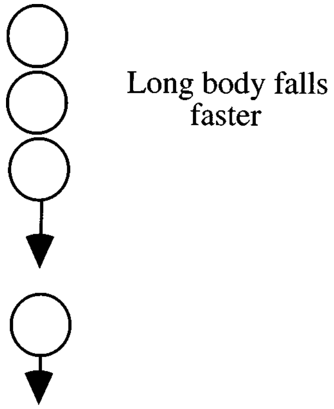

Fig. 2 Formation of long chains in Newtonian and viscoelastic fluids. This chain configuration is unstable in Newtonian fluids whereas it is stable in viscoelastic fluids in slow flows.

effects the long chain structure becomes unstable and tumbles at higher Reynolds numbers. Such turning happens at nonzero Reynolds numbers in Newtonian fluids, whereas in viscoelastic fluids it happens at relatively higher Reynolds numbers depending on the fluid (Liu and Joseph [9]).

There are various mechanisms at work in the case of a single sphere falling behind a chain of spheres. The trailing sphere is not always attracted to the chain. In viscoelastic fluids, it is seen that there is attraction if the separation between the trailing sphere and the chain is not very large. As shown in Fig. 3, the trailing sphere detaches from the chain when the distance between them exceeds a critical value (Joseph [6]). This observation is similar to that seen in the experiments by Riddle et al. [2]. However, sometimes, an attached sphere in a chain gets separated. In this case the critical separation for detachment is zero. Although this phenomenon looks similar to that observed by Riddle et al. [2], it is not clear if it is caused by the same mechanism. It is also not clear whether the phenomenon of critical distance in chains is peculiar to the viscoelastic fluid model. It is difficult to experimentally study this phenomenon in Newtonian fluids since a perfectly aligned chain configuration is not stable. However, this difficulty can be overcome in numerical simulations.

In this paper, we study the phenomenon of detachment of particles from a chain. We perform two-dimensional dynamic simulation of particles in Newtonian and Oldroyd-B fluids. In our simulations, there are $N$ particles (cylinders) in the leading chain and a trailing particle is placed with some initial separation. We found that the detachment of a particle from a chain is not peculiar to the viscoelastic fluid model. It can also be observed in Newtonian fluids under certain ideal conditions.

In the next section, we will make a brief mention of the numerical method. Then we will present results on chaining in Newtonian and viscoelastic (Oldroyd-B) fluids. In the end conclusions will be presented.

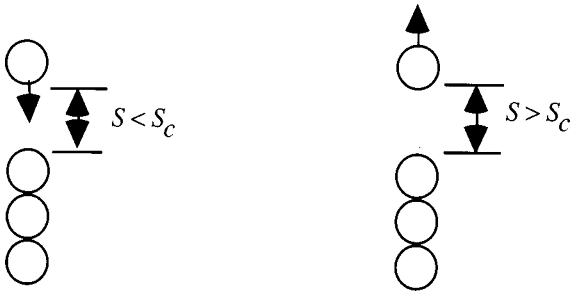

Fig. 3 Phenomenon of critical distance for chains settling in viscoelastic fluids

## 2 The Numerical Scheme

The numerical scheme is described in detail by Hu [10] and Hu and Patankar [11]. This scheme solves the full non-linear Navier-Stokes equations for the fluid in conjunction with the Newton's equation of motion for the particles. For a viscoelastic fluid, the momentum equation is coupled with the constitutive equation of an Oldroyd-B fluid. The equations are solved by the EVSS formulation.

A finite element technique based on moving unstructured grids is used to simulate the motion of large numbers of particles in a flowing liquid. A generalized Galerkin finite element formulation, which is second-order accurate in space, is used to discretize the equations. Upwinding is not used in the convective terms. An arbitrary Lagrangian-Eulerian (ALE) technique is adopted to deal with the motion of the particles. At each time step, the grid is updated according to the motion of the particles and checked for element degradation. If an unacceptable element distortion is detected, a new finite element grid is generated and the flow fields are projected from the old grid to the new grid. The generalized ALE Galerkin finite element approach used here gives rise to a set of nonlinear algebraic equations, which are solved via a quasi-Newton scheme. The corresponding linearized system is solved by an iterative solver using a preconditioned generalized minimal residual algorithm. Initially, the particles are positioned in the fluid with a zero velocity. The particles are then released and the motion of the combined fluid/particle system is simulated using a procedure in which the positions of the particles and of the mesh are updated explicitly, while the velocities of the fluid and the solid particles are determined implicitly. Hu [10] and Hu and Patankar [11] have reported convergence tests and benchmark solutions for this numerical scheme.

## 3 Nondimensional Parameters

Consider a viscoelastic (Oldroyd-B) fluid with constant properties. Let $\eta$ be the viscosity, $\lambda_1$ be the relaxation time and $\lambda_2$ be the retardation time of the fluid. Let $d$ be the diameter of the circular particle, $g$ be the gravitational acceleration, $\rho_s$ be the density of the particle and $\rho_f$ be the density of the fluid. Let $S_c$ be the critical distance of separation and let there be $N$ particles in the leading chain. Considering the width of the channel to be large enough to exclude the wall effects we get

$$S_c = f(d,\rho_s,\rho_f,\eta,\lambda_1,\lambda_2,g,N), \tag{1}$$

where $f$ is some function. Applying Buckingham's Pi theorem we can write:

$$\left(\frac{S_c}{d}\right) = f\left(N, \frac{\rho_s}{\rho_f}, \frac{\eta}{\rho_f d\sqrt{gd}}, \frac{\lambda_1\eta}{\rho_f d^2}, \frac{\lambda_2}{\lambda_1}\right). \tag{2}$$

Note that:

$$\frac{\eta}{\rho_f d\sqrt{gd}} \equiv \frac{\mathrm{Fr}^{0.5}}{\mathrm{Re}} \quad \text{and} \quad \frac{\lambda_1\eta}{\rho_f d^2} \equiv \frac{\mathrm{De}}{\mathrm{Re}},$$

where Re is the Reynolds number, Fr is the Froude number, and De is the Deborah number. The ratio of dimensionless numbers is used in the expression for critical distance since the characteristic velocity of the problem is not known beforehand. We use an Oldroyd-B model with $\lambda_2/\lambda_1 = 1/8$. $\lambda_1 = 0$ or $\lambda_2/\lambda_1 = 1$ results in a Newtonian fluid.

## 4 Chaining in a Newtonian Fluid

A vertically falling chain configuration is unstable in Newtonian fluids. In our simulations we consider a chain sedimenting along the centerline of a vertical channel (Fig. 4). The width of the

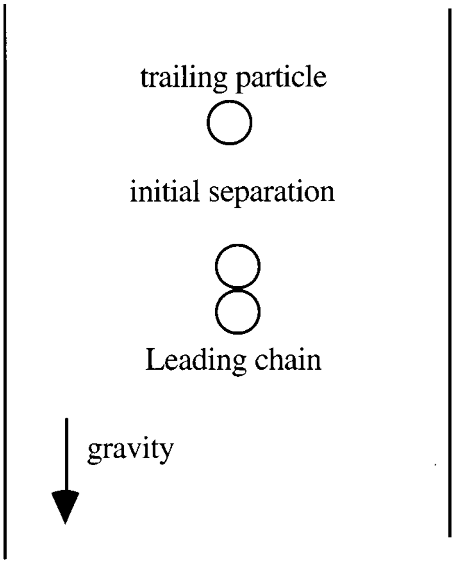

**Fig. 4 Numerical simulations are performed in a channel with the walls wide apart (the channel width is 15 times the particle diameter)**

channel is taken large enough to minimize the wall effects. Due to the symmetry of the problem, the vertical chain configuration is stable during the simulations even in a Newtonian fluid.

**4.1 Phenomenon of Critical Distance of Separation.** To demonstrate the phenomenon of critical distance of separation in a Newtonian fluid we consider a case with $N=2$, $\rho_s/\rho_f=1.01$ and $\mathrm{Fr}^{0.5}/\mathrm{Re}=0.026$. Figure 5 depicts the plot of velocities of the leading chain and the trailing particle as a function of time for three different initial separations. If the trailing particle falls with a velocity less than that of the leading chain then we have separation; if it falls faster then we have attachment. No detachment is said to occur if the magnitude of the difference in velocities of the trailing particle and the leading chain is less than $10^{-4}$. Figure 5 shows that for zero initial separation all the particles fall with a common velocity indicating no detachment.

Note that the initial separation is not exactly equal to zero during the simulations. We set the initial distance of separation between all adjacent particles to 0.01 times the particle diameter. Separation between particles in a liquid is never exactly zero unless cavitation occurs. We do not consider this phenomenon. Hence there is always a thin layer of fluid between the particles. In our simulations we have a ''collision scheme'' which keeps the particles separated by some minimum distance (Hu and Patankar [11]). If the particles stay together, the separation distance is found to reduce to the one set by the collision scheme in all our simulations. This is as close as the particles can get and is equivalent to zero separation for the purpose of our simulations.

When the initial separation is increased to 1.5 times the diameter of the particles we see that the trailing particle falls faster, indicating attachment. On further increasing the initial distance of separation to two times the diameter of the particle, we see that the trailing particle now falls slower than the leading chain indicating further separation. This clearly indicates that the phenomenon of critical distance in a sedimenting chain is not peculiar to the viscoelastic fluid model and can be seen in Newtonian fluids as well.

The leading chain behaves like a long body and tends to fall faster than a single particle (the long body effect). Consequently, if the trailing particle is far behind the leading chain there is separation. But when the trailing particle is in the wake of the leading chain it experiences reduced drag and may fall faster than the leading chain, causing attachment. Thus we see attraction due to the wake effect. Competition between the long body effect and the wake effect gives rise to the phenomenon of critical distance of separation in a Newtonian fluid.

**4.2 Effect of Number of Particles in the Leading Chain.** Consider a case with $\rho_s/\rho_f=1.005$ and $\mathrm{Fr}^{0.5}/\mathrm{Re}=0.026$. The initial distance of separation between the leading chain and the trailing particle is zero. We consider $N=2$ and 3. Figure 6 shows that for $N=2$ all the particles fall with a common velocity indicating no detachment. For $N=3$, the leading chain falls faster than the trailing particle, indicating detachment. Increase in the number of particles in the leading chain induces detachment.

Increase in the number of particles in the leading chain increases both, the long body effect and the wake effect (there is a stronger wake behind a chain falling faster). The long body effect dominates as the number of particles in the leading chain is increased. Consequently, the critical distance of separation decreases with increase in the number of particles in the leading chain.

**4.3 Effect of Density Ratio.** We set $N=3$ and $\mathrm{Fr}^{0.5}/\mathrm{Re}=0.026$. The initial distance of separation between the trailing particle and the leading chain is zero. We consider two cases with $\rho_s/\rho_f=1.005$ and 1.01, respectively. Figure 7 shows that the trailing particle separates from the leading chain when the density

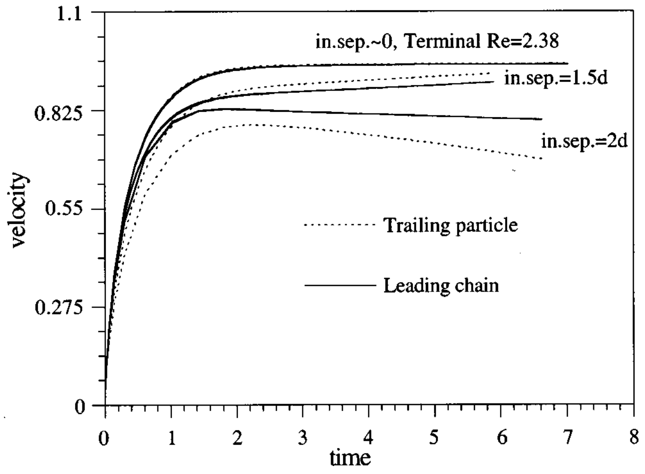

**Fig. 5 Phenomenon of critical distance in Newtonian fluids, $N=2$, $\rho_s/\rho_f=1.01$ and $\mathrm{Fr}^{0.5}/\mathrm{Re}=0.026$**

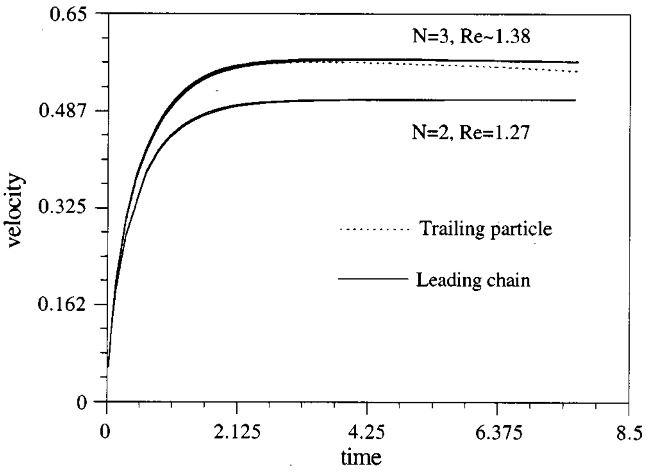

**Fig. 6 Effect of number of particles in the leading chain. Initial separation ~0, $\rho_s/\rho_f=1.005$ and $\mathrm{Fr}^{0.5}/\mathrm{Re}=0.026$.**

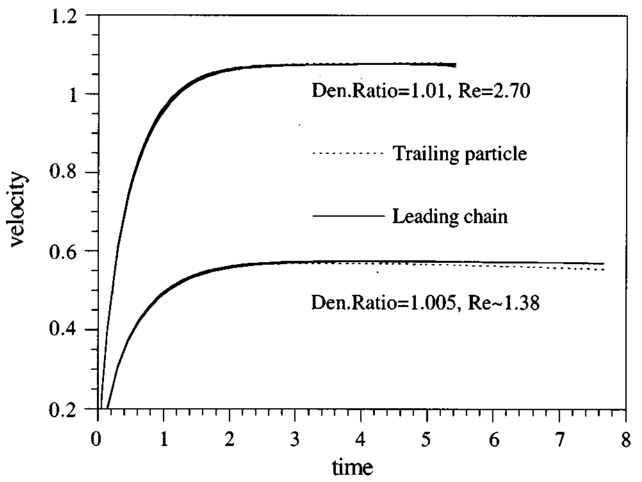

**Fig. 7 Effect of density ratio. Initial separation ∼0, $N=3$ and $\mathrm{Fr}^{0.5}/\mathrm{Re}=0.026$.**

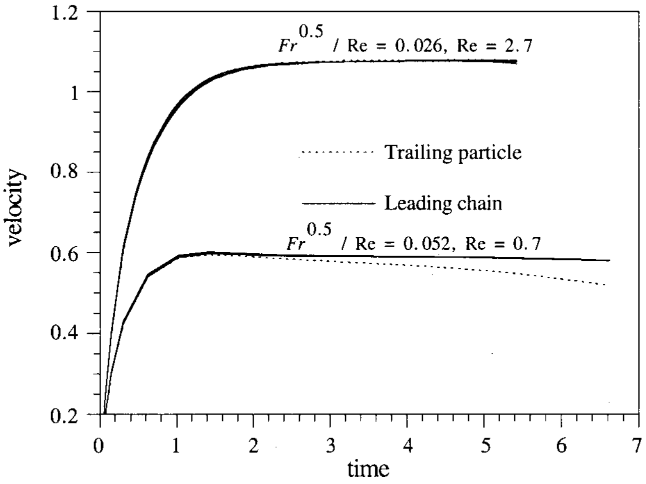

**Fig. 8 Effect of viscosity. Initial separation ∼0, $N=3$ and $\rho_s/\rho_f=1.01$.**

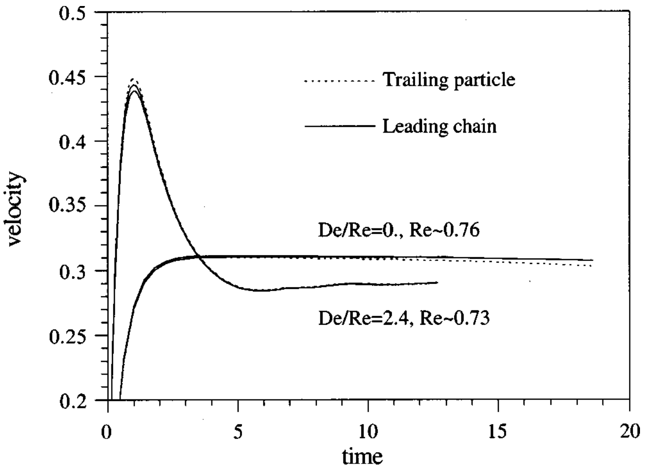

**Fig. 9 Effect of fluid elasticity. Initial separation ∼0, $N=2$, $\rho_s/\rho_f=1.003$ and $\mathrm{Fr}^{0.5}/\mathrm{Re}=0.026$.**

ratio is 1.005. When the particles are denser ($\rho_s/\rho_f=1.01$), there is no detachment. Increasing the density ratio increases the wake effect (indicated by higher Reynolds number) which induces attachment. This causes the critical distance of separation to increase with increase in the density ratio.

**4.4 Effect of Viscosity.** We now set $N=3$ and $\rho_s/\rho_f=1.01$. The initial distance of separation between the trailing particle and the leading chain is zero. Increase in the viscosity of the fluid is manifested through increase in $\mathrm{Fr}^{0.5}/\mathrm{Re}$. We consider two cases with $\mathrm{Fr}^{0.5}/\mathrm{Re}=0.026$ and 0.052, respectively. Figure 8 shows that the trailing particle remains attached to the leading chain when $\mathrm{Fr}^{0.5}/\mathrm{Re}=0.026$. Increasing the viscosity increases the drag on the particles and reduces the Reynolds number (Fig. 8). The inertia effects become less dominant at lower Reynolds number, reducing the wake effect. This causes the critical distance of separation to decrease with an increase in the viscosity of the fluid.

## 5 Chaining in Viscoelastic Fluids

We consider an Oldroyd-B fluid with $\lambda_2/\lambda_1=1/8$ and $\mathrm{De}/\mathrm{Re}=2.4$. In the case of Newtonian fluids, $\mathrm{De}/\mathrm{Re}=0$. We study the effect of viscoelastic properties by comparing chains in an Oldroyd-B fluid and a Newtonian fluid while keeping all other parameters the same. Consider a case with $N=2$, $\rho_s/\rho_f=1.003$, and $\mathrm{Fr}^{0.5}/\mathrm{Re}=0.026$. The initial separation between the trailing particle and the leading chain is zero. Figure 9 shows that the trailing particle gets detached in the Newtonian fluid whereas in the Oldroyd-B fluid there is no detachment. This suggests that the elasticity of the fluid induced attachment. The tendency to attach in a viscoelastic fluid is due to the normal stress effects as explained by Joseph [6].

Riddle et al. [2] had observed that for large initial separation (greater than 5 times the diameter of the particle) the trailing particle tends to detach due to some viscoelastic effects. As mentioned before, this has not yet been explained theoretically and is not captured in any of the numerical simulations. Our simulations do not capture this effect either. Nevertheless, it should be noted that the tendency to detach due to the viscoelastic effects (as observed by Riddle) is important for large initial separations whereas the tendency to detach due to the long body effect is active even for zero initial separations. Thus, for small initial separations, long body effect is a dominant phenomenon and especially so for the detachment of the last particle from a chain.

Figure 10 shows the separation of particles from a chain in viscoelastic fluids. It shows that the last two particles in a chain of six particles are detached from the chain one after the other.

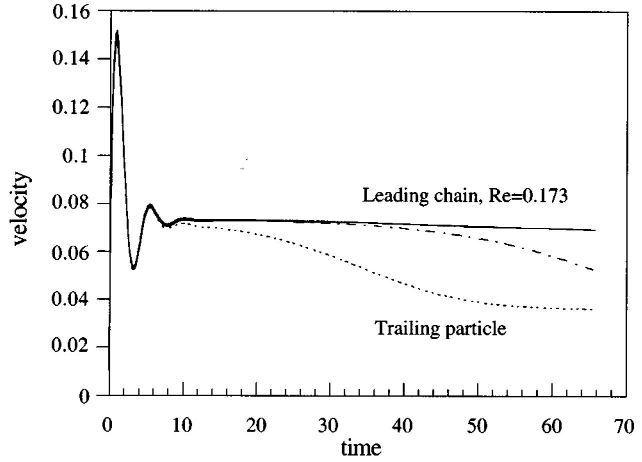

**Fig. 10 Sequential separation of particles from a chain of six particles in a viscoelastic fluid, $\rho_s/\rho_f=1.001$, $\mathrm{Fr}^{0.5}/\mathrm{Re}=0.026$ and $\mathrm{De}/\mathrm{Re}=2.4$**

## 6 Conclusions

In this paper, we have investigated the phenomenon of detachment of a trailing particle from a leading chain, frequently observed in sedimentation experiments involving viscoelastic fluids. We performed two-dimensional dynamic simulation of particles in Newtonian and Oldroyd-B fluids. We found that the detachment of a particle from a chain is not peculiar to the viscoelastic fluid models. It can also be observed in Newtonian fluids under certain ideal conditions.

A chain of particles behaves like a long body and tends to fall faster than a single particle, inducing detachment (the long body effect). The mechanisms that work against this are the wake effect and the normal stress effect. The wake of the leading chain reduces the drag on the trailing particle. This causes attraction. In a viscoelastic fluid, the normal stress effect also causes attraction. The long body effect competes with the wake and normal stress effects to give rise to the phenomenon of critical distance of separation. If the initial separation of the trailing particle from the leading chain is less than this critical distance then there is attraction otherwise there is separation. The critical distance of separation depends on various flow parameters. Knowledge of the functional form of this dependence can be used to determine the rheological properties of the fluid.

In our numerical simulations, we chose a wide channel to minimize the effect of channel walls. In some experiments, the particles (spheres) are dropped in a slit whose gap is slightly bigger than the particle diameter. This confines the particles to move in two dimensions. In this configuration, the long body effect will be reduced since the drag on a chain of spheres will be more linearly dependent on the length of the chain. In an infinite domain, the drag on a chain increases logarithmically with the length of the chain in the creeping flow limit.

## Acknowledgment

This work was supported by the National Science Foundation under an HPCC Grand Challenge Grant ECS-9527123 and CTS 94-10022 and by the Research Foundation of the University of Pennsylvania.

## Nomenclature

$d$ = diameter of circular particles
De = $\lambda_1 U/d$; Deborah number
Fr = $U^2/gd$; Froude number
$g$ = acceleration due to gravity
$N$ = number of particles in the leading chain
Re = $\rho_f U d/\eta$; Reynolds number
$S$ = separation between particles (see Figs. 1 and 3)
$S_c$ = critical distance of separation for the detachment of the trailing particle
$U$ = characteristic velocity of the problem (defined as the velocity of the leading chain)
$\eta$ = dynamic viscosity of the fluid
$\lambda_1$ = relaxation time of the fluid
$\lambda_2$ = retardation time of the fluid
$\rho_f$ = density of the fluid
$\rho_s$ = density of the solid particles

## References

[1] Goldman, A. J., Cox, R. G., and Brenner, H., 1966, ''The slow motion of two identical arbitrarily oriented spheres through a viscous fluid,'' Chem. Eng. Sci., **21**, pp. 1151–1170.

[2] Riddle, M. J., Narvaez, C., and Bird, R. B., 1977, ''Interactions between two spheres falling along their line of centers in a viscoelastic fluid,'' J. Non-Newtonian Fluid Mech., **2**, pp. 23–35.

[3] Leal, L. G., 1979, ''The motion of small particles in non-Newtonian fluids,'' J. Non-Newtonian Fluid Mech., **5**, pp. 33–78.

[4] Brunn, P., 1980, ''The motion of rigid particles in viscoelastic fluids,'' J. Non-Newtonian Fluid Mech., **7**, pp. 271–288.

[5] Brunn, P., 1977, ''Interaction of spheres in a viscoelastic fluid,'' Rheol. Acta, **16**, pp. 461–465.

[6] Joseph, D. D., 1996, ''Flow induced microstructure in Newtonian and viscoelastic fluids,'' Keynote presentation (paper no. 95a) at the *5th World Congress of Chemical Engineering, Particle Technology Track, Second Particle Technology Forum*, San Diego, CA.

[7] Feng, J., Huang, P. Y., and Joseph, D. D., 1996, ''Dynamic simulation of sedimentation of solid particles in an Oldroyd-B fluid,'' J. Non-Newtonian Fluid Mech., **63**, pp. 63–88.

[8] Bird, R. B., Armstrong, R. C., and Hassager, O., 1987, *Dynamics of Polymeric Liquids, Vol. 1*, Wiley-Interscience, New York.

[9] Liu, Y. J., and Joseph, D. D., 1993, ''Sedimentation of particles in polymer solutions,'' J. Fluid Mech., **255**, pp. 565–595.

[10] Hu, H. H., 1996, ''Direct simulation of flows of solid-liquid mixtures,'' Int. J. Multiphase Flow, **22**, pp. 335–352.

[11] Hu, H. H., and Patankar, N. A., 1999, ''Simulation of particulate flows in Newtonian and viscoelastic fluids,'' to appear in the Int. J. Multiphase Flow.

# Flow Characteristics of Transitional Boundary Layers on an Airfoil in Wakes

**H. Lee**[1]
Graduate Student

**S.-H. Kang**
Professor

School of Mechanical and
Aerospace Engineering,
Seoul National University,
Seoul 151-742, Korea

*Transition characteristics of a boundary layer on a NACA0012 airfoil are investigated by measuring unsteady velocity using hot wire anemometry. The airfoil is installed in the incoming wake generated by an airfoil aligned in tandem with zero angle of attack. Reynolds number based on the airfoil chord varies from $2.0\times10^5$ to $6.0\times10^5$; distance between two airfoils varies from 0.25 to 1.0 of the chord length. To measure skin friction coefficient identifying the transition onset and completion, an extended wall law is devised to accommodate transitional flows with pressure gradient and nonuniform inflows. Variations of the skin friction are quite similar to that of the flat plate boundary layer in the uniform turbulent inflow of high intensity. Measured velocity profiles are coincident with families generated by the modified wall law in the range up to $y^+=40$. Turbulence intensity of the incoming wake shifts the onset location of transition upstream. The transitional region becomes longer as the airfoils approach one another and the Reynolds number increases. The mean velocity profile gradually varies from a laminar to logarithmic one during the transition. The maximum values of rms velocity fluctuations are located near $y^+=15-20$. A strong positive skewness of velocity fluctuation is observed at the onset of transition and the overall rms level of velocity fluctuation reaches 3.0–3.5 in wall units. The database obtained will be useful in developing and evaluating turbulence models and computational schemes for transitional boundary layer.*
[S0098-2202(00)01603-5]

## Introduction

The flow over the blades of turbomachinery are usually highly three dimensional, turbulent, and unsteady due to their complex geometry and interaction between the rotating and nonrotating blades. The flows are transitional over a considerable part of the blade, especially in machines of compact design and small size. Therefore correct prediction of skin-friction and heat transfer coefficients in the transitional boundary layer are important for developing highly efficient compressor blades and predicting hot spots on turbine blades. However, the transition procedure is complex and affected by many parameters. Many studies investigating the flow structure and modeling the transition procedure have been done in the past. Most of them have focused on steady flows with highly turbulent freestream, pressure gradient, streamline curvature and unsteadiness (see review papers by Mayle [1]; Walker [2]). However, it is still interesting to expand our knowledge of physical aspects of the transitional boundary layer (e.g., bypass transition developing on the blade in the highly turbulent steady flows).

Many studies on the effects of freestream turbulence and pressure gradient have been performed on flat plates, since they are the most influential parameters on the boundary layer transition. The isolated and combined effects of freestream turbulence and adverse pressure gradients were studied parametrically, based on turbulent intermittency in the boundary layer (Gostelow et al. [3]; Gostelow and Walker, [4]). They reported similar transition behavior based on the measured intermittency and the linear combination of laminar and turbulent properties. Conditionally sampled turbulence does not show fully developed turbulent flow characteristics, and the nonturbulent part does not show laminar flow characteristics. Therefore, linearly combining the laminar and turbulent properties is questionable even for flows without pressure gradient (Kuan and Wang [5]; Sohn and Reshotko [6]).

Mislevy and Wang [7,8] investigated the effects of adverse pressure gradients on momentum and thermal structures for a developing boundary layer. They reported that highly turbulent shear layer is generated in the near wall ($y^+=7$) pretransition region. They also observed a broader region of streamwise velocity fluctuation in the transverse direction unlike the zero pressure gradient flows.

The European Research Community on Flow Turbulence and Combustion (ERCOFTAC) special interest group made an experimental database of the transitional boundary layer, and applied the available turbulence models to verify them for transitional flows (Savill [9]). However, a turbulence model for accurate prediction of the transition on the blades in various conditions is not available. More data are needed to validate turbulence models and CFD techniques.

The present study provides an experimental data set of a transitional boundary layer on the NACA0012 airfoil located in the turbulent wake generated by another upstream airfoil. The transitional boundary layer on an airfoil in the nonuniformly distributed freestream velocity profile is a more realistic case of turbomachinery flow, since there are extra strain and curvature effects. Jeon and Kang [10] measured boundary layers on a flat plate in wakes. They reported that the Computational Preston tube Method (CPM), proposed by Nitsche et al. [11], is a simple and convenient method to measure the skin friction in the transitional boundary layer. However, it is quite difficult to obtain accurate data over the flat plate due to thickness of the leading edge specially in the nonuniform flow. Numerical schemes also have difficulties in accurate treatment of the knife edge, since grid generation is usually developed for round edges of turbomachinery blades. The boundary layer flow on the NACA0012 airfoil devel-

---

[1] Present address: Senior Research Engineer, LG Cable, Ltd., 555, Hogye-Dong, Dongan-Ku, Anyang-Si, Kyounggi 431-080, Korea.

Contributed by the Fluids Engineering Division for publication in the JOURNAL OF FLUIDS ENGINEERING. Manuscript received by the Fluids Engineering Division February 4, 1999; revised manuscript received February 14, 2000. Associate Technical Editor: D. Williams.

ops under an adverse pressure gradient on the curved surface except in the vicinity of the leading edge. Strong turbulence intensity of the incoming wake over the leading edge of the airfoil stimulates the boundary layer transition. The wakes were usually generated by putting rods of small diameter upstream in previous studies. In such cases, unnecessary vortex shedding appeared from the cylinder and large velocity defects were hard to obtain. More natural and stable wake profiles of high turbulence intensity could be obtained by installing another airfoil upstream in the present study. The flow condition of the present study represents flows in the turbomachinery more closely than that of a flat plate. We expect that these data will contribute to development and validation of turbulence models and computational schemes for transitional flows. Since the flows are carefully measured at low Reynolds numbers, the data are also quite useful and interesting for people to develop low speed and small airfoils.

## Experimental Program

**Facility and Instrumentation.** The experiment was conducted in a closed-type wind tunnel. At a flow speed of 30 m/s, the background turbulence level was 0.3 percent (low-pass filtered at 10 kHz) and the flow uniformity 0.36 percent. The variation of the static pressure in the test section without airfoils is less than 0.5 percent of dynamic pressure. Two NACA0012 airfoils are vertically mounted in tandem with zero angle of attack at the center of test section (W 600 mm×H 300 mm×L 2000 mm). The upstream airfoil has 44 static pressure holes of 0.8 mm and the downstream airfoil has 40 holes. The schematic of the arrangement is shown in Fig. 1. Strips of sandpaper (220 grade) are pasted on both sides of the upstream airfoil between $X=175$ and 195 mm to generate a stable wake flow. Streamwise mean velocity and velocity fluctuations are measured with a single hot wire probe (DANTEC 55P15). The anemometer is calibrated using a standard Pitot tube and the output is fitted to a fourth order polynomial. The output of the hot wire anemometer is low-pass filtered at 3 kHz and sampled with 6 k samples/s for 20 s by the 12-bit analog to digital conversion board (Data Translation 2833) installed in a PC (Intel 80386). The probe is traversed vertically normal to the wall by a traverse unit with 0.01 mm resolution installed on the roof of the test section and controlled automatically by the PC. The incoming wake profiles are measured with X-wire probe (DANTEC 55P63). A single wire calibration procedure was applied to each wire independently on the base of effective velocity (cosine cooling law). The instantaneous velocity $u$ and $v$ were obtained by adding or subtracting each effective velocity component. Forty-eight channels of Scanivalve with a pressure transducer (MKS 220CD) are used to measure multi-point static pressures.

**Measuring Skin Friction.** Although the skin friction is an important parameter for boundary layers, it is difficult to measure in the transitional region. Jeon and Kang [10] showed that CPM with a proper correlation of the displacement factor is useful for measuring the skin friction in transitional boundary layers. In the present study, we extended the wall law given by CPM to include the effects of pressure gradients; the hot-wire measurement of the mean velocity is employed to determine the unknown parameters in CPM, instead of using conventional multi-sized Preston tubes. The initial distance of the hot wire from the wall, $y_0$ is also an unknown parameter in the extended wall law to obtain the wall shear stress. The extended wall law assumes following family of profile with three free parameters $(K_1,K_2,K_3)$.

$$u^+=\int_0^{y^+}\frac{2(1+K_3y^+)}{1+[1+4(K_1y^+)^2(1+K_3y^+)(1-\exp(-y^+\sqrt{1+K_3y^+}/K_2))^2]^{0.5}}dy^+ \tag{1}$$

where $u^+$ is the streamwise mean velocity and $y^+$ is normal distance from the wall in the wall unit. $K_1$, $K_2$ and $K_3$ correspond to the von Karman constant $\kappa$, the van Driest constant $A^+$, and the pressure gradient parameter $K_3=p^+=\nu/\rho u_\tau^3(dp/dx)$, respectively, in the fully turbulent boundary layer. Here $K_2$ is set to the standard value of 26. Therefore three unknowns, $K_1$, friction velocity $u_\tau$, and $y_0$ are determined using measured values of velocity in the region of $y^+=5-40$. The values of $u_\tau$ and $y_0$ are initially obtained by a conventional linear fit ($u^+=y^+$) with three or four mean velocity data near the wall. With these initial values, the three unknowns are determined by iteration of Eq. (1). The correlation of displacement factor of Preston tubes in the CPM is very important for the measurement of skin friction, because errors of CPM mostly depend on displacement factor (Kang et al. [12]). However, in our measurement, the errors due to the displacement factor are not existent because interaction between hot-wire and wall is negligible even at $y^+=5$.

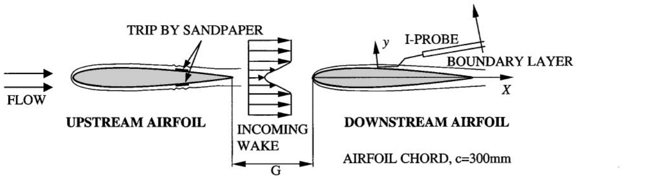

**Fig. 1 Schematic of the arrangement of airfoils**

Recently, Choi et al. [13] calculated the transitional boundary layer on a flat plate using the Direct Numerical Simulation technique. Skin friction computed directly by DNS is compared with that computed by the extended wall law using the DNS data, as shown in Fig. 2. The maximum deviation between the two values is 5.6 percent. This shows that the extended wall law can be successfully used to measure skin friction.

**Uncertainty Analysis.** The uncertainty levels for hot-wire measurements are estimated according to Yavzukurt [14]. The

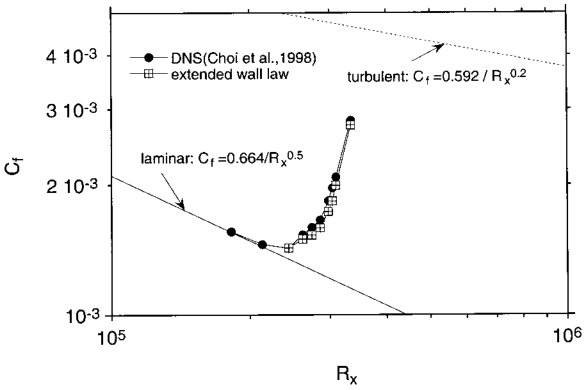

**Fig. 2 Comparison of the extended wall law with the DNS data for skin friction**

major uncertainty comes from the difference of the hot-wire output before and after the measurement; this is due to air temperature variation and the dust contamination. Air temperature variation during measurement was within 0.3. The maximum deviation of calibrated velocity is 2.0 percent when compared with the recalibrated velocity after the measurement. Combining other uncertainty factors with the flow condition and calibration of the I-probe, the uncertainty level for the measurement of I-probe is 2.35 percent. Mean velocity and the rms velocity fluctuation were obtained by real-time data reduction technique. Therefore, they have the same uncertainty levels. The range of uncertainty analysis for I-probe measurement (in the boundary layer) is restricted to $u \geqslant 4$ m/s, because meaningful data were obtained within this range for the boundary layer measurements.

In addition to the factors considered in the I-probe measurement, misalignment of the probe to the flow must be considered for the X-probe measurements. Simply we put the mean yaw angle of the wire as 45 degree following specifications of the maker. No yaw angle calibrations were made. Since the probe misalignment is within one degree, the total uncertainty level for the X-wire velocity measurement is 2.96 percent.

In the transition region, we applied the extended wall law to estimate the skin friction coefficient. The maximum deviation between the modified wall law and the measured velocity profile was 2.25 percent. We simply estimated the uncertainty level of the friction velocity by the extended wall law with the change of mean velocity within 2.25 percent deviations. We found that the uncertainty level of the friction velocity was 4.2 percent (8.4 percent for skin-friction coefficient, $C_f$).

## Experimental Results and Discussion

The alignment of the airfoil is confirmed by checking symmetric static pressure distributions on the airfoil, which are shown in Fig. 3. The solid line shows the potential flow solution considering wall blockage, and dotted line shows the values in the infinite domain. For the single airfoil, the measured distributions of pressure with different flow speeds coincide well with the calculated results on the both sides as in Fig. 3(*a*). From the leading edge to 11.5 percent of chord, the flow accelerates under favorable pressure gradient, and decelerates after that under adverse pressure gradient. When an airfoil is installed in the wake, the pressure distribution on the downstream airfoil changes due to the wake as shown in Fig. 3(*b*). As the distance between two airfoils decreases, the mean velocity defect of the incoming flow increases as expected. The minimum $C_p$ on the downstream airfoil increases and moves downstream.

**Table 1 Transition extents in 6 cases tested**

| CASE | Distance between airfoils | Reynolds number ($\times 10^5$) | $X_S/c$ | $(X_E-X_S)/c$ |
|---|---|---|---|---|
| CASE 0 | Single airfoil | 6.0 | 185/300 | 50/300 |
| CASE 1 | $G/c=1.0$ | 6.0 | 60/300 | 95/300 |
| CASE 2 | $G/c=1.0$ | 4.0 | 75/300 | 100/300 |
| CASE 3 | $G/c=1.0$ | 2.0 | 105/300 | 120/300 |
| CASE 4 | $G/c=0.5$ | 2.0 | 95/300 | 110/300 |
| CASE 5 | $G/c=0.25$ | 2.0 | 85/300 | 90/300 |

Profiles of the mean velocity, turbulence intensity and Reynolds shear stress are measured using an X-wire to confirm two-dimensionality of the wake at three locations ($Z/c=0$, $\pm 0.35$ at 1.5 chord downstream of the single airfoil in the uniform flow, CASE0. The X-wire measurements showed that the wake flow is two-dimensional and the wake thickness is about 10 mm. Boundary layer velocity profiles were measured along the mid-span of the downstream airfoil. The transition regions for six cases are determined from the measured skin friction coefficients and summarized in Table 1. CASE1, CASE2, and CASE3 are to investigate the effects of Reynolds number for the distance between two airfoils of one chord length. CASE3, CASE4, and CASE5 were performed to see the effects of distance between two airfoils for fixed Reynolds number.

**Boundary Layer in the Uniform Flow.** Transitional boundary layer on the airfoil in a uniform flow, without an upstream airfoil (CASE0), was measured as a baseline case. Variations of skin friction coefficient are shown in Fig. 4. Transition starts at $R_\theta=500$ ($X=185$ mm) and ends at $R_\theta=860$ ($X=235$ mm). Transition is assumed to start and end at the locations of local minimum and maximum values of skin friction, respectively. Local skin friction in the laminar region is smaller than that of the flat plate boundary layer under zero pressure gradient due to the adverse pressure gradient on the airfoil. In the turbulent region, the value of skin friction is 20 percent smaller than that of the zero pressure gradient boundary layer, which agrees well with the re-

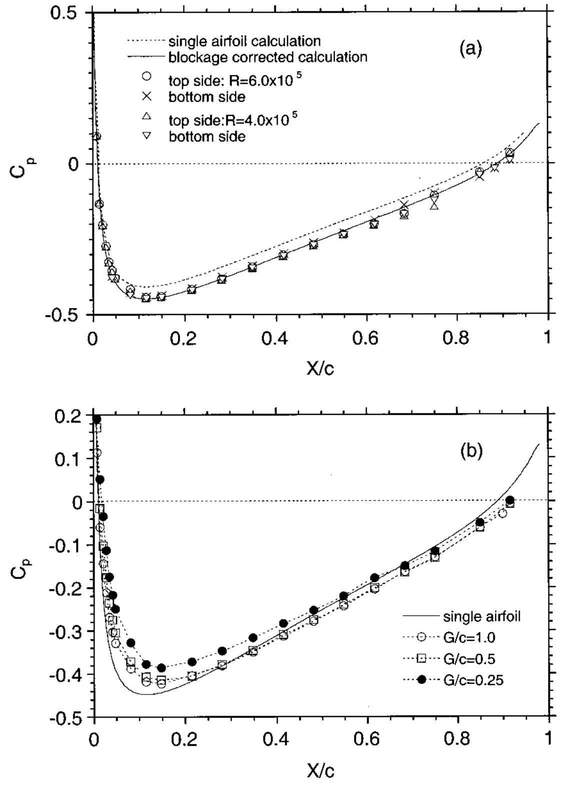

**Fig. 3 Distributions of static pressure (*a*) for single airfoil and (*b*) for airfoil in wakes (uncertainty for $C_p$ is ±0.015)**

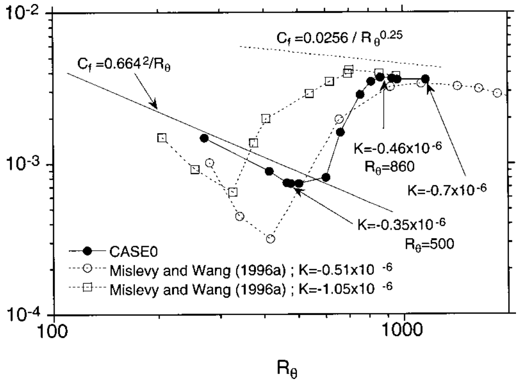

**Fig. 4 Variations of skin friction for CASE0 (uncertainty for $C_f$ is ±8.4%)**

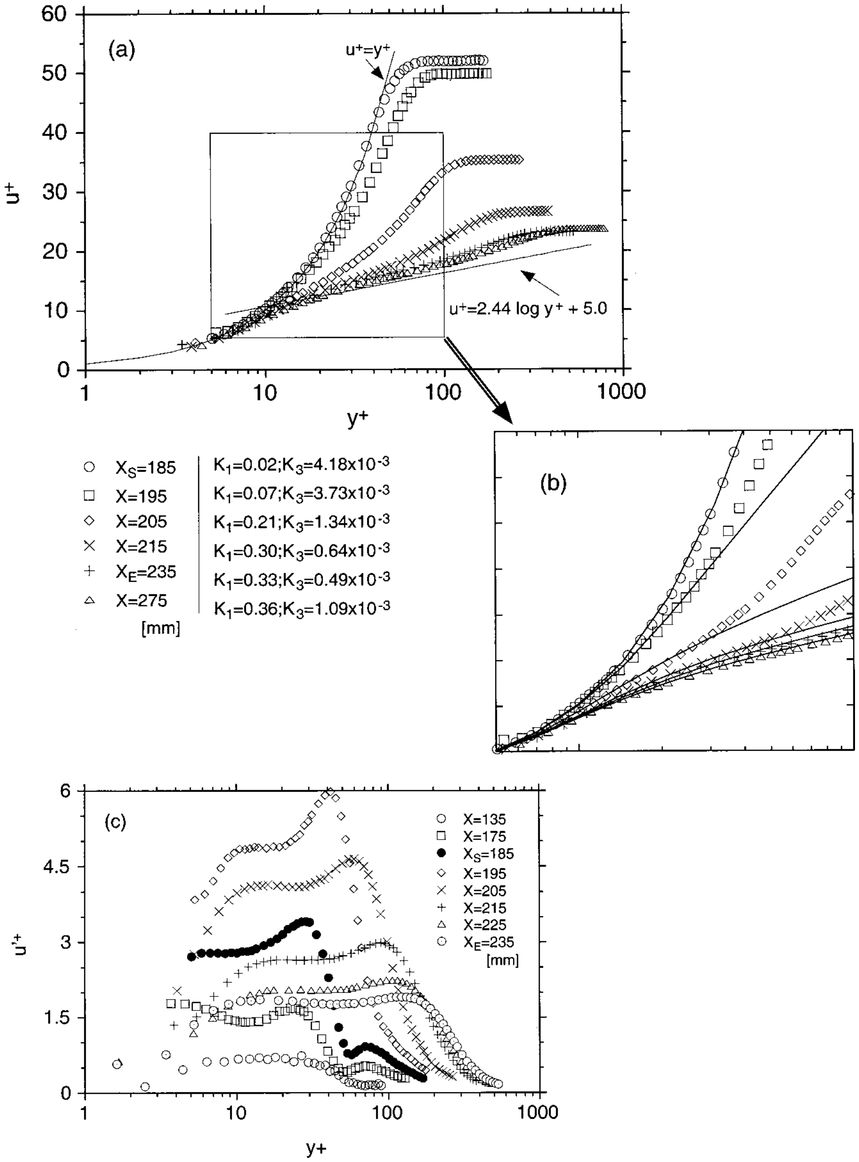

**Fig. 5 Profiles of (*a*) streamwise mean velocity, (*b*) enlarged view of (*a*) and (*c*) rms velocity fluctuation for CASE0 (uncertainties for $u^+$ and $u'^+$ are ±4.8%)**

sults of flat plate boundary layer under adverse pressure gradient (Mislevy and Wang [7]; the transition onset Reynolds number at the start of transition decreases even for weak adverse gradient). Although there are no experimental data of skin friction on airfoils at low Reynolds numbers, Kerho and Bragg [15] studied transitional flow on a NACA0012 airfoil using an intermittency signal. They reported that the transition starts at $X/c = 0.65$ and the length of transition is, $(X_E - X_S)/c = 0.125$ at $R = 7.5 \times 10^5$ based on chord length. In spite of the difference in test conditions, the extent of transition and the onset location of transition are quite similar to the results of the present study.

Several profiles of streamwise mean velocity are shown in Fig. 5(*a*). Experimentally determined parameters of the extended wall law are also given in Fig. 5(*a*). The boundary layer thickness, $\delta$ $(u = 0.99u_e)$ is 0.8–6.0 mm from $X = 135$ to 275 mm. Before the onset of transition, velocity profiles coincide well with the relation $u^+ = y^+$ up to $y^+ = 20$. The measured velocity near the wall of $y^+ < 4$ deviates from the law of the wall due to wall cooling effect of the hot-wire. From the onset of transition, the mean velocity profile slowly changes and converges to the logarithmic profile after $X = 235$ mm. The velocity profile in the logarithmic region after the end of transition is still steeper than that of the flat plate turbulent boundary layer under zero pressure gradient. This is expected because the turbulent boundary layer on the airfoil, even after the end of transition, does not reach the equilibrium state. An enlarged view of Fig. 5(*a*) over the region of $5 \leqslant y^+ \leqslant 100$ is shown in Fig. 5(*b*) with corresponding profiles of the extended wall law. The valid region for the extended wall law becomes large from $y^+ \leqslant 30$ just after the onset of transition to $y^+ \leqslant 100$ at the end of transition.

The rms profiles of streamwise velocity fluctuation are shown in Fig. 5(*c*). The transition onset in this study corresponds to the location of turbulent spot creation. Thus, there are large velocity fluctuations in the pre-transition, so called laminar like region, due to Tollmien-Schlichting (T-S) waves and their nonlinear interaction. As the transition starts, the fluctuation grows quickly. Just after the onset of transition ($X = 195$ mm), the maximum value of $u'^+$ becomes as high as 6.0 (13 percent of freestream velocity) at $y^+ = 40$. The value of $u'^+$ is nearly constant between $y^+ = 10$ and 20. The location of local maximum moves to the boundary layer edge during the transition. It suggests that vortices generated dur-

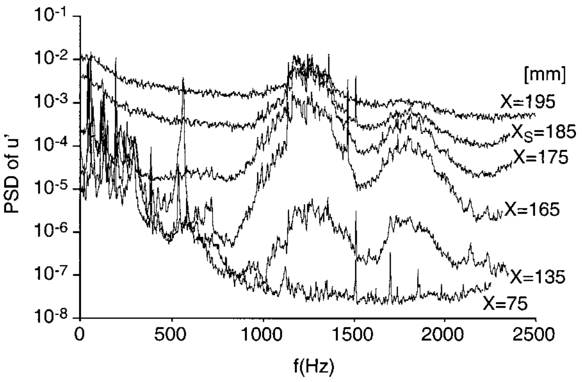

**Fig. 6 Power spectral density of velocity fluctuation for CASE0**

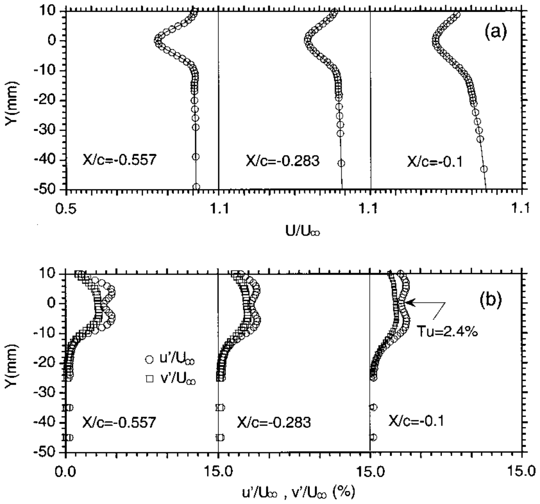

**Fig. 7 Profiles of (*a*) streamwise mean velocity and (*b*) turbulence intensities of the upstream wake for CASE1 (uncertainties for *u*, *u*′ and *v*′ are ±2.96%)**

ing the transition period move upward from the wall. The distribution of $u'^{+}$ form a typical fully turbulent flow as expected. Just before the onset of transition, $X=175$ mm, $u'^{+}$ shows two peaks at $y^{+}=5$ and 30, whose values are about 1.8. As the boundary layer develops, the outer peak moves to the external boundary layer and the inner peak is flattened. The value of $u'^{+}$ is nearly 3.0 between $y^{+}=5$ and 15 at $X=185$ mm (transition onset), 5.0 between $y^{+}=10$ and 20 at $X=195$ mm, and 4.1 between $y^{+}=10$ and 30 at $X=205$ mm (mid-transition). The peak point of $u'^{+}$ continues to move to the external boundary layer during the transition. The streamwise turbulence intensity at the location of maximum $u'^{+}$ is almost 80 percent of the total turbulence intensity, implying high anisotropy due to streamwise vortices.

Power spectral densities (PSD) of velocity fluctuation near the wall ($y/\delta \cong 0.1$) at several streamwise locations are shown in Fig. 6. In the region of $X=135$–175 mm, two dominant peaks of the PSD appear around 1200 and 1800 Hz. The primary peak occurs at 1200 Hz, which corresponds to a two-dimensional T-S wave. At $X=135$ mm, far away from the onset of the transition, T-S waves develop up to the transition onset point (peaks at $f=1200$ and 1800 Hz). The waves grow and the values of PSD become more than $10^3$ times that at $X=185$, where turbulent spots develop. After that, T-S waves do not grow anymore; the spectrum becomes more flattened and shows a similar distribution of fully turbulent flow. Walker and Gostelow [16] reported that there appears a primary peak corresponding to a T-S wave and several harmonics for mild adverse pressure gradient flows; this trend is similar to our case.

**Effect of Incoming Wake on the Boundary Layer.** With the baseline data for the uniform flow described above, the effects of the wake on the boundary layer development and transition are investigated. The effects of Reynolds number and distance between the two airfoils are discussed.

**Reynolds Number Effect.** The characteristics of the boundary layer developing in wakes are quite different from those of a single airfoil in a uniform flow because turbulence intensity, length scale and mean strain in the wake strongly affect the transition mechanism. Mean velocity and turbulence intensity profiles of the incoming wake for CASE1 ($R=6.0\times10^5$) are shown in Figs. 7(*a*) and (*b*), respectively. As the wake approaches the nose of the downstream airfoil, the velocity profile becomes disturbed due to the blockage. The $u'$-maximum occurs at the location of maximum shear stress and $v'$ maximum occurs at the centerline of the wake as usual case. The measured data show good wake symmetry. The wake thickness is about 60 percent of airfoil thickness as seen in Fig. 7(*a*). As Reynolds number decreases, the thickness of the wake increases and the velocity defect decreases as expected. At $X/c=-0.557$ the velocity defect decreases from 15 percent of $U_\infty$ to 10 percent as $R$ decreases from $6.0\times10^5$ to $2.0\times10^5$. The turbulent intensities of the wake ($Tu$) at $X/c=-0.1$ increase from 2.4 percent (CASE1) and 2.7 percent (CASE2) to 3.7 percent (CASE3).

To determine the range of transition, we show distributions of skin friction coefficient for $G/c=1.0$ for different Reynolds-number cases with respect to $X$ or $R_X$ in Figs. 8(*a*) and (*b*), respectively. In the transition region, the skin friction increases

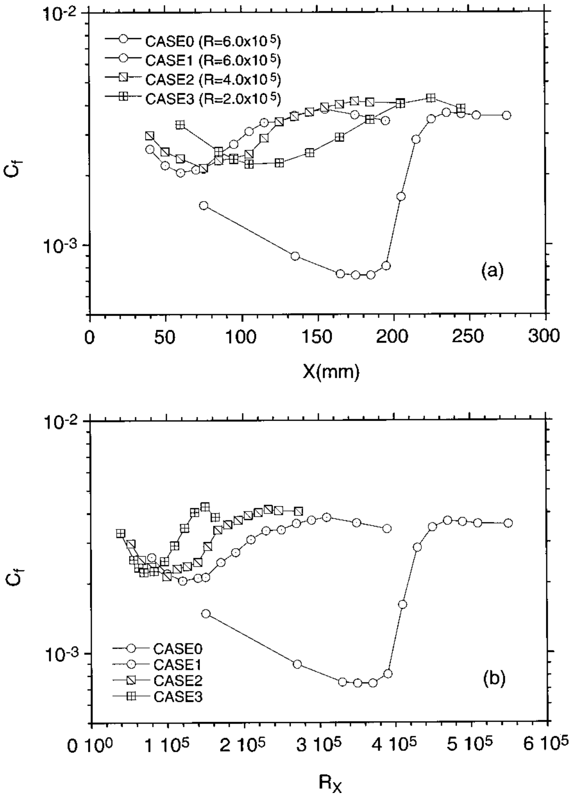

**Fig. 8 Variations of skin friction for different Reynolds numbers with respect to (*a*) chordwise location and (*b*) Reynolds number based on chordwise location (uncertainty for $C_f$ is ±8.4%)**

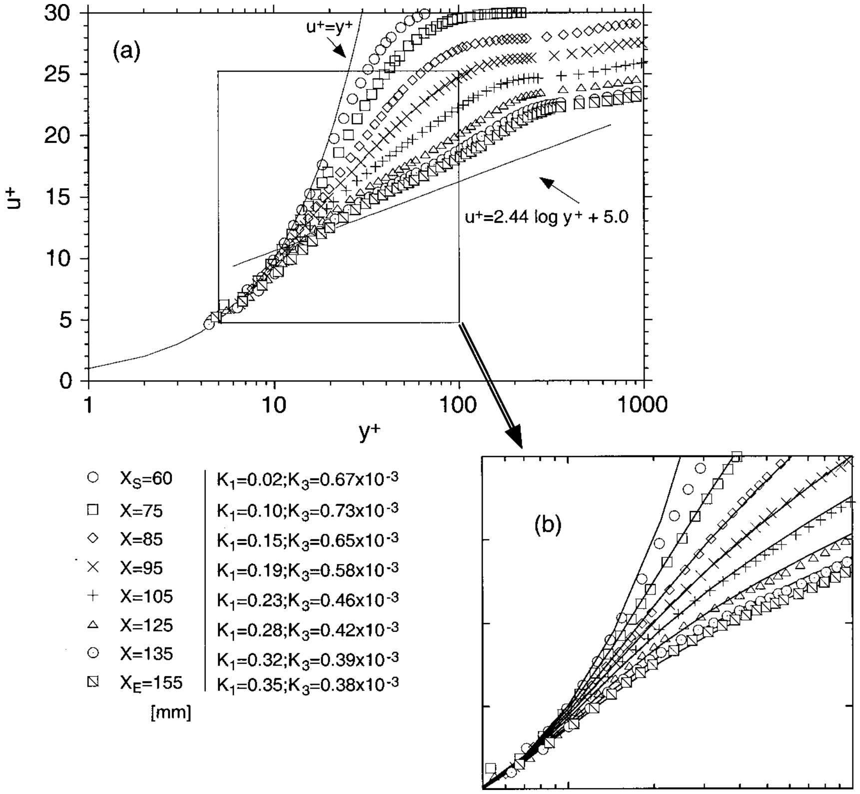

**Fig. 9 Profiles of (*a*) streamwise mean velocity for CASE1 and (*b*) enlarged view of (*a*) (uncertainty for $u^+$ is ±4.8%)**

much more gradually than in the natural transition of the baseline CASE0. The transition commences much earlier than that in CASE0, which is typical of bypass transition in a turbulent free stream. This will be discussed in detail later.

Profiles of streamwise mean velocity for CASE1 are shown in Fig. 9(*a*) in wall units with parameters of extended wall law obtained during the CPM procedure. An enlarged view of Fig. 9(*a*) for the range of $5 \leqslant y^+ \leqslant 100$ is shown in Fig. 9(*b*) with profiles of extended wall law. A new laminar like boundary layer start to develop from the leading edge in the external shear layer of the incoming wake. The new layer shows a typical linear profile of $u^+ = y^+$ over the transition onset location ($X = 60$ mm). During the transition, the mean velocity profile changes gradually from a laminar one to a logarithmic one. At the end of the transition, the logarithmic region is relatively short due to the low Reynolds number ($R = 6.0 \times 10^5$); the slope of the logarithmic profile is steeper than that of a flat plate boundary layer. As the Reynolds number decreases, the logarithmic region becomes shorter at the end of transition due to the adverse pressure gradient (not shown here). The valid region for the extended wall law at the onset of transition decreases for $5 \leqslant y^+ \leqslant 20$, since the incoming wake disturbs the boundary layer. As the flow moves downstream, the valid region of the extended wall law grows. At the end of transition, this region grows up to $y^+ \leqslant 100$, corresponding to the inner region for the turbulent boundary layer. The extended wall law is valid for the newly developing layer near the wall, and such information is carefully used to obtained the wall shear stress using the CPM.

The rms distributions of streamwise velocity fluctuation for CASE1 ($R = 6.0 \times 10^5$) and CASE3 ($R = 2.0 \times 10^5$) are shown in Figs. 10(*a*) and (*b*), respectively. The maximum value of $u'^+$ reaches 3.5 (12 percent of free stream velocity) just after the onset of transition ($X = 75$ mm). Although this value is much lower than that of CASE0, this does not mean that turbulence is suppressed

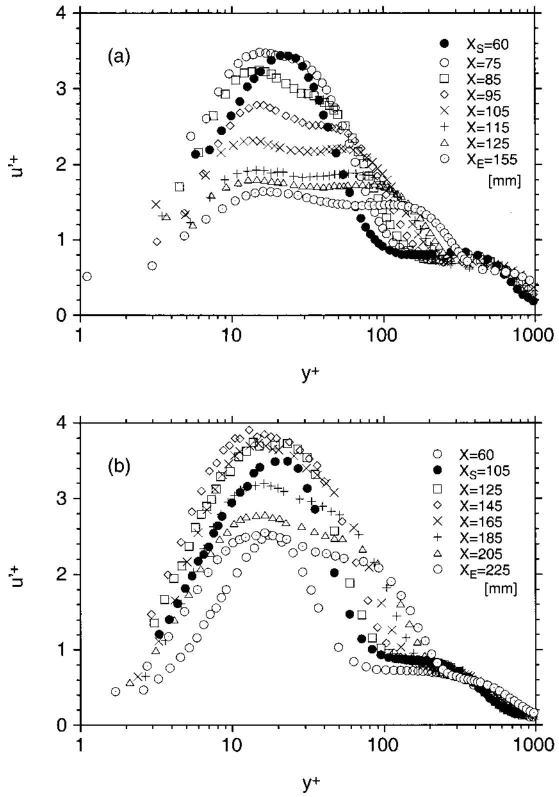

**Fig. 10 Profiles of rms velocity fluctuation (*a*) for CASE1 and (*b*) for CASE3 (uncertainty for $u^+$ is ±4.8%)**

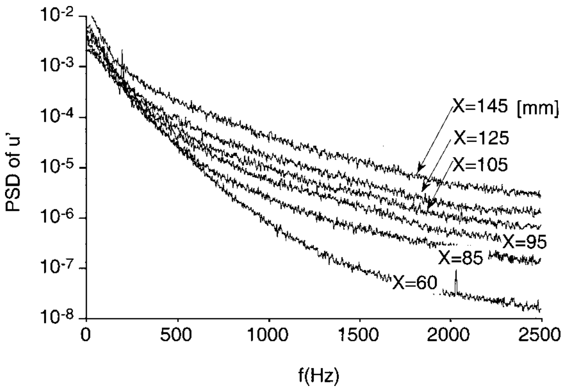

**Fig. 11 Streamwise variation of power spectral density for CASE3 at $y^+=5$**

by the wake; it simply implies that the transition occurs much earlier in wakes as seen in Fig. 8; thus, the skin friction coefficient is larger for CASE1–3. The location of maximum $u'^+$ occurs at around $y^+=20$ during the transition for CASE1–3, and moves a little closer to the wall although it moves away from the wall for CASE0. Note that the peak $u'^+$ around $y^+=20$ at transition onset reaches 3.5 for CASE1 and CASE3. For CASE3, $u'^+$ reaches its maximum value of about 4.0 at $y^+=20$ and $X=145$ mm (initial stage of transition). The local maximum of $u'^+$ occurs at $y^+=20$ through transition, and their values decrease to 2.5 at $X=225$ mm (the final stage of transition). At the end of the transition, the peak values of $u'^+$ are 1.8, 1.9 and 2.4 for CASE1, CASE2, and CASE3, respectively. This shows that the reducing flow speed improves the near wall resolution of the hot wire. However, the characteristics of the boundary layer are nearly unchanged. The skewness distribution of the velocity fluctuation is quite similar for three cases (not shown).

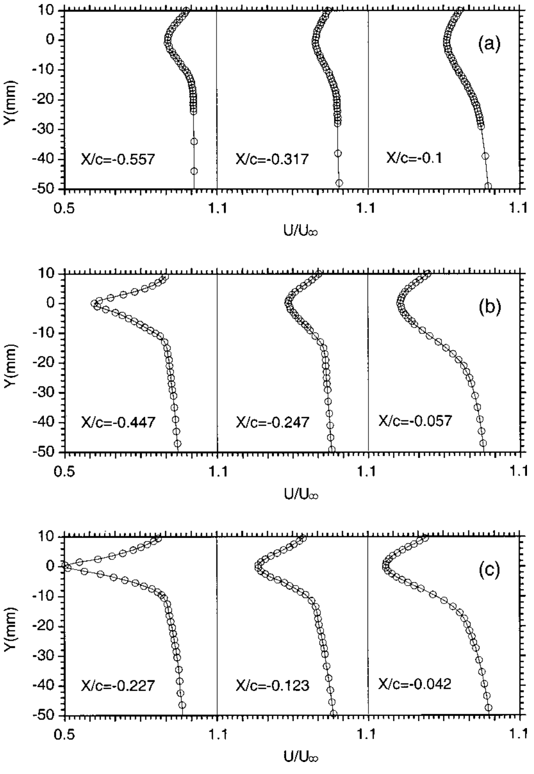

**Fig. 12 Streamwise mean velocity profiles of incoming wakes (*a*) for CASE3, (*b*) for CASE4 and (*c*) for CASE5 (uncertainty for *u* is ±2.96%)**

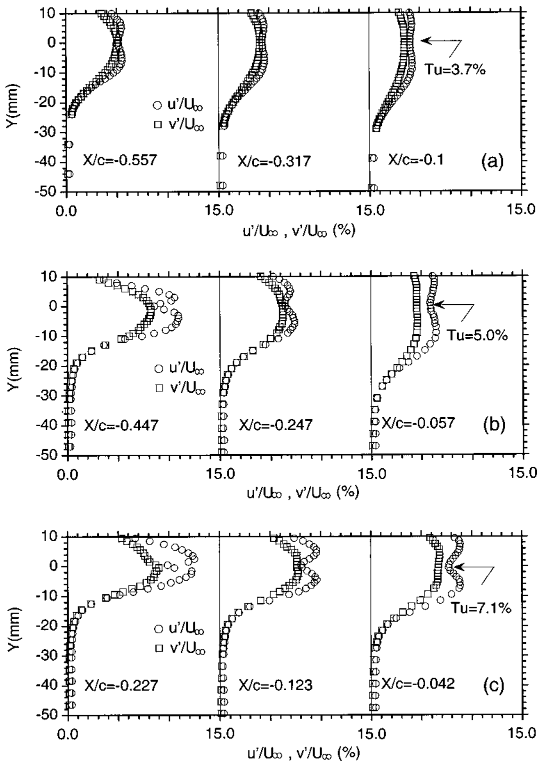

**Fig. 13 Profiles of turbulence intensities of incoming wakes (*a*) for CASE3, (*b*) for CASE4 and (*c*) for CASE5 (uncertainties for *u*′ and *v*′ are ±2.96%)**

For CASE3 of a relatively low Reynolds number, the PSD of velocity fluctuation in Fig. 11 shows that the flow is fully random throughout the transition region. PSD distributions for CASE1–3 are different from the one for CASE0 (PSDs for CASE1–3 are almost the same; CASE3 is shown only). During the transition, there is no dominant peak as for CASE0, implying that the transition processes do not experience T-S wave formation; it directly passes to spot formation.

**Airfoil Distance Effect.** As the distance between the two airfoils decreases, the turbulence intensity and the velocity defect of the incoming wake increases, and the wake thickness decreases as shown in Figs. 12(*a*), (*b*), and (*c*). Turbulence intensity profiles of

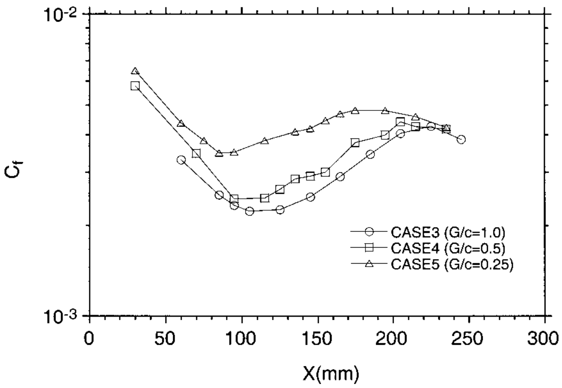

**Fig. 14 Variations of skin friction for different airfoil distances (uncertainty for $C_f$ is ±8.4%)**

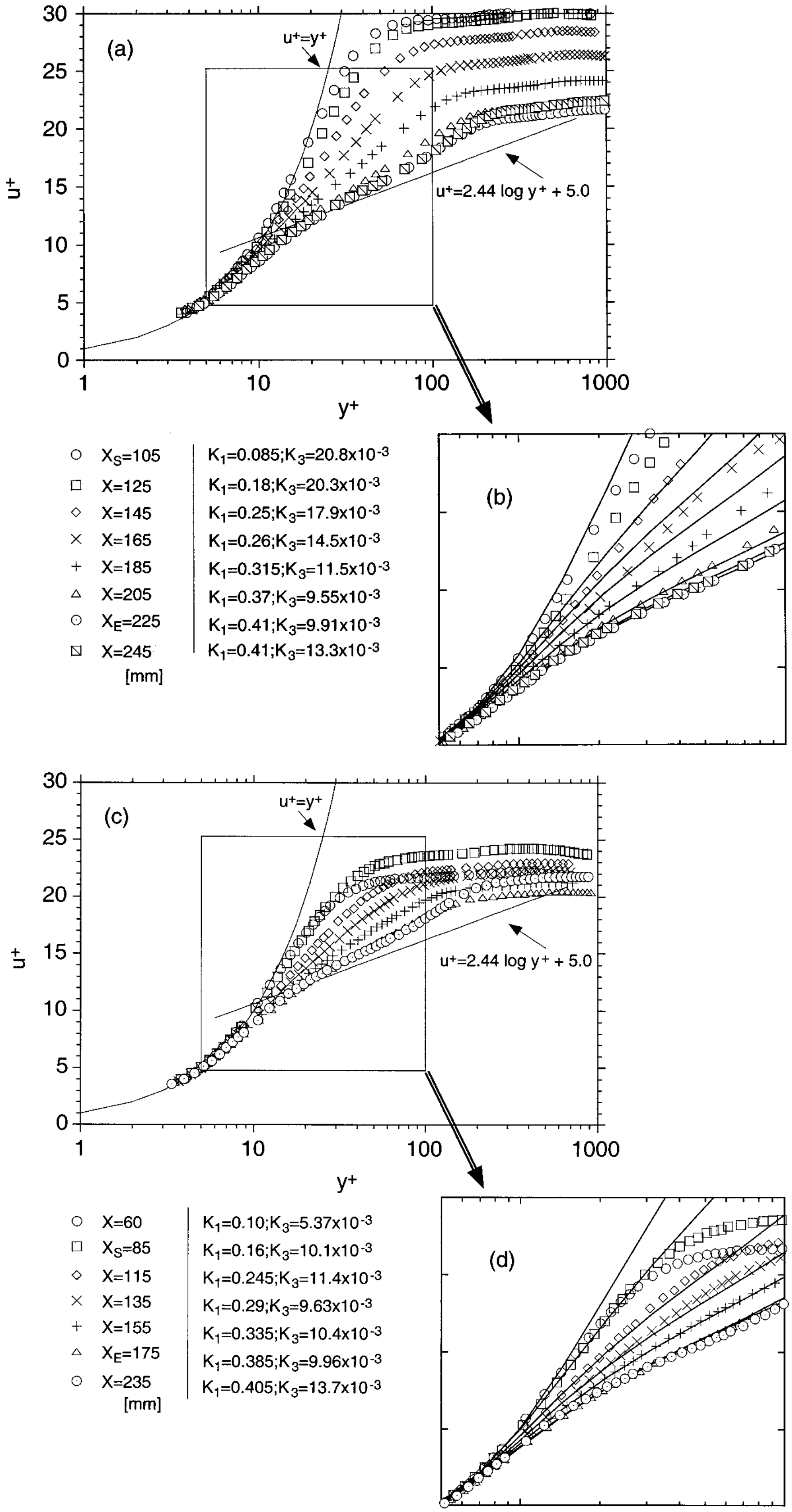

**Fig. 15 Profiles of streamwise mean velocity (*a*) for CASE3, (*b*) enlarged view of (*a*), (*c*) for CASE5 and (*d*) enlarged view of (*c*) (uncertainty for $u^+$ is ±4.8%)**

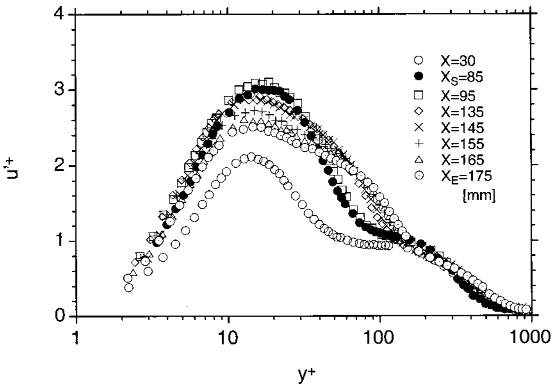

**Fig. 16 Profiles of rms velocity fluctuation for CASE5 (uncertainty for $u'^+$ is ±4.8%)**

the incoming wake at three locations for each case are shown in Figs. 13(*a*), (*b*), and (*c*). As the distance between the two airfoils decreases, the difference between $u'$ and $v'$ gradually increases, i.e., the flow becomes more anisotropic; the maximum $u'$ and turbulence intensity increase as expected.

As the turbulence intensity increases, the skin friction over the blade increases, transition onset location moves upstream, and the length of transition region decreases as shown in Fig. 14. Differences in $C_f$ for CASE3–5 in the laminar region are much larger than those for CASE1–3 in Fig. 8. For CASE1–3, the starting points of virtual boundary layer are the same; however, wake thickness are all different for CASE3–5, so that interaction between the incoming wake and boundary layer changes the virtual starting point of boundary layer. As a result, $C_f$-distributions in CASE3–5 show larger differences than those do in CASE1–3. However, the slope of $C_f$-variation before transition is similar for these three cases.

The streamwise mean velocity profiles for CASE3 ($G/c=1.0$) and CASE5 ($G/c=0.25$) are shown in Figs. 15(*a*) and (*c*); enlarged views of (*a*) and (*c*) with profiles of extended wall laws are shown in Figs. 15(*b*) and (*d*), respectively. The *u*-profile shows a gradual variation starting from the linear distribution at the transition onset to a logarithmic one at the end of transition. Valid region for the extended wall law grows from $y^+ \leqslant 15$ (at the onset of transition) to $y^+ \leqslant 100$ (at the end of transition) for both cases. The extended wall law cannot represent the initial incoming wake. However, as fluid moves downstream, the boundary layer thickness grows, so that the valid limit of the extended wall law increases as $X$ increases, which is shown by Figs. 15(*b*) and (*d*), respectively. In CASE5, the differences in $u$ outside the boundary layer along the streamwise direction are much smaller than those in CASE3, because $C_f$ -variation is smaller in CASE5 shown in Fig. 14.

The $u'^+$ profiles for CASE5 ($G/c=0.25$) are shown in Fig. 16. The maximum of $u'^+$ (16 percent of $U_\infty$) occurs in the interval of $y^+=15-20$ as in CASE1. At transition onset point, the values of maximum $u'^+$ are 3.5 and 3.0 for CASE3 (Fig. 10(*b*)) and CASE5 (Fig. 15), respectively. These values are consistent with the criteria for transition onset suggested by Sharma et al. [17] and Mayle and Schulz [18]. During transition, the $u'^+$ profiles become flattened near the peak. The region for flattened profiles corresponds to the one for the logarithmic profile and grows in the streamwise direction, which is consistent with the mean velocity profiles. At the end of the transition, the flattened profile extends up to $y^+=80$, suggesting that the logarithmic region develops up to $y^+=80$. The tails of $u'^+$-profiles above $y^+=100$ are due to the incoming wakes; however, the exact location of the wake is hard to determine from the $u'^+$-profile. This will be discussed in details from the skewness data.

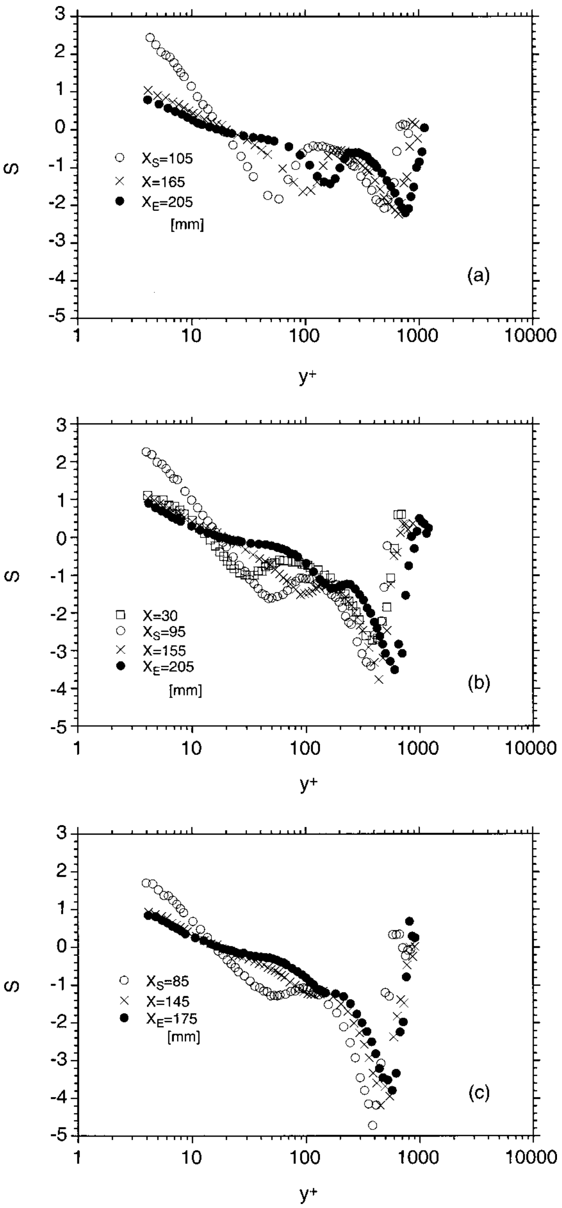

**Fig. 17 Skewness profiles (*a*) for CASE3, (*b*) for CASE4 and (*c*) for CASE5 (uncertainty for *S* is ±7.05%)**

Skewness distributions show the edges of the boundary layer and wake more clearly as shown in Fig. 17. The maximum positive skewness appears at the onset of transition near the wall in all cases. At the onset point, the turbulent region occurs intermittently and produces a lot of *u*-fluctuation around it as shown in Fig. 19. This results in a positive peak of skewness as in Fig. 17(*a*). As the fluid moves downstream, the spot extends and spreads in both time and space, thus the value of the positive peak decreases. The skewness distribution always shows two valleys during transition. Inner valleys represent the remains of the incoming wake. Since the boundary layer grows in the streamwise direction, these valleys move away from the wall. As the distance between the two airfoils decreases, the inner valley loses its identity at the end of the transition. This is because the incoming wake is initially located closer to the centerline for CASE5 as shown in Fig. 12. Thus, the incoming wake maintains its identity closer to the wall, even after transition for CASE5 (Fig. 17), than for CASE3. Thus, the inner valley loses its identity faster than CASE3 as the logarithmic region grows at almost the same rate

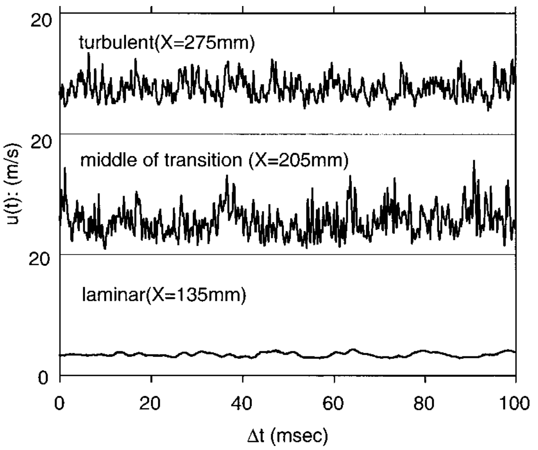

**Fig. 18 Velocity signals at $y/\delta=0.1$ for CASE0**

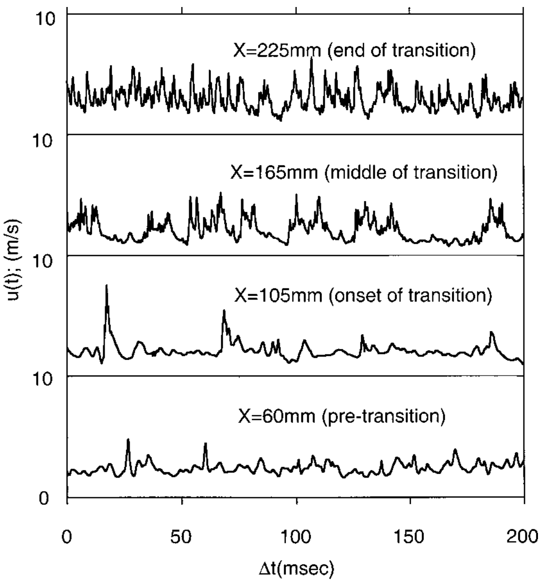

**Fig. 19 Velocity signals near the wall ($y^{+}=5$) for CASE3**

for CASE3–5. An interesting observation is that skewness distributions are quite different during the transition for CASE3–5 (when incoming wakes are different). However, at the end of transition, all three cases have the same skewness distribution for $y^{+}\leqslant 100$. This suggests that the dynamics of newly developing boundary layer is not affected by the variation of incoming wakes. This validates the use of common turbulence models after transition irrespective of the freestream turbulence.

**Velocity Signals.** The instantaneous velocity signals from a hot wire anemometer (HWA) for 100 ms at $y/\delta=0.1$ are shown in Fig. 18 for CASE0. However, it is difficult to decide whether the instantaneous flow is turbulent, since the velocity fluctuation in the boundary layer grows during transition. This is consistent with the report by Mislevy and Wang [8] that the magnitude of three-dimensional instability can be of the same order of that of turbulent spots. Thus, it seems to be meaningless to determine the transition onset location from intermittency. They reported that the adverse pressure gradient affects and disguises the turbulent spots, even under weak pressure gradient, and the magnitude of waves can be of the same order as the magnitude of turbulent spots.

For CASE3 where the incoming wake is present, the velocity signal is more intermittent than that for CASE0 at the onset of the transition as shown in Fig. 19. However, it is not proper to determine the onset point by intermittency, because velocity signal before transition is also intermittent. In the middle of the transition, the small-scale fluctuation is more apparent than that at the onset of the transition. At the end of the transition, the small-scale turbulence grows completely, and the velocity signal becomes the same as that in CASE0.

## Conclusion

We have obtained a database for the transitional boundary layers on an NACA0012 airfoil in various incoming wakes. This can be used to validate turbulence models and simulation schemes for turbomachinery in the future. Conclusions of the present study are as follows:

1 We have extended the CPM procedure by using ''the extended wall law'' to include the pressure gradient effect. This approach is successfully applied it to flows around airfoils with/without incoming wakes to determine the onset and the end of the transition. This extended wall law is found to be consistent with the velocity profiles which vary from laminar to turbulent ones.

2 Bypass transition occurs in flows around an airfoil when incoming wake is turbulent.

3 When an incoming wake is present, the transition onset shifts upstream and the transition length becomes smaller as Reynolds number increases and as the airfoil gap decreases.

4 In the transition region, the value of maximum $u'^{+}$ occurs in the interval of $y^{+}=15$–$20$ and the value is 3.0–3.5 for different inflow conditions at transition onset point.

5 The skewness is found to be an effective measure to locate the various regions when the boundary layer and the incoming wake interact with each other. The skewness is also found to be a good indicator for the onset of transition since it reaches the positive peak at the onset of the transition.

## Acknowledgments

The present work was supported by the grant of Korea Ministry of Education (96ME-B04) and Turbo and Power Machinery Research Center at Seoul National University. We gratefully acknowledge this support and thank Dr. Jinhee Jeong for helpful discussions.

## Nomenclature

$A^{+}$ = van Driest constant
$c$ = chord length of airfoil
$C_p$ = static pressure coefficient, $2(p-p_\infty)/\rho U_\infty^2$
$C_f$ = skin friction coefficient, $2\tau_w/\rho u_e^2$
$K$ = acceleration parameter, $(\nu/u_\infty^2)(du_\infty/dx)$
$G$ = distance between two airfoils
$K_1$, $K_2$, $K_3$ = parameters of CPM
$u_\tau$ = friction velocity
$p$ = static pressure
$R$ = Reynolds number based on airfoil chord, $U_\infty c/\nu$
$R_X$ = Reynolds number based on chordwise distance, $U_\infty X/\nu$
$R_\theta$ = Reynolds number based on momentum thickness, $u_e\theta/\nu$
$S$ = skewness factor
$Tu$ = inlet turbulence intensity, $\sqrt{(u^2+2v^2)/3}/U_\infty(\%)$
$U_\infty$ = flow speed at far upstream
$U,u$ = streamwise mean velocity
$u(t)$ = instantaneous velocity
$u^{+}$ = normalized mean velocity, $u/u_\tau$
$u'$ $v'$ = rms of streamwise and normal velocity fluctuation
$u'^{+}$ = normalized rms velocity fluctuation, $u'/u_\tau$

$x$ = streamwise distance
$X$ = longitudinal coordinate from leading edge
$y$ = normal distance from the wall
$y^+$ = dimensionless distance from the wall, $u_\tau y/\nu$
$y_0$ = initial distance of the probe from the wall
$Y$ = normal coordinate to $XZ$ plane
$Z$ = spanwise coordinate
$\delta$ = boundary layer thickness
$\kappa$ = von Karman constant
$\nu$ = dynamic viscosity of air
$\theta$ = momentum thickness
$\rho$ = density of air
$\tau_w$ = wall shear stress

## Subscripts

$\infty$ = far upstream value
$e$ = freestream value
$E$ = end of transition
$S$ = onset of transition

## References

[1] Mayle, R. E., 1991, ''The Role of Laminar-Turbulent Transition in Gas Turbine Engines,'' ASME J. Turbomach., **113**, pp. 509–537.

[2] Walker, G. J., 1993, ''The Role of Laminar-Turbulent Transition in Gas Turbine Engines: A Discussion,'' ASME J. Turbomach., **115**, pp. 207–217.

[3] Gostelow, J. P., Blunden, A. R., and Walker, G. J., 1994, ''Effects of Free-Stream Turbulence and Adverse Pressure Gradients on Boundary Layer Transition,'' ASME J. Turbomach., **116**, pp. 392–404.

[4] Gostelow, J. P., and Walker, G. J., 1991, ''Similarity Behavior in Transitional Boundary Layers Over a Range of Adverse Pressure Gradients and Turbulence Levels,'' ASME J. Turbomach., **113**, pp. 617–625.

[5] Kuan, C. L., and Wang, T., 1990, ''Investigation of the Intermittent Behavior of Transitional Boundary Layer Using a Conditional Averaging Technique,'' Exp. Therm. Fluid Sci., **3**, pp. 157–170.

[6] Sohn, K. H., and Reshotko, E., 1991, ''Experimental Study of Boundary Layer Transition with Elevated Freestream Turbulence on a Heated Flat Plate,'' NASA CR 187068.

[7] Mislevy, S. P., and Wang, T., 1996, ''The Effects of Adverse Pressure Gradients on Momentum and Thermal Structures in Transitional Boundary Layers: Part 1—Mean Quantities,'' ASME J. Turbomach., **118**, pp. 717–727.

[8] Mislevy, S. P., and Wang, T., 1996, ''The Effects of Adverse Pressure Gradients on Momentum and Thermal Structures in Transitional Boundary Layers: Part 2—Fluctuation Quantities,'' ASME J. Turbomach., **118**, pp. 728–736.

[9] Savill, A. M., 1995, *Transition Modeling for Turbomachinery III*, A Final Summary of ERCOFTAC Transition SIG progress for the 3rd workshop.

[10] Jeon, W. P., and Kang, S. H., 1995, ''Measurements of Transitional Boundary Layer on a Flat Plate Using a Computational Preston Tube Method,'' Exp. Fluids, **20**, pp. 29–37.

[11] Nitsche, W., Thuenker, R., and Haberland, C., 1983, ''A Computational Preston Tube Method,'' *Turbulent Shear Flows 4*, Bradbury, L. J. S. et al., Springer-Verlag, New York, pp. 261–276.

[12] Kang, S.-H., Shin, S.-H., Lee, H.-K., and Jeon, W.-P., 1998, ''Prediction of Wall Shear Stress in a Transitional Boundary Layer on a Flat Plate Based on the Principle of Computational Preston Tube Method,'' 1998, *Proceedings of the 4th KSME-JSME Fluids Engineering Conference*, Pusan, Korea, pp. 489–492.

[13] Choi, M.-R., Choi, H., and Kang, S.-H., 1998, ''Characteristics of the Late-Stage Transition in a Flat Plate Boundary Layer,'' *Proceedings of the 4th KSME-JSME Fluids Engineering Conference*, Pusan, Korea, pp. 481–484.

[14] Yavzukurt, S., 1984, ''A Guide to Uncertainty Analysis of Hot-Wire Data,'' ASME J. Fluids Eng., **106**, pp. 181–186.

[15] Kerho, M. F., and Bragg, M. B., 1997, ''Airfoil Boundary-Layer Development and Transition With Large Leading-Edge Roughness,'' AIAA J., **35**, No. 1, pp. 75–84.

[16] Walker, G. J., and Gostelow, J. P., 1990, ''Effects of Adverse Pressure Gradients on the Nature and Length of Boundary Layer Transition,'' ASME J. Turbomach., **112**, pp. 198–205.

[17] Sharma, O. P., Wells, R. A., Schlinker, R. H., and Bailey, D. A., 1982, ''Boundary Layer Development on Turbine Airfoil Suction Surfaces,'' ASME J. Eng. Power, **104**, pp. 698–706.

[18] Mayle, R. E. and Schulz, A., 1997, ''The Path to Predicting Bypass Transition,'' ASME J. Turbomach., **119**, pp. 405–411.

**M. F. Tachie**
Research Assistant,

**D. J. Bergstrom**
Professor,

Department of Mechanical Engineering,
University of Saskatchewan,
Saskatoon, Canada S7N 5A9

**R. Balachandar**
Associate Professor,
Department of Civil Engineering,
University of Saskatchewan,
Saskatoon, Canada S7N 5A9

# Rough Wall Turbulent Boundary Layers in Shallow Open Channel Flow

*An experimental study was undertaken to investigate the effects of roughness on the structure of turbulent boundary layers in open channels. The study was carried out using a laser Doppler anemometer in shallow flows for three different types of rough surface, as well as a hydraulically smooth surface. The flow Reynolds number based on the boundary layer momentum thickness ranged from 1400 to 4000. The boundary layer thickness was comparable with the depth of flow and the turbulence intensity in the channel flow varied from 2 to 4 percent. The defect profile was correlated using an approach which allowed both the skin friction and wake strength to vary. The wake parameter was observed to vary significantly with the type of surface roughness in contradiction to the ''wall similarity'' hypothesis. Wall roughness also led to higher turbulence levels in the outer region of the boundary layer. The profound effect of surface roughness on the outer region as well as the effect of channel turbulence on the main flow indicates a strong interaction, which must be accounted for in turbulence models.* [S0098-2202(00)00803-8]

## Introduction

The turbulent boundary layer is likely the most important engineering flow from a practical viewpoint, since it is encountered in so many industrial and environmental applications. The skin friction characteristics of boundary layers have been studied extensively and almost continuously over the past ninety years. Yet, there still remains numerous important research questions regarding the structural characteristics of turbulent boundary layers, and directly related to this, our ability to model or predict such flow parameters as the skin friction coefficient in practically relevant, i.e., complex, flow configurations. One feature of turbulent boundary layers which continues to warrant the attention of researchers, both experimental and computational, is surface roughness and its effect on momentum transport in the boundary layer (Patel [1]). Surface roughness is not only widely encountered in industrial flow applications such as flow over turbine blades or flow through duct systems, but it becomes critically important in environmental flows, where surface roughness is dominant. In this paper, the topic of surface roughness will be investigated in the context of relatively shallow open channel flows. Although there are clear differences between the canonical zero pressure gradient boundary layer and that in open channel flow, the effect of surface roughness on the velocity field is found to be similar.

Nikuradse [2] carried out extensive measurements in pipes roughened by sand grains and established the framework of our understanding of rough wall turbulent flow. Since then, it has come to be accepted that with increasing Reynolds number the skin friction of a rough wall turbulent flow deviates from that of the smooth wall and becomes dependent on the relative length scale of the roughness as well as the Reynolds number (Tani and Motohashi [3]). At still higher Reynolds numbers, the skin friction becomes independent of Reynolds number and depends solely on the roughness scale. This regime has come to be called ''fully rough.'' The earliest rough wall experiment on a two-dimensional turbulent boundary layer is that of Prandtl and Schlichting [4]. Their study led to the well-known Prandtl-Schlichting formula for skin friction for a fully rough plate.

For both smooth and rough surfaces, the mean velocity profile can be thought to comprise two regions. In the inner region, the appropriate velocity scale is the friction velocity $U_\tau$, and the length scale is the viscous length scale $\nu/U_\tau$ (here, $\nu$ is the kinematic viscosity) and/or roughness height $k$, for a rough surface. In the outer region, $U_\tau$ remains an appropriate velocity scale, but the characteristic length scale is now the boundary layer thickness $\delta$ (or for a pipe the diameter, $d$). Following Millikan [5], most undergraduate texts teach that the overlap between the inner and outer regions is characterized by a ''universal'' logarithmic velocity profile sometimes referred to as the law of the wall. This profile leads to the skin friction correlation for smooth surfaces. The effect of roughness is to produce a downward shift in the logarithmic profile, which is commonly expressed by the roughness function $\Delta U^+$. Hama [6] showed that this function is related to the local skin friction coefficient $C_f$. For a rough wall boundary layer, the complete velocity profile may be written in the following form

$$U^+=\frac{1}{\kappa}\ln y^+ + C-\Delta U^+ + \frac{2\Pi}{\kappa}w\left(\frac{y}{\delta}\right) \tag{1}$$

where, $U^+=U/U_\tau$, $y^+=yU_\tau/\nu$, $\kappa$ is the Karman constant, $C$ is a smooth wall constant, $\Delta U^+$ is the roughness shift, $\Pi$ is the Coles wake parameter and $w$ is a universal function of $y/\delta$. For a rough surface, $y$ is defined as the distance from the top plane of the roughness elements to the point of interest plus the distance to the virtual origin denoted $\varepsilon$. Typical values of the two constants in Eq. (1) are $\kappa=0.41$ and $C=5.0$, but these values vary slightly between experiments.

The outer region of a boundary layer is most often studied using the velocity defect law, which relates the difference between the freestream velocity $U_e$ and the local velocity $U$ to the distance from the wall and the outer pressure gradient, i.e.,

$$U_e^+-U^+=g\left(\frac{y}{\delta},\frac{\delta^*}{\tau_w}\frac{dP_e}{dx}\right) \tag{2}$$

Nikuradse established that for pipe flow, the velocity defect law is valid except close to the wall, no matter whether the wall is smooth or rough. Clauser [7] and Hama [6] demonstrated the validity of the velocity defect law for boundary layer flows on both smooth and rough walls. Since these earlier studies, significant attention has been given to rough surfaces (Furuya and Fujita [8], Perry and Abell [9]; Bandyopadhyay [10]; Perry et al. [11]; as

---

Contributed by the Fluids Engineering Division for publication in the JOURNAL OF FLUIDS ENGINEERING. Manuscript received by the Fluids Engineering Division March 23, 1999; revised manuscript received February 14, 2000. Associate Technical Editor: D. Williams.

well as the review by Raupach et al. [12]). The velocity distribution in open channel flows has also been studied in the context of inner and outer layers, see for example, Nezu and Rodi [13] and Xinyu et al. [14].

A topic of current debate is the effect of surface roughness on the velocity characteristics in the outer layer. Using Eq. (1), the specific form of the defect law becomes:

$$U_e^+ - U^+ = \frac{2\Pi}{\kappa}\left[w(1) - w\left(\frac{y}{\delta}\right)\right] - \frac{1}{\kappa}\ln\left(\frac{y}{\delta}\right) \tag{3}$$

which indicates that the velocity deficit in the outer region is strongly dependent on the magnitude of the wake parameter $\Pi$. The wake parameter is generally regarded as dependent on streamwise location. Coles [15] initially proposed that for a smooth-wall zero pressure gradient turbulent boundary layer, $\Pi$ would be 0.55 at high Reynolds numbers, but later [16] gave an asymptotic value of 0.62. The recent smooth wall experiments by Osaka et al. [17] exhibited a Reynolds number dependence for $\Pi$. However, an asymptotic value of 0.62 was observed at sufficiently high $\mathrm{Re}_\theta$. For subcritical smooth-wall open channel flows, Nezu and Rodi [13] also reported a Reynolds number dependence, but indicated that the wake parameter remains nearly constant at $\Pi \cong 0.2$ for sufficiently high Reynolds numbers. Xinyu et al. [14] made LDA measurements in super-critical open channel flows at varying bed slopes and obtained a value of $\Pi \cong 0.3$. In the event that $\Pi$ is independent of the streamwise distance $x$, the velocity defect ratio $(U_e^+ - U^+)$ turns out to be a function of $y/\delta$ alone (Tani [18]). Tani [18] commented that $(U_e^+ - U^+)$ is also a weak function of $C_f$, and this dependence precludes the possibility of even approximate equilibrium for smooth wall boundary layers (Tani and Motohashi [3]). As will be shown later, incorrect wake strength may contaminate an estimate of the skin friction coefficient, and hence the roughness shift, in rough wall flows.

In considering the effects of surface roughness, often the specific characteristics of the roughness elements has been given minimal attention. Two main types of roughness have been identified in the literature. Following the terminology of Perry et al. [19], these are referred to as *k*-type or *d*-type roughness. If the roughness function depends on Reynolds number based on the roughness height and friction velocity ($k^+ = kU_\tau/\nu$), it is termed *k*-type roughness. Experiments have shown that the *k*-type scaling is not obeyed by grooved surfaces when the cavities are narrow or on a smooth surface with a series of depressions. This type of roughness scales with outer variables (the boundary layer thickness, $\delta$, or the pipe diameter, $d$) and is known as *d*-type.

It has been generally accepted that a *k*-type roughness only influences the flow structure in the immediate vicinity of the surface. For a rough-wall boundary layer, the wall similarity hypothesis (proposed by Townsend [20] and slightly modified by Perry and Abell [9]) states that outside the roughness sublayer, turbulent motions are independent of the wall roughness at sufficiently high Reynolds numbers. This would suggest that the turbulence structure over a significant portion of the boundary layer should be unchanged in spite of significant alterations to the surface characteristics of the wall. However, recently evidence has been brought forward which challenges the notion that wall roughness effects are confined to the roughness sublayer. For example, recent low freestream turbulence experiments on rough surfaces (see for example, Krogstad et al. [21]) have shown a significant deviation of the wake strength from that proposed by Coles. The *d*-type roughness experiment of Osaka and Mochizuchi [22] at $\mathrm{Re}_\theta$=5300 gave $\Pi = 0.68$. More recently, Young and Bergstrom [23] obtained $\Pi = 0.43$ for a perforated plate. A number of previous rough wall experiments were re-evaluated by Tani [18] and the $\Pi$ values obtained fell in the range of 0.4–0.7. Mills and Hang [24] remarked that extensive rough wall turbulence experiments carried out at Stanford University gave skin friction coefficients that deviate from Prandtl-Schlichting formulation by as much as 25 percent. They attributed the disparity to the neglect of the role of the wake component of the velocity profile in the Prandtl-Schlichting formulation.

Two additional factors that complicate the analysis of rough-wall boundary layers are the effects of (1) an external pressure gradient and (2) freestream turbulence. In the open channel flows being considered here, the pressure gradient is negligible since the change in the free surface elevation is small. On the other hand, the boundary layer is affected by the moderate levels of turbulence generated upstream of the roughness test section. For smooth-wall boundary layers at elevated turbulence intensity (Tu), Bradshaw [25] argued that the log-law holds when there is local equilibrium in the near wall region. Hancock and Bradshaw [26] measured various terms in the turbulence energy transport equation at $\mathrm{Tu} \leqslant 6$ percent and found the boundary layer to be in local equilibrium. More recently, Thole and Bogard [27] extended the existing smooth-wall data to turbulence intensity values as high as $\mathrm{Tu} = 20$ percent. Among other findings, they confirmed the validity of the log-law at high freestream turbulence and noted significant alterations of the outer region of the boundary layer. Based on the measured velocity spectrum, they found that at $\mathrm{Tu} = 20$ percent, the freestream turbulence penetrates deep into the wall region. Experimental evidence also suggests that the strength of the wake is strongly altered at high freestream turbulence levels. Blair [28] and Hancock and Bradshaw [29,26] showed that as the freestream turbulence increases, the outer region of the boundary layer exhibits a depressed wake region. At a turbulence level of $\mathrm{Tu} = 5$ percent for example, the wake was essentially nonexistent. In the recent smooth-wall study of Thole and Bogard [27], an asymptotic value of $\Pi = -0.5$ was observed.

The summary discussion above indicates that there is reasonable grounds to suggest that surface roughness in a turbulent boundary layer can modify the mean velocity profile, even outside the roughness sublayer. In support of this hypothesis, the present paper reports some new measurements of the mean velocity profile in a shallow open channel flow for three different types of roughness elements, as well for a hydraulically smooth surface. Of specific interest is the effect of roughness on the strength of the wake, as well as the variation in skin friction resulting from different velocity defect profiles. Consideration is also given to the effect of the upstream turbulence intensity on the boundary layer structure. Although comparisons will be made to similar studies which considered flat plate boundary layer flows, it is important to recognize that in an open channel flow, the outer edge of the boundary layer is influenced by the free surface which causes a local maximum in the streamwise velocity component to occur a distance below the surface. This effect modifies the magnitude of the wake parameter, which is further modulated by the effects of surface roughness as shown in the results presented below.

## Experimental Setup and Procedure

The experiments were conducted in a rectangular cross-section open channel flume. The flume was 0.8 m wide, 0.6 m deep, and 10 m long. The sidewalls of the flume were made of transparent tempered glass to facilitate velocity measurements using a laser Doppler anemometer. A contraction and several stilling arrangements used to reduce any large-scale turbulence in the flow preceded the straight section of the channel. The channel bottom was made of brass and the slope was adjustable. For the present experiments, the channel bottom was set to be horizontal. The change in water surface elevation was less than 1 mm over a streamwise distance of 600 mm implying a negligible pressure gradient. Figure 1 shows a schematic of a typical velocity distribution in an open channel. In contrast to the canonical zero pressure gradient boundary layer, the velocity profile decreases gradually from its maximum value at $y = \delta$ to a slightly lower value at the free surface, $y \approx h$. The free surface is also known to damp the wall-normal velocity fluctuation.

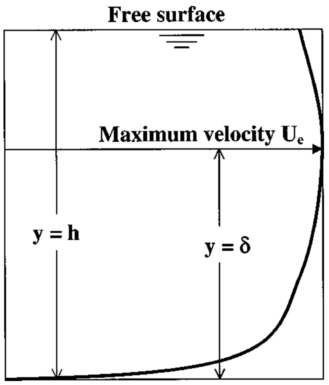

Fig. 1 Schematic of typical velocity profile in an open channel

Table 1 Summary of test conditions

| Test | Type of surface | Depth, h (mm) | $U_e$ (m/s) | Tu (%) (at $y = \delta$) | $\delta$ (mm) | $\theta$ (mm) | H | $Re_\theta$ |
|---|---|---|---|---|---|---|---|---|
| SM 1 | Smooth | 100 | 0.737 | 3.1 | 46 | 3.56 | 1.29 | 2625 |
| SM 2 | Smooth | 80 | 0.331 | 3.3 | 48 | 4.17 | 1.33 | 1380 |
| SM 3 | Smooth | 50 | 0.463 | 2.4 | 40 | 3.37 | 1.31 | 1750 |
| PF 1 | Perforated | 100 | 0.702 | 3.3 | 42 | 3.49 | 1.35 | 2450 |
| PF 2 | Perforated | 75 | 0.604 | 3.2 | 40 | 3.73 | 1.35 | 2250 |
| PF 3 | Perforated | 50 | 0.482 | 3.1 | 35 | 2.90 | 1.41 | 1400 |
| SG 1 | Sand grain | 100 | 0.622 | 3.2 | 50 | 4.20 | 1.37 | 2620 |
| SG 2 | Sand grain | 75 | 0.495 | 3.5 | 41 | 3.97 | 1.37 | 1970 |
| SG 3 | Sand grain | 50 | 0.448 | 2.5 | 39 | 3.48 | 1.38 | 1560 |
| WM 1 | Wire mesh | 100 | 0.773 | 2.9 | 45 | 5.07 | 1.50 | 3920 |
| WM 2 | Wire mesh | 75 | 0.675 | 2.8 | 42 | 4.80 | 1.50 | 3240 |
| WM 3 | Wire mesh | 50 | 0.519 | 2.5 | 40 | 4.97 | 1.52 | 2580 |

Three types of surface roughness were employed. A 1.4 mm thick and 1.5 m long sheet with circular perforations arrayed in a hexagonal pattern was used as one of the surfaces. The perforation diameter was 2.2 mm with a 4.0 mm spacing between centers, giving an openness ratio of about 43 percent. A 1.2 mm diameter sand grain roughness was coated on to a 1.75 m long plywood sheet using a double-sided tape. The third rough surface employed was a 1.3 m long stainless steel wire mesh. The mesh was made of 0.6 mm wires with 7.0 mm centerline spacing, giving a ratio of centerline spacing to wire diameter of about 12. Figure 2 shows sections of the perforated and wire mesh roughnesses.

To ensure a turbulent boundary layer, a trip was located 3.5 m downstream of the contraction and spanning the width of the flume. The trip was composed of 3 mm (median diameter) pebbles glued to the bottom of the channel as a 40 mm long strip. The perforated plate (PF) and sand grain roughness (SG) were located at about 1.1 m downstream of the trip, while the wire mesh screen was located 1.2 m downstream of the trip. A reference axial position ($x=0$) was located 1.3 m downstream of the trip. For the smooth wall (SM), measurements were made at an axial station of $x=0.50\,\text{m}$. For the wire mesh roughness (WM), measurements were made at axial locations of $x=0.30$ and 0.50 m for each test condition. The measurements on the perforated plate and sand grain roughness were conducted at $x=0.10$, 0.25, and 0.52 m, for each test condition.

Velocity measurements were carried out along the centerline using a single-component fiber-optic laser Doppler anemometer (Dantec Inc). The present system uses a 300 mW, air-cooled Argon-Ion laser (Ion Laser Technology). The laser Doppler anemometer system was operated in a backscatter mode. Details of the operating parameters of the laser Doppler anemometer can be found in Balachandar and Ramachandran [30] and are omitted here for brevity. The fiber optic probe was mounted on a three-dimensional traversing mechanism. Each direction of the traversing arrangement was stepper motor driven and controlled by a computer. Preliminary experiments were conducted to examine the variation of mean velocity profiles in the spanwise direction at the first measurement location for each surface roughness. The flow was found to be two-dimensional with a variation of less than 1 percent of the freestream velocity ($U_e$). Close to the bottom wall (i.e., $y\leqslant 0.8\,\text{mm}$), $y$-steps of 0.05 mm were used to ensure that sufficient data were taken in this range. This was necessary to allow a dependable estimate of $U_\tau$ for the smooth plate by resolving the velocity gradient at the wall.

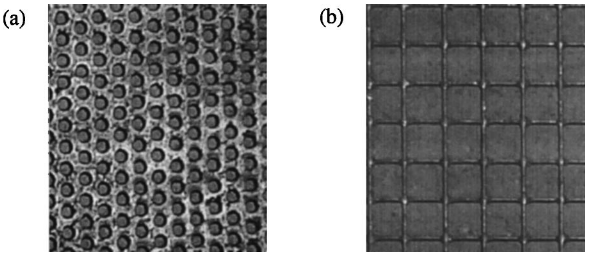

Fig. 2 Types of rough surfaces used: (*a*) perforated plate (PF), (*b*) wire mesh (WM)

In the present experiments, a freestream velocity in the range $0.33\leqslant U_e\leqslant 0.77\,\text{m/s}$ was considered. A summary of the test conditions is provided in Table 1. Here, the turbulence intensity (Tu) of the external flow is specified at $y=\delta$. From the test conditions specified in Table 1, the boundary layer thickness varied from approximately 80 percent of the channel depth at low speed to approximately 50 percent of the depth at higher speeds.

## Determination of Shear Stress

One of the central questions in boundary layer experiments is the determination of the wall shear stress, and hence the friction velocity. Different methods used include direct measurement (e.g., with a floating element gauge), performing a momentum balance, or by fitting the mean velocity to a standard profile. For a smooth wall turbulent boundary layer ($\Delta U^+=0$), the wall shear stress is commonly determined by fitting to the mean velocity profile measured near the wall (known as a ''Clauser plot''). The velocity profile is assumed to follow a logarithmic form, i.e.,

$$U^+=\kappa^{-1}\ln y^+ + C \tag{4}$$

The use of a Clauser plot technique is well established for smooth-wall low-freestream turbulence boundary layers, and has also been assumed to be valid in high freestream turbulence flows (Hancock and Bradshaw [26]; Thole and Bogard [27]). For a smooth surface, if a sufficient number of data points is obtained very close to the wall ($y^+<5$) a more dependable estimate of $U_\tau=(\tau_w/\rho)^{1/2}$ can be obtained from the slope of the velocity profile in the viscous sublayer using the relation

$$\tau_w=\mu\frac{dU}{dy} \tag{5}$$

where $\tau_w$ is the wall shear stress, $\rho$ is the fluid density and $\mu$ is the absolute viscosity of the fluid.

Previous rough wall experiments demonstrate that a Clauser technique may not be reliable (Perry et al. [19]). For a turbulent boundary layer developing over a rough surface, Eq. (1) is assumed to describe the mean velocity. Then, description of a measured velocity profile on a rough wall requires the determination of four parameters, namely: $U_\tau$, $\Delta U^+$, $\Pi$ and $\varepsilon$. A reduction in the number of parameters to be fitted is obtained by choosing to work with the velocity defect form of the velocity profile given by Eq. (3). By subtracting $U^+$ from its value $U_e^+$ at the edge of the boundary layer, the roughness parameter $\Delta U^+$ is eliminated. A commonly used form for the velocity distribution in zero pressure gradient boundary layers on rough surfaces is Hama's [6] formulation. For small values of $y/\delta$, Eq. (3) is dominated by the logarithmic term and is therefore written as

$$U_e^+ - U^+ = -\frac{1}{\kappa}\ln\left(\frac{y}{\delta^* U_e^+}\right) - 0.6 \quad (y/\delta^* U_e^+ \leqslant 0.045) \tag{6}$$

For larger values of $y/\delta$, the wake contribution dominates and Hama proposed the following function

$$U_e^+ - U^+ = 9.6\left[1-\left(\frac{10v}{3\delta^* U_e^+}\right)\right]^2 \quad (y/\delta^* U_e^+ > 0.045) \tag{7}$$

In both cases, the displacement thickness $\delta^*$, is used as the reference length scale. Equations (6) and (7) connect smoothly at $y/\delta^* U_e^+ = 0.045$ or $y/\delta = 0.15$. Bandyopadhyay [10] suggests that the Hama profile could be fitted to obtain a reliable estimate of $U_\tau$ irrespective of the surface. He also argued that since the Clauser technique matches the profile in the logarithmic region, which is thin, there are only a few data points to work with. In contrast, the profile matching using Hama's formulation covers virtually the entire region.

It has been observed (Bandyopadhyay [10]; Perry et al. [11]; Krogstad et al. [21]) that the value of skin friction velocity $U_\tau$ obtained from the Hama formulation (Eqs. (6) and (7)) is consistently higher than that obtained from either a momentum balance or by extrapolating the Reynolds stress to the wall. Bradshaw [31] suggested that this may be due to the strength of the wake, as implied by Eq. (7), being too small. With recent evidence of the dependence of $\Pi$ on $\mathrm{Re}_\theta$, roughness and (high) turbulence levels, the usefulness of a defect law such as that of Hama which fixes the value of $\Pi$ may be limited for the present experimental conditions. Krogstad et al. [21] employed a formulation that does not implicitly fix $\Pi$ but rather allows its value to be optimized. They used the formulation proposed by Finley et al. [32], and later used by both Granville [33] and Hancock and Bradshaw [29], namely,

$$w\left(\frac{y}{\delta}\right) = \frac{1}{2\Pi}\left[(1+6\Pi)-(1+4\Pi)\left(\frac{y}{\delta}\right)\right]\left(\frac{y}{\delta}\right)^2 \tag{8}$$

Equation (8) is the simplest polynomial satisfying the two boundary conditions (correct slope and function values) both near the wall and the boundary layer edge. Krogstad et al. [21], combined Eqs. (3) and (8) to obtain

$$f = \frac{U}{U_e} = 1 + \frac{U_\tau}{\kappa U_e}\left\{\ln\left(\frac{y}{\delta}\right) - (1+6\Pi)\left[1-\left(\frac{y}{\delta}\right)^2\right] + (1+4\Pi)\left[1-\left(\frac{y}{\delta}\right)^3\right]\right\} \tag{9}$$

which is a more sophisticated expression for the mean velocity profile which can be fitted to the experimental data to obtain the optimized values of $U_\tau$, $\Pi$, and $\varepsilon$. Of special importance is the explicit determination of the wake strength $\Pi$, and the expectation of a more accurate estimate of the friction velocity, $U_\tau$. The virtual origin, $\varepsilon$, is generally a small fraction of the roughness height, $k$, which itself is small relative to the boundary layer thickness $\delta$. For example, Krogstad et al. [21] reported a typical value of $\varepsilon/k = 0.25$ for their 0.69 mm thick wire mesh measurement. Except in the very near wall region where the value of $\varepsilon$ is comparable to $y$, the effect of $\varepsilon$ will be negligible over a significant portion of the flow. In the present study, our focus is on the outer part of the flow and no attempt was made to determine $\varepsilon$. For the rough wall measurements reported herein, the wall normal distance, $y$, was measured relative to the top of the roughness elements. As mentioned earlier, the principal object of the present study is to examine the effect of surface roughness on the outer layer, more specifically on $\Pi$ values. In order to bring this effect out more clearly, the use of Eq. (3), in conjunction with Eq. (8), is preferred in the present discussion. Although not shown, the curve fits resulting from Eq. (9) were considered and found to compare favorably with the experimental data of $U/U_e$.

## Results and Discussion

**Mean Velocity Profiles.** Figure 3 shows the distribution of the mean velocity profiles in physical coordinates. The profiles for each type of roughness collapse onto each other, although there is some Reynolds number dependence for all profiles except the wire-mesh. The characteristic ''blunt'' profile typical of a turbulent boundary layer is clearly evident. The effect of roughness is to increase the surface drag resulting in the velocity profile of the rough surface being less ''full'' when compared to a smooth surface profile. It is also clear from this figure that the wire mesh exhibits the highest deviation from the smooth profile while the perforated plate shows the least deviation. This suggests that even though the wire itself has the smallest diameter (0.6 mm compared with 1.2 mm for the sand grain, and 1.4 mm for the perforation depth), the mesh roughness exhibits the greatest resistance for the present set of test conditions. Further evidence of this trend will be discussed later.

The values of $U_\tau$ and $\Pi$ in the present study were determined following an optimization procedure similar to that outlined in Krogstad et al. [21]. The optimization was carried out by fitting Eq. (3) to the experimental data, using Eq. (8) for the wake function. Specifically, we sought the iterated value of $U_\tau$ and $\Pi$ that gave the best fit to Eq. (3) while ensuring a log-linear relation with $\kappa = 0.41$. In Fig. 4, fits of Eq. (3) to some of the present experimental data (Tests SM2, PF1, SG3 and WM2) are shown. Following Press et al. ([34], p. 502), we computed the chi-square distribution of the fitted curve and the experimental data in the range $0.1 \leqslant y/\delta \leqslant 1$ as a quantitative measure of the goodness-of-fit for the plots shown in Fig. 4. It was noted that the fits gave a good representation of the experimental data at 99.5 percent confidence level. For the smooth wall, $U_\tau$ was also determined by fitting a straight line to $U^+ = y^+$ for $y^+ < 5$ following the procedure outlined in Balachandar and Ramachandran [30]. The difference between the smooth-wall $U_\tau$ values as obtained from the two

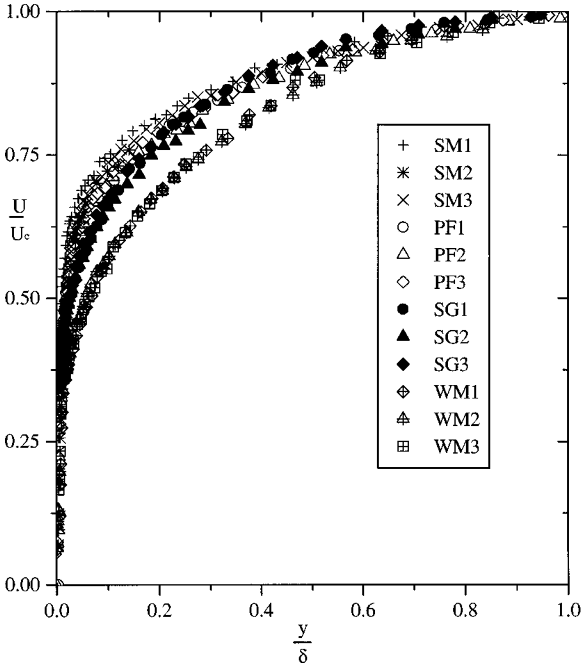

**Fig. 3 Variation of mean velocity in outer coordinates for rough and smooth surfaces (uncertainty in $U/U_e$: ±2 percent, $y/\delta$: ±4 percent)**

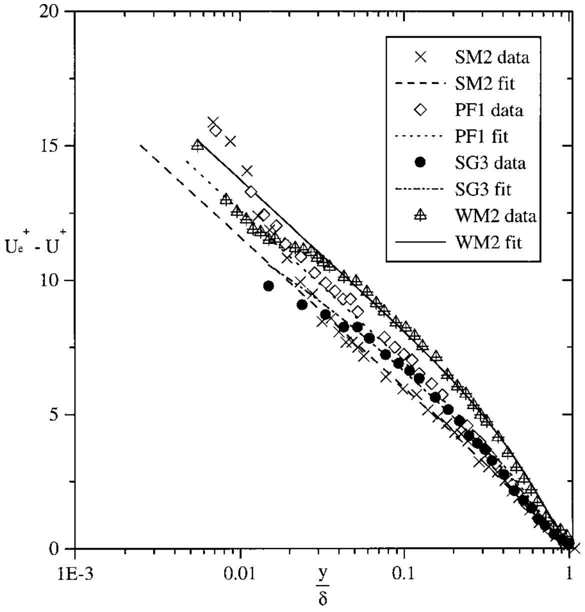

**Fig. 4 Determination of Π and $U_\tau$: Fit to Eq. (4) (uncertainty in $U^+$: ±4 percent for smooth surface and ±6 percent for rough surfaces, $y/\delta$: ±4 percent)**

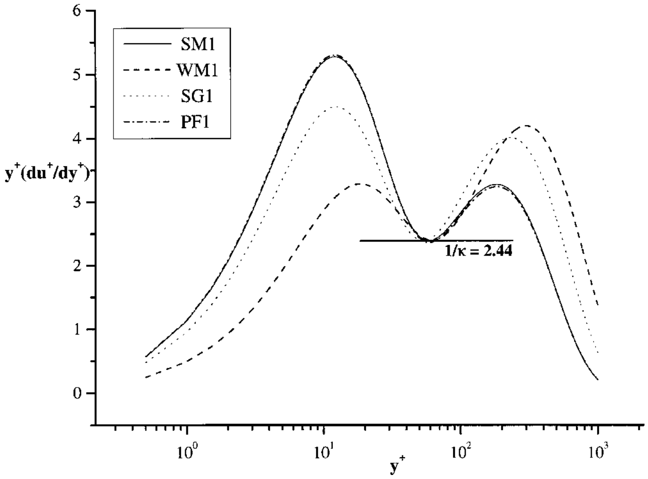

**Fig. 5 Determination of log-law constant, $\kappa$ (uncertainty in $y^+dU^+/dy^+$: ±6 percent)**

different methods was for all cases less than 4 percent. The $U_\tau$ and Π values obtained for all data sets are summarized in Table 2, together with the experimental values of the skin friction coefficient, the roughness function $\Delta U^+$, and the roughness Reynolds number, $k^+$. Similar to the observations made by Krogstad et al. [21] for a zero pressure gradient boundary layer, there is a clear variation in the relative strength of the wake with the type of roughness. Specifically, the smooth plate has the lowest wake strength ($\Pi = 0.08$) while the wire mesh has the highest strength ($\Pi = 0.48$). The value of $\Pi = 0.08$ obtained for the present smooth plate is similar to the value of 0.1 noted by Kirkgoz and Ardichoglu [35], but lower than $\Pi = 0.16$ obtained by Nezu and Rodi [13] in their open channel flow experiments at similar test conditions. The present value ($\Pi = 0.08$) is, however, quite different from the suggested value of 0.55 for a typical smooth wall zero pressure gradient boundary layer. This difference is most likely due to both the free surface effect present in open channel flow and the elevated turbulence levels.

In order to ensure that $\kappa = 0.41$, a plot of $y^+(dU^+/dy^+)$ versus $y^+$ was obtained for each measurement. A typical set of plots is shown in Fig. 5. As indicated by Spalart [36] and Balachandar and Ramachandran [30], the value of $\kappa^{-1}$ can be established by seeking the minimum value of the curve in the generally accepted log-law region. It should be pointed out that this procedure was very sensitive to noise so that direct use of experimental data was avoided to obtain $dU^+/dy^+$. Instead, a best fit to the experimental data was used. The present results indicate that the von-Karman constant $\kappa$ was indeed 0.41 for all the test conditions. This value is comparable to $\kappa = 0.412$ reported by Nezu and Rodi [13] at similar test conditions.

**Table 2 Summary $U_\tau$, Π and other related parameters**

| Test | $Re_\theta$ | $U_\tau$ (cm/s) | $C_{fx}\,10^{-3}$ | Π | ΔU | $k^+$ |
|---|---|---|---|---|---|---|
| SM 1 | 2625 | 3.24 | 3.80 | 0.11 | | |
| SM 2 | 1380 | 1.55 | 4.39 | 0.10 | | |
| SM 3 | 1750 | 2.10 | 4.14 | 0.08 | | |
| PF 1 | 2450 | 3.05 | 3.61 | 0.35 | | |
| PF 2 | 2250 | 2.60 | 3.71 | 0.36 | | |
| PF 3 | 1400 | 2.20 | 4.20 | 0.30 | | |
| SG 1 | 2620 | 2.95 | 4.50 | 0.25 | 2.8 | 35 |
| SG 2 | 1970 | 2.28 | 4.22 | 0.30 | 1.8 | 27 |
| SG 3 | 1560 | 2.10 | 4.39 | 0.24 | 1.5 | 25 |
| WM 1 | 3920 | 4.13 | 5.70 | 0.48 | 7.1 | 25 |
| WM 2 | 3240 | 3.55 | 5.53 | 0.49 | 6.2 | 21 |
| WM 3 | 2580 | 2.75 | 5.56 | 0.45 | 5.8 | 17 |

The distributions of the velocity defect for the smooth wall data sets in the present study are shown in Fig. 6(*a*). The solid line is a fit to Hama's function (Eqs. (6) and (7)) which is representative of a correlation which fixes the value of Π implicitly. For the purpose of comparison, the results of Thole and Bogard [27] at both lower and higher freestream turbulence values are also shown. It should be noted that the study of Thole and Bogard [27] considered a boundary layer with significant and sustained freestream turbulence, while our data pertains to a shallow open channel flow where the notion of "freestream" becomes ambiguous. Even though our study considered a boundary layer in an open channel, the smooth data fall within the envelope of Thole and Bogard's boundary layer data for a zero pressure gradient. In Fig. 6(*a*), the defect velocity profiles for all data sets are consistently lower than would be predicted by Hama's functions. In fact, if one insists on the smooth plate flow (Test SM3) following the Hama fit, a $U_\tau$ value of about 0.0165 m/s (compared with 0.0210 m/s obtained from Eqs. (3) and (8)) would be predicted. This would give a skin friction coefficient that is 40 percent lower than otherwise obtained. It should be recalled that for the smooth case, the value of $U_\tau$ obtained previously closely matched that determined from the slope of the velocity profile at the wall. Following Bradshaw [31], one is tempted to attribute the consistently lower values of $U_\tau$ obtained from the Hama function (and hence $C_f$) to the strength of the wake, as implied by Eq. (7), being too large for our experiments. In Fig. 6(*b*) all the data sets (smooth and rough surfaces) from the present experiment are shown. Consistent with the Π values summarized in Table 2, the wire mesh surface which has the highest Π value follows the Hama formulation most closely. If one used the Hama formulation for the wire mesh, the skin friction coefficient predicted would still be 4–7 percent lower than those summarized in Table 2. Similar to Krogstad et al. [21], one may conclude from Fig. 6(*b*) that the velocity profiles for the rough wall boundary layers being studied are significantly different from the smooth case both in the wall region, and also in the outer part of the flow.

The velocity profiles normalized using wall parameters are shown in Fig. 7. The strengths of the wake produced by the perforated plate and sand grain roughness are nearly equal (Π

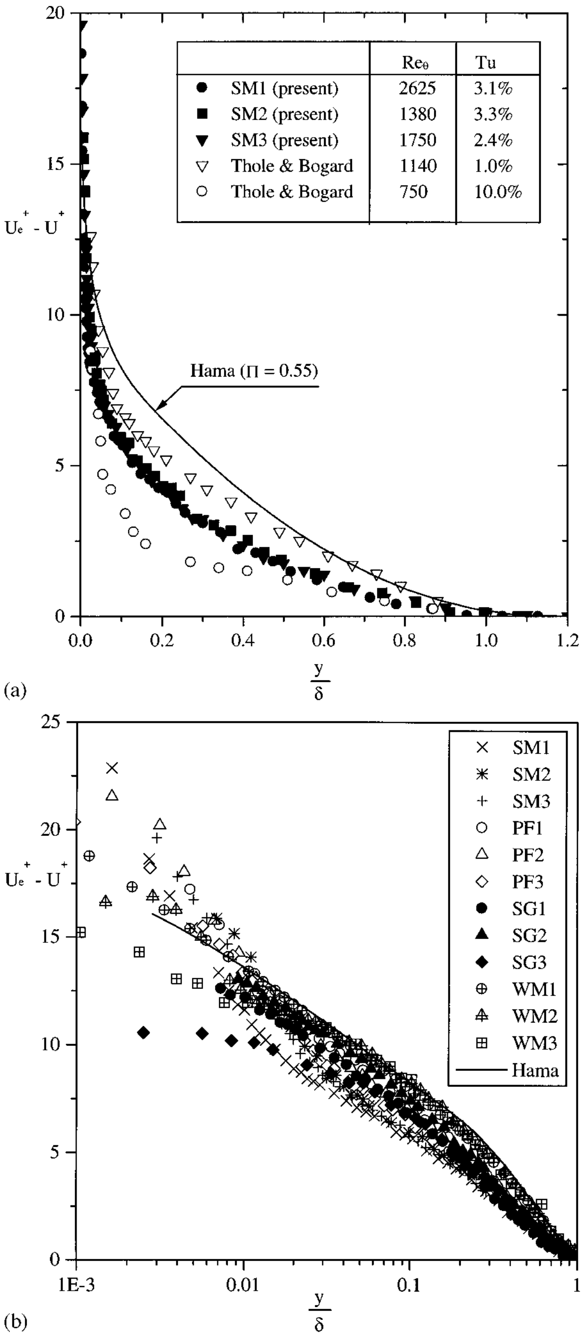

**Fig. 6** (***a***) **Velocity defect distribution for smooth wall: present and previous data. (*b*) Velocity defect distribution for smooth and rough surfaces: solid line is a fit to Hama profile ($\Pi = 0.55$)**

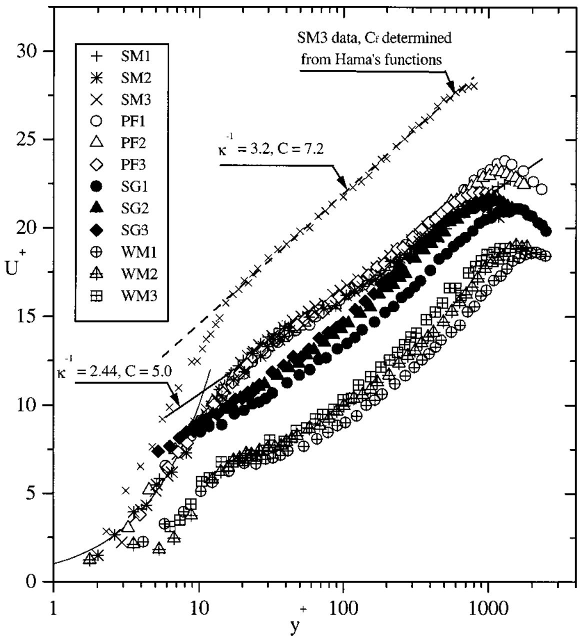

**Fig. 7 Velocity distribution in inner coordinates (uncertainty in $y^+$: ±4 percent)**

$=0.24-0.36$), while the wire mesh has the strongest wake strength. The evident reduction of the wake strength for all the profiles may be attributed to the relatively higher turbulence levels in the outer channel flow as well as the free surface effect. As mentioned earlier, the wake component for the smooth plate is almost nonexistent; these results are similar to those of Hancock and Bradshaw [29,26] for a boundary layer at similar turbulence levels. In fact, if the friction velocity obtained from a Hama formulation is employed for the SM3 data, a slope of $\kappa^{-1}=3.2$ and additive constant of $C=7.2$ will be required for the experimental data to follow the well-established log-law (see Fig. 7). Furthermore, the universality of $u^+=y^+$ will be invalidated. This result leads one to conclude that use of a correlation such as Hama's which implicitly fixes the wake strength at $\Pi=0.55$ is an erroneous approach for the open channel flow boundary layer being studied.

In Fig. 7, the effect of surface roughness is to shift the velocity profile down, and to the right, relative to the profile on a smooth wall. This effect can easily be discerned with the wire mesh providing the largest shift. The shift in the velocity profile and to a lesser degree the shape of the profile are strongly dependent on the type of roughness employed. The roughness function of each profile and the corresponding roughness Reynolds number ($k^+ = kU_\tau/v$) are summarized in Table 2. One notes that even though the mesh diameter is only half as thick as the average diameter of the sand grains, it gave the highest roughness function. The amount of shift produced by the perforated plate is minimal. For the tests conducted on the perforated plate (Tests PF1, PF2, and PF3), no noticeable shift ($\Delta U^+$) was observed suggesting that the mean velocity profile is essentially similar to the smooth wall data except for the strength of the wake.

Figure 8 shows the variation of the skin friction coefficient, $C_f$ with $\mathrm{Re}_\theta$ for all surfaces, albeit for only a narrow range of Reynolds numbers. The broken line is a fit to the recent low-turbulence intensity smooth-wall empirical relation of Osaka et al. [17]. Also shown for the purpose of comparison is the skin friction coefficient correlation derived from a one-seventh-power law for smooth turbulent boundary layer, i.e., $C_f=0.02\,\mathrm{Re}_\delta^{-1/6}$. The present $C_f$ values for the smooth surface are consistently higher than the low turbulence correlations. The agreement between the present data and the skin friction correlation based on the power law improves as $\mathrm{Re}_\theta$ increases while a better agreement is observed in comparison to the correlation of Osaka et al. [17] at lower $\mathrm{Re}_\theta$. One should recall that an increase in freestream turbulence necessarily increases the skin friction coefficient. The deviation of the present skin friction coefficient (for an open channel) on a smooth surface from those predicted for a boundary layer in low freestream turbulence is comparable to that predicted by Hoffmann and Mohammadi [37] at similar turbulence levels. As one would expect, the skin friction coefficients for the sand grain and wire mesh data are significantly higher than the smooth wall data. Contrary to expectation, however, the skin friction values obtained for the perforated plate are slightly lower than the

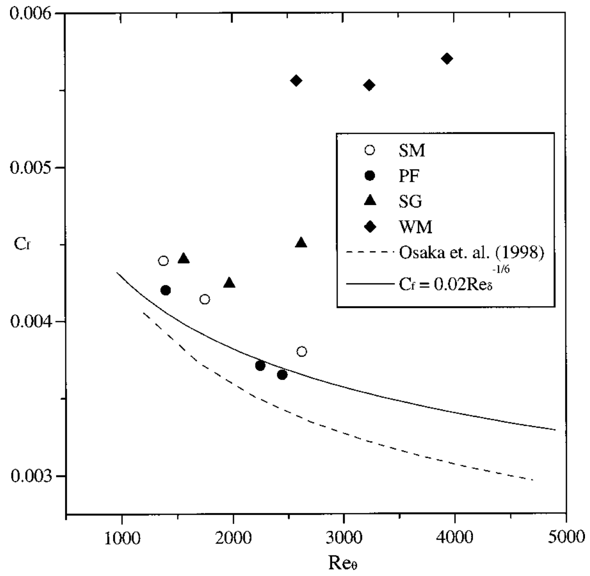

**Fig. 8 Variation of skin friction coefficient with $Re_\theta$ for smooth and rough surfaces (uncertainty in $C_f$: ±6 percent for smooth surface and ±12 percent for rough surfaces, $Re_\theta$: ±5 percent)**

smooth surface data, although they are higher than the corresponding low-turbulence skin friction values. Attempts were made to vary the $C_f$ values for either the perforated plate or the smooth surface to avoid this apparent contradiction. However, such attempts gave $C_f$ values that predicted significantly larger log-law slopes for the smooth surface or significantly lower slopes for the perforated plate. Furthermore, the resulting fits to Eq. (3) were generally not good. One may recall from Fig. 7 that the perforated plate produced no shift in comparison with the smooth wall plots. Assuming that the strength of the wake is related to the value of $C_f$, one may expect a less significant alteration of the skin friction for the perforated plate.

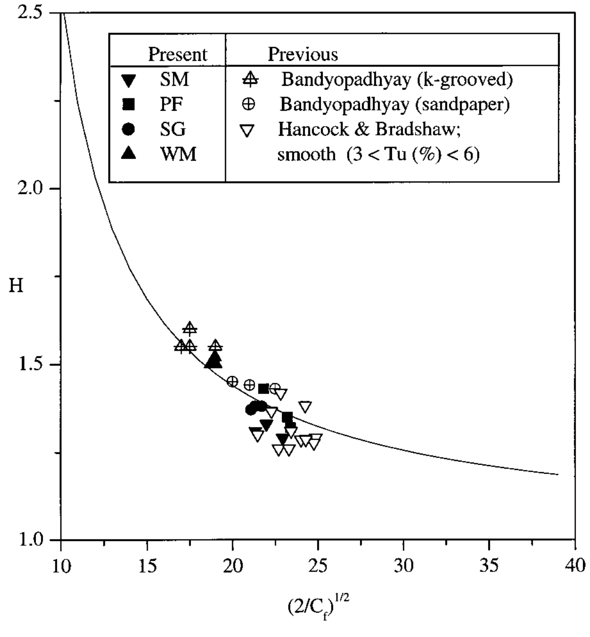

**Fig. 9 Variation of shape factor ($H$) with skin friction coefficient ($C_f$) for smooth and rough surfaces at different freestream turbulence values (uncertainty in $H$: ±4 percent)**

The variation of the shape factor $H$ with $C_f$ is shown plotted in Fig. 9. Also shown are the rough wall boundary layer data set (sandpaper and $k$-grooved surfaces) of Bandyopadhyay [10] at low turbulence levels, and the smooth wall data of Hancock and Bradshaw [26] at moderately high turbulence levels. The solid line represents the fit to the following equation

$$H=\left[1-G\sqrt{\frac{C_f}{2}}\right]^{-1} \tag{10}$$

where, $G$ is the Clauser shape parameter. Following Bandyopadhyay [10], we adopted a constant value of $G=6.1$. The agreement between the fit and both the smooth and rough wall experimental data is reasonable, irrespective of the type of roughness and irrespective of the distinction between open channel and zero pressure gradient boundary layers. One can infer that as the roughness effect increases, $H$ increases and $(2/C_f)^{1/2}$ decreases in Fig. 9. The present wire mesh data and the low-intensity $k$-grooved results of Bandyopadhyay are concentrated at the far left of Fig. 9, while the present smooth data and those of Hancock and Bradshaw [26] are found at the far right in the figure. The present sand grain and low-intensity sandpaper data of Bandyopadhyay [10] lie between these two extremes. This zonal distribution according to type of surface suggests that the effect of surface-type dominates the freestream turbulence effect in the vicinity of the wall.

## Turbulence Intensity

Before considering the results for the rough surfaces, the streamwise turbulence intensity for the smooth case will be compared to other measurements reported in the literature in order to assess the effect of the turbulence intensity of the exterior flow. Although comparisons are made to the boundary layer measurements of Thole and Bogard [27] and Hancock and Bradshaw [29] at similar and different freestream turbulence intensities, the present case considers an open channel flow where the flow region outside the boundary layer is somewhat different, both in terms of mean flow structure and turbulence length scale.

The distribution of the streamwise turbulence intensity for the smooth wall tests is shown in Fig. 10 using the friction velocity and the boundary layer thickness as the normalizing scales. The agreement between the present smooth data and the other studies at comparable intensities appears reasonable. Specifically, the

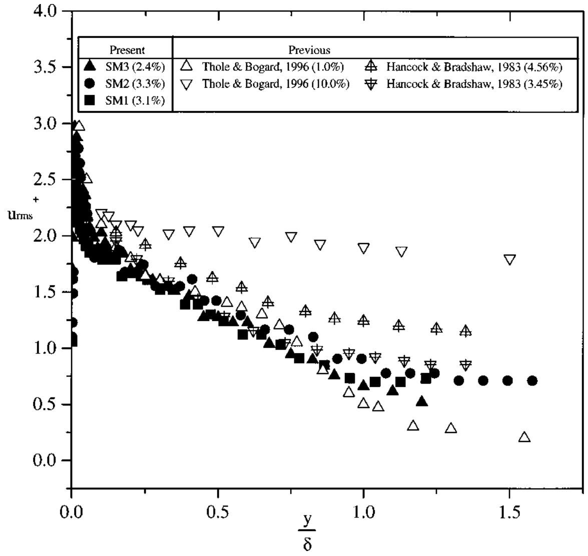

**Fig. 10 Variation of turbulence intensity on smooth surfaces at various freestream turbulence levels (uncertainty in $u^+_{rms}$: ±5 percent, $y/\delta$: ±5 percent)**

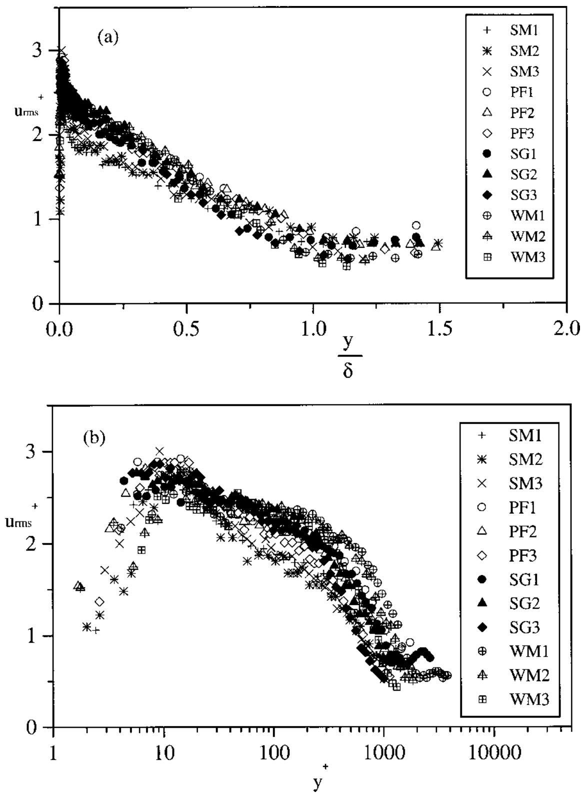

**Fig. 11 Variation of turbulence intensity for (*a*) smooth and (*b*) rough surfaces (uncertainty in $u^+_{rms}$: ±5 percent for smooth surface and ±8 percent for rough surfaces)**

present data and the data of Hancock and Bradshaw at Tu=3.45 percent are similar in the range $y<0.75\delta$. Figure 10 suggests that as the freestream turbulence increases, the intensity profile becomes more flat, implying that the outer turbulence is penetrating more deeply into the boundary layer.

In Fig. 11(*a*) and 11(*b*) all the data sets (smooth and rough surfaces) obtained in the present experiment are shown. In Fig. 11(*a*) the boundary layer thickness is used as the normalizing length scale, while in Fig. 11(*b*) the viscous length scale is adopted. From Fig. 11(*b*), the location ($y^+_{max}$) at which each data set attains its maximum value appears to be confined to the range $10<y^+_{max}<15$. It is also evident from Fig. 11 that the smooth wall and perforated plate data exhibit slightly higher peak values. The smooth-wall intensities, however, fall more rapidly and beyond $y^+\sim 20$, they become consistently lower than all the other data sets up to $y^+\sim 300$. In general, at similar outer turbulence levels, the turbulence intensity profiles tend to be more flat as the roughness effect increases. This is a clear evidence of the influence of roughness extending beyond the roughness sublayer.

## Conclusions

Velocity measurements were obtained in the turbulent boundary layer created by a shallow open channel flow for both smooth and three different rough surfaces using a laser-Doppler anemometer. A velocity defect profile was fitted to each experimental data set to determine the strength of the wake and the skin friction coefficient. Finally, in order to assess the effect of the moderate turbulence intensity level in the channel flow outside the boundary layer, the data were compared to both smooth and rough wall boundary layer data in the literature for different freestream turbulence intensities. The major conclusions of the study are as follows:

1 The effect of roughness on both the mean velocity and, to a lesser extent, the streamwise turbulence intensity, varied for the three different roughness elements.

2 The value of the wake parameter, $\Pi$, was also observed to vary with roughness element. For each of the rough surfaces, the value of $\Pi$ increased over the smooth wall value in this experiment, approximately $\Pi=0.08-0.11$.

3 In fitting the velocity defect law, the correlation used by Krogstad et al. [21], which did not fix the value of $\Pi$ implicitly, was found to yield a more consistent and accurate estimate for the skin friction coefficient than a formulation such as that of Hama which fixes the value of $\Pi$.

4 Comparisons with boundary layer data in the literature for elevated freestream turbulence intensities suggest that one effect of the higher turbulence level in the channel flow outside the wall region was to increase the skin friction coefficient. However, this effect was observed to diminish as the wall roughness increased.

5 Finally, even though the boundary layer in an open channel flow is influenced by the free surface, many of the flow characteristics, in particular those that pertain to surface roughness, are similar to those observed in a canonical zero pressure gradient boundary layer.

A general conclusion of the present study is that bed surface effects, in this case due to roughness, can influence the flow structure in the outer region of the boundary layer, which contradicts the wall similarity hypothesis. This conclusion has important implications for predictive models for near-wall flows, which then face the challenging task of incorporating the specific effects of different roughness elements. A final observation is that the non-confinement of rough wall effects to the inner region and the penetration of outer turbulence intensity deep into the wall region suggests that rough-wall flows in the presence of elevated turbulence intensities may be an ideal flow for studying the interactions between the inner and outer regions of the turbulent boundary layer.

## Acknowledgments

The financial support of the Natural Sciences and Engineering Research Council of Canada (NSERC) to the first author in the form of a postgraduate scholarship and to the second author in the form of a research grant is gratefully acknowledged. The financial support of NSERC to the third author in the form of an equipment grant is also gratefully acknowledged. As well, the authors thank the reviewers of the paper for their comments and suggestions, many of which have been reflected in the final version for improved clarity and explanation.

## References

[1] Patel, V. C., 1998, ''Perspective: Flow at High Reynolds Number and over Rough Surfaces—Achilles Heel of CFD,'' ASME J. Fluids Eng., **120**, pp. 434–444.
[2] Nikuradse, J., 1933, Stromungsgesetze in rauhen Rohren, VDI Forschungsheft No. 361.
[3] Tani, I., and Motohashi, T., 1985, ''Non-Equilibrium Behavior of Turbulent Boundary Layer Flows,'' Proc. Jpn. Acad., **B61**, pp. 333–340.
[4] Prandtl, L., and Schlichting, H., 1934, das Wiederstandagesetz rouher Platten, Werft Reedere Hafen, **15**, pp. 1–4.
[5] Millikan, C. B., 1938, ''A Critical Discussion of Turbulent Flows in Channels and Circular Tubes,'' *Proc. 5th Int. Cong. Appl. Mech.*, Cambridge, pp. 386–392.
[6] Hama, F. R., 1954, ''Boundary Layer Characteristics for Smooth and Rough Surfaces,'' Trans. Soc. Naval Archit. Mar. Eng., **62**, 333–358.
[7] Clauser, F. H., 1954, ''Turbulent Boundary Layers in Adverse Pressure Gradients,'' J. Aeronaut. Sci., **21**, pp. 91–108
[8] Furuya, Y., and Fujita, H., 1967, ''Turbulent Boundary Layers on a Wire-Screen Roughness,'' Bull. JSME, **10**, pp. 77–86
[9] Perry, A. E., and Abell, C. J., 1977, ''Asymptotic Similarity of Turbulence Structures in Smooth- and Rough-Walled Pipes,'' J. Fluid Mech., **79**, pp. 785–799
[10] Bandyopadhyay, P. R., 1987, ''Rough-Wall Turbulent Boundary Layers in the Transition Regime,'' J. Fluid Mech., **180**, pp. 231–266.
[11] Perry, A. E., Lim, K. L., and Henbest, S. M., 1987, ''An Experimental Study

of the Turbulence Structure in Smooth- and Rough-Wall Boundary Layers,'' J. Fluid Mech., **177**, pp. 437–466.

[12] Raupach, M. R., Antonia, R. A., and Rajagopalan, S., 1991, ''Rough Wall Turbulent Boundary Layers,'' Appl. Mech. Rev., **44**, pp. 1–25.

[13] Nezu, I., and Rodi, W., 1986, ''Open-Channel Flow Measurements with a Laser Doppler Anemometer,'' J. Hydraul. Eng., **112**, No. 5, pp. 335–355.

[14] Xinyu, L., Zengnan, D., and Changzhi, C., 1995, ''Turbulent Flow in Smooth-Wall Open Channels with Different Slopes,'' J. Hydraul. Res., **33**, No. 5, pp. 333–347.

[15] Coles, D. E., 1956, ''The law of the Wake in the Turbulent Boundary Layer,'' J. Fluid Mech., **1**, pp. 191–226.

[16] Coles, D. E., 1987, ''Coherent Structure in Turbulent Boundary Layers,'' *Perspectives in Turbulence Studies*, pp. 93–114, Springer-Verlag.

[17] Osaka, H., Kameda, T., and Mochizuki, S., 1998, ''Re-Examination of the Reynolds-Number-Effect on the Mean Flow Quantities in a Smooth Wall Turbulent Boundary Layer,'' JSME Int. J., Ser. B, **41**, No. 1, pp. 123–129.

[18] Tani, I., 1987, ''Turbulent Boundary Layer Development over Rough Surfaces,'' Perspectives in Turbulence Studies, Meier H. U., and Bradshaw, P., eds., Springer-Verlag, pp. 223–249.

[19] Perry, A. E., Schofield, W. H., and Joubert, P. N., 1969, ''Rough Wall Turbulent Boundary Layers,'' J. Fluid Mech., **37**, pp. 383–413.

[20] Townsend, A. A., 1976, *The Structure of Turbulent Shear Flow*, Cambridge University Press.

[21] Krogstad, P. A., Antonia, R. A., and Browne, L. W. B., 1992, ''Comparison between Rough- and Smooth-Wall Turbulent Boundary Layers,'' J. Fluid Mech., **245**, pp. 599–617.

[22] Osaka, H., and Mochizuki, S., 1988, ''Coherent Structure of a *d*-type Rough Wall Boundary Layer,'' *Transport Phenomena in Turbulent Flows: Theory Experiment and Numerical Simulation*, Hirata, M., and Kasagi, N., eds., pp. 199–211.

[23] Young, S., and Bergstrom, D. J., 1997, ''Turbulence Measurements in a Rough Wall Boundary Layer,'' *Proceedings of Eleventh Symposium on Turbulent Shear Flows*, Grenoble, Sept. 8–10, 14–18.

[24] Mills, A. F., and Hang, X., 1983, ''On the Skin Friction Coefficient for a Fully Rough Flat Plate,'' ASME J. Fluids Eng., **105**, pp. 364–365.

[25] Bradshaw, P., 1978, *Topics in Applied Physics, Turbulence*, Bradshaw, P., ed., Vol. 12, 2nd ed., New York, Springer-Verlag.

[26] Hancock, P. E., and Bradshaw, P., 1989, ''Turbulence Structure of a Boundary Layer Beneath a Turbulent Freestream,'' J. Fluid Mech., **205**, pp. 45–76.

[27] Thole, K. A., and Bogard, D. G., 1996, ''High Freestream Turbulence Effects on Turbulent Boundary Layers,'' ASME J. Fluids Eng., **118**, pp. 276–284.

[28] Blair, M. F., 1983, ''Influence of Free-Stream Turbulence on Turbulent Boundary Layer Heat Transfer and Mean Profile Development: Part II Analysis and Results,'' ASME J. Heat Transfer, **105**, pp. 41–47.

[29] Hancock, P. E., and Bradshaw, P., 1983, ''Effect of Free-Stream Turbulence on Turbulent Boundary Layers,'' ASME J. Fluids Eng., **105**, pp. 284–289.

[30] Balachandar, R., and Ramachandran, S., 1999, ''Turbulent Boundary Layers in Low Reynolds Number Shallow Open Channel Flows,'' ASME J. Fluids Eng., **121**, No. 3, pp. 684–689.

[31] Bradshaw, P., 1987, ''Wall Flows,'' *Turbulent Shear Flows 5*, Durst, F., Launder, B. E., Lumley, J. L., Schmidt, F. W., and Whitelaw, J. H., eds., pp. 171–175.

[32] Finley, P. J., Phoe, Khoo Chong, and Poh, Chin Jeck, 1966, ''Velocity Measurements in a Thin Turbulent Wake Layer,'' La Houille Blanche, **21**, pp. 713–721.

[33] Granville, P. S., 1976, ''A Modified Law of the Wake for Turbulent Shear Layers,'' ASME J. Fluids Eng., **98**, pp. 578–580.

[34] Press, W. H., Flannery, B. P. Teukolsky, S. A., and Vetterling, W. T., 1987, *Numerical Recipes*, Cambridge University Press.

[35] Kirkgoz, M. S., and Ardichoglu, M., 1997, ''Velocity Profiles of Developing and Developed Open Channel Flow,'' J. Hydraul. Eng., **123**, No. 12, pp. 1099–1105.

[36] Spalart, P. R., 1988, ''Direct Numerical Simulation of a Turbulent Boundary Layer Up to $R_\theta = 1410$,'' J. Fluid Mech., **187**, pp. 61–69.

[37] Hoffmann, J. A., and Mohammadi, K., 1991, ''Velocity Profiles for Turbulent Boundary Layers Under Freestream Turbulence,'' ASME J. Fluids Eng., **113**, pp. 399–404.

[38] Cardoso, A. H., Graf, W. H., and Gust, G., 1989, ''Uniform Flow in a Smooth Open Channel,'' J. Hydraul. Res., **27**, No. 5, pp. 603–616.

[39] Dvorok, F. A., 1969, ''Calculation of Turbulent Boundary Layers on Rough Surfaces in Pressure Gradients,'' AIAA J., **7**, pp. 1752–1759.

[40] Schultz-Grunow, 1941, ''New Frictional Resistance Law for Smooth Plates,'' NACA TM 986.

[41] Smith, D. W., and Walter, J. H., 1959, ''Skin-Friction Measurement in Incompressible Flow,'' NACA TR-R 26.

**Anupam Dewan**
Associate Professor,
Department of Mechanical Engineering,
Indian Institute of Technology,
Guwahati–781 031, India
e-mail: adewan@iitg.ernet.in

**Jaywant H. Arakeri**
Associate Professor,
Department of Mechanical Engineering,
Indian Institute of Science,
Bangalore–560 012, India
e-mail: jaywant@mecheng.iisc.ernet.in

# Use of $k-\epsilon-\gamma$ Model to Predict Intermittency in Turbulent Boundary-Layers

*The intermittency profile in the turbulent flat-plate zero pressure-gradient boundary-layer and a thick axisymmetric boundary-layer has been computed using the Reynolds-averaged $k-\epsilon-\gamma$ model, where k denotes turbulent kinetic energy, $\epsilon$ its rate of dissipation, and $\gamma$ intermittency. The Reynolds-averaged model is simpler compared to the conditional model used in the literature. The dissipation equation of the Reynolds-averaged model is modified to account for the effect of entrainment. It has been shown that the model correctly predicts the observed intermittency of the flows.*
[S0098-2202(00)02403-2]

## 1 Introduction

Turbulent boundary-layers are intermittent close to the free-stream where the flow alternates between turbulent and irrotational states. Intermittency at a point is defined as the fraction of time flow is turbulent at that point. Characteristics of the outer intermittent region are important for understanding the entrainment process, in which the outer irrotational fluid becomes turbulent by acquiring vorticity. This process is governed mainly by large eddies. The interface separating turbulent and nonturbulent zones is influenced by eddies of all sizes and is sharp, irregular and changes rapidly. The prediction of intermittency ($\gamma$) of wall-bounded flows has not received much attention as intermittency is not as important as the skin friction coefficient and drag which are governed mainly by the near wall dynamics.

Eddy-viscosity based $k-\epsilon$ model is widely used to compute wall-bounded and free-shear flows. Byggstoyl and Kollmann [1] proposed a conditional $k-\epsilon-\gamma$ model in which momentum equations for the turbulent and irrotational zones and transport equations for turbulent kinetic energy and its dissipation are solved, with a contribution of the turbulent-irrotational interface to these equations. They solved the intermittency transport equation based on the turbulent zone quantities. Subsequently, they extended their model to the second moment closure (Byggstoyl and Kollmann [2]). The second-moment conditional model is difficult to implement for wall-bounded flows as near wall modifications for such models are much more complex compared to the eddy-viscosity based models.

Recently, Cho and Chung [3] proposed the $k-\epsilon-\gamma$ model based on the Reynolds-averaged quantities, which is simpler compared to the conditional $k-\epsilon-\gamma$ model. The model of Cho and Chung [3] is superior to the conditional $k-\epsilon-\gamma$ and second moment models in predicting the intermittency of free-shear flows. They showed that the effect of entrainment on the rate of dissipation of turbulent kinetic energy considered in their model removes the weaknesses of the standard $k-\epsilon$ model in predicting different nonbuoyant free-shear flows (axisymmetric jet, plane far wake, and plane mixing-layer). The standard $k-\epsilon$ model overpredicts the growth rate and turbulent quantities of the axisymmetric jet and underpredicts that of the plane far wake and the plane mixing-layer. The $k-\epsilon-\gamma$ of Cho and Chung [3] has been extended to the plane momentumless wake (Ahn and Sung [4]), axisymmetric plume (Dewan et al. [5]) and plane plume (Kalita et al. [6]). Recently, Wang and Derksen [7] have used the $k-\epsilon-\gamma$ model to investigate developing turbulent flow in a pipe. They have showed that transport equation for intermittency based on the Reynolds-averaged quantities eliminates the need for the wall functions and thus the $k-\epsilon-\gamma$ model can be applied to complicated wall-bounded turbulent flows.

The zero pressure-gradient flat-plate boundary layer is the simplest test case for the model. Measurements in an axisymmetric boundary-layer flow on the outer surface of a circular cylinder with boundary-layer thickness greater than the cylinder radius $a$ ($\delta/a>1$; hence termed thick) show that the intermittency is larger compared to the flat-plate boundary-layer. Thick axisymmetric boundary-layer flow is relevant to several engineering applications (Dewan and Arakeri [8]) and is a good test case for the model.

The objective of this paper is to study the Reynolds-averaged $k-\epsilon-\gamma$ model for the flat plate and thick axisymmetric boundary-layers. Section 2 provides the details of the turbulence model and the numerical method used. The modeling of the intermittency equation and the effect of intermittency on mean and turbulent quantities has also been described in Section 2. Section 3 compares the predicted mean and turbulent quantities with measurements for the two flows.

## 2 Governing Equations and Turbulence Model

The following equations in the cylindrical coordinate system are solved. The boundary-layer assumptions are assumed to be valid. The computations for the flat plate boundary-layer are made in the limiting case with $r/a\rightarrow 0$, where $a$ is the cylinder radius.

*Continuity*:

$$\frac{\partial u}{\partial x}+\frac{1}{r}\frac{\partial}{\partial r}(rv)=0 \tag{1}$$

*Streamwise Momentum Equation*:

$$u\frac{\partial u}{\partial x}+v\frac{\partial u}{\partial r}=\frac{1}{r}\frac{\partial}{\partial r}\left[[r(\nu+\nu_t)]\frac{\partial u}{\partial r}\right] \tag{2}$$

$u$ and $v$ are the mean velocities in the streamwise ($x$) and radial ($r$) directions, respectively.

### 2.1 $k-\epsilon-\gamma$ Model.

In the present work we have used the following eddy viscosity relation proposed by Cho and Chung [3] to account for the contribution of the outer irrotational fluid

$$\nu_t=c_\mu\left[1+c_{\mu g}\frac{k^3}{\epsilon^2}\frac{1-\gamma}{\gamma^3}\frac{\partial\gamma}{\partial r}\frac{\partial\gamma}{\partial r}\right]\frac{k^2}{\epsilon} \tag{3}$$

---

Contributed by the Fluids Engineering Division for publication in the JOURNAL OF FLUIDS ENGINEERING. Manuscript received by the Fluids Engineering Division July 8, 1999; revised manuscript received March 27, 2000. Associate Technical Editor: P. Bradshaw.

where, $\gamma$ denotes intermittency and the model constant $c_{\mu g}=0.10$. In the limit of fully turbulent flow ($\gamma=1$) the above relation reduces to the standard eddy-viscosity relation

$$\nu_t = c_\mu \frac{k^2}{\epsilon} \tag{4}$$

where, the standard $k-\epsilon$ model constant $c_\mu=0.09$. Intermittency ($\gamma$) profile, turbulent kinetic energy ($k$), and its dissipation ($\epsilon$) are obtained from the following transport equations.

*Turbulent Kinetic Energy*:

$$u\frac{\partial k}{\partial x} + v\frac{\partial k}{\partial r} = \frac{1}{r}\frac{\partial}{\partial r}\left[\left[r\left(\nu+\frac{\nu_t}{\sigma_k}\right)\right]\frac{\partial k}{\partial r}\right] + P_k - \epsilon \tag{5}$$

*Rate of Turbulent Kinetic Energy Dissipation*:

$$u\frac{\partial \epsilon}{\partial x} + v\frac{\partial \epsilon}{\partial r} = \frac{1}{r}\frac{\partial}{\partial r}\left[\left[r\left(\nu+\frac{\nu_t}{\sigma_\epsilon}\right)\right]\frac{\partial \epsilon}{\partial r}\right] + c_{\epsilon 1}\frac{\epsilon}{k}P_k + c_{\epsilon 4}\Gamma\frac{\epsilon^2}{k} - c_{\epsilon 2}\frac{\epsilon^2}{k} \tag{6}$$

where, $P_k=\nu_t S^2$ is the production of turbulent kinetic energy with mean strain rate $S=[\partial u/\partial r+\partial v/\partial x]$. For the near wall region, the low-Re $k-\epsilon$ model of Chien was used, which is quite accurate in predicting the near wall quantities for the flat plate boundary-layer (Patel et al. [9]). The predicted characteristics of the outer region are independent of the near-wall modifications as in the outer region all the low-Re $k-\epsilon$ models reduce to the standard $k-\epsilon$ model. Therefore, the near wall version used in the model is not important. $c_{\epsilon 1}=1.35$, $c_{\epsilon 2}=1.88$, $\sigma_k=1.0$ and $\sigma_\epsilon=1.3$ are the constants of Chien's low-Reynolds number $k-\epsilon$ model (Patel et al. [9]). In the present work we have added the third term on the RHS of the dissipation equation and its effect is discussed in the next section. It may be noted that in Section 3.1 predictions using the low-Re $k-\epsilon$ model of Chien (termed as the $k-\epsilon$ model in the present paper) employ the standard eddy viscosity relation (4).

**2.2 Intermittency.** Libby [10] was the first to propose a model for a guessed transport equation for the intermittency. Dopazo [11] derived an exact transport equation for intermittency by multiplying the instantaneous continuity equation by the intermittency indicator function and taking the ensemble average. The intermittency indicator function is used to distinguish between the two zones and is equal to one in the turbulent zone and zero in the nonturbulent zone. The exact intermittency equation involves terms accounting for the transport of intermittency due to the relative motion of turbulent and nonturbulent zones, and production terms. The following modeled equation for intermittency is solved

$$u\frac{\partial \gamma}{\partial x} + v\frac{\partial \gamma}{\partial r} = D_g + S_g \tag{7}$$

$D_g$ represents the transport of $\gamma$ due to the mean velocity difference between the turbulent and irrotational fluids and is effective only in the intermittent region. The following diffusion model for $D_g$ is used (Cho and Chung [3]): $D_g=(1/r)(\partial/\partial r)[r(1-\gamma)(\nu_t/\sigma_g)(\partial\gamma/\partial r)]$, with the model constant $\sigma_g=1.0$.

$S_g$ represents the conversion rate of the outer irrotational fluid into the turbulent fluid and involves the geometry of the interface. The following model for $S_g$ is used, with the model constants $c_{g1}=1.6$, $c_{g2}=0.15$, $c_{g3}=0.16$ (Dewan et al. [5])

$$S_g = c_{g1}\gamma(1-\gamma)\frac{P_k}{k} + c_{g2}\frac{k^2}{\epsilon}\frac{\partial\gamma}{\partial x_j}\frac{\partial\gamma}{\partial x_j} - c_{g3}\gamma(1-\gamma)\frac{\epsilon}{k}\Gamma \tag{8}$$

The last term in the model for $S_g$ accounts for the effect of entrainment. This term, however, is negligible for most flows. Here $\Gamma=(k^{5/2}/\epsilon^2)U_i/(U_kU_k)^{1/2}(\partial U_i)/(\partial x_j)(\partial\gamma/\partial x_j)$ is the intermittency interaction invariant and is a measure of the change in intermittency due to the entrainment (Cho and Chung [3]). In the present work with boundary-layer assumptions $\Gamma$ is approximately equal to $k^{5/2}/\epsilon^2\,\partial u/\partial r\,\partial\gamma/\partial r$. The magnitude of $\Gamma$ depends on the rate of entrainment. If the entrainment is by the inward movement of the outer irrotational fluid (as in a jet or in a plume) then $\gamma$ at a fixed location decreases and vice-versa. A reduction in $\gamma$ means reduction in turbulent length scale $l$ or an increase in $\epsilon$ as $l \simeq k^{3/2}/\epsilon$.

Cho and Chung [3] proposed this model by modifying the model of Byggstoyl and Kollmann [2] which was used with the conditional $k-\epsilon$ and Reynolds stress transport models. Dewan et al. [5] modified the model of Cho and Chung [3] to account for the effect of buoyancy on intermittency and studied intermittency of the axisymmetric plume. Recently, Kalita et al. [6] have applied this model to the plane plume. Note that the intermittency equation does not require any special near wall treatment. Cho and Chung [3] also modified the dissipation equation (6) by adding the term $c_{\epsilon 4}\Gamma\epsilon^2/k$ with the model constant $c_{\epsilon 4}=0.1$. This term accounts for the effect of entrainment and is significant. Its inclusion in the dissipation equation removes the limitations of the standard $k-\epsilon$ model in predicting different free-shear flows (described in Section 1).

**2.3 Numerical Method.** The governing equations were solved using the control volume method (Patankar [12]). Power-law scheme (Patankar [12]) in the cross-stream direction and upwind scheme (Anderson et al. [13]) in the stream-wise direction were used. Grid independence was checked and achieved. For one typical case with $\mathrm{Re}_a=736$ increasing the number of radial grids from 100–150 resulted in the changes in $C_f$ and $H$ at $\mathrm{Re}_{\theta,ax}=4350$ by the two models within 0.3 percent. The computations reported in this paper are using 100 radial grid points. To resolve sharp gradients close to the wall about 30 grid points were located within $y^+=50$. An axial step size equal to the smaller of five sublayer thickness and 25 percent of momentum thickness was used (Patel et al. [9]).

At the wall $u$ and $k$ were set to be zero, $\epsilon$ was computed based on Chien's low-Re $k-\epsilon$ model and the intermittency was set to unity at the wall (Wang and Derksen [7]). At the free-stream the variables $k$, $\epsilon$, and $\gamma$ were set to zero. Computations were started sufficiently upstream of the region of interest. At the starting point a small trigger in the values of $k$ and $\epsilon$ was given to initiate turbulent flow. Computations were made to study the dependence of results on the free-stream turbulence level defined by $T=1/U_\infty[2k/3]^{1/2}$ (White [14]) by considering three values of $T$ equal to 0.5 percent, 1 percent, and 2 percent, where $U_\infty$ is the free-stream velocity. The results reported in the present paper are independent of values of $k$ and $\epsilon$ at the starting point and the value of free-stream turbulence level. The code was validated with the results reported by Patel et al. [9] for the flat plate boundary-layer using the low-Re $k-\epsilon$ model and for the axisymmetric jet by Cho and Chung [3] using the Reynolds-averaged $k-\epsilon-\gamma$ model. The predicted $C_f$, $H$, mean and turbulent quantities were within 2 percent of those reported in the above references (Dewan [15]).

## 3 Results and Discussion

**3.1 Flat Plate Boundary-Layer.** Figures 1 and 2 compare the predicted intermittency and turbulent kinetic energy profiles at $\mathrm{Re}_\theta=2600$ with measurements by Klebanoff [16] for the flat plate boundary-layer with zero pressure gradient. The prediction of intermittency by the conditional $k-\epsilon-\gamma$ model of Byggstoyl and Kollmann [1] and the prediction of turbulent kinetic energy profile by low-Re $k-\epsilon$ model of Chien (hereafter termed as the $k-\epsilon$ model) have also been shown in Figs. 1 and 2, respectively. The prediction of intermittency by the Reynolds-averaged $k-\epsilon-\gamma$ model is superior to that by the conditional $k-\epsilon-\gamma$ model (Fig. 1). While using the Reynolds-averaged $k-\epsilon-\gamma$ model, the Eq. (6) for dissipation has been modified to account for the effect of entrainment, by adding the term containing intermittency interaction invariant $\Gamma$. The effect of entrainment on dissipation depends on the direction of motion of the interface and its magnitude de-

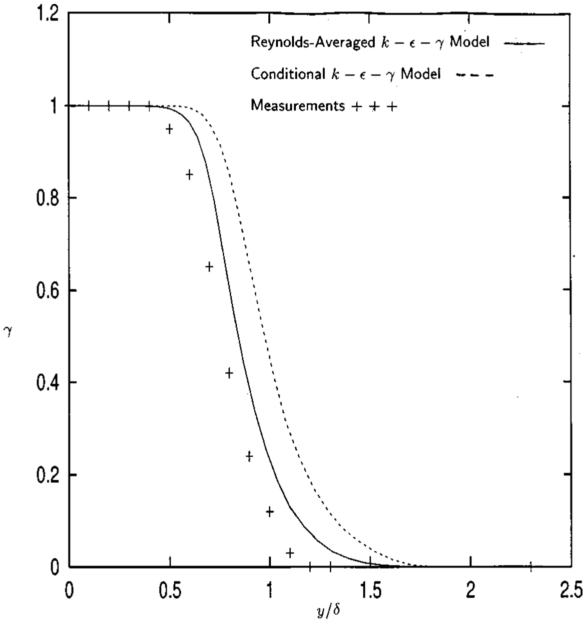

Fig. 1 Predicted intermittency profiles for the flat plate boundary layer at $Re_\theta=2600$ compared with the measurements

pends on the rate of entrainment. For boundary-layer flow the effect is to slightly increase dissipation (or decrease $k$) in the outer intermittent region (Fig. 2). The overall deviation between predictions by the two models and measurements in the outer region (Fig. 2) is due to the different values of the model constants used in Chien's low-Re $k-\epsilon$ model (Patel et al. [9]). Table 1 shows that the values of the skin friction coefficient and shape factor predicted by the two models are almost the same.

There is a debate in the literature on the effect of the outer irrotational fluid to the eddy viscosity. Based on the DNS data for the flat plate boundary-layer, Cazalbou and Bradshaw [17] have shown that close to the free-stream the standard eddy-viscosity model fails as here the value of the constant $c_\mu$ in the eddy-viscosity relation becomes three to four times its original value of 0.09. They suggested that this is probably due to the intermittent nature of the flow close to the free stream in wall-bounded and free-shear flows. It may be noted that the predictions of the eddy-viscosity by the relation (3) are consistent with the observations of Cazalbou and Bradshaw [17] and show a large increase in the value of the constant $c_\mu$ close to the free-stream.

Table 1 Predicted skin friction coefficient and shape factor for flat plate boundary-layer at $Re_\theta=2600$ compared with the measurements

| Quantity | Measurement | Low-Re $k-\epsilon-\gamma$ model | Low-Re $k-\epsilon$ model |
|---|---|---|---|
| $C_f \times 10^3$ | 3.42 | 3.41 | 3.43 |
| $H$ | - | 1.34 | 1.35 |

**3.2 Thick Axisymmetric Boundary-Layer.** For this flow the computations have been compared with measurements for the following three cases: (a) $Re_a=4800$ and $\delta/a=4.59$; (b) $Re_a=3200$ and $\delta/a=7.57$; and (c) $Re_a=736$ and $Re_{\theta,ax}=4350$ ($\delta/a \simeq 40$). Transverse curvature effects in the outer region become more important as the value of $\delta/a$ increases. Figure 3 compares Reynolds shear stress profiles for the case (a). Figures 4 and 5 compare intermittency and Reynolds shear-stress profiles for the case (b). The measurements of intermittency profile by Lueptow and Haritonidis [18] and of Reynolds shear-stress profile by Lueptow et al. [19] have also been shown in Figures 3, 4, and 5 for comparison. For the case (b) the predicted intermittency profile by the model is one over larger boundary layer thickness compared to the flat plate boundary-layer and the agreement with the measurements is good (Figs. 1 and 4). Here larger $\gamma$ is observed because of less constraint on the motion of eddies compared to the flat-plate boundary-layer. With an increase in $\delta/a$ the Reynolds shear-stress in the outer region decays faster compared to the flat plate boundary-layer as turbulence generated in the near wall region sustains larger area compared to flat plate boundary-layer (Fig. 3). The decay of Reynolds shear-stress in the outer region is larger

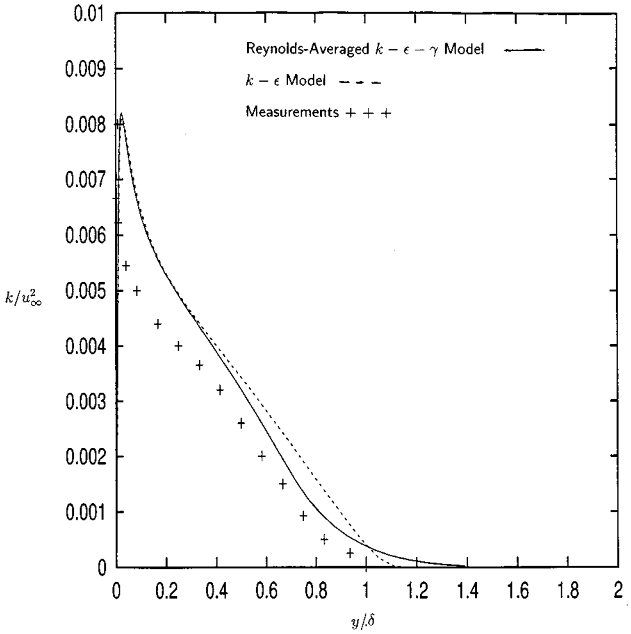

Fig. 2 Predicted turbulent kinetic energy profiles for the flat plate boundary-layer at $Re_\theta=2600$ compared with the measurements

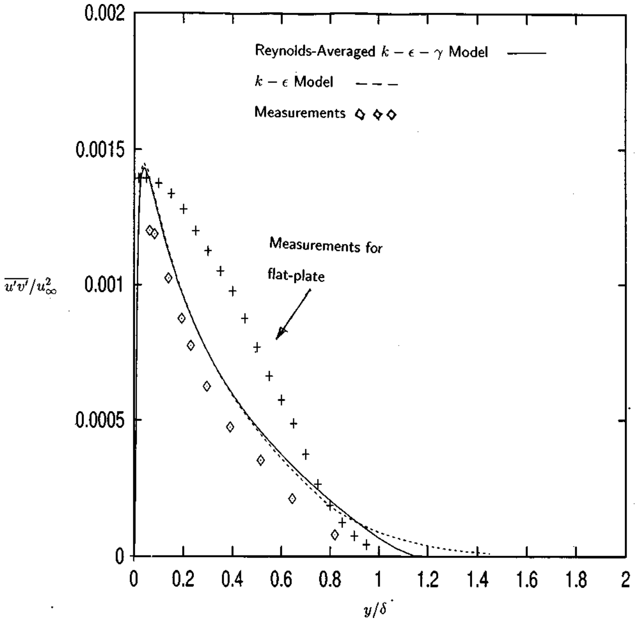

Fig. 3 Predicted Reynolds shear-stress profiles for thick axisymmetric boundary-layer ($Re_a=4800$, $\delta/a=4.59$) compared with the measurements

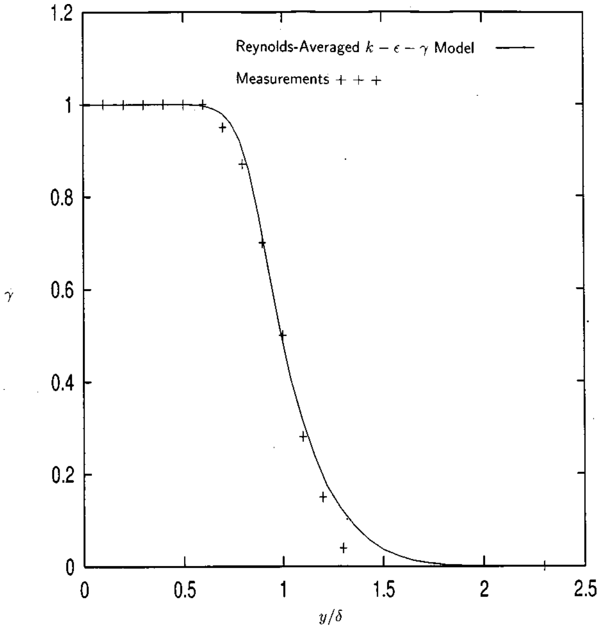

**Fig. 4 Predicted intermittency profile for thick axisymmetric boundary-layer ($Re_a=3200$, $\delta/a=7.57$) compared with the measurements**

for the case (b) compared to the case (a) because of larger value of the boundary-layer thickness in the latter. The models correctly predict this behavior (Figs. 3 and 5).

Tables 2, 3, and 4 compare the predicted skin friction coefficient and shape factor with the measurements by Lueptow et al. [19] for cases (a) and (b) and Willmarth et al. [20] for case (c) of thick axisymmetric boundary-layer. Here $Re_a=U_\infty a/v$ and $Re_{\theta,ax}=U_\infty\theta_{ax}/v$, where $U_\infty$ is the free-stream velocity, $a$ is the cylinder radius, $\theta_{ax}$ is the momentum thickness for axisymmetric flows (Willmarth et al. [20]), and $v$ is the kinematic viscosity. Underprediction in the maximum value of Reynolds shear stress profiles by the two models for the case (b) of thick axisymmetric boundary-layer (Fig. 5) leads to underprediction of the skin friction coefficient (Table 3). Results for other cases also show similar trends. The large underprediction in $C_f$ for thick axisymmetric boundary layers by different low-Re $k-\epsilon$ models has been discussed by Dewan and Arakeri [8]. They have shown that different low-Reynolds number modifications to the standard $k-\epsilon$ model are unsatisfactory in predicting the near-wall characteristics of such flows. They have shown that a small modification to the zero equation model of Cebeci [21,22] by replacing the standard expression of displacement thickness for planar flows by that for axisymmetric flows leads to superior predictions compared to that using different low-Re $k-\epsilon$ models.

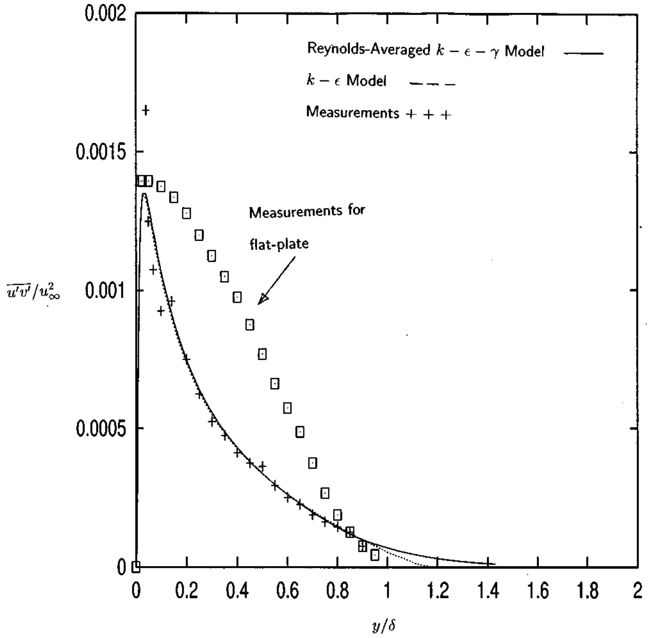

**Fig. 5 Predicted Reynolds shear-stress profiles for thick axisymmetric boundary-layer ($Re_a=3200$, $\delta/a=7.57$) compared with the measurements**

**Table 2 Predicted skin friction coefficient and shape factor for thick axisymmetric boundary-layer at $Re_a=4800$ and $\delta/a=4.59$ compared with the measurements**

| Quantity | Measurement | Low-Re $k-\epsilon-\gamma$ model | Low-Re $k-\epsilon$ model |
|---|---|---|---|
| $C_f\times 10^3$ | 4.61 | 3.84 | 3.80 |
| $H$ | - | 1.16 | 1.16 |

**Table 3 Predicted skin friction coefficient and shape factor for thick axisymmetric boundary-layer at $Re_a=3200$ and $\delta/a=7.57$ compared with the measurements**

| Quantity | Measurement | Low-Re $k-\epsilon-\gamma$ model | Low-Re $k-\epsilon$ model |
|---|---|---|---|
| $C_f\times 10^3$ | 4.80 | 3.88 | 3.85 |
| $H$ | - | 1.113 | 1.116 |

**Table 4 Predicted skin friction coefficient and shape factor for thick axisymmetric boundary-layer at $Re_a=736$ and $Re_{\theta,ax}=4350(\delta/a\simeq 40)$ compared with the measurements**

| Quantity | Measurement | Low-Re $k-\epsilon-\gamma$ model | Low-Re $k-\epsilon$ model |
|---|---|---|---|
| $C_f\times 10^3$ | 7.84 | 4.74 | 4.72 |
| $H$ | 1.115 | 1.045 | 1.047 |

Tables 2, 3, and 4 show that the $k-\epsilon-\gamma$ model with the effect of intermittency on dissipation does not lead to any improvement in the predicted skin friction coefficient compared to the low-Re $k-\epsilon$ model of Chien. The predicted mean and turbulent quantities by the two models are almost same. This is because the effect of entrainment on dissipation accounted for in the Reynolds averaged $k-\epsilon-\gamma$ model marginally affects the flow in the outer region only. In contrast, for most free-shear flows the Reynolds-averaged $k-\epsilon-\gamma$ significantly improves predictions compared to the standard $k-\epsilon$ model.

The results show that the present Reynolds-averaged $k-\epsilon-\gamma$ model accurately predicts the outer region of wall-bounded flows. The fact that this model is also appropriate for different free-shear flows shows that it could be a universal model for intermittency.

## 4 Concluding Remarks

We have shown that the $k-\epsilon-\gamma$ model based on the Reynolds averaged quantities is adequate to predict the intermittency of wall-bounded flows. Making near wall modifications to this model as used in any low Reynolds number version of the $k-\epsilon$ model results in a model which can be used to study the near wall and outer characteristics of the turbulent flat plate boundary-layer and thick axisymmetric boundary-layers. This model is appropriate to study intermittency of different free-shear flows and removes the weaknesses of the standard $k-\epsilon$ model for free-shear flows. Because of its simplicity the Reynolds-averaged $k-\epsilon-\gamma$ model could be extended, with small modifications, to the axisymmetric plume and plane plume, buoyancy driven free-shear flows. The flow in a plume is more complex than in nonbuoyant free-shear flows with buoyancy affecting mean and turbulent quantities.

## Acknowledgments

The first author thanks Council for Scientific and Industrial Research (CSIR), Government of India, for financial support through the award of Research Associateship at Department of Mechanical Engineering, Indian Institute of Science, Bangalore.

## References

[1] Byggstoyl, S., and Kollmann, W., 1981, ''Closure Model for Intermittent Turbulent Flows,'' Int. J. Heat Mass Transfer, **24**, No. 11, pp. 1811–1822.
[2] Byggstoyl, S., and Kollmann, W., 1986, ''A Closure Model for Conditioned Stress Equations and its Application to Turbulent Shear Flows,'' Phys. Fluids, **29**, pp. 1430–1443.
[3] Cho, J. R., and Chung, M. K., 1992, ''A $k-\epsilon-\gamma$ Equation Turbulence Model,'' J. Fluid Mech., **237**, pp. 301–322.
[4] Ahn, J. W., and Sung, H. J., 1995, ''Prediction of Two-Dimensional Momentumless Wake by $k-\epsilon-\gamma$ Model,'' AIAA J., **33**, No. 4, pp. 611–617.
[5] Dewan, A., Arakeri, J. H., and Srinivasan, J., 1997, ''A New Turbulence Model for the Axisymmetric Plume,'' Appl. Math. Model., **21**, pp. 709–719.
[6] Kalita, K., Dewan, A., and Dass, A. K., 2000, ''Computation of the Turbulent Plane Plume using $k-\epsilon-\overline{t'^2}-\gamma$ Model,'' Appl. Math. Model., **24**, No. 11, pp. 815–826.
[7] Wang, Y. Q., and Derksen, R. W., 1999, ''Prediction of Developing Turbulent Pipe Flow by a Modified $k-\epsilon-\gamma$ Model,'' AIAA J., **37**, No. 2, pp. 268–270.
[8] Dewan, A., and Arakeri, J. H., 1996, ''Comparison for Four Turbulence Models for Wall-Bounded Flows Affected by Transverse Curvature,'' AIAA J., **36**, No. 4, pp. 842–844.
[9] Patel, V. C., Rodi, W., and Scheuerer, G., 1985, ''Turbulence Models for Near-Wall and Low Reynolds Number Flows: A Review,'' AIAA J., **23**, No. 9, pp. 1308–1319.
[10] Libby, P. A., 1975, ''On the Prediction of Intermittent Turbulent Flows,'' J. Fluid Mech., **68**, pp. 273–295.
[11] Dopazo, C., 1977, ''On Conditioned Averages for Intermittent Turbulent Flows,'' J. Fluid Mech., **81**, pp. 433–439.
[12] Patankar, S. V., 1980, *Numerical Heat Transfer and Fluid Flow*, Hemisphere Publishing, New York.
[13] Anderson, D. A., Tannehill, J. C., and Pletcher, R. H., 1984, *Computational Fluid Mechanics and Heat Transfer*, Hemisphere, New York.
[14] White, F. M., 1991, *Viscous Fluid Flow*, McGraw-Hill, NY.
[15] Dewan, A., 1996, ''Turbulence Modelling of Thick Axisymmetric Wall-Bounded Flows and Axisymmetric Plume,'' Ph.D. thesis, Department of Mechanical Engineering, Indian Institute of Science, Bangalore, India.
[16] Klebanoff, P. S., 1955, ''Characteristics of Turbulence in a Boundary Layer with Zero Pressure Gradient,'' NACA Report 1247.
[17] Cazalbou, J. B., and Bradshaw, P., 1993, ''Turbulent Transport in Wall-Bounded Flows. Evaluation of Model Coefficients Using Direct Simulation,'' Phys. Fluids, **5**, No. 12, pp. 3233–3239.
[18] Lueptow, R. M., and Haritonidis, J. H., 1987, ''The Structure of the Turbulent Boundary Layer on a Cylinder in Axial Flow,'' Phys. Fluids, **30**, No. 10, pp. 2993–3005.
[19] Lueptow, R. M., Leehey, P., and Stellinger, T., 1985, ''The Thick, Turbulent Boundary Layer on a Cylinder: Mean and Fluctuating Velocities,'' Phys. Fluids, **28**, No. 12, pp. 3495–3505.
[20] Willmarth, W. W., Winkel, R. E., Sharma, L. K., and Bogar, T. J., 1976, ''Axially Symmetric Turbulent Boundary Layers on Cylinders: Mean Velocity Profiles and Wall Pressure Fluctuations,'' J. Fluid Mech., **76**, pp. 35–64.
[21] Cebeci, T., 1970, ''Laminar and Turbulent Incompressible Boundary-Layers on Slender Bodies of Revolution in Axial Flow,'' ASME J. Basic Eng., **92**, No. 3, pp. 545–554.
[22] Cebeci, T., 1973, ''Eddy Viscosity Distribution in Thick Axisymmetric Turbulent Boundary Layer,'' ASME J. Fluids Eng., **95**, No. 2, pp. 319–326.

**N. Kim**
Research Associate

**D. L. Rhode**
Professor
e-mail: drhode@mengr.tamu.edu

Department of Mechanical Engineering,
Texas A&M University,
College Station, TX 77843-3123

# Streamwise Curvature Effect on the Incompressible Turbulent Mean Velocity Over Curved Surfaces

*A curvature law of the wall, which determines the mean velocity profile, is analytically derived for near-wall turbulent flows to include strong curved-channel wall curvature effects through a perturbation analysis. The new law allows improved analysis of such flows, and it provides the basis for improved wall function boundary conditions for their computation (CFD), even for strong curvature cases. The improved law is based on the algebraic eddy viscosity and curvature-corrected mixing length concepts, the latter of which is a linear function of the gradient Richardson number. To include the complete Richardson number effects, the local streamline curvature effects in the gradient Richardson number are kept. To overcome the mathematical difficulty of keeping all of these local streamline curvature terms, an innovative nonconstant-parameter perturbation solution technique is successfully applied.* [S0098-2202(00)00903-2]

## Introduction

Turbulent flows along curved walls with finite curvature can be classified as complex shear flows due to the appearance of an extra strain rate introduced by the wall curvature. The effect of convex wall curvature on the near-wall turbulent flow is to suppress the outward diffusion of turbulent kinetic energy from the wall, whereas the opposite is true for concave wall curvature (Bradshaw [1,2], So and Mellor [3–5], So [6,7], Meroney and Bradshaw [8], Hunt and Joubert [9], Barlow and Johnston [10]). The common experimental observation made is that wall curvature reduces the distance from the wall over which the classical log-law for a flat plate is accurate. It was also found that the fractional changes in the skin friction coefficient on a curved wall are an order of magnitude greater than the ratio of boundary layer thickness $\delta$ to the radius of curvature of the wall $R$. Accordingly, the near-wall dimensionless mean velocity profile on curved walls deviates from that on flat walls.

There exist two basically different flow situations near a curved wall: (a) the curved channel case with one near-wall velocity and shear stress in a plane parallel to the wall, and (b) the swirling-axial case with an additional velocity and stress component which act in the curvature axis (i.e., axial) direction. Not surprisingly, the local flow details are substantially different for these cases. For example, for the swirling-axial case the near-wall vector resultant velocity is not exactly in the opposite direction to that of the corresponding resultant shear stress, whereas for the curved channel case they are generally considered to be exactly opposite in direction. Furthermore, there is an extremely wide range of the $\tau_{rx}/\tau_{r\theta}$ ratio that can occur for the swirling-axial cases, and thus certain analysis assumptions are typically needed there regarding an anisotropic mixing length, stress-strain rate relationships, $y^+$ and $w^*$ definitions, etc. Because of the different near-wall physics a log law specifically for curved channel flows, as well as one specifically for swirling-axial flows, is needed.

As a result of the analogy between flows with curved streamlines and buoyancy-induced flows, Bradshaw [1,2] proposed a correction to the mixing length distribution as a linear function of the gradient Richardson number $\mathrm{R_i}$ [i.e., $l_c=\kappa y(1-\beta \mathrm{R_i})$] to account for the streamline curvature effect on the turbulence. Different mixing length corrections were derived by So and Mellor [3] and So [7] as nonlinear functions of the $\mathrm{R_i}$ number. The $\mathrm{R_i}$ number used for curved flows is a dimensionless parameter representing a measure of the production of turbulence by centrifugal forces to that by shear effects. Meroney and Bradshaw [8] developed a curvature wall law using a mixing length correction based on a momentum integral equation assuming that the velocity profile in the inner layer is proportional to $y^{1/5}$. Also, So [6] developed a curvature wall law using a similar mixing length correction. In their derivation, however, approximate forms of the $\mathrm{R_i}$ number were used to obtain closed analytic solutions avoiding mathematical complexity.

Wilcox and Chambers [11] proposed a curvature wall law from a singular perturbation after simplifying the $k-\omega$ turbulence model according to the boundary layer approximation and adding extra curvature terms. In addition, Galperin and Mellor [12] used an algebraic Reynolds stress model to obtain a curvature law assuming an equilibrium, constant-flux layer over curved surfaces.

The objective of the present investigation is the development and analysis of an improved curvature law for the strongly curved (convex as well as concave) channel case. This improved law features the incorporation of the complete $\mathrm{R_i}$ number expression on a local, rather than an averaged, basis with the goal of obtaining an increased range of accurate applicability.

## Development

Following the linear mixing correction suggested by Bradshaw [1,2], the law of the wall on curved surfaces can be obtained by integrating the shear stress in the near-wall region using

$$\tau_{r\theta}=\rho l_c^2\left(\frac{dw}{dr}-\frac{w}{r}\right)^2 \tag{1}$$

with

$$l_c=\kappa y(1-\beta \mathrm{R_i}) \tag{2}$$

where the empirical constant $\beta$ was originally proposed to have a value between 4 and 5 for a concave wall, and between 7 and 8 for a convex wall. The particular form of the gradient Richardson number $\mathrm{R_i}$ used here is suggested by So [13] as

---

Contributed by the Fluids Engineering Division for publication in the JOURNAL OF FLUIDS ENGINEERING. Manuscript received by the Fluids Engineering Division March 23, 1999; revised manuscript received February 14, 2000. Associate Technical Editor: D. Williams.

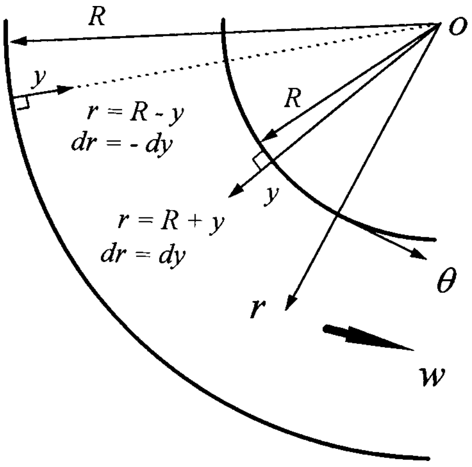

**Fig. 1 Definition of coordinates for the concave and convex surfaces**

$$\mathrm{R_i}=\frac{2\,\dfrac{w}{R\pm y}\left(\dfrac{dw}{dr}+\dfrac{w}{R\pm y}\right)}{\left(\dfrac{dw}{dr}-\dfrac{w}{R\pm y}\right)^2} \tag{3}$$

Note that the previous use of the gradient Richardson number in wall law derivations involved only approximations to the above definition, i.e., $\mathrm{R_i}=2(w/R)/(dw/dr)$ by Meroney and Bradshaw [8] and $\mathrm{R_i}=8.33(y/R)$ by So [6]. Substituting Eq. (3) into the mixing length correction and combining it with the shear stress, one obtains a dimensionless, nonlinear, ordinary differential equation as

$$f^3-\{1+(3+2\beta)g\}f^2+(2g+3g^2)f-\{g^2-(2\beta-1)g^3\}=0 \tag{4}$$

where the definitions of $f=\kappa y^+(dw^+/dy^+)$ and $g=\kappa y^+w^+/(y^+\pm R^+)$ are used with the dimensionless variables defined as $w^+=w/w^*$, $y^+=w^*y/\nu$, $R^+=w^*R/\nu$ and the wall shear velocity $w^*=(\tau/\rho)^{1/2}$. The negative sign for $R^+$ and $dr=-dy$ are used for concave wall curvature, and vice versa for convex curvature (see Fig. 1). It is implied in the derivation of Eq. (4) that a local equilibrium layer exists in the near-wall region and that the shear stress is constant in the normal direction within the layer (So and Mellor [5], Barlow and Johnston [10], Gibson [14], Galperin and Mellor [12]).

Two important facts arise regarding the functions *f* and *g*. First, the classical (i.e., non-curved) law of the wall for $w^+$ is obtainable when *f* equals unity. This occurs as the function *g* (which contains the curvature effects) goes to zero, or equivalently as $R^+$ approaches infinity for the case of a flat plate. Second, the function *g* is much smaller than *f* in order of magnitude for the range of $y^+$ near the wall over which the law of the wall applies, even with strong curvature ($R^+\approx 10{,}000$). This is equivalent to the statement that the gradient Richardson number is much smaller than unity in the near-wall region (So and Mellor [4], Hunt and Joubert [9]).

Because Eq. (4) has no exact analytical solution, an innovative perturbation technique similar to that of Kim and Rhode [15] was applied taking the function *g* as the nonconstant perturbation parameter based on the aforementioned observation concerning the functions *f* and *g*. The first step is to consider the nonlinear differential equation as a nonlinear algebraic equation. Taking the curvature function *g* as the perturbation parameter denoted as $\varepsilon$, one obtains a nonlinear algebraic equation for *f* as

$$f^3-f^2-\{(3+2\beta)f^2-2\,f\}\varepsilon+(3f-1\,)\varepsilon^2+(2\beta-1)\varepsilon^3=0 \tag{5}$$

Next, the function *f* and the mean velocity $w^+$ are expanded in terms of $\varepsilon$ as

$$f=f_0+\varepsilon f_1+\varepsilon^2 f_2+O(\varepsilon^3)\quad\text{and} \tag{6}$$

$$w^+=w_0^++\varepsilon w_1^++\varepsilon^2 w_2^++O(\varepsilon^3) \tag{7}$$

from which one obtains the relationship between $f_i$ and $w_i^+$ as

$$\sum_{i=0}^{\infty}\varepsilon^i f_i=\kappa y^+\sum_{i=0}^{\infty}\frac{d(\varepsilon^i w_i^+)}{dy^+} \tag{8}$$

Unlike conventional perturbation approaches [16], where the perturbation parameter is usually chosen as the dimensionless group of constants in the governing equation, the present formulation uses a nonconstant perturbation parameter which includes both the dependent and independent variables in its definition. This is why the $\varepsilon^i$ term appears in the derivative on the right-hand side of Eq. (8). Substituting Eq. (6) into Eq. (5) and equating the terms containing $\varepsilon^i$ on both sides gives the algebraic relationship among the $f_i$ as

$$\varepsilon^0{:}\,f_0^3-f_0^2=0$$

$$\varepsilon^1{:}\,3f_0^2f_1-(3+2\beta)f_0^2-2\,f_0f_1+2\,f_0=0$$

$$\varepsilon^2{:}\,3f_0^2f_2-2\,f_0f_2+3f_0f_1^2-2(3+2\beta)f_0f_1-f_1^2+2\,f_1+3f_0-1=0$$

which give the solutions as $f_0=1$, $f_1=1+2\beta$, and $f_2=4\beta$ and etc. Note that the zeroth-order solution corresponds to the classical law of the wall while the higher-order solutions of $f_i$ account for the curvature effect, and thus are functions of $\beta$. Through a careful term-by-term examination of Eq. (8), one finds the relationship between $f_i$ and $w_i^+$ as

$$f_0=\kappa y^+\frac{dw_0^+}{dy^+}+\kappa y^+\frac{w_1^+}{y^+\pm R^+}f_0 \tag{9}$$

$$f_1=\kappa w_1^++\kappa y^+\frac{w_1^+}{y^+\pm R^+}f_1+2\kappa y^+\frac{w_2^+}{y^+\pm R^+}f_0 \tag{10}$$

$$f_2=2\kappa w_2^++\kappa y^+\frac{w_1^+}{y^+\pm R^+}f_2+2\kappa y^+\frac{w_2^+}{y^+\pm R^+}f_1 \tag{11}$$

A careful examination of $w_2^+/w_1^+$, which is obtainable by combining Eqs. (10) and (11), revealed that the ratio is always smaller than 1.1 for both convex and concave curvature when $R^+$ is larger than 10,000. Therefore one can conclude that the second- and higher-order $w_i^+$ solutions are reasonably negligible in the practical application range of $y^+$ if $R^+$ is not much smaller than 10,000. Accordingly, by solving the algebraic equation [Eq. (10)] for $w_1^+$ and the ordinary differential equation [Eq. (9)] for $w_0^+$, one obtains the approximate solution for $w^+$ as

$$\left\{1-\frac{f_1y^+}{(1+f_1)y^+\pm R^+}\right\}w^+=\frac{1}{\kappa}\ln\frac{y^+}{\alpha}-\frac{1}{\kappa}\frac{f_1}{1+f_1}\ln\left\{\frac{(1+f_1)y^+\pm R^+}{(1+f_1)\alpha\pm R^+}\right\}+\alpha\left\{\frac{\alpha\pm R^+}{(1+f_1)\alpha\pm R^+}\right\} \tag{12}$$

where $\alpha$, which is chosen (as for a noncurved surface) approximately as 10.5, is the $y^+$ location where the wall law profile and the linear sublayer meet, and the curvature term $f_1$ has been evaluated as $1+2\beta$. The + and − sign notation corresponds to convex and concave curvature, respectively. The classical law of the wall is recovered when $R^+$ approaches infinity in Eq. (12), which corresponds to a flat plate. Note that the effect of surface roughness is not included, as a hydrodynamically smooth surface has been assumed. It is expected that there exists little correlation between surface roughness and wall curvature, thus a conventional technique to account for the surface roughness on a flat plate can be applied. Also, a simplication to Eq. (12) can be made without loss of accuracy by neglecting the second term on the right-hand side because the magnitude of the first term on the right-hand side is much greater than that of the second term in most of the practical CFD $y^+$ range. For example, the magnitude of the second term is just 1 percent of that of the first term at $y^+=100$ when $R^+$ is 30,000.

## Discussion

It has been observed that pairs of longitudinal roll cells, which are similar to Taylor-Goertler vortices, often exist along concave walls (Meroney and Bradshaw [8], So and Mellor [3]) resulting in spanwise variations of flow structure, whereas the convex wall curvature does not create such roll cells. Because of the limitation of two-dimensionality of the present analysis, the present law is unable to show the three-dimensional spanwise variation of the mean turbulence structure. Instead, it is assumed in the present study that the mixing length correction effectively represents the spanwise-averaged, two-dimensional flow changes due to concave curvature.

Because of the nature of perturbation analysis, the present solution, i.e., Eq. (12), deviates (underpredicts) from a more accurate numerical solution (from the fourth-order Runge-Kutta method) of Eq. (4) as the local value of function $g$ increases (i.e., $R^+$ decreases and/or $y^+$ increases). However, a careful examination validated the use of the present solution with accuracy in a practical $y^+$ range even for strong curvature cases. For example, the relative error from the numerical solution is less than 3 percent for both concave and convex cases when $R^+$ is 10,000 and $y^+$ is 200.

The present curvature law of the wall is compared with the measurements obtained with different curvature and other previous laws (Meroney and Bradshaw [8], So [6], Wilcox and Chambers [11]). In the comparison the following constants were consistently applied: $\alpha=10.5$, $\kappa=0.415$. Thus $w^+=2.43\ln y^++4.9$ was obtained for the classical log-law profile. One should be reminded that the constants are not universally fixed, but vary somewhat according to each individual's preference. Thus a different combination of the constants may be applied. In the comparison, $\beta=4$ is used for both concave and convex curvature for the present law, whereas different values are used for the other laws as given in the literature by their developers.

In Fig. 2 the mean velocity profiles are compared for a concave wall where $R^+$ is approximately 35,000. The symbols represent the measured profiles at different streamwise locations by So and Mellor [5]. By comparison with measurements, it is shown that the classical log-law is limited to a small range of $y^+$ only out to approximately 50. The curves of the present law and Meroney and Bradshaw [8] show very good agreement with measurements, whereas the curve for the classical log-law largely over-estimates as $y^+$ exceeds about 100. A similar trend of the mean velocity profiles and reduced log-law region was observed near a concave wall by Barlow and Johnston [10] as shown in Fig. 3, where $R^+$ is approximately 10,100. It is found here again that the present curvature law of the wall agrees with measurements increasingly well as one proceeds in the flow direction. Note that the deviation from the classical log-law profile begins at an even lower $y^+$ value than was found in Fig. 2 due to the increased curvature effect. However, one should be reminded that the wall law values for concave curvature were shown in a spanwise averaged sense as discussed earlier. A maximum value of $w^+$, followed by a decrease in its value, always occurs in the outer layer for all compared curvature laws of the wall, whereas this does not appear in the measurements. One of the possible reasons for this may be overestimation of the mixing length correction in the outer layer, especially for the empirical constant $\beta$.

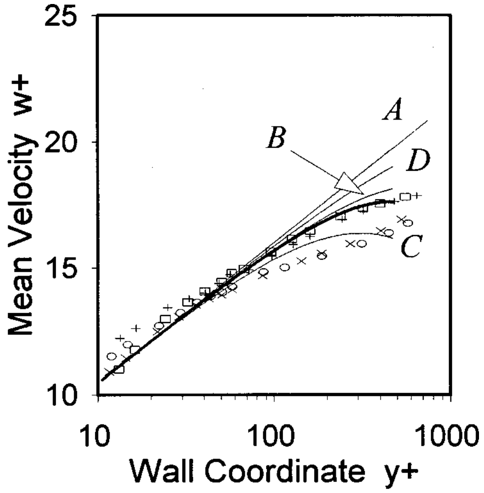

**Fig. 2 Comparison of the present curvature law of the wall (——) with measurements (So and Mellor [5]) along a concave wall ($R^+=35{,}000$); [(—*A*—): the classical log-law, (—*B*—): Meroney and Bradshaw [8], (—*C*—): Wilcox and Chambers [11], and (—*D*—): So [6]]; [(○○○): $x=159.49$ cm, (×××): $x=166.95$ cm; (+++): $x=174.47$ cm; (□□□): $x=182.37$ cm].**

Figure 4 shows the comparison of the mean velocity profiles on a convex wall with strong curvature where $R^+$ is approximately 13,500 (Galperin and Mellor [12]). It is shown that the deviation from the log law is opposite to that of the concave case. The present law is shown to be generally in closest agreement with measurements. A similar result can be found in Fig. 5 where the convex $R^+$ is approximately 17,400 (So and Mellor [4]). Here again one finds a very narrow $y^+$ range where the classical log-law is realistic. Thus it is clear that the currently common use of the classical log-law as a wall function form of a wall boundary condition in the CFD computation of flows on curved walls

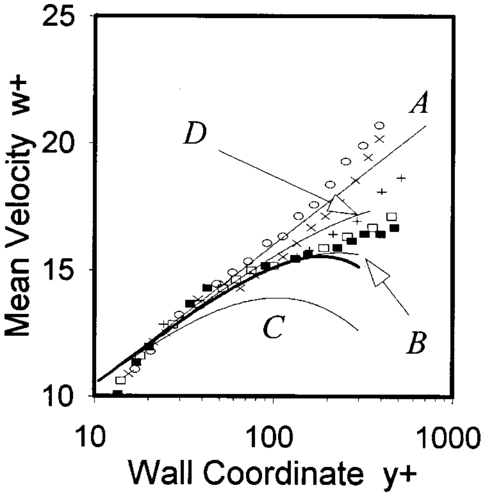

**Fig. 3 Comparison of the present curvature law of the wall (——) with measurements (Barlow and Johnston [10]) along a concave wall ($R^+=10{,}100$); [(—*A*—): the classical log-law, (—*B*—): Meroney and Bradshaw [8], (—*C*—): Wilcox and Chambers [11], and (—*D*—): So [6]]; [(○○○): flat; (×××): $\theta=15$ deg; (+++): $\theta=30$ deg; (□□□): $\theta=60$ deg; (■■■): $\theta=75$ deg].**

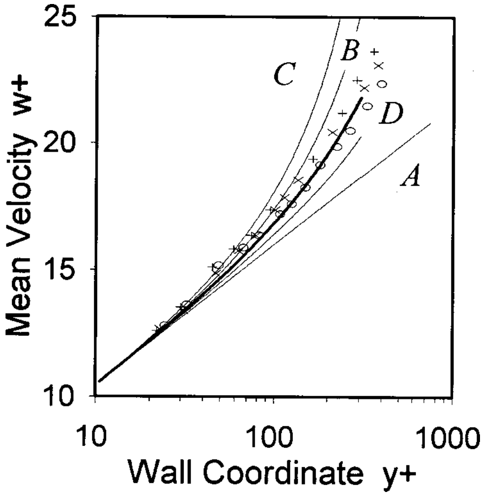

**Fig. 4 Comparison of the present curvature law of the wall (——) with measurements along a convex wall ($R^+=13{,}500$); [(—*A*—): the classical log-law, (—*B*—): Meroney and Bradshaw [8], (—*C*—): Wilcox and Chambers [11], and (—*D*—): So [6]]; [measurements were adapted from Gibson [14] and Galperin and Mellor [12]]; [(○○○): $x/\delta_0=9.0$; (×××): $x/\delta_0=14.3$; (+++): $x/\delta_0=21.7$].**

should be avoided. The deviation of the mean velocity from the classical log-law profile is primarily due to the term in the left-hand-side parenthesis, which is the first-order perturbed solution in the present law.

Note that the use of the previously recommended $\beta$ value of 7–8 for convex wall with the present wall law does not give good agreement with measurements. However, a $\beta$ value of 4, which is the same value as the one used for the concave case, was found to result in better agreement. It is well coincident with the result derived by So and Mellor [3] through an analytical and experimental correlation. Discussions of the different choices for $\beta$ values can be found in Galperin and Mellor [12], So [7,13], and Adams and Johnston [17].

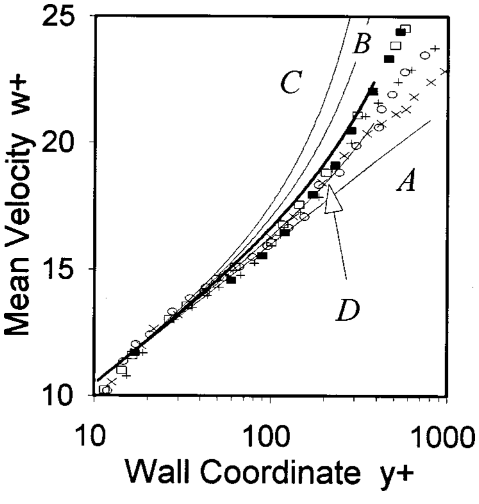

**Fig. 5 Comparison of the present curvature law of the wall (——) with measurements (So and Mellor [4]) along a convex wall ($R^+=17{,}400$); [(—*A*—): the classical log-law, (—*B*—): Meroney and Bradshaw [8], (—*C*—): Wilcox and Chambers [11], and (—*D*—): So [6]]; [(○○○): $x=61.0$ cm; (×××): $x=138.4$ cm; (+++): $x=149.9$ cm; (□□□): $x=170.2$ cm; (■■■): $x=180.3$ cm].**

In the comparisons with measurements (Figs. 2–5), it has been shown that the profiles of the laws of the wall are not in good agreement with measurements for $y^+$ lower than 20. One possible reason for this disagreement seems to be the existence of the buffer layer in the region where the present equilibrium layer assumption is not valid. Also note that for all measured cases the mean velocity profiles vary at different streamwise locations. This variation occurs due to the streamwise change of wall shear stress, thus changing $w^*$ and $R^+$ as the wall curvature effect develops (Barlow and Johnston [10]). However, all of the curvature laws were plotted using the fully developed $R^+$ value as the reference curvature parameter. Therefore, it is possible to obtain a slightly different comparison of the mean velocity profiles when the changes of $R^+$ are considered along the downstream direction.

## Summary

In contrast to the two previous mixing-length derivations of a curvature law of the wall, which used only approximated (i.e., incomplete $\mathrm{R_i}$ number) corrections to the mixing length, the present derivation keeps all of the streamline curvature details in the $\mathrm{R_i}$ number definition on a local, rather than on an averaged basis. In order to incorporate the local curvature effect and handle the resulting increase of mathematical complexity, an innovative nonconstant-parameter perturbation analysis similar to Kim and Rhode [15] was applied. Specific findings are:

1 The new curvature law is found to give good agreement with measurements for all four test cases.

2 It is now more clear that the complete-$\mathrm{R_i}$ number mixing length curvature correction well describes the effect of wall curvature on the turbulence structure in the near-wall region.

3 For best agreement with the measurements considered, it appears that the empirical constant $\beta$ in the mixing length correction is around 4 for both convex and concave cases. This finding agrees with the previous results obtained by So and Mellor [3]. Because of its empirical nature, however, the universality of the $\beta$ value is not clear, and needs more investigation.

## Nomenclature

$k$ = turbulent kinetic energy
$l_c$ = corrected turbulent mixing length
$r$ = coordinate in radial direction
$R$ = radius of wall curvature
$\mathrm{R_i}$ = gradient Richardson number
$w$ = velocity along curved wall
$w^*$ = wall shear velocity $[=(\tau/\rho)^{1/2}]$
$x$ = coordinate along curved wall
$y$ = coordinate normal to curved wall
$\alpha$ = $y^+$ where the law of the wall region begins
$\beta$ = empirical constant
$\delta$ = turbulent boundary layer thickness
$\varepsilon$ = perturbation parameter
$\kappa$ = von Karman constant
$\nu$ = kinematic viscosity of fluid
$\theta$ = coordinate in circumferential direction
$\rho$ = density of fluid
$\tau$ = shear stress
$\omega$ = turbulent dissipation rate

### Superscript

$+$ = dimensionless wall quantity

## References

[1] Bradshaw, P., 1969, ''The Analogy Between Streamline Curvature and Buoyancy in Turbulent Shear Flow,'' J. Fluid Mech., **36**, pp. 177–191.
[2] Bradshaw, P., 1973, ''Effects of Streamline Curvature on Turbulent Flows,'' AGARDograph No. 169.
[3] So, R. M. C., and Mellor, G. L., 1972, ''An Experimental Investigation of Turbulent Boundary Layers Along Curved Surfaces,'' NASA CR-1940.

[4] So, R. M. C., and Mellor, G. L., 1973, ''Experiment on Convex Curvature Effects in Turbulent Boundary Layers,'' J. Fluid Mech., **60**, pp. 43–62.

[5] So, R. M. C., and Mellor, G. L., 1975, ''Experiment on Turbulent Boundary Layers on a Concave Wall,'' Aeronaut. Q., **XXVI**, pp. 25–40.

[6] So, R. M. C., 1975, ''Effects of Streamline Curvature on the Law of the Wall,'' Proc. 12th Annual Meeting, Society of Engineering Science, The University of Texas at Austin, Texas, pp. 787–796.

[7] So, R. M. C., 1975, ''A Turbulence Velocity Scale For Curved Shear Flows,'' J. Fluid Mech., **70**, pp. 37–57.

[8] Meroney, R. N., and Bradshaw, P., 1975, ''Turbulent Boundary-Layer Growth over a Longitudinally Curved Surface,'' AIAA J., **13**, pp. 1448–1453.

[9] Hunt, I. A., and Joubert, P. N., 1979, ''Effects of Small Streamline Curvature on Turbulent Duct Flow,'' J. Fluid Mech., **91**, pp. 633–659.

[10] Barlow, R. S., and Johnston, J. P., 1988, ''Structure of a Turbulent Boundary Layer on a Concave Surface,'' J. Fluid Mech., **191**, pp. 137–176.

[11] Wilcox, D. C., and Chambers, T. L., 1977, ''Streamline Curvature Effects on Turbulent Boundary Layers,'' AIAA J., **15**, pp. 574–580.

[12] Galperin, B., and Mellor, G. L., 1991, ''The Effects of Streamline Curvature and Spanwise Rotation on Near-Surface, Turbulent Boundary Layers,'' ZAMP, **42**, pp. 565–583.

[13] So, R. M. C., 1977, ''Turbulence Velocity Scales for Swirling Flows,'' *Turbulence in Internal Flows*, Murthy, S. N. B., ed., Hemisphere.

[14] Gibson, M. M., 1988, ''Effects of Surface Curvature on the Law of the Wall,'' *Near-Wall Turbulence*, Kline, S. J., and Afgan, N. H., eds., Hemisphere.

[15] Kim, N., and Rhode, D. L., 1999, ''Swirling Streamline-Curvature Law of The Wall From a Novel Perturbation Analysis,'' Numer. Heat Transfer, Part B, **36**, pp. 331–350.

[16] Aziz, A., 1984, *Perturbation Methods in Heat Transfer*, Hemisphere.

[17] Adams, E. W., and Johnston, J. P., 1984, ''A Mixing-Length Model for the Prediction of Convex Curvature Effects on Turbulent Boundary Layers,'' ASME J. Fluids Eng., **106**, pp. 142–148.

# A Simultaneous Variable Solution Procedure for Laminar and Turbulent Flows in Curved Channels and Bends

**Jianrong Wang**[1]
Graduate Research Assistant

**Siamack A. Shirazi**
Associate Professor

Department of Mechanical Engineering,
The University of Tulsa,
Tulsa, OK 74104

*Direct Numerical Simulation of turbulent flow requires accurate numerical techniques for solving the Navier-Stokes equations. Therefore, the Navier-Stokes equations in general orthogonal and nonorthogonal coordinates were employed and a simultaneous variable solution method was extended to solve these general governing equations. The present numerical method can be used to accurately predict both laminar and turbulent flow in various curved channels and bends. To demonstrate the capability of this numerical method and to verify the method, the time-averaged Navier-Stokes equations were employed and several turbulence models were also implemented into the numerical solution procedure to predict flows with strong streamline curvature effects. The results from the present numerical solution procedure were compared with available experimental data for a 90 deg bend. All of the turbulence models implemented resulted in predicted velocity profiles which were in agreement with the trends of experimental data. This indicates that the solution method is a viable numerical method for calculating complex flows.* [S0098-2202(00)01803-4]

## Introduction

Advances in computing power of supercomputers and computational fluid dynamics will soon allow direct numerical solution of complex turbulent flows in complex geometries. However, direct numerical simulation of turbulent flow requires accurate numerical techniques for solving the Navier-Stokes equations. The simultaneous variable solution method proposed by Bentson and Vradis [1] is an attractive method for solving the Navier-Stokes equations because of its numerical accuracy, efficiency and robustness. The method proposed by Bentson and Vradis was later extended to two-dimensional laminar flow in curved boundaries (Vradis et al. [2]) and to three-dimensional flow in the Cartesian coordinates by Prado [3]. However, the applicability of the method to highly curved geometries was not addressed by the previous investigators. Thus, the simultaneous variable method for solving the Navier-Stokes proposed by Bentson and Vradis [1] has been extended and generalized to the Navier-Stokes equations in general curvilinear coordinates. Additionally, to make the solution procedure useful and practical for its use in current engineering applications, the method was extended to turbulent flow computations by implementing several turbulence models. Turbulence models implemented include modified versions of the mixing-length model developed by Baldwin and Lomax [4] and the low-Reynolds-number two-equation $k$-$\tau$ model developed by Speziale et al. [5]. In addition to numerical difficulties encountered in turbulent flow computations, turbulent flow in curved channels is dominated by strong streamline curvature effects. These effects considerably change the behavior of the turbulent kinetic energy and the dissipation rate (Cheng and Farokhi [6]). Thus, two different methods were used to modify the $k$-$\tau$ model for strong streamline curvature effects. One method was to include the Richardson flux number in the turbulent time scale, $\tau$, transport equation and the other method was to directly modify the eddy viscosity expression. The results with and without modifications to the $k$-$\tau$ model as well as other turbulence models used are evaluated by comparing velocity profiles and turbulent kinetic energy predictions with experimental data for a 90 deg bend. The predictions from the standard $k$-$\varepsilon$ model in a commercially available CFD code were also compared with present results and with experimental data.

## Development of the Numerical Solution Procedure

**1 Vradis and Bentson Simultaneous Variable Solution Method.** Vradis et al. [2] developed a simultaneous variable solution method for solving laminar flow in two-dimensional straight and expanding channels using the orthogonal and nonorthogonal curvilinear coordinate systems. But, this method is not applicable to highly curved channels and bends as it is discussed in this section.

In the present work, the simultaneous variable solution method was extended to turbulent flow computations by using the time-averaged continuity and momentum equations for a steady, incompressible, Newtonian, and two-dimensional flow. Assuming that the Reynolds stresses are linearly proportional to the strain rate tensor by a turbulent or a scalar eddy viscosity, the equations used are

$$\frac{\partial u}{\partial x}+\frac{\partial v}{\partial y}=0 \tag{1}$$

$$u\frac{\partial u}{\partial x}+v\frac{\partial u}{\partial y}=-\frac{1}{\rho}\frac{\partial p}{\partial x}+\frac{\partial}{\partial x}\left\{2\nu_e\frac{\partial u}{\partial x}\right\}+\frac{\partial}{\partial y}\left\{\nu_e\left(\frac{\partial u}{\partial y}+\frac{\partial v}{\partial x}\right)\right\} \tag{2}$$

$$u\frac{\partial v}{\partial x}+v\frac{\partial v}{\partial y}=-\frac{1}{\rho}\frac{\partial p}{\partial y}+\frac{\partial}{\partial x}\left\{\nu_e\left(\frac{\partial u}{\partial x}+\frac{\partial v}{\partial x}\right)\right\}+\frac{\partial}{\partial y}\left\{2\nu_e\frac{\partial v}{\partial y}\right\} \tag{3}$$

where $u$, $v$, and $p$ are the time-averaged velocity components in the Cartesian $x$ and $y$ directions and time-averaged pressure, respectively. The effective viscosity $\nu_e$ is defined as

$$\nu_e=\nu+\nu_\tau \tag{4}$$

---

[1] Currently with Baker Atlas, Houston, Texas.

Contributed by the Fluids Engineering Division for Publication in the JOURNAL OF FLUIDS ENGINEERING. Manuscript received by the Fluids Engineering Division March 18, 1998; revised manuscript received February 7, 2000. Associate Technical Editor: G. Erlebacher.

where $\nu$ is the fluid kinematic viscosity, $\nu_\tau$ is turbulent eddy viscosity which is calculated from an appropriate turbulence model discussed in the Turbulence Modeling section.

The above equations were transformed into nonorthogonal curvilinear coordinates by

$$\frac{\partial}{\partial x}=\left(y_\eta \frac{\partial}{\partial \xi}-y_\xi \frac{\partial}{\partial \eta}\right)\frac{1}{J} \tag{5a}$$

$$\frac{\partial}{\partial y}=\left(-x_\eta \frac{\partial}{\partial \xi}+x_\xi \frac{\partial}{\partial \eta}\right)\frac{1}{J} \tag{5b}$$

where $\eta$ and $\xi$ are the coordinates in the transformed computational space, and $J$ is the Jacobian of the transformation defined by $J=x_\xi y_\eta-\chi_\eta y_\xi$.

Using the staggered grid method, Eq. (1) was discretized at the center of the cell where pressure is defined. Equations (2) and (3) were discretized at the $u$ velocity location and $v$ velocity location, respectively. The convective terms in the transformed equations were discretized by the second-order accurate upwind scheme. The diffusion terms were discretized by the second-order centered difference scheme. The boundary conditions for velocities and pressure were treated in a similar manner as Vradis et al. [2]; the boundary condition for pressure used a modified equation (Eq. (6)) which includes the effective viscosity for turbulent flows

$$\begin{aligned}\frac{J}{\rho}\frac{\partial p}{\partial \eta}=&x_\eta y_\xi \frac{\partial}{\partial \eta}\left(\nu_e\frac{y_\xi}{J}\frac{\partial u}{\partial \eta}\right)+x_\eta x_\xi \frac{\partial}{\partial \eta}\left(\nu_e\frac{x_\xi}{J}\frac{\partial u}{\partial \eta}\right)\\&+y_\eta x_\xi \frac{\partial}{\partial \eta}\left(\nu_e\frac{x_\xi}{J}\frac{\partial v}{\partial \eta}\right)+y_\eta y_\xi \frac{\partial}{\partial \eta}\left(\nu_e\frac{y_\xi}{J}\frac{\partial v}{\partial \eta}\right)\\&-\left(y_\eta \frac{\partial v}{\partial \eta}+x_\eta \frac{\partial u}{\partial \eta}\right)\left(y_\eta\frac{\partial}{\partial \xi}\left(\nu_e\frac{y_\xi}{J}\right)+x_\eta \frac{\partial}{\partial \xi}\left(\nu_e\frac{x_\xi}{J}\right)\right)\end{aligned} \tag{6}$$

The resulting system of algebraic finite-difference equations are nonlinear due to the convective terms. The equations were linearized by freezing the coefficients of convective terms to the previous iteration level. Finally, a system of linear equations are formed with a block tridiagonal coefficient matrix of 3×3 elements

$$\begin{vmatrix} B_1 & C_1 & & & \\ A_2 & B_2 & C_2 & & \\ & . & . & . & \\ & & & A_n & B_n \end{vmatrix}\begin{vmatrix} W_1 \\ W_2 \\ . \\ W_n \end{vmatrix}=\begin{vmatrix} E_1 \\ E_2 \\ . \\ E_n \end{vmatrix} \tag{7}$$

where, $W_i=[u_{ij},v_{ij},p_{ij}]^T$, $A_i,B_i,C_i$ are 3×3 coefficient matrices. In the above 3×3 matrices, the first three rows, that is, $a_{1j}$, $b_{1j}$, and $c_{1j}$, result from discretizing the continuity equation. The second three rows result from discretizing the $y$ momentum equation. The last three rows are obtained from discretizing the $x$ momentum equation. The system of Eq. (7) was solved by a block tridiagonal solution method described in Anderson et al. [7].

Using the above procedure, turbulent flow in a straight channel was computed. In the computation of turbulent flow in straight channels, the method was found to be robust and no under-relaxation parameters were necessary for either velocity or pressure, and the method worked well. However, when this method was applied to a 90 deg bend, the method resulted in singular matrices and the method failed. By conducting numerical experimentation, it was found that singularities in the coefficient matrices resulted for bend angles, $\theta$ (measured from the inlet as shown in Fig. 1), greater than 70 deg. To investigate the reason for this, the discretized system of equations was considered. The source of the problem was found to be in the ''$B$ matrix.'' In Eq. (7), the diagonal matrix $B_i$ is given by

$$B_i=\begin{vmatrix} b_{11} & b_{12} & 0 \\ b_{21} & b_{22} & b_{23} \\ b_{31} & b_{32} & b_{33} \end{vmatrix} \tag{8}$$

The elements of this matrix that cause problem arise from discretization of the continuity equation and the pressure terms in the momentum equations. Some of the elements in $B_i$ arise from discretizing the continuity equation (Eq. (1)). These elements are

$$b_{11}=y_\eta/\Delta\xi, \quad b_{12}=-x_\xi/\Delta\eta \tag{9}$$

Other elements that cause problem arise from the pressure term of the momentum Eqs. (2) and (3). They are

$$b_{23}=\frac{x_\xi}{\rho\Delta\eta}, \quad b_{33}=-\frac{y_\eta}{\rho\Delta\xi} \tag{10}$$

where $\xi$ represents the stream-wise direction and $\eta$ represents the transverse direction as shown in Fig. 1.

As the bend angle approaches 90 deg, the derivatives, $x_\xi$ and $y_\eta$ approach zero (at $\theta=90$ deg, $x_\xi=y_\eta=0$). This means that in this region the elements $b_{11}=b_{12}=b_{13}=b_{23}=b_{33}=0$ and the matrix becomes singular (the determinant of matrix $B$ is zero). Therefore, it was found that this method with the form of governing equations used above is not suitable for highly curved geometries such as 90 deg bends and channels.

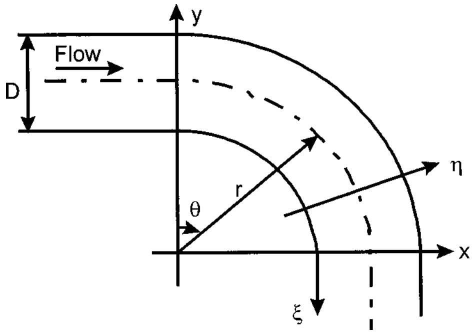

**Fig. 1 Coordinate system of bend**

**2 Generalization of the Simultaneous Variable Solution Method.** The simultaneous variable solution method described above is efficient, accurate and robust. However, the form of the governing equations used above limits its applications to small bend angles. This method becomes more generally applicable if the Navier-Stokes equations using the covariant or contravariant components, employing the orthogonal or nonorthogonal curvilinear coordinates, are used. In this study, the equations in orthogonal curvilinear coordinates (Warsi [8]) were used. The equations are

Momentum equations:

$$\begin{aligned}&\frac{U}{h_1}\frac{\partial U}{\partial \xi}+\frac{V}{h_2}\frac{\partial U}{\partial \eta}+\frac{UV}{h_1h_2}\frac{\partial h_1}{\partial \eta}-\frac{V^2}{h_1h_2}\frac{\partial h_2}{\partial \xi}\\&\quad=-\frac{1}{h_1^2}\frac{\partial h_1}{\partial \xi}\tau_{\xi\xi}+\frac{1}{h_1^2h_2}\left\{\frac{\partial}{\partial \xi}(h_1h_2\tau_{\xi\xi})+\frac{\partial}{\partial \eta}(h_1^2\tau_{\xi\eta})\right\}\\&\quad\quad-\frac{1}{h_1h_2}\frac{\partial h_2}{\partial \xi}\tau_{\eta\eta}\end{aligned} \tag{11}$$

$$\frac{U}{h_1}\frac{\partial V}{\partial \xi}+\frac{V}{h_2}\frac{\partial V}{\partial \eta}+\frac{UV}{h_1h_2}\frac{\partial h_2}{\partial \eta}-\frac{U^2}{h_1h_2}\frac{\partial h_1}{\partial \xi}$$

$$=-\frac{1}{h_1h_2}\frac{\partial h_1}{\partial \eta}\tau_{\xi\xi}+\frac{1}{h_2^2h_1}\left\{\frac{\partial}{\partial \xi}(h_2^2\tau_{\xi\eta})+\frac{\partial}{\partial \eta}(h_1h_2\tau_{\eta\eta})\right\}$$

$$-\frac{1}{h_2^2}\frac{\partial h_2}{\partial \eta}\tau_{\eta\eta} \qquad (12)$$

Continuity equation:

$$\frac{\partial}{\partial \xi}(h_2U)+\frac{\partial}{\partial \eta}(h_1V)=0 \qquad (13)$$

where $U$ is defined as the velocity in the stream-wise, $\xi$, direction, and $V$ is defined as the transverse velocity component or the velocity component in the direction normal to stream-wise, $\eta$, or the direction normal to the flow direction, and $h_1$ and $h_2$ are geometric terms. The stress $\tau_{ij}$ in Eqs. (11) and (12) is

$$\tau_{ij}=-p\,\delta_{ij}+2\,\nu_e D_{ij} \qquad (14)$$

where $D_{ij}$ is the mean rate of strain tensor.

Equations (11)–(13) were discretized and solved simultaneously to obtain flow velocity components and pressure. In discretization of Eqs. (11)–(13), the convection terms were discretized by the second-order upwind scheme; all other terms were discretized by the second-order central difference scheme. The boundary conditions for the velocity components were obtained by a second-order polynomial extrapolation. The details of this extrapolation procedure and the results can be found in Wang [9]. The pressure boundary conditions were obtained by simplifying Eq. (12) using the no-slip boundary conditions, i.e., $U=0$ and $V=0$ at the wall. All terms in the remaining equation were discretized by the second-order central difference scheme at the wall. To close the system of equations, the next step was to define the eddy viscosity by employing a turbulence model.

## Turbulence Modeling in Curved Ducts

Two-equation turbulence models and algebraic Reynolds stress models are commonly used for engineering predictions of turbulent flows. Among the two-equation turbulence models, the standard $k$-$\varepsilon$ model and its variants are most widely used. But, in the ASME's CFD Biathlon (Freitas [10]), it was shown that the standard $k$-$\varepsilon$ model provides different solutions when using different CFD codes. This may be caused by the different wall function treatments in the different CFD codes. In the present work, several other turbulence models were considered, namely, a modified version of the Baldwin-Lomax mixing-length model, a low-Reynolds-number two-equation $k$-$\tau$ turbulence model developed by Speziale et al. [5] and an algebraic Reynolds stress model developed by Thangam et al. [11]. None of these models require a wall function. The $k$-$\tau$ model has the advantage that the turbulence time scale $\tau$ has a natural boundary condition at the wall ($\tau=0$) and it is a low-Reynolds-number model. Therefore, the $k$-$\tau$ model does not need the wall function treatment at the wall. The various turbulence models that are used and their modification are described below.

**1 The Mixing-Length Model.** The mixing-length model proposed by Baldwin and Lomax [4] was used in the present numerical method for its efficiency and simplicity. In the mixing-length model of Baldwin and Lomax [4], the turbulent eddy viscosity was related to a length scale and a velocity scale, by

$$\nu_\tau\begin{cases}(\nu_\tau)_{\text{inner}}=\ell^2|\omega| & y\leqslant y_{\text{crossover}}\\ (\nu_\tau)_{\text{outer}}=K_mC_{cp}F_{\text{wake}}F_{kleb} & y>y_{\text{crossover}}\end{cases} \qquad (15)$$

where: $y_{\text{crossover}}$ is the value of $y$ where $(\nu_\tau)_{\text{outer}}=(\nu_\tau)_{\text{inner}}$, and $\ell=\kappa y[1-\exp(-y^+/A^+)]$, $|\omega|$ is the magnitude of vorticity vector, $y^+=u_\tau y/\nu$; $u_\tau$ is the frictional velocity, $\kappa=0.4$, $A^+=26$, $K_m=0.0168$ and $C_{cp}=1.6$. In Eq. (15), $F_{\text{wake}}$ and $F_{kleb}$ are given by following equations

$$F_{kleb}=1(\text{no intermittency is used for internal flows}) \qquad (16)$$

$$F_{\text{wake}}=\text{the smaller of}\left\{\begin{matrix} y_{\max}F_{\max}\\ \text{or}\\ C_{wk}y_{\max}u_{\text{dif}}^2/F_{\max}\end{matrix}\right\} \qquad (17)$$

where $C_{wk}=0.25$, $y_{\max}$ and $F_{\max}$ are determined from Eq. (18). $F_{\max}$ is the maximum value of $F(y)$ that occurs in a profile and $y_{\max}$ is the value of $y$ at which $F_{\max}$ occurs.

$$F(y)=y|\omega|[1-\exp(-y^+/A^+)] \qquad (18)$$

Modification of $u_\tau$ which was used in defining $y^+$ was conducted to overcome its singularity ($\tau_w=0$) in the separated flow region. The modified $u_\tau$ is given by the following expression (Baldwin and MacCormak [12])

$$u_\tau=\frac{1}{2}\left(\sqrt{|\tau_w|/\rho}+\kappa\left|y\frac{\partial U}{\partial y}\right|_{y^+=60}\right) \qquad (19)$$

**2 The $k$-$\tau$ Model (Speziale et al. [5]).** In the $k$-$\tau$ model, the turbulent eddy-viscosity is related to the turbulent kinetic energy, $k$, and the turbulence time scale, $\tau$, by

$$\nu_\tau=C_\mu f_\mu k\tau \qquad (20)$$

where $C_\mu=0.09$, $f_\mu=[1+3.45/\sqrt{\text{Re}_t}]\tanh(y^+/70)$ and $\text{Re}_t=k\tau/\nu$, $f_\mu$ is the wall damping function that is needed for asymptotic consistency.

The transport equation for the turbulent kinetic energy, $k$, is

$$\vec{V}\cdot\nabla k=2\,\tau_{ij}^t:D_{ij}-k/\tau+\nabla\cdot\left(\left(\nu+\frac{\nu_\tau}{\sigma_k}\right)\nabla k\right) \qquad (21)$$

where $\nu_\tau$ is the turbulent eddy viscosity computed by Eq. (20), $\sigma_k=1.4$ is an empirical constant, $\overline{V}$ is the fluid mean velocity vector, $\nabla$ is the gradient operator defined in the two dimensional case as: $\nabla=(1/h_1)(\partial/\partial\xi)\vec{e}_1+(1/h_2)(\partial/\partial\eta)\vec{e}_2$. $\tau_{ij}^t$ is the Reynolds stress tensor which is defined as $\tau_{ij}^t=-(2/3)k\delta_{ij}+2\nu_\tau D_{ij}$. $\delta_{ij}$ is the Kroneker delta and $D_{ij}$ is the mean rate of the strain tensor.

The turbulent time scale $\tau$ of Eq. (20) is modeled by the following equation

$$\vec{V}\cdot\nabla\tau=2(1-C_{el})\frac{\tau}{k}\tau_{ij}^t:D_{ij}+\frac{2}{k}\left(\nu+\frac{\nu_\tau}{\sigma_{\tau1}}\right)\nabla k\cdot\nabla\tau$$

$$-\frac{2}{\tau}\left(\nu+\frac{\nu_\tau}{\sigma_{\tau2}}\right)\nabla\tau\cdot\nabla\tau+\nabla\cdot\left(\left(\nu+\frac{\nu_\tau}{\sigma_{\tau2}}\right)\nabla\tau\right)+C_{e2}f_2-1 \qquad (22)$$

where $i$, $j$, $\tau_{ij}^t$, and $\nu$, $\nu_\tau$ have the same meaning as Eq. (21). $C_{e1}=1.44$ $C_{e2}=1.83$ $\sigma_{\tau1}=\sigma_{\tau2}=1.36$, and $f_2$ is the wall damping function that is needed for asymptotic consistency for the turbulent time scale transport equation which is given by

$$f_2=\left[1-\frac{2}{9}\exp\left(-\frac{\text{Re}_t^2}{36}\right)\right][1-\exp(-y^+/5)]^2.$$

*Modifications of the $k$-$\tau$ Turbulence Model.* The two-equation turbulence models, including the $k$-$\tau$ model (Speziale et al. [5]), do not include the streamline curvature effects. Therefore, modifications of the $k$-$\tau$ model were conducted by including these effects. Currently, there are several ways of modifying the two-equation turbulence model to include the streamline curvature effects. Two methods were selected, which are: (i) including the Richardson flux number in the $\tau$ transport equation as used by Tamamidis and Assanis [13], and (ii) modifying the eddy-viscosity expression as suggested by Cheng and Farokhi [6] for the $k$-$\varepsilon$ model. In this work, both modifications were extended to the $k$-$\tau$ turbulence model equations.

After including the Richardson curvature number modification, the turbulent time scale $\tau$ transport Eq. (22) becomes

$$\begin{aligned}\vec{V}\cdot\nabla\tau=&2(1-C_{el})\frac{\tau}{k}\tau_{ij}^{t}:D_{ij}+\frac{2}{k}\left(\nu+\frac{\nu_\tau}{\sigma_{\tau 1}}\right)\nabla k\cdot\nabla\tau\\ &-\frac{2}{\tau}\left(\nu+\frac{\nu_\tau}{\sigma_{\tau 2}}\right)\nabla\tau\cdot\nabla\tau+\nabla\cdot\left(\left(\nu+\frac{\nu_\tau}{\sigma_{\sigma 2}}\right)\nabla\tau\right)\\ &+(C_{e2}f_2(1-C_rR_{it})-1)\end{aligned}\tag{23}$$

where $Cr=0.3$, and $\mathrm{R}_{\mathrm{it}}$ is the curvature Richardson number given by

$$R_{it}=\tau^2\frac{U}{r^2}\frac{\partial(rU)}{\partial r}\tag{24}$$

where $r$ is the radius of curvature, $U$ is the velocity in the streamwise direction.

An alternative way to modify the turbulent eddy viscosity is by including pressure strain which is neglected in the standard $k$-$\tau$ model. Based on the pressure strain model of Launder et al. [14] and after some manipulations, the eddy viscosity expression, i.e., Eq. (20) becomes

$$\nu_\tau=f_\mu k\tau\left(1-\phi p_r\frac{\tau}{k}\right)\phi,\quad \phi=\frac{1-C_2}{p_r\tau/k-1+C_1}\tag{25}$$

where $C_1$ and $C_2$ are empirical constants ($C_1=1.5$, $C_2=-0.35$), and $p_r$ is the production of turbulent kinetic energy.

**3 The Standard *k*-*ε* Model.** In this investigation, a commercially available CFD code, called CFX® (CFX [15]) is also used. Several different turbulence models are available in CFX, but only the standard (high-Reynolds-number) $k$-$\varepsilon$ model employing a standard wall function was used for comparison to the present models. (Equations used in CFX are also presented by Wang [9].) Not much work has been done to validate this CFD code in the literature; a work by Edwards et al. [16] discusses validation of this CFD code for two- and three-dimensional flows.

## Numerical Solution

The time-averaged Navier-Stokes equations were discretized and solved simultaneously to obtain the flow velocity components and pressure. In discretization of the transport equations, the convection terms were discretized by the second-order upwind scheme. Other terms were discretized by the second-order centered difference scheme. The discretized equations were solved iteratively by a method described by Bentson and Vradis [1]. After one iteration and solving for the velocity components and pressure, the turbulent eddy viscosity was updated by solving the governing equations for the turbulence models.

The accuracy of the numerical solution was checked by refining the computational grid. The procedure used to determine the rate of convergence is described by Blottner [17]. Richardson's extrapolation was used to perform an extrapolation of the results to ''zero-mesh width,'' i.e., the exact solution. The truncation error in the calculation of the streamwise flow velocity, at the centerline and at 75 deg downstream of the bend (the geometry for this case is described below, see Fig. 6), was used to determined the rate of convergence.

Using this procedure, the convergence and accuracy of the numerical solution was checked by refining the grid in both the streamwise and normal directions. The truncation error in calculated value of the centerline velocity as a function of the grid spacing in each direction was determined by comparing the calculated values with the ''exact'' or the extrapolated value. A typical result is shown in Fig. 2 for turbulent flow in the 90 deg bend discussed below. The line shown in Fig. 2 has the slope of 2, indicating second order accuracy (Blottner [17]). For the results shown in Fig. 2, as well as other cases considered, nonuniform grids were used. Figure 2 was based on 20, 40, 80, and 160 grid points in the $\eta$ direction for the 90 deg bend calculations. Figure 2 indicates that if 60 to 70 points are used in the $\eta$ direction, the accuracy of the calculated velocity at the centerline can be expected to be larger than or about 2 to 3 percent. Also, note that the rate of convergence of the numerical results agrees with the theoretical result if the grid is sufficiently refined (for approximately 60 or more grid points in the $\eta$ direction). A total of 150 grids were used in the streamwise direction of which, 30 nonuniform grids were used in the upstream section, 60 uniform grids were used in the bend section and 60 nonuniform grids were used in the downstream section. A grid refinement study was conducted in the streamwise direction by doubling the number of grids in each section. The results obtained at several locations were examined and the results were nearly the same (relative error for velocities were less than one percent). Therefore, for the comparison of the results, 150 grids in the streamwise direction were used.

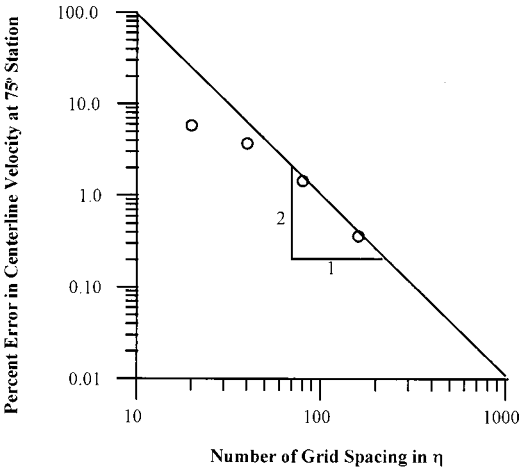

**Fig. 2 Typical grid refinement results**

## Results and Discussion

**Channel Flows.** Results using the present numerical solution procedure were first compared with the results obtained by Vradis et al. [2] for laminar flow and very good agreement were observed. Turbulent flow in a straight channel studied by Hussain and Reynolds [18] was used as the next test case for the simultaneous variable solution method using the $k$-$\tau$ turbulence model and the mixing-length model. The flow was computed using 50 nonuniform grid points in the $y$ direction such that the value of $y^+$ for the first grid point near the wall was about 0.5. The channel is long enough to allow the flow to become fully developed. Given the inlet parabolic or logarithmic velocity profile, the simultaneous variable solution method converged with no relaxation for the velocity components and pressure. The predicted mean velocity profiles using the mixing-length model and the $k$-$\tau$ model are compared with experimental data of Hussain and Reynolds [18] and are shown in Fig. 3. In Fig. 3, the velocity is normalized by the centerline velocity, and the distance from the wall, $y$, is normalized by half of the channel height. It can be seen that the prediction using the $k$-$\tau$ model agrees very well with the experimental data. The agreement between the mixing-length model (denoted by M-L) prediction and data is also good. In Fig. 4, it can be seen that the $k$-$\tau$ model yields a logarithmic velocity profile and the prediction agrees very well with the experimental data.

In Fig. 5, prediction of turbulent kinetic energy using the $k$-$\tau$ model is compared with Kim et al. [19] prediction that uses a low-Reynolds-number $k$-$\varepsilon$ model and with the direct numerical

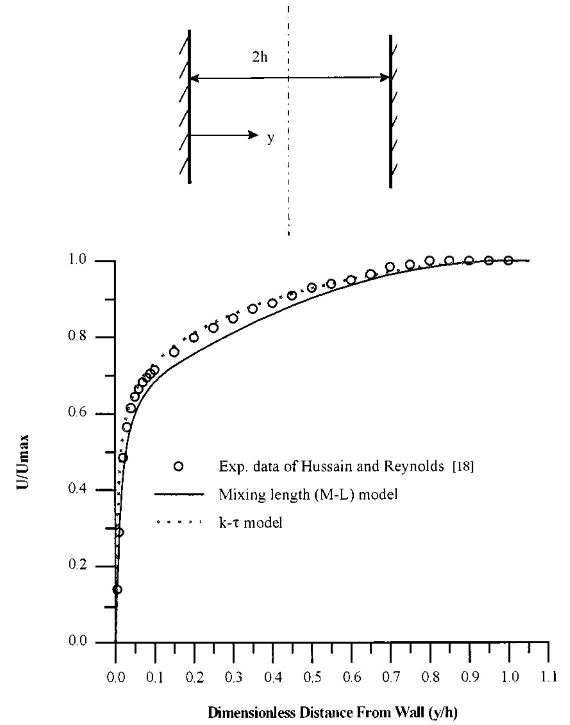

**Fig. 3 Channel flow dimensionless velocity profiles (Re =32,300)**

simulation results from them. From this figure, it can be seen that the $k$-$\tau$ model gives a better prediction of the peak of turbulent kinetic energy than the low-Reynolds-number $k$-$\varepsilon$ model in the near-wall region.

**Turbulent Flow in 90 Deg Bend.** Turbulent flow in a 90 deg curved channel or bend with the Reynolds number of 224,000 was investigated experimentally and numerically by Kim and Patel [20] and was selected as the next test case for flow model verification. The experimental data was gathered for a 90 deg curved duct of a rectangular cross section with an aspect ratio of one-to-six and a curvature radius to height ratio of 3.5 ($(R_0+R_i)/(2H)=3.5$). The flow velocities and turbulent quantities were measured at stations U1, U2, 15 deg, 45 deg, 75 deg, and D1 which are shown in Fig. 6. The overall experimental uncertainty reported for the streamwise velocity component ($U$) was reported to be 1.5 percent and for the turbulent stress measurement was about 5 percent for $\overline{U'U'}$ and 10 percent for other turbulent stress components. The numerical simulation was carried out starting at the U1 station (see Fig. 6) and ending at the down stream end of the duct. To specify inlet conditions at the inlet (U1 station), velocity and turbulent kinetic energy profiles were obtained from curve fits to the experimental data. The results using the mixing-length mode with $150\times70$ (150 in streamwise direction and 70 across the channel) grid points are shown in the following figures and were used to compare with solutions from other models. The results using the commercially available CFD code (CFX) are also presented. In the computation of the flow field using the present numerical model, no under-relaxation parameters were used in the solution procedure for the velocity components and pressure. However, when the ratio of the bend curvature radius to channel height was below 2, (i.e., $(R_o+R_i)/(2H)<2$), under-relaxation factors for the velocity components were needed to obtain a converged solution. The results presented below are compared with the experimental data at the centerplane of the rectangular duct.

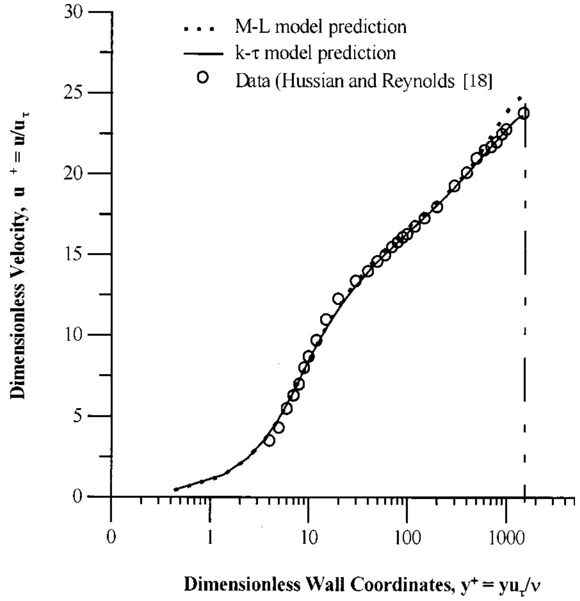

**Fig. 4 Channel flow dimensionless velocity profiles in the wall coordinates (Re=32,300)**

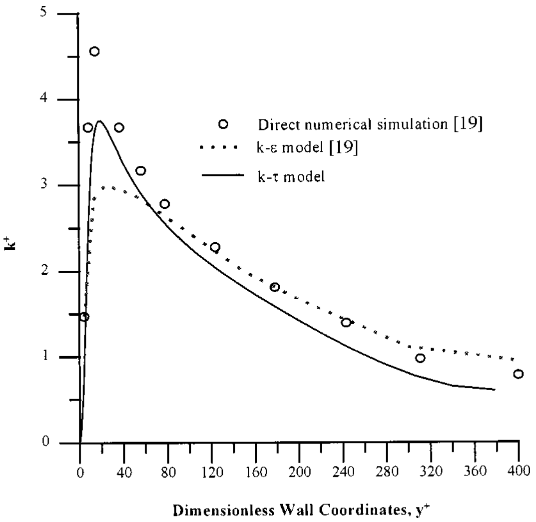

**Fig. 5 Turbulent kinetic energy predictions for a channel flow (Re=7,725)**

For the $k$-$\tau$ model and the modified $k$-$\tau$ model, the $y^+$ values for the first grid point away from the wall was selected to be 0.3 $\sim$0.6 (note that $y^+$ varies along the bend). For the standard $k$-$\varepsilon$

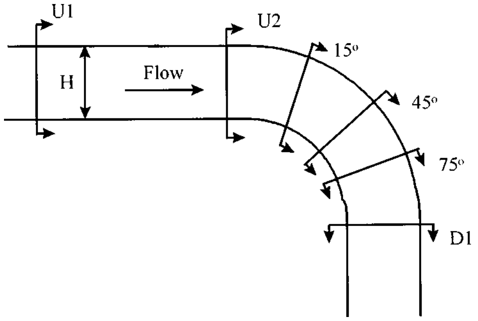

**Fig. 6 Velocity measurement locations in a 90 degree bend (Kim and Patel [20])**

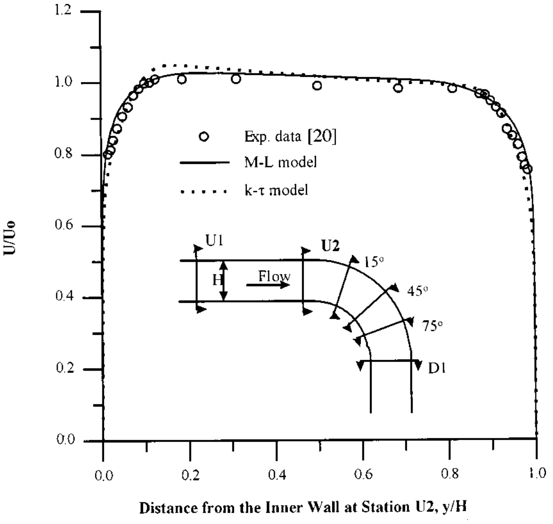

Fig. 7 Predicted velocity profiles using mixing-length model and $k$-$\tau$ model versus data (Kim and Patel [20]) at U2 Station, $U_0$ is the centerline velocity at station U1

model used in CFX, the $y^+$ values for the first grid points away from the wall was around 40–100. This is due to the wall function that is used in the standard $k$-$\varepsilon$ model.

Figure 7 shows the predicted streamwise velocity profile using the mixing-length (denoted by M-L) model and the $k$-$\tau$ model compared with the experimental data at the U2 station. Figures 8 and 9 show the predicted streamwise velocity profile by the mixing-length model and the $k$-$\tau$ model compared with the experimental data at the 15, 45, 75 deg and D1 stations. It can be seen that at downstream regions, such as the D1 station, the model predictions near the walls of the channel are not as good as their predictions at the upstream stations. Overall however, it is surprising that the simple mixing-length model used in this work gives pretty good velocity predictions as compared with the experimental data for this complex turbulent flow near the inner wall. The $k$-$\tau$ model gives slightly better predictions in the outer wall region than the mixing length model. Figure 10 shows the velocity profiles at the 75 deg station predicted by the original $k$-$\tau$ model denoted by $k$-$\tau$ model; the $k$-$\tau$ model with the Richardson curvature number modification in the $\tau$ transport equation denoted by $k$-$\tau$ model with Rit for $\tau$ equation; and the $k$-$\tau$ model with modified eddy viscosity by including pressure strain denoted by $k$-$\tau$

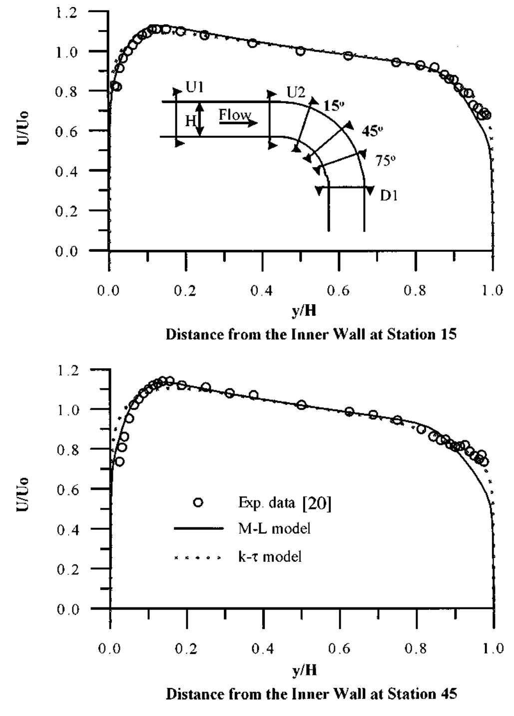

Fig. 8 Predicted velocity profiles using mixing-length model and $k$-$\tau$ model versus data (Kim and Patel, [20]) at 15 and 45 deg stations

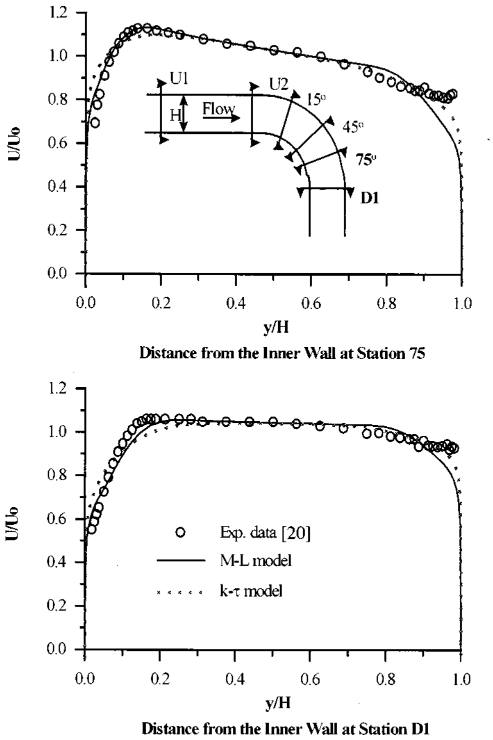

Fig. 9 Predicted velocity profiles using mixing-length model and $k$-$\tau$ model versus data (Kim and Patel [20]) at 75 deg and D1 stations

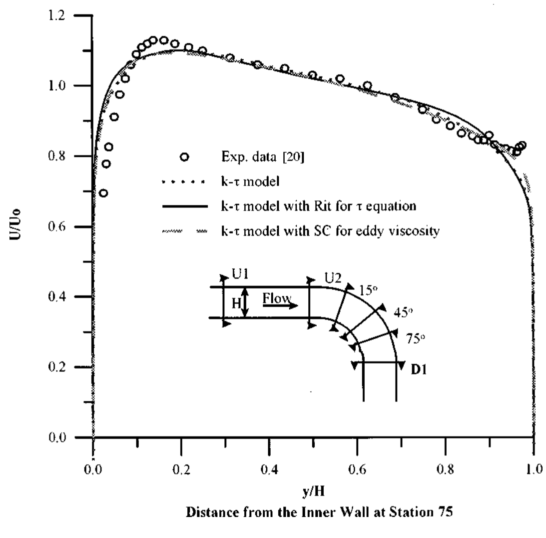

Fig. 10 Predicted velocity profiles using $k$-$\tau$ models versus data (Kim and Patel [20]) at 75 deg station

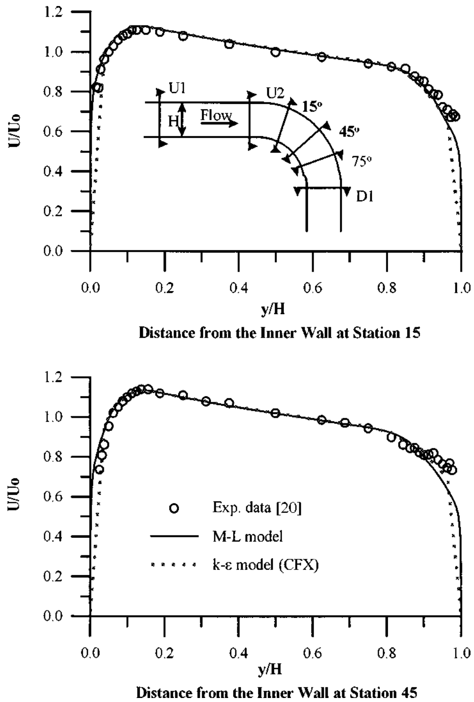

**Fig. 11 Predicted velocity profiles using mixing-length and *k*-*ε* models versus data (Kim and Patel data [20]) at 15 and 45 deg stations**

model with SC for eddy viscosity. It can be seen that the modified versions of the *k*-*τ* model give velocity profiles that are similar to the standard *k*-*τ* model prediction.

Figures 11 and 12 show predictions of the velocity profiles using CFX and employing the standard *k*-*ε* model as compared with the mixing-length model with the present numerical method and the experimental data at the 15, 45, 75 deg and D1 stations. Again, at the downstream regions of the bend where streamline curvature effects become stronger, such as 75 deg and D1 stations, the model predictions near the channel walls are not as good as the predictions at the upstream stations. Overall, both the *k*-*ε* and the mixing-length models give similar velocity profiles.

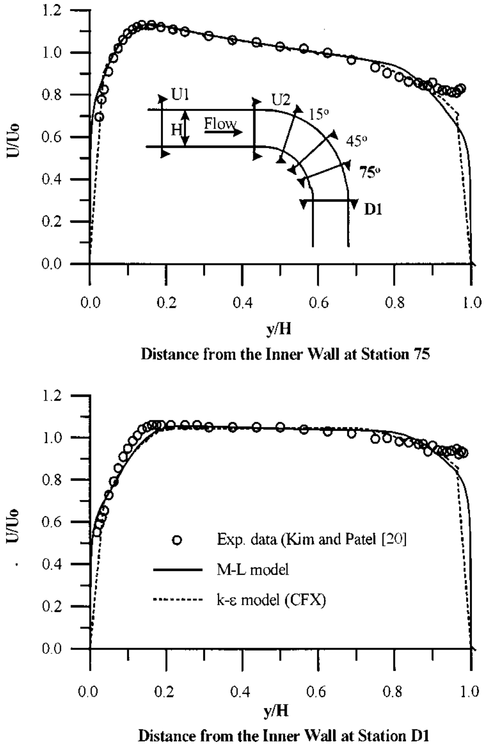

**Fig. 12 Predicted velocity profiles using mixing-length and *k*-*ε* model versus data (Kim and Patel [20]) at 75 deg and D1 stations**

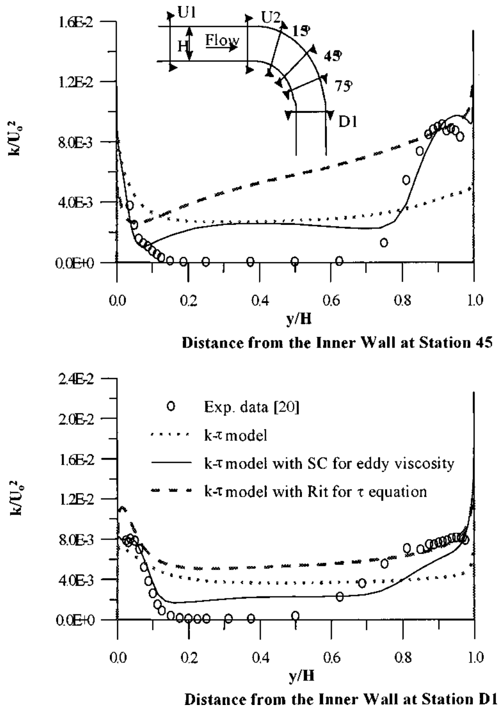

**Fig. 13 Predicted turbulent-kinetic energy profiles using *k*-*τ* models versus data (Kim and Patel [20]) at 45 deg and D1 stations**

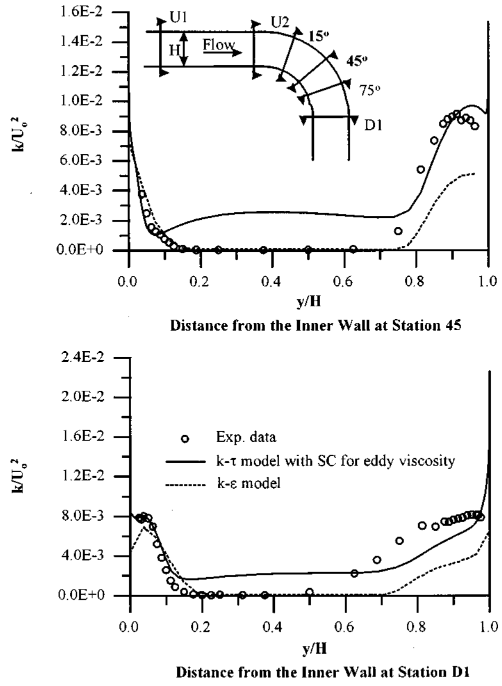

**Fig. 14 Predicted turbulent kinetic energy profiles using modified *k*-*τ* and *k*-*ε* models versus data (Kim and Patel [20]) at 45 deg and D1 stations**

Figure 13 shows comparison of turbulent kinetic energy profiles between the present numerical model predictions and the experimental data at 45 deg and D1 stations. This figure shows that the $k$-$\tau$ model with streamline curvature effects correction in eddy viscosity agrees better with the data than the other models. A comparison between the standard $k$-$\varepsilon$ model (in CFX) and the modified $k$-$\tau$ model is shown in Fig. 14. It is observed that the modified $k$-$\tau$ model agrees better with the data in the near wall region of the outer wall than the standard $k$-$\varepsilon$ model.

It is worth mentioning that a three-dimensional simulation of flow in the channel that is considered in this work was conducted by Sotiropoulos and Patel [21]. They used a standard $k$-$\varepsilon$ model, similar to one that is also used in this study. The results obtained by Sotiropoulos and Patel for three-dimensional simulations are almost identical to the results that are obtained in this study with CFX for a two-dimensional simulation. Therefore, the effects of the secondary flows that normally appear in the transverse cross section of curved ducts may be small for this channel flow where the aspect ratio is high. The turbulence models used in the present work may not accurately capture all of the physics of turbulent flow in this complex turbulent flow. The results, however, indicate that the present numerical solution procedure is a viable tool for solving the Navier-Stokes equations in highly curved geometries.

## Summary and Conclusions

An efficient and accurate simultaneous variable solution technique for solving the Navier-Stokes equations has been extended to general orthogonal and nonorthogonal coordinates and turbulent flow computations. The numerical solution procedure is now capable of handling flows in highly curved channels and bends. In addition, several turbulence models were implemented into the numerical solution procedure to predict turbulent flows with strong streamline curvature effects. Turbulence models used are the modified versions of the mixing-length model developed by Baldwin and Lomax [4], the two-equation low-Reynolds-number $k$-$\tau$ model developed by Speziale et al. [5], the algebraic Reynolds stress model of Thangam et al. [11], and the standard $k$-$\varepsilon$ model with a wall function.

The $k$-$\tau$ model was tested for flows in a straight channel and a curved channel with streamline curvature effects. It is found that although this model gives very good results in a straight channel, its prediction of streamwise velocity profile was not much better than the standard $k$-$\tau$ model and the simple mixing-length model in the 90 deg bend. A comparison between the standard $k$-$\varepsilon$ model and the modified $k$-$\tau$ model in the 90 deg bend indicates that the modified $k$-$\tau$ model agrees better with the data in the near wall region of the outer wall than the standard $k$-$\varepsilon$ model. Therefore, the $k$-$\tau$ model needs to be further tested and refined to accurately predict complex turbulent flows. Predictions of turbulent kinetic energy profiles in a 90 deg bend indicates that modification of the $k$-$\tau$ model for streamline curvature effects was necessary to obtain reasonable agreement with the experimental data.

## Acknowledgments

This work was supported by the Erosion/Corrosion Research Center (E/CRC) at The University of Tulsa. The authors wish to acknowledge comments and support of Drs. John Shadley and Edmund Rybicki during the course of this study.

## References

[1] Bentson, J., and Vradis, G., 1987, ''A Two-stage Pressure Correction Technique for the Incompressible Navier-Stokes Equations,'' AIAA-87-0545, paper presented at the AIAA 25th Aerospace Sciences Meeting, Reno, NV.
[2] Vradis, G., Zalak, V., and Bentson, J., 1992, ''Simultaneous Variable Solutions of the Incompressible Steady Navier-Stokes Equations in General Curvilinear Coordinate Systems,'' ASME J. Fluids Eng., **114**, pp. 299–307.
[3] Prado, M., 1995, ''A Block Implicit Numerical Solution Technique for Two-Phase Multi-Dimensional Steady-State Flow,'' Ph.D. dissertation, The University of Tulsa, Tulsa, Oklahoma.
[4] Baldwin, B. S., and Lomax, H., 1978, ''Thin Layer Approximation and Algebraic Model for Separated Turbulent Flows,'' AIAA Paper No. 78-257, AIAA 16th Aerospace Sciences Meting, Huntsvill, AL.
[5] Speziale, C. G., Abid, R., and Anderson, E. C., 1992, ''Critical Evaluation of Two-equation Models for Near-wall Turbulence,'' AIAA J., **30**, No. 2, pp. 324–331.
[6] Cheng, G. C., and Farokhi, S., 1992, ''On Turbulent Flows Dominated by Curvature Effects,'' ASME J. Fluids Eng., **114**, pp. 52–57.
[7] Anderson, D. A., Tannehill, J. C., and Pletcher, R. H., 1984, *Computational Fluid Mechanics and Heat Transfer*, Hemisphere, NY.
[8] Warsi, Z. U. A., 1992, *Fluid Dynamics Theoretical and Computational Approaches*, CRC Press.
[9] Wang, J., 1997, ''Modeling Flow, Erosion and Mass Transfer in Elbows,'' Ph.D. dissertation, The University of Tulsa, Tulsa, Oklahoma.
[10] Freitas, C. J., 1995, ''Perspective: Selected Benchmarks From Commercial CFD Codes,'' ASME J. Fluids Eng., **117**, pp. 208–218.
[11] Thangam, S., Abid, R., and Speziale, C. G., 1992, ''Application of a New $K$-$\tau$ Model to Near Wall Turbulent Flows,'' AIAA J., **30**, No. 2, pp. 552–554.
[12] Baldwin, B. S., and MacCormack, R. W., 1976, ''Modification of The Law of The Wall and Algebraic Turbulence Modeling for Separated Boundary Layers,'' AIAA Paper No. 76-350, AIAA 9th Fluid and Plasma Dynamics Conference, San Diego, CA.
[13] Tamamidis, P., and Assanis, D. N., 1993, ''Numerical Simulation of Turbulent Flows in Complex Geometries Using Curvature Modified $k$-$\varepsilon$ models,'' ASME FED-Vol. 155, Turbulent Flows. pp. 113–118.
[14] Launder, B. E., Reece, G. J., and Rodi, W., 1975, ''Progress in the Development of a Reynolds-Stress Turbulence Closure,'' J. Fluid Mech., **68**, Part 3, pp. 537–568.
[15] CFX®, 1997, *CFX-4.2: Solver*, AEA Technology, Oxford, United Kingdom
[16] Edwards, J. E., Erdal, F. M., McLaury, B. S., and Shirazi, S. A., 1999, ''Validation of a CFD code for tangentially injected swirling flows and flow in 90 deg Elbows,'' Paper No. FEDSM99-6785, 3rd ASME/JSME Joint Fluids Engineering Conference, July 18–23, San Francisco, CA.
[17] Blottner, F. G., 1975, ''Investigation of Some Finite-Difference Techniques for Solving the Boundary layer Equations,'' Comput. Methods Appl. Mech. Eng., **6**, pp. 1–30.
[18] Hussain, A. K. M. F., and Reynolds, W. C., 1975, ''Measurements in Fully Developed Turbulent Channel Flow,'' ASME J. Fluids Eng., **97**, pp. 568–579.
[19] Kim, J., Moin, P., and Moser, R., 1987, ''Turbulent Statistics in Fully Developed Channel Flow at Low Reynolds Number,'' J. Fluid Mech., **177**, pp. 133–166.
[20] Kim, Wu J., and Patel V. C., 1993, ''An Experimental Study of Boundary-Layer Flow in A Curved Rectangular Duct,'' Data for Validation of CFD codes (and ASME J. Fluids Eng. Data Bank), FED-Vol. 146, pp. 13–28.
[21] Sotiropoulos, F., and Patel, V. C., 1992, ''Flow in Curved Ducts of Varying Cross-section,'' IIHR Report No. 358, Iowa Institute of Hydraulic Research, The University of Iowa, Iowa City, Iowa.

# A Flow Visualization Study of Vortex Interaction With the Wake of a Sphere

**M. Sun**
Graduate Research Assistant

**J. S. Marshall**
Associate Professor
e-mail: jeffrey-marshall@uiowa.edu

Iowa Institute of Hydraulic Research and
Department of Mechanical Engineering,
The University of Iowa,
Iowa City, IA 52242

*A study of the interaction between an initially columnar intake vortex (hereinafter referred to as the primary vortex) and vortex structures in the wake of a single sphere (hereinafter referred to as secondary vortices) is performed using a series of flow visualization experiments, in which a sphere is towed toward a stationary vortex with ambient axial flow and gradually decelerated to rest at a specified distance from the vortex core axis. Both the primary vortex core and the boundary layer of the sphere are visualized using laser-induced fluorescent dyes of two different colors, which are illuminated either with a laser sheet or a laser volume. The strength of the primary vortex is measured using particle-image velocimetry, which is also used to measure the strength of the secondary vortices in select cases. The form of the sphere wake in the presence of the primary vortex and the effect of the induced velocity from the secondary vortices on the primary vortex are studied for different values of the vortex-sphere separation distance, the sphere diameter, and the primary vortex core radius. Weak secondary vortices are observed to induce formation of small-amplitude waves of varying core area on the primary vortex, eventually forming a turbulent sheath surrounding the primary vortex. Stronger secondary vortices have an increasingly strong effect on the primary vortex, including large-amplitude variation in core area, outward ejection of fluid from the primary vortex core, and breakdown of the primary vortex.* [S0098-2202(00)01403-6]

## 1 Introduction

Vortex interaction with blunt bodies is of importance in a wide variety of fluid flow applications, ranging from flow-induced noise and vibrations in aerodynamic and turbomachinery applications to turbulence modification by particles, bubbles, or droplets in two-phase flows. For problems of noise and vibration sources in aerodynamic and turbomachinery applications, vortices generated by upstream blades, vortices present in the ambient (atmospheric) turbulence, or intake vortices interact with the fuselage of the aircraft and downstream control surfaces or rotors. A discussion of the effects of vortex-body interaction in rotorcraft aerodynamics, for instance, is given by Sheridan and Smith [1]. In turbulent two-phase flows, it is known that the presence of a dispersed particulate phase may either suppress or enhance the turbulent kinetic energy of the fluid (Crowe et al. [2]). Data on turbulence modification in two-phase flows compiled from a variety of sources by Gore and Crowe [3] show that turbulence enhancement occurs when the particle sizes are larger than about 10 percent of the turbulence integral length scale and turbulence attenuation occurs for smaller particle sizes. Gore and Crowe [3] propose that the particle wake generation in the turbulent flow is primarily responsible for turbulence enhancement.

Numerous studies of vortex interaction with blades and cylindrical bodies have been performed, as described in the review articles by Rockwell [4], Doligalski et al. [5], and Kim and Komerath [6]. Some of this literature includes the effects on the primary vortex of secondary vorticity shed from the body surface (due to the vortex-induced flow), including a recent study by Krishnamoorthy and Marshall [7] on vortex interaction with a thin blade and studies by Liou et al. [8] and Krishnamoorthy et al. [9] on vortex interaction with a circular cylinder. However, very little work has been reported on viscous vortex interaction with bodies, such as a sphere, in which the body wake plays a significant role during interaction with the vortex. The present paper reports on an experimental study of vortex interaction with a sphere wake, where we use the sphere as representative of a wake-generating body immersed in a vortex flow.

Previous work on inviscid vortex-sphere interaction is reported by Dhanak [10], who uses a vortex filament approximation, together with a cut-off model (Moore and Saffman [11]) for the singularity in self-induced filament velocity, to compute the bending of the vortex in the presence of the sphere. Dhanak also derives a linear approximation for small vortex displacements when the sphere is sufficiently distant. Pedrizzetti [12] examines the vortex-induced boundary layer development on a sphere for the case of instantaneous startup of the vortex from rest, using the vortex filament model to predict the external vortex-induced flow. Sound generation during vortex-sphere interaction is studied using an inviscid flow model by Knio and Ting [13] and experimentally by Minota et al. [14].

The sphere wake generated by a columnar vortex flow at low sphere Reynolds numbers ($20 \leqslant \mathrm{Re}_S \leqslant 100$) is examined in a series of numerical computations by Kim et al. [15,16], both for a single columnar vortex and for a vortex pair. The sphere is held fixed in these computations and the vortex is advected at some fixed distance above the sphere by a uniform flow. This Reynolds number is below the critical value for periodic vortex shedding from the sphere, and the sphere wake decays substantially over a distance of a few sphere radii. One effect of the vortex-induced velocity field is to cause the sphere wake to become asymmetric at Reynolds numbers for which the sphere wake is symmetric in a uniform flow.

We also note that several recent studies have examined aspects of vortex-vortex interaction that are pertinent to the topic of the current paper. In particular, Melander and Hussain [17] report a direct numerical simulation study of a large-scale vortex immersed in background turbulence, and similar computations using rapid distortion theory are reported by Miyazaki and Hunt [18]. A review of turbulence evolution in the vicinity of large-scale vortex flows is given by Marshall and Beninati [19], which includes discussion of both the modifications to the turbulence due to the flow

---

Contributed by the Fluids Engineering Division for publication in the JOURNAL OF FLUIDS ENGINEERING. Manuscript received by the Fluids Engineering Division January 7, 2000; revised manuscript received May 18, 2000. Associate Technical Editor: K. Zaman.

induced by the vortex and the modifications to the vortex induced by the turbulence. Computations of an individual vortex loop wrapping about an initially columnar vortex are reported by Krishnamoorthy and Marshall [7]. A study of the axisymmetric interaction between a columnar vortex and a series of periodic vortex rings (of both same sign and alternating sign vorticity) wrapped around the columnar vortex is given by Marshall [20], in which it is shown that weak vortex rings induce standing wave oscillations on the columnar vortex but strong vortex rings strip vorticity in thin sheets from the outer part of the columnar vortex.

The present paper reports on a series of flow visualization experiments that examine the interaction of the wake generated by a spherical body brought to rest near an initially columnar (*primary*) vortex for Reynolds numbers sufficiently high that unsteady vortex shedding occurs from the sphere. The focus of the study is to examine the entrainment of the sphere wake into the vortex and the response of the primary vortex to interaction with the sphere wake (*secondary*) vortices. The experiments investigate this interaction for different values of the sphere diameter $D$ and vortex-sphere separation distance $S$ using a combination of flow visualization using laser-induced fluorescence (LIF) and quantitative measurements using particle-image velocimetry (PIV). A variety of different interaction processes are observed to occur in the experiments depending upon the vortex-sphere separation distance and the sphere diameter relative to the vortex core radius. These interactions include entrainment of the sphere wake into the primary vortex core, formation of waves of varying core area on the primary vortex, generation of an upstream propagating breakdown on the primary vortex by the induced velocity from the sphere wake vortices, and attraction and intermittent attachment of the primary vortex to the sphere surface.

The experimental apparatus and procedures are described in Section 2, along with characterization of the primary vortex flow field. The experimental results, reported in Sections 3–4, illustrate different regimes of vortex-sphere interaction as the parameters $S/D$ and $D/\sigma_0$ are varied. Conclusions are given in Section 5.

## 2 Experimental Setup and Procedure

A sketch of the experimental apparatus is given in Fig. 1. The primary vortex is generated in water in a cylindrical inner tank (diameter $H=30$ cm), about which is placed an outer rectangular tank (101 cm×43 cm cross-section and 123 cm high) that houses the sphere and the support arms of the two carriage. Water is circulated through the system via tangential inlet jets at the top of the inner cylindrical tank and an outlet orifice at the tank bottom. A steady vortex is generated within about 20–30 minutes after starting the water circulation along the center axis of the inner cylindrical tank. The vortex is trapped at the top of the cylindrical tank by an inverted funnel that is sealed at the top with a Plexiglas plate, which both stabilizes the vortex and increases the core radius. The sphere is supported by a 3 mm diameter hollow metal rod, placed on the side of the sphere opposite the vortex. Five sphere sizes are used in the experiments, with diameters of 9.5 mm, 19 mm, 25 mm, 38 mm, and 50 mm.

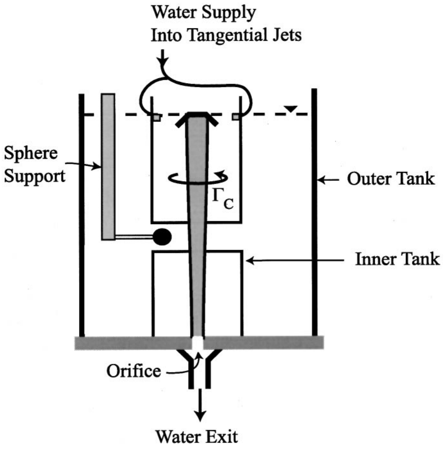

Fig. 1 Schematic of the experimental apparatus, showing the circular inner tank and rectangular outer tank, the water inlet and exit, the primary vortex, the sphere and the sphere support

The sphere is initially translated toward the vortex at a constant velocity of 0.01 m/s, and is then gradually brought to rest (at a deceleration of 0.05 m/s$^2$) at a separation distance $S$ between the sphere leading edge and the vortex symmetry axis. The sphere towing speed is set by a computer-controlled screw drive mechanism, so as to minimize vibrations and maintain a specified towing speed and deceleration rate. Experiments with different sphere translation and deceleration rates did not produce qualitatively different results.

The laser-induced fluorescence technique is used for flow visualization, with solutions of dyes that fluoresce at two different colors. The primary vortex is visualized using dye that fluoresces red (Sulfurhodamine 640) and the sphere wake is visualized with a dye that fluoresces yellow (Rhodamine chloride 590) when exposed to light with wavelength in the range 500–600 nm. The dyes are excited by the green line of a continuous argon ion laser (with wavelength in the range 457–514 nm). Photographs are taken using both a 35 mm still camera and a standard video camera, with frame rates of approximately 4 and 30 frames per second, respectively. The green laser light is filtered out so that only the emitted light of the dyes is recorded on film. A sketch showing the different laser sheet imaging planes and the parameters governing the sphere-vortex interaction is given in Fig. 2. Most of the visualization is performed in a vertical plane that slices through the symmetry axis of the primary vortex and the sphere center (labeled A in Fig. 2). In some cases, visualization is also performed either in a horizontal plane that bisects the sphere (labeled B in Fig. 2) or in a volumetric section of the flow.

The yellow dye is gravity fed into the sphere boundary layer from an external reservoir. The flow rate of yellow dye can be finely controlled by adjusting the gravity head and a needle valve placed in the feed line. The yellow dye enters into the boundary layer through 25 small holes (1 mm diameter) for spheres with diameter greater than 20 mm and through 13 holes for spheres

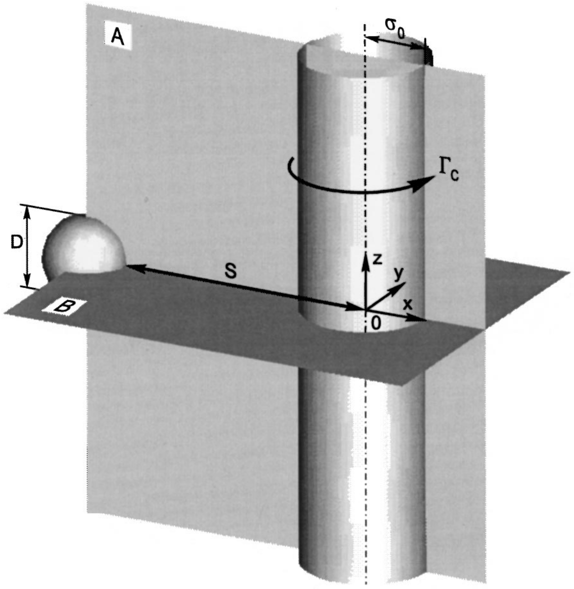

Fig. 2 Sketch illustrating the coordinate system, the parameters $\sigma_0$, $\Gamma_C$, $S$, and $D$ used to characterize vortex-sphere interaction, and the position of the (A) vertical and (B) horizontal laser sheet illumination planes

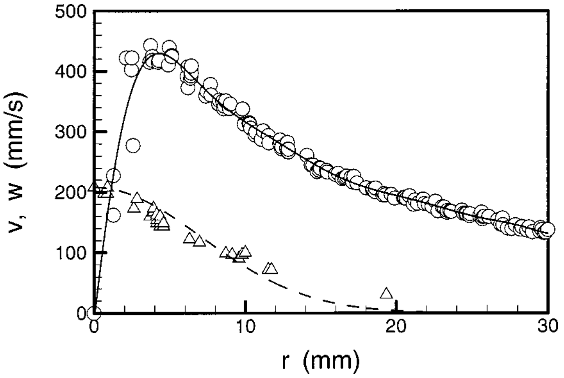

**Fig. 3 Experimental data for azimuthal velocity *v* (circles) and axial velocity *w* (triangles) for the primary vortex as a function of radial distance *r* from the center of the inner cylindrical tank. Best-fit curves are drawn for the azimuthal velocity (solid line) and axial velocity (dashed line).**

with diameter less than 20 mm. The holes are distributed evenly around the sphere surface. Red dye is injected into the primary vortex within the inverted funnel at the top of the inner cylindrical tank, and carried downward by the ambient axial flow within the vortex core. The LIF photographs have been digitally processed to insert the sphere profile and to convert the colors to grayscale, with the yellow dye appearing darker than the red dye.

The azimuthal velocity field within and outside the primary vortex core is measured using a particle-image velocimetry (PIV) system, which uses a double-pulsed Nd:YAG laser synchronized with a CCD camera (1317×1035 pixels). Data processing is performed using autocorrelation with the TSI *Insight* software with a time increment of $\Delta t = 0.7$ ms near the vortex core and $\Delta t = 1.0$ ms for the outer part of the vortex. The PIV data is obtained with a spacing of about 1 mm between vectors and 50 percent overlap of interrogation regions. Neutrally buoyant polycrystalline particles are used for flow seeding, with specific gravity $1.00 \pm 0.02$ and with more than 90 percent of the particle diameters less than 10 $\mu$m. The seed particles are formed into a milky suspension that is injected into the flow through the inverted funnel at the top of the inner cylindrical tank. PIV images are acquired after the particles have dispersed thoroughly within the test region. The instantaneous PIV data (circular symbols) in Fig. 3, acquired from five different images, scatter about the best-fit curve (solid line) with root-mean-square deviation of 3.6 percent of the maximum azimuthal velocity. The core radius $\sigma_0$ is set equal to the value of $r$ at which the best-fit curve has a maximum, and the circulation $\Gamma_C$ is obtained by fitting the expression $\Gamma_C/2\pi r$ for azimuthal velocity from a line vortex to the measured data for large values of $r$.

The axial velocity profile $w(r)$ of the primary vortex is measured by photographing the motion of a large number of small (0.5–1 mm diameter) neutrally buoyant immiscible dye globules (bromobenzene and paraffin oil mixed in proportion along with a fat soluble dye), which are released through a hypodermic needle at the top of the tank and carried downward by the vortex axial flow. The measured axial velocity profile is well fit by a Gaussian function of the form

$$w(r) = w_{\max} \exp(-r^2/\sigma_1^2), \tag{1}$$

where $\sigma_1$ is another measure of the vortex core radius and $w_{\max}$ is the axial velocity on the vortex centerline. The axial velocity data (triangular symbols in Fig. 3) have a root-mean-square scatter about the fit (1) (dashed curve) of 8.3 percent of $w_{\max}$. The average axial velocity over the core radius, $w_0$, is defined by

$$w_0 = \frac{2}{\sigma_1^2} \int_0^{\sigma_1} r w(r) dr \cong 0.63 w_{\max}. \tag{2}$$

For the experiments reported in this paper, the measures $\sigma_0$ and $\sigma_1$ of core radius, based on the azimuthal and axial velocity components, respectively, are $\sigma_0 = 4.5 \pm 1.0$ mm and $\sigma_1 = 10 \pm 2$ mm. The maximum axial velocity is $w_{\max} = 208 \pm 20$ mm/s and the average axial velocity over the core radius is $w_0 = 131 \pm 15$ mm/s. The vortex circulation is $\Gamma_C = 24 \times 10^3 \pm 1 \times 10^3$ mm$^2$/s.

The PIV method is also used to investigate the velocity component in the radial direction for the primary vortex. An estimate of the radial velocity associated with the primary vortex in the interval between 2–4 core radii $\sigma_0$ from the vortex center is obtained by dividing the observed radial displacement $\Delta R$ of the streamlines after one rotation by the time interval $\Delta t$ required for the fluid to rotate about the vortex core at that radius. The average radial velocity in this interval, $-2.8$ mm/s, has a magnitude of about 1 percent of the local azimuthal velocity magnitude.

The primary vortex is held in a fixed state for all experiments, with axial flow parameter $A \equiv 2\pi\sigma_0 w_0/\Gamma_C = 0.15 \pm 0.05$ and vortex Reynolds number $\mathrm{Re}_V \equiv \Gamma_C/\nu \cong 2.5 \times 10^4$. The axial flow parameter is much less than the critical value of about 0.7 (Marshall [21]), such that waves of variable core area can propagate both upstream and downstream on the vortex core (i.e., the vortex is subcritical). The axial flow parameter does not have a major effect on the vortex-sphere interaction except for cases where the sphere is very close to the vortex core, and the primary vortex behavior in the current experiments is expected to be typical of other subcritical vortex states. Letting $U_S = \Gamma_C/2\pi(S + 0.5D)$ denote the ambient velocity induced by the columnar vortex at the location of the sphere center, the sphere Reynolds number $\mathrm{Re}_S \equiv U_S D/\nu = \mathrm{Re}_V/2\pi(0.5 + S/D)$ varies in the experiments in the range 1000–4000. The experiments examine the sphere wake-vortex interaction for values of the ratio $S/D$ spanning the interval $-0.5 \leqslant S/D \leqslant 3$. At the lower limit, $S/D = -0.5$, the sphere center lies in the center of the inner cylindrical tank (on the initial position of the vortex symmetry axis). For each value of $S/D$, experiments with five different values of $D/\sigma_0$ (ranging from 2.1 to 11.1) are performed.

Other dimensionless parameters implicit in the experimental setup are assumed to have negligible effect. For instance, the effect of the tank wall is believed to be small since the ratio $D/H$ of sphere diameter to inner tank diameter ranges from 0.03 to 0.17, with $D/H$ less than 10 percent for all but the largest sphere diameter. Likewise, the vortex is assumed to be nearly columnar at the start of each experiment, since flow visualization pictures indicate that the gradient in vortex core radius, $d\sigma_0/dz$, is less than 2 percent within the experimental measurement region (which spans approximately five sphere diameters along the vortex on either side of the body).

## 3 Effect of Vortex on Sphere Wake

When a sphere is placed in the vicinity of the primary vortex, the vortex-induced flow generates "secondary vorticity" on the sphere surface that diffuses outward and is convected behind the sphere to form the sphere wake. For very large values of $S/D$ ($S/D \gg 1$), the flow induced by the vortex at the sphere location is nearly uniform and the sphere wake closely resembles that caused by uniform translation of a sphere in a still fluid. The form of the vortex structures present in the wake of a sphere immersed in a uniform flow has been studied by numerous investigators for sphere Reynolds numbers in the range 300–$10^4$ (Achenbach [22], Magarvey and Bishop [23], Magarvey and MacLatchy [24], Sakamoto and Haniu [25], Taneda [26]). For sphere Reynolds numbers greater than about 300–400, this flow is dominated by nearly periodic shedding of hairpin vortex loops. These vortex structures form an interconnected "street" of hairpin vortices, which is illustrated schematically by Achenbach [22] and reproduced in Fig. 4. For Reynolds numbers just above the critical value for onset of vortex shedding (up to about Re≅420), this hairpin vortex street appears very regular, with each loop of nearly the same strength and with the same spacing and orientation. As the Reynolds num-

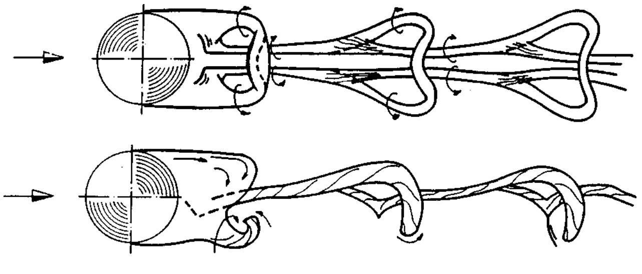

Fig. 4 Schematic representation of the interconnected vortex loop structures in the wake of a sphere immersed in a uniform flow (reproduced from Achenbach [22])

ber is further increased, the hairpin vortex street becomes increasingly irregular, both in terms of the vorticity separation point on the body surface and the orientation of the vortex loops far away from the body. Evidence for the presence of vortex loops with alternating sign vorticity, which can be viewed as an extreme case of hairpin oscillation with the vortex loop detachment point on alternating sides of the sphere, is presented by Sakamoto and Haniu [25] for Reynolds numbers greater than about 800 and in computations by Tomboulides et al. [27] and Johnson and Patel [28].

As $S/D$ decreases in the vortex-sphere interaction problem and approaches unity (but still with the sphere outside of the primary vortex core), the vortex-induced flow past the sphere becomes increasingly nonuniform, with higher velocity on the side of the sphere closest to the primary vortex. The wake form in this case becomes similar to the problem of a sphere immersed in a uniform shear flow, which was studied by Sakamoto and Haniu [29]. These authors report that the sphere wake configuration (i.e., the general form of the wake vortex structures) in a shear flow does not differ substantially from that in a uniform flow. Sakamoto and Haniu [29] make the following observations on the effect of background shear on the sphere wake: (1) the point of vorticity detachment from the body shifts toward the high-velocity side of the sphere and remains fixed, (2) the wake vortex loops are always shed from the high-velocity side of the sphere and do not exhibit the irregular oscillation in orientation characteristic of the sphere wake in uniform flow for $\mathrm{Re}_S > 420$, (3) the critical Reynolds number for onset of periodic vortex shedding decreases with shear rate, and (4) the Strouhal number of the shed vortex loops increases slightly with shear rate. The data of Sakamoto and Haniu [29] are reported for values of the shear parameter $K \equiv GD/U_S$, where $G$ is the shear gradient, ranging between about 0.05 and 0.25. The shear parameter can be interpreted simply as the difference in the ambient velocity on the two sides of the sphere divided by the mean ambient flow speed relative to the sphere. For the vortex-sphere interaction problem, the effective shear parameter at the sphere location can be estimated from the difference of the vortex-induced velocity on the near and far sides of the sphere and written in terms of $S/D$ as

$$K = \frac{1+2(S/D)}{2(S/D)(1+S/D)}. \tag{3}$$

The range $0.05 \leqslant K \leqslant 0.25$ considered by Sakamoto and Haniu [29] corresponds approximately to variation of $S/D$ over the interval $3.6 \leqslant S/D \leqslant 19.5$ for the vortex-sphere interaction problem.

The effect of the vortex on the sphere wake is examined in the current paper for values of $S/D$ of 2 and 3, corresponding to a sphere Reynolds number in the range 1000–1500. For these values of $S/D$, the discussion in the previous paragraph suggests that the shear induced by the vortex has a strong effect on the sphere wake. An LIF photograph showing a cross-section of the sphere wake in the horizontal plane B is given in Fig. 5 for a case with $S/D = 2$ and $D/\sigma_0 = 4.3$. Cross-sections of the nose region of the hairpin loops are clearly visible for a distance of about four sphere diameters behind the sphere. Beyond this distance, the hairpin loops have drifted slightly in the vertical direction, so that the horizontal light sheet passes instead through one of the loop legs. The point of wake detachment from the sphere is noticeably shifted toward the primary vortex, corresponding to the high-velocity side of the sphere. The wake vortex loops are observed to both advect azimuthally around the primary vortex and to drift radially inwards toward the primary vortex. This radial drift, which eventually leads to an entrainment of the wake vortices into the primary vortex core, is consistent with the direction of the self-induced velocity of vortex loops of a single sign shed only from the high-velocity side of the sphere, as indicated by the results of Sakamoto and Haniu [29] for a sphere immersed in a uniform shear flow. Similar inward radial drift of the secondary vortex structures is observed in the computations of vortex-cylinder interaction by Gossler [30].

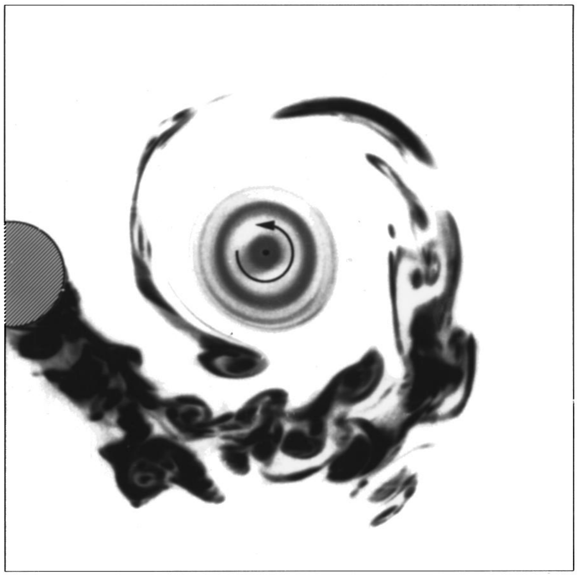

Fig. 5 LIF photograph in the horizontal plane $B$ showing the sphere wake entrainment into the primary vortex core for a case with $D/\sigma_0 = 4.3$ and $S/D = 2$

A schematic diagram showing the form of a single loop-like secondary vortex structure as it wraps around the primary vortex, as well as the definitions of various parameters used to characterize the secondary vorticity structure, is given in Fig. 6. The experimentally observed values of vortex loop radial drift rate varies from between 4–7 times the measured maximum radial velocity of the vortex without the sphere present (see Section 2), so this radial drift must be controlled by the flow induced by the wake vortex loops. The inward drift of the wake vortex loops appears to be led by the loop nose, which is the region with greatest curvature of the vortex lines and hence the largest self-induced velocity. As the nose of a vortex loop propagates radially inward, it encounters greater azimuthal velocity than do points along the loop legs. This difference in azimuthal velocity with radial position gives rise to stretching of the vortex loops, resulting over time in elongation of the loops, increase in loop spacing, and decrease in loop core cross-sectional area.

A heuristic model for the radial drift rate of the secondary vortex loops can be formulated using the local-induction approximation (LIA) to write

$$\frac{dR}{dt} \cong -\frac{\Gamma_S \kappa}{4\pi}[\ln(8/\kappa\sigma_S) + B], \tag{4}$$

where $B$ is an O(1) quantity that in LIA is assumed to be small in comparison to the logarithmic term in (4) (Arms and Hama [31]).

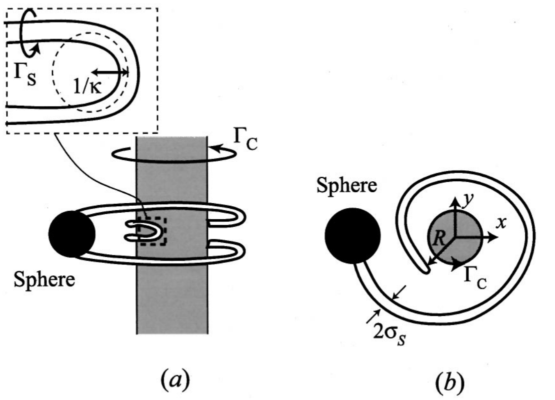

**Fig. 6 Schematic diagram showing the loop-like form of the secondary vortex structures and the parameters $\sigma_S$, $\Gamma_S$, $\kappa$, and $R$ used to characterize the secondary vortex entrainment into the primary vortex: (*a*) side view, (*b*) top view**

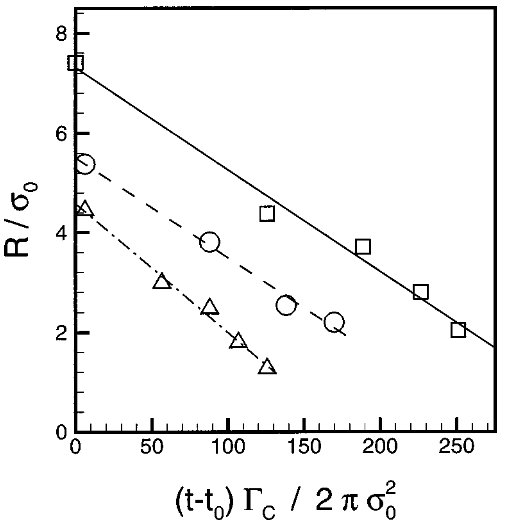

**Fig. 7 Experimental data for variation of radial position $R(t)$ of the nose of a wake loop from the primary vortex center and the best-fit lines for cases with $S/D=2$ and three different values of $D/\sigma_0$: 4.2 (circles), 5.6 (triangles), 8.5 (squares)**

The loop nose curvature $\kappa$ is affected both by the axial self-induced velocity due to curvature of the loop legs from wrapping around the primary vortex and by the stretching of the loop during the entrainment process. The first of these effects tends to decrease $\kappa$ while the second tends to increase $\kappa$. The flow visualization experiments suggest that $\kappa$ remains approximately constant as the loops wrap around the primary vortex. Variation of the loop core radius during entrainment is not significant since this term appears only in the integrand of the logarithm in (4).

If we therefore assume that the right-hand side of (4) is approximately constant during entrainment of the vortex loop, the radial position $R(t)$ of the wake loop should decrease linearly in time. This simple model neglects both the velocity induced by other vortex loops in the wake and the velocity induced by the azimuthal vorticity field within the primary vortex. Nevertheless, the assumption of linear variation of $R$ with time is in good agreement with the experimental data for all cases examined for values of $R$ between the initial value and about 1–2 times the core radius of the primary vortex. For example, typical entrainment data for the wake vortex loops is shown in Fig. 7 for cases with $S/D=2$ and three different values of $D/\sigma_0$. We note that the initial time for data recording, $t_0$, differs for the different cases studied, so only the slope of the data in this figure is significant. For values of $R/\sigma_0$ less than about 1.5, significant deviation from the linear variation is observed, which is believed to be due to a combination of the effect of strong curvature of the loop legs from wrapping around the primary vortex and the effect of velocity induced by azimuthal vorticity generated within the primary vortex.

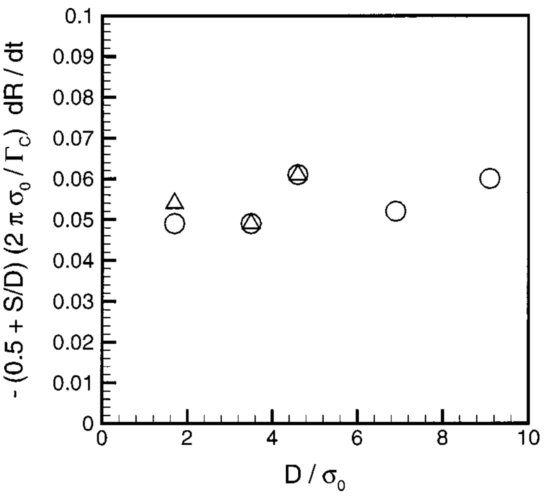

**Fig. 8 Plot of experimental data for the dimensionless entrainment rate as a function of $D/\sigma_0$. Cases with $S/D=2$ are denoted by a circle, and cases with $S/D=3$ are denoted by a triangle.**

The circulation $\Gamma_S$ of a secondary vortex loop for sufficiently large values of $S/D$ is expected to be proportional to the product of the mean velocity past the sphere $U_S=\Gamma_C/[2\pi(2+0.5D)]$ and the sphere diameter $D$. Dividing $dR/dt$ by $U_S(D/\sigma_0)$ yields a dimensionless radial drift rate that is expected to vary only as a function of $D/\sigma_0$. The dimensionless radial drift rate, plotted versus $D/\sigma_0$ in Fig. 8, is found to vary between 0.048 and 0.062 without any perceptible variation with $D/\sigma_0$ for the different experimental cases considered in the present study.

## 4 Effect of Sphere Wake on Vortex

As the secondary vortex loops wrap around the primary vortex, they induce stretching of the primary vortex core in the region in-between the loop legs and axial compression of the primary vortex outside of this region. This axial stretching/compression results in thinning of the primary vortex core in-between the two loop legs and bulging of the core on either side of the loop legs. For cases where $S/D$ is large, the wake loops are weak compared to the primary vortex and they have only a small effect on the primary vortex, accumulating over a long time to form a sheath of weak turbulence surrounding the primary vortex core. The loops in this case cause small perturbation waves on the outer surface of the primary vortex core, but have no dramatic effect on the vortex. A LIF photograph showing a cross-section in the vertical plane A for a case with weak wake loops is given in Fig. 9(*a*) (for $S/D=3$ and $D/\sigma_0=4.3$). The labels 1–3 in this figure identify three pairs of cross-sections of a single wake vortex loop, where cross-section pair 3 has made one full rotation and cross-section pair 2 has made one-half rotation more than cross-section pair 1 around the primary vortex. Each cross-section pair contains two patches, indicating cross-sections of the two loop legs with vorticity orientated in opposite directions. As the loops begin to move into the outer regions of the primary vortex core, the axial flow within the primary vortex advects the loops downward. The pronounced decrease in core radius as the loop wraps around the primary vortex is clearly evident in this figure. The separation distance between the legs of the loops appears to remain on the order of the sphere diameter. A close-up view of the interaction of a single loop with

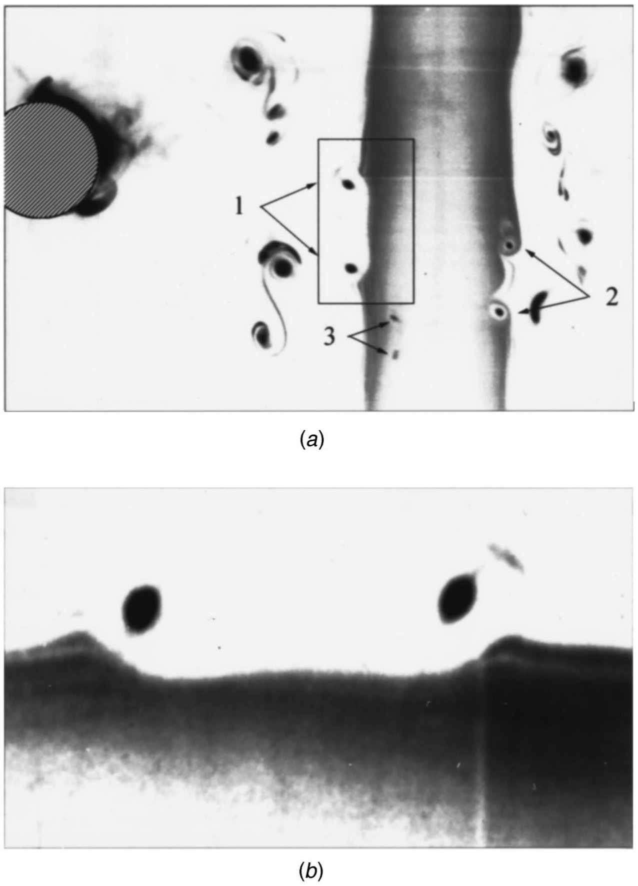

**Fig. 9 LIF photograph showing a cross-section of the wake vortices in the vertical plane *A* for a case with $D/\sigma_0=4.3$ and $S/D=3$. Figure 9(*a*) shows an overview with three cross-sections of a wake loop and Fig. 9(*b*) shows a close-up of the region marked by a rectangle in (*a*) showing the primary vortex response to a single cross-section of the loop.**

the primary vortex is shown in Fig. 9(*b*) for the part of the flow in Fig. 9(*a*) marked by a rectangle. The thinning of the primary vortex in-between the two cross-sections of the loop legs and the vortex bulging just outside of the loop legs is clearly observed in this figure, although the amount of variation in vortex core area is small because the loop strength is weak compared to the strength of the primary vortex.

As $S/D$ decreases, the wake loop strength correspondingly increases. For example, a LIF photograph of a flow cross-section in the vertical plane A is shown in Fig. 10 for a case with $S/D=2$ and $D/\sigma_0=4.3$. Two cross-section pairs of a wake vortex loop are observed, with one located on either side of the primary vortex. The response of the primary vortex is qualitatively similar to that shown for weak wake loops in Fig. 9, although the vortex thinning and bulging is more pronounced due to the fact that the wake loops are stronger. Also, fluid appears to be ejected from the primary vortex and to wrap around the loop legs in certain cases, as observed for the upper right-hand loop cross-section in Fig. 10. The distance separating the loop legs increases with time due to the self-induced velocity caused by curvature of the legs around the primary vortex.

A sample of instantaneous PIV data for a cross-section of a secondary vortex loop leg, corresponding to the region marked by a rectangle in Fig. 10, is given in Fig. 11(*a*) for the velocity vectors and in Fig. 11(*b*) for the streamlines in the $r-z$ plane. The velocity cannot be resolved near the secondary vortex core center due to the combined effects of out-of-plane motion and high rotation rate. The strength of the vortex loop is obtained by drawing a circuit surrounding the core of the vortex loop and numerically integrating the tangential velocity component about this circuit. The circulation ratio $\Gamma_S/\Gamma_C$ is found to be $0.10\pm0.02$ for the case shown in Figs. 10–11, for which $S/D=2$ and $D/\sigma_0=4.3$. For a case with sphere diameter increased to $D/\sigma_0=8.4$, and $S/D$ maintained at 2, the circulation ratio increases to $\Gamma_S/\Gamma_C=0.18\pm0.02$. The reported uncertainty in $\Gamma_S$ is evaluated by repeating the circulation measurement for different circuits surrounding the loop core. In the case of weak sphere wake vortices (corresponding to large $S/D$), it is difficult to obtain PIV data for vertical cross-sections of the wake vortex loops due to the strong out-of-plane flow induced by the azimuthal velocity of the primary vortex. PIV measurements of the vortex loop cross-sections were

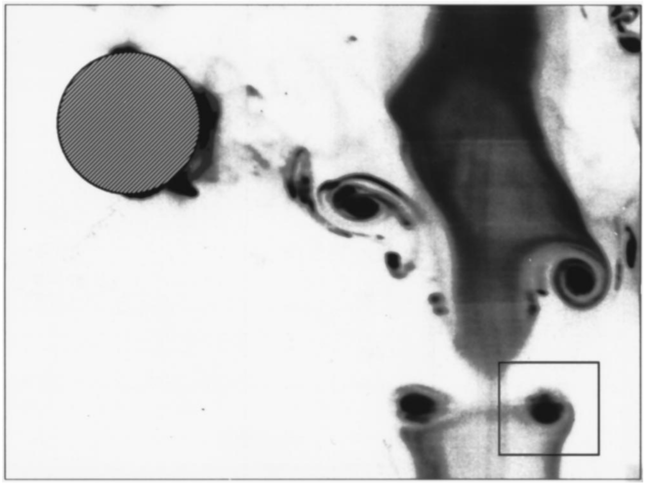

**Fig. 10 LIF photograph showing interaction of the primary vortex with a single strong vortex loop in the vertical plane A for a case with $D/\sigma_0=4.3$ and $S/D=2$**

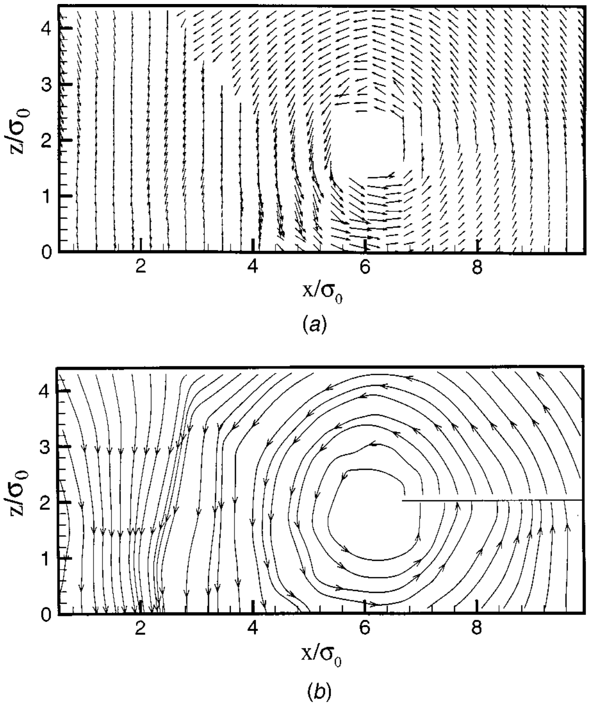

**Fig. 11 PIV data for the region marked by a rectangle in Fig. 10, showing (*a*) velocity vectors and (*b*) streamlines in the *x-z* plane**

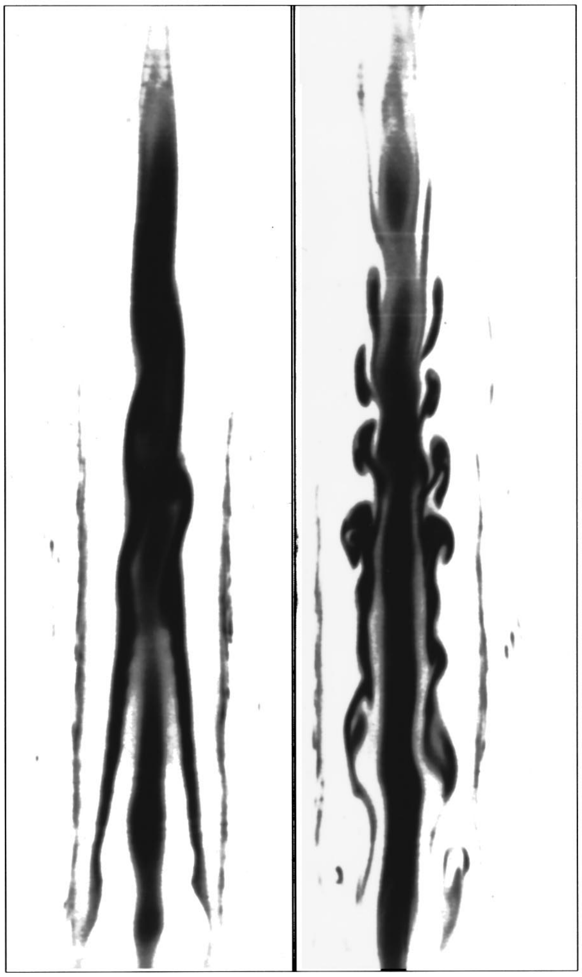

(*a*) (*b*)

**Fig. 12 LIF photographs showing an upward traveling vortex breakdown, for a case with $D/\sigma_0=4.3$ and $S/D=1$. The flow is illuminated in a vertical plane, where the bottom of the plane is 27 cm above the sphere center. In (*a*), the leading part of the breakdown is observed to have the form of a kink in the vortex, which is followed in (*b*) by organized turbulent structures wrapped around the inner part of the vortex core.**

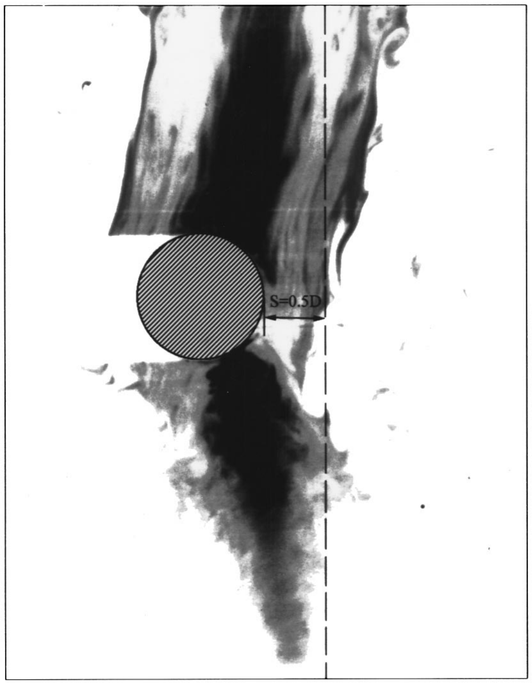

**Fig. 13 LIF photograph showing the vortex after attachment onto the sphere surface. The flow is illuminated in the vertical plane A, for a case with $D/\sigma_0=4.3$ and $S/D=0.5$. A dashed line indicates the axis of the undisturbed vortex.**

successful only for cases with fairly strong wake vortex loops, for which the velocity induced by the loop is sufficiently large compared to the azimuthal velocity induced by the primary vortex.

For cases with sufficiently strong vortex loops, the primary vortex is observed to respond to the velocity field induced by the wake vortices by formation of a traveling vortex breakdown that propagates upward on the vortex. LIF photographs showing the cross-section of the primary vortex during and immediately after passage of the breakdown are shown in Fig. 12(*a*,*b*) for a case with $S/D=1$ and $D/\sigma_0=4.3$. In this figure, the flow is illuminated in a vertical plane that is raised above the sphere, such that the bottom of the photograph is located at a distance of 27 cm above the sphere center. The vortex breakdown initially has the form of a sudden spiral kink in the primary vortex, as shown in Fig. 12(*a*). Behind the spiral kink, double helical oscillations are observed that degenerate into turbulence wrapped around a central columnar vortex. A vertical cross-section in Fig. 12(*b*) shows organized turbulent structures wrapped around the primary vortex just after passage of the vortex breakdown spiral. Data for vortex breakdown propagation speeds are given in Table 1 for cases with $D/\sigma_0=4.3$ and different values of $S/D$. The breakdown speed is obtained by measuring the distance traveled by the spiral kink using a video camera over 3–4 video frames, and the uncertainty in propagation speed measurement is estimated to be less than 2 percent. Cases with no vortex breakdown sometimes exhibit small-amplitude bending or axisymmetric waves on the vortex upstream of the sphere position, with amplitude on the order of 10–20 percent of the vortex core radius. These waves could be clearly distinguished from cases with vortex breakdown, for which there exist large-amplitude helical waves on the vortex core with amplitude on the order of 1–3 times the core radius, and subsequent degeneration of these waves into turbulence. Spiral breakdown forms similar to that observed in the current experiments have been reported by numerous other investigators for delta wing vortices and swirling flow in tubes (see review articles by Hall [32] and Leibovich [33]). Traveling breakdowns similar to that observed in the current experiments are examined in previous theoretical and experimental work on vortex-blade interaction by Marshall [34], Krishnamoorthy and Marshall [35], and Marshall and Krishnamoorthy [36].

**Table 1 Data for propagation speed *W* of the upward propagating vortex breakdown induced by the sphere wake vorticity for experiments with $D/\sigma_0=4.3$**

| $S/D+0.5$ | $2\pi\sigma_0 W/\Gamma_C$ |
|---|---|
| 0 | 0.41 |
| 0.5 | 0.30 |
| 1.0 | 0.29 |
| 1.5 | 0.25 |

When the sphere is brought very close to the primary vortex, the primary vortex is found to become attracted to the sphere and may even attach to the sphere surface. The primary vortex attachment to the sphere typically occurs a few seconds after the sphere is brought to rest and lasts for a period of 2–3 seconds. After this time, the primary vortex detaches from the sphere and reforms along its initial axis in front of the sphere, exhibiting large-amplitude bending oscillations near the sphere leading edge. A

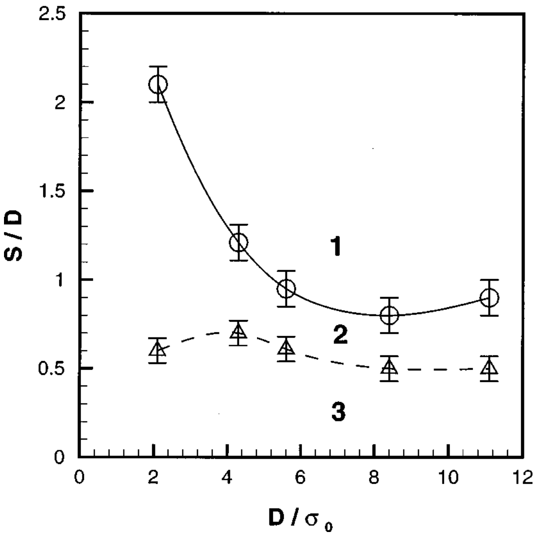

**Fig. 14 Regime plot summarizing the occurrence of breakdown of the primary vortex (circles) due to interaction with the sphere wake and intermittent vortex attachment to the sphere (triangles). Best-fit solid and dashed curves are drawn to indicate three different flow regimes: (1) no vortex breakdown or attachment to sphere, (2) vortex breakdown but no attachment to sphere, (3) both vortex breakdown and attachment to sphere. Experimental uncertainty is indicated by error bars attached to the data points.**

LIF photograph in the vertical plane A showing an example of vortex attachment to the sphere is given in Fig. 13 for a case with $S/D=0.5$ and $D/\sigma_0=4.3$. The initial axis of the primary vortex is indicated in this figure by a dashed line. The axial flow within the primary vortex core passes around the sphere in order to reach the lower half of the primary vortex core. In all cases examined for which the primary vortex attaches to the sphere, a traveling breakdown propagates upward on the primary vortex and the vortex core radius is significantly greater above than below the sphere.

The apparent primary vortex attraction to the sphere observed in our experiments is similar to that predicted from inviscid theory by Dhanak [10] and Pedrizzetti [12]. This inviscid attraction occurs because the vortex is deflected to one side by the induced velocity from the vortex image in the presence of the sphere. The side deflection leads to curvature of the vortex filament, which generates a self-induced velocity that drives the vortex into the sphere. While this mechanism may underlie the observed vortex attraction to the sphere, we suspect the actual vortex response to be quite a bit more complex. In particular, when the sphere is placed close to the primary vortex, its wake is quite strong. The wake vortices are observed to impact back onto the front end of the sphere after one rotation around the primary vortex, forming a donut-shape annulus of wake vorticity. The role that the sphere wake plays in modifying the primary vortex attraction to the sphere is complex and not yet understood.

The conditions for onset of breakdown of the primary vortex and of attachment of the vortex to the sphere are indicated in Fig. 14 in the space of the two parameters $S/D$ and $D/\sigma_0$. The primary vortex response to the sphere is categorized in this map in terms of three regimes. In regime 1, the sphere is sufficiently distant from the vortex that neither vortex breakdown nor attachment to the sphere occur. In regime 2 only vortex breakdown occurs, and in regime 3 both breakdown and intermittent vortex attachment to the sphere occur. The critical value of $S/D$ for onset of vortex breakdown is found to decrease rapidly with increase in $D/\sigma_0$ for $D/\sigma_0<6$, but to asymptote to $(S/D)_{12}\cong 0.8\pm 0.1$ for $D/\sigma_0>6$. The critical value of $S/D$ for onset of vortex attachment to the sphere is nearly independent of $D/\sigma_0$, with $(S/D)_{23}\cong 0.6\pm 0.1$.

## 5 Conclusions

An experimental study has been performed of the interaction between an initially columnar primary vortex with the wake of a sphere decelerated to a fixed position within the flow field. The results are categorized using two dimensionless parameters formed from the vortex-sphere separation distance $S$, the sphere diameter $D$, and the vortex core radius $\sigma_0$. The sphere wake appears to have the form of a series of hairpin vortices that are entrained into the primary vortex core while rotating around the vortex. The wake entrainment rate is controlled by the self-induced velocity of the secondary wake vortex structures. The strength of the secondary vortices increases as the ratio $S/D$ decreases (for $S/D$ larger than about unity). Weak secondary vortices cause only small-amplitude waves on the primary vortex core, until after long time a turbulent sheath of vorticity originating from the sphere wake surrounds the primary vortex. For stronger secondary vortices, the primary vortex core exhibits substantial thinning in the region in-between the secondary vortex loop legs loops and bulging outside of this region. Sufficiently strong secondary vortices are observed to induce an upward propagating vortex breakdown on the primary vortex. The breakdown has the form of a spiral kink, followed by a double-helical oscillation that eventually breaks down into turbulence. For cases where the sphere is placed quite close to the primary vortex, the vortex becomes attracted to the sphere, resulting in an intermittent attachment of the primary vortex onto the sphere surface. Both onset of vortex breakdown and of vortex attachment to the sphere are mapped in the space of the two parameters $S/D$ and $D/\sigma_0$.

Typical applications of vortex interaction with wake-generating bodies occur in situations where the body is moving relative to the vortex. For instance, in a turbulent two-phase flow, the particles may have significant motion relative to an eddy if the Stokes number, based on the eddy length and velocity scales, is of order unity or greater. It would therefore be of interest in future work to examine the extent to which the results reported in the current paper can be extended to cases where the sphere is translated steadily past the vortex. Also, while most of the phenomena reported in the paper are believed to be essentially inviscid (once the vorticity is shed into the sphere wake), it would be of interest to examine modification of the observations reported here for sphere Reynolds numbers in-between the range 1000–4000 considered in the current study and the range 20–100 considered in the computations of Kim et al. [15]. Sphere Reynolds numbers in the range 100–1000 are of particular importance for many two-phase flow problems.

Despite the need for further work, the present results should be of use for assessing the effect of particle wakes on turbulent coherent structures in two-phase flow problems. For instance, if the maximum and mean values of the separation distance between a particle center and an energy-containing eddy are assumed to be approximately one-half and one-quarter, respectively, of the turbulence integral length scale $l$, then the parameter $S/D$ employed in the current experiments can be approximated as $S/D\cong 0.25(l/D)-0.5$. The experimental data compilation of Gore and Crowe [3] indicates that particle wakes will enhance the fluid turbulence if $D/l>0.1$, which using the above relationship implies $S/D<2$. This range of $S/D$ is observed in the present experiments to coincide with conditions where the sphere wake vortices have a significant influence on, and may possibly lead to breakdown of, the primary vortex. The present study therefore indicates that under conditions where the particle wakes enhance fluid turbulence, the wake vortices will have a significant effect on the coherent structures of the turbulent flow. This observation may have bearing, for instance, on the experimental findings of Rashidi et al. [37] for two-phase turbulent wall layers, who report that large particles act to increase the frequency of fluid ejections from the wall layer, thereby increasing the production of turbulent kinetic energy. Increased ejection frequency is consistent with the notion that the particle wake vortices act to decrease the length and time scales of the turbulent coherent structures, either by directly inducing breakup of the turbulent structures or by inducing large perturbations of these structures, which enhance the existing instabilities of the large-scale turbulence.

## Acknowledgments

The authors thank Dr. S. Krishnamoorthy for his assistance in setting up the experiments and data acquisition systems. Funding for this research was provided by the U.S. Army Research Office under grant number DAAH04-96-1-0081 to The University of Iowa. Dr. T. L. Doligalski is the program manager.

## Nomenclature

$A$ = vortex axial flow parameter $[A \equiv 2\pi\sigma_0 w_0/\Gamma_C]$
$B$ = O(1) parameter in the local induction approximation
$D$ = sphere diameter
$G$ = shear gradient
$H$ = inner cylindrical tank diameter
$K$ = shear parameter $[K \equiv GD/U_S]$
$l$ = turbulence integral length scale
$r$ = distance from center of primary vortex $[r \equiv (x^2 + y^2)^{1/2}]$
$R$ = distance between secondary vortex nose and primary vortex axis
$\mathrm{Re}_S$ = sphere Reynolds number $[\mathrm{Re}_S \equiv U_S D/\nu]$
$\mathrm{Re}_V$ = vortex Reynolds number $[\mathrm{Re}_V \equiv \Gamma_C/\nu]$
$S$ = vortex-sphere separation distance
$t$ = time
$U_S$ = velocity induced by primary vortex at sphere center $[U_S \equiv \Gamma_C/2\pi(S+0.5D)]$
$w_0$ = average primary vortex axial velocity
$w_{\max}$ = maximum primary vortex axial velocity
$W$ = vortex breakdown propagation speed
$\Gamma_C$ = primary vortex strength
$\Gamma_S$ = secondary vortex strength
$\kappa$ = secondary vortex loop nose curvature
$\nu$ = kinematic viscosity
$\sigma_0$ = primary vortex core radius, based on azimuthal velocity
$\sigma_1$ = primary vortex core radius, based on axial velocity
$\sigma_S$ = secondary vortex core radius

## References

[1] Sheridan, P. F., and Smith, R. F., 1980, ''Interactional Aerodynamics—A New Challenge to Helicopter Technology,'' J. Am. Helicopter Soc., **25**, No. 1, pp. 3–21.
[2] Crowe, C. T., Troutt, T. R., and Chung, J. N., 1996, ''Numerical Models for Two-Phase Turbulent Flows,'' Annu. Rev. Fluid Mech., **28**, pp. 11–43.
[3] Gore, R. A., and Crowe, C. T., 1989, ''Effect of Particle Size on Modulating Turbulence Intensity,'' Int. J. Multiphase Flow, **15**, pp. 279–285.
[4] Rockwell, D., 1998, ''Vortex-Body Interactions,'' Annu. Rev. Fluid Mech., **30**, pp. 199–229.
[5] Doligalski, T. L., Smith, C. R., and Walker, J. D. A., 1994, ''Vortex Interactions With Walls,'' Annu. Rev. Fluid Mech., **26**, pp. 573–616.
[6] Kim, J. M., and Komerath, N. M., 1995, ''Summary of the Interaction of a Rotor Wake With a Circular Cylinder,'' AIAA J., **33**, No. 3, pp. 470–478.
[7] Krishnamoorthy, S., and Marshall, J. S., 1998, ''Three-Dimensional Blade-Vortex Interaction in the Strong Vortex Regime,'' Phys. Fluids, **10**, No. 11, pp. 2828–2845.
[8] Liou, S. G., Komerath, N. M., and McMahon, H. M., 1990, ''Measurement of the Interaction Between a Rotor Tip Vortex and a Cylinder,'' AIAA J., **28**, No. 6, pp. 975–981.
[9] Krishnamoorthy, S., Gossler, A. A., and Marshall, J. S., 1999, ''Normal Vortex Interaction With a Circular Cylinder,'' AIAA J., **37**, No. 1, pp. 50–57.
[10] Dhanak, M. R., 1981, ''Interaction Between a Vortex Filament and an Approaching Rigid Sphere,'' J. Fluid Mech., **110**, pp. 129–147.
[11] Moore, D. W., and Saffman, P. G., 1972, ''The Motion of a Vortex Filament With Axial Flow,'' Philos. Trans. R. Soc. London, Ser. A, **272**, pp. 403–429.
[12] Pedrizzetti, G., 1992, ''Close Interaction Between a Vortex Filament and a Rigid Sphere,'' J. Fluid Mech., **245**, pp. 701–722.
[13] Knio, O. M., and Ting, L., 1997, ''Vortical Flow Outside a Sphere and Sound Generation,'' SIAM (Soc. Ind. Appl. Math.) J. Appl. Math., **57**, pp. 972–981.
[14] Minota, T., Kambe, T., and Murakami, T., 1988, ''Acoustic Emission From Interaction of a Vortex Ring With a Sphere,'' Fluid Dyn. Res., **3**, pp. 357–362.
[15] Kim, I., Elghobashi, S., and Sirignano, W. A., 1995, ''Unsteady Flow Interactions Between an Advected Cylindrical Vortex Tube and a Spherical Particle,'' J. Fluid Mech., **288**, pp. 123–155.
[16] Kim, I., Elghobashi, S., and Sirignano, W. A., 1997, ''Unsteady Flow Interactions Between a Pair of Advected Vortex Tubes and a Rigid Sphere,'' Int. J. Multiphase Flow, **23**, No. 1, pp. 1–23.
[17] Melander, M. V., and Hussain, F., 1993, ''Coupling Between a Coherent Structure and Fine-Scale Turbulence,'' Phys. Rev. E, **48**, pp. 2669–2689.
[18] Miyazaki, T., and Hunt, J. C., 2000, ''Linear and Nonlinear Interactions Between a Columnar Vortex and External Turbulence,'' J. Fluid Mech., **402**, pp. 349–378.
[19] Marshall, J. S., and Beninati, M. L., 2000, ''Turbulence Evolution in Vortex-Dominated Flows,'' *Advances in Fluid Mechanics*, Vol. 25, *Nonlinear Instability, Chaos, and Turbulence II*, Debnath, L., and Riahi, D. N., eds., WIT Press, Southampton, England, pp. 1–40.
[20] Marshall, J. S., 1997, ''The Flow Induced by Periodic Vortex Rings Wrapped Around a Columnar Vortex Core,'' J. Fluid Mech., **345**, pp. 1–30.
[21] Marshall, J. S., 1993, ''The Effect of Axial Pressure Gradient on Axisymmetrical and Helical Vortex Waves,'' Phys. Fluids A, **5**, pp. 588–599.
[22] Achenbach, E., 1974, ''Vortex Shedding From Spheres,'' J. Fluid Mech., **62**, No. 2, pp. 209–221.
[23] Magarvey, R. H., and Bishop, R. L., 1961, ''Transitional Ranges for Three-Dimensional Wakes,'' Can. J. Phys., **39**, pp. 1418–1422.
[24] Magarvey, R. H., and MacLatchy, C. S., 1965, ''Vortices in Sphere Wakes,'' Can. J. Phys., **43**, pp. 1649–1656.
[25] Sakamoto, H., and Haniu, H., 1990, ''A Study on Vortex Shedding From Spheres in a Uniform Flow,'' ASME J. Fluids Eng., **112**, pp. 386–392.
[26] Taneda, S., 1956, ''Experimental Investigation of the Wake Behind a Sphere at Low Reynolds Numbers,'' J. Phys. Soc. Jpn., **11**, No. 10, pp. 1104–1108.
[27] Tomboulides, A. G., Orszag, S. A., and Karniadakis, G. E., 1993, ''Direct and Large-Eddy Simulation of Axisymmetric Wakes,'' AIAA paper AIAA-93-0546.
[28] Johnson, T. A., and Patel, V. C., 1999, ''Flow Past a Sphere up to a Reynolds Number of 300,'' J. Fluid Mech., **378**, pp. 19–70.
[29] Sakamoto, H., and Haniu, H., 1995, ''The Formation Mechanism and Shedding Frequency of Vortices From a Sphere in Uniform Shear Flow,'' J. Fluid Mech., **287**, pp. 151–171.
[30] Gossler, A. A., 1999, ''A Tetrahedral Element Lagrangian Vorticity Method With Application to Vortex-Cylinder Interaction,'' Ph.D. dissertation, University of Iowa, Iowa City, Iowa.
[31] Arms, R. J., and Hama, F. R., 1965, ''Localized-Induction Concept on a Curved Vortex and Motion of an Elliptic Vortex Ring,'' Phys. Fluids, **8**, No. 4, pp. 553–559.
[32] Hall, M. G., 1972, ''Vortex Breakdown,'' Annu. Rev. Fluid Mech., **4**, pp. 195–218.
[33] Leibovich, S., 1983, ''Vortex Stability and Breakdown: Survey and Extension,'' AIAA J., **22**, No. 9, pp. 1192–1206.
[34] Marshall, J. S., 1994, ''Vortex Cutting by a Blade. Part I. General Theory and a Simple Solution,'' AIAA J., **32**, No. 6, pp. 1145–1150.
[35] Krishnamoorthy, S., and Marshall, J. S., 1994, ''An Experimental Investigation of 'Vortex Shocks','' Phys. Fluids, **6**, No. 11, pp. 3737–3741.
[36] Marshall, J. S., and Krishnamoorthy, S., 1997, ''On the Instantaneous Cutting of a Columnar Vortex With Non-Zero Axial Flow,'' J. Fluid Mech., **351**, pp. 41–74.
[37] Rashidi, M., Hetsroni, G., and Banerjee, S., 1990, ''Particle-Turbulence Interaction in a Boundary Layer,'' Int. J. Multiphase Flow, **16**, No. 6, pp. 935–949.

**D. Schinas**

**D. S. Mathioulakis**
Assistant Professor,
e-mail: mathew@fluid.mech.ntua.gr

Department of Mechanical Engineering,
Fluids Section,
National Technical University of Athens,
Zografos 15710, Greece

# Pulsating Flow in a 90 Degree Bifurcation

*The pulsating flow field in a 90 deg bifurcation was examined by performing LDV measurements in a model with square cross-sections and equal branch flow rates. The three-dimensional separation zones of both branches were studied revealing details of their temporal evolution. During acceleration the flow was attached, but close to the peak flow condition, separation initiated at both branches. The basic feature of the reverse flow zones at a given time instant was that these shrank streamwise in a direction perpendicular to the bifurcation plane and grew at the symmetry plane. Flow instabilities were strong in the horizontal branch during acceleration, in contrast to the vertical branch in which these appeared during deceleration. Comparison of this flow field for a particular time instant with the flow field under steady inlet conditions and similar Re, revealed that for the steady case the flow separated in the horizontal branch upstream of the unsteady case.* [S0098-2202(00)03002-9]

## Introduction

The unsteady flow in a curved duct or a duct branch constitutes an interesting fluid mechanics problem, due to the formation of time dependent separation zones associated with vortex shedding, time varying shear stresses, as well as strong secondary motions. From a practical point of view, the study of such flows assists in gaining more understanding about the origin of vascular diseases like atherosclerosis which happens to occur at branches and curves of the human circulatory system.

Previous work has been done mainly in vitro at duct branches of various angles between parent and daughter tubes and various flow waveforms. The shape of the branches has been normally based on models of blood vessels like the aorta, carotid etc. with circular or rectangular cross sections, whereas the inlet flow waveforms are pulsating (e.g., sinusoidal with a nonzero mean) or physiologic ones.

Fernandez et al. [1] studied numerically the steady and unsteady flow in a symmetric bifurcation of rectangular cross section giving emphasis upon the separated region. Siouffi et al. [2] using a pulsed Doppler ultrasonic velocimeter in a symmetric bifurcation of rectangular cross-sections realized that during acceleration the maximum of the velocity in a branch was shifted toward the center of the cross section in contrast to the highly skewed profiles of the steady case. They also found that the downstream influence of the branch was damped out by the unsteadiness, compared to steady case results. Rindt et al. [3] validated a computer code with LDA data obtained in a two-dimensional bifurcation of the human carotid artery. Using flow visualization and three-dimensional LDA measurements Naiki et al. [4] found in an aortic bifurcation model that during acceleration the flow was stabilized, in contrast to the highly disturbed flow during deceleration. Sung and Yoganatham [5] employing a human pulmonary model found that the velocity profiles under physiologic waveforms were quite uniform during acceleration tending to become skewed at peak systole and in the deceleration phase, during which the secondary flow was significant. Ku and Giddens [6] in a carotid bifurcation model found that flow separation was retarded at the bifurcation apex when acceleration took place, in contrast to steady flow which separated under the same Re. Using flow visualization in an abdominal aorta model, with its main branches under rest and exercise conditions, the flow patterns were identified during all phases of a physiologic waveform, being quite complex during the deceleration phase (Petersen et al. [7]). Moore et al. [8] in a similar model, employing magnetic resonance imaging as velocimeter, found that during exercise conditions flow reversal was reduced, but the velocity profiles were more skewed due to the higher Dean number.

Wall shear stress measurements were carried out by Yawaguchi and Kohtoh [9] in a 45 deg curved bifurcation under steady and pulsatile conditions by using an electrochemical method. In the branch wall of the smaller radius of curvature the shear stresses under steady conditions were found to take smaller values than at the opposite wall (of higher radius) varying in the streamwise direction like a damped sine wave. The same tendency was also observed in the instantaneous shear stresses for the time varying case, but with higher excursions at maximum flow rate. A numerical study by Kawaguti and Hamano [10] focusing on the shear stress distribution in a 90 deg 2-D bend under pulsating conditions and low Re predicted an amplitude shear stress peak at the main duct a little upstream of the bifurcation apex. Perktold and Rappitsch [11] in a numerical study predicted the flow in a carotid bifurcation with rigid and distensible walls, which showed the separated regions on several cross sections, and more recently Perktold et al. [12] compared the numerical results with LDA measurements in a realistic coronary branch.

The objective of this work was to study experimentally the flow field in a 90 deg bifurcation under pulsating conditions. Although the most appropriate model for bioengineering applications would include circular ducts, it was decided to use square ducts instead. The simplicity of their shape would ease any comparisons with numerical predictions, allowing also comparisons with the flow field under steady conditions recorded in the same model. Moreover, the majority of the relevant published works include only two profiles in each cross sectional area passing through the center of the ducts. In the present work, the plane walls of the model allowed LDA measurements to be made in the whole cross-section, a necessary condition for the detailed description of this three-dimensional flow field.

## Experimental Procedure

This work constitutes an extension of a previous study, in which the flow field of a 90 deg bifurcation of square cross-sections ($40\times40$ mm$^2$) (see Fig. 1) was examined under steady inlet conditions (Mathioulakis et al. [19]). In order to minimize any flow disturbances entering the model, it was connected upstream to a straight square duct 2 m long, and the latter to the exit of a convergent nozzle of 25:1 contraction ratio attached to a settling chamber. In the present work, flow (water) entering the

---

Contributed by the Fluids Engineering Division for publication in the JOURNAL OF FLUIDS ENGINEERING. Manuscript received by the Fluids Engineering Division September 22, 1998; revised manuscript received February 26, 2000. Associate Technical Editor: D. R. Williams.

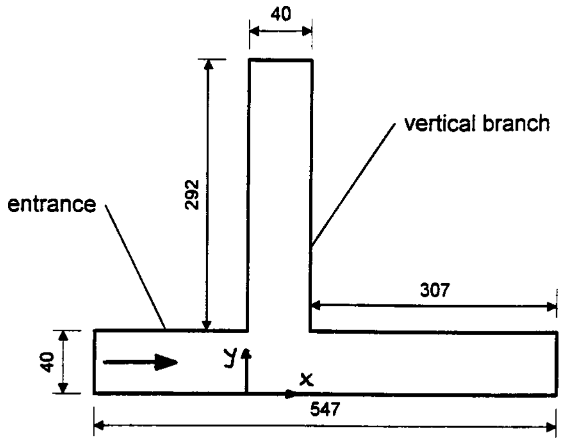

**Fig. 1 Bifurcation model (dimensions in mm) coordinate system**

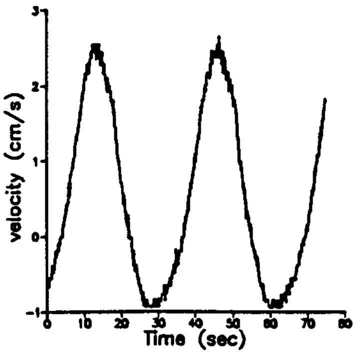

**Fig. 2 Typical velocity time-record at model's inlet**

model was time dependent, being increased and decreased via a rotating spherical valve which disturbed the flow established by gravity. The valve was located downstream of the model, and opened and closed in a periodic way by a PC controlled stepper motor (400 steps per revolution) and a 60:1 gear ratio speed-reducer. The high gear ratio was necessary for the smooth rotation of the valve about its closed position, for a total angle of 10 degrees. It should be noted that the flow was not significantly affected by the motion of the valve when it was open more than 10 degrees, due to low induced hydraulic losses. In order to make the flow vary harmonically as possible, the motion of the valve was adjusted, following a trial-and error-procedure, by changing the width and the number of pulses sent to the stepper motor controller. Figure 2 includes a typical velocity time record at the model inlet.

The axial velocity component was measured by a one component Laser Doppler Velocimeter, with a measuring volume estimated to be $100\times 600\,\mu$m with the longer dimension along the bisector of the laser beams (for more details see Mathioulakis et al. [19]). Measurements were taken at a grid of 81 points (4 mm apart), at each measuring station, which corresponded to a cross section of the duct. All measuring points are referred to a Cartesian coordinate system ($x$, $y$, $z$) as shown in Fig. 1, whose origin is located at the beginning of the bifurcation, with direction $z$ being normal to the bifurcation plane.

Before initiating the measurements in the bifurcation model, the pulsating flow field in a straight square duct of the same cross-section was studied. The period $T$, varied from 279.6 s to 11.15 s so that the Womersley parameter $\alpha(a=R\sqrt{\omega/\nu})$ where $R$ is the hydraulic radius, took values from 2.9 to 14.4. It was found from this study that for $\alpha=2.9$ the velocity profiles did not differ during acceleration and deceleration, so that the flow behaved essentially like a quasi-steady one. Increasing $\alpha$, caused the unsteadiness to become more pronounced. However, for high $\alpha$ (above 10), the flow tended to become uniform, with high values of the velocity gradient only close to the walls (see also McDonald [14] and Hughes and How [15]). Therefore, it was decided for the present study to use $\alpha=8.76$ or $T=32.7$ s which is a physiological value (Pedersen et al. [7] and Bharadvaj et al. [16]). The flow was not quasi-steady and the LDV could record the spatial velocity gradients in the selected measuring grid. The velocity signal digitized with a sampling rate of 10 Hz was conditionally averaged over 5 periods (Jin and Clark [17] suggest two periods to satisfy ergodicity for Re peak value of 1200) with time instant $t=0$ corresponding to a value close to the minimum flow rate. This rather small number of periods was a trade off between a reduction of the integration time and the smoothness of the obtained velocity profiles. Downstream of the bifurcation where flow instabilities were significant, time records were smoothed out before phase averaged contours were obtained. Maximum precision error for a 95 percent confidence level was of the order of ±4 mm/s, or 7.5 percent of maximum velocity.

Based on volume flow meters, inlet mean flow rate was 1210 ml/min ±2 percent while the mean flow rates of the two branches were equal within an uncertainty of ±3 percent. Performing a spatial integration of the velocity distribution at the model entrance, the flow peak was found to be equal to 2500 ml/min, namely, Re varied between 0 to 1150 with a mean value of 560. Based on ensemble averaged profiles at the entrance of the model the flow rate for 8 time instants within a period $T$ was calculated as follows:

| t/T | 1 | 2 | 3 | 4 | 5 | 6 | 7 | 8 |
|---|---|---|---|---|---|---|---|---|
| ml/min | 340 | 1251 | 2390 | 2500 | 1682 | 590 | 28 | 0.17 |

Velocity measurements were carried out at three regions in the model, namely at its entrance, its extension, referred to as the horizontal branch, and its vertical branch. Since preliminary measurements had shown that the upstream influence of the bifurcation was not significant, more attention was focused upon both branches of the bifurcation where the flow separated from the bottom of the horizontal branch ($y=0$) and the sharp bifurcation edge of the vertical branch ($x=0$, $y=40$ mm). Therefore, in the horizontal branch six stations were examined from $x=0$ to $x=50$ mm, being 10 mm apart while in the vertical one four stations, namely at $y=44$ mm, 56 mm, 67 mm and 80 mm were examined.

## Results and Discussion

**(a) Model Entrance and Horizontal Branch.** The unsteady character of the flow at the model entrance and its extension is depicted in Fig. 3 for three time instants, namely during acceleration ($t=3T/8$), flow peak ($t=4T/8$) and deceleration ($t=6T/8$). The phase-averaged axial velocity contours of Fig. 3(*a*) ($x=-160,20,40$ mm) show that there are no flow separation zones during acceleration, in contrast to flow peak (Fig. 3(*b*), $x=0,20,40$ mm) at which these appear at $x\geq 20$ mm, growing further during deceleration. It is important to notice that although the flow rate between time instants $3T/8$ and $4T/8$ increases only by 4.6 percent, there is a significant change of the flow field. Therefore in this unsteady flow it is the time dependent pressure gradient which controls the flow rather than the Reynolds number.

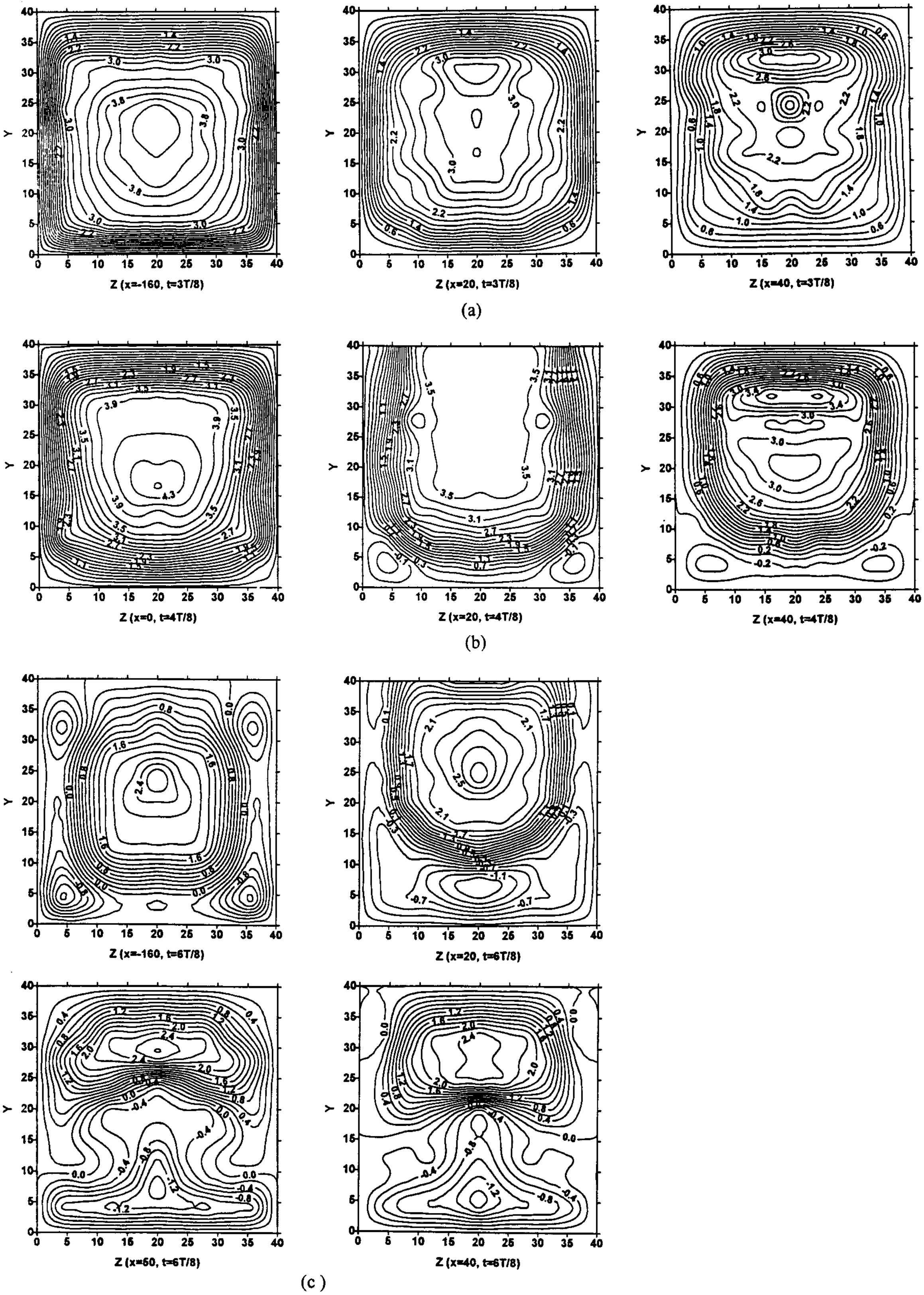

(a)

(b)

(c)

Fig. 3 Horizontal branch axial velocity contours (cm/s), (*a*) Flow acceleration, (*b*) flow peak, (*c*) Flow deceleration

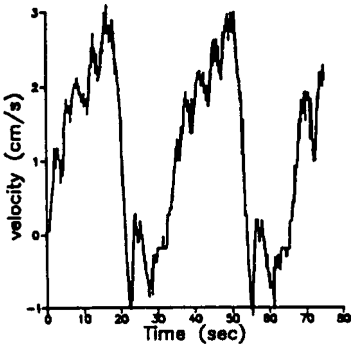

**Fig. 4 Horizontal branch. Perturbed velocity time record.**

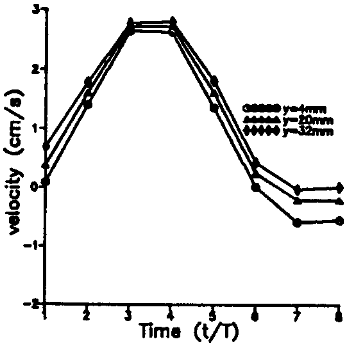

**Fig. 6 Entrance region. Near wall velocity time-records ($x=-10$ mm).**

Apparently, the imposed favorable pressure gradient for the acceleration of the fluid shadows the adverse pressure gradient due to the bifurcation itself, washing out any negative flow regions of the deceleration phase. This phenomenon of reattachment has been identified by others like Rindt et al. [3,18], Ku et al. [6], Perktold et al. [11]. At flow peak the flow in the entrance region is attached, while at $x=20$ mm it separates from both corners of the bottom wall and further downstream there are negative velocities across the whole width of the bottom wall.

During the deceleration phase (Fig. 3(*c*), $x=-160,20,40,50$ mm) not only do these separated regions grow, but there is also negative flow in the entrance region of the model and especially at the four corners of the duct. The most significant feature of the flow field for $x\geqslant 0$ is that at a given time instant the separated region close to the vertical walls ($z=0$, $z=40$ mm) is progressively reduced streamwise, in contrast to the middle section $z=20$ mm where this increases. More specifically, at station $x=10$ mm to $x=50$ mm this reverse flow region increased linearly from $y=8$ m to $y=24$ mm, with higher negative velocities at the midspan plane ($z=20$ mm). Due to these higher negative velocities, the flow accelerated in the remaining part of the cross sectional area, reducing the back flow in these regions. A similar behavior was recorded under steady inlet conditions for $\mathrm{Re}=1200$ (Mathioulakis et al. [19]) in the same model, in which downstream of $x=114$ mm the flow became positive over the whole cross section. It is clear that in this kind of flow field, separation and reattachment is a complex process. The three-dimensional character of steady laminar flow in rectangular bifurcations has been studied numerically by Neary et al. [20] where interesting topological features were revealed.

The time-records in the present study were perturbed in the region $x\geqslant 0$ (see Fig. 4) with a mean frequency of 0.4 Hz and especially during the acceleration phase. This is attributed to coherent vortices being generated at the separated region and shed during this phase, the existence of which was verified through flow visualization. However, it should be pointed out that the peak to peak velocity amplitude in this region was of the same order like that at the model entrance. Based on previous works treating two-dimensional unsteady external flows (Mezaris and Telionis [21], Mathioulakis and Telionis [22,13]) where the amplitude was magnified in the separated shear layers several times with respect to the freestream amplitude, it was expected to have a similar phenomenon in this configuration. However, the confinement of the flow between the four walls of the ducts and its strong three-dimensional character may give an explanation for the suppression of the velocity amplitude in this case.

The influence of the unsteadiness was examined through the phase-averaged profiles at the midspan plane ($z=20$ mm) in order to make comparisons with the steady case (Mathioulakis et al. [19]). Axial velocity profiles were drawn for $z=20$ mm and three time instants about the middle of the period (see Fig. 5, $x=10,20,30,40$ mm) which corresponded to about the same Re of steady case. We notice from this figure that the flow downstream of the bifurcation is attached until the flow peak is reached and then this separates from a point between $x=20$ and 30 mm (on plane $z=20$ mm), its region growing in an upstream direction as well as from the bottom to the ceiling of the duct. It should be mentioned that in the steady case the flow separated at $x=10$ mm, namely about 1/2 diameter upstream. Therefore, there is a solid indication that unsteadiness moves the separated regions downstream. The same observation has been made also in pulsating external flows of small amplitude (Mathioulakis and Telionis [13]). An estimate of the wall shear stress variation in time and space can be obtained from the closest to the wall (4 mm) velocity distribution. Although this distance is not so small (about 10 percent of the duct width) we believe that since the flow was laminar, shear stresses varied in proportion to these velocity changes. Fig-

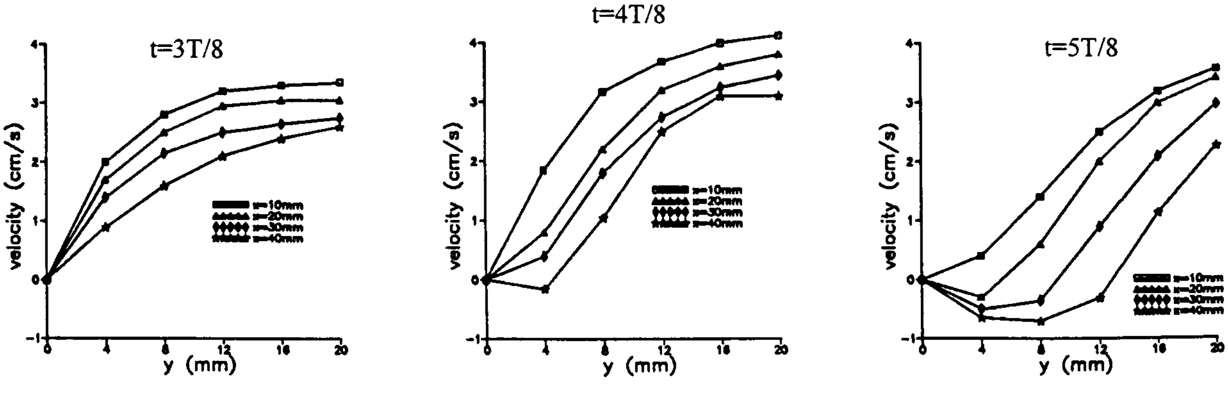

**Fig. 5 Horizontal branch. Instantaneous velocity profiles at $t=3,4,5\,T/8$ and $z=20$ mm.**

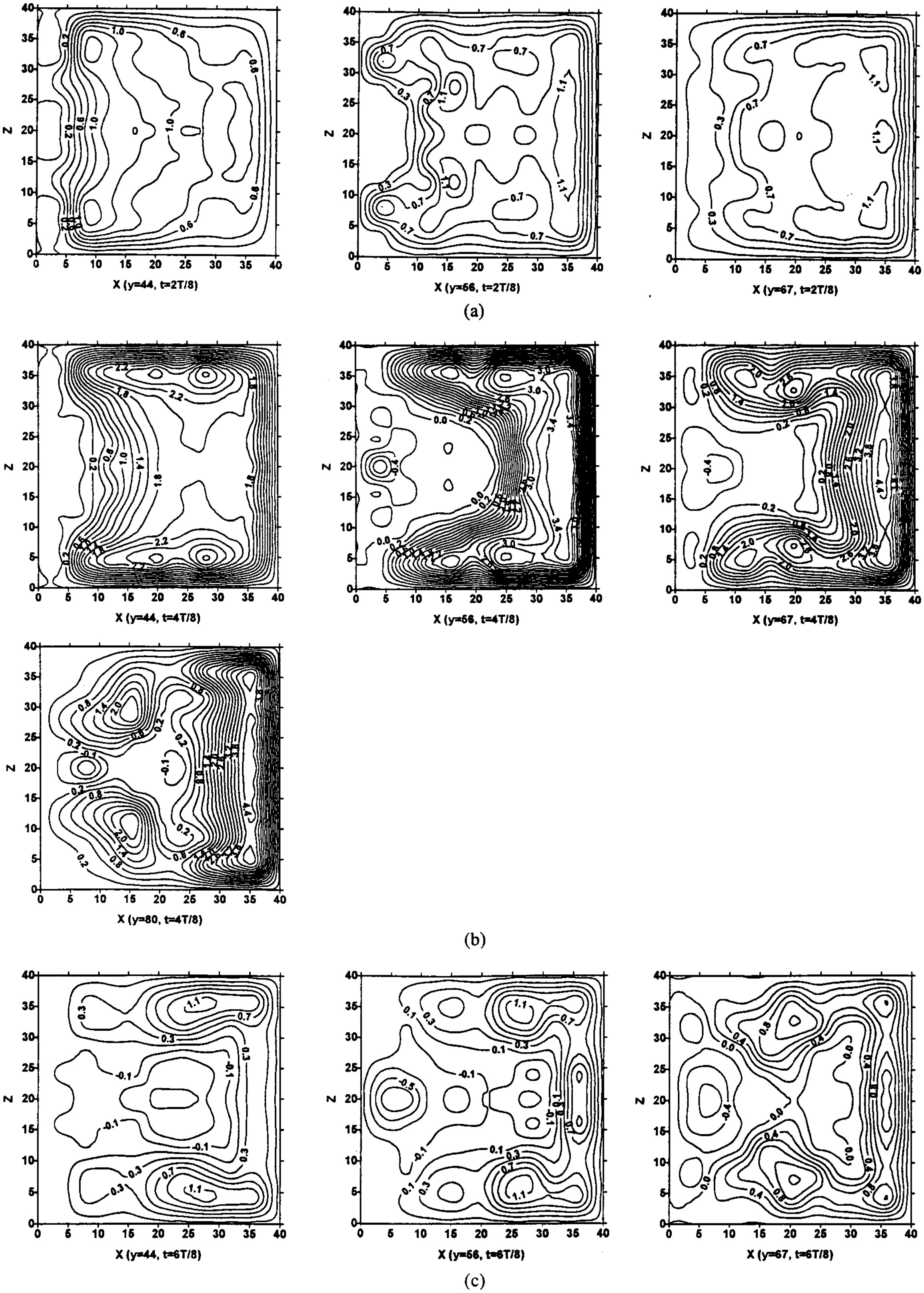

**Fig. 7 Vertical branch axial velocity contours (cm/s). (*a*) Flow acceleration, (*b*) flow peak, (*c*) flow deceleration.**

ure 6 includes three time records of the near wall velocity at $y=4$, 20 and 32 mm, a little upstream of the bifurcation ($x=-10$ mm). The conclusions drawn from this figure are: (a) there is an increase of the shear stresses from the bottom to the ceiling of the duct, (b) their spatial differences become minimum at flow peak, and (c) their amplitude does not differ significantly in space. The same tendencies were also found downstream of the bifurcation, at $x=10$ mm.

**(b) Vertical Branch.** Phase-averaged axial velocity con-

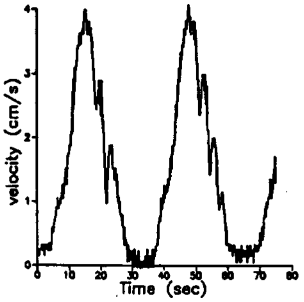

**Fig. 8 Vertical branch. Perturbed velocity time record.**

tours are shown for this branch in Fig. 7 during acceleration ($t=2T/8$), flow peak ($t=4T/8$) and deceleration ($t=6T/8$). It is interesting to notice that despite the 90 degree bending of the streamlines the flow during acceleration (Fig. 7(*a*), $y=44,56,67\,\mathrm{mm}$) is essentially attached, excluding a very thin region across the sharp bifurcation leading edge ($x=0$) where at stations $y=44$ mm and $y=56$ mm the flow is stagnant. At flow peak (Fig. 7(*b*), $y=44,56,67,80$ mm) and deceleration (Fig. 7(*c*), $y=44,56,67\,\mathrm{mm}$) reverse flow is present, as in horizontal branch. Namely, flow separates from the bifurcation sharp leading edge ($x=0$, $y=40\,\mathrm{mm}$), diverting the flow toward the remaining three walls of the tube where it exhibits higher velocities. As expected, the maximum of the velocities is located close to the bifurcation trailing edge ($x=40$ mm) due to centrifugal forces, in contrast to the horizontal branch which is closer to the duct center. A similar feature of the separated flow evolution in space like in horizontal branch happens here: namely, the reversed flow shrinks streamwise in a direction normal to the bifurcation plane, so that the flow becomes positive at the two corners of $x=0$ earlier than at the center of the cross-section. The only difference between the horizontal and vertical branch is that for the latter this process is stronger, which is most probably due to secondary velocities which provide momentum to the retarded fluid of the separated regions. Therefore the skewness of the profiles is diminished faster normal to the bifurcation plane ($z$) than along the radial direction ($x$), in the streamwise direction. Similar behavior was observed in the steady case, but there the skewness of the profiles was stronger.

The temporal variation of the velocity in the vertical branch was smooth only in a thin region close to the three walls where the flow was attached. In the remaining area the instabilities of the detached flow were predominant, especially during the deceleration phase. A characteristic velocity time record is shown in Fig. 8. The disturbed flow during deceleration has been also verified by others (Naiki et al. [4] Sung and Yoganatham [5], Pedersen et al. [7]). However, it should be reminded that in the present work quite the opposite was happening in the horizontal branch. This difference might be attributed to the secondary flow which is strong in this branch. According to the experimental evidence of Rieu et al. [23] in a symmetric bifurcation with rectangular cross-sections under pulsatile conditions, the secondary motion was enhanced during the deceleration phase, which might disturb the flow in our case as well.

According to the velocity profiles the shear stresses are expected to take high values at the three sides of the cross-section where the flow is attached, with the highest at the wall opposite of the bifurcation leading edge, being maximum at the peak of the flow. Similar conclusions are drawn from a recent numerical work by Shipkowitz et al. [24] which emphasized the wall shear stress distribution in four branches of a human aorta (iliac and renal branches). They predicted high stresses at the inner walls of the branches and lower at the outer ones.

## Conclusions

LDA measurements were performed in a 90 deg bifurcation square section model under pulsating inlet conditions with Re varying in the interval 0 to 1150, Womersley parameter 8.76 and equal branch flow rates. The main objective of this work was to present a detailed picture of this unsteady three-dimensional flow field, providing data for the whole cross-sectional area of the ducts, information which is missing in the majority of the published relevant works. Axial phase-averaged contours depicted the flow field at characteristic time instants within a period, namely during acceleration, flow peak, and deceleration. During acceleration the flow was attached in the parent tube and its extension although for similar Re but under steady conditions this was separated. At flow peak reversed flow zones appeared downstream of $x=0$, first at both corners of the bottom wall ($x=20$ mm) and further downstream negative flow covered the whole width of the bottom wall. In the deceleration phase back flow appeared upstream of the bifurcation at the four corners of the duct while downstream of this, a large portion of the lower part of the cross-section was covered by negative flow. The characteristic feature of the flow for this phase and $x>0$ is that the reversed flow region shrinks along the parallel to the bifurcation plane walls ($z=0$, $z=40\,\mathrm{mm}$) for increasing $x$ stations, while at the same time it expands at mid-plane ($z=20\,\mathrm{mm}$). A similar process was recorded for the steady case. Due to instabilities of the detached shear layers the velocity time records in the horizontal branch were disturbed including frequencies higher than the fundamental, especially during the acceleration phase, but the velocity amplitude was of the same order like the inlet one.

In the vertical branch where the flow turned an angle of 90 deg the flow field resembled the steady one, being less skewed. The flow, separated from the bifurcation leading edge, forced the fluid toward the remaining three walls of the cross-section. During the acceleration phase the flow was attached but at flow peak and later on it separated, forming a region of negative velocities whose width increased in both directions, in a plane normal to the axial flow of this branch until the end of the period. However, again like in horizontal branch, the separated region shrank streamwise in a direction normal to the bifurcation plane. Excluding a thin region close to the walls where the flow was varying in time smoothly, in the rest of the cross-section flow instabilities were significant. In contrast to the horizontal branch, here the instabilities appeared during the deceleration phase, probably due to enhancement of secondary motions during this phase. Finally, according to the near wall velocity values the shear stresses increased from the bottom to the ceiling for the horizontal branch and from the bifurcation leading edge to the opposite wall for the vertical branch.

Although the results of this work cannot be applied directly to haemodynamic applications mainly due to the noncircular shape of the ducts, it is noteworthy to observe that global flow characteristics had the same trends as in physiologic flows e.g., reverse flow zones and wall shear stresses temporal variation. Moreover, we believe that the simple geometry of the model provided an easier understanding of this unsteady flow field.

## Acknowledgements

This work was partly supported by the General Secretariat of Research and Technology of Greece in the context of the research program ''Haemodynamic Parameters in Arteriosclerosis.'' Thanks are also extended to the valuable criticism of the reviewers.

## References

[1] Fernandez, R. C., De Witt, K. J., and Botwin, M. R., 1976, ''Pulsatile flow through a bifurcation with applications to arterial disease,'' J. Biomech., **9**, pp. 575–580.

[2] Siouffi, M., Pelissier, R., Farahifar, D., and Rieu, R., 1984, ''The effect of unsteadiness on the flow through stenoses and bifurcations,'' J. Biomech., **17**, pp. 299–315.

[3] Rindt, C. C. M., Vosse, F. N. v. d., Steenhoven, A. A. v., and Janssen, J. D., 1987, ''A numerical and experimental analysis of the flow field in a two-dimensional model of the human carotid artery bifurcation,'' J. Biomech., **20**, No. 5, pp. 499–509.

[4] Naiki, T., Hayasi, K., and Takemura, S., 1995, ''An LDA and flow visualization study of pulsatile flow in an aortic bifurcation model,'' Biorheology, **32**, pp. 43–59.

[5] Sung, H-W., and Yoganatham, A. P., 1990, ''Axial flow velocity patterns in a normal human pulmonary artery model: Pulsatile in vitro studies,'' J. Biomech., **23**, pp. 201–214.

[6] Ku, D. N., and Giddens, D. P., 1987, ''Laser Doppler anemometer measurements of pulsatile flow in a model carotid bifurcation,'' J. Biomech., **20**, pp. 407–421.

[7] Pedersen, E. M., Yoganatham, A. P., and Lefebvre, X. P., 1992, ''Pulsatile flow visualization in a model of the human abdominal aorta and aortic bifurcation,'' J. Biomech., **25**, pp. 935–944.

[8] Moore, J. E., and Ku, D. N., 1994, ''Pulsatile velocity measurements in a model of the human abdominal aorta under simulated and postprandial conditions,'' ASME J. Biomech. Eng., **116**, pp. 107–111.

[9] Yamaguchi, R., and Kohtoh, K., 1994, ''Sinusoidal variation of wall shear stess in daughter tube through 45 deg branch model in laminar flow,'' J. Biomech. Eng., **116**, pp. 119–126.

[10] Kawaguti, M., and Hamano, A., 1980, ''Numerical study on bifurcating flow of a viscous fluid. II. Pulsatile flow,'' J. Phys. Soc. Jpn., **49**, pp. 817–824.

[11] Perktold, K., and Rappitsch, G., 1995, ''Computer simulation of local blood flow and vessel mechanics in a compliant carotid artery bifurcation model,'' J. Biomech., **28**, No. 7, pp. 845–856.

[12] Perktold, K., Hofer, M., Rappitsch, G., Loew, M., Kuban, B. D., and Friedman, M. H., 1998, ''Validated computation of physiologic flow in a realistic coronary artery branch,'' J. Biomech., **31**, pp. 217–228.

[13] Mathioulakis, D. S., and Telionis, D. P., 1989, ''Pulsating flow over an ellipse at an angle of attack,'' J. Fluid Mech., **204**, pp. 99–121.

[14] Mcdonald, D. A., 1974, *Blood Flow in Arteries*, textbook, Edward Arnold, London.

[15] Hughes, P. E., and How, T. V., 1994, ''Pulsatile velocity distribution and wall shear rate measurement using pulsed doppler ultrasound,'' J. Biomech., **27**, No. 1, pp. 103–110.

[16] Bharadvaj, B. K., Mabon, R. F., and Giddens, D. P., 1982, ''Steady flow in a model of the human carotid bifurcation, Part I-Flow visualization, Part 2-Laser-Doppler anemometer measurements,'' J. Biomech., **15**, pp. 349–378.

[17] Jin, W., and Clark, C., 1993, ''A correlation method for determining the number of sampling cycles required for pulsating flow analysis using LDA,'' J. Biomech., **27**, No. 9, pp. 1179–1181.

[18] Rindt, C. C. M., and Steenhoven, A. A. v., 1996, ''Unsteady flow in a rigid 3-D model of the carotid artery bifurcation,'' J. Biomech., **118**, pp. 90–96.

[19] Mathioulakis, D. S., Pappou, Th., and Tsangaris, S., 1997, ''An experimental and numerical study of a 90° bifurcation,'' Fluid Dyn. Res., **19**, pp. 1–26.

[20] Neary, V. S., and Sotiropoulos, F., 1996, ''Numerical investigation of laminar flows through 90-degree diversions of rectangular cross-section,'' Comput. Fluids, **25**, pp. 95–118.

[21] Mezaris, T. B., and Telionis, D. P., 1980, ''Visualization and measurement of separating oscillatory laminar flow,'' AIAA Paper 80–1420.

[22] Mathioulakis, D. S., and Telionis, D. P., 1987, ''Velocity and vorticity distributions in periodic separating laminar flow,'' J. Fluid Mech., **184**, pp. 303–333.

[23] Rieu R., Pelissier, R., and Deplano, V., 1990, ''Flow in rigid and arterial graft bifurcation models,'' Biomechanical Transport Processes, F. Mosora, ed., pp. 115–123.

[24] Shipkowitz, T., Rodgers, V. G. J., Frazin, L. J., and Chandran, K. B., 1998, ''Numerical study on the effect of steady axial flow development in the human aorta on local shear stresses in abdominal aortic branches,'' J. Biomech., **31**, pp. 995–1007.

**Ashraf Farag**
Delphi Thermal Systems,
A&E Building 6,
200 Upper Mountain Road,
Lockport, NY 14094
e-mail: faragaa@hotmail.com

**Jeffery Hammersley**
e-mail: jeff@mco.edu

**Dan Olson**

Center of Environmental Medicine,
Medical College of Ohio,
3000 Arlington Ave.,
Toledo, OH 43699

**Terry Ng**
MIME Department,
University of Toledo,
Toledo, OH 43606
e-mail: tng@top.eng.utoledo.edu

# Mechanics of the Flow in the Small and Middle Human Airways

*Steady divergent flow (inspiration directed) is measured using Laser Doppler Velocimetry in a large-scale model carefully mimicing the morphometry of small human airways. The anatomical features, which induced vorticity in the flow from vorticity free entrance flow, are evaluated under conditions of convective similitude. The flow pattern in the daughter tubes is typical of laminar flow within the entrance to sharp bends (Dean number >500) with rapid development of strong secondary flows (maximum secondary velocity is 45 percent of mean axial velocity). The secondary flow consists of two main vortices, with two smaller and weaker secondary vortex activities toward the inner wall of curvature. There appears to be time dependent interaction with these vortices causing warbling at specific flow conditions. The calculated vorticity transport along the flow axis showed interaction between the viscous force at the new boundary layer development along the carinal wall and centrifugal force of curvature, with a significant influence by the upstream flow prior to entering the actual flow division. This interplay results in an overshoot of the calculated vorticity transport comparable to flow entering curved bends and suppression for the tendency to separate at the inner wall of these tight bends. The maximum primary flow velocities are skewed toward the carinal side (outer wall of curvature) and development of a second peak occurred with convection of the high velocity elements toward the inner wall of curvature by the strong secondary flow.*
[S0098-2202(00)01903-9]

## Introduction

Early studies that dealt with the transport of air in the human lung were focused on overall resistance to the breathing [1], and the mechanics of regional ventilation [2]. However little attention had been focused on the flow characteristics in individual bronchi. West and Hugh-Jones [3] were the first to focus on the flow characteristics by visualizing the flow of water in casts of trachea and main bronchi. They showed that disturbed flow was evident at all physiological flow rates even with local Reynolds number of 200. Schroter and Sudlow [4] studied the flow profiles in two successive generations of large-scale symmetrical models of junction of the human bronchial tree. They observed that small variations in the sharpness of the flow divider and radius of curvature of the walls creating the daughter branched tubes markedly influenced the flow. The basic flow pattern they observed had been reconfirmed in several subsequent observations ([5–8] and [9]). Flow visualization denoted prominent but complex secondary flows, which were poorly predicted by hot wire techniques for air speeds of these magnitudes. They showed that a pair of vortices was established in the daughter tube during inspiration while a set of four vortices was established in the parent tube during the expiration.

To overcome the unreliability of the hot wire at very low speed which is the case for the flow inside the human airways, Olson [7] designed a pulsed-probe anemometer to measure steady three-dimensional velocity fields typical of pulmonary trachea-bronchial airflows. Apparently, Olson was the first to measure the secondary current in the bifurcating tubes with both flat and parabolic inlet velocity profiles. The downstream development of the secondary velocities showed rapid and complex development of the pair of vortices observed qualitatively by Schroter and Sudlow [4].

Chang and El-Masry [9] studied the primary flow in a four generation asymmetric model of the human trachea and central bronchi using hot wire anemometer. They measured velocity distributions at two different flow rates characteristic of quiet and mild exercise respiration for both inspiratory and expiratory flows. The axial velocity profiles contrasted to other observations showed a high degree of asymmetry with peak velocities near the carinal side for both flat profile and jet like profile at the entrance to the bifurcation.

One should bear in mind that using hot wire anemometer to measure the secondary velocities is inaccurate since the secondary component in most part represents a small portion of the axial component, especially where the axial component gets small (i.e., near the wall). Indeed Isabey and Chang [10] faced that problem.

Yao Zhao and Baruch Lieber [11,12] used a two-velocity component Laser Doppler Anemometer and water as a working medium to measure the velocity field in a 70 deg symmetrical bifurcation with lesser curvature than previous studies. The water medium did not allow simultaneous matching of Reynolds and dean numbers to the presumed physiological conditions.

It should be noted here that Olson [7] used realistic airway geometry based on a real size lung cast. On the other hand, researchers such as Chang and El-Masry [9], and Yao and Lieber [11] claimed that using a realistic geometry complicates performing detailed measurements. Therefore, they used an idealized bifurcation. The first used a kind of idealized model to achieve both correct airway geometry and ease of measurements, but no geometrical details have been reported. The latter used an idealized symmetric model based on mathematical expressions to simplify the complicity of the flow geometry, especially for computational use. Yao and Lieber assumed that the cross sectional area is conserved throughout the bifurcation, which violates the realistic bifurcation as reported by Horsfield et al. [13].

The present work is carried out within the context of a project in which the flow patterns in symmetric and asymmetric bifurcations with different geometrical parameters, based on realistic airway geometry [13,14], are investigated using laser-Doppler velocimetry. As a first step in the investigation, the steady flow development in the average anatomical model of the small airway bronchi and bronchioles, a 70 deg symmetrical bifurcation model with 1/7 curvature ratio, is investigated. Both axial and secondary velocity profiles, measured at several axial locations in the bifurcation model, will be presented in this paper. This study is the ''baseline'' observation for an airway structure to function analy-

---

Contributed by the Fluids Engineering Division for publication in the JOURNAL OF FLUIDS ENGINEERING. Manuscript received by the Fluids Engineering Division August 10, 1999; revised manuscript received May 3, 2000. Associate Technical Editor: S. Banerjee.

sis. The observed flow patterns have high influence on convective mixing, particle deposition, volume flow distribution, gaseous scrubbing, and convective-diffusive axial dispersion mechanism; all critical features for respiration.

## Experimental Procedure

The model used in the experiments is sketched in Fig. 1(*a*). It consists of two halves of Perspex produced by milling. The model has 2-in. diameter parent tube, 1.5-in. diameter daughter tube, and 10.5 radius of curvature, yielding a curvature ratio of 1/7. The transition zone, the area between the parent and daughter tube, is subdivided into an ''elliptical region'' and a ''carinal region.'' The elliptical region is defined as beginning with the onset of the transition zone (i.e., beginning branch expansion) and ending at a point where the lateral arc of this elliptical cross section (major axis) approximates the smaller daughter tube's circularity. At this point the curvature of the parent tube's lateral walls has blended into the curvature of the daughter tube's lateral wall as shown in Fig. 1(*a*). Beyond this elliptical expansion, a prism-shaped carinal region is defined. This carinal region consists of a complex three-dimensional shape that exhibits progressive carinal indentation and ends at the circular onset of the daughter branch. The later point occurs at the midpoint of the carinal spur. In the elliptical region of the transition zone, the cross section changes shape from circular to elliptical keeping the cross section area constant while in the carinal region the area increases by 13 percent. The geometry of the model tested represents the mean anatomical details of branch points in the 4 to 16 branching. It corresponds to medium to small bronchi and bronchioles to terminal bronchial conducting airways at the entrance to the zone of the lung where oxygen is passively diffused into the blood.

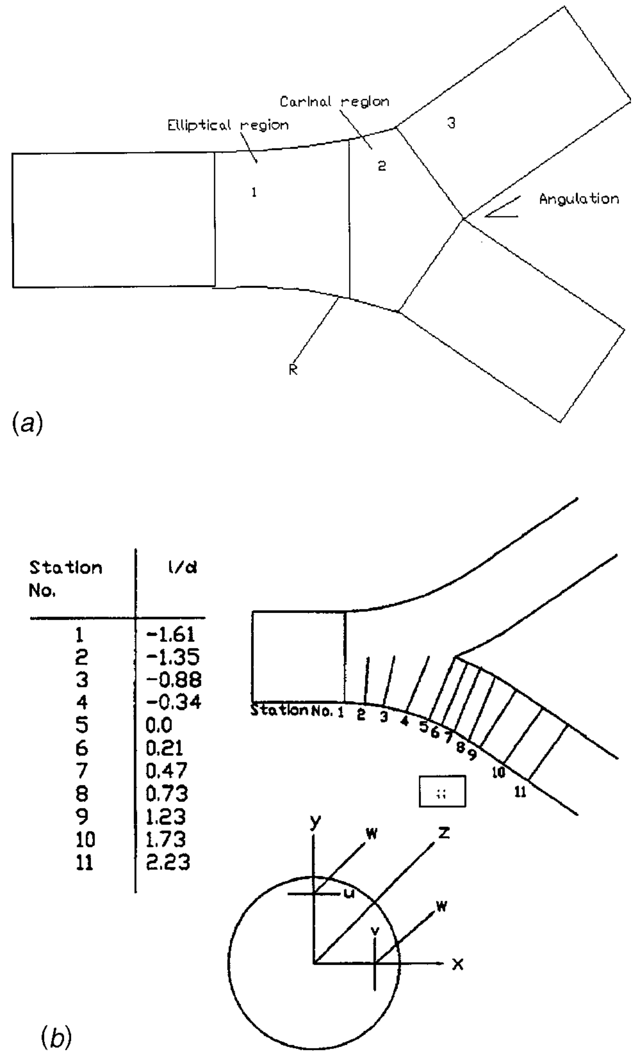

**Fig. 1** (***a***) **Symmetrical model configuration; (*b*) (i) measurement stations and (ii) velocity components**

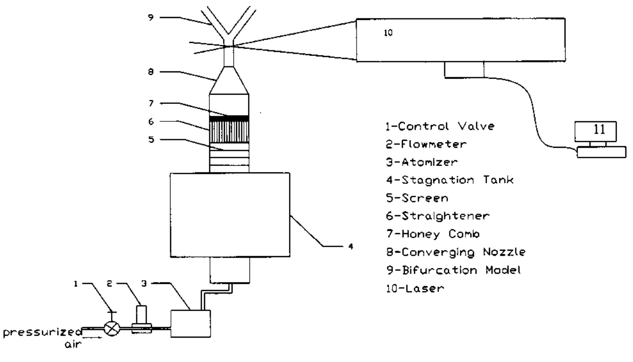

**Fig. 2 Flow system**

The model is placed in a flow system shown in Fig. 2. Seeding the air with salt using a six-jet atomizer (Model 9306, TSI inc.) yielded the best LDV signal. The seeded air passed through a stagnation tank and conditioned through sets of perforated discs, fine screens, and straightener before entering the model. After passing through the model, the air discharged to the atmosphere through a 10-diameter long circular tubes at the exit of the two daughter branches to minimize feed forward disturbances from the atmosphere. A Hastings Model HFM mass flowmeter upstream of the atomizer is used to monitor the flow. The output of the flowmeter is displayed and monitored on a computer during each experiment. A control band of ±1 percent of the desired flow rate was set for each experiment. Data acquisition would pause whenever the flow rate drifted outside the band, and would resume when the regulator brings the flow back within the band.

Velocity measurements are carried out at eleven axial locations in the bifurcation: $l/d=-1.61$, $-0.88$, $-0.34$, 0.0, 0.21, 0.47, 0.73, 1.23, 1.73, and 2 (where $l$ is the axial length and $d$ is the daughter tube diameter). Position 0 is at the flow divider, and the transition from the circular inlet to the daughter tube entrance starts from $l/d=-1.61$ as shown in Fig. 1(*b*). The locations are chosen according to the expected rate of velocity alterations. The velocity components are measured in rectangular grids at each axial location along arrays parallel and perpendicular to the plane of symmetry [15]. The laser is placed on a three-dimensional traversing mechanism driven by three stepper motors, allowing a traversing resolution of 0.025 mm in all directions. At each point the laser beams are placed at two different planes in the model—the plane of bifurcation and the normal plane—by combinations of turning the optics train 90 deg and the model was turned 90 deg around its axis. This yields four velocity components at each crossing point between the horizontal and vertical arrays: two cross velocity components, $u$ and $v$ in $x$ and $y$ directions, respectively, and two measurements for the same axial component, $w$ in $z$ direction from two different planes (see Fig. 1(*b*)). The two measurements of the same axial component allowed an estimation of the uncertainty based on repeatability. The uncertainty, which is defined based on the difference between the two measurements at each crossing point, was estimated to be ±1.85 percent of the mean entrance velocity. This uncertainty might come from the inaccuracy of placing the model relative to the LDA measurement volume and variations in the mean flow rate. Based on 60 data points, the correlation coefficients between the uncertainty and the velocity gradient, mean velocity, rms, and the position inside the model were 0.448, $-0.216$, 0.353, and 0.13439, respectively. This shows that the uncertainty is most correlated to the velocity gradient. The difference between the measured and calculated total flow rates was 4.85 percent. This represents the overall accuracy of the measurements, including the uncertainty of calculating the volume flow rate in 3-D flow with high swirling motion based on finite measurement grids. Looking at the overall accuracy of the measurements, 4.85 percent, and the repeatability of the measurements, ±1.85 percent, one might realize two major sources of the uncertainty. The first one is the accuracy in adjusting the flow to the same value at the beginning of each experiment. The second is the accuracy of predicting the flow rate based upon finite measurement grids. However, the uncertainty is within the expected limit in such a three-dimensional flow with high swirling motions.

## Results

Figure 3 shows the overall development of the axial velocity field from the inlet to the parent tube to the exit at one of the daughter tubes and at Re=1500. Position $l/d=0.0$ is at the flow divider, with minus and positive signs indicating respectively locations upstream and downstream of the flow divider. The veloc-

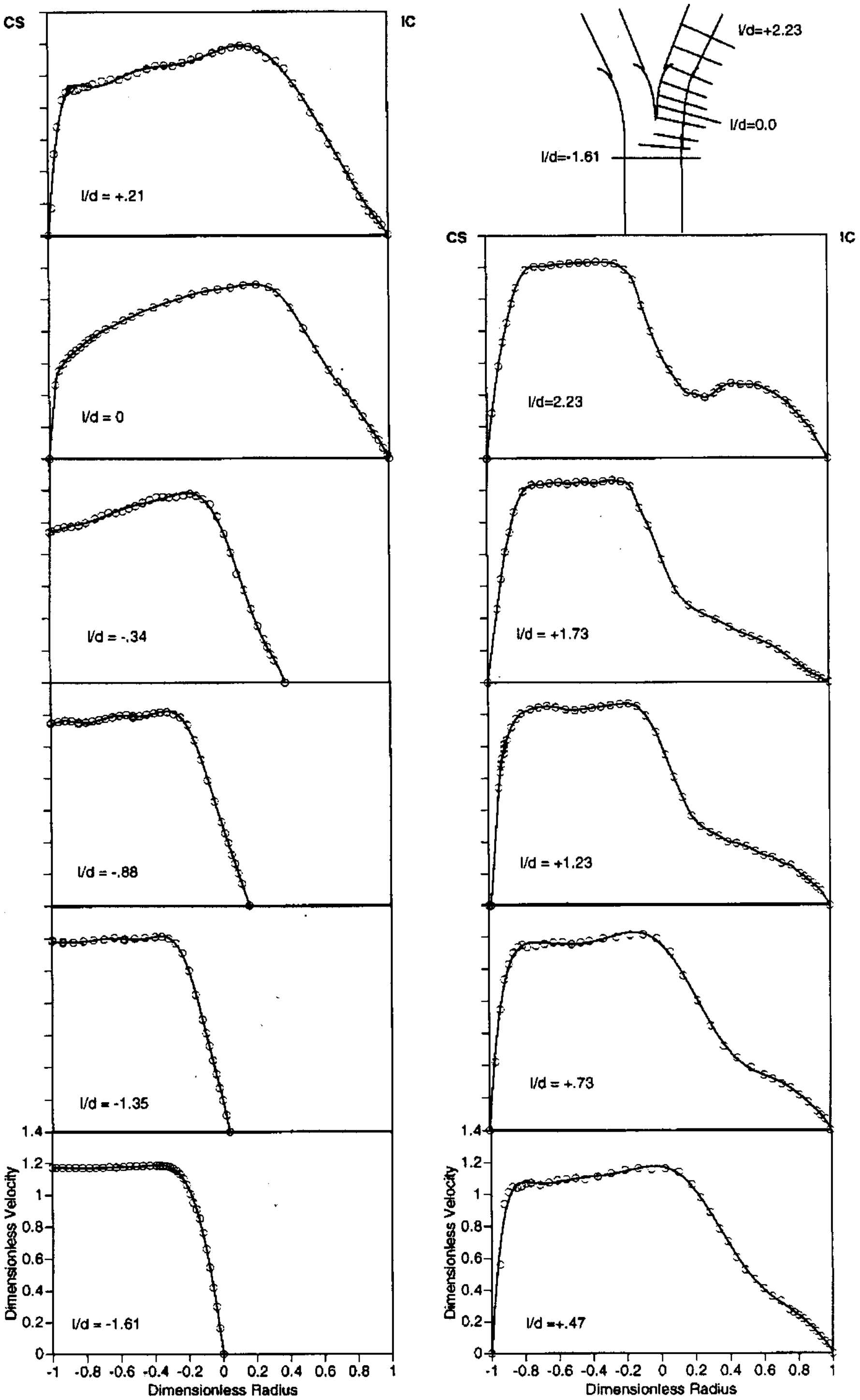

**Fig. 3 Downstream development of the primary velocity in the plane of bifurcation at Re=1500; CS is the carinal side and IC is the inner of curvature**

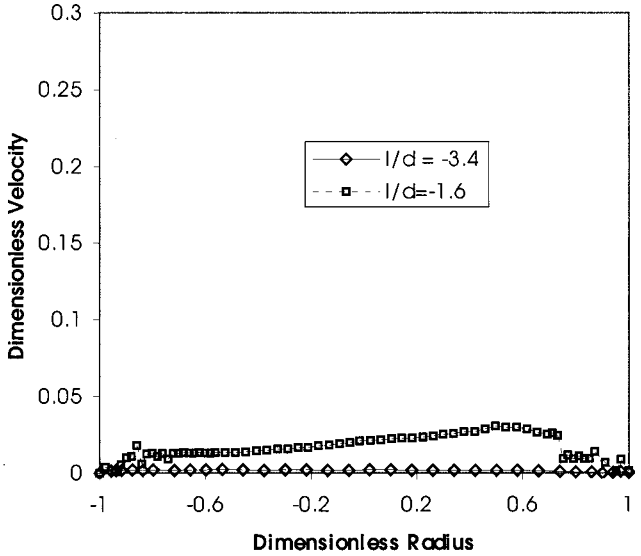

**Fig. 4 Secondary flow at the inlet to the model ($l/d=-3.4$) and first measuring location ($l/d=-1.61$); CS is the carinal side and IC is the inner of curvature**

ity is normalized to the mean velocity at the inlet to the model. The radial distance is normalized to the parent tube radius in the parent tube and the transition zone, and is normalized to the daughter tube radius in the daughter tube. Flows in different regions of the model will be discussed in the following sections.

## Inlet Conditions

In any bifurcating flow with high secondary flow, a well-defined inlet flow is of special importance. The inlet flow condition is investigated in detail to determine the inlet mean velocity profile, and the presence of secondary flow or high fluctuation level that might trigger flow instability.

The flow system yielded a flat profile at the entrance of the model, with a boundary layer thickness of 10 percent of the diameter at Re=1500 based on the diameter of the parent tube. Also the flow system ensured that the flow is going parallel to the axis of the model to within ±0.5 degree. Figure 4 shows the secondary flow at the inlet of the model, $l/d=-3.4$, and at the first measuring location, $l/d=-1.61$, where the transition zone starts. It is clear that essentially no secondary flow is observed at the inlet of the model. Even at $l/d=-1.61$ no significant secondary flow is observed. The fluctuation level of the incoming flow is also crucial. Since in any point within the flow field, it is important to decide whether any instability is due to the fluctuation in the incoming flow or introduced by certain bifurcating parameters. The fluctuation level, represented as rms of the mean axial velocity, is investigated for different Reynolds numbers and different arrangements of the flow conditioning. The fluctuation level at Re=1500 is 0.75 [15].

## Transition Zone

Figure 5 shows the secondary velocity distributions in the transition zone at $l/d$ locations of $-0.88$ and $-0.34$. The two measuring planes are placed perpendicular to the local axis of the daughter tube, or at 10 and 19 deg with respect to the axis of the parent tube respectively. Along the local normal plane at $l/d=-0.88$, the flow is going toward the centerline. The magnitude of the secondary flow velocity decreases while the boundary layer thickness increases toward the minor axis. At the minor axis, an inflection point can be seen to develop at the wall, signifying an onset of reversal flow inside the secondary flow boundary layer. At $l/d=-0.34$ in Fig. 6, the normal plane secondary velocity indicates that the reversal flow becomes more pronounced. The secondary flow boundary layer thickness increases as one moves across the major axis toward the innermost axis or the inner wall of curvature (Fig. 7). This indicates that the centrifugal force becomes more effective in shifting the flow toward the center of the transition zone where the flow divider eventually locates.

Figure 3 shows that the flow divider affects the primary flow in the plane of bifurcation in the transition zone. Figure 6, however, shows that the primary velocity in the normal plane stays flat throughout the same region. The influence of the wedge-shaped divider is thus confined mainly to planes normal to its leading edge. Figure 3 shows that the effect is relatively pronounced at $l/d=-0.34$, and decreases as one moves upstream from the flow divider such that it is barely noticeable at $l/d=-1.35$. At the beginning of the transition zone at $l/d=-1.61$ the velocity profile is essentially flat, indicating that the upstream influence of the flow divider is not significant upstream of this location. At the end of the transition zone and at the entrance to the daughter tubes, the flow is skewed toward the inner wall of curvature of the daughter tube.

The exit of the transition zone represents the entrance flow to the daughter tubes. The flow in this zone is affected by the changing cross-sectional shape, the increasing cross-sectional area, and the downstream flows in the daughter tubes.

## Daughter Branches

The overall development of the flow in the plane of bifurcation within a daughter tube can be seen in Figs. 4 and 5. In the axial flow, an inflection point starts to appear in the profile at $l/d=0.47$ indicating the initiation of the double humped profile. As shown in Fig. 5, this phenomenon is related to the secondary flow development that brings the higher velocity fluid from the vicinity of the outer wall outwards the inner wall of curvature. The inflection point becomes more pronounce as the flow proceeds downstream and eventually develops to a double peak profile at $l/d=2.23$.

Figure 5 shows the secondary velocity distributions inside the daughter tube at several axial locations. In comparison to a curved tube model with a similar geometry, the secondary flow in the daughter tube develops faster downstream from the flow divider, which agrees with Sobey's expectation [16]. The maximum secondary flow occurs approximately between 25 deg (the inlet to the daughter tube) and 28 deg compared to 40 and 60 deg in a curved tube model with a similar curvature. At the inlet of the daughter tube, the tangential component of the secondary flow is in general similar to that found at the corresponding location within a curved tube model except it is more developed. However, the component of the secondary flow in the plane of bifurcation does not agree with that of a curved tube at the outer wall of curvature. This disagreement may be related to the development of a secondary vortex near the inner wall of curvature. The secondary vortex becomes evident at $l/d=0.47$ and apparently reaches its maximum strength at the end of the curve section at $l/d=1.23$.

## Shear Stress Distribution

The magnitude of wall shear stress, or the velocity gradient is an important parameter for the problem being studied. Figure 8 shows the gradient of the axial velocity component on the carinal side, inner wall, and the upper (or the lower wall) at different downstream locations. Generally, the axial velocity gradients follow the developments of the boundary layer thickness on those locations. On the carinal side, the gradient is very high at the inlet to the daughter tube where a new boundary layer starts to develop. Inside the daughter tube, the velocity gradient decreases very rapidly near the inlet. At a small distance further downstream, the rate of the decrease slows significantly. On the inner wall, the velocity gradient is much lower than that on the carinal side, and the rate of the decrease is more gradual in general. On the upper or the lower wall, the velocity gradient decreases slightly in the

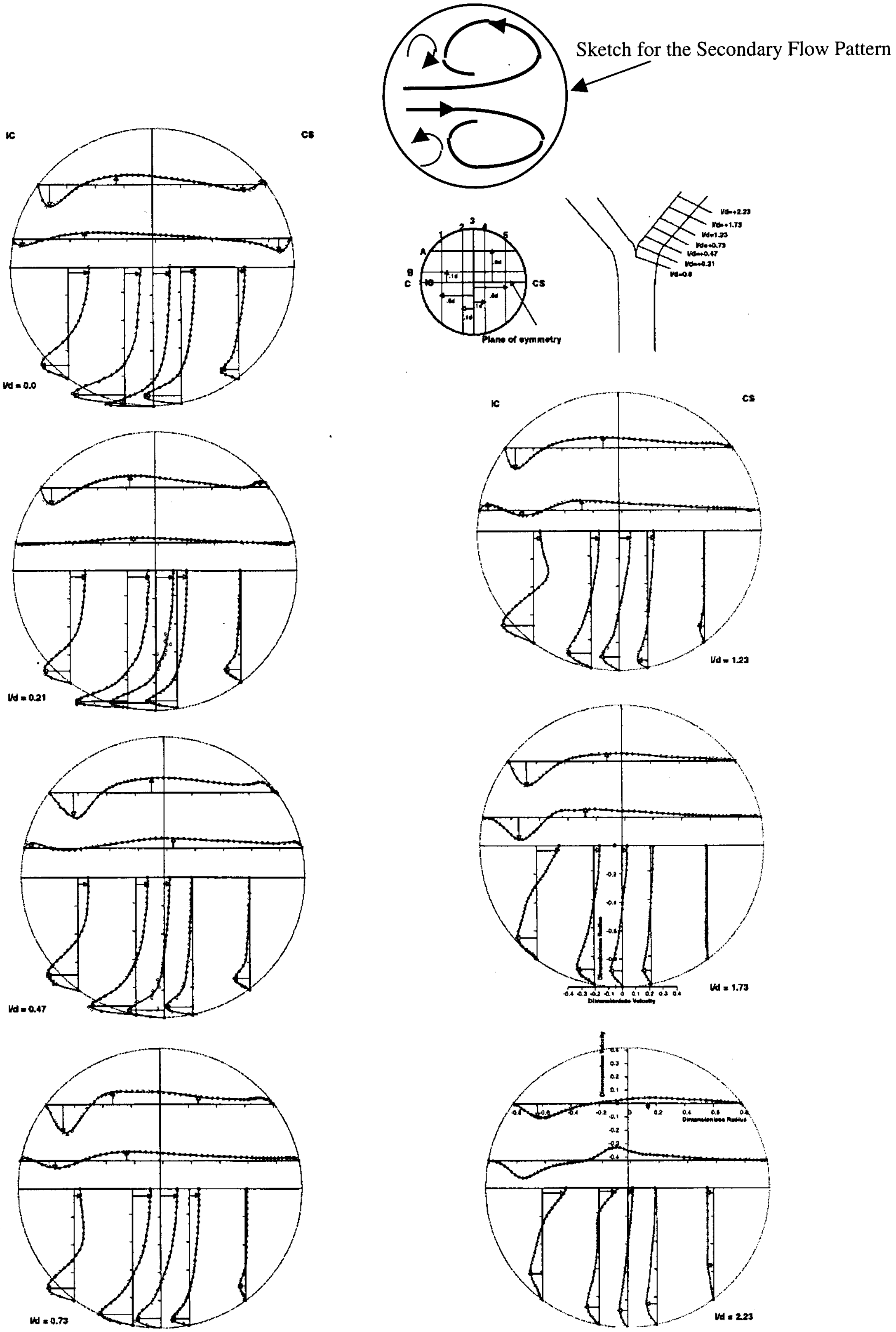

Fig. 5 Secondary velocity components in the normal plane and plane of bifurcation at different axial locations from the flow divider $(l/d=0.0)$ at Re=1500

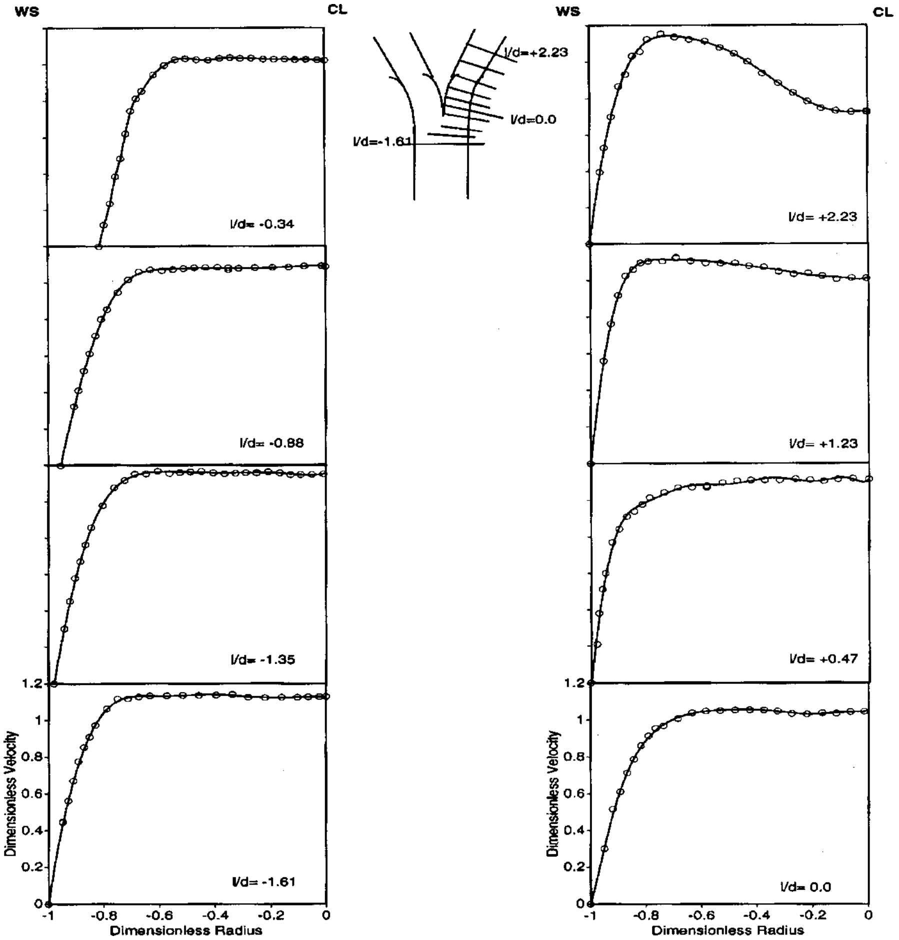

**Fig. 6 Downstream development of primary velocity in the normal plane at different axial locations (*l/d*) at Re=1500; CS is the carinal side and IC is the inner of curvature**

transition zone. After entering the daughter tube, the velocity gradient increases as one move downstream and then decreases in the straight section of the daughter tube. The initial increase in the velocity gradient in the daughter tube is related to the development of the low velocity region at the inlet to the daughter tube, which in turn depends on the development secondary current.

## Discussions

Figure 3 shows that the axial flow pattern undergoes a significant shifting as the flow proceeds downstream the flow divider. This flow shifting can be described quantitatively by calculating the first moment of the axial flow at each axial location

$$\left\langle \frac{X}{a} \right\rangle = \frac{\int_{-1/2\pi}^{1/2\pi}\int_{0}^{a}(WX/a)\,r\,dr\,d\phi}{\int_{-1/2\pi}^{1/2\pi}\int_{0}^{a}W\,r\,dr\,d\phi} \qquad (1)$$

where $W$ is the axial velocity and $a$ is the daughter tube radius.

Since the data are obtained over a Cartesian grid as defined in Section 2, the data are transferred to the cylindrical coordinates and then Eq. (1) is performed numerically over the cylindrical grid. Figure 9 shows the first moment at the inlet and exit of the daughter tube in the bifurcation model. Results from the curved tube experiments of Agrawal [17] and Olson and Snyder [18] are included for comparison. Figure 9 shows that the center of momentum or first moment is shifted toward the outer wall. This indicates one fundamental difference between the bifurcation model and the curved tube model. In the bifurcation model the center of momentum is shifted toward the carinal side, while in a curve tube model it is shifted toward the inner wall of curvature. This indicates the strong influence of the entrance condition to the daughter tube on the flow development. Additionally, the results indicate the importance of the geometry of the transition zone in the bifurcation model as predicted by other Sobey [16] and Synder and Olson [19].

The secondary current can be quantified more conveniently by defining a mean vorticity $\zeta$. Olson and Synder [18] defined three circulation paths as shown in Fig. 10. The inviscid core path is taken along the plane of symmetry and the upper surface of the tube, the maximum circulation path is taken along the plane of symmetry and the locations of maximum secondary velocity, and the boundary layer path is simply the difference between the first two paths. The mean vorticity $\zeta$ is defined as:

$$\zeta = \frac{\Gamma}{A} = \frac{1}{A}\oint_{s} V\cdot dS \qquad (2)$$

where $S$ is taken as defined above for the three different paths. Olson and Synder [18] scaled the transverse motion in the central core to the radius of the tube, $a$, and the boundary layer swirl to $(aR)^{1/2}$, where $R$ is the radius of curvature. As can be seen in Fig. 10, the general characteristics of the mean axial vorticity development are comparable to the curved tube. The vorticity overshoots before approaching a steady value, with the rate of development being faster in the bifurcation. Overall, the bifurcation produces less mean axial vorticity compared to the corresponding locations in the curved tube except in the boundary layer at the entrance to the daughter tube.

**Comparison With Previous Work.** Yao Zhou and B. Lieber [11] used a simplified bifurcation model that does not represent

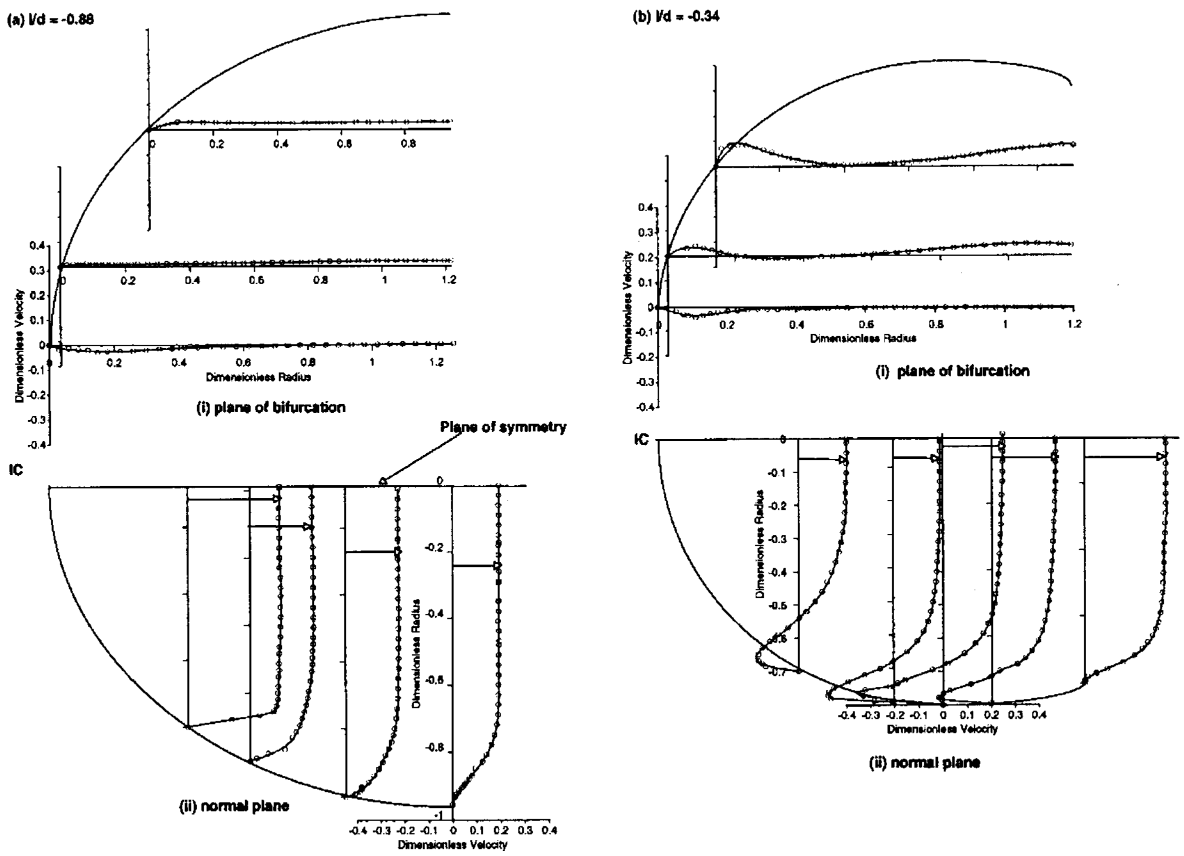

**Fig. 7 Secondary velocity components in the transition zone at two different axial locations, Re=1500; CS is the carinal side and IC is the inner of curvature**

any anatomical branch. The general features of the primary velocities in both the plane of bifurcation and the normal plane are evident in both works, the flow is skewed toward the outer wall of curvature in the plane of bifurcation and an ''*M*'' shaped profile is observed in the normal plane. However, the development of the inflection point and the appearance of the second peak in the primary component close to the inner wall of curvature are more pronounce in the present work. The appearance of the second peak is very important in stepping up the velocity gradient at the inner wall of curvature and consequently preventing flow separation as can be seen in Fig. 3. Some differences do exist regarding the development of the secondary velocities. They concluded that the tangential component of the secondary flow don't undergo a significant decay inside the curved section of the daughter tube for Reynolds number lower than 2089. This does not agree with the results reported here for Re=1500. As shown in Fig. 5, the tangential component of the secondary flow does decrease significantly in the curved section of the daughter tube. It decreases, for example at the centerline, from 36 percent at $l/d=0.0$ to 13.4 percent at $l/d=+1.23$, end of the curvature, and reaches 6 percent at $l/d=+2.23$, exist of the model. Also our results for even lower Reynolds numbers, not shown here, support our conclusion. In the transition zone, Yao and Lieber observed only a diminished magnitude of the secondary velocities while in this study strong secondary velocities were observed in the transition zone. Vestiges of the secondary velocities were observed as far as $l/d=-1.61$ upstream the ridge, see Fig. 10.

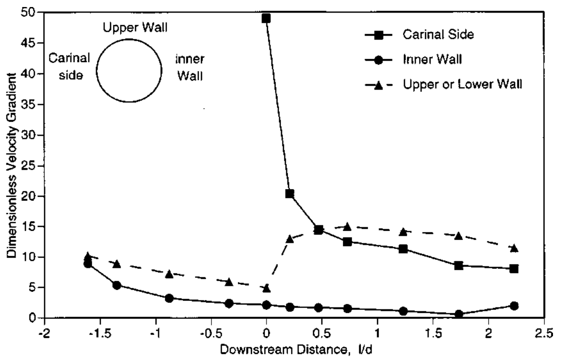

**Fig. 8 Dimensionless wall axial velocity gradients at different downstream locations ($l/d$) at Re=1500**

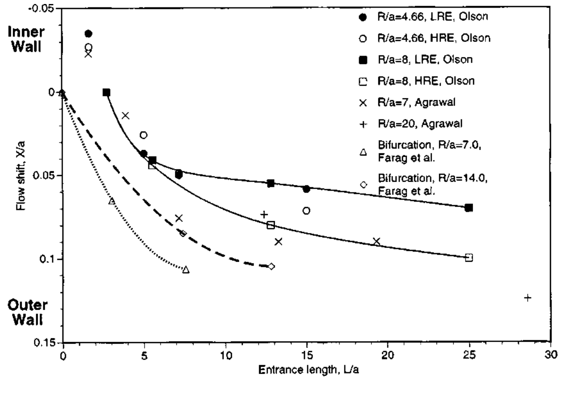

**Fig. 9 The downstream evolution of the transverse shifts in the axial velocity, expressed as the first moment ($X/a$), Re =1500**

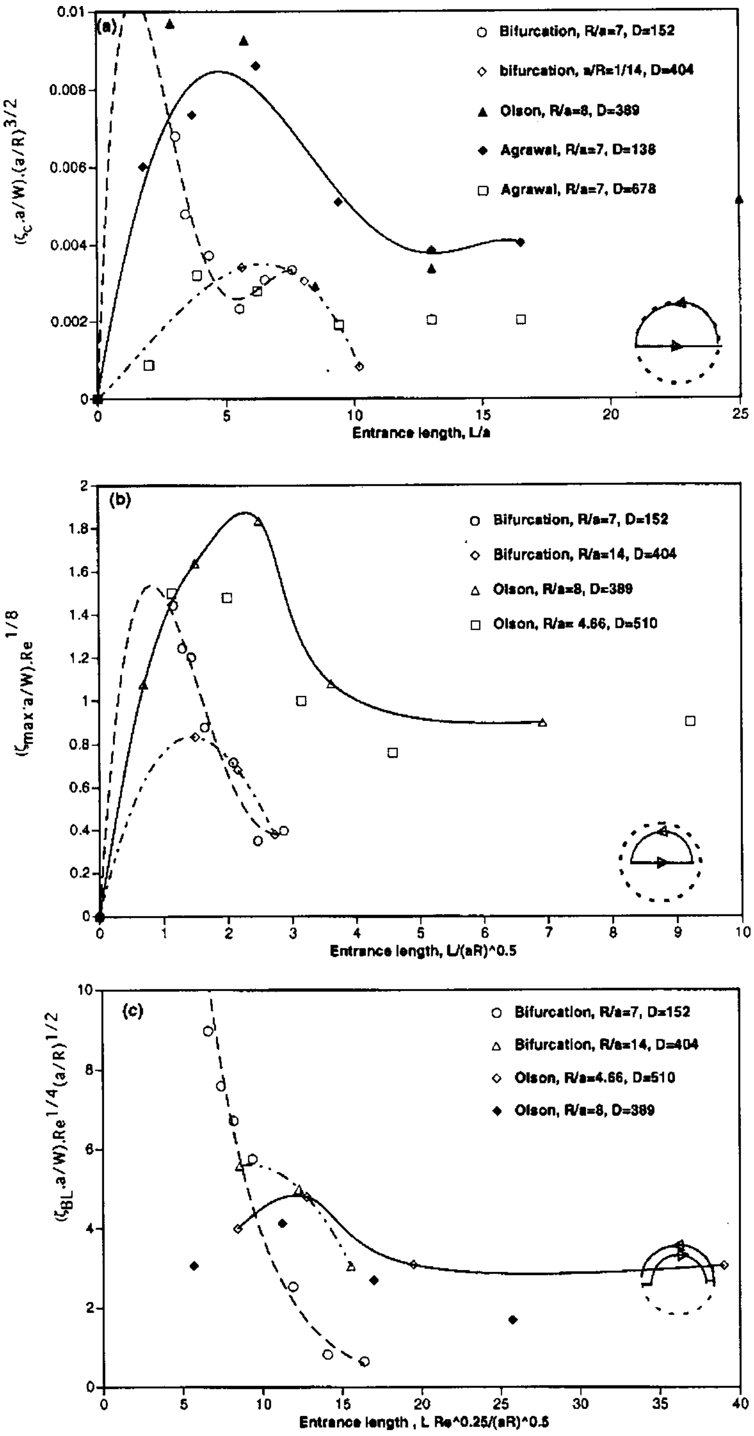

**Fig. 10 Development of the mean axial vorticity compared to the curved tube: (*a*) in central core; (*b*) on maximal circulation path; (*c*) in the boundary layer**

## Conclusions

The flow in a symmetric bifurcation model typical to human airways is studied. The primary and secondary velocities at several streamwise locations are measured, and comparisons with several previous studies were made. The results reveal that while the general features of the flows are similar, there are significant differences in several important flow characteristics among models. In addition to the bifurcation angle and radius of curvature of the daughter tube, the geometry of the transition zone between the parent and daughter branches appears to play a key role in phenomena such as local flow separation, the development of secondary vortices, the wall shear stress, and the overall development of the flow.

## References

[1] Dubois, A. B. 1964, ''Resistance to Breathing,'' Handbook of Physiology, Sec. 3, Respiration, Vol. 1, Fenn W. O., and Rahn, H., eds., Washington D. C., Am. Physiol. Soc. pp. 451–452.

[2] West J. B., 1966, ‘‘Regional Differences in Blood and Ventilation in the Lung,’’ *Advances in Respiratory Physiology*, Caro, C. G., ed., London.

[3] West, J. B., and Hugh-Jones, P., 1959, ‘‘Patterns of Gas Flow in the Upper Bronchial Tree,’’ J. Appl. Physiol., **14**, pp. 753–759.

[4] Schroter, R. C., and Sudlow, M. F., 1969, ‘‘Flow Patterns In Models of The Human Bronchial Airways,’’ Respir. Physiol., **7**, pp. 341–355.

[5] Schreck, R. M., and Mockros, L. F. 1970, ‘‘Fluid Dynamics in the Upper Pulmonary Airways,’’ AIAA 3rd Fluid and Plasma Dynamics Conference, Los Angeles, CA.

[6] West, J. B., 1960, ‘‘The Measurements of Bronchial Air Flow,’’ J. Appl. Physiol., **15**, pp. 976–978.

[7] Olson, D. E. 1971, ‘‘Fluid Mechanics Relevant to Respiration Flow Within Curved or Elliptical Tubes and Bifurcation Systems,’’ Ph.D. thesis, Imperial College London, Dec.

[8] Pedley, T. J., Schrter, R. C., and Sudlow, M. F., 1977, ‘‘Review: Gas Flow and Mixing in the Airways,’’ Bioengineering Aspects of the Lung, West, J. B., ed., Marcel Dekker, New York.

[9] Chang, H. K., and El-Masry, A. Osama, 1982, ‘‘A Model Study of Flow Dynamics in Human Central Airways Part I: Axial Profiles,’’ Respir. Physiol., **49**, pp. 75–95.

[10] Isabey, D., and Chang, H. K., 1982, ‘‘A Model Study of Flow Dynamics in Human Central Airways Part I: Secondary Flow Profiles,’’ Respir. Physiol., **49**, pp. 97–113.

[11] Zhao, Y., and Baruch, L. B., 1994, ‘‘Steady Inspiratory Flow in a Model Symmetric Bifurcation,’’ ASME J. Fluids Eng., **116**, pp. 488–496.

[12] Zhao, Y., and Baruch, L. B., 1994, ‘‘Steady Expiratory Flow in a Model Symmetric Bifurcation’’ ASME J. Fluids Eng., **116**, pp. 318–323.

[13] Horsfield, K., Dart, G., and Olson, E. D., 1971, ‘‘Models of Human Bronchial Tree,’’ J. Appl. Phys., **31**, No. 2.

[14] Hammersley, R. J., and Olson, E. D., 1992, ‘‘Physical Models of the Smaller Pulmonary Airways,’’ J. Appl. Physiol., **72**, No. 6, pp. 2402–2414.

[15] Farag, Ashraf, 1988, ‘‘Fluid Mechanics of Symmetric and Asymmetric Bifurcation Models Typical to Middle and Small Human Airways,’’ Ph.D. thesis, The University of Toledo, Ohio, Apr.

[16] Sobey, J. I., 1976, ‘‘Inviscid Secondary Motions in a Tube of Slowly Varying Ellipticity,’’ J. Fluid Mech., **73**, pp. 621–639.

[17] Agrawal, Y., Talbot, L., and Gong, K., 1978, ‘‘Laser Anemometer Study of Flow Development in Curved Circular Pipes,’’ J. Fluid Mech., **85**, pp. 497–518.

[18] Olson, D. E., and Synder, B., 1985, ‘‘The Upstream Scale of Flow Development in Curved Circular Pipes,’’ J. Fluid Mech., **150**, pp. 139–158.

[19] Synder, B., and Olson, E. D., 1989, ‘‘Flow Development in a Model Airway Bronchus,’’ J. Fluid Mech., **207**, pp. 379–392.

**Kazumi Tsunoda**
Lecturer,
Department of Mechanical Engineering,
Shibaura Institute of Technology,
Tokyo, 108-8548, Japan
e-mail: ktsunoda@sic.shibaura-it.ac.jp

**Tomohiko Suzuki**
Namiki Precision Jewel Co., Ltd.
Tokyo, 123-8511, Japan

**Toshiaki Asai**
Graduate Student,
Department of Mechanical Engineering,
Shibaura Institute of Technology,
Tokyo, 108-8548, Japan

# Improvement of the Performance of a Supersonic Nozzle by Riblets

*This paper describes an experimental study of supersonic internal flow over a riblet surface mounted on a channel wall to reduce pressure loss and improve the performance of a supersonic nozzle. The magnitude of the static pressure in the pressure-rise region observed in channels with riblet surface became lower than that for a smooth surface, and the significance of its difference was indicated by uncertainty analysis estimated at 95 percent coverage. The Mach number distributions obtained by traversing a Pitot-tube showed that the separation point moved downstream and the size of the separation region became small when using riblets. Furthermore, it was found that the stagnation pressure loss reduction was as large as 56 percent in the uniform supersonic flow field at a Mach number of 2.0, and 29 percent in the separation region.* [S0098-2202(00)00103-6]

## 1 Introduction

It is well known that, in a thermofluid machinery utilizing a supersonic internal flow, a turbulent boundary layer developing along the channel wall causes unfavorable frictional drag, and gives rise to large entropy production by the interaction with shock waves. These phenomena play a major role in momentum and energy losses of working fluid; therefore, an establishment of a method of a turbulent boundary layer control has been expected to improve the performance of the thermofluid machinery.

A riblet, which is a longitudinally microgrooved surface, is one of the passive drag-reduction techniques, and its systematic research was initiated at NASA Langley Research Center in order to reduce the fuel costs of airlines. Since Walsh [1] showed that symmetric triangular or semi-circular with sharp peak riblets produced turbulent drag reduction as much as 8 percent, the effectiveness of riblets has been demonstrated by many researchers. Moreover, with recent advances in experimental techniques and direct numerical simulation (DNS), progress was made toward understanding the drag-reduction mechanism by riblets. Bacher and Smith [2] performed hydrogen-bubble flow visualization to investigate the behavior of low-speed streak structure above riblet surfaces. Choi [3] observed the change of the near-wall structure in the turbulent boundary layer by using hot-wire/film anemometry and smoke-wire technique with a sheet of laser light. Suzuki and Kasagi [4] measured the turbulent flow-field in the near-wall region with the aid of a three-dimensional particle tracking velocimetry (3-D PTV), and showed that the turbulent intensities and the Reynolds shear stress were decreased near riblet surface. The first DNS of a turbulent flow over riblet surfaces was performed by Chu and Karniadakis [5]. Their results suggested that the drag reduction achieved was approximately 6 percent in the translational and turbulent regimes. Choi et al. [6] also solved the three-dimensional Navier-Stokes equations via DNS to shed light on the mechanism of drag-reduction by riblets, and discussed the drag modification mechanism based on the relationship between the average diameter of streamwise vortices and the spacing of riblets.

As was mentioned above, riblets can modify the near-wall structures of the turbulent boundary layer without additional power, and hence they have been expected to be an attractive tool for drag-reduction in many engineering applications. On the other hand, since riblets are passive means of drag-reduction, we have to obtain information about the characteristics of riblets under various flow conditions in a wide range of Reynolds numbers, in order to apply riblets to the practical flow-field. In contrast to numerous studies of riblets at low speed, few studies at high Reynolds number (i.e., transonic or supersonic speed) have so far been carried out. For instance, Squire and Savill [7] examined the effects of riblets on drag-reduction at high subsonic speed by using a blowdown-type wind tunnel with V-groove riblets mounted on the floor of the tunnel. In this experiment, a maximum drag-reduction of about 7 percent was obtained at a Mach number of 0.88. They also observed shock wave/boundary layer interactions on riblet surfaces at a Mach number of 1.5 with the shadowgraph photograph flow visualization technique. Gaudet [8] measured the wall shear stress on a riblet surface at a Mach number of 1.25. He indicated that drag-reduction on the order of 7 percent was achieved at optimum flow conditions, and that misalignment of a riblet with the flow direction should be smaller than 30 deg. Their studies suggested that riblets can reduce the skin-friction drag in a high speed flow-field. However, these experiments deal with supersonic external flows, and the characteristics of the riblets for a supersonic internal flow remains still unknown.

This paper describes an experimental study of the riblets mounted on the wall surface of a supersonic nozzle. The performance of applications utilizing a supersonic internal flow is generally estimated by nozzle efficiency, diffuser efficiency, stagnation pressure loss and so on. We therefore have to know the effect of riblets on these efficiencies, in order to operate the applications at the appropriate conditions. In the present work, from the comparison of pressure distributions in the supersonic nozzle with a riblet surface and a smooth surface, we determined the nozzle performance quantitatively on the basis of a stagnation pressure loss.

## 2 Experimental Apparatus and Measurement Procedures

All experiments were carried out in an indraft supersonic wind tunnel installed with an asymmetric, two-dimensional converging/diverging (CD) nozzle as shown in Fig. 1. The air introduced into the CD nozzle is accelerated up to the maximum Mach number of 2.3, and finally exhausted into the vacuum tank with a volume of 1.976 m$^3$. The experimentation time was about 25 seconds under the present experimental conditions. A cross-sectional configuration of the nozzle is depicted in Fig. 2 showing the principal dimensions. The nozzle has a 400 mm long rectangular working section of constant width 30 mm, and the location of the throat is 75 mm downstream of the nozzle inlet. For the riblets experi-

---

Contributed by the Fluids Engineering Division for publication in the JOURNAL OF FLUIDS ENGINEERING. Manuscript received by the Fluids Engineering Division August 24, 1999; revised manuscript received May 2, 2000. Associate Technical Editor: K. Zaman.

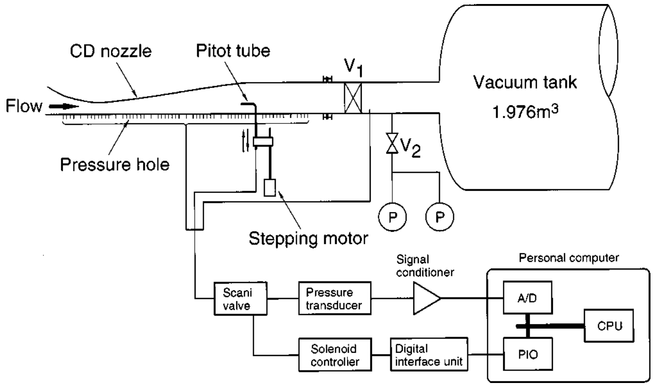

**Fig. 1 Experimental apparatus and schematic diagram of measurement system**

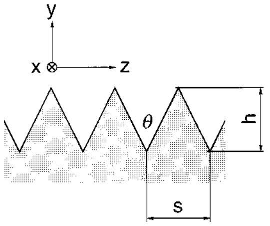

| | θ (deg) | s (mm) | h (mm) |
|---|---|---|---|
| Channel A | 97 | 0.050 | 0.022 |
| Channel B | 85 | 0.050 | 0.027 |

**Fig. 3 Cross-sectional view of the riblet surface with principal dimension**

ments, a thin polyethylene terephthalate (PET) film on which micro-grooves were machined regularly was attached to the flat bottom wall over the whole surface by an adhesive tape. We investigated two kinds of triangular cross-section riblets, having the same rib spacing and different heights as shown in Fig. 3. In the present paper, we call the nozzle with these riblets surfaces as ''Channel A'' ($s=0.050$ mm, $h=0.022$ mm) and ''Channel B'' ($s=0.050$ mm, $h=0.027$ mm), respectively. The experimental results obtained from Channel A and B were compared to those from the channel with the flat bottom wall to which a smooth film was attached.

In order to obtain the wall static pressure distributions, pressure holes of 1.5 mm diameter were arranged on the top converging/diverging wall at 25 mm intervals along the streamwise direction. The spatial distribution of stagnation pressure was measured by traversing a flattened Pitot-tube with the tip dimensions of 0.8 mm width and 0.4 mm height. Measurement values obtained from flattened Pitot-tube were checked against those from conventional cylindrical Pitot-tube. It was found from this comparison that there was no significant effect of the probe tip on measurement values and time response. The Pitot-tube was driven by the one-direction transverse gear with stepping motor which has a positioning accuracy of ±0.1 mm, and automatically moved away from the bottom wall to the top wall at 0.25 mm intervals. Measurements of static and stagnation pressure were conducted by a multichannel pressure management system (Scanivalve, 48D9GM). Output voltage from differential pressure transducer (Scanivalve, PDCR23D) is acquired every 0.01 s by a personal computer through A/D converter, and converted into pressure signals by fitting the pressure-voltage curve which was calibrated statically at the operating condition. A Mach number in the nozzle was calculated from the wall static pressure and the stagnation pressure using isentropic relationship. The static pressure measurement through the boundary layer revealed that the static pressure was almost constant along the direction normal to the bottom wall, thus, the variation of the static pressure was not considered significant when the transverse distribution of Mach number was calculated. Moreover, the mean streamwise velocity profile was deduced from the Mach number distribution by assuming the constant stagnation temperature, which corresponds to the adiabatic wall condition.

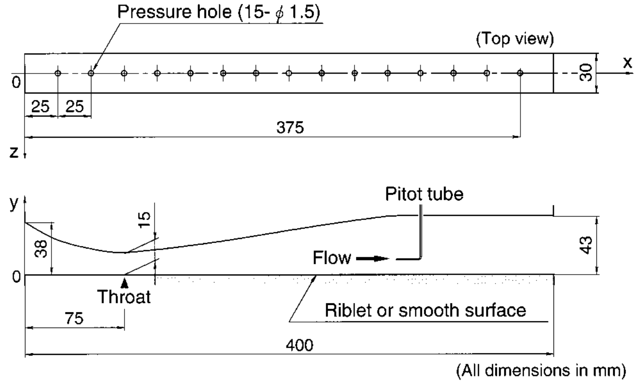

**Fig. 2 Schematic cross-sectional view of the converging/diverging (CD) nozzle and coordinate system**

## 3 Results and Discussion

**3.1 Wall Static Pressure Distributions.** Since riblets would lead to a drag reduction in a turbulent boundary layer, it is necessary to comprehend the growth of boundary layer in the nozzle. Figure 4 shows the streamwise velocity profiles in the boundary layer developing over the smooth surface for the operating pressure ratio of $P_b/P_{0S}=0.1$. The air flow is accelerated to supersonic flow in the measurement region, and core flow Mach number achieved to $M=2.3$ at $x=225$ mm, as will be shown later. It can be seen from Fig. 4 that measurement values are in reasonable agreement with the power law profile for a turbulent boundary layer. For the low pressure ratio ($P_b/P_{0S}\leqslant 0.2$), we observed similar velocity profiles as seen in Fig. 4, and thus, we recognized the growth of a turbulent boundary layer above the bottom wall under the present operating condition.

The wall static pressure distributions along the streamwise direction are plotted in Fig. 5 for various operating pressure ratios. Each data of $P_g/P_{0S}$ represents the average value obtained from

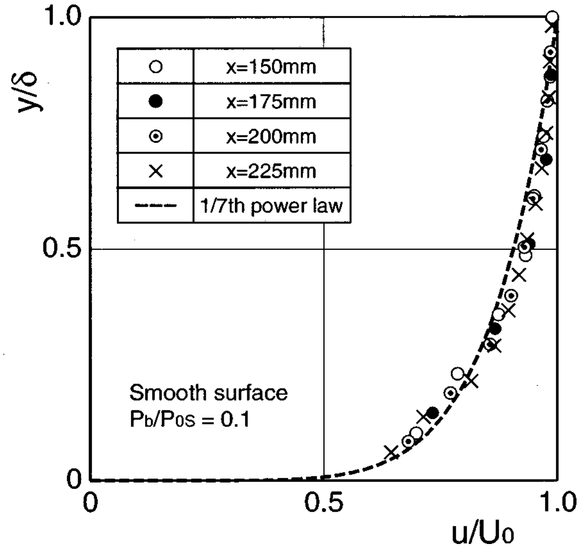

**Fig. 4 Nondimensionalized streamwise velocity profiles in boundary layer (uncertainty in $u/U_0=\pm0.019$ and in $y/\delta=\pm0.0015$)**

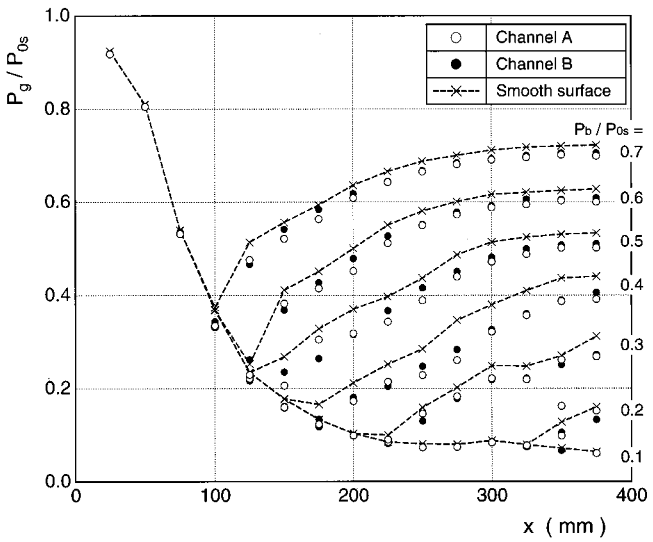

**Fig. 5 Wall static pressure distributions along the *x*-direction for various operating pressure ratios**

10 independent measurements. When the operating pressure ratio is small enough to allow an adiabatic expansion throughout the nozzle, i.e., $P_b/P_{0S} \leqslant 0.2$, the static pressure distributions for Channel A and B are in close agreement with the distribution for the smooth channel. On the other hand, for the case of $P_0/P_{0S} \geqslant 0.3$, we can see that the wall static pressures for Channel A and B are lower than that for the smooth channel downstream of the initial pressure rise point. In particular, when the pressure ratio reaches $P_b/P_{0S}=0.4$ and 0.5, the start point of pressure rise on the riblet surface shifted about 25 mm downstream of that for the smooth surface. For cases with higher pressure ratio of $P_b/P_{0S} \geqslant 0.6$, however, the location where the static pressure starts to increase is almost the same for all channels, and the pressure difference between the riblet surfaces and the smooth surface becomes small with an increase in the operating pressure ratio.

In order to discuss whether the wall static pressure difference shown in Fig. 5 is quantitatively significant, we evaluate the uncertainty intervals associated with the pressure measurement at 95 percent coverage. As mentioned in the previous section, the voltage signal from the pressure transducer is amplified by a signal conditioner, and sampled digitally with the A/D converter. The bias limit of the pressure transducer is within $\pm 0.06$ percent including nonlinearity and hysteresis. This value is considered to be negligible compared to other elemental bias limits. Therefore, the bias limit occurring from the signal conditioner and A/D converter is dominant in all subsequent data processing, and the overall system bias limit is estimated to be 645 Pa. Figure 6 presents the resulting uncertainty which is calculated from the overall system bias limit and the precision index based on a series of pressure measurements. In the region of 100 mm$\leqslant x \leqslant$300 mm, where pressure difference is clearly observed for $0.3 \leqslant P_b/P_{0S} \leqslant 0.6$, the uncertainty interval of nondimensionalized wall static pressure at 95 percent coverage is $P_g/P_{0S} = \pm 0.0065$. It can be found that this uncertainty interval is small enough that the pressure difference between Channel A or B and smooth channel is significant in the present experiment. The wall static pressure distributions measured for $P_b/P_{0S} \geqslant 0.3$ indicate the occurrence of a shock wave/boundary layer interaction. Therefore we can confirm that riblets have the effect of changing the static pressure distribution in the shock wave/boundary layer interaction region in the supersonic nozzle.

### 3.2 Flow Pattern in the Channel.

Wall static pressure increases gradually along the streamwise direction. This phenomenon is closely related to the interaction between a shock wave and a boundary layer. Therefore, the behavior of the pressure distribution discussed in the previous section suggests that an examination of the variation of flow properties through the boundary layer is quite important.

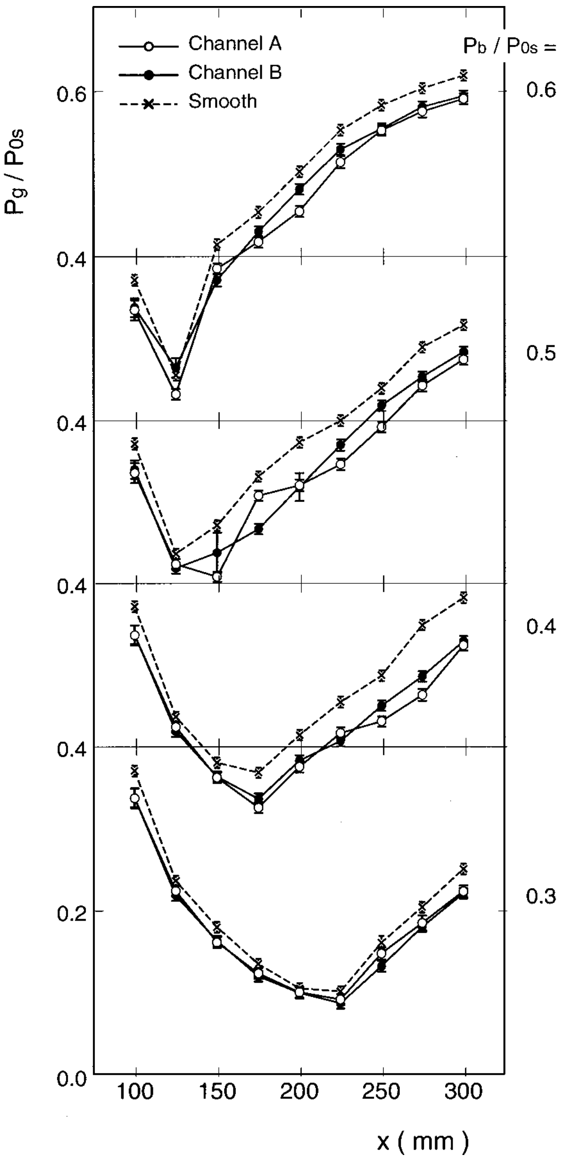

**Fig. 6 Uncertainties of wall static pressure measurement. Error bars extend uncertainty interval at 95 percent coverage.**

To illustrate the overall appearance of the flow-fields, the development of Mach number profiles in Channel A is compared with that in the smooth channel in Fig. 7. For the two pressure ratios $P_b/P_{0S}=0.1$ and 0.2, Mach number profiles in Channel A are in good agreement with those in the smooth channel, and the uniform flow field, whose maximum Mach number is $M=2.3$ at $x=250$ mm, is produced for $x \leqslant 275$ mm. The flow above the bottom wall is slightly decelerated due to the back pressure variation near the nozzle exit ($x \geqslant 300$ mm), but a shock wave or a separation bubble is not observed. When the pressure ratio reaches $P_b/P_{0S}=0.3$, the decelerated flow at the bottom wall side develops a large scale separation, in which there is a difference in the profile between the two channels. In particular, the differences observed at $x=225$ mm and 250 mm suggest that a flow deceleration in Channel A starts downstream compared to the smooth channel. This trend corresponds to the fact that the start point of a pressure rise for Channel A moves to $x=225$ nm which is slightly

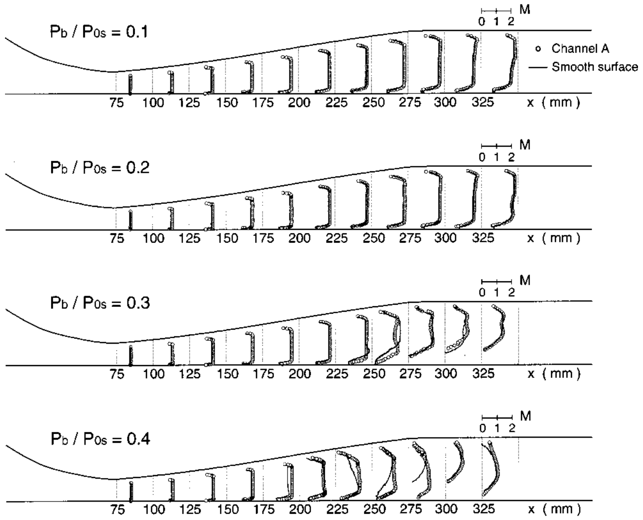

**Fig. 7 Development of Mach number profile along the *x*-direction for Channel A and the smooth channel (uncertainty in $M=\pm 0.09$ for Channel A and in $M=\pm 0.07$ for the smooth channel)**

downstream of the separation point for the smooth channel, as seen in Figs. 5 or 6. For $P_b/P_{0S}=0.4$, the Mach number at $x=175$ mm in Channel A, where the gradual pressure rise occurs, is higher than that in the smooth channel. Furthermore, a flow separation above the bottom wall still appears at $x\approx 250$ mm in the smooth channel and downstream of $x=275$ mm in Channel A, respectively. Therefore, we can find from these results that riblets have the effects of shifting the separation point downstream and of restricting the growth of the separation region.

In Fig. 8, we compare the Mach number profiles developing in Channel B with those in the smooth channel. For $P_b/P_{0S}\leqslant 0.2$, a uniform supersonic core flow is realized in the region of 75 mm $\leqslant x\leqslant 275$ mm of Channel B, and the behavior of the Mach number profile closely resembles the results obtained from the other two channels. On the other hand, there exist some differences in the Mach number profile among three channels for $P_b/P_{0S}=0.3$. From the transition in the Mach number profile, the separation point on the bottom wall is estimated to be in the region of 250 mm$<x<275$ mm for the smooth channel, and in the region of $x\geqslant 275$ mm for Channel B, respectively. Taking into account the result discussed in Fig. 7, it is found that the separation appearing in Channel B extends within a narrow region compared with that in Channel A, and the separation point moves downstream. When $P_b/P_{0S}=0.4$, the size of the separation region in Channel B is smaller than that in the smooth channel, but larger than that in Channel A, in contrast to the case of $P_b/P_{0S}=0.3$. These facts mean that there exists an optimum riblet size in restricting a separation and it is determined in accordance with the flow conditions, such as pressure ratio and Mach number.

**3.3 Reduction in Stagnation Pressure Loss by Riblets.** In order to operate a supersonic nozzle with high performance, it is required to keep pressure loss small through the nozzle, and thus, we have to comprehend the behavior of a stagnation pressure in a supersonic nozzle with riblet surface. In the present study, we generate stagnation pressure distributions in the *x*-*y* plane in the center of the nozzle by using over 1200 Pitot-pressure data measured in the region of 75 mm$\leqslant x\leqslant$325 mm.

In Figs. 9 and 10, contour plots of nondimensionalized stagnation pressure $P_0/P_{0S}$ obtained from three channels are compared for the two operating pressure ratios which characterize the typical flow-pattern in the present experiment. When $P_b/P_{0S}=0.1$ (Fig. 9), the highest stagnation pressure region which is bounded by broken line occupies the supersonic core flow region and exists for $x<250$ mm in Channel A and B, and for $x<225$ mm in the smooth channel, respectively. Furthermore, in the downstream of all channels, a low stagnation pressure region extends from the bottom wall side, which corresponds to the flow deceleration region as seen in Figs. 7 and 8. It is suggested from the above comparison that riblets improve the flow-field in the supersonic flow regime, although there is no clear difference in Mach number profile among the three channels. For $P_b/P_{0S}=0.4$ (Fig. 10), it is apparently shown that a high stagnation pressure is maintained near the riblet surface, especially for Channel A. In addition, the size of the lowest stagnation pressure region ($P_0/P_{0S}=0.3$) observed in channel A is smaller than that for the other two channels. Although there are no noticeable differences between the contour pattern for Channel B and that for the smooth channel, lower contour lines above the riblet surface of Channel B slightly approach to the bottom wall compared to contour patterns for the smooth channel. Therefore, it is found from these facts and the previous discussion of Mach number profile, that the riblet

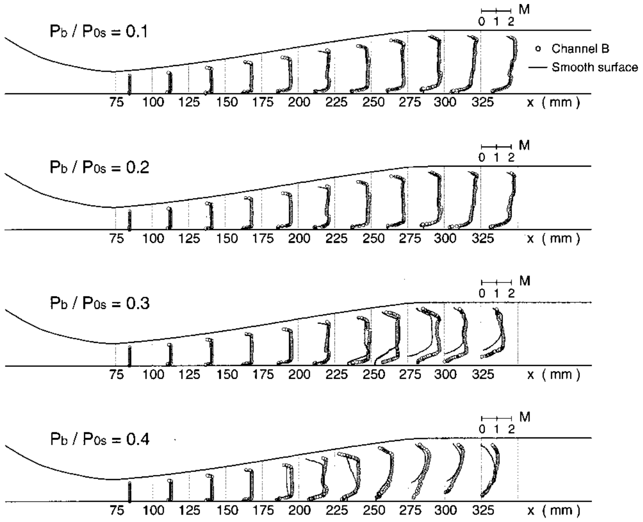

**Fig. 8 Development of Mach number profile along the *x*-direction for Channel B and the smooth channel (uncertainty in $M=\pm 0.08$ for Channel B and in $M=\pm 0.07$ for the smooth channel)**

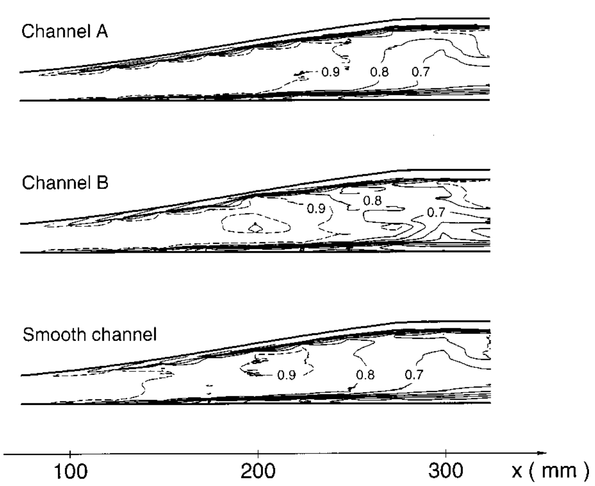

**Fig. 9 Contour plots of stagnation pressure for the operating pressure ratio of $P_b/P_{0S}=0.1$ (uncertainty in $P_0/P_{0S}=\pm 0.0066$ for Channel A, in $P_0/P_{0S}=\pm 0.0097$ for Channel B and in $P_0/P_{0S}=\pm 0.0068$ for the smooth channel)**

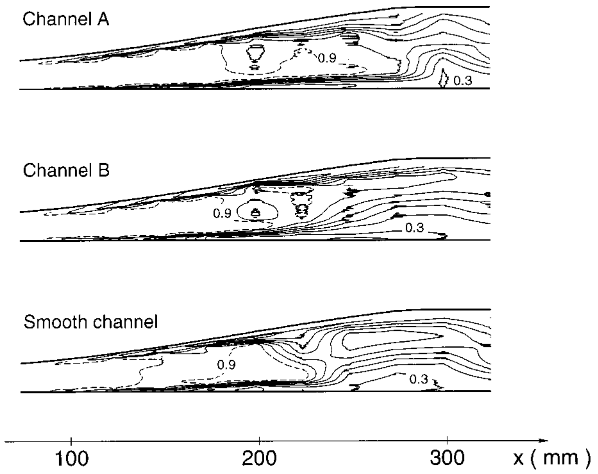

**Fig. 10 Contour plots of stagnation pressure for the operating pressure ratio of $P_b/P_{0S}=0.4$ (uncertainties: refer to the caption of Fig. 9)**

mounted on a nozzle wall delays occurrence of a separation and yields the improvement of a stagnation pressure field.

For the complex flow-field where a separation region develops with the increase of an operating pressure ratio, it is important to investigate the relationship between the local variation of a stagnation pressure and the overall performance of a supersonic nozzle. Hence, we introduce the averaged stagnation pressure which is defined as the integral mean over the channel height $H$ as follows:

$$\overline{P_0}=\frac{1}{H}\int_0^H P_0(x,z)dz \tag{1}$$

The averaged stagnation pressure distributions along the streamwise direction are presented for the three channels in Fig. 11. At the throat location of $x=75$ mm, the stagnation pressure of the air flow has almost the same value as that at the channel inlet. As the air flows downstream, the initial stagnation pressure decreases, and finally, 25~50 percent of the inlet stagnation pressure is lost at $x=325$ mm. When $P_b/P_{0S}=0.1$ and 0.2, we can observe the reduction in a stagnation pressure loss in the region of 125 mm $\leqslant x \leqslant$ 275 mm for Channel A and B. In particular, the stagnation pressure for Channel A is remarkably higher than that for the other two channels, at $x=150$ mm, 175 mm, and 200 mm. The stagnation pressure distribution upstream of $x=225$ mm for $P_b/P_{0S}=0.3$ and upstream of $x=175$ mm for $P_b/P_{0S}=0.4$, are in fair agreement with the distribution for $P_b/P_{0S}\leqslant 0.2$, and the reduction of a pressure loss is also observed. At $x=175$ mm, where the large reduction in a stagnation pressure loss is realized, the difference of $\overline{P_0}/P_{0S}$ between Channel A and the smooth channel is $\overline{P_0}/P_{0S}=0.078\sim 0.13$, and the difference between Channel B and the smooth channel is $\overline{P_0}/P_{0S}=0.022\sim 0.10$, respectively. These values are found to be larger than the experimental errors, because the uncertainty interval for nondimensionalized stagnation pressure is $\overline{P_0}/P_{0S}=\pm 0.0065\sim\pm 0.0066$ for Channel A, $\overline{P_0}/P_{0S}=\pm 0.0091\sim\pm 0.0097$ for Channel B, and $\overline{P_0}/P_{0S}=\pm 0.0064\sim\pm 0.0068$ for the smooth channel, respectively. Therefore, we can recognize that a stagnation pressure loss is reduced by riblets in a supersonic flow regime.

On the other hand, in Channel A and B, a stagnation pressure decreases rapidly beyond $x=225$ mm for $P_b/P_{0S}=0.3$, and $x=175$ mm for $P_b/P_{0S}=0.4$, respectively. Downstream of these locations, a flow separation occurs as mentioned earlier, thereby a low stagnation pressure in the separation region reduces the integral mean of a stagnation pressure. In particular, a large amount of reduction in a stagnation pressure loss is observed in the region of 225 mm$\leqslant x \leqslant$275 mm of Channel A, with decrease in the size of a separation region.

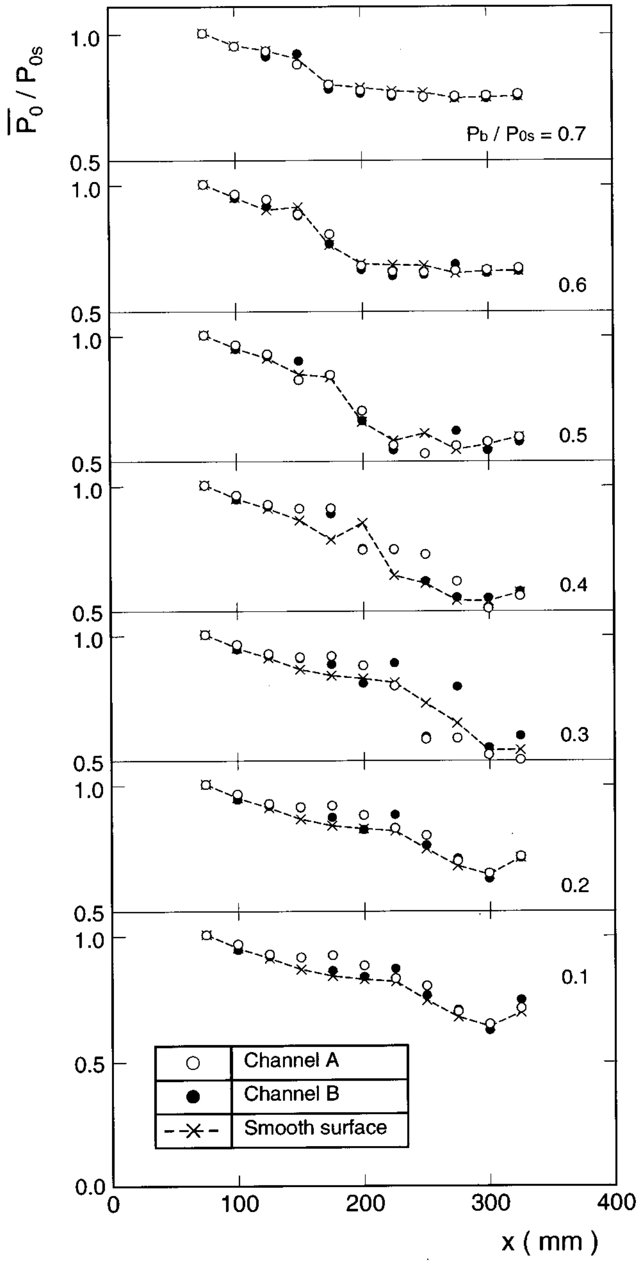

**Fig. 11 Streamwise variation of stagnation pressure, defined as the integral mean over the channel height, for various operating pressure ratios**

**3.4 Riblets Efficiency.** The above mentioned phenomena indicate that riblets influence the flow-field with a high-Mach number, and thus, it is necessary to investigate the dependence of a riblet efficiency on a flow Mach number. For the present purpose, we define the reduction ratio of a stagnation pressure loss as follows

$$\eta_l=1-\frac{P_l^R}{P_l^S}, \tag{2}$$

where $P_l=1-\overline{P_0}/P_{0S}$ is the amount of a stagnation pressure loss

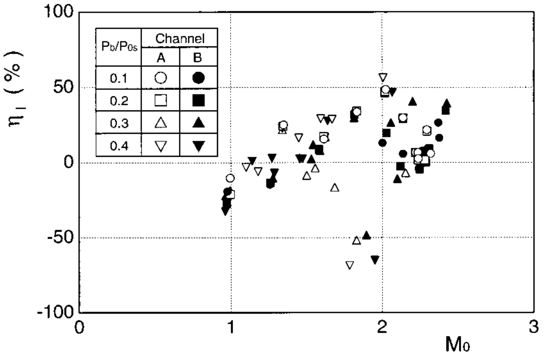

**Fig. 12 Reduction ratio in stagnation pressure loss as a function of Mach number**

at each measurement section, and the superscripts of ''*R*'' and ''*S*'' represent the riblet channel and the smooth channel, respectively.

Figure 12 summarizes characteristics of $\eta_l$ as a function of the maximum Mach number $M_0$ at each measurement section. All of the data plotted in Fig. 12 are the results obtained for $P_b/P_{0S} \leqslant 0.4$, where a supersonic core flow is kept. Here, the evaluated uncertainty interval associated with $\eta_l$ is $\pm 3.6 \sim \pm 6.4$ percent. This figure shows that $\eta_l$ increases with Mach number throughout the range of $1.0 < M_0 < 2.0$ for both channels. In particular, for the flow-field in Channel A, where the flow in the core region stays supersonic downstream of the throat and there is no shock wave or separation, riblets result in a high efficiency of $\eta_l = 46 \sim 56$ percent at $M_0 = 2.0$. At $P_b/P_{0S} = 0.4$ for Channel A, $\eta_l$ of $16 \sim 29$ percent is achieved in the range of $1.4 < M_0 < 1.7$. The condition in this case corresponds to a flow-field in which the separation region above the riblets surface is smaller than that above the smooth surface. In contrast, there exist few data having a negative value in the range of $1.8 < M_0 < 2.0$, which means an increase of a stagnation pressure loss. In this case, a stagnation pressure is maintained at high value near the riblet surface. However, since the stagnation pressure in the core flow region is strongly reduced by a shock-wave, the stagnation pressure averaged in the wall-normal direction finally decreases.

**3.5 Estimation of Optimum Riblets Size.** A large number of drag measurements have revealed the optimum riblet height $h^+$ and spacing $s^+$. Here, $h^+$ and $s^+$ are represented in law of the wall coordinate, and defined as follows

$$h^+ = \frac{hu_\tau}{\nu}, \quad s^+ = \frac{su_\tau}{\nu}, \tag{3}$$

where $u_\tau$ is the friction velocity and $\nu$ is the kinematic viscosity, respectively. For instance, Walsh [1] indicated that the optimum $h^+$ and $s^+$ required to obtain a maximum drag reduction is $h^+ = s^+ = 12$ for V-groove riblets having the aspect ratio of $h/s = 1.0$. Walsh and Lindemann [9] reported that the maximum drag-reduction of 7 to 8 percent was achieved for V-groove riblets with $h^+ = 13$ and $s^+ = 15$. Furthermore, Walsh [1], Square and Savill [7], and Gaudet [8] suggested that, when riblets are designed for $h^+ < 30$ and $s^+ < 30$, a net drag reduction can be expected over a wide range of Reynolds numbers. In this section, we try to evaluate the optimum size of riblets under the present experimental conditions and compare it with the conventional results.

Figure 13 shows streamwise velocity profile in the law of the wall coordinate at $x = 150$ and 175 mm for the smooth channel. In the case of an incompressible turbulent boundary layer, mean-velocity profile near the wall is written in the form of the law of the wall as

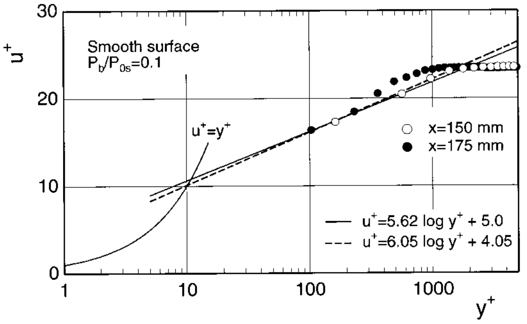

**Fig. 13 Streamwise velocity profile in law of the wall coordinate (uncertainty in $u^+ = \pm 0.4$ and in $y^+ = \pm 3.2$)**

$$\frac{u}{u_\tau} = \frac{1}{0.41} \ln \frac{u_\tau y}{U_0} + 5.0 \tag{4}$$

However, it is difficult to apply Eq. (4) to compressible turbulent boundary layer, since a variation of mass-density loses the uniqueness of definition of a friction velocity $u_\tau$. In order to solve this problem, Winter and Gaudet [10] introduced effective friction velocity $u_\tau^i$ which was defined as the following equation

$$u_\tau^i = \sqrt{\frac{1}{2} F_c C_f} \cdot U_0, \quad F_c = \sqrt{1 + 0.2 M_0^2} \tag{5}$$

And finally, they proposed law of the wall equation as follows

$$\frac{u}{u_\tau^i} = \frac{1}{0.38} \ln \frac{u_\tau^i y}{U_0} + 4.05 \tag{6}$$

They reported that the empirical equation (5) gave the best fit to the measurement data for the range of $1.4 < M_0 < 2.8$. In the present experiment, the free-stream Mach number was $2.2 \sim 2.4$, and hence we used the above mentioned relationship to estimate the skin friction coefficient. The experimental results are in good agreement with the law of the wall equation, and the skin friction coefficient determined by Clauser's method (Clauser [11]) is $C_f = 0.0028$ at $x = 150$ mm and $C_f = 0.0027$ at $x = 175$ mm, respectively. These values seem to be reasonable for the turbulent boundary layer, although the spatial resolution in the Pitot-tube traverse is too coarse to resolve the near-wall structure. With reference to these values, we calculate riblets sizes of $h^+$ and $s^+$ by assuming the local skin friction coefficient to be within a range of $0.002 < C_f < 0.004$ for $1.5 < M < 2.0$. Consequently, the riblet spacing is $20.0 < s^+ < 33.5$ for Channel A and B. The riblet height is $8.8 < h^+ < 14.7$ for Channel A and $10.8 < h^+ < 18.1$ for Channel B, respectively. These results are satisfied with the conditions of $h^+ < 30$ and $s^+ < 30$, and so we find that the conventional optimum size of riblets is also applicable to the supersonic internal flow. Therefore, the drag-reduction mechanism for the supersonic internal flow may be considered to be related to the restriction of the movement of streamwise vortices and similar to the drag reduction mechanisms for low speed flows. Both are in the same drag reduction regime ($h^+ < 30$, $s^+ < 30$). However, in order to clarify the drag-reduction mechanism, detailed study of the near wall structure for turbulent boundary layers in a supersonic flow-field is expected as a future work.

## 4 Conclusions

The flow-field in the supersonic nozzle with a riblet surface was experimentally investigated. The effects of riblets on the nozzle performance were discussed based on the reduction ratio in the stagnation pressure loss. The comparison of the experimental results between the riblet channels and the smooth channel lead to the following conclusions:

1 The magnitude of the static pressure in the pressure-rise region observed in the riblet channels becomes lower than that for the smooth channel, and it is found that its difference is significant by uncertainty analysis estimated at 95 percent coverage.

2 The streamwise development of Mach number distributions shows that the separation point moves downstream and the size of a separation region becomes smaller by using riblets.

3 When the flow-field without a shock wave and a separation is realized, the highest stagnation pressure area, which occupies the supersonic core flow region in the riblet channel, is extended compared with the smooth channel. For the flow-field with a separation, a high stagnation pressure is maintained near the riblet surface and the size of the lowest stagnation pressure region becomes smaller than that for the smooth channel.

4 To obtain a quantitative estimation of riblets efficiency, the reduction ratio in a stagnation pressure loss is introduced, and hence, it is found that the efficiency achieved up to 56 percent in the uniform flow-field at a Mach number of 2.0, and 29 percent in the flow-field with a separation above a riblet surface. It is suggested from this fact that riblets improve the performance of a supersonic nozzle with or without flow separation.

## Acknowledgment

This work was supported through the Grant-in-Aid for Encouragement of Young Scientists (No. 07750204) by the Ministry of Education, Science and Culture.

$C_f$ = local skin friction coefficient $= 2\tau_w/\rho U_0^2$
$F_c$ = compressibility factor
$H$ = channel height
$h$ = riblets height
$M$ = Mach number
$M_0$ = maximum Mach number
$P_b$ = back pressure measured at the inlet of vacuum tank
$P_g$ = wall static pressure
$P_0$ = stagnation pressure
$\overline{P_0}$ = integral mean of stagnation pressure (equation (1))
$P_{0S}$ = upstream stagnation pressure
$s$ = riblets spacing
$U_0$ = maximum velocity
$u$ = time-mean velocity in the $x$-direction
$u_\tau$ = friction velocity
$x,y,z$ = coordinate system with origin at the center of the leading edge of the bottom wall: $x$, streamwise; $y$, wall-normal; $z$, spanwise
$\delta$ = boundary layer thickness (distance from wall at which $u = 0.99U_0$)
$\eta_l$ = reduction ratio in stagnation pressure loss (Eq. (2))
$\nu$ = kinematic viscosity of air
$\rho$ = density of air
$\tau_w$ = wall shear stress

### Superscripts

$(\ )^+$ = nondimensionalized value by $u_\tau$ and $\nu$

## References

[1] Walsh, M. J., 1982, ''Turbulent Boundary Layer Drag Reduction Using Riblets,'' AIAA Paper, 82-0169.
[2] Bacher, E. V., and Smith, C. R., 1985, ''A Combined Visualization-Anemometry Study of the Turbulent Drag Reducing Mechanisms of Triangular Micro-Groove Surface Modifications,'' AIAA Paper, 85-0548.
[3] Choi, K.-S., 1989, ''Near-Wall Structure of a Turbulent Boundary Layer with Riblets,'' J. Fluid Mech., **208**, pp. 417–458.
[4] Suzuki, Y., and Kasagi, N., 1994, ''Turbulent Drag Reduction Mechanism Above a Riblet Surface,'' AIAA J., **32**, No. 9, pp. 1781–1790.
[5] Chu, D. C., and Karniadakis, G. E., 1993, ''A Direct Numerical Simulation of Laminar and Turbulent Flow over Riblet-Mounted Surfaces,'' J. Fluid Mech., **250**, pp. 1–42.
[6] Choi, H., Moin, P., and Kim, J., 1993, ''Direct Numerical Simulation of Turbulent Flow over Riblets,'' J. Fluid Mech. **255**, pp. 503–539.
[7] Squire, L. C., and Savill, A. M., 1987, ''Some Experiences of Riblets at Transonic Speeds,'' *Proc. Intl. Conf. on Turbulent Drag Reduction by Passive Means, Royal Aero. Soc.*, pp. 392–407.
[8] Gaudet, L., 1989, ''Properties of Riblets at Supersonic Speed,'' Appl. Sci. Res., **46**, No. 6, pp. 245–254.
[9] Walsh, M. J., and Lindemann, A. M., 1984, ''Optimization and Application of Riblets for Turbulent Drag Reduction,'' AIAA Paper, 84-0347.
[10] Winter, K. G., and Gaudet, L., 1973, ''Turbulent Boundary-Layer Studies at High Reynolds Numbers at Mach Numbers between 0.2 and 2.8,'' Aeronautical Research Council Reports and Memoranda, No. 3712.
[11] Clauser, F. H., 1954, ''Turbulent Boundary Layers in Adverse Pressure Gradients,'' J. Aeronaut. Sci., **21**, pp. 91–108.

**Sankar L. Saha**
Graduate Student,
Graduate School of Engineering,
Yokohama National University,
79-5 Tokiwadai, Hodogaya-ku,
Yokohama, 240-8501, Japan
e-mail: saha@mach.me.ynu.ac.jp

**Junichi Kurokawa**
Professor
e-mail: kuro@mach.me.ynu.ac.jp

**Jun Matsui**
Associate Professor
e-mail: jmat@post.me.ynu.ac.jp

**Hiroshi Imamura**
Research Associate
e-mail: ima@post.me.ynu.ac.jp

Department of Mechanical Engineering,
Yokohama National University,
79-5 Tokiwadai, Hodogaya-ku,
Yokohama, 240-8501, Japan

# Suppression of Performance Curve Instability of a Mixed Flow Pump by Use of J-groove

*In order to control and suppress performance curve instability characterized by the positive slope of head-capacity curve of a mixed flow pump, a very simple passive method utilizing shallow grooves mounted on a casing wall parallel to the pressure gradient (J-groove) is proposed. The optimum groove dimension and location for suppressing such an instability are determined experimentally. Results show that shallow grooves of adequate dimension and proper location can suppress such instability perfectly without decreasing the pump maximum efficiency. The remarkable effect of shallow grooves is to decrease both the swirl strength and the propagation of reverse flow at the impeller inlet region, through angular momentum absorption owing to mixing of groove reverse flow and swirl flow, yielding recovery of impeller theoretical head.* [S0098-2202(00)02603-1]

## Introduction

The radial grooves mounted on stationary casing wall of a LOX-Pump had a remarkable effect on reducing swirl of rotational flow at the back of the impeller. Even though the grooves were very shallow, such as only of 0.5 mm in depth, they could reduce the swirl strength considerably (Kurokawa et al. [1]). It is, therefore, predicted that the idea of utilizing this mechanism could be one possible way of controlling and suppressing several anomalous phenomena caused by rotational flow, such as rotating stall in vaneless and vaned diffusers, performance curve instability characterized by positive slope of head-capacity curve, rotating cavitation, and draft tube surge.

According to Greitzer [2], various complicated devices have been developed and proposed to suppress each of these anomalous phenomena, but a common and simple method of suppressing these phenomena has not been proposed.

Performance curve instability, characterized by positive slope of head-capacity curve, sometimes causes severe pressure oscillation and vibration, and hinders normal and smooth operation. According to Hergt and Starke [3] there are two types of instabilities in a diffuser pump. One is caused by back flow at an impeller inlet (called Part Load Whirl, PLW) and the other is caused by back flow in a diffuser channel (called Full Load Instability, FLI). According to Kurokawa et al. [4], the former (PLW) is caused by a sudden drop of theoretical head due to the swirl of reverse flow at the impeller inlet of a mixed flow pump. According to Kurokawa [5], the latter (FLI) is caused by rotating stall in a diffuser pump.

To suppress instability and surge of a mixed flow pump, an active method of water jet injection at the impeller inlet has been proposed recently, where jet injection in the counter rotating direction of the impeller has been found effective to enlarge the stall margin between the design point and the positive slope region of the head-flow characteristic (Goto [6]). To suppress the instability caused by stall and surge of axial, centrifugal compressors and fans, passive methods of casing treatments have also been proposed ([7–19]). The active control method proposed by Goto [6] requires complicated mechanisms and utilizes additional machinery that eventually decrease the overall efficiency and reliability.

The present study is thus aimed at a very simple common passive method of suppressing the performance curve instability by utilizing shallow grooves mounted parallel to the pressure gradient on the casing wall of a mixed flow pump. Such shallow grooves mounted parallel to the pressure gradient are termed ''**J-grooves**.'' Hereafter groove means J-groove.

The authors proposed in their previous work [20,21] similar types of grooves (radial shallow grooves i.e., parallel to the pressure gradient and thus J-groove) to suppress rotating stall in the vaneless and vaned diffusers.

## Mechanism of Suppressing Swirl by J-groove

Radial shallow grooves (J-groove) of proper dimension mounted on diffuser wall/walls had been able to suppress rotating stall perfectly in both a vaneless diffuser (Kurokawa et al. [20]) and a vaned diffuser (Kurokawa et al. [21]) for the entire flow range. Even though the grooves were very shallow such as $d = 1$ mm, the increase in flow angle was significant. A strong groove flow e.g., for $\phi = 0.10$, 30 percent of the main flow in grooves of $n = 32$, $d = 3$ mm, $w = 10$ mm on the upper wall of the diffuser (width 18 mm) was shown to flow against the main flow. Experimental findings and theoretical considerations (Kurokawa et al. [20]) revealed that the remarkable effects of J-groove are caused by the following two mechanisms; one is a remarkable decrease in tangential velocity at the diffuser inlet owing to mixing between the main flow and the groove reverse flow, and the other is a remarkable increase in radial velocity due to the groove reverse flow. Both effects have the same contribution to increase the flow angle.

## Experimental Apparatus

The mixed flow pump tested in this experiment is shown schematically in Fig. 1. It is equipped with an impeller of 5 blades, a diffuser of 7 guidevanes, and a swirl stop about 20 mm upstream of the impeller inlet tip. $N_s$ and $\omega$ of the impeller are 830 and 0.33, respectively. The impeller inlet angle $\beta_1$ is 21.0 deg and outlet angle $\beta_2$ is 31.4 deg. The impeller tip clearance is 0.7 mm and inlet and outlet tip radii are 97.6 mm and 123.5 mm, respec-

---

Contributed by the Fluids Engineering Division for publication in the JOURNAL OF FLUIDS ENGINEERING. Manuscript received by the Fluids Engineering Division May 18, 1999; revised manuscript received March 27, 2000. Associate Technical Editor: D. Williams.

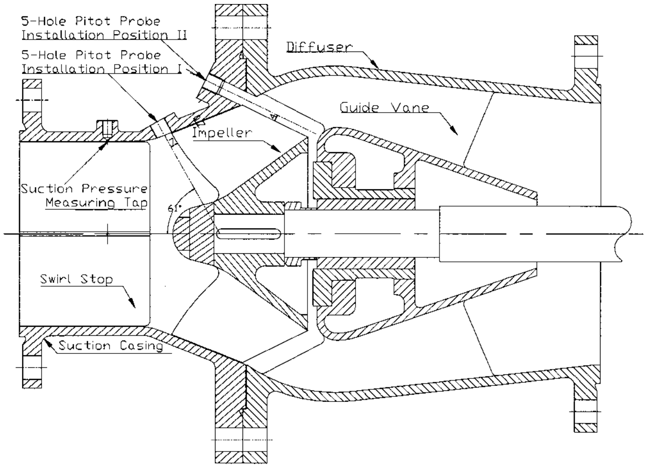

Fig. 1 Mixed flow pump tested (Ns=830)

tively. The suction and discharge pressure measuring taps are located 61.5 mm upstream and 713.0 mm downstream of the impeller inlet tip, respectively. Pump discharge is calculated from the pressure difference across an orifice of radii ratio 0.8. All the pressure differences in this experiment for the steady cases are measured with differential pressure cell transducers of suitable capacities. The impeller is driven at a constant speed of 1460 rpm, and the blade tip clearance is kept fixed at 0.7 mm throughout all experiments. The test Reynolds No. $R_e = 2U_2 r_2/\nu$ is $3.6\times10^6$.

Because the positive slope of the head-capacity curve is caused by the rapid drop of theoretical head due to a strong swirl of reverse flow at the impeller inlet of a mixed flow pump (Kurokawa et al., [4]), the J-groove is utilized upstream of the impeller inlet. This anticipates that the groove flow would suppress both the swirl and reverse flow at low flow region, and might not affect the pump performance at the high flow region including the Best Efficiency Point (BEP).

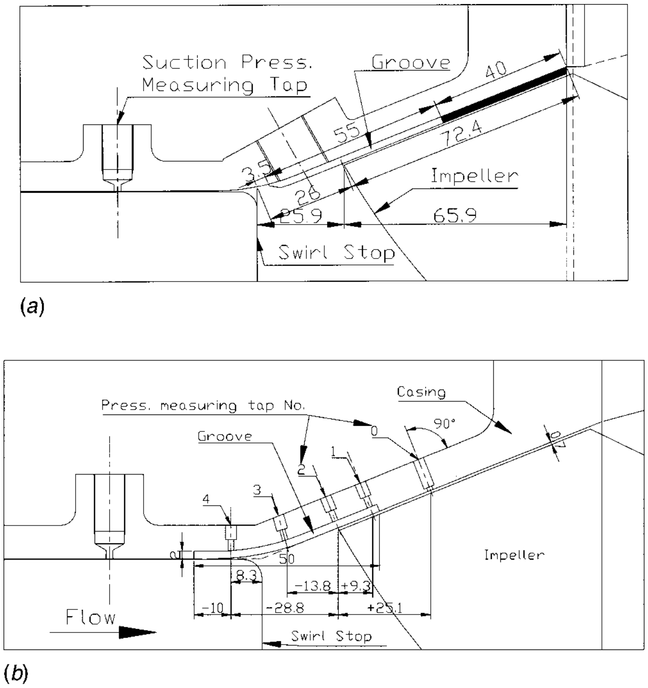

Fig. 2 Location of J-groove on the casing wall, (*a*) Grooves formed on the surface of the casing wall, (*b*) grooves formed under the surface of the casing wall

When the J-groove is installed in the test pump, a remarkable improvement of head-capacity and efficiency curve is attained as described later. Because it is believed that the groove dimensions ($w$, $d$, $l$, $n$) and location would influence the performance-curve instability, various combinations of dimensions and locations are tested, and finally the optimum combination is determined.

Initially the grooves are formed by thin rubber pieces pasted on the surface of the casing wall by a quick-drying adhesive, as shown in Fig. 2(*a*). However, from the practical point of view, the grooves are to be formed by machining. The hill part of the groove should be flat to the upstream and downstream casing wall. To realize the utility of J-groove in such a practical case, further tests were performed by altering the casing wall as shown in Fig. 2(*b*). The casing wall is trimmed to a slot of 4 mm in depth in the region of the optimum location, and rubber pieces are pasted in the slot to form J-grooves of different patterns. The hill surfaces of the grooves are finished flush with the upstream and downstream connecting wall.

To examine the mechanism of angular momentum absorption resulting from the mixing of groove reverse flow and swirl flow, pressure gradients between holes No. 0–4 (Fig. 2(*b*)) on the bottom and hill of the groove and the suction pressure measuring tap are measured for a wide flow range. The velocity distributions at the section 7 mm upstream of the impeller inlet tip are also measured with traversing a 5-hole Pitot probe.

## Results and Discussions

**(1) Original Performance Curves of the Test Pump.** The original performance characteristics of the test pump are shown by the symbol ○ in Fig. 3. The performance curve instability with a rapid drop of head-capacity and efficiency curve can be seen clearly at $\phi = 0.135$, which is about 65 percent of the BEP and is referred to as critical flow coefficient. The flow range of performance curve instability is seen from 30 percent to 65 percent of the BEP.

**(2) Effect of J-grooves on Instability.** Comparisons of test results are illustrated in Fig. 3 for three different cases i.e., no groove, J-groove of $28^n\times4\ \mathrm{mm}^d\times5\ \mathrm{mm}^w$ and that of $28^n\times2\ \mathrm{mm}^d\times10\ \mathrm{mm}^w$. The third case (□) represents the optimum dimension of the J-groove determined by the present study.

Comparing with no groove (○), a remarkable improvement is seen for the J-groove of $28^n\times2\ \mathrm{mm}^d\times10\ \mathrm{mm}^w$ (□). No positive slope of the head-capacity curve is seen. It can be seen that the

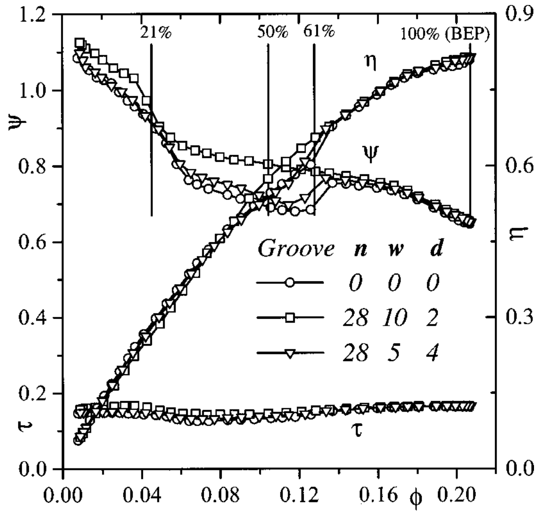

Fig. 3 Comparison of performance curves. Uncertainties of $\phi$, $\psi$, $\tau$, and $\eta$ are ±1.4 percent; ±0.7 percent; ±1.1 percent and ±2 percent, respectively

grooves do not produce additional hydraulic loss, as because the efficiency increases in the flow range of the performance curve instability, and the maximum efficiency is not influenced at all.

However, in case of J-groove of $28^n \times 4\ \mathrm{mm}^d \times 5\ \mathrm{mm}^w$(▽), only a slight improvement is attained. A large instability still remains, although the total sectional area of J-groove is same in both the cases. This indicates that the width of J-groove has key importance.

**(3) Velocity and Pressure Measurements.** In order to understand the reason for the remarkable improvement in head-capacity curve, the changes in meridional and tangential velocity distributions at the impeller inlet between the J-groove of optimum dimension ($28^n \times 2\ \mathrm{mm}^d \times 10\ \mathrm{mm}^w$) and no groove are shown in Fig. 4.

The velocity distributions shown are measured for the BEP ($\phi = \phi_n$, denoted by ○) and for $\phi/\phi_n = 0.73$(□), 0.61(△), 0.50(▽) and 0.21(◇). It is already shown in Fig. 3 that the flow at which performance curve instability occurs is about 65 percent of the BEP, and unstable range is about 30 percent–65 percent of the BEP. The comparison of △ with ▲ and ▽ with ▼ reveals the mechanism of suppressing the instability by J-groove.

Figure 4 clearly shows that the reverse flow with large swirl velocity begins at a flow a little higher than $\phi/\phi_n = 0.61$, which coincides well with the onset of the performance curve instability shown in Fig. 3.

Comparison of velocity distributions for $\phi/\phi_n = 0.61$ (△ with ▲) are shown in Fig. 4; however it is not a fair comparison as the flow was unstable and fluctuated suddenly in case of no groove. However, for $\phi/\phi_n = 0.50$, the flow was much more stable and it is fair to compare. Thus the comparison of ▽ with ▼ reveals that $V_\theta$ is largely decreased and the region of reverse flow ($V_m < 0$) is also reduced by the J-groove.

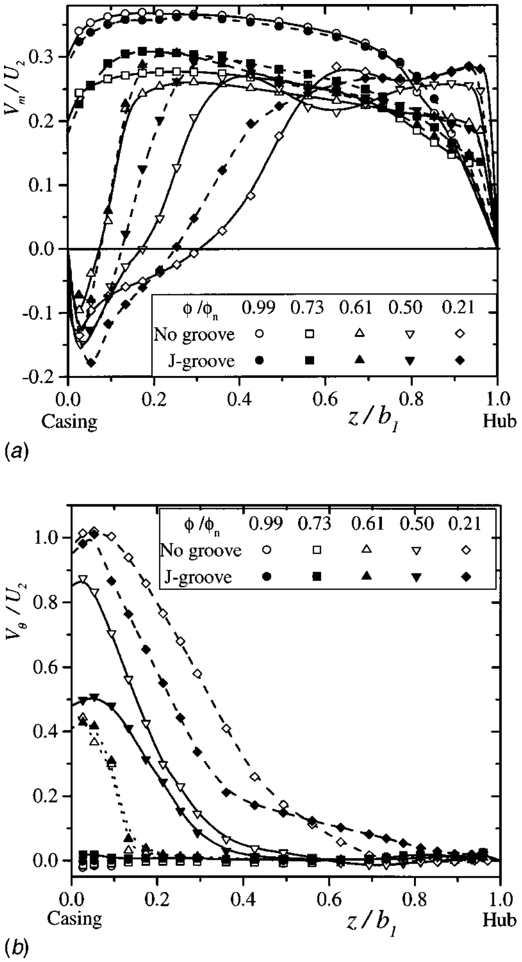

(*a*)

(*b*)

**Fig. 4 Velocity distribution at the impeller inlet section. Uncertainties of $V_m/U_2$; $V_\theta/U_2$ and $z/b_1$ are ±3.3 percent; ±3.3 percent and ±2.2 percent, respectively. (*a*) Meridional velocity component, (*b*) tangential velocity component**

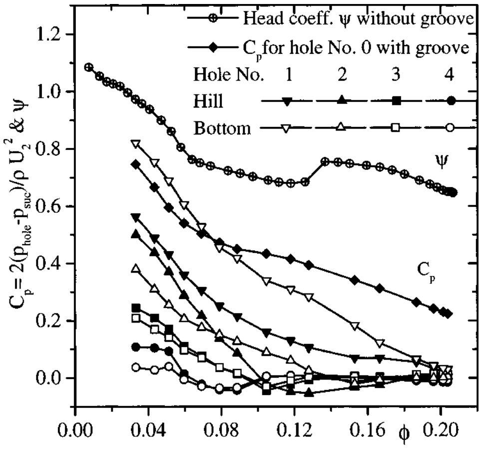

**Fig. 5 Comparison of pressure coefficient at the hill and bottom of J-groove. Uncertainties of $C_p$; $\phi$ and $\psi$ are ±1 percent, ±1.4 percent and ±0.7 percent, respectively**

To understand this phenomenon, the pressure gradient in the axial direction along the casing surface is shown in Fig. 5 only for the optimum J-groove dimension. Here two kinds of pressure coefficients, i.e., static pressure coefficients at the bottom and hill of the J-grooves are shown. Holes No. 0–4 in Fig. 5 correspond to the pressure measuring taps No. 0–4 shown in Fig. 2(*b*). $C_p$ is defined by the nondimensional pressure difference between hole and suction tap i.e., $\Delta p = p_{\mathrm{hole}} - p_{\mathrm{suc}}$.

It is seen from Fig. 5 that all the pressure coefficients at the BEP are almost equal except for the pressure at hole No. 0, which is about 25 mm downstream of the impeller inlet tip. This means that the optimum groove location is a low pressure rise region such that no groove flow occurs and causes no effect on the stable region. It is also seen that the pressure of hole No. 1 at the bottom of the groove is exceptionally high, especially in the low flow region and at the hill is moderate. Pressure in the other holes show slight differences in the stable flow range ($\phi > 0.135$). However, when the performance curve instability occurs at $\phi = 0.135$, low pressure rises in the main flow direction and pressure of holes No. 1 and 2 at the bottom of grooves are higher than at the hill, until the unstable range exists (30 percent–65 percent of the BEP). The pressure of holes No. 3 and 4 at the bottom and hill of groove remains the same. When the flow is lower than the unstable range ($\phi < 30$ percent of the BEP), the pressure of hole No. 1 at the bottom of the groove becomes exceptionally high compared to the hill as mentioned earlier, but the pressures of holes No. 2, 3, and 4 at the bottom of the groove fall lower than at the hill.

The above results reveal that at the onset of instability, a jet flow forms automatically in the J-groove, and flows against the main flow up to a low pressure region where it mixes with and increases the main flow.

Based on the mechanism of radial grooves (Kurokawa et al. [20]), suppression of swirl and inlet reverse flow in the present case is also caused by mixing between the swirl flow and the groove reverse flow. In the J-groove, a jet flow occurred (due to the sharp pressure gradient) in the opposite direction of the main flow. This groove flow has no angular momentum, but the main flow has large angular momentum near the wall when the impeller inlet swirl occurred. So a large angular momentum absorption occurred when the groove reverse flow mixes with the main flow

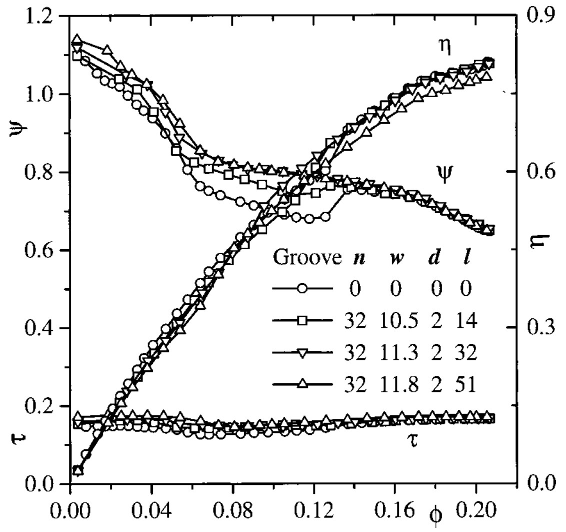

**Fig. 6 Effect of groove length on instability. Uncertainties of $\phi$, $\psi$, $\tau$, and $\eta$ are ±1.4 percent; ±0.7 percent; ±1.1 percent and ±2 percent, respectively**

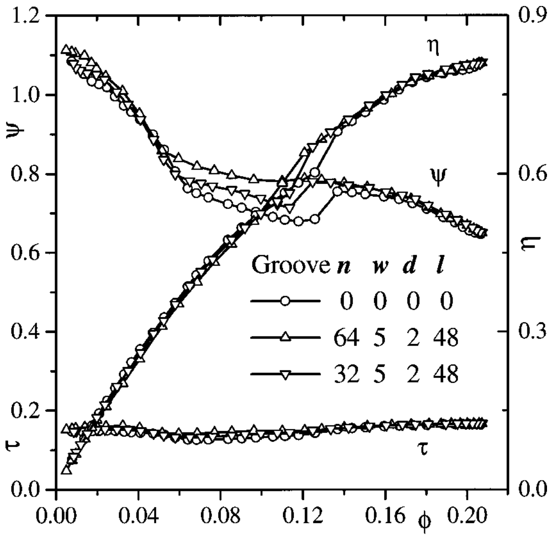

**Fig. 8 Effect of groove number on instability. Uncertainties of $\phi$, $\psi$, $\tau$, and $\eta$ are ±1.4 percent; ±0.7 percent; ±1.1 percent and ±2 percent, respectively**

near the wall. If the impeller inlet flow had no swirl, then the groove reverse flow would not have any angular momentum absorption.

It can, therefore, be mentioned that the mechanism of J-groove is quite different from those of casing treatments ([7]–[19]). The J-groove does not utilize any additional equipment such as chamber, air-separator, recess vane, honeycomb, Amann et al. [11], Miyake et al. [16,17], Azimian et al. [18], and Smith [19]. Rather it utilizes the flow behavior itself. Either the geometry or the location or both of the J-groove are different from those in the conventional casing treatments, such as the circumferential, radial, axial, skewed, reversed skewed, blade-angle groove/slot used by Boyce et al. [9], Amann et al. [11], Takata and Tsukuda [12], Greitzer et al. [13], Fujita and Takata [15], and Smith [19].

**(4) J-Groove Dimension and Location and Their Effects on Instability.** To obtain the optimum groove dimension and location, the effects of the J-groove dimension on suppressing the instability is studied using the groove patterns shown in Fig. 2. Several characteristic curves are illustrated in Figs. 6, 7, 8, and 9 corresponding to the variation of $l$, $d$ and $w$, $n$ and the location of J-groove.

Figure 6 reveals that the optimum groove length is about 32 mm. The longer grooves decrease the maximum efficiency, whereas the shorter grooves can not attain perfect suppression of instability although they are very effective (the decimal in the width dimension is the average of length-wise varying width).

Figure 7 indicates that the optimum groove depth is in the range of $d \leqslant 2$ mm for the case of $w = 10$ mm. Grooves those are too deep decrease the efficiency in the low discharge range. It also indicates that the performance curve instability is not improved by the grooves of $w = 5$ mm. However, from Fig. 8, the grooves of $w = 5$ mm can attain sufficient suppression of instability when the number of grooves is doubled.

From Fig. 9 (where, $+l$ and $-l$ indicate the portion of the length of groove downstream and upstream of the impeller inlet tip, respectively) it is seen that the insertion of long grooves into

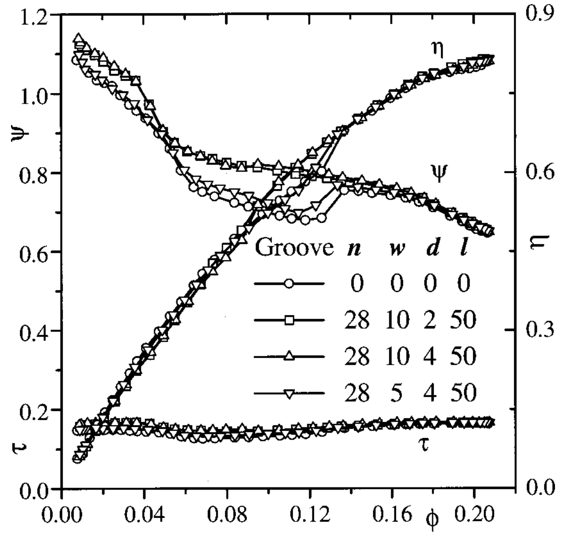

**Fig. 7 Effect of groove depth and width on instability. Uncertainties of $\phi$, $\psi$, $\tau$, and $\eta$ are ±1.4 percent; ±0.7 percent; ±1.1 percent and ±2 percent, respectively**

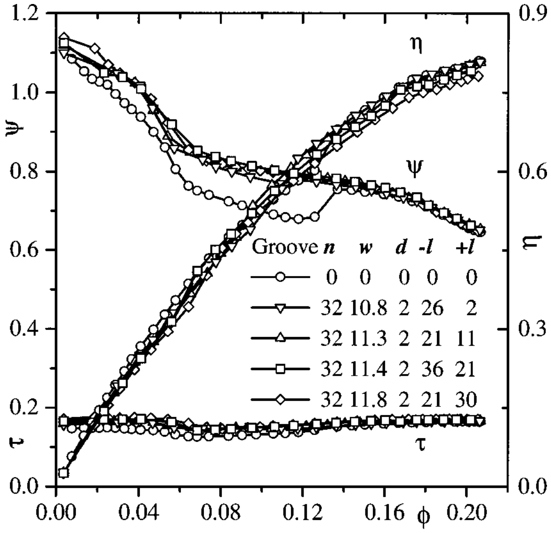

**Fig. 9 Effect of groove location on instability. Uncertainties of $\phi$, $\psi$, $\tau$, and $\eta$ are ±1.4 percent; ±0.7 percent; ±1.1 percent and ± 2 percent, respectively**

the impeller channel yields stability, but reduces efficiency whereas the shorter grooves can not attain stability. Here it can be mentioned that insertion of the long portion of grooves into the impeller channel reduces the impeller work.

From the application, machining and cost point of view, the shallow depth and lower number of J-grooves is the best. Thus the optimum dimension of J-groove within the tested range is as $d \leqq 2$ mm, $l = 50$ mm, $w = 10$ mm, and $n = 28$ and the optimum location is from 39 mm upstream to about 11 mm downstream of the impeller inlet.

**(5) Pressure Pulse and Frequency Analyses.** To examine the pressure pulse and pulse frequency around the impeller outlet and in the groove region of impeller inlet, pressure pulse measurements with semiconductor pressure transducers have been performed and FFT analyses have been done for J-groove and no groove cases.

Pressure pulse and pulse frequency at 26 mm upstream of the impeller outlet tip are seen to be similar at the BEP for the J-groove and no groove (not shown) cases. For $\phi/\phi_n = 0.61$, the amplitude of the pulsed pressure for the J-groove was seen to be 90 percent of the no groove case as shown in the window view in Fig. 10(*a*).

The pressure pulse spectrum for $\phi/\phi_n = 0.61$ for J-groove and no groove are also shown in Fig. 10(*a*). The blade passing frequency (NZ) of the tested pump is 122 Hz. The results show that the frequency distribution and power spectra for both cases agree well and there is no rotating stall.

The pressure pulse (not shown) at the hill of J-groove and with no groove, 9.3 mm downstream of the impeller inlet tip, were seen to be similar at the BEP for both the cases, but were more unstable in the case of no groove than at the hill of J-groove. An increased fluctuation amplitude occurred with decreased flow.

The pressure pulse frequency distribution for $\phi/\phi_n = 0.61$ at impeller inlet region for the no groove case and hill of the J-groove are shown in Fig. 10(*b*). The results show that the frequency distribution for both the cases are mostly an agreement, but the power spectra for the no groove cases are higher. These high power spectra and pressure pulsations in no groove compared to that of J-groove are considered to be due to the strong inlet swirl.

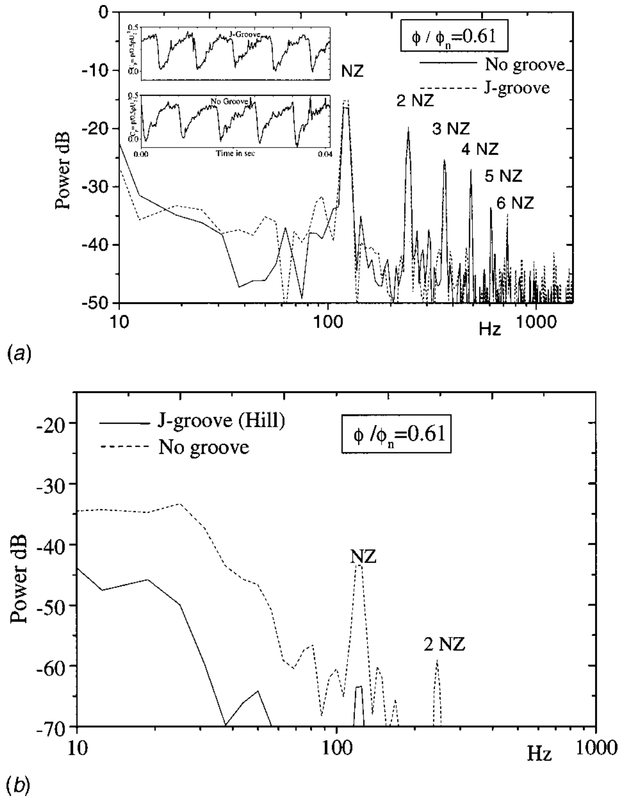

**Fig. 10 Wall pressure fluctuation. (*a*) 26 mm upstream of the impeller outlet tip, (*b*) 9.3 mm downstream of the impeller inlet tip**

**(6) Criteria of Optimum J-groove Dimension.** The effects of length, depth, width, and number of J-grooves are correlated. Again the width is more effective than the depth. To gain performance curve stability without an efficiency penalty, there must be consistency among the number, depth, width, length and location of J-groove.

From the experimental results, a logical number is deduced and defined as the J-groove Efficient No. (JE No.).

$$\text{JE No.} = \text{WR}\times\text{VR}\times\text{WDR}\times\text{DLDR} \qquad (1)$$

where, WR=Width Ratio i.e., total groove width ($n\times w$) divided by circumferential casing length at the groove mean depth and casing mean diameter, VR=Volume Ratio i.e., total groove volume ($n\times l\times w\times d$) divided by the impeller inlet volume (impeller inlet area×impeller tip axial length), WDR=Width Depth Ratio i.e., $w/d$ and DLDR=Downstream Length Depth Ratio, i.e., length of groove downstream of the impeller inlet tip ($+l$) divided by depth of groove ($d$).

The significance of the JE No. is shown in Fig. 11, where the abscissa represents the JE No. and the ordinates represent head instability and drop of maximum efficiency. Here head instability is defined as the ratio of sudden drop of head coefficient in case of J-groove compared to the no groove case. Although the uncertainty measurement of efficiency is about 2 percent, Fig. 12 clearly shows the trend of the maximum efficiency drop against J.E. No. It is seen that to gain perfect stability, the JE No. should be $\geqq 0.17$. It can be seen that groove geometry at lower JE No. is narrow or short or lacks the optimum location (e.g., less insertion of the groove into the downstream side) or a low number of grooves. This causes insufficient angular momentum absorption, and fails to suppress sufficient swirl strength and eventually fails to gain stability. On the contrary, groove geometry which has a JE No. larger than 0.17 is too wide or too long or lacks the optimum location (e.g., too much insertion of groove into the downstream

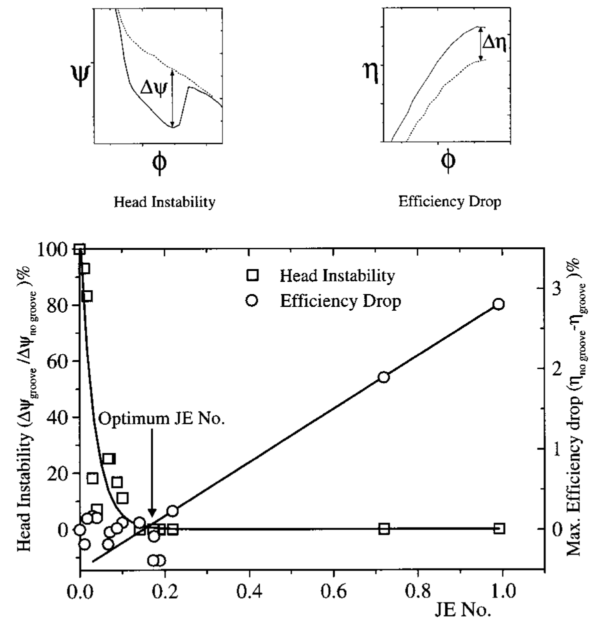

**Fig. 11 Criteria of optimum J-groove dimension. Uncertainty of JE No. is ±6.6 percent**

side) or too large in number of grooves and excessive angular momentum absorption occurs including strong groove reverse flow demanding large shaft power and decreases the maximum efficiency. Hence the optimum groove geometry is that JE No.$=0.17$.

## Conclusions

The conclusions are summarized as follows.

The J-groove of optimum dimension and proper location can suppress the performance curve instability completely, and can make a stable pump operation possible for the entire flow range.

The J-groove of optimum dimension and proper location does not decrease the peak efficiency, rather it increases the efficiency in the flow range of performance curve instability.

Velocity and pressure measurements have revealed the mechanism of suppressing the instability as described below.

Groove flow flows against the main flow and mixes with the swirl flow near the impeller inlet tip region, while reducing the swirl strength and the region of reverse flow in the critical flow and low flow range. Because the onset of inlet swirl causes a sudden drop of the pump theoretical head and thus causes the performance curve instability, the reduction of swirl strength and the region of the reverse flow by the J-groove makes the performance curve instability disappear. The present method thus utilizes absorption of angular momentum by the groove reverse flow owing to mixing with the swirl flow.

The optimum J-groove dimension and location are determined. The groove location has key importance and grooves are to be mounted parallel to the pressure gradient on the casing wall from the upstream of the impeller leading edge, and should be inserted into the impeller channel. Grooves those are too deep and wide decrease the peak efficiency, hence shallow and wide grooves are recommended.

Pressure pulse measurements depict that there is no rotating stall either in the case of the J-groove or in the case of no groove. The J-groove does not create additional pressure pulses.

From the present study, together with the former study [20,21], it has been confirmed that the J-groove is a simple common passive method of suppressing instabilities caused by rotational flow, such as rotating stall in vaneless and vaned diffusers and performance curve instability of a mixed flow pump.

## Acknowledgments

The present study was conducted under the aid of grant-in aid for Scientific Research #09555062. The authors express their sincere gratitude.

## Nomenclature

$A$ = flow area [m$^2$]
$b$ = impeller width [mm]
$C_p$ = pressure coefficient [$\Delta p/0.5\rho U_2^2$]
$d$ = depth of J-groove [mm]
$g$ = acceleration due to gravity [m/s$^2$]
$H$ = total head [m]
$l$ = length of J-groove [mm]
$n$ = number of J-groove
$N$ = revolution per minute [rpm]
$N_s$ = specific speed [m, m$^3$/min, rpm]
$p$ = pressure [Pa]
$P$ = power [N-m/s]
$Q$ = flow rate [m$^3$/s]
$r$ = radius or radial position [mm]
$U$ = impeller speed [m/s]
$V$ = fluid velocity [m/s]
$\overline{V}$ = area average velocity [m/s]
$w$ = width of J-groove [mm]
$z$ = distance from the casing wall [mm]
$\eta$ = efficiency
$\nu$ = kinematic viscosity of fluid [m$^2$/s]
$\omega$ = nondimensional specific speed [$(N/60)\sqrt{Q}/(gH)^{3/4}$]
$\phi$ = flow coefficient [$Q/A_2U_2$]
$\rho$ = density of fluid [kg/m$^3$]
$\psi$ = head coefficient [$H/(U_2^2/2g)$]
$\Delta\psi$ = drop of head coefficient
$\tau$ = shaft power coefficient [$P/0.5\rho A_2 U_2^3$]

### Subscripts

1 = inlet (at root mean square radius)
2 = outlet (at root mean square radius)
$m$ = meridional component
$n$ = best efficiency point
$\theta$ = tangential component

## References

[1] Kurokawa, J., Kamijo, K., and Shimura, T., 1994, ‘‘Axial Thrust Behavior in LOX-Pump of Rocket Engine,’’ AIAA J. Propulsion Power, **10**, No. 2, pp. 244–250.
[2] Greitzer, E. M., 1981, ‘‘The Stability of Pumping System,’’ ASME J. Fluids Eng., **103**, pp. 193–242.
[3] Hergt, P., and Starke, J., 1985, ‘‘Flow Patterns Causing Instabilities in the Performance Curves of Centrifugal Pumps with Vaned Diffusers,’’ *Proceedings 2nd International Symposium*, Texas A & M Univ., pp. 67–75.
[4] Kurokawa, J., Kitahora, T., and Jiang, J., 1994, ‘‘Performance Prediction of Mixed-Flow Pumps Using Inlet Reverse Flow Model,’’ *Proceedings 17th IAHR Symp.*, Beijing, Vol. 1, pp. 177–188.
[5] Kurokawa, J., 1992, ‘‘Performance Curve Instability of a Diffuser Pump Due to a Rotating Stall and Some Control Method,’’ *Proceedings of the 16th IAHR Symposium, Sao Paulo*, Vol. 2, pp. 723–732.
[6] Goto, A., 1994, ‘‘Suppression of Mixed-Flow Pump Instability and Surge by the Active Alteration of Impeller Secondary Flows,’’ ASME J. Turbomach., **116**, pp. 621–628.
[7] Osborn, W. M., Lewis, Jr., G. W., and Heidelberg, L. J., 1971, ‘‘Effect of Several Porous Casing Treatments on Stall Limit and on Overall Performance of an Axial-Flow Compressor Rotor,’’ NASA TN D-6537.
[8] Moore, R. D., Kovich, G., and Blade, R. J., 1971, ‘‘Effect of Casing Treatment on Overall and Blade-Element Performance of a Compressor Rotor,’’ NASA TN D-6538.
[9] Boyce, M. P., Schiller, R. N., and Desai, A. R., 1975, ‘‘Study of Casing Treatment Effects in Axial Flow Compressors,’’ ASME Paper No. 74-GT-89.
[10] Prince, D. C., Jr., Wisler, D. C., and Hilvers, D. E., 1975, ‘‘A Study of Casing Treatment Stall Margin Improvement Phenomena,’’ ASME Paper No. 75-GT-60.
[11] Amann, C. A., Nordenson, G. E., and Skellenger, G. D., 1975, ‘‘Casing Modification for Increasing the Surge Margin of a Centrifugal Compressor in an Automotive Turbine Engine,’’ ASME J. Eng. Power, **97**, pp. 329–336.
[12] Takata, H., and Tsukuda, Y., 1977, ‘‘Stall Margin Improvement by Casing Treatment—Its Mechanism and Effectiveness,’’ ASME J. Eng. Power, **99**, pp. 121–133.
[13] Greitzer, E. M., Nikkanen, J. P., Haddad, D. E., Mazzaway, R. S., and Joslyn, H. D., 1979, ‘‘A Fundamental Criterion for the Application of Rotor Casing Treatment,’’ ASME J. Fluids Eng., **101**, pp. 237–243.
[14] Smith, G. D. J., and Cumptsy, N. A., 1984, ‘‘Flow Phenomena in Compressor Casing Treatment,’’ ASME J. Eng. Gas Turbines Power, **106**, pp. 532–541.
[15] Fujita, H., and Takata, H., 1984, ‘‘A Study on Configurations of Casing Treatment for Axial Flow Compressors,’’ Bull. JSME, **27**, pp. 1675–1681.
[16] Miyake, Y., Noji, I., Nishikawa, Y., and Murata, S., 1985, ‘‘The Performance Characteristic of an Air-Separator of an Axial Flow Fan,’’ Bull. JSME, **28**, pp. 1659–1666.
[17] Miyake, Y., Inaba, T., and Kato, T., 1987, ‘‘Improvement of Unstable Characteristics of an Axial Flow Fan by Air-Separator Equipment,’’ ASME J. Fluids Eng., **109**, pp. 36–40.
[18] Azimian, A. R., Elder, R. L., and McKenzie, A. B., 1990, ‘‘Application of Recess Vaned Casing Treatment to Axial Flow Fans,’’ ASME J. Turbomach., **112**, pp. 145–150.
[19] Smith, Jr., L. H., 1994, ‘‘NASA/GE Fan and Compressor Research Accomplishments,’’ ASME J. Turbomach., **116**, pp. 555–569.
[20] Kurokawa, J., Saha, S. L., Matsui, J., and Kitahora, T., 2000, ‘‘Passive Control of Rotating Stall in a Parallel-Wall Vaneless Diffuser by Radial Grooves,’’ ASME J. Fluids Eng., **122**, pp. 90–97.
[21] Kurokawa, J., Saha, S. L., Matsui, J., and Kitahora, T., 1997, ‘‘A New Passive Control of Rotating Stall in Vaneless and Vaned Diffusers by Shallow Grooves,’’ *Proceedings of International Conference on Fluid Engineering*, Tokyo, Vol. 2, pp. 1109–1114.

**Daniel O. Baun**
Graduate Research Assistant and ROMAC Lab Engineer,
Department of Mechanical Aerospace and Nuclear Engineering,
University of Virginia, Charlottesville, VA 22903-2442
e-mail: dob2e@virginia.edu

**Lutz Köstner**
Project Engineer,
Salzgitter Pumpen AG, Salzgitter, Germany

**Ronald D. Flack**
Professor and Department Head,
Department of Mechanical Aerospace and Nuclear Engineering,
University of Virginia,
Charlottesville, VA 22903-2442
e-mail: rdf@virginia.edu

# Effect of Relative Impeller-to-Volute Position on Hydraulic Efficiency and Static Radial Force Distribution in a Circular Volute Centrifugal Pump

*The hydraulic performance and radial hydraulic force characteristics of a circular volute centrifugal pump are strongly affected by the impeller to volute relative position. For a typical design configuration the geometric center of the impeller will be coincident with the volute geometric center. However, assembling a circular volute pump with the impeller center eccentric from the volute center can radically alter both the hydraulic performance and the radial hydraulic force characteristics. In particular, at the design flow coefficient an optimum impeller to volute relative position exists where the efficiency is maximized and the resultant radial force is minimized. At the optimal relative position a 5 percent and a 3.5 percent increase in the efficiency was realized compared to the centered positions for the circular and spiral volutes, respectively. In addition the nondimensional resultant radial force at the design flow coefficient was reduced from 0.045 at the centered position to 0.005 at the optimal position for the circular casing. This value of radial thrust is similar in magnitude to the radial thrust for the spiral volute operating at the design flow coefficient. By assembling a circular volute pump with the appropriate relative impeller to volute position the design simplicity of a circular volute can be utilized without compromising pump hydraulic performance or radial force characteristics as compared to a typical spiral volute.* [S0098-2202(00)02303-8]

## Introduction

The need to understand and quantify the hydraulic interaction forces that are developed by a centrifugal impeller operating in a volute or diffuser pump is best supported by tracking the history of research in this area. Binder et al. [1], Acosta et al. [2], and Stepanoff [3] conducted some of the earliest documented investigations on impeller forces in centrifugal pumps. Stepanoff proposed a simple empirical model based on impeller geometry, pump operating head and the normalized pump capacity for the calculation of resultant radial forces. Agostinelli et al. [4] extended Stepanoff's model to account for the effect of specific speed on radial forces. Biheller [5] developed a universal equation to predict static radial pump forces applicable for a wide range of pump types and operating conditions. Hergt and Krieger [6] measured the impeller forces and moments on a range of specific speed pumps with spiral volutes. In addition, the effect of impeller center with respect to the volute center at 4 equally spaced angular positions and one eccentricity ratio was reported. Kanki et al. [7] examined the effect of number of impeller blades on the radial forces in double volute and vaned diffuser casing pumps. Chamieh et al. [8] investigated hydrodynamic impeller forces and stiffness matrices for a single volute and circular volute centrifugal pump. More recently, de Ojeda et al. [9] combined the exit momentum flux and static pressure distributions around the impeller of a double volute pump to evaluate a total resultant radial thrust. In addition to experimental investigations, numerous analytical studies have been undertaken to predict the radial hydraulic forces in centrifugal pumps, Domm and Hergt [10], Lorett and Gopalakrishnan [11], and Fongang et al. [12] to name only a few. Despite the voluminous research done on hydraulic forces, very little work has been reported in the open literature on the effect of impeller to volute relative position on the hydraulic performance or radial hydraulic force characteristics of centrifugal pumps. The present paper investigates the effect of impeller to volute relative position on both hydraulic performance and radial hydraulic forces in a circular volute end suction laboratory centrifugal pump.

## Test Apparatus

de Ojeda et al. [9] and Baun and Flack [13] have documented the pump and flow loop discussed in this paper. Therefore, only the apparatus details specifically pertinent to the new results presented in this paper will be reviewed. The nominal design point of the pump is 6.3 l/s (100 USGPM) at 2.03 m (6.66 ft) total dynamic head at an operating speed of 620 rpm. These parameters give a design specific speed, $N_s = 0.547$ (1495 US units), a design flow coefficient, $\phi_n = 0.061$, and a design head coefficient, $\psi_n = 0.458$. The details of the pump hydraulic design are given in Figs. 1, 2, and 3: the impeller, the spiral volute casing, and the circular volute casing, respectively. The pump casing consisted of a radially split pressure chamber into which volute inserts were installed. The volute inserts were securely located by clamping the front and back halves of the pressure casing together. O-rings around the flow path perimeter of the volute inserts ensured a positive seal between the volute insert and the front and back pressure chamber walls. The flow path profiles for the different volute inserts were NC machined from Plexiglas sheets and have a two-dimensional cross section as shown in Figs. 2 and 3. All surfaces of the volute flow paths were constructed of polished (optically clear) Plexiglas. The volute cut water to impeller radius ratios, $r_{3CV}/r_2$ and $r_{3SV}/r_2$, were 1.688 and 1.063 for the circular and spiral volutes, respectively. The volute throat areas, $A_{\text{th}} = L_{\text{th}}$

---

Contributed by the Fluids Engineering Division for publication in the JOURNAL OF FLUIDS ENGINEERING. Manuscript received by the Fluids Engineering Division July 2, 1999; revised manuscript received May 15, 2000. Associate Technical Editor: B. Schiavello.

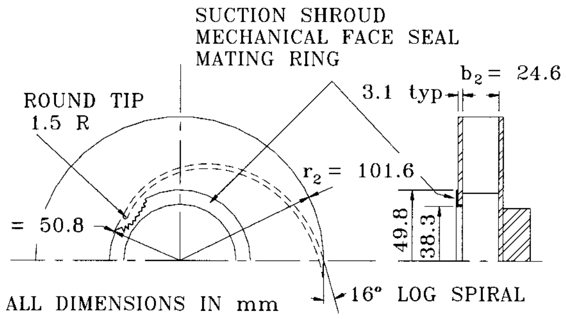

**Fig. 1 Plexiglas impeller**

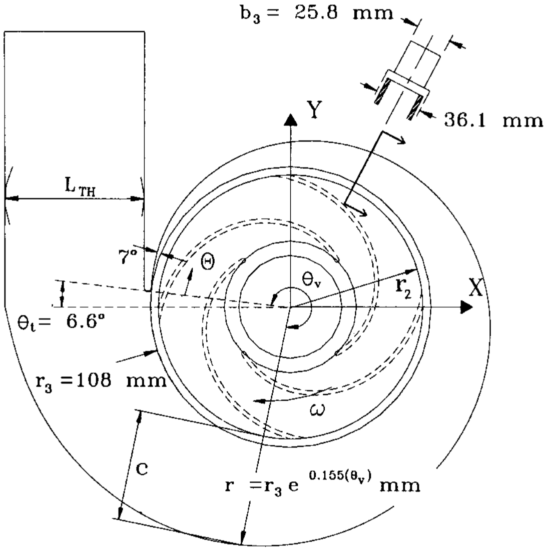

**Fig. 2 Spiral volute (SV)**

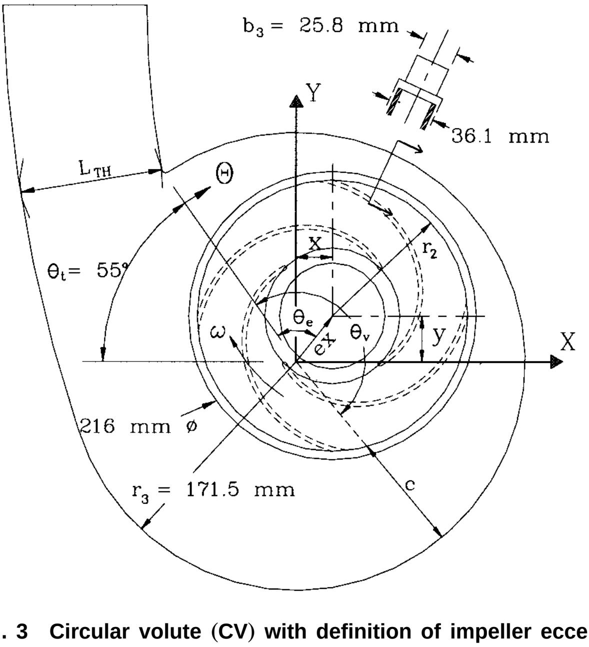

**Fig. 3 Circular volute (CV) with definition of impeller eccentricity**

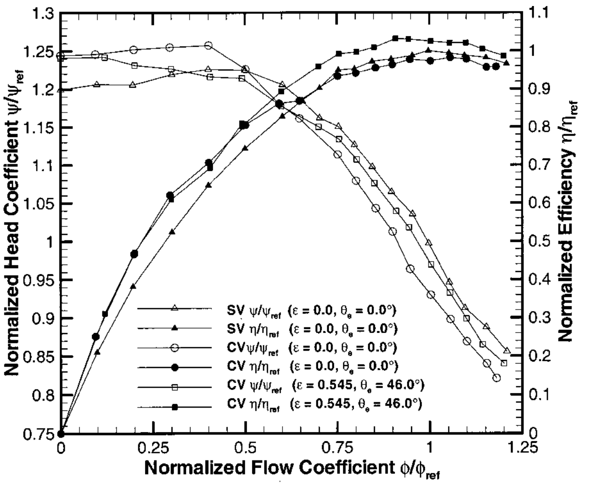

**Fig. 4 Hydraulic performance: centered SV, centered CV and optimally located CV ($\varepsilon \approx 0.55$, $\theta_e \approx 46$ deg). (Uncertainties: $\Delta\phi/\phi_{ref} \approx \pm 0.01$; $\Delta\psi/\psi_{ref} \approx \pm 0.007$; $\Delta\eta/\eta_{ref} \approx \pm 0.01$.)**

$\times b_3 = 2785$ mm$^2$ (4.3 in.$^2$), are identical between the circular and the spiral volute casings. Figure 4 shows the normalized hydraulic performance for the spiral volute, the centered circular volute, and the circular volute located at the optimal eccentric position (detailed discussion to follow). The best efficiency head and flow coefficients of the spiral volute in the centered condition, $\psi_{SV,\mathrm{bep},\varepsilon=0} \equiv \psi_{\mathrm{ref}}$ and $\phi_{SV,\mathrm{bep},\varepsilon=0} \equiv \phi_{\mathrm{ref}}$, respectively, are used to normalize *all* head and flow coefficient data. To facilitate simple and direct comparison of the efficiency between the two volutes and the various relative positions tested, all efficiencies have been normalized by the efficiency of the centered spiral volute at the design flow which corresponds to the bep and hence is symbolized by, $\eta_{SV,\mathrm{bep},\varepsilon=0} \equiv \eta_{\mathrm{ref}}$. The mechanical setup, stuffing box seal, suction shroud seal, magnetic bearings, couplings and shroud clearances were the same between the spiral volute and the circular volute at all eccentric test positions. Therefore, normalized efficiencies greater than one, $\eta/\eta_{\mathrm{ref}} > 1$, represent an increase in hydraulic efficiency while normalized efficiencies less than one, $\eta/\eta_{\mathrm{ref}} < 1$, represent a decrease in hydraulic efficiency. The pump rotor is supported radially and axially with magnetic bearings that also serve as active load cells for the measurement of hydraulic forces. The static and dynamic properties of the load cells have been rigorously characterized and a detailed assessment of their respective measurement uncertainties have been quantified, Baun et al. [14] and Fittro et al. [15]. In addition, verification of the hydraulic force measurement capabilities of the apparatus was demonstrated on a spiral volute centrifugal pump, Baun and Flack [13].

## Test Program

A testing program was conducted to study the effect of impeller to volute relative position on hydraulic performance and static impeller force for a centrifugal pump with a circular volute casing. The circular volute insert was centered in the front half of the pressure casing with dowel pins. From this position inside micrometers were used to map the clearance around the outside perimeter of the volute insert and the adjacent pressure casing wall. To set the volute in an eccentric position the dowel pins were removed and gauge-blocks and/or shims were inserted between the outer perimeter of the volute insert and the adjacent pressure casing walls. The casing insert was positioned to a tolerance of 0.13 mm (0.005 in.). For each eccentric test case the casing insert was repositioned with gauge blocks and clamped firmly in place between the two pressure casing halves. A search for the relative impeller to volute position that produced the highest hydraulic efficiency was conducted by systematically varying the volute center position relative to the impeller center and measuring the resulting pump hydraulic performance and radial force characteristics. Twenty discrete test positions were used as shown in Fig. 5. The nondimensional eccentricity ratio, $\varepsilon$, and attitude angle, $\theta_e$, of the twenty test positions are given in Table 1.

## Experimental Technique

The experimental technique used to make the static/time averaged impeller force measurements was described, in detail, by Baun and Flack [13]. The only addition to these procedures was to make *in situ* force calibrations on each magnetic bearing/load cell. This was accomplished by applying know weights normal to the axis of the shaft with a pulley-and-cable apparatus. The component of the applied load acting on each bearing was determined and compared to the indicated bearing force as obtained from Baun and Flack [13], Eq. (5),

$$F_X = \tfrac{1}{2} k_{th} \mathbf{I}^T \mathbf{N}^T \mathbf{R}^{-T} \mathbf{A}_x \mathbf{R}^{-1} \mathbf{N} \mathbf{I}$$

$$F_Y = \tfrac{1}{2} k_{th} \mathbf{I}^T \mathbf{N}^T \mathbf{R}^{-T} \mathbf{A}_y \mathbf{R}^{-1} \mathbf{N} \mathbf{I}.$$

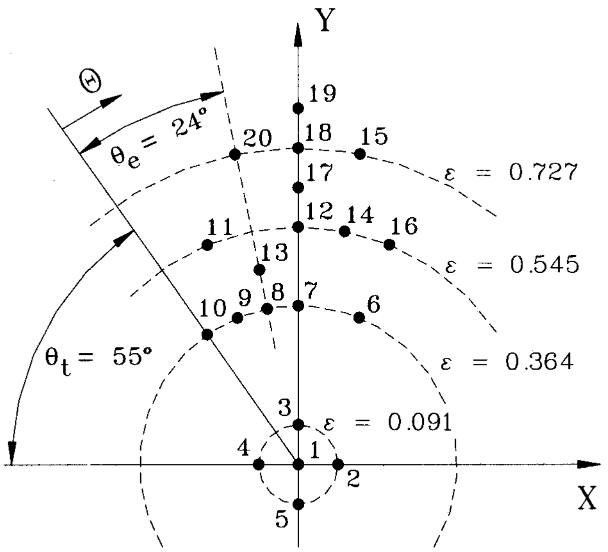

**Fig. 5 Matrix of test positions. (Uncertainties: $\Delta\varepsilon \approx \pm 0.003$, $\Delta\theta_e \approx \pm 0.15$ deg.)**

**Table 1 List of test positions for CV**

| Position No. | Eccentricity Ratio (ε) | Attitude Angle (θe) |
|---|---|---|
| 1 | 0 | 125.0 |
| 2 | 0.091 | 125.0 |
| 3 | 0.091 | 35.0 |
| 4 | 0.091 | 305.0 |
| 5 | 0.091 | 215.0 |
| 6 | 0.364 | 57.5 |
| 7 | 0.364 | 35.0 |
| 8 | 0.364 | 24.0 |
| 9 | 0.364 | 12.5 |
| 10 | 0.364 | 0.0 |
| 11 | 0.545 | 12.5 |
| 12 | 0.545 | 35.0 |
| 13 | 0.455 | 24.0 |
| 14 | 0.545 | 46.0 |
| 15 | 0.727 | 46.0 |
| 16 | 0.545 | 57.5 |
| 17 | 0.636 | 35.0 |
| 18 | 0.727 | 35.0 |
| 19 | 0.818 | 35.0 |
| 20 | 0.727 | 24.0 |

The calibration factor, $k_{th}$, was then adjusted based on a linear regression of the applied load versus the indicated load. The addition of this procedure reduced the nondimensional uncertainty of a typical force measurement from approximately 0.008 to approximately 0.002. This reduction in the force measurement uncertainty was primarily achieved by eliminating the strong dependence of the force uncertainty, $\Delta F$, on the uncertainty in the shaft centering position, $\Delta x$ and $\Delta y$, within the magnetic bearings as given by Baun and Flack [13], Eq. (7),

$$\Delta F = \left[ \left( \frac{\partial F}{\partial k} \Delta k \right)^2 + \left( \frac{\partial F}{\partial i_e} \Delta i_e \right)^2 + \left( \frac{\partial F}{\partial i_n} \Delta i_n \right)^2 + \left( \frac{\partial F}{\partial i_w} \Delta i_w \right)^2 + \left( \frac{\partial F}{\partial i_s} \Delta i_s \right)^2 + \left( \frac{\partial F}{\partial \theta} \Delta \theta \right)^2 + \left( \frac{\partial F}{\partial x} \Delta x \right)^2 + \left( \frac{\partial F}{\partial y} \Delta y \right)^2 + \left( \frac{\partial F}{\partial b} \Delta b \right)^2 \right]^{0.5}.$$

Approximately 90 percent of the total force uncertainty, $\Delta F$, was due to the magnetic bearing gap uncertainties, $\Delta x \approx \Delta y \approx \pm 0.00001\,\mathrm{m}$ ($\pm 0.00025$ in.) which in turn are due primarily to unavoidable system misalignment introduced during apparatus assembly.

## Results

**Translation Along *Y*-Axis ($\theta_e = 35$ deg).** A representative plot of the head and efficiency characteristics for a progressive series ($\theta_e = \text{constant} = 35$ deg, $0.364 \leqslant \varepsilon \leqslant 0.818$) of impeller to volute relative positions is shown in Fig. 6. For reference the normalized head coefficient, $\psi/\psi_{\text{ref}}$, versus the normalized flow coefficient, $\phi/\phi_{\text{ref}}$, at the centered position, $\varepsilon = 0.0$, is included. For low normalized flow coefficients, $\phi/\phi_{\text{ref}} < 0.2$, the $\psi/\psi_{\text{ref}}$ characteristic for the centered case is the highest with a shutoff value of approximately 1.245. In contrast for high normalized flow coefficients, $\phi/\phi_{\text{ref}} > 0.8$, the $\psi/\psi_{\text{ref}}$ characteristic for the centered case is the lowest. Focusing attention on the characteristics for $\theta_e = \text{constant} = 35$ deg, $0.364 \leqslant \varepsilon \leqslant 0.818$ a clear progression in the normalized head coefficient is seen as the relative position is moved along the positive $y$-axis from $\varepsilon = 0.364$ to $\varepsilon = 0.818$. The normalized shutoff head coefficient drops from 1.23 to 1.19. The general shape of the normalized head coefficient curves at low normalized flow coefficients, $\phi/\phi_{\text{ref}} < 0.3$, changes from having a positive slope for $\varepsilon = 0.364$, to being almost flat for $\varepsilon = 0.545$, to having an increasingly negative slope for $\varepsilon = 0.636$, $\varepsilon = 0.727$, and $\varepsilon = 0.818$. At higher normalized flow coefficients, $\phi/\phi_{\text{ref}} > 0.7$, the variation in the head characteristic between each position is less pronounced, however, a clear trend is still evident. All the curves, with the exception of $\varepsilon = 0.818$, intersect between the normalized flow coefficients of 0.9 and 1.0. At higher flow rates, $\phi/\phi_{\text{ref}} > 1.0$, the ordering of the head coefficient curves are reversed from the ordering at shutoff. The progression in the normalized efficiency, $\eta/\eta_{\text{ref}}$, is more difficult to identify on a lined plot such as Fig. 6 because the changes are small. As the relative position is systematically varied from $\varepsilon = 0.364$ to $\varepsilon = 0.727$ two trends are apparent: (1) The peak normalized efficiency increases from 0.985 to 1.04. (2) The normalized flow coefficient at which the peak normalized efficiency occurs increases from 1.0 to 1.1. The peak normalized efficiency drops to about 1.0 as the eccentricity is increased to $\varepsilon = 0.818$. The normalized efficiency for the centered case is the lowest for normalized flow rates above about 0.7.

Representative plots of the magnitude of the nondimensional resultant radial force, $F$, and the orientation of the resultant force

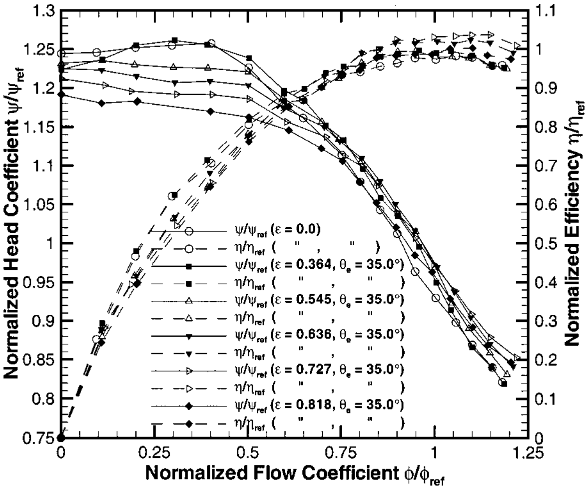

**Fig. 6 Variation of normalized head coefficient and normalized efficiency with relative position along *Y*-axis for the CV. (Uncertainties: $\Delta\phi/\phi_{\mathrm{ref}}\approx\pm0.01$; $\Delta\psi/\psi_{\mathrm{ref}}\approx\pm0.007$; $\Delta\eta/\eta_{\mathrm{ref}}\approx\pm0.01$.)**

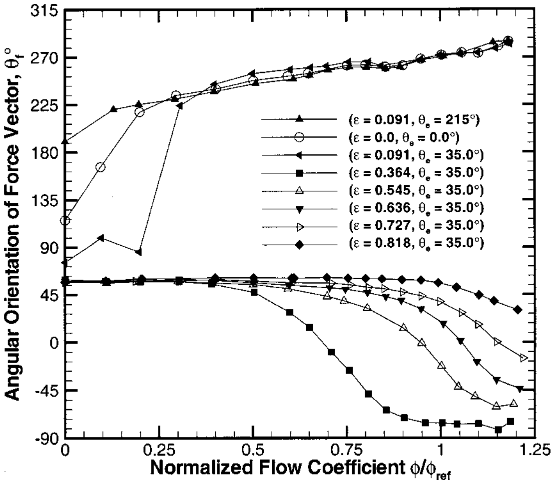

**Fig. 8 Variation of resultant force vector orientation ($\theta_f$) with relative position along *Y*-axis for the CV. (Uncertainties: $\Delta\phi/\phi_{\mathrm{ref}}\approx\pm0.01$; $\Delta F\approx\pm0.002$; $\Delta\varepsilon\approx\pm0.003$; $\Delta\theta_e\approx\pm0.15$ deg.)**

vector, $\theta_f$, as a function of the impeller to volute relative position along the *Y*-axis are shown in Figs. 7 and 8, respectively. These figures include the forces at the centered position ($\varepsilon=0.0$) and the forces for a small positive ($\varepsilon=0.092$, $\theta_e=35.0$ deg) and negative ($\varepsilon=0.092$, $\theta_e=215.0$ deg) perturbations about the center along the *Y*-axis. Figure 7 shows that the centered condition produces the smallest force magnitude at shutoff, $F=0.015$, but a large force magnitude, $F=0.045$, at the design flow condition. However, the force magnitude characteristic for the centered condition is nearly flat for $\phi/\phi_{\mathrm{ref}}>0.7$. In contrast when the impeller is at the relative position, $\varepsilon=0.818$, $\theta_e=35.0$ deg, the largest shutoff force is observed, $F=0.133$ and a minimum force, $F=0.02$, is observed at the normalized flow coefficient, $\phi/\phi_{\mathrm{ref}}\approx1.2$. The general shape of the resultant radial force characteristic for the positions, $\varepsilon=0.545$, 0.636, 0.727 and 0.818 are similar to the shape of the resultant force characteristic of a spiral volute pump. The shape of the radial force characteristic for a spiral volute pump, which is well known, is characterized by a maximum at shut-off and a minimum near the design flow rate, Stepanoff [3].

Systematic trends in the orientation of the resultant radial force vector, $\theta_f$, as the relative position is changed are clearly illustrated in Fig. 8. As the relative position is varied from $\varepsilon=0.092$, $\theta_e=215.0$ deg to $\varepsilon=0.364$, $\theta_e=35.0$ deg the orientation of the force vector at shutoff changes progressively from 190–58 deg. The orientation of the force vector at shutoff remains constant at 58 deg for all other eccentricity ratios ($\varepsilon=0.545$, 0.636, 0.727, and 0.818). Above the normalized flow coefficient, $\phi/\phi_{\mathrm{ref}}>0.3$, the orientation of the resultant force vectors for the relative positions, $\varepsilon=0.092$, $\theta_e=215$ deg, $\varepsilon=0.0$, $\theta_e=0.0$ deg, and $\varepsilon=0.092$, $\theta_e=35$ deg all converge and become approximately collinear. In addition, the angular orientation of the force vectors for these three positions becomes increasingly positive as the flow coefficient increases ($\theta_f\approx284$ deg at runout) indicating that the resultant force vector is rotating in the direction of impeller rotation. This contrasts with the angular orientations of the force vectors for positions, $\varepsilon=0.364$, 0.545, 0.636, 0.727 and 0.818. These positions all have a common value, $\theta_f\approx58$ deg, at shutoff, are collinear for normalized flow coefficients less than 0.3 and rotate opposite to the direction of impeller rotation as the flow coefficient is increased. The force orientations at run-out for these five positions vary progressively from $\theta_f\approx-75$ deg at $\varepsilon=0.364$, $\theta_e=35.0$ deg to $\theta_f\approx30$ deg at $\varepsilon=0.818$, $\theta_e=35.0$ deg.

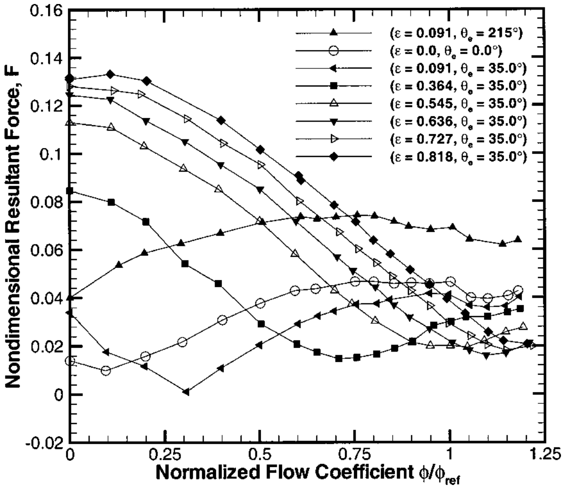

**Fig. 7 Variation of nondimensional resultant force (*F*) with relative position along *Y*-axis for the CV. (Uncertainties: $\Delta\phi/\phi_{\mathrm{ref}}\approx\pm0.01$; $\Delta F\approx\pm0.002$; $\Delta\varepsilon\approx\pm0.003$; $\Delta\theta_e\approx\pm0.15$ deg.)**

**Force Contour Plots.** Nondimensional resultant radial force contour plots at the normalized flow coefficients, $\phi/\phi_{\mathrm{ref}}=0.0$, 0.5, 0.75 and 1.0 are shown in Figs. 9, 10, 11, and 12, respectively. These contour plots were generated using all 20 test cases as given in Table 1 and shown in Fig. 5. The contour level scales are consistent between figures. A nondimensional force gradient, $|dF/d\varepsilon|$, is defined as the change in force resulting from a change in relative position. To calculate the force gradient at each flow rate the hydraulic center, point of minimum force, (or center of the 0.0–0.01 contour level) was selected. This point will have a nondimensional force magnitude of approximately 0.005. A line was extended from the hydraulic center perpendicularly across 3 complete contour levels. The force gradient, $|dF/d\varepsilon|$, was then calculated as, ($dF\equiv0.035/d\varepsilon\equiv$length of line). An eccentric test position corresponding to the hydraulic center was not taken at each flow rate. Therefore, Figs. 10 and 11 do not show a 0.0–0.01 force contour level and the hydraulic center was approximated as the center of the lowest contour level shown on each respective figure. In addition to force magnitude contour levels, Figs. 9–12, show force orientation vectors, $\theta_f$, at each of the test positions.

Figure 9, force contours at $\phi/\phi_{\mathrm{ref}}=0$, shows that the hydraulic center occurs at the relative position $\varepsilon=0.092$, $\theta_e=305.0$ and that the magnitude of the force gradient, $|dF/d\varepsilon|$ is approximately 0.23. Comparing Fig. 10, $\phi/\phi_{\mathrm{ref}}=0.5$, to Fig. 9, $\phi/\phi_{\mathrm{ref}}=0$, re-

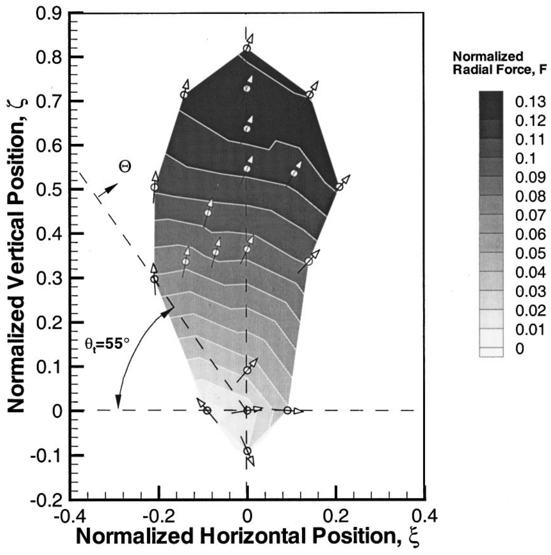

**Fig. 9 Nondimensional force contours ($F$) at the normalized flow coefficient, $\phi/\phi_{\text{ref}}=0.0$ for the CV. (Uncertainties: $\Delta F\approx\pm0.002$; $\Delta\phi/\phi_{\text{ref}}\approx\pm0.01$; $\Delta\xi\approx\pm0.001$; $\Delta\zeta\approx\pm0.001$.)**

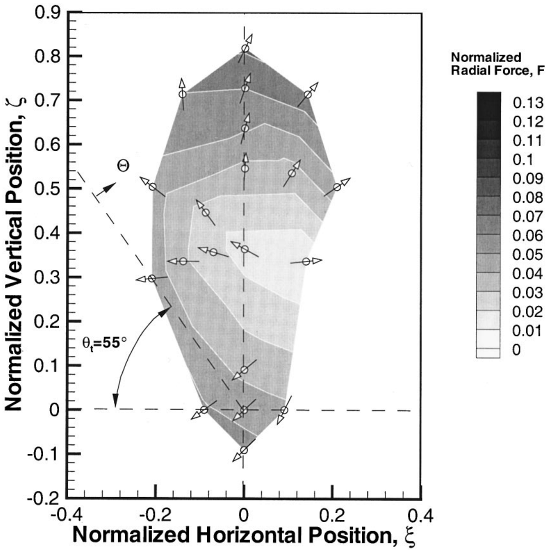

**Fig. 11 Nondimensional force contours ($F$) at the normalized flow coefficient, $\phi/\phi_{\text{ref}}=0.75$ for the CV. (Uncertainties: $\Delta F\approx\pm0.002$; $\Delta\phi/\phi_{\text{ref}}\approx\pm0.01$; $\Delta\xi\approx\pm0.001$; $\Delta\zeta\approx\pm0.001$.)**

veals that: (1) As the flow coefficient is increased the hydraulic center shifts to $\varepsilon\approx0.2$, $\theta_e\approx30.0$ deg. (2) The force gradient has decreased to approximately 0.18 as indicated by a reduction in the number of contour levels from 13 to 10. Progressing to Fig. 11, $\phi/\phi_{\text{ref}}=0.75$, the trends observed between Figs. 9 and 10 are continued: (1) The hydraulic center has moved up and to the right and is approximately located at $\varepsilon=0.42$, $\theta_e=40.0$ deg. (2) The number of contour levels has decreased to 7 resulting in a reduction in the force gradient to approximately 0.15. Figure 12, radial force contours at $\phi/\phi_{\text{ref}}=1.0$, shows a continuation of the trends previously observed between Figs. 9, 10, and 11. The hydraulic center has continued to move up and to the right farther into the first quadrant and is now located at $\varepsilon=0.545$, $\theta_e=46.0$ deg. The number of contour levels has decreased to 5 and the force gradient has decreased to approximately 0.12. Figures 9–12 show that the relative impeller to volute positions which minimize the total radial impeller force at each flow rate form a continuous locus of points originating near $\varepsilon=0.092$, $\theta_e=305.0$ at $\phi/\phi_{\text{ref}}=0.0$ and extending in a line oriented at $\theta_e\approx46.0$. The force gradient decreases from approximately 0.23 to 0.12, a factor of 1.9, as the normalized flow coefficient increases from 0.0 to 1.0, respectively.

The force orientation vectors, $\theta_f$, in each of Figs. 9–12 show a consistent characteristic of radiating outwards (away) from the hydraulic center with a slight (clockwise) twist in the direction of impeller rotation. Using this qualitative observation, the force gradients can be resolved into radial and tangential components and interpreted as radial and cross-coupled position stiffnesses, respectively. The radial position stiffnesses are negative, in the same direction as the displacements, and the cross coupled stiffnesses act in the tangential direction such that forward impeller whirl will be promoted.

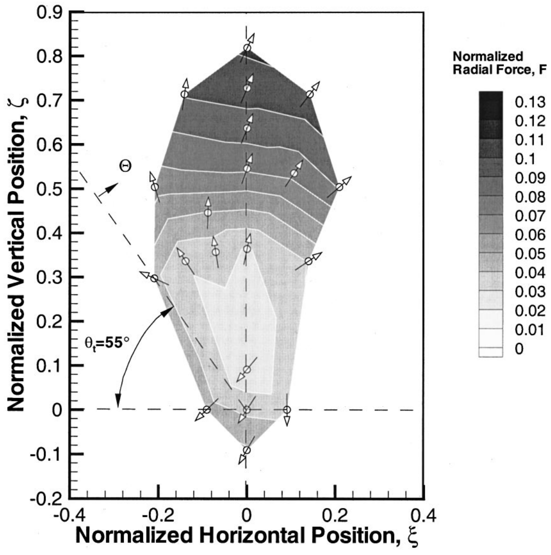

**Fig. 10 Nondimensional force contours ($F$) at the normalized flow coefficient, $\phi/\phi_{\text{ref}}=0.5$ for the CV. (Uncertainties: $\Delta F\approx\pm0.002$; $\Delta\phi/\phi_{\text{ref}}\approx\pm0.01$; $\Delta\xi\approx\pm0.001$; $\Delta\zeta\approx\pm0.001$.)**

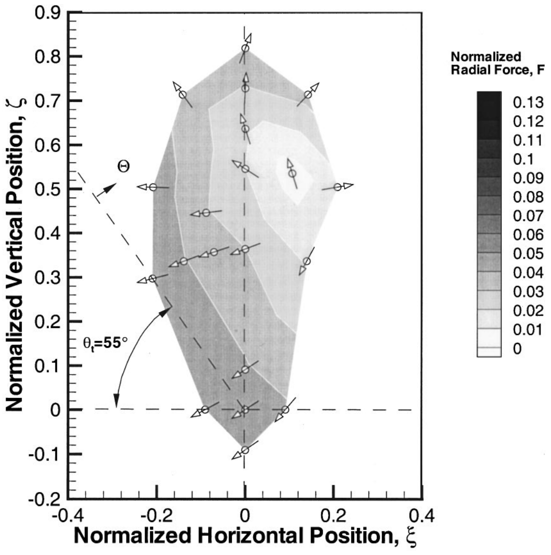

**Fig. 12 Nondimensional force contours ($F$) at the normalized flow coefficient, $\phi/\phi_{\text{ref}}=1.0$ for the CV. (Uncertainties: $\Delta F\approx\pm0.002$; $\Delta\phi/\phi_{\text{ref}}\approx\pm0.01$; $\Delta\xi\approx\pm0.001$; $\Delta\zeta\approx\pm0.001$.)**

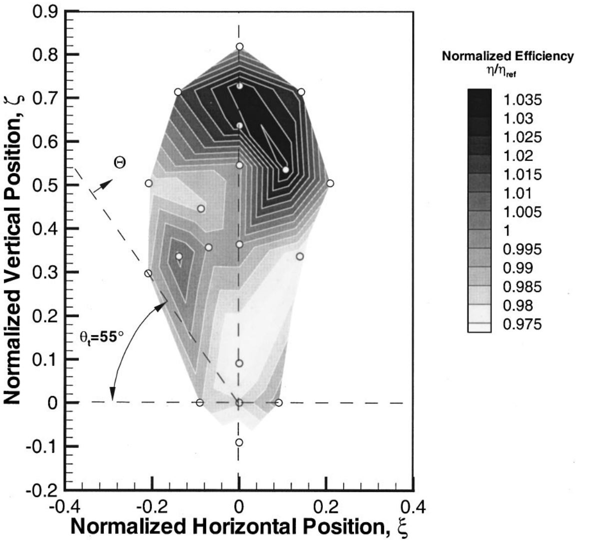

**Fig. 13 Normalized efficiency contours ($\theta_f$) at the normalized flow coefficient, $\phi/\phi_{ref}=1.0$ for the CV. (Uncertainties: $\Delta\eta/\eta_{ref}\approx\pm0.01$; $\Delta\phi/\phi_{ref}\approx\pm0.01$; $\Delta\xi\approx\pm0.001$; $\Delta\zeta\approx\pm0.001$.)**

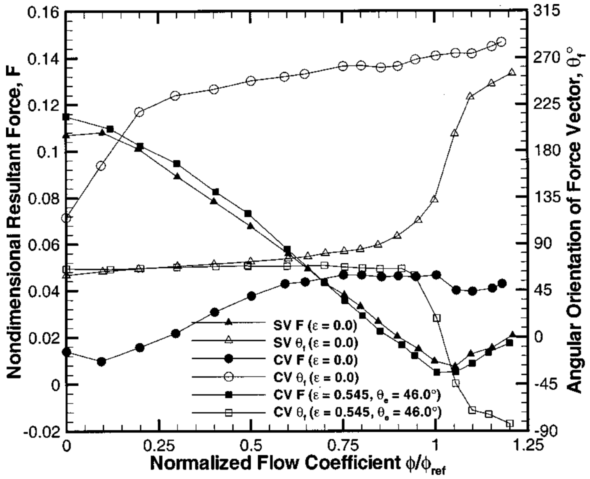

**Fig. 14 Magnitude and orientation of resultant hydraulic force: centered SV, centered CV and optimally located CV ($\varepsilon\approx0.55$, $\theta_e\approx46$ deg). (Uncertainties: $\Delta\phi/\phi_{ref}\approx\pm0.01$; $\Delta F\approx\pm0.002$; $\Delta\theta_e\approx\pm0.15$ deg.)**

**Efficiency Contour Plots.** A normalized efficiency, $\eta/\eta_{ref}$, contour plot at the design flow, $\phi/\phi_{ref}=1.0$, is shown in Fig. 13. The efficiencies used to generate this contour plot are not necessarily the highest efficiencies observed at each particular test position, but rather the efficiencies at the design flow, $\phi/\phi_{ref}=1.0$. As with the force contour plots, this contour plot was generated using all 20 test cases as given in Table 1 and shown in Fig. 5. There are multiple efficiency islands in this plot. However, the efficiency island centered near $\varepsilon=0.545$, $\theta_e=46.0$ deg is distinctly higher than the others, with a maximum normalized magnitude of 1.035. This contour is located at the same relative volute to impeller position as the minimum force contour at the design flow coefficient, $\phi/\phi_{ref}=1.0$ (Fig. 12). Around this position the efficiency contours are close together, indicating steep efficiency gradients, and the maximum efficiency contour has a small area indicating that the optimum efficiency condition is limited to a small range of impeller to volute relative positions.

**Comparison of Optimum Position With *SV* and Centered *CV*.** Figure 4 shows a comparison of the hydraulic performance for the spiral volute, the centered circular volute ($\varepsilon=0.0$) and the optimally positioned circular volute ($\varepsilon=0.545$, $\theta_e=46.0$ deg). The centered circular volute has a lower hydraulic efficiency for all normalized flow coefficients above 0.5 as compared with the spiral volute. At the design flow, $\phi/\phi_{ref}=1.0$, the centered circular volute has a normalized efficiency, $\eta/\eta_{ref}\approx0.985$. However, the normalized efficiency of the circular volute increases to 1.035 when the impeller is located at the optimal eccentric position. Figure 14 shows a comparison of the resultant radial force, $F$, and the orientation of the force vectors, $\theta_f$, for the same three volute configurations. The optimally located circular volute has a radial force characteristic with virtually identical magnitude to that of the spiral volute over the complete flow range. However, the angular orientations of the resultant force vectors for the spiral volute and the optimally located circular volute are quite different. From shut-off to $\phi/\phi_{ref}=0.5$, the angular orientations of the force vectors are approximately the same at 63.0 deg. For $\phi/\phi_{ref}>0.5$ the force vector for the spiral volute begins to rotate in the positive direction (direction of impeller rotation) while the force vector for the optimally placed circular volute rotates in the negative direction. Between the normalized flow coefficients, $0.9<\phi/\phi_{ref}<1.1$, the orientation angles for both volutes diverge sharply. At run-out the total angle swept by the force vectors are +192 and −148 deg for the spiral volute and the optimally located circular volute, respectively.

The shut-off and run-out vector orientations, the directions of rotation, and the total angles swept from shut-off to run-out by the force vectors for the spiral volute and the centered circular volute are entirely consistent with their respective counterparts as reported in the literature, Stepanoff [3]. Figure 15 is included as a comparison of the normalized volute areas, $A_v$, as a function of angular position, $\theta_v$, measured form the volute tongue for the spiral volute, centered circular volute ($\varepsilon=0.0$) and optimally located circular volute ($\varepsilon=0.545$, $\theta_e=46.0$ deg). The volute area for the optimally located circular volute converges for $0<\theta_v<46$ deg, diverges for 46 deg$\leq\theta_v<225$ deg then converges again between 225 deg$\leq\theta_v<288$ deg before diverging into the discharge section of the volute. The observed differences in the angular orientation of the force vector for the optimally located circular volute are likely due to two factors: (1) The flow exiting the impeller does not experience a strong interaction with the volute tongue. In contrast, Miner et al. [16] showed that for a spiral volute the tongue stagnation point rotates from the discharge (throat) side of the tongue to the inside (impeller side) of

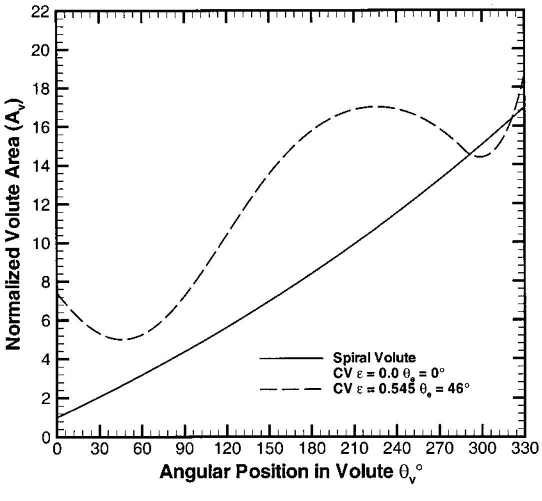

**Fig. 15 Normalized volute area ($A_V$) versus angular position in volute ($\theta_V$)**

the tongue as the flow rate is increased from shutoff. Therefore, the local high pressure region associated with the tongue stagnation point rotates in the direction of impeller rotation. (2) As the recirculating flow is accelerated through the converging flow channel, $0\ \text{deg} < \theta_v < 46.0\ \text{deg}$ (Fig. 15), a Bernoulli effect produces a low-pressure zone. This low-pressure zone grows as the capacity is increased, causing the resultant force vector to rotate towards it, in the direction of the volute tongue or opposite the direction of impeller rotation.

## Conclusions

The effect of impeller to volute relative position on hydraulic performance and radial impeller force characteristic for a circular volute casing pump were investigated. The results for a circular volute casing with $r_{3CV}/r_2 = 1.688$ were compared with the corresponding measurements for a spiral volute casing with $r_{3SV}/r_2 = 1.063$ and $N_s = 0.547$; the two volutes had the same throat areas. The following important observations were made:

1 An optimum impeller to volute relative position was found for the circular volute pump characterized by an eccentricity ratio, $\varepsilon \approx 0.545$, and attitude angle, $\theta_e \approx 46.0$ deg.

2 At the optimum position an increase in hydraulic efficiency of about 5 percent and 3.5 percent over that of the centered circular volute and the spiral volute, respectively, was observed at the design flow coefficient.

3 At the optimum position the magnitude of the radial force characteristic for the circular volute is virtually identical to that of the spiral volute over the full flow range.

4 For low flow coefficients, $\phi/\phi_{\text{ref}} < 0.8$ the angular orientation of the force vectors are approximately the same for both the optimally located circular volute and the spiral volute. As the flow coefficient increases above the design coefficient the orientation of the force vectors diverge, becoming increasingly negative for the optimally located circular volute and increasingly positive for the spiral volute. Above the design flow coefficient the force orientation vectors for each volute asymptotically approach a common value.

5 The head, efficiency, and resultant radial force characteristics of a circular volute pump can be varied in a systematic fashion by assembling the pump with the appropriate impeller to volute relative position.

6 Impeller to volute relative positions exist for which head curve stability is improved at low flows (shutoff) while the head coefficient is reduced at bep and runout flows.

7 There exists a locus of impeller to volute relative positions along which the total force is minimized at a particular flow rate.

8 As the flow coefficient is increased from $\phi/\phi_{\text{ref}} = 0$ to $\phi/\phi_{\text{ref}} = 1.0$, the sensitivity of the force gradient to a displacement away from the point of minimum force decreases.

9 The minimum force line represents a locus of unstable equilibrium points. As the relative impeller position moves away from the point of minimum force the components of the force gradient are predominantly radial, in the same direction as the displacement, with a small tangential component oriented in the direction of impeller rotation. In a dynamic system where the impeller is mounted on a flexible shaft these forces will act to destabilize forward impeller whirl.

The results reported above are for one specific speed, $N_s = 1495$, and one volute to impeller diameter ratio $r_{3CV}/r_2 = 1.688$. More studies on the effect of volute to impeller relative position in circular volute casing pumps of higher specific speeds and smaller volute to impeller radius ratios are needed. These additional studies should focus on head curve stability improvements at low flow rates as well as efficiency improvements at high flow rates. The findings reported in this paper suggest the feasibility of using a circular volute casing in place of a more conventional spiral volute casing while improving the hydraulic efficiency and maintaining virtually the same radial force characteristic.

## Acknowledgments

This research was sponsored by the Rotating Machinery and Controls (ROMAC) Industrial Research Program at the University of Virginia.

## Nomenclature

$A_V$ = normalized volute flow area $(c)/(r_{3SV} - r_2)$
$b_2$ = flow passage width at impeller exit
$b_3$ = volute width
$c$ = clearance between volute and impeller
$ex$ = eccentricity $((x^2 + y^2)^{1/2})$
$f$ = resultant hydraulic force
$F$ = nondimensional force $(f/(\rho\pi r_2^3\omega^2 b_2))$
$g$ = acceleration of gravity
$H$ = pump total discharge head
$L_{\text{th}}$ = volute throat height
$N_s$ = specific speed $(\omega Q^{1/2}/(gH)^{3/4})$
$P_{\text{input}}$ = motor torque$\times\omega$
$O$ = volume flow rate
$r_2$ = impeller outer radius
$r_3$ = volute cut water radius
$X$, $Y$ = coordinate directions
$x$ = $X$ direction displacement from center
$\xi$ = nondimensional $x$ position $(x/(r_3 - r_2))$
$y$ = $Y$ direction displacement from center
$\zeta$ = nondimensional $y$ position $(y/(r_3 - r_2))$
$\Delta$ = uncertainty (generic)
$\varepsilon$ = eccentricity ratio $(ex/(r_3 - r_2))$
$\phi$ = flow coefficient $(Q/(\omega 2\pi r_2^2 b_2))$
$\psi$ = head coefficient $(gH/(\omega^2 r_2^2))$
$\omega$ = impeller angular velocity
$\rho$ = fluid density
$\eta$ = efficiency $(\rho gHQ/P_{\text{input}})$
$\Theta$ = volute frame angular coordinate direction
$\theta_e$ = eccentricity vector orientation angle (volute frame)
$\theta_f$ = force vector orientation angle (volute frame)
$\theta_t$ = tongue angle (volute frame)
$\theta_v$ = angular position in volute (volute frame)

### Subscripts

$n$ = SV design conditions
bep = best efficiency point
ref = reference condition (SV, bep, $\varepsilon = 0$)

### Abbreviations

SV = spiral volute
CV = circular volute
NC = numerically controlled

## References

[1] Binder, R. C., and Knapp, R. T., 1936, ''Experimental Determination of the Flow Characteristics in the Volutes of Centrifugal Pumps,'' Trans. ASME, **58**, No. 8, p. 659.
[2] Acosta, A. J., and Bowerman, R. D., 1957, ''An Experimental Study of Centrifugal Pump Impellers,'' Trans. ASME, **79**, pp. 1821–1831.
[3] Stepanoff, A. J., 1957, *Centrifugal and Axial Flow Pumps*, Wiley, NY.
[4] Agostinelli, A., Nobles, D., and Mockridge, C. R., 1960, ''An Experimental Investigation of Radial Thrust in Centrifugal Pumps,'' ASME J. Eng. Power, **80**, pp. 120–126.
[5] Biheller, H. J., 1965, ''Radial Forces on the Impeller of Centrifugal Pumps with Volute, Semivolute, and Fully Concentric Casings,'' ASME J. Eng. Power, **85**, pp. 319–323.
[6] Hergt, P., and Krieger, P. 1972, ''Radial Forces and Moments Acting on the Impeller of Volute Casing Pumps,'' *Proceedings of the Fourth Conference of Fluid Machinery*, Budapest, pp. 599–619.
[7] Kanki, H., Kawata, Y., and Kawatani, T., 1981, ''Experimental Research on the Hydraulic Excitation Force on the Pump Shaft,'' *Proceedings, ASME De-*

*sign Engineering Technical Conf.*, 81-DET-71, Sept., Hartford, CT.

[8] Chamieh, D. S., Acosta, A. J., Brennen, C. E., Caughey, T. K., and Franz, R., 1985, ''Experimental Measurements of Hydrodynamic Radial Forces and Stiffness Matrices for a Centrifugal Pump Impeller,'' ASME J. Fluids Eng., **107**, pp. 307–315.

[9] de Ojeda, W., Flack, R. D., and Miner, S. M., 1995, ''Laser Velocimetry Measurements in a Double Volute Centrifugal Pump,'' Int. J. Rotat. Mach., **1**, Nos. 3–4, pp. 199–214.

[10] Domm, U., and Hergt, P., 1970, ''Radial Forces on Impeller of Volute Casing Pumps,'' *Flow Research on Blading*, Elsevier, NY, pp. 305–321.

[11] Lorett, J. A., and Gopalakrishnan, S., 1986, ''Interaction Between Impeller and Volute of Pumps at Off-Design Conditions,'' ASME J. Fluids Eng., **108**, pp. 12–18.

[12] Fongang, R., Colding-Jorgenson, J., and Nordman, R., 1998, ''Investigation of Hydrodynamic Forces on Rotating and Whirling Centrifugal Pump Impellers,'' ASME J. Turbomach., **120**, pp. 179–185.

[13] Baun, D. O., and Flack, R. D., 1999, ''A Plexiglas Research Pump with Calibrated Magnetic Bearing/Load Cells for Radial and Axial Hydraulic Force Measurements,'' ASME J. Fluids Eng., **121**, pp. 126–132.

[14] Baun, D. O., Fittro, R. L., and Maslen, E. H., 1997, ''Force versus Current and Air Gap Calibration of a Double Acting Magnetic Thrust Bearing,'' ASME J. Eng. Gas Turbines Power, **119**, pp. 942–948.

[15] Fittro, R. L., Baun, D. O., Maslen, E. H., and Allaire, P. E., 1997, ''Calibration of an 8-Pole Planar Radial Magnetic Actuator,'' 97-GT-108, ASME Gas Turbine Conference, Orlando, FL, June.

[16] Miner, S. M., Beaudoin, R. J., and Flack, R. D., 1989, ''Laser Velocimeter Measurements in a Centrifugal Flow Pump,'' ASME J. Turbomach., **111**, July, pp. 205–212.

# Effect of Wake Disturbance Frequency on the Secondary Flow Vortex Structure in a Turbine Blade Cascade

**Christopher G. Murawski**
Research Engineer,
Propulsion Directorate,
Air Force Research Laboratory, USAF,
Wright Patterson AFB, OH 45433

**Kambiz Vafai**
Professor, Fellow ASME,
Department of Mechanical Engineering,
The Ohio State University, Columbus, OH 43210

*An experimental study of the effect of wake disturbance frequency on the secondary flow vortices in a two-dimensional linear cascade is presented. The flow Reynolds numbers, based on exit velocity and suction side surface length were 25,000, 50,000 and 85,000. Secondary flow was visualized by injecting smoke into the boundary layer and illuminating it with a laser light sheet located at the exit of the cascade. To simulate wakes from upstream blade rows, a set of spanwise cylinders were traversed across the front of the blade row. The flow visualization results with a single wake disturbance reveal that the recovery time of the secondary flow vortex structure decreases as the wake traverse velocity is increased. The results of flow visualization with multiple wakes showed that wake disturbance frequencies below the axial chord flow frequency allowed complete recovery of the secondary flow vortex structure before the next wake encounters the blade leading edge. Wake disturbance frequencies that exceeded the axial chord flow frequency resulted in no observable recovery of the secondary flow vortex structure. Axial chord flow frequency is defined as the axial velocity in the cascade divided by the axial chord length of the turbine blade.* [S0098-2202(00)02203-3]

## Introduction

The losses in a turbine stage may be divided into three categories: endwall secondary flow loss, profile loss, and end wall tip clearance loss (Sharma and Butler [1]). Secondary flow in a turbine passage is created by two mechanisms: the boundary layer interaction with the leading edge creates a horseshoe vortex, and streamwise vorticity is created in the blade passage from the momentum defect in the boundary layer as the flow turns through the blade passage. The vortices entrain the freestream flow and endwall boundary layer. As a result, secondary flow regions embody considerable momentum losses resulting in total pressure losses, which are detrimental to overall turbine efficiencies.

The development of secondary flow in a stationary linear turbine cascade was documented by Wang et al. [2] using still photography, smoke wires, and a laser light sheet. Their secondary flow vortex model accurately depicts the near endwall flow behavior in a stationary linear cascade. Similar flow behavior was observed in the present study, and shall be discussed later.

Low pressure turbine aerodynamics has received greater attention recently through efforts of Halstead [3], Murawski et al. [4], Qiu and Simon [5], Lake et al. [6], and Matsunuma et al. [7]. It is well established that for some low pressure turbine blades, that as the flow Reynolds number decrease to low levels the profile loss increases. In a study of annular cascade flow, Matsunuma et al. [7] found that as Reynolds numbers decrease, the endwall passage vortices increase in size, resulting in significantly higher secondary flow losses. Gregory-Smith et al. [8], utilizing a linear turbine cascade, also showed that as the endwall boundary layer thickness increases, which occurs as Reynolds numbers decrease, the passage vortices become broader.

Wake interaction occurs in the gas turbine engine environment due to the relative motion of the rotors and stators. Numerous experimental efforts have been conducted in which moving cylinders were placed upstream of test blades to study the effect of simulated wake interactions on midspan flow phenomena (Doorly [9], Dullenkopf et al. [10], Han et al. [11], and Halstead [12]). Using moving cylinders to study the details of unsteady wake disturbances on a downstream blade row has proven to be a valuable research tool, and we have employed a similar technique in our work.

Previous research efforts into unsteady wake disturbances on downstream blade rows have concentrated on the mid-span region of the turbine cascades. The research presented here will focus on the effects of wake disturbances on the secondary flow vortices in the endwall region of a turbine cascade. During wake passing events, four phenomena contribute to the disturbance of the secondary flow vortex structure. They are: the dynamic changes to the inlet flow angle as a result of the velocity deficit in the wake, the effect of the velocity deficit (negative jet) in the wake, elevated levels of turbulence in the wake, and wake disturbance frequency. The experimental effort presented in this paper will not address the quantitative distribution of these effects. The vortex structure will be affected by dynamic changes in the inlet flow angle. This will not result in the complete destruction of the vortex. Secondary flow vortices will exist in high freestream turbulence environments. However, during a wake passing event the temporary change in local turbulence level, as well as, the velocity deficit in the wake compound to destroy the secondary vortex structure. In the gas turbine engine, wakes from upstream stages are generated continuously. The frequency of these wakes will have an effect on the stability of the secondary vortex structures.

The purpose of this research is to investigate the effect of wake frequency on the secondary flow vortex structure. This research was conducted in a linear turbine cascade in order to study the flow field in greater detail than are possible in actual turbine engines. The flow Reynolds numbers were 25,000, 50,000, and 85,000. To visualize the three-dimensional vortices, the boundary layer flow was seeded with mineral oil smoke and illuminated by a laser sheet. The illuminated flow was recorded using a high-speed video camera at 200 frames per second.

---

Contributed by the Fluids Engineering Division for publication in the JOURNAL OF FLUIDS ENGINEERING. Manuscript received by the Fluids Engineering Division August 10, 1999; revised manuscript received March 27, 2000. Associate Technical Editor: D. Williams.

## Experimental Method

**Experimental Apparatus.** A linear cascade was employed to study the low pressure turbine airfoil. A schematic of the test apparatus is provided in Fig. 1. Air is pulled through the apparatus by a 20 HP motor operating a centrifugal blower in the suction mode. Air flow through the test rig is controlled by a variable speed motor controller. The wind tunnel inlet bell-mouth directs the flow through a 53 cm square by 20 cm deep honeycomb flow straightener. The flow continues through a 7:1 converging nozzle to the 11.4 cm by 40.6 cm flow channel.

The cascade used in this experiment is illustrated in Fig. 2. It contains four geometrically identical, low pressure turbine blades with an axial chord length of 10.36 cm, and a span-to-chord length aspect ratio of 1.1. The suction surface length is 15.24 cm. The pitch-to-chord ratio (solidity) is 0.88 and the flow is turned through 95 deg. The three flow Reynolds number cases in this study were 25,000, 50,000, and 85,000. Reynolds number is based on exit flow velocity and suction side surface length.

The wake generator was designed to model an actual gas turbine engine blade passage. The wake generator contains a moving floor and ceiling shuttle into which cylinders are inserted. The wake generator assembly is traversed across the tunnel in the transverse direction. These wake generators traverse, remaining inline with the linear turbine cascade at all times. The cylinders are utilized to simulate the wakes generated by the vane row upstream of the blade rotor. The cylinders are located 6.35 cm upstream of the airfoil row. The wake generator cylinders are 9.5 mm diameter with a 91.7 mm pitch. The cylinders are driven across the flow path by a mechanism at velocities from 0.5 m/s to 5.0 m/s. The total translation distance was 38.1 cm. The velocity was sustained by driving a push bar with a 1 horsepower DC electric motor. The velocity history of the translation slide was recorded using a slotted bar and a photo-diode assembly.

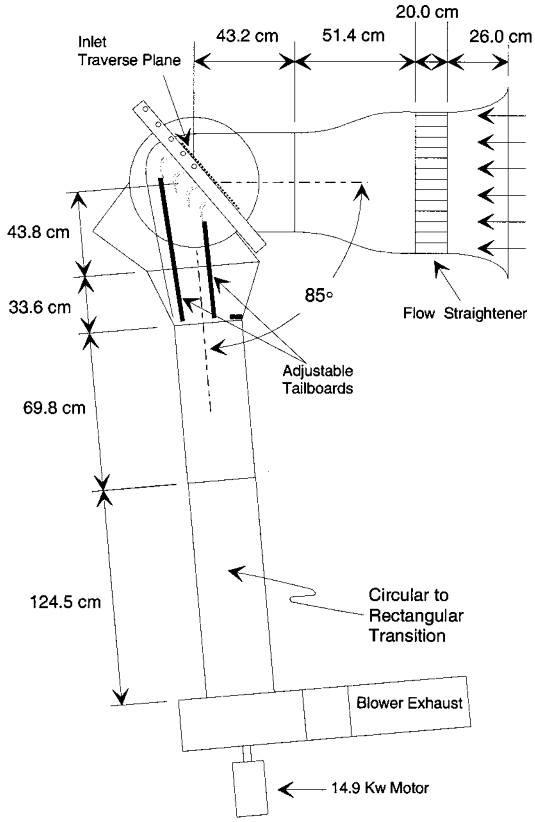

Fig. 1 Experimental setup

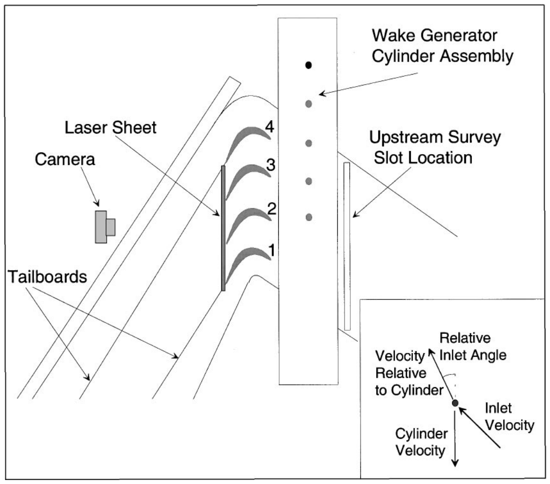

Fig. 2 Test section

**Flow Visualization.** The test section walls are constructed of clear plastic for visual access to the test section. Smoke was produced by an Aerolab smoke generator which vaporizes mineral oil. The smoke from the generator was injected into a 1.6 cm diameter copper tube located at the upper and lower edges of the inlet of the bellmouth. The smoke was ejected through fourteen 0.48 cm holes in the copper pipe. The smoke traveled into the bellmouth and remained within the boundary layer. This method of flow visualization has some advantages over the smoke wire method employed by Wang et al. [2] as the wires can create local turbulence in the flow field, while the method used in this study does not create extra turbulence. This method has the same limitation of requiring that the Reynolds number remain low in order to record clear video images. The beam from a 5 W ($Nd:YVO_4$) laser was expanded into a sheet to illuminate the flow, allowing imaging of the smoke laden vortices. The laser emitted a visible beam that was green (532 nm). The location of the laser sheet is illustrated in Fig. 2. When the wake generator was not used, video images were recorded at 30 frames per second using a Panasonic CCD camera with a 1:1.4 25 mm Electrophysics TV Lens, shutter speed of 1/500th of a second, and lens aperture of f1.4. When the wake generator was used, a high speed video system was required to capture the vortex-wake interaction. High speed video images were recorded at 200 frames per second using a NAC Inc. camera. The same lens was utilized, with a shutter speed of 1/2000th of a second, and an aperture of f2.6.

**Instrumentation.** Instantaneous local velocities were measured using a single element hot-wire probe. Mean inlet velocity and total pressure measurements were made using a pitot-static probe. The airfoil's surface static pressures were measured using 22 static pressure ports installed at midspan on the surface of one blade. The surface static pressure test blade was inserted in blade position 2 in the test section. One pressure tap is located near the front stagnation point, nine surface pressure taps are on the pressure side of the test blade and 12 static pressure taps are on the suction side of the test blade. The ports are connected to stainless steel tubing manifolded to a Scanivalve selector. Three different Validyne pressure transducers were used to cover the range of cascade pressures. Instrumentation output voltages were acquired using a National Instruments Data Acquisition Board. National Instruments LabVIEW software was utilized for data acquisition.

The experimental uncertainties were determined based on the method of Kline and McClintock [13]. The uncertainty of the velocity measurements resulting from pressure transducers and single wire, hot wire anemometer velocity measurements was calculated to be less than 2 percent. The maximum uncertainty in the pressure coefficient was calculated to be less than 4 percent.

## Results

**Inlet Velocity Profile.** To verify an acceptable inlet flow, a velocity survey was performed using a single-element hot-wire probe. The survey was taken two blade chords upstream of the leading edges of the cascade blades at mid-tunnel height. The maximum variation from the mean inlet velocity was 3.57 percent, which occurred at a Reynolds number of 50,000. The average inlet freestream turbulence intensity was 0.61 percent.

**Surface Static Pressure Surveys.** Figure 3 illustrates the surface static pressure survey for the cascade at the Reynolds numbers used in this study. For all Reynolds numbers, the flow is attached for the whole length of the pressure side, which is the lower portion of the plot. The suction side is the top portion of Fig. 3. For all Reynolds numbers, the results show a separation occurring near 68 percent axial chord on the suction side. The largest boundary layer separation on the suction side was recorded for a Reynolds number of 25,000. As the Reynolds number is increased the point of flow reattachment moves forward, thus decreasing the size of the separation bubble. These results are similar to those reported by Murawski et al. [4] and Murawski and Vafai [14,15] in the same cascade used in this study, and Qui and Simon [5] and Lake et al. [6] in larger test rigs with the same blade goemetry.

**Secondary Flow Symmetry.** The linear cascade in this experimental study has a chord to height ratio of one. At low Reynolds numbers, large regions of secondary flow will exist. Figure 4 is an image of the secondary flow as it exits the cascade. A large vortex is seen in the corner of the endwall and suction side of each test blade. The vortices at the exit of the cascade have grown to dominate a large portion of the blade passage. A two-dimensional flow region is still present at the exit of the cascade on the centerline of each blade. The two-dimensional region is approximately 2.54 cm in height.

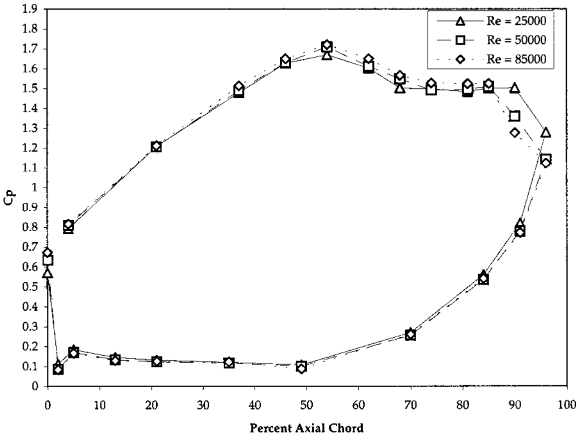

**Fig. 3 Static pressure survey**

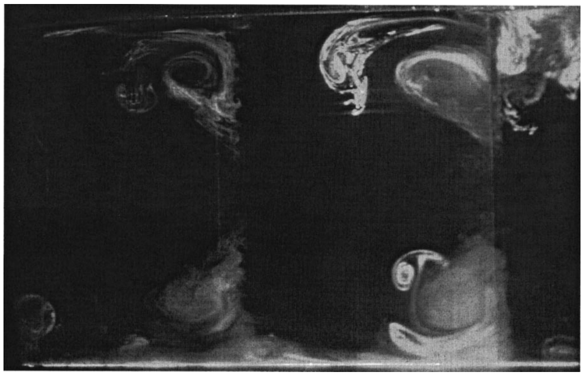

**Fig. 4 Secondary flow vortex structure at the Cascade Exit Plane**

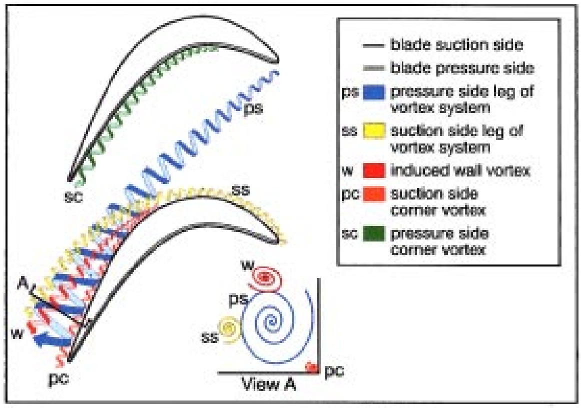

**Fig. 5 Secondary flow vortex structure model**

The behavior of the secondary flow seen in this study is very similar to that observed by Wang et al. [2]. In Fig. 4 the secondary flow vortex structure at the exit plane of the suction surface of the blade contains four vortices. Figure 5 is provided to explain the origin of these vortices in a linear turbine cascade. Figure 5 was created by applying the Wang et al. [2] flow model to our present results. The largest vortex is the passage vortex, which is created from the pressure side leg of the horseshoe vortex system. From the video it was seen that the passage vortex is very stable, and remained fixed in place. Two smaller vortices are wrapped around the passage vortex. Wang et al. [2] had shown that these vortices are the suction side leg of the horseshoe vortex and a wall vortex induced by the passage vortex. The fourth vortex is a small suction side corner vortex which is present in the corner of the endwall and the suction surface, under the larger multi-vortex structure.

**Wake Generator Motion.** Three configurations of the wake generator were tested. The first case was the wake generator operated without any rods in place to study the effect on the vortex structure of the moving shuttle without cylinders. The second case was the wake generator fitted with a single bar, to study the response of the secondary flow vortex structure to a single wake disturbance. The third case was the study of multiple wakes, with the intention to simulate the blade/wake interaction in real gas turbine engines.

Figure 6 illustrates typical velocity histories for each of the wake generator cases. Table 1 provides a summary of the wake generator characteristics. The wake generator assembly traverses from the pressure side toward the suction side of the blade set, moving across the front of the blade set from blade 4 toward blade 1. The wake generator assembly velocity was varied by setting the wake generator motor at 10 percent, 20 percent, 50 percent, and 80 percent of its maximum speed. The wake generator moves for 0.35 seconds for a motor setting of 10 percent, to 0.1 seconds for a motor setting of 80 percent. The high-speed video camera records at 200 frames per second, resulting in 70 frames for a motor setting of 10 percent and 20 frames for a motor setting of 80 percent. The wake generator assembly motion and the high speed video camera frame rate was more than adequate to record the reaction of the vortex structure to the flow disturbances.

**Characteristics of Wakes From Cylinders.** The wake generator assembly was traversed at different speeds which results in wakes with different characteristics. Table 2 presents the characteristics of the wakes from the wake generator cylinders. This experiment was conducted at three different Reynolds numbers

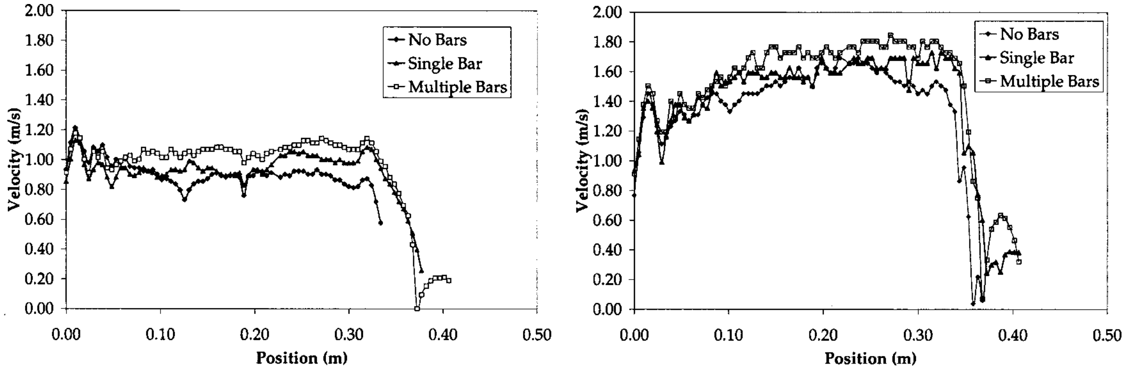

a) 10%

b) 20%

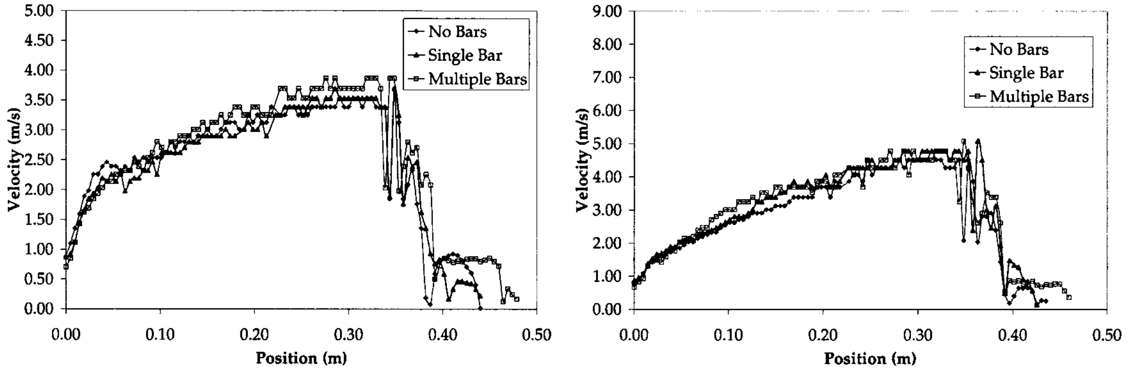

c) 50%

d) 80%

**Fig. 6 Wake generator velocities with motor control set at (*a*) 10 percent, (*b*) 20 percent, (*c*) 50 percent, and (*d*) 80 percent**

(25,000, 50,000, and 85,000) and four motor generator settings (10 percent, 20 percent, 50 percent, and 80 percent of total motor speed). The relative inlet angle of the wake approaching the blade set varies with changes in the flow Reynolds number and wake generator traversing velocity. At a steady inlet velocity, as the velocity of the wake generator cylinder increases the relative inlet angle of the wake approaching the blade goes down. For the case of Reynolds number of 25,000, the inlet angle varies by threefold from about 36 degrees at low wake generator speed (wake generator motor setting of 10 percent) to 13 degrees at the highest wake generator speeds (wake generator motor setting of 80 percent). At the higher Reynolds number case of 85,000, the change in inlet angle is about 5 to 3. The change in flow Reynolds number and relative inlet angle of the wakes has an effect on the wake/blade secondary flow interaction.

**Table 1 Wake generator characteristics**

| Wake Generator Motor Setting | Wake Case | Steady State Velocity (m/s) | Frequency of Wakes (Hz) | Time at Constant Velocity (Sec) |
|---|---|---|---|---|
| 10% | None<br>Single<br>Multiple | 0.90<br>1.00<br>1.07 | None<br>None<br>11.66 | 0.295 |
| 20% | None<br>Single<br>Multiple | 1.59<br>1.69<br>1.81 | None<br>None<br>19.73 | 0.110 |
| 50% | None<br>Single<br>Multiple | 3.39<br>3.53<br>3.69 | None<br>None<br>40.23 | 0.037 |
| 80% | None<br>Single<br>Multiple | 4.51<br>4.78<br>4.78 | None<br>None<br>52.11 | 0.021 |

Table 2 shows that the Reynolds numbers (based on relative velocity and cylinder diameter) from the wake generator cylinders remain below 9000. The relative velocity is the velocity the wake generator cylinder experiences by vector addition of the inlet flow velocity and motion of the wake generator. At these Reynolds numbers, the boundary layer on the wake generator cylinder is laminar and the boundary layer will separate at 80 degrees from the leading edge of the cylinder (Incropera and DeWitt [16]).

The characteristics of the wakes from the cylinders were not measured in this study. However, the cylinder wake characteristics should not differ from the result reported by Halstead et al. [12]. Halstead et al. [12] measured the wake characteristic of cylindrical rods and summarized their findings in several graphs which we will use to estimate wake width, total velocity deficit, peak turbulence intensity and turbulence intensity width. The width of the cylinder wake at the leading edge of the downstream blades was 1.905 cm. The total velocity deficit of about 25 percent, peak turbulence intensity in the cylinder wake of 14 percent, and turbulence intensity wake width of 3.096 cm.

### Moving Wake Generator Cases

*Moving Shuttle With No Wake Generators.* Moving the shuttle with no wake generators was investigated to determine if a short duration moving floor segment ahead of the blade set would destroy the secondary vortex structure. In this case, the 50-cm wide shuttle moves in front of the blade set, from the suction side

**Table 2 Characteristics of the wake generator cylinder**

| Wake Generator Motor Setting | Wake Case | Relative Inlet Angle (degrees) | Wake Generator Re # |
|---|---|---|---|
| Reynolds Number = 25000 | | | |
| 10% | None<br>Single<br>Multiple | 35.99<br>34.56<br>33.62 | None<br>2259<br>2309 |
| 20% | None<br>Single<br>Multiple | 27.82<br>26.91<br>25.88 | None<br>2829<br>2930 |
| 50% | None<br>Single<br>Multiple | 17.11<br>16.60<br>16.06 | None<br>4478<br>4625 |
| 80% | None<br>Single<br>Multiple | 13.74<br>13.12<br>13.12 | None<br>5734<br>5734 |
| Reynolds Number = 50000 | | | |
| 10% | None<br>Single<br>Multiple | 43.92<br>42.90<br>42.20 | None<br>3759<br>3810 |
| 20% | None<br>Single<br>Multiple | 37.62<br>36.83<br>35.93 | None<br>4273<br>4361 |
| 50% | None<br>Single<br>Multiple | 26.87<br>26.27<br>25.61 | None<br>5775<br>5923 |
| 80% | None<br>Single<br>Multiple | 22.66<br>21.83<br>21.83 | None<br>6994<br>6994 |
| Reynolds Number = 85000 | | | |
| 10% | None<br>Single<br>Multiple | 48.04<br>47.35<br>46.88 | None<br>5912<br>5965 |
| 20% | None<br>Single<br>Multiple | 43.65<br>42.97<br>42.27 | None<br>6390<br>6465 |
| 50% | None<br>Single<br>Multiple | 34.60<br>34.04<br>33.42 | None<br>7764<br>7904 |
| 80% | None<br>Single<br>Multiple | 30.52<br>29.66<br>29.66 | None<br>8937<br>8937 |

toward the pressure side of the blade. For all the flow cases the reaction of the secondary flow is similar. The moving wall segment in front of the blade set does not destroy the vortex structures. None of the vortices appear to change size during the duration of the shuttle movement. The passage vortex is pulled closer to the suction side. The vortices that ride on top of passage vortex are also pulled toward the suction surface. The suction side corner vortex remains intact and is also pulled toward the corner as the floor traverses across the front of the blade set. As the velocity of the traversing floor is increased, the vortices react in the same manner. The secondary flow vortices respond quicker as the speed of the shuttle is increased. The moving floor never destroys the secondary flow vortex system. However, the vortices respond more quickly to the increased speed of the flow disturbance.

**Single Wake Disturbances.** A single wake generator rod was traversed across the front of the blade passage to document the reaction and recovery behavior of the secondary flow vortex structure. The data collected in Table 3 were recorded using a constant source laser and a video camera with a 200 Hz frame rate. Images captured from the high speed video camera were not of sufficient quality for presentation in printed form. For illustrative purposes, clearer images were recorded using a pulsed laser and a digital camera with a frame rate of 30 Hz. Figure 7 presents the flow visualization results with one wake disturbance event using the pulsed laser. The flow behavior seen is exactly the same as that captured by the high frame rate camera. An undisturbed vortex structure is seen in Fig. 7(*a*) because the single wake generator has not been activated. The vortex structure is relatively stable and similar to that seen in Fig. 4. Blade 2 is located at the center/right portion of Fig. 7. Blade 3, which is on the left side of Fig. 7, shows an undisturbed vortex structure in both images. In Fig. 7(*b*) the single wake generator cylinder is located upstream of Blade 2. At the left of Fig. 7(*b*), the vortex structure on blade 3 is intact. At the center/right portion of this image the single wake generator cylinder destroys the secondary flow structure.

**Table 3 Single wake vortex recovery results**

| Reynolds Number | Wake Generator Motor Setting (%) | Vortex Recovery Time (Sec.) |
|---|---|---|
| 25000 | 10 | 0.08 |
| | 20 | 0.06 |
| | 50 | 0.04 |
| | 80 | 0.04 |
| 50000 | 10 | 0.06 |
| | 20 | 0.06 |
| | 50 | 0.05 |
| | 80 | 0.03 |
| 85000 | 10 | 0.02 – 0.025 |
| | 20 | 0.02 – 0.025 |
| | 50 | 0.02 |
| | 80 | 0.02 |

A single wake disturbance is sufficient to temporarily disrupt the vortex structure. The vortex structure was disrupted in every case. Once the wake disturbance had passed, the secondary vortex structure re-establishes quickly. The disruption-to-recovery time recorded by the time-indexed high-speed video recorder varied with the wake generator motor speed and is presented in Table 3. This table shows that for the lower Reynolds number cases (25,000 and 50,000) the vortex recovery time is reduced by half

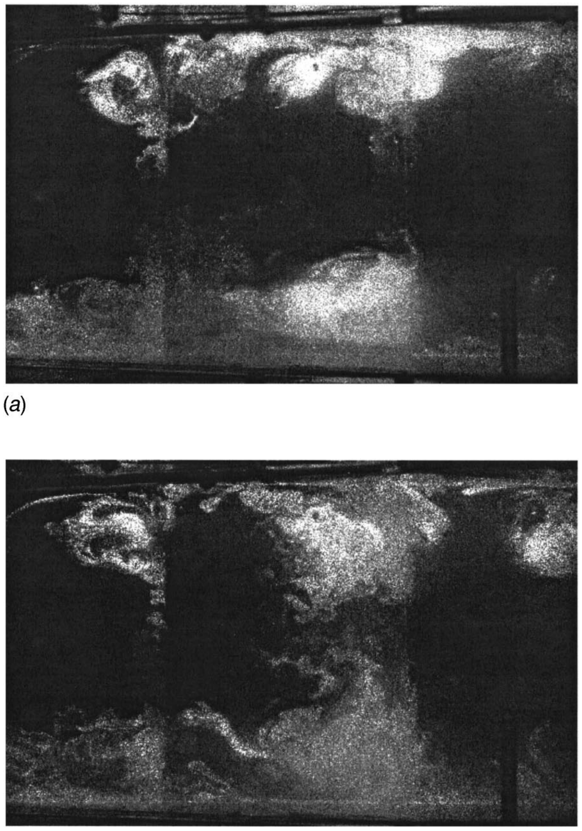

(*a*)

(*b*)

**Fig. 7 Flow visualization with single wake passing event. (*a*) Undisturbed vortex structure; (*b*) one vortex structure intact and one vortex structure destroyed**

when comparing the lowest (10 percent) and the highest (80 percent) wake generator motor settings. For a Reynolds number of 85,000, the vortex recovery time does not differ in each case. For the lower Reynolds number cases the vortex recovery time is affected by the large change in relative inlet angle and wake Reynolds number. Using Table 2 and Table 3, it is seen that the largest drop in vortex recovery time occurs when the relative inlet angle is halved. For example, at Reynolds number 25,000, the vortex recovery time (Table 3) significantly reduces from wake generator motor setting of 10 percent to 50 percent. However, when the Reynolds number is 85,000, the relative inlet angle only decreases by 40 percent from the lowest to highest wake generator motor setting, resulting in only a minimal change in vortex recovery time.

For the lower Reynolds number cases, it was shown that the time for vortex recovery decreased because the relative angle of the wake had decreased. Each wake of the wake generator cylinder may be viewed as a local region of highly turbulent, momentum deficient flow. Each blade cuts the wake as it interacts with the blade's leading edge, then each passage swallows a highly turbulent slug of wake flow. When the relative angle of the wake is decreased, the interaction time at the leading edge is decreased and the quantity of turbulent flow through the blade passage is also decreased. These factors result in a quicker vortex recovery time.

Figure 8 illustrates a single wake disruption of the vortex system in the linear cascade. The following sequence of wake and vortex interaction resulted from studying the high-speed video images. As the shuttle containing the single wake disturbance cylinder moves, the entire vortex structure reacts to the motion of the floor ahead of the blade set by migrating closer to the suction surface. The wake first strikes the pressure side of blade 3. The wake is cut by blade 3, at the same time the leading edge horseshoe vortex is destroyed. The cut wake begins to convect through the blade passage. When the wake encounters the suction side of blade 2, it disrupts the pressure side leg of the horseshoe vortex system. At the same time that this occurs, the leading edge of blade 2 will cut the wake, creating a highly turbulent slug that will move through the blade passage. The highly turbulent slug is too well mixed to contain coherent vortex structures. Before the wake contacts blade 2, the horseshoe vortex system on blade 3 has recovered from the single wake disturbance. Immediately following the wake, the passage vortex reappears briefly without the top riding pressure side leg of the horseshoe vortex system. Afterwards, three smaller vortices (wall vortex induced by the passage vortex, suction side leg of the horseshoe vortex system and suction side corner vortex) rejoin the passage vortex in a semi-stable system. It should be reiterated that this process occurs in a small window of time, from disruption to resurrection of the secondary flow vortex system.

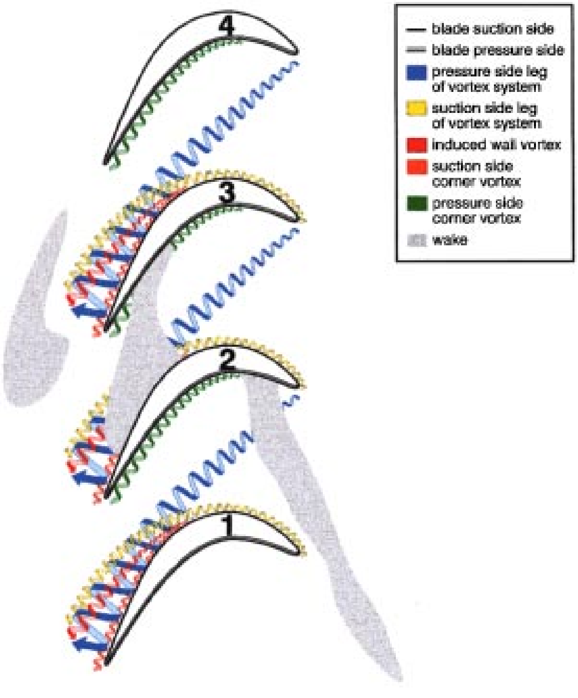

Fig. 8 Single wake flow model

**Multiple Wake Disturbances.** All the wake generator cylinders were installed to record the reaction of the secondary flow vortex structure with multiple wake disturbances. The observations in Table 4 were recorded by using a constant source laser sheet and a high speed (200 Hz frame rate) video camera. However, as in the previous section, the video images were not of sufficient quality to present in printed format. Therefore, for illustrative purposes, Fig. 9 presents the flow behavior for multiple wake passing events with images recorded using a pulsed laser and a digital camera (30 Hz frame rate). The flow behavior outlined in Fig. 9 is similar to the flow behavior seen on the high speed video. The disruption of the secondary flow vortex system is a very dynamic process. Figure 9(*a*) shows the undisturbed vortex structure, prior to the start of the wake generation. The wake generator moves from left to right in this figure. In Fig. 9(*b*) the multiple bar wake generator has entered the wind tunnel and is disturbing the vortex structure on blade 3 (left side of image), while the vortex structure from blade 2 (center/right side of image) remains intact. Fig. 9(*c*) shows the vortex structure has recovered on blade 3 as the wake generator has moved to a point midway between the cascade blades. The vortex structure is intact on blades 2 and 3. In Fig. 9(*d*), cylinders on the multiple bar wake generator have moved to a point in front of each cascade blade and results in the destruction of the vortex structure on both blades 2 and 3.

For each case the bar spacing is held constant. The velocity of the wake generator shuttle changes from case-to-case which results in a change in passing frequency of wake disturbance events. Referring to Table 1, as the velocity of the wake generator system increases the frequency of the wake increases. It should be noted that at a turbine blade flow Reynolds number of 50,000, the time for the flow to traverse the blade set in the axial direction is approximately 0.0382 seconds. This may also be restated as an axial chord flow frequency. The frequency of axial flow through the turbine blade cascade, is 26.2 Hz. The axial chord flow frequency ($f_f$) for each Reynolds number case is provided in Table 4.

Figure 10 illustrates the multiple wake passing results observed with the high speed video camera for a Reynolds number of 50,000. At the lowest wake generator motor setting (10 percent and 20 percent), it was observed that the vortex structure was disrupted by each wake passing event. However, the time between each wake passing event is long enough to enable the vortex

Table 4 Multiple wake vortex recovery results

| Reynolds Number | Wake Generator Motor Setting (%) | Frequency of Wakes ($f_w$) (Hz) | $\frac{f_w}{f_f}$ | Observation |
|---|---|---|---|---|
| 25000<br>$f_f$ =13.1 Hz | 10 | 11.66 | 0.89 | Recovery |
| | 20 | 19.73 | 1.50 | None |
| | 50 | 40.23 | 3.07 | None |
| | 80 | 52.11 | 3.98 | None |
| 50000<br>$f_f$ =26.2 Hz | 10 | 11.66 | 0.45 | Recovery |
| | 20 | 19.73 | 0.75 | Recovery |
| | 50 | 40.23 | 1.53 | None |
| | 80 | 52.11 | 1.99 | None |
| 85000<br>$f_f$ =44.5 Hz | 10 | 11.66 | 0.26 | Recovery |
| | 20 | 19.73 | 0.44 | Recovery |
| | 50 | 40.23 | 0.90 | Recovery |
| | 80 | 52.11 | 1.17 | None |

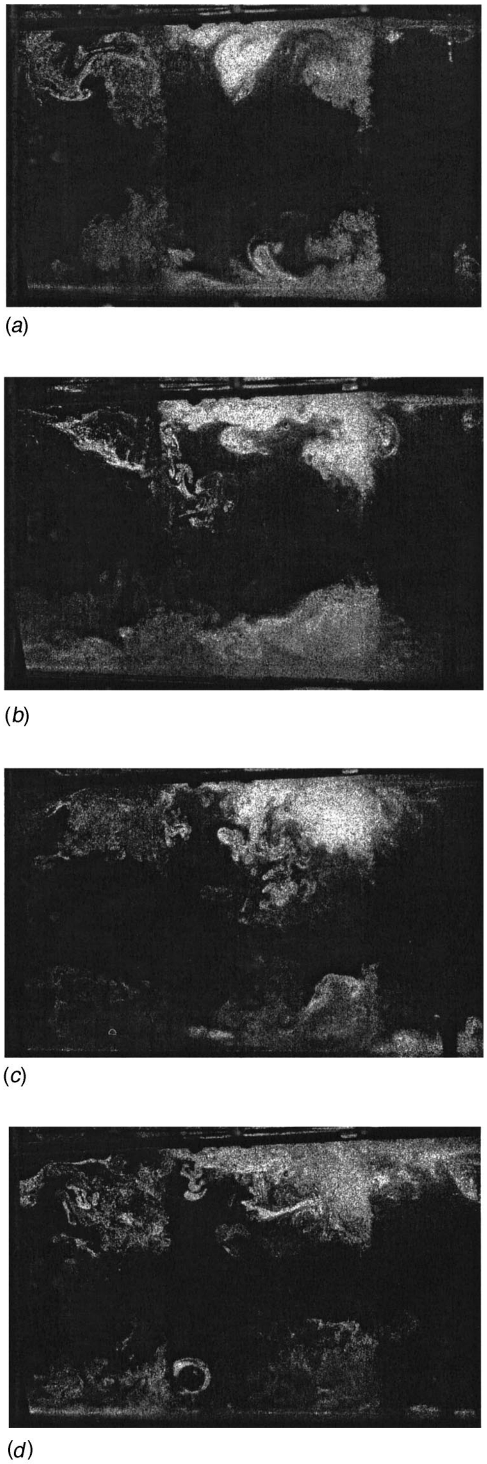

**Fig. 9 Flow visualization with multiple wake passing events. (*a*) Undisturbed vortex structure; (*b*) One vortex structure destroyed and one vortex structure intact; (*c*) Upstream wakes about to destroy vortex structures; (*d*) Upstream wakes destroying both vortex structures**

structure to recover (see Table 4). The vortex pattern was short lived, and was quickly disrupted by the next wake passing event. At higher wake generator motor speeds (wake generator motor setting of 50 percent and 80 percent), the interval between wake disturbance is so close that it will not allow the secondary flow vortex structure to regenerate.

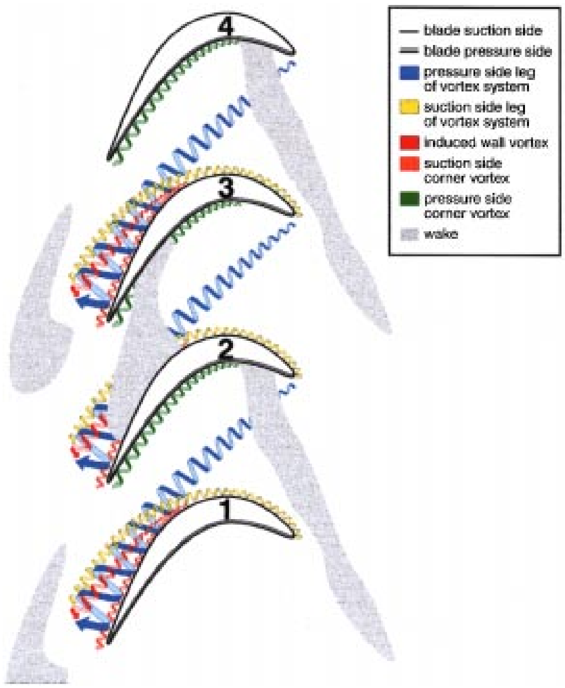

**Fig. 10 Multiple wake with vortex recovery flow model**

The wake disturbance destroyed the vortex structure in a similar manner as seen in the single wake disturbance case. Once the wake passes the leading edge of the blade, the horseshoe vortex begins to regenerate. For the Reynolds number case of 50,000, the single wake passing disturbance case at 10 percent and 20 percent wake generator motor setting established that the vortex structure would reassert itself in 0.06 seconds (16.6 Hz). As seen in Table 4, the 10 percent and 20 percent wake generator motor setting case for multiple wakes established wake frequency of about 11.66 and 19.73 wakes per second, respectively. Since the time between wakes in the 20 percent case is less than the single wake vortex reestablishment time of 0.06 seconds, we may conclude that vortex recovery time is not as important as the ratio of wake disturbance frequency to axial chord flow frequency. For both low wake generator motor setting cases the frequency of the wakes was below the axial chord flow frequency of 26.2 Hz. The secondary flow vortex system is able to reestablish and grow through the blade passage before the next wake hits the blade leading edge.

For Reynolds number of 50,000 and wake generator motor settings of 50 percent and 80 percent of the maximum power, there was no visible recovery of the secondary flow vortex structure at the exit of the blade passage. Table 4 shows that the wake disturbance frequency for the wake generator motor setting of 50 percent and 80 percent was 40.23 Hz and 52.11 Hz, respectively. These wake frequencies exceed the turbine axial chord flow frequency of 26.2 Hz. There is not sufficient time between wake passing disturbances to allow for the recovery of the secondary flow vortex structure in the blade passage.

Table 4 shows that the trend described above is valid for the other Reynolds numbers. The vortex structure only recovers when the frequency of the wake disturbances are below the axial chord flow frequency.

## Conclusions

The present study investigated the reaction of the secondary flow vortex structure in a turbine cascade with variable wake frequency. Reynolds number was varied from 25,000, 50,000, and 85,000. The secondary vortex structure recorded in this study was compatible with established secondary flow theory. Cylinders were traversed across the front of the blade row to simulate turbine blade disturbances. The velocity of the wake generator assembly was varied from 1.0 m/s to 4.8 m/s. The high-speed camera, with a frame rate of 200 frames per second, proved adequate to visualize the reaction of the vortex structure to the flow disturbances.

The flow visualization was carried out for three different cases.

First, the movement of the wake generator shuttle with no wake generators was investigated. The short duration shuttle motion without wake generators did not destroy the secondary flow structure. In each case, vortices remained intact and were temporarily pulled to the pressure side of the turbine blade. The vortex structure returned to its original configuration when the wake generator shuttle stopped moving. The vortices respond quicker, but in a similar manner, as the shuttle speed was increased.

Next, a single wake generator rod was placed in the shuttle and traversed across the front of the blade set at various velocities. The single wake disturbance temporarily disrupted the vortex structure. When the relative inlet angle of the wake was decreased by half, from the low to high speed wake generator assembly cases, the vortex recovery times were decreased by half. The higher wake generator velocity resulted in a decreased relative inlet angle and a decreased quantity of higher turbulence wake flow through the blade passage. It was observed that the secondary vortex structure began to recover even while a neighboring blade is immersed in a wake disturbance event.

Finally, all the wake generators were installed and run at varied velocities. The space between the wake generator cylinders was kept constant which created wake disturbance frequencies from 12 Hz to 52 Hz. It is shown that to sustain the destruction of the secondary flow vortex structure, the wake disturbance frequency must exceed the axial chord flow frequency. When the wake disturbance frequency is below the axial chord flow frequency, the secondary flow vortex structure is able to re-establish itself between each wake disturbance event.

The ratio of wake passing frequency to axial chord flow frequency in a gas turbine engine will be dependent on the number of blades, rotational speed, and the mass flow through the engine. Secondary flows create the second greatest profile losses in the high-pressure turbine stage (film cooling losses are the greatest). Low-pressure turbines contain blades with larger aspect ratios, therefore the secondary flows have a lesser affect on total profile losses. If these vortices are attenuated, the resulting reduction in total pressure loss will result in improved stage performance. Most high-pressure turbine stages will have a ratio of wake passing frequency to axial chord flow frequency greater than 1, therefore the secondary flow vortex structure will not recover between wake disturbances. In the low-pressure turbine, at certain design points, the secondary flow vortex structure will recover between wake disturbance events.

## Acknowledgments

The authors are grateful for the assistance from members of the Air Force Research Laboratory Basic Aerothermal Research Program and the support of Dr. Paul King of the AFIT Aeronautical Engineering Department for use of the linear cascade. The authors would also like to acknowledge the technical and financial support provided by the Turbine Branch of the Air Force Research Laboratory's Propulsion Directorate.

## Nomenclature

$Cp$ = local pressure coefficient $((P_{Tin}-P_{Si})/\frac{1}{2}\rho U_{\mathrm{OUT}}^2)$
$d$ = wake generator cylinder diameter
$f_f$ = axial chord flow frequency
$f_w$ = wake disturbance frequency
$P_{Si}$ = static pressure along the blade surface
$P_{Tin}$ = total pressure at inlet of the blade set
Re = Reynolds number $(U_{\mathrm{OUT}}\,(\mathrm{SSL})/v)$
SSL = suction surface length
Tu = freestream turbulence intensity $(u'_{\mathrm{rms}}/\overline{u}_{\mathrm{local}})$
$U_{\mathrm{OUT}}$ = average velocity out of the blade set
$u'_{\mathrm{rms}}$ = root mean square of fluctuating component of streamwise velocity
$\overline{u}_{\mathrm{local}}$ = local mean streamwise velocity
$x$ = distance downstream from cylinder
$v$ = kinematic viscosity
$\rho$ = density

## References

[1] Sharma, O. P., and Butler, T. L., 1987, ''Prediction of Endwall Losses and Secondary Flows in Axial Flow Turbine Cascades,'' ASME J. Turbomach., **109**, pp. 229–236.
[2] Wang, H.-P., Olson, S. J., Goldstein, R. J., and Eckert E. R. G., 1995, ''Flow Visualization in a Linear Turbine Cascade of High Performance Turbine Blades,'' ASME Paper No. 95-GT-7.
[3] Halstead, D. E., 1996, ''Boundary Layer Development in Multi-Stage Low Pressure Turbines,'' Ph.D. dissertation, Iowa State University.
[4] Murawski, C. G., Sondergaard, R., Rivir, R. B., Vafai, K., Simon, T. W., and Volino, R. J., 1997, ''Experimental Study of the Unsteady Aerodynamics in a Linear Cascade with Low Reynolds Number Low Pressure Turbine Blades,'' ASME Paper No. 97-GT-95.
[5] Qui, S., and Simon, T. W., 1997, ''An Experimental Investigation of Transition as Applied to Low Pressure Turbine Suction Surface Flows,'' ASME Paper No. 97-GT-455.
[6] Lake, J. P., King, P. I., and Rivir, R. B., 1999, ''Reduction of Separation Losses on a Turbine Blade with Low Reynolds Number,'' AIAA Paper No. 99-0242.
[7] Matsunuma, T., Abe, H, and Tsutsui, Y., 1999, ''Influence of Turbine Intensity on Annular Turbine Stator Aerodynamics at Low Reynolds Numbers,'' ASME Paper No. 99-GT-151.
[8] Gregory-Smith, D.G., Graves, C. P., and Walsh, J. A., 1988, ''Growth of Secondary Losses and Vorticity in an Axial Turbine Cascade,'' ASME J. Turbomach., **110**, pp. 1–8.
[9] Doorly, D. J., 1988, ''Modeling the Unsteady Flow in a Turbine Rotor Passage,'' ASME J. Turbomach., **110**, pp. 27–37.
[10] Dullenkopf, K., Shulz, A., and Wittig, S., 1991, ''The Effect of Incident Wake Conditions on the Mean Heat Transfer on an Airfoil,'' ASME J. Turbomach., **113**, pp. 412–418.
[11] Han, J.-C., Zhang, L., and Ou, S., 1993, ''Influence of Unsteady Wake on Heat Transfer Coefficient From a Gas Turbine Blade,'' ASME J. Heat Transfer, **115**, pp. 104–115.
[12] Halstead, D. E., Wisler, D. C., Okiishi, T. H., Walker, G. J., Hodson, H. P., and Shin, H.-W., 1995, ''Boundary Layer Development in Axial Compressors and Turbines Part 4 of 4: Computations and Analysis,'' ASME Paper No. 95-GT464.
[13] Kline, S. J., and McClintock, F. A., 1953, ''Describing Uncertainties in Single-Sample Experiments,'' Mech. Eng. (Am. Soc. Mech. Eng.), **75**, pp. 3–8.
[14] Murawski, C. G., and Vafai, K., 1999, ''Effect of Variable Axial Chord on a Low Pressure Turbine Blade,'' AIAA J. Propulsion and Power, **15**, pp. 667–674.
[15] Murawski, C. G., and Vafai, K., 2000, ''An Experimental Investigation of the Effect of Freestream Turbulence on the Wake of a Separated Low-Pressure Turbine Blade at Low Reynolds Numbers,'' ASME J. Fluids Engineering, **122**, pp. 431–433.
[16] Incropera, F. W., and DeWitt, D. P., 1985, *Fundamentals of Heat and Mass Transfer*, 2nd ed., Wiley, New York.

**Motomu Nakashima**
Research Associate
e-mail: motomu@mech.titech.ac.jp

**Kyosuke Ono**
Professor

Faculty of Engineering,
Tokyo Institute of Technology,
2-12-1 O-okayama, Meguro-ku,
Tokyo 152-8552, Japan

# Numerical Study of the Thrust, Energy Consumption, and Propulsive Efficiency of a Three Joint Bending Propulsion Mechanism

*In our previous paper, we proposed a numerical method based on the discrete vortex method for a bending propulsion mechanism of fish or cetaceans in water, and we demonstrated its validity by comparing the results with an experiment using a three joint bending propulsion mechanism. In this paper, using this numerical method, we will analyze the characteristics of the thrust, energy consumption, and propulsive efficiency of a three joint bending propulsion mechanism in terms of normalized propulsive speed and the phase differences of the adjacent joints. We found that the thrust decreases due to the increase in the lift force as the normalized propulsive speed increases when all the joints move in phase. We also found that the propulsive efficiency has a maximum value when the normalized propulsive speed is 0.8 and when all the phase differences between the joints are 100 degrees.* [S0098-2202(00)01203-7]

## 1 Introduction

The swimming movements of fish or cetaceans (accompanied by the undulatory motion of their bodies) is of interest to scientists and engineers; therefore, this topic has been studied by many researchers from a hydrodynamical perspective. One primary subject in this field of research is the lunate tail, which is seen among fast swimming animals. Lighthill [1] applied the two-dimensional airfoil theory of aerodynamics to the caudal fin of fish and analyzed the characteristics of the thrust and the propulsive efficiency in terms of the amplitude ratio between the heaving and pitching motions and the location of the pitching axis. He found that the maximum propulsive efficiency value of the fin exceeds 90 percent if the flow does not separate from the fin. Following Lighthill's study, there have been many theoretical studies about the same topic. Wu [2], for example, also analyzed the two-dimensional flat wing and compared his theory with experimental measurements of a porpoise's tail. Katz and Weihs [3] analyzed the propulsive performance of an airfoil with chordwise flexibility. Chopra [4,5] extended this study to include three-dimensional rectangular wing and two-dimensional wing with large amplitude. In addition, Chopra and Kambe [6], Cheng and Murillo [7], Bose et al. [8], and Karpouzian et al. [9] studied the performance of the three-dimensional lunate tail. Triantafyllou et al. [10] showed experimentally that the optimal efficiency of an oscillating foil is obtained at the frequency of the maximum amplification of the wake vortices.

Another important subject is their undulatory bodies. Lighthill [11] applied the slender body theory of aeronautics to the transverse oscillatory movements of slender fish whose cross-section varies gradually. He showed that the propulsive efficiency (which is defined as the ratio of the forward work necessary to overcome frictional drag and the total work necessary to produce both thrust and vortex wake is essentially very high. Wu [12] extended this theory to include slender fish, whose transverse cross-section to the rear of their maximum span section was a lenticular in shape with pointed edges. Katz and Weihs [13] analyzed a slender wing with passive chordwise flexibility. Cheng et al. [14] developed the fully three-dimensional rectangular or triangular plate theory.

The authors' final goal, which will be discussed in a future paper, is to design and produce a bending propulsion mechanism for practical use. However, since it is not desirable from a mechanical perspective to build a mechanical and control system with numerous joints which can completely simulate the smooth undulatory motion of fish or cetaceans by their highly flexible spine, we will have to design a propulsion mechanism with fewer joints which can be built and controlled easily. Therefore, first, we have to establish a theoretical method which is applicable to that types of multiple joint propulsion mechanism and will have to analyze the mechanics of propulsion mechanism because all of the studies to date (as we mentioned above) are not about a multiple joint propulsion mechanism but are about the lunate tail (one plate) or the undulatory body (smoothly waving plate).

Therefore, the authors have already developed a numerical method which is suitable for multiple joint propulsion mechanism based on the discrete vortex method in our previous paper (Nakashima and Ono [15]). The discrete vortex method is widely used to calculate the flow around simple objects (for example, an airfoil with separated flow done by Katz [16]), and it is easy to formulate and requires less calculation than other more precise but time-consuming numerical methods (for example, the finite difference and the finite element methods). We also have shown its validity by comparing its results with an experiment about a three joint propulsion mechanism and found that the experimental propulsive speeds were 65–80 percent of the predicted values.

The goal of this paper is not to study the characteristics of the propulsive speed (which was done in our previous paper), but to provide other important propulsive characteristics (i.e., thrust, energy consumption, and propulsive efficiency) of a three joint bending propulsion mechanism using our developed method. Since the motion of the mechanism has too many degrees-of-freedom to analyze it globally, we therefore have focused on the motion of a more simple one, i.e., with the same amplitudes of the joint angles for all three joints and with uniform phase differences of the adjacent joint angles.

---

Contributed by the Fluids Engineering Division for publication in the JOURNAL OF FLUIDS ENGINEERING. Manuscript received by the Fluids Engineering Division December 6, 1999; revised manuscript received March 13, 2000. Associate Technical Editor: A. Ghoniem.

## 2 Numerical Method and Definition of Analyzed Quantities

Figure 1 illustrates an analytical model of the four-link and three-joint bending propulsion mechanism in water. We have assumed that the leading edge of the first link can move freely only in the $x$ direction because our experimental setup has a structure that uses an air slider to avoid the instability of an unsupported mechanism. According to the discrete vortex method, the shear layers shed from the trailing edge of the bending propulsion mechanism and the boundary of the mechanism are approximately represented by the point vortices. Pressure forces $F_{px}$ and $F_{py}$ (which act on the bending propulsion mechanism) can be calculated by the following Blasius equation

$$F_{px} - iF_{py} = \frac{i\rho}{2}\oint_C \left(\frac{dW}{dz}\right)^2 dz + i\rho\frac{\partial}{\partial t}\oint_C \overline{W}\,\overline{dz}. \tag{1}$$

Using the point vortices, Eq. (1) is rewritten in the form

$$\begin{aligned} F_{px} - iF_{py} &= \sum_{j=1}^{M} f_{px(j)} - i\sum_{j=1}^{M} f_{py(j)} \\ &= \rho\Bigg[-i(u_\infty - iv_\infty)\sum_{j=1}^{M}\Gamma_{bv(j)} \\ &\quad - \frac{1}{2\pi}\sum_{j=1}^{M}\sum_{k=1}^{N}\Gamma_{bv(j)}\Gamma_{sv(k)}\frac{1}{z_{sv(k)} - z_{bv(j)}} \\ &\quad + i\sum_{j=1}^{M}\frac{\partial\Gamma_{bv(j)}}{\partial t}\overline{z}_{bv(j)} + i\sum_{k=1}^{N}\frac{\partial\Gamma_{sv(k)}}{\partial t}\overline{z}_{sv(k)}\Bigg]. \end{aligned} \tag{2}$$

In the square bracket of Eq. (2), the first term represents the quasi-steady lift force, the second represents the lift force due to the shed vortices in the wake, and the third and fourth represent the inertial force of the added mass of fluid.

Since drag due to fluid viscosity cannot be taken into account in the discrete vortex method, this type of drag has been empirically identified in an experiment that measured the flow speed of the tank and the drag (Nakashima and Ono [15]). From that experiment, we found that drag $F_D$ for our experimental setup can be represented as the function of flow speed $U$ in the form

$$F_D = 0.327\ U^{1.7}\ [\mathrm{N}]. \tag{3}$$

The mass of the bending propulsion mechanism is represented by a set of discretized lumped masses ($m_{(j)}$). The joint angles of the mechanism change sinusoidally in the form

$$\theta_p(t) = \theta_{p\,\max}\sin(\omega t - \Phi_p) \quad (p = 1\sim 3,\ \Phi_1 = 0). \tag{4}$$

Thus, the motion of the mechanism is determined by solving the following two equations of motion

$$\sum_{j=1}^{M}\left(m_{(j)}\frac{\partial^2 x_{bv(j)}}{\partial t^2}\right) = \sum_{j=1}^{M} f_{x(j)} \tag{5}$$

$$\sum_{j=1}^{M}\left(I_{(j)}\frac{\partial^2 \theta_{bv(j)}}{\partial t^2}\right) = \sum_{j=1}^{M} T_{\theta(j)} \tag{6}$$

where Eqs. (5) and (6), respectively, represent the translation motion in the $x$ direction for the mass center and the angular motion around the mass center. These two motions are solved simultaneously with the boundary conditions of the fluid flow. We have presented an iterative calculation for this coupled system and have discussed its validity in a previous paper (Nakashima and Ono [15]).

Since the motion of the mechanism has too many degrees-of-freedom to analyze it globally, in this paper, we have focused on the motion of a more simple one, i.e., with the same amplitudes of the joint angles for all three joints and with uniform phase differences of the adjacent joint angles. We should note that the motion of the mechanism in this simplification can represent the traveling wave motion if the number of joints is large enough. This uniform phase difference is represented for a three joint mechanism in the form

$$\Phi_2 = \phi_0, \tag{7}$$

$$\Phi_3 = 2\phi_0. \tag{8}$$

In the computer simulation, all quantities were calculated in the normalized system. The steady average propulsive speed is defined as $\overline{U}$ where the symbol $\overline{\phantom{x}}$ represents the averaged value. Using $L$ and $T$, $\overline{U}$ is normalized in the form

$$\overline{U}^* = \overline{U}T/L \tag{9}$$

where * represents the normalized value.

The normalized input power required for the motion is computed as the sum of the required power of the three joints. All of the power of the joints is calculated as the product of the normalized torque and the bending angular speed. Thus, the normalized power is represented as

$$E^*(t) = \sum_{p=1}^{3} T_p^*(t)\frac{\partial\theta_p}{\partial t}. \tag{10}$$

The normalized averaged energy consumption $\overline{E}^*$ is defined as time average of $E^*(t)$ over one period of time. We have further defined propulsive efficiency $\eta$ as the ratio of the normalized average energy $\overline{E}_{fx}^*$ consumed for the drag due to fluid viscosity in one period of time to the total consumed energy $\overline{E}^*$, in other words,

$$\eta = \frac{\overline{E}_{fx}^*}{\overline{E}^*}. \tag{11}$$

In addition, energy consumption $\overline{E}^*$ can be divided into four components in the form:

$$\overline{E}^* = \overline{E}_{px}^* + \overline{E}_{fx}^* + \overline{E}_{py}^* + \overline{E}_{fy}^* \tag{12}$$

where $E_{px}$ and $E_{py}$ are the energy consumed for the pressure force in the $x$ direction and the $y$ direction, and the $E_{fy}$ is the energy consumed for the drag due to fluid viscosity in the $y$ direction. Since the pressure force and the drag due to fluid viscosity in $x$ direction balance for the one period in steady state, we can say that $\overline{E}_{px}^* \simeq -\overline{E}_{fx}^*$ when the velocity of every position of the mechanism in the $x$ direction can be regarded as equal. Since $\overline{E}_{fy}^*$ is very small, we finally obtained

$$\eta \simeq \frac{\overline{E}_{fx}^*}{\overline{E}_{py}^*} = \frac{-\overline{E}_{px}^*}{\overline{E}_{py}^*}. \tag{13}$$

This relationship of propulsive efficiency $\eta$ is used in Section 3.3.

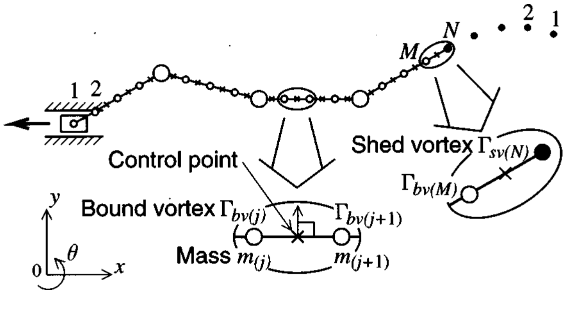

**Fig. 1 Analytical model of a three joint bending propulsion mechanism**

## 3 Results and Discussion

**3.1 Thrust Characteristics When $\phi_0 = 0$ Deg.** First, we analyzed the thrust characteristics in terms of the normalized propulsive speed. Figure 2 shows the thrust (pressure force) $\bar{F}^*_{px}$, its components $\bar{F}^*_{px1}$, $\bar{F}^*_{px2}$, and drag $\bar{F}^*_D$ as the function of normalized propulsive speed $\bar{U}^*$ when all of the joint amplitudes are 5.2 deg. The inertial force of the added mass $\bar{F}^*_{px1}$ comes from the first and second terms of Eq. (2), and lift force $\bar{F}^*_{px2}$ comes from the third and fourth terms. Thus, the sum of components $\bar{F}^*_{px1}$ and $\bar{F}^*_{px2}$ equals total thrust $\bar{F}^*_{px}$. Note that, in this calculation, the propulsive speed is not solved by our iterative method but is given beforehand as the constant value. Therefore, the force balance in the $x$ direction is not yet retained. Components $\bar{F}^*_{px1}$, $\bar{F}^*_{px2}$ and their resultant force $\bar{F}^*_{px}$ are defined as positive values when they produce a positive thrust, while $\bar{F}^*_D$ is defined as a positive value when it produces positive drag.

Figure 2($a$) shows the results when $\phi_0 = 0$ deg and ($b$) shows the results when $\phi_0 = 100$ deg. These two values of phase difference $\phi_0$ were chosen because they are special values. In other words, we have already found that the highest propulsive speed is obtained when $\phi_0 = 0$ deg (Nakashima and Ono [15]), and we will see in Section 3.3 that the highest propulsive efficiency is obtained when $\phi_0 = 100$ deg. As seen in Fig. 2($a$), when $\phi_0 = 0$ deg, $\bar{F}^*_{px}$ is almost constant in the range of small $\bar{U}^*$ and then quadratically decreases as $\bar{U}^*$ increases. The value of $\bar{U}^*$ where the $\bar{F}^*_{px}$-line and the $\bar{F}^*_D$-line intersect is the equilibrium normalized propulsive speed.

Let us consider this characteristics of thrust $\bar{F}^*_{px}$ in light of its components $\bar{F}^*_{px1}$ and $\bar{F}^*_{px2}$. As seen in Fig. 2($a$), inertial force $\bar{F}^*_{px1}$ is almost proportional to $\bar{U}^*$. This is because the inertial force of the added mass is proportional to $\bar{\Gamma}^*_{bv}$ (as shown in Eq. (2)) and $\bar{\Gamma}^*_{bv}$ is almost proportional to $\bar{U}^*$. However, $\bar{F}^*_{px1}$ has a positive certain value as $\bar{U}^*$ decreases to zero. This is because $\bar{\Gamma}^*_{bv}$ does not become zero when $\bar{U}^*$ is zero because of the motion velocity of the mechanism. On the other hand, lift force $\bar{F}^*_{px2}$ quadratically decreases. The reason for this is that the lift force is proportional to $(\bar{\Gamma}^*_{bv} \cdot \bar{U}^*)$ (as shown in Eq. (2)) and that $\bar{\Gamma}^*_{bv}$ is almost proportional to $\bar{U}^*$. The reason why the lift force is negative is that the pitching motion of the whole mechanism is a reactive motion. Therefore, the resultant force $\bar{F}^*_{px}$ is almost constant in the range of a small $\bar{U}^*$ and then quadratically decreases as $\bar{U}^*$ increases.

Let us examine the above-mentioned results schematically. Figure 3 shows the motion of the bending propulsion mechanism during a half of a period of time for various normalized speeds, where the leading edge of the first link is arranged at the same point although it propels. In Fig. 3, for a small normalized propulsive speed (Fig. 3($a$), for example), the bending motion of the mechanism is dominant while the pitching motion of the whole mechanism is much smaller. On the other hand, as for a large normalized propulsive speed (Fig. 3($e$), for example), the pitching motion of the whole mechanism seems to be dominant and its bending motion is much smaller than the pitching motion. This pitching motion is caused by the lift force that is produced by uniform flow $\bar{U}^*$ with the mechanism's cambered posture. Therefore, the lift force becomes dominant in the case of a large normalized propulsive speed.

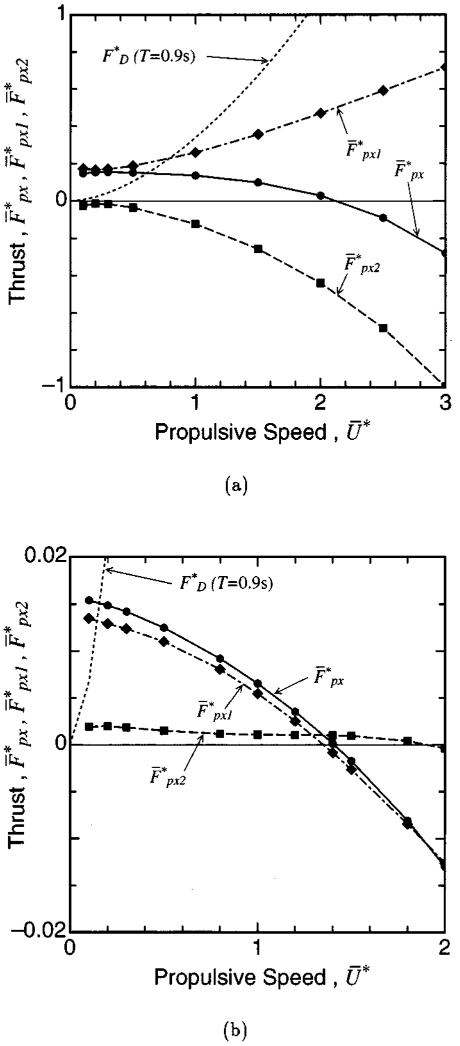

**Fig. 2 Thrust $\bar{F}^*_{px}$, its components $\bar{F}^*_{px1}$, $\bar{F}^*_{px2}$, and drag $\bar{F}^*_D$ as functions of $\bar{U}^*$ when $\theta_{p\,\max} = 5.2$ deg ($p = 1 \sim 3$): ($a$) $\phi_0 = 0$ deg, ($b$) $\phi_0 = 100$ deg**

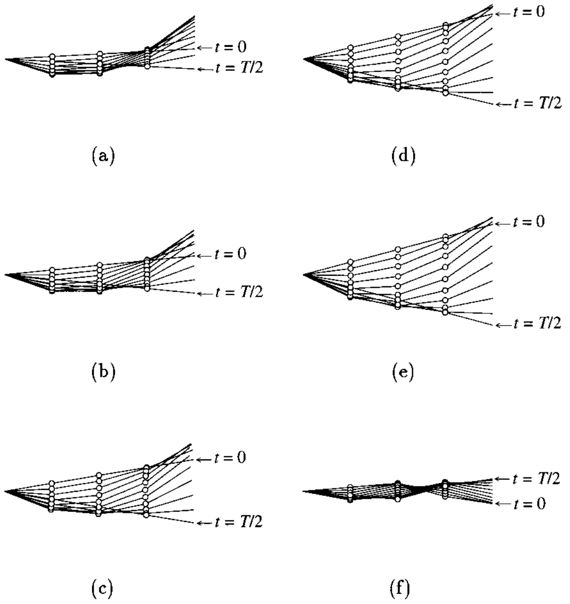

**Fig. 3 Motions of the bending propulsion mechanism during half a period of time: ($a$) $\bar{U}^* = 0.31$, $\phi_0 = 0$ deg, ($b$) $\bar{U}^* = 0.62$, $\phi_0 = 0$ deg, ($c$) $\bar{U}^* = 1.11$, $\phi_0 = 0$ deg, ($d$) $\bar{U}^* = 1.88$, $\phi_0 = 0$ deg, ($e$) $\bar{U}^* = 2.14$, $\phi_0 = 0$ deg, ($f$) $\bar{U}^* = 0.16$, $\phi_0 = 100$ deg**

**3.2 Thrust Characteristics When $\phi_0 = 100$ deg.** Next, Fig. 2(*b*) shows the thrust characteristics when $\phi_0 = 100$ deg. Here, the inertial force of the added mass $\bar{F}^*_{px1}$ is positive when $\bar{U}^* \approx 0$. However, it decreases as $\bar{U}^*$ increases in contrast to the case of $\phi_0 = 0$ deg. This difference between two cases is caused by the difference between the two motions of the mechanism. In other words, when $\phi_0 = 0$ deg, the posture of the mechanism becomes a cambered shape, as is shown in Figs. 3(*a*)–(*e*). However, when $\phi_0 = 100$ deg, the motion of the mechanism is thought to be an undulatory (traveling wave) motion (although it is not clearly observed in Fig. 3(*f*)) because the second joint is lagged for 100 deg behind the first joint and the third joint is also lagged for 100 deg behind the second joint. As for this traveling wave motion, thrust is produced when the traveling speed of the wave is faster than the propulsive speed. Therefore, when the traveling speed is constant (i.e., phase difference $\phi_0$ is constant), the increase in the propulsive speed causes the thrust to decrease, as is seen in Fig. 2(*b*).

On the other hand, lift force component $\bar{F}^*_{px2}$ is very small for all $\bar{U}^*$ value. This is caused by the fact that the mechanism almost doesn't have a cambered posture (which causes the lift force) in contrast to $\phi_0 = 0$ deg.

**3.3 Characteristics of Energy Consumption and Propulsive Efficiency.** Figure 4 shows propulsive efficiency $\eta$ as the function of phase difference $\phi_0$ for various normalized propulsive speed $\bar{U}^*$. As is shown in this figure, propulsive efficiency $\eta$ reaches its maximum when $\phi_0 = 100$ deg and $\bar{U}^* \approx 1.0$. Thus, we have shown more detailed characteristics of propulsive efficiency $\eta$ in terms of normalized propulsive speed when $\phi_0 = 100$ deg in Fig. 5. As shown in this figure, propulsive efficiency $\eta$ was at its maximum (0.65) when $\bar{U}^* = 0.8$. In order to examine these results, let us consider the characteristics of the energy consumption components. Figure 5 also shows the averaged energy consumption components $\bar{E}^*_{px}$, $\bar{E}^*_{py}$ as functions of $\bar{U}^*$ when $\phi_0 = 100$ deg. As seen in Fig. 5, $-\bar{E}^*_{px}$ is zero when $\bar{U}^* \approx 0$, and at first increases as $\bar{U}^*$ increases, but, finally, rapidly decreases. This is caused by the fact that the thrust decreases monotonously from a positive value at $\bar{U}^* \approx 0$ (as is shown in Fig. 2(*b*)) and that $-\bar{E}^*_{px}$ is the product of the thrust and $\bar{U}^*$. On the other hand, $\bar{E}^*_{py}$ at first increases from a positive value, and decreases after peaking, as is seen in Fig. 5. Therefore, propulsive efficiency $\eta$ (which is the ratio of $-\bar{E}^*_{px}$ to $\bar{E}^*_{py}$ as shown in Eq. (13)) increases first from zero as $\bar{U}^*$ increases, and, finally, rapidly decreases.

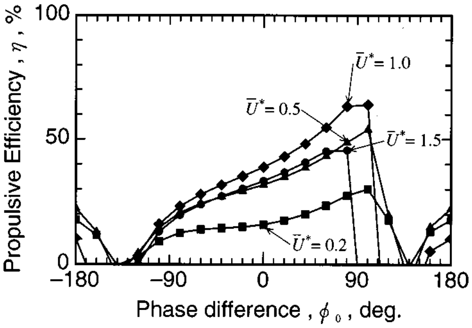

**Fig. 4 Propulsive efficiency $\eta$ as the function of the uniform phase difference $\phi_0$ for various normalized speed $\bar{U}^*$**

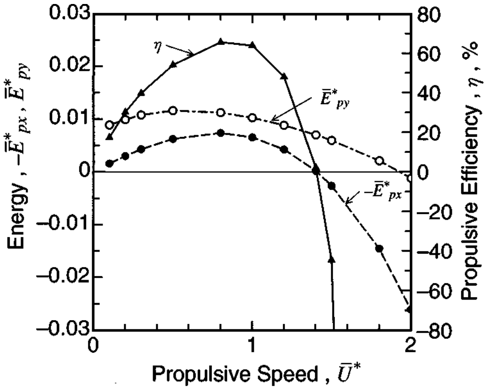

**Fig. 5 Propulsive efficiency $\eta$ and its components $\bar{E}^*_{px}$ and $\bar{E}^*_{py}$, as functions of $\bar{U}^*$ when $\theta_{p\,\max} = 5.2$ deg ($p = 1 \sim 3$), $\phi_0 = 100$ deg**

## 4 Conclusions

In this paper, we numerically analyzed the characteristics of the thrust, the energy consumption, and the propulsive efficiency of a three joint bending propulsion mechanism in which all the joints have the same amplitudes and uniform phase differences. The results are summarized as follows:

1 From an analysis of the thrust characteristics, we found that, when all the joints moved in phase, the inertial force (which generates positive thrust) increased proportionally with the normalized propulsive speed. The lift force (which generates negative thrust) increased proportionally to the second power of the normalized propulsive speed. Thus, the resultant thrust decreases due to the increase in the lift force as the normalized propulsive speed. In addition, we found that, when the uniform phase difference was 100 degrees, the inertial force generated thrust due to the undulatory motion of the mechanism, and that the lift force was almost zero.

2 From an analysis of the energy consumption and propulsive efficiency, the maximum propulsive efficiency was 0.65 when the normalized propulsive speed was 0.8 and when the uniform phase difference was 100 degrees.

## Acknowledgments

The authors are grateful for the many constructive suggestions from the referees.

## Nomenclature

$M$ = number of bound vortices
$N$ = number of shed vortices
$x_{bv}, y_{bv}$ = coordinates of the bound vortex
$x_{sv}, y_{sv}$ = coordinates of the shed vortex
$t$ = time
$\Gamma_{bv}$ = strength of the bound vortex
$\Gamma_{sv}$ = strength of the shed vortex
$m_{(j)}$ = mass of discretized lumped mass
$\theta_{bv}$ = angle from the mass center at the bound vortex point
$I_{(j)}$ = moment of inertia of the lumped mass about the mass center
$f_{px(j)}, f_{py(j)}$ = pressure force of the $j$th point
$f_{x(j)}, f_{y(j)}$ = sum of the pressure force and drag due to the fluid viscosity of the $j$th point
$F_{px}, F_{py}$ = pressure force
$F_{px1}, F_{py1}$ = pressure force due to inertial force of the added mass
$F_{px2}, F_{py2}$ = pressure force due to lift force
$T_\theta$ = moment acting on the mechanism
$u_{(j)}, v_{(j)}$ = velocity of the $j$th point
$u_\infty, v_\infty$ = velocity of the uniform flow
$i$ = $\sqrt{-1}$
$z$ = $x + iy$
$W$ = complex velocity potential

$\rho$ = fluid density
$F_D$ = drag due to fluid viscosity
$\theta_p$ = bending angle of the $p$th joint
$T_p$ = torque of the $p$th joint
$\theta_{max}$ = amplitude of the joint angle
$\omega$ = angular frequency of the joint angle
$\Phi_p$ = phase difference from the first joint
$\phi_0$ = phase difference of each joint
$\overline{U}$ = average propulsive speed
$\overline{U}^*$ = normalized propulsive speed $=\overline{U}T/L$
$U_0$ = velocity of the transverse wave
$L$ = total length of the bending propulsion mechanism
$T$ = period of the motion of the bending propulsion mechanism
$m_a$ = actual mass in the normalized unit area
$\overline{E}$ = consumed energy
$E_{px}, E_{py}$ = energy consumed by the pressure force
$E_{fx}$, $E_{fy}$ = energy consumed by the drag due to fluid viscosity
$\eta$ = propulsive efficiency
$\overline{(\ )}$ = time average of ( )
$(\ )^*$ = normalized value of ( ) by $L$, $T$, and $m_a$

## References

[1] Lighthill, M. J., 1970, ''Aquatic Animal Propulsion of High Hydromechanical Efficiency,'' J. Fluid Mech., **44**, No. 2, pp. 265–301.

[2] Wu, T. Y., 1971, ''Hydromechanics of Swimming Propulsion. Part 2. Some Optimum Shape Problem,'' J. Fluid Mech., **46**, No. 3, pp. 521–544.

[3] Katz, J., and Weihs, D., 1978, ''Hydrodynamic Propulsion by Large Amplitude Oscillation of an Airfoil with Chordwise Flexibility,'' J. Fluid Mech., **88**, No. 3, pp. 485–497.

[4] Chopra, M. G., 1974, ''Hydromechanics of Lunate-Tail Swimming Propulsion,'' J. Fluid Mech., **64**, No. 2, pp. 375–391.

[5] Chopra, M. G., 1976, ''Large Amplitude Lunate-Tail Theory of Fish Locomotion,'' J. Fluid Mech., **74**, No. 1, pp. 161–182.

[6] Chopra, M. G., and Kambe, T., 1977, ''Hydromechanics of Lunate-Tail Swimming Propulsion. Part 2,'' J. Fluid Mech., **79**, No. 1, pp. 49–69.

[7] Cheng, H. K., and Murillo, L., 1984, ''Lunate-Tail Swimming Propulsion as a Problem of Curved Lifting Line in Unsteady Flow. Part 1. Asymptotic Theory,'' J. Fluid Mech., **143**, pp. 327–350.

[8] Bose, N., Lien, J., and Ahia, J., 1990, ''Measurements of the Bodies and Flukes of Several Cetacean Species,'' Proc. R. Soc. London, Ser. B, **242**, pp. 163–173.

[9] Karpouzian, G., Spedding, G., and Cheng, H. K., 1990, ''Lunate-Tail Swimming Propulsion. Part 2. Performance Analysis,'' J. Fluid Mech., **210**, No. 4, pp. 329–351.

[10] Triantafyllou, G. S., Triantafyllou, M. S., and Grosenbaugh, M. A., 1993, ''Optimal Thrust Development in Oscillating Foils with Application to Fish Propulsion,'' J. Fluids Struct., **7**, pp. 205–224.

[11] Lighthill, M. J., 1960, ''Note on the Swimming of Slender Fish,'' J. Fluid Mech., **9**, pp. 305–317.

[12] Wu, T. Y., 1971, ''Hydromechanics of Swimming Propulsion. Part 3. Swimming and Optimum Movements of Slender Fish with Side Fins,'' J. Fluid Mech., **46**, No. 3, pp. 545–568.

[13] Katz, J., and Weihs, D., 1979, ''Large Amplitude Unsteady Motion of a Flexible Slender Propulsor,'' J. Fluid Mech., **90**, No. 4, pp. 713–723.

[14] Cheng, J. Y., Zhuang, L. X., and Tong, B. G., 1991, ''Analysis of Swimming Three-Dimensional Waving Plates,'' J. Fluid Mech., **232**, pp. 341–355.

[15] Nakashima, M., and Ono, K., 1996, ''Numerical and Experimental Study of the Propulsive Speed of the Three Joint Bending Propulsion Mechanism,'' ASME J. Fluids Eng., **118**, No. 1, pp. 134–141.

[16] Katz, J., 1981, ''A Discrete Vortex Method for the Non-steady Separated Flow over an Airfoil,'' J. Fluid Mech., **102**, pp. 315–328.

**J. L. Lage**
Associate Professor,
Mechanical Engineering Department,
Southern Methodist University,
P.O. Box 750337, Dallas, TX 75275-0337

**B. V. Antohe**
Technology Development Staff Member,
MicroFab Technologies Inc.,
Plano, TX 75074

# Darcy's Experiments and the Deviation to Nonlinear Flow Regime

*Many important technological and natural processes involving flow through porous media are characterized by large filtration velocity. It is important to know when the transition from the linear flow regime to the quadratic flow regime actually occurs to obtain accurate models for these processes. By interpreting the quadratic extension of the original Darcy equation as a model of the macroscopic form drag, we suggest a physically consistent parameter to characterize the transition to quadratic flow regime in place of the Reynolds number, Re. We demonstrate that an additional data set obtained by Darcy, and so far ignored by the community, indeed supports the Darcy equation. Finally, we emphasize that the cubic extension proposed in the literature, proportional to $Re^3$ and mathematically valid only for $Re \ll 1$, is irrelevant in practice. Hence, it should not be compared to the quadratic extension experimentally observed when $Re \geqslant O(1)$.*
[S0098-2202(00)01703-X]

## Introduction

By taking the semivariogram of one set of Darcy's experimental data to verify the validation of Darcy equation, Davis et al. [1] concluded that "... Darcy's law was not validated by Darcy's experiment." A natural question is: If Darcy's law is not validated by the experimental data, would there be a valid extension of it? This question is not new, neither are the inconsistencies behind previous attempts to answer it.

Our purpose is to provide a fresh look into the proposed nonlinear extensions to the Darcy equation by revisiting some of the historical events following the publication of Darcy's book (Darcy [2]). We also reinterpret the physical phenomenon behind the deviation from Darcy equation to propose a physically consistent dimensionless parameter for determining the transition to nonlinear regime. This is a very important issue to the accurate modeling of many important technological and natural processes, such as horizontal strip casting (Kuznetsov, [3]), enhanced cooling of electronics (Lage et al. [4], Antohe et al. [5]), and underground contaminant transport (Lage [6]).

Finally, we consider an experimental data set obtained by Darcy that satisfies the Darcy equation. This particular data set has been ignored by, or unknown to, those questioning the validity of the Darcy equation.

## Historic Events

It was in 1856 that Henry Philibert Gaspard Darcy (Darcy [2]) had his report on the public fountains of Dijon published. The more technical aspects of his essay were detailed in seven appendices.

In Appendix *D* (pp. 559–603), Darcy describes an experimental apparatus built to test the hydraulic efficiency of a uniform cross-section sand filter under steady unidirectional flow. The experimental results obtained by Darcy were presented in terms of volumetric flow rate $Q$ (in liters per minute) and pressure difference across the filter (in meters of water-column). Using the filter cross-section surface area $s$ to find the average Darcy, or seepage, fluid speed $U=Q/s$, the height of the filter medium column $e$, and the total pressure difference across the filter $\Delta p$, Darcy found a coefficient $k$ called *hydraulic conductivity*, related to the filter medium, correlating the pressure-drop and the average fluid speed as

$$\frac{\Delta p}{e}=\frac{1}{k}U \qquad (1)$$

It is worth mentioning that the empirical hydraulic Eq. (1), called here the *Darcy equation*, differs from the equation

$$\frac{\Delta p}{e}=\left(\frac{\mu}{K}\right)U \qquad (2)$$

presented as *Darcy's Law* in most textbooks and papers. Equation (2) has the hydraulic conductivity $k$ of the original Eq. (1) substituted by $K/\mu$, where $K$ is called *specific permeability*, a hydraulic parameter independent of fluid properties, and $\mu$ is the fluid dynamic viscosity.

Only years after the publication of Eq. (1), the effect of fluid viscosity was observed, indirectly, by changing the temperature of the fluid flowing through the filter, as reported by Hazen [7]. It was not until much later that the fluid viscosity appeared as an individual parameter in the Darcy equation, e.g., in Krüger [8]. We refer to Eq. (2) as the *Hazen-Darcy equation* to distinguish it from the original Darcy equation, Eq. (1).

Observe that Eqs. (1) and (2) are *global* (or *macroscopic*) equations, i.e., they do not infer the complicated fluid-solid interactions taking place inside each tortuous flow path (pores) of the porous material.

Arsène Jules Emile Juvénal Dupuit (Dupuit [9]) (and not Forchheimer [10], as believed by many), drawing a parallel between Prony's equation for modeling flow in open channels (Prony [11]) and flow through porous media, was the first to proposed an extension to Eq. (2), namely

$$0=\frac{\Delta p}{e}-\alpha U-\beta U^2 \qquad (3)$$

The physical phenomenon responsible for the quadratic term of Eq. (3) is the *form force* imposed to a fluid by any solid surface obstructing the flow path. This resistive (to unidirectional flow) force was proposed by Newton ([12] pp. 260–262) to be proportional to the fluid density and to the average fluid velocity square. Using this concept together with Eq. (2), Eq. (3) is rewritten as the *Hazen-Dupuit-Darcy equation*,

---

Contributed by the Fluids Engineering Division for publication in the JOURNAL OF FLUIDS ENGINEERING. Manuscript received by the Fluids Engineering Division August 27, 1998; revised manuscript received April 26, 2000. Associate Technical Editor: M. Dhaubhadel.

$$0 = \frac{\Delta p}{e} - \frac{\mu}{K} U - C \rho U^2 \tag{4}$$

where $C$ is a form coefficient related to the geometry of the solid permeable medium and $\rho$ is the fluid density. The last two terms of Eq. (4) represent the lumped viscous drag and the lumped form drag, respectively, imposed by the solid porous matrix to the flowing fluid. Although these two effects are always present in the flow, the viscous effect will predominate at low enough fluid speeds. We regard Eq. (4) as a *macroscopic momentum balance equation* of fluid flow through a porous medium.

Ward [13] proposed to replace the form parameter $C$ in Eq. (4) by $c/K^{1/2}$, where the dimensionless parameter $c$ was believed to be a universal constant. Ward's suggestion results from a dimensional analysis involving only four basic parameters, i.e., he assumed that the pressure-drop versus fluid-speed relationship, Eq. (4), would depend only on $U$, $K$, $\rho$, and $\mu$. Therefore, the form coefficient $C$ would depend on the permeability $K$ of the medium. This is incorrect because the permeability, as linked to viscous drag, relates to the *effective surface area* of the solid porous matrix. The form coefficient $C$, on the other hand, does not depend on the extent of the surface, but on the *form* of the solid matrix (form defined as the variation of the cross section area of the solid matrix). Moreover, if Ward's suggestion was correct then $c$ should be a universal constant, something which has been shown, for instance by Beavers et al. [14] and Antohe et al. [15], not to be the case.

## Inertial Force

The concept of *inertial force* is traced back to Newton's *Philosophiae naturalis principia mathematica*, *The Principia*, Newton [12]. At the beginning of his book, Newton presents eight definitions forming the basis for his three Laws. The two most important definitions for us are definition no. 2, or the definition of *quantity of motion*, and no. 3, or the definition of *inertial force* or the force that measures how difficult it is to change the quantity of motion of a body. Together with Newton's second law, we can state that the *change in quantity of motion* is identical to the *inertial force* that is equal to the *resultant* of all forces acting upon the body.

Observe that the left side of Eq. (4) being zero reminds us that, macroscopically, the fluid in and out of a permeable medium with uniform cross-section, under unidirectional and steady flow, retains its quantity of motion (or momentum). Therefore, the fluid has zero macroscopic inertial force.

Because Eq. (4) is *macroscopic* in nature, the right-side terms represent, macroscopically, all the considered forces acting upon the fluid. Of special interest is the rightmost term of Eq. (4), the term arising from the *form force*, often referred to as the *inertia force* or the *inertia term*. This terminology is confusing because with constant macroscopic momentum, the flow presents zero inertial force. Even if referring to the effect of the *microscopic* (pore level) inertial force of the fluid, this terminology is inappropriate still because the microscopic inertial force must be equal to the resultant of *all forces* acting on the fluid within a pore. But we know that the form force is only one of the forces acting on the fluid within a pore (viscous forces at the pore level will also affect the change of quantity of movement—or the inertial force—of the fluid).

The confusion is created, we believe, because the form force is proportional to $U^2$, and in certain cases the fluid inertial force (or the time rate of momentum change) is also written as velocity square. We know, however, that the rightmost term of Eq. (4) corresponds to a force, which happens to vary with $U^2$. This force is *inertial related* as much as any other force is, i.e., via Newton's second law. Another strongly distinctive factor is that the microscopic form force is not proportional to the fluid viscosity but in general the microscopic inertial force, or the force resisting the change of movement at the pore level, is.

The *inertia dogma* of flow in porous media has influenced many scientists to generate other misconceptions. For instance, a comment made by Barak [16] led Hassanizadeh and Gray [17] to incorrectly correct a *typo* on their original paper by stating that '' . . . macroscopic inertial forces have been shown to be small at the onset of nonlinear flow . . . '' - *macroscopic inertia forces* (or convective inertia) are zero in steady unidirectional flow through a homogeneous and isotropic porous medium.

The desire by many investigators to obtain a macroscopic equation similar to Eq. (4) from the microscopic Navier-Stokes (N-S) equation governing the fluid flow inside each pore is also influenced by the inertia dogma. See, for instance, Wodie and Levy [18] who suggested that the linear term of Eq. (4) can be obtained from the viscous term of the N-S equation by performing a double-scale asymptotic expansion on pressure and velocity (to first order) followed by the volumetric averaging of the resulting equation. They went on to indicate that for very slow flow (Reynolds number much smaller than unity), in the case of macroscopic isotropy and assuming the convective inertia term of the N-S equation to be of the same order of the viscous term, a second order approximation leads to a macroscopic equation similar to Eq. (4) but with the rightmost term being cubic in the fluid speed instead of quadratic. The same result was obtained also by Mei and Auriault [19] via theory of homogenization. They then concluded that the quadratic deviation from Eq. (2) must be associated with the anisotropy of the porous medium. An important aspect overlooked in their analysis is the fact that the quadratic deviation from Eq. (2) has been observed experimentally even for isotropic media. Moreover, the deviation is observed at a Reynolds number of the order unity or greater, hence outside the validity range of their analysis.

## The Reynolds Number

In several studies, e.g., Wyckoff et al. [20], Ward [13], Fand et al. [21], the permeability based Reynolds number,

$$\mathrm{Re}_K = \frac{\rho U K^{1/2}}{\mu} \tag{5}$$

was used to indicate the departure from the linear Hazen-Darcy model, Eq. (2), in fully developed steady unidirectional flow through a porous medium, a direct consequence of the *inertia dogma*.

Some other authors, like Wodie and Levy [18], prefer using a characteristic pore length scale in place of $K^{1/2}$ in Eq. (5). The Reynolds number definition used recently by Firdaouss et al. [22] can make things even more confusing. Indeed, a Reynolds number can be written in terms of the fluid pressure-drop

$$\mathrm{Re}_{\Delta P} = \frac{\Delta P a^3 \rho}{L \mu^2} \tag{6}$$

where $a$ and $L$ are the microscopic (pore scale) and the macroscopic length scales of the medium, respectively, and assuming the term $a^2 \Delta P/\mu L$ as representing the velocity scale of the flow. But this velocity scale is correct, from Eq. (4), only if $K$ and $a^2$ have the same scale and when the pressure-drop versus fluid-speed relationship is linear. Observe that for high fluid speed the pressure-drop becomes proportional to $U^2$, which suggests from Eq. (6) a Reynolds number also proportional to $U^2$ what is inconsistent with the usual definition of the Reynolds number.

Because steady, fully developed and unidirectional flow through a uniform cross-section duct has zero macroscopic inertia, the Reynolds numbers of Eqs. (5) or (6) have no physical meaning, i.e., they should not be confused with a quantity representing the ratio between macroscopic inertial and viscous forces. This observation is simply an extension to flow through a porous medium of what has been remarked by Batchelor [23], and more recently by Bejan [24], regarding steady, fully developed flow of a *clear* (of porous medium) fluid.

We made an important point when we wrote *macroscopic inertia* in the previous paragraph. Observe that the Reynolds number (Re) currently used to predict the transition from linear to quadratic flow regime in porous media is based on the macroscopic fluid speed. When attempting to use the macroscopic Re to infer transition from linear to quadratic regime, one is ignoring the lack of pore-scale information brought about by the macroscopic Re.

Lack of physical meaning (in a macroscopic sense) and lack of pore-scale information hinder the use of the macroscopic Re as a parameter to predict the transition to nonlinear regime.

Using a Reynolds number to characterize the zero-inertia, steady unidirectional flow through a porous media leads to other abnormalities, such as, for instance, the writing of the form force term as function of the fluid kinematic viscosity, as done recently by Firdaouss et al. [22], p. 335.

Even more surprising is the use of a Reynolds number to estimate the macroscopic transition from a viscous dominated flow regime (Eq. (2), or linear regime) to a form dominated regime (Eq. (4), or quadratic regime). The Reynolds number has no information on the form drag effect. What should be used to characterize the departure from the linear regime, we suggest, is the physically meaningful ratio between the form force $D_C$ and the viscous force $D_\mu$, from Eq. (4)

$$\frac{D_C}{D_\mu}=\frac{C\rho U^2}{\left(\frac{\mu}{K}\right)U}=\frac{\rho CK}{\mu}U \tag{7}$$

Observe that there is no ambiguity in the definition of the force-ratio Eq. (7). There are no possible choices of scales as in the case of trying to define a proper Reynolds number (see comment on p. 334, Section 2.1, of Firdaouss et al. [22]). Also, Eq. (7) requires prior knowledge of the form factor $C$ value for the medium, an obvious prerequisite for determining when the form force becomes predominant.

Therefore, the transition from linear to quadratic regime is indeed media-specific (contrary to what has been traditionally advocated). The transition is that of the drag switching from being linear to quadratic with the fluid speed, and the drag depends on the form (shape) and extent of the interface fluid-solid within the porous medium. Hence, the transition must depend on the internal geometry of the porous media, i.e., be media-specific as we propose.

Unfortunate as the previous statement might be, our proposition is a challenge to theoreticians and, more importantly, to experimentalists working with fluid flow through porous media. There is a need to investigate how the geometry of the porous matrix affects the drag effect. Very little is known in this regard.

Coincidentally, the use of $D_C/D_\mu$ reduces the scattering of experimental hydraulic data obtained with permeable media of very different forms as shown in Fig. 1 of Macdonald et al. [25], p. 200—note their Reynolds number is identical to Eq. (7), with $C$ replaced by $c/K^{1/2}$.

## Darcy's Experimental Data

Darcy [2] presents the results of *five* carefully performed experiments. Four of them, using different sand-column height ($e=0.58$, 1.14, 1.71, and 1.70 meter) and keeping the pressure under the filter equal to the atmospheric pressure, were reported on p. 592 of his manuscript. Table 1 presents the set of experimental results obtained using $e=0.58$ m, in terms of average fluid speed $U$ and total pressure difference across the filter $\Delta p$, assuming water at 10°C ($\rho=999.7\,\text{kg/m}^3$). Asterisks denote tests performed under strong pressure oscillation.

By assuming that only the two last data points of Table 1 follow the Darcy equation, Firdaouss et al. [22] attempted to indicate that the entire data set of Table 1 could not be fitted by the Darcy equation. However, Davis et al. [1] presented the curve fit of the same data showing a reasonably good fit. We present our own curve fit in Fig. 1, using the Darcy equation, Eq. (1), and the quadratic Eq. (4). Indeed, the quadratic curve fit seems better.

**Table 1 Modified experimental data for $e=0.58$ m**

| $U(10^{-3}$ m/s) | $\Delta p$(kPa) | $k(10^{-8}$ m$^3$s/kg) |
|---|---|---|
| 5.09 | 106.8* | 2.76 |
| 4.82 | 96.7* | 2.89 |
| 4.24 | 84.1* | 2.92 |
| 4.05 | 79.7* | 2.95 |
| 3.78 | 74.8 | 2.93 |
| 2.62 | 49.2 | 3.09 |
| 2.48 | 48.1 | 2.99 |
| 2.08 | 39.2 | 3.08 |
| 1.33 | 23.1 | 3.33 |
| 0.62 | 10.9 | 3.30 |

Firdaouss et al. [22] went on to show, again assuming only the two last data points of Table 1 as satisfying Eq. (1), that a normalization technique based on the Reynolds number at maximum pressure-drop indicates a deviation to cubic flow regime. The normalization is based on calculating the quantity

$$y=\frac{\dfrac{\Delta p}{eU}-\dfrac{1}{k}}{\left(\dfrac{\Delta p}{eU}\right)_{\max}-\dfrac{1}{k}} \tag{8}$$

from each data point, and then plotting the results versus the corresponding ratio $x=\Delta p/\Delta p_{\max}$.

From Eq. (8) we conclude that the experimental data points satisfying Eq. (1) exactly will have $y=0$. If the data follow the quadratic extension to Darcy equation, then $y$ should be linear with $x$. If the data follow a cubic pressure-drop versus fluid-speed relation, then $y$ versus $x$ should follow a quadratic curve.

Although not explicitly stated in their paper, it seems that at least one point of a certain data set must be assumed to follow Eq. (1) so that the hydraulic conductivity $k$ (or the permeability $K$) necessary in Eq. (8) can be determined. Unfortunately, the results of the Firdaouss et al. [22] normalization technique depend strongly on the value of $k$, which depends on how $k$ is determined. If one assumes, for instance, that only the last data point of Table 1 satisfies the Darcy equation and then obtain a value for $k$ from it, this value will differ from the value obtained when using the last two points and, by consequence, the results from the normalization technique will be different.

As a practical example of how sensitive the normalization technique is to the chosen value of $k$, we present the two graphs of Fig. 2. The upper graph is the result of the normalization proposed

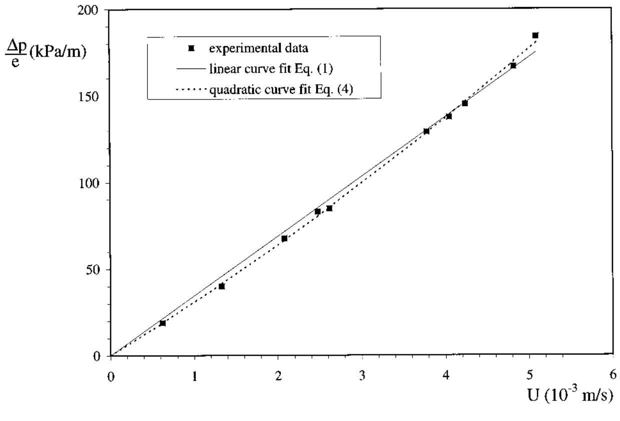

**Fig. 1 Darcy experimental data of Table 1, and least-square linear and quadratic curve fits**

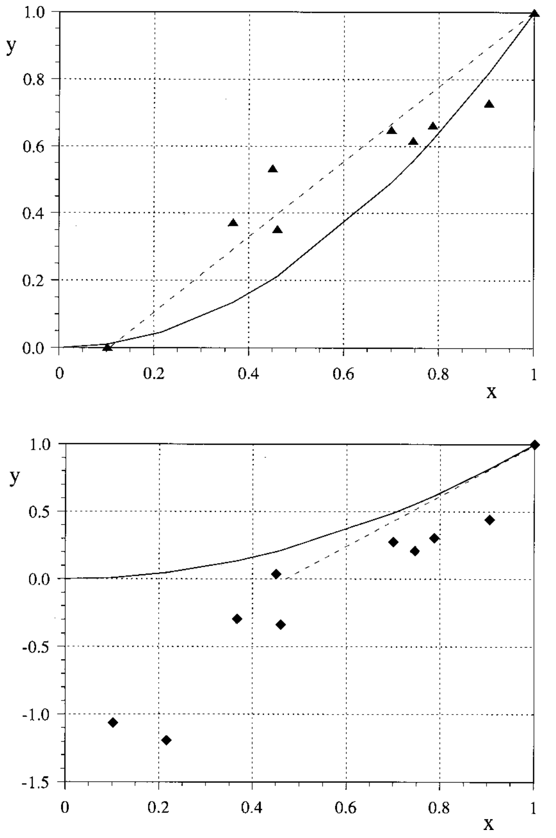

**Fig. 2 Normalization results of data in Table 1—continuous lines are for quadratic *y-x* relation; dashed lines are for linear *y-x* relation. Upper graph: $k=3.30\times10^{-8}$ m$^3$s/kg obtained from a single data point. Lower graph: $k=3.00\times10^{-8}$ m$^3$s/kg from best linear fit of five points.**

by Firdaouss et al. [22] using $k=3.30\times10^{-8}$ m$^3$s/kg obtained by considering only the last point of Table 1 as satisfying Eq. (1). The results can be compared with the *y*-versus-*x* linear (dashed line) and quadratic (continuous line) profiles, shown in the graph.

Observe that the *y*-versus-*x* graphs of Firdaouss et al. [22] assume the linear profile to start at the origin $y=x=0$, as if only the point $\Delta p=U=0$ satisfied Eq. (1). However, the linear profile should start from the first point believed to deviate from Eq. (1), for which $y\neq0$, because the data points with smaller $\Delta p$ were assumed to follow Eq. (1) (so that $k$ or $K$ could be determined), therefore, they must yield $y=0$ when using Eq. (8). If the graphs of Firdaouss et al. [22] are redrawn with this correction in mind, the discrepancy between linear and quadratic deviation becomes much smaller. See the upper graph of Fig. 2, for instance, where the data seems to follow more closely the linear profile than the quadratic profile.

The weakness of the Firdaouss et al. [22] normalization procedure is that one can not determine beforehand how many (or which) data points in Table 1 (or from any experimental data set) satisfy the Darcy equation. Now, observe the lower graph of Fig. 2. This graph presents the results of the same normalization technique, but in this case using Eq. (8) with $k=3.00\times10^{-8}$ m$^3$s/kg resulting from considering the last five data values of Table 1 as following Eq. (1) (in this case, $k$ is determined from the best linear curve-fit of the last five data points, passing through the origin). Observe how different the results are when compared with the upper graph. Even some negative values are obtained for *y*, in which case the normalization technique is meaningless. Again, considering the linear profile starting from the last data point used to determine $k$ we observe a better agreement between linear profile and the experimental results than with the quadratic profile.

Davis et al. [1] have applied a different validation technique to the original Darcy equation, considering only the data of Table 1. The suggested method tests if there is any correlation between the residuals, defined as

$$\delta(U_i)=\frac{1}{e}[\Delta p(U_i)-\Delta p_t(U_i)] \tag{9}$$

where we calculate a theoretical pressure drop $\Delta p_t$ for every fluid speed using the theoretical model to be validated, and then compare the results with the $\Delta p$ values obtained experimentally. In case of validating the Darcy model, Eq. (1), one must determine first the $k$ value from the best curve fitting. For the quadratic extension model, Eq. (4), one must determine $k(=K/\mu)$ and $C$ from the best fitting.

The semivariance used to estimate the *correlation* between the residuals is presented in more detail by Delhomme [26]. Briefly, the semivariance is a function of the *lag-distance* (distance between two experimental points) and defined as

$$\sigma(\Delta U)=\frac{1}{2N(\Delta U)}\sum_{i=1}^{N(\Delta U)}[\delta(U_i+\Delta U)-\delta(U_i)]^2 \tag{10}$$

where $U_i$ is a certain fluid speed, $\Delta U$ is the *lag-distance* between two experimental fluid speeds, and $N(\Delta U)$ is the number of pairs of experimental points $\Delta U$ units apart. If the semivariance tends to a finite value as the *lag-distance* $\Delta U$ increases then the residuals do not correlate and the theoretical model is valid. Otherwise, the residuals correlate and the theoretical model is invalid.

The results of Davis et al. [1] to validate the Darcy equation based upon the data in Table 1 indicated an increase in variance as the fluid speed (or pressure drop) increases, in other words, an apparent systematic relationship between the residuals. Based on these results Darcy original equation would not be validated by this experimental data set. One of the possible causes, as suggested by Davis et al. [1], could be a *systematic measurement error*. A more likely explanation is simply the departure from the linear flow regime.

To substantiate our point, we first assume the data of Table 1 to follow the linear model, Eq. (1). We then curve fit the data and obtain $k=K/\mu=2.909\times10^{-8}$ m$^3$ s/kg from the best fit. With this $k$ value and Eq. (1), we calculate a theoretical pressure drop $\Delta p_t$ for every fluid speed and compare the results with the experimental $\Delta p$ values of Table 1. In this case, the maximum pressure-drop deviation defined as $|\Delta p-\Delta p_t|/\Delta p$ is 14.8 percent. Repeating the same procedure, but now assuming the data to follow the quadratic model, Eq. (4), instead of Eq. (1), we obtain $k=3.385\times10^{-8}$ m$^3$s/kg, $C=1.1689\times10^6$ m, and a maximum deviation of 3.8 percent only.

Moreover, the variance technique for testing the suitability of Eq. (4) reveals smaller residuals and more uniform variance, as shown in Figs. 3 and 4. It is evident that the quadratic model correlates better the experimental data of Table 1.

Using Eq. (5) the maximum Reynolds number for the data of Table 1 is $\mathrm{Re}_K=0.0235$, a value well below the usual value of 0.1 for transition to quadratic regime. So, based on the Reynolds number criterion the flow should be in the linear regime. On the other hand, the maximum ratio of form to viscous forces, Eq. (7), is 0.2 indicating that the magnitudes of these forces are in fact less dissimilar than suggested by the Reynolds number criterion.

The fifth, and so far ignored, or unknown, data set was obtained by Darcy with $e=1.1$ m and the results presented in p. 593 of his report, shown on Table 2. Contrary to what is stated in Firdaouss et al. [22], p. 336, *this* is the most extensive of all data sets.

An analysis of the experimental data in Table 2 leads to $k=2.809\times10^{-8}$ m$^3$s/kg from the linear Eq. (1), with 7.4 percent maximum pressure-drop deviation. For the quadratic Eq. (4) we have: $k=2.909\times10^{-8}$ m$^3$s/kg, $C=0.4293\times10^6$ m, and a maxi-

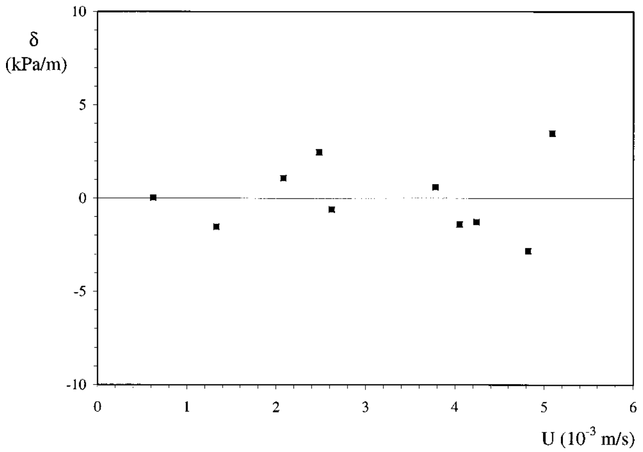

**Fig. 3 Residuals between the experimental pressure drop of Table 1 and the theoretical pressure drop obtained from the quadratic Eq. (4) with $K/\mu = k = 3.385\times10^{-8}$ m$^3$s/kg, and $C = 1.1689\times10^6$ m**

mum deviation of 7.1 percent. The corresponding fitting curves are shown in Fig. 5. There is no clear indication that the quadratic is better than the linear equation as either one seems to correlate fairly well the experimental data of Table 2 (within what one would expect to be the experimental uncertainty of the data collected by Darcy).

The semivariance technique applied to Table 2 points toward a similar conclusion. In Figs. 6 and 7 we present the residuals and the semivariances of the experimental data to the linear model, Eq. (1). In Figs. 8 and 9 the residuals and the semivariances from the quadratic model, Eq. (4), are presented. Both cases present very similar results with the semivariance tending to a finite value as $\Delta U$ increases. In this case both models seem valid, so the effect of the quadratic extension to Darcy equation must be negligible.

The maximum Reynolds number from the data of Table 2 is:

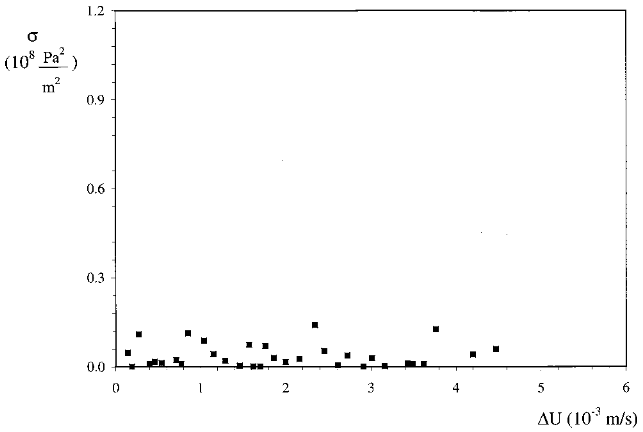

**Fig. 4 Variance of the residuals between the experimental pressure drop of Table 1 and the theoretical pressure drop obtained from the quadratic Eq. (4)**

**Table 2 Modified experimental data for $e = 1.1$ m**

| $U(10^{-3}$ m/s) | $\Delta p$ (kPa) | $k(10^{-8}$ m$^3$s/kg) |
|---|---|---|
| 3.26 | 128.3* | 2.79 |
| 3.17 | 126.3* | 2.76 |
| 3.12 | 123.4* | 2.78 |
| 3.02 | 121.7 | 2.73 |
| 3.14 | 121.1 | 2.85 |
| 2.58 | 95.0 | 2.99 |
| 2.10 | 82.8* | 2.79 |
| 1.70 | 65.8 | 2.84 |
| 1.37 | 56.7* | 2.66 |
| 1.50 | 54.7 | 3.01 |
| 0.78 | 29.2 | 2.93 |
| 0.72 | 29.2* | 2.71 |

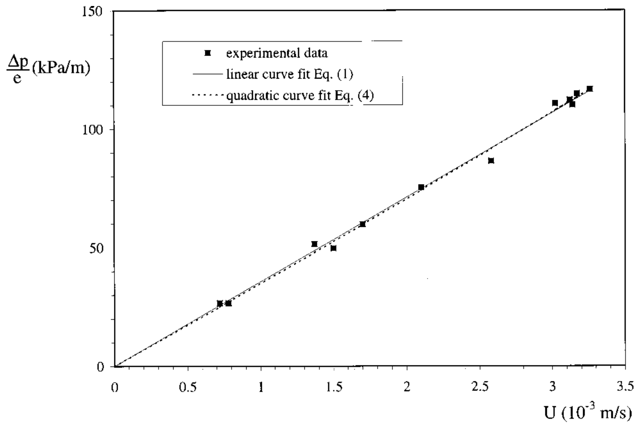

**Fig. 5 Darcy experimental data of Table 2, and least-square linear and quadratic curve fits**

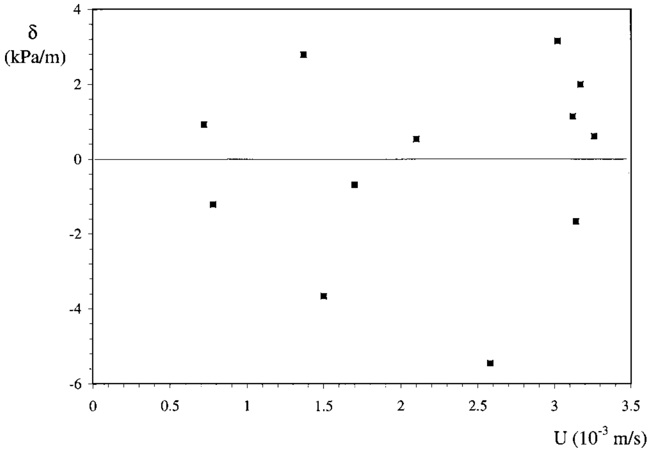

**Fig. 6 Residuals between the experimental pressure drop of Table 2 and the theoretical pressure drop obtained from the Darcy Eq. (1) with $k = 2.809\times10^{-8}$ m$^3$s/kg.**

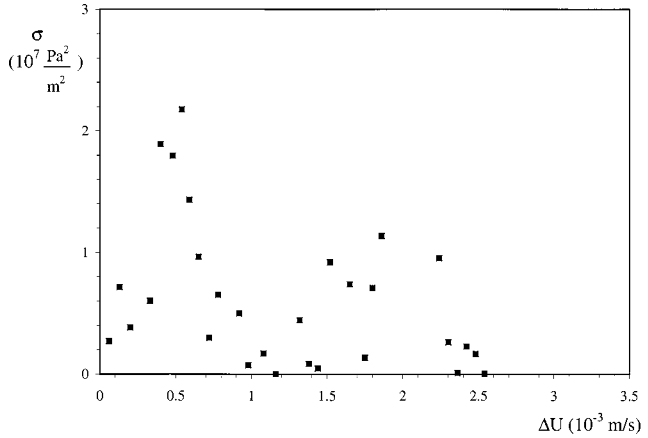

**Fig. 7 Variance of the residuals between the experimental pressure drop of Table 2 and the theoretical pressure drop obtained from the Darcy Eq. (1)**

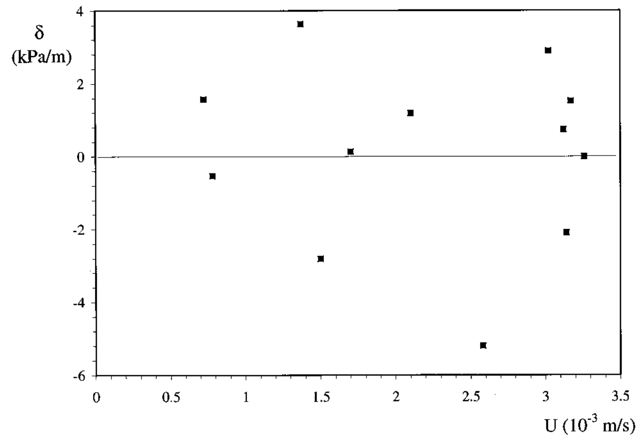

**Fig. 8 Residuals between the experimental pressure drop of Table 2 and the theoretical pressure drop obtained from the quadratic Eq. (4) with $K/\mu = k = 2.909\times10^{-8}$ m$^3$s/kg, and $C = 0.4293\times10^6$ m**

$Re_K = 0.0151$, and the maximum ratio of form to viscous forces is only 0.04. Both parameters indicating that the viscous forces predominate. Therefore, the so far overlooked fifth experimental data set presented by Darcy indeed seems to support the Darcy equation.

## Cubic Extension

Mei and Auriault [19] presented a theory valid for isotropic homogeneous medium showing that a cubic extension to the Darcy equation evolves from the inertia term of the Navier-Stokes equation, as long as the Reynolds number is *much smaller than unity*. They note that '... it is not possible to use these data {available experimental data} to draw any conclusion on the inertia correction.'

Firdaouss et al. [22] also presented a theory (similar to the theory presented by Wodie and Levy [18]) to demonstrate that the deviation from the linear flow regime (Darcy equation) can not be quadratic in velocity but cubic. Their fundamental hypothesis is that the seepage velocity of the fluid through a periodic porous medium is unaffected by reversing the pressure gradient.

The seepage velocity is invariant with the reverse of the pressure gradient only if: (1) the form factor $C$ in Eq. (4) is invariant when reversing the flow; or (2) the form force $D_c$ is negligible. Therefore, the only way to physically satisfy their hypothesis without imposing the isotropicity of $C$ is for the quadratic velocity deviation to be zero.

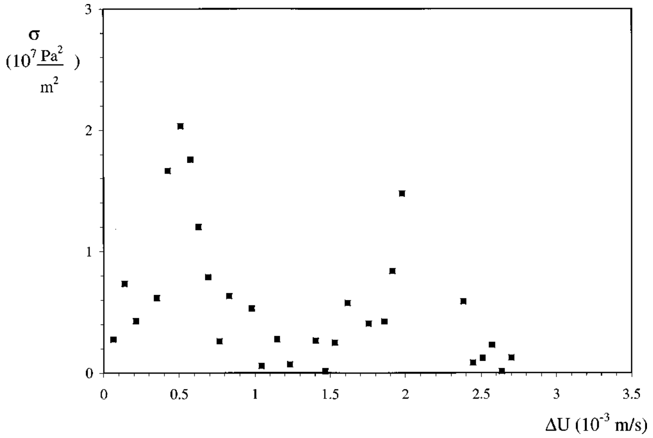

**Fig. 9 Variance of the residuals between the experimental pressure drop of Table 2 and the theoretical pressure drop obtained from Eq. (4)**

From their conclusion that the deviation must be cubic in velocity we observe a direct relationship between the order of the term $Re_{\Delta P}$ in their hypothesis and the order of the deviation. If one hypothesizes that when the pressure gradient is reversed the seepage velocity is also reversed up to a perturbation term of order $O(Re_{\Delta P})$, instead of $O(Re_{\Delta p}{}^2)$ as in their equation (3.12), then the deviation turns out to be quadratic in velocity instead of cubic.

As the cubic extension can also be written in terms of $Re^3$, and the analysis is only valid for $Re \ll 1$, the effect of this cubic extension on the pressure-drop is irrelevant in practice (this was pointed out by Mei and Auriault [19]). This aspect is supported by considering Eq. (3) of Koch and Ladd [27], p. 36, together with the results for $k_0$ and $k_2$ shown in their Fig. 1. Observe that even for $Re = 3$ (greater than unity), the cubic term accounts for only 1.25 percent of the total pressure drop (a value, in fact, within the numerical error, estimated at 3 percent, see p. 35).

## Conclusions

A careful historical review provides the correct interpretation of the physical meaning of the quadratic velocity extension, proposed by Dupuit [9], to the original Darcy equation. This quadratic extension modeling the bulk form drag force effect of the solid porous matrix depends only on a form factor and on the fluid density.

Although our paper is not concerned only with the history of science, we should never forget the educational impact of published papers. Let alone history, our emphatic reference to Dupuit's work (which should be a required reading for those working in the field of flow through porous media) brings to light a fundamental contribution ignored by many: the physical explanation behind including a quadratic velocity term to the original Darcy equation. The explanation, not found in Forchheimer's work, is given by Dupuit who educates us on the inclusion of the quadratic term in Darcy's equation to account for the form drag imposed by the porous matrix on the fluid flow. This fundamental piece of information is enough to disallow the misleading use of *inertia-related* terminology in reference to the quadratic term.

Therefore, the use of a parameter representing the ratio of inertia forces to friction forces, such as the Reynolds number, in a criterion to determine transition from linear to quadratic macroscopic flow regime is physically inconsistent. A new dimensionless parameter representing the ratio between viscous and form forces is proposed to predict the transition.

Although one of the data sets presented by Darcy seems indeed to follow the quadratic extension model proposed by Dupuit, a second data set in Darcy's manuscript so far neglected by the community supports the Darcy equation.

A cubic velocity extension to the Darcy equation finds no experimental support at the present. This deviation, mathematically restricted to very small Reynolds numbers, is completely independent from the quadratic deviation and it has no relevance in practice. Moreover, no physical justification for a cubic term is available at the moment.

## References

[1] Davis, P. A., Olague, N. E., and Goodrich, M. T., 1992, ''Application of a Validation Strategy to Darcy's Experiment,'' Adv. Water Resour., **15**, pp. 175–180.

[2] Darcy, H. P. G., 1856, *Les Fontaines Publiques de la Ville de Dijon*, Victor Dalmont, Paris. Davis, P. A., and Goodrich, M. T., 1990, ''A Proposed Strategy for the Validation of Ground-Water Flow and Solute Transport Models,'' *Proc. GEOVAL-90 Conf.*, Stokholm, Sweden.

[3] Kuznetsov, A. V., 1997, ''Investigation of the Coupled Heat Transfer, Fluid Flow and the Solute Transport During the Strip Casting Process,'' Int. J. Heat Mass Transf., **40**, pp. 2949–2961.

[4] Lage, J. L., Weinert, A. K., Price, D. C., and Weber, R. M., 1996, ''Numerical Study of a Low Permeability Microporous Heat Sink for Cooling Phased-Array Radar Systems,'' Int. J. Heat Mass Transf., **39**, pp. 3633–3647.

[5] Antohe, B. V., Lage, J. L., Price, D. C., and Weber, R. M., 1996, ''Numerical Characterization of Micro Heat Exchangers using Experimentally Tested Porous Aluminum Layers,'' Int. J. Heat Fluid Flow, **17**, pp. 594–603.
[6] Lage, J. L., 1997, ''Contaminant Transport Through Single Fracture with Porous Obstructions,'' ASME J. Fluids Eng. **119**, pp. 180–187.
[7] Hazen, A., 1893, ''Some Physical Properties of Sand and Gravels with Special Reference to Their Use in Filtration,'' *Massachusetts State Board of Health*, *Twenty-fourth Annual Report*, p. 541.
[8] Krüger, E., 1918, ''Die Grundwasserbewegung,'' Int. Mitt. Boden., **8**, p. 105.
[9] Dupuit, A. J. E. J., 1863, *Études Théoriques et Pratiques sur le Mouvement des aux dans les Canaux Découverts et a Travers les Terrains Perméables*, Victor Dalmont, Paris.
[10] Forchheimer, P., 1901, ''Wasserbewegun durch Boden,'' Z. Ver. Deutsch. Ingen., **45**, pp. 1782–1788.
[11] Prony, R. de, 1804, *Recherches Physico-mathématiques sur la Théorie des Eaux Courants*, Paris.
[12] Newton, I., 1687, *Philosophiae Naturalis Principia Mathematica* [1995, *The Principial*, Translated by Andrew Motte, Prometheus Books, New York].
[13] Ward, J. C., 1964, ''Turbulent Flow in Porous Media,'' J. Hydraul. Div., Am. Soc. Civ. Eng., **90**, HY 5, pp. 1–12.
[14] Beavers, G. S., Sparrow, E. M., and Rodenz, D. E., 1973, ''Influence of Bed Size on the Flow Characteristics and Porosity of Randomly Packed Beds of Spheres,'' ASME J. Appl. Mech., **40**, pp. 655–660.
[15] Antohe, B. V., Lage, J. L., Price, D. C., and Weber, R. M., 1997, ''Experimental Determination of Permeability and Inertia Coefficients of Mechanically Compressed Aluminum Porous Matrices,'' ASME J Fluids Eng. **119**, pp. 404–412.
[16] Barak, A. Z., 1987, ''Comments on 'High Velocity Flow in Porous Media','' Transp. Porous Media, **2**, pp. 533–535.
[17] Hassanizadeh, S. M., and Gray, W. G., 1988, ''Reply to Comments by Barak on High Velocity Flow in Porous Media,'' Transp. Porous Media, **3**, pp. 319–321.
[18] Wodie, J.-C., and Levy, T., 1991, ''Correction non Linéare de la loi de Darcy,'' C. R. Acad. Sci. Paris, **312**, Série II, pp. 157–161.
[19] Mei, C. C., and Aurialt, J.-L., 1991, ''The Effect of Weak Inertia on Flow Through a Porous Medium,'' J. Fluid Mech., **222**, pp. 647–672.
[20] Wyckoff, R. D., Botset, H. G., Muskat, M., and Reed, D. W., 1934, ''Measurement of Permeability of Porous Media,'' Bull. Am. Assoc. Petrol. Geol., **18**, pp. 161–190.
[21] Fand, R. M., Kim, B. Y. K., Lam, A. C. C., and Phan, R. T., 1987, ''Resistance to the Flow of Fluids Through Simple and Complex Porous Media Whose Matrices are Composed of Randomly Packed Spheres,'' ASME J. Fluids Eng. **109**, pp. 268–274.
[22] Firdaouss, M., Guermond, J.-L., and Le Quéré, P., 1997, ''Nonlinear Corrections to Darcy's Law at Low Reynolds Numbers,'' J. Fluid Mech., **343**, pp. 331–350.
[23] Batchelor, G. K., 1987, *An Introduction to Fluid Dynamics*, Cambridge University Press, (reprint of 1st edition 1967), p. 215.
[24] Bejan, A., 1984, *Convection Heat Transfer*, 2nd ed., Wiley, New York, pp. 99–100.
[25] Macdonald, I. F., El-Sayed, M. S., Mow, K., and Dullien, F. A. L., 1979, ''Flow Through Porous Media - Ergun Equation Revisited,'' Ind. Eng. Chem. Fundam., **18**, pp. 199–208.
[26] Delhomme, J. P., 1978, ''Kriging in the Hydrosciences,'' Adv. Water Resour., **1**, pp. 251–266.
[27] Koch, D. L., and Ladd, A. J. C., 1997, ''Moderate Reynolds Number Flows Through Periodic and Random Arrays of Aligned Cylinders,'' J. Fluid Mech., **349**, pp. 31–66.

**Bulent Yesilata**

**Alparslan Öztekin**

**Sudhakar Neti**

**Jacob Kazakia**

Department of Mechanical Engineering
and Mechanics,
Lehigh University,
Bethlehem, PA 18015

# Pressure Measurements in Highly Viscous and Elastic Fluids

*Pressure measurements in flows of highly viscous and elastic fluids are of practical importance in polymer processing and rheology systems. Special problems arise during such pressure measurements. High fluid viscosity results in excessive dynamic response time (rise time) of the pressure measuring systems. This is true for systems that consist of manometers as well as pressure transducers attached to the base of a small hole at the wall. We model the dynamic response and examine related disturbing effects. These systematic errors in pressure measurements include hole-pressure effects, instabilities in cavity flow, and the time lag of the disturbance wave. We consider static and dynamic flow systems of a polymer solution (PIB/C14/PB Boger fluid) to study these problems and show that instantaneous pressure measurements in these systems can effectively be performed.* [S0098-2202(00)02703-6]

## 1 Introduction

In industrial polymer processing systems such as extrusion, injection molding and fiber spinning, monitoring the pressure during the process is of great importance. Pressure measurements can be used to characterize the temporal structure of complex flows of polymeric fluids (Yesilata et al. [1,2] Kim et al. [3]). Pressure data can also be used to characterize rheological properties of the fluid (Bird et al. [4], Walters [5], Hatzikiriakos and Dealy [6], Dealy [7]).

Measurements of static pressure with low viscosity Newtonian fluids (water, air, etc.) is considered quite routine since no special problems arise up to frequency responses of about 1 KHz. On the other hand, for highly viscous and/or elastic fluids (typical polymeric fluids) pressure measurements could be problematic even for moderate frequency response (1 Hz). Problems encountered include dynamic response time of the measuring system and other systematic disturbances. Understanding and resolving these problems related to pressure measurements are the primary focus of this work.

Dynamic response of pressure measurements using recessed transducers may have severe limitations (Walters [5], Tanner and Pipkin [8]). Due to that and possibly other considerations, pressure measurements in polymeric fluids have been performed mostly using transducers mounted flush over a surface. Even for flush-mounted transducers other difficulties may persist. Since the size of pressure-sensing element is usually relatively large, it is difficult to mount these transducers over a surface of a duct that is small in size and obtain ‘‘local’’ pressure measurements. This is particularly true in rheological devices that usually include dies (a capillary or slit) (Macosco [9]). Another significant problem is in mounting these transducers over a curved surface. This is not only practically difficult, but is also a possible source of measurement errors. Differential pressure measurements are advantageous when sensitive measurements are to be made, but it is impractical to measure differential pressures using flush-mounted transducers (Lodge and De Vargas [10]).

In this paper, we study and model the parameters that influence dynamic response of standing columns (manometry) and of recessed transducers. We thus establish the feasibility of using such systems for dynamic pressure measurements. We also consider some possible disturbances to the pressure distribution in the flow resulting from the presence of a small hole at the wall bounding the fluid (Broadbent et al. [11], Joseph [12], Lodge [13,14]), and assess the pressure measurement errors due to these disturbances. One such error is caused by non-Newtonian elastic normal stress and fluid inertia, and it is referred to as *hole-pressure* effect. Instabilities of flow in and past a cavity of highly viscous and elastic fluids are another source of flow-related disturbances to pressure measurement. Pressure measuring systems with pressure taps include a creeping flow past a deep cavity, and such flows are subject to elastically-driven flow transitions (Pakdel and McKinley [15], Kim et al. [3]). The issue of time lag in pressure measurements caused by the slow propagation of the disturbance wave (Kazakia and Rivlin [16], Yoo and Joseph [17]) is also considered in this work as yet another possible source of systematic errors.

The experiments and theoretical models that characterize the dynamic response of the pressure measuring systems are described in Section 2. Systematic disturbances to the pressure measurements are discussed in Section 3, and results are summarized in Section 4.

## 2 Dynamic Response of the Measurement System

Two types of pressure measuring systems are considered. These are: (1) fluid-filled columns (manometry) and (2) transducers connected to flow pipes by fluid-filled columns. We describe theoretical and experimental modeling that identifies the parameters determining the response time of both of these systems.

The test fluid used in the present experimental measurements is a PIB based polymer solution, referred as PIB Boger fluid. It consists of a solution of 0.31 percent polyisobutylene (PIB) dissolved in 94.86 percent polybutene (PB) and 4.83 percent tetradecane (C14). The rheology of the fluid is given elsewhere (Shiang et al. [18]). The fluid is highly viscous and elastic. The viscometric properties of the test fluid were measured using the Rheometrics RDA-II rheometer. The zero-shear-rate viscometric properties are $\eta_p \cong 17$ Pas, $\eta_s \cong 31$ Pas, $\eta_0 \cong 48$ Pas, and $\lambda_1 \cong 2$ s, all determined at 23.5°C. Here $\lambda_1$ is the zero-shear-rate Oldroyd relaxation time, $\eta_p$ and $\eta_s$ are, respectively, zero-shear-rate polymeric and solvent contributions to the total viscosity, $\eta_0 = \eta_s + \eta_p$. Flow and pressure measurements in this work are performed at temperatures between 23°C and 24°C.

Section 2.1 describes the experimental setup, measurement methods as well as the theoretical model, and the solution of equations governing fluid-filled columns (manometry). Results of experimental measurements and theoretical predictions are presented and discussed in this section. Corresponding information for transducer systems is presented in Section 2.2.

### 2.1 Rise Time in Vertical Tube Systems (Manometry).

Measurement of static pressure with standing columns of liquids is very common since it is simple, inexpensive, and reliable. Al-

---

Contributed by the Fluids Engineering Division for publication in the JOURNAL OF FLUIDS ENGINEERING. Manuscript received by the Fluids Engineering Division May 3, 1999; revised manuscript received May 9, 2000. Associate Technical Editor: M. Dhaubhadel.

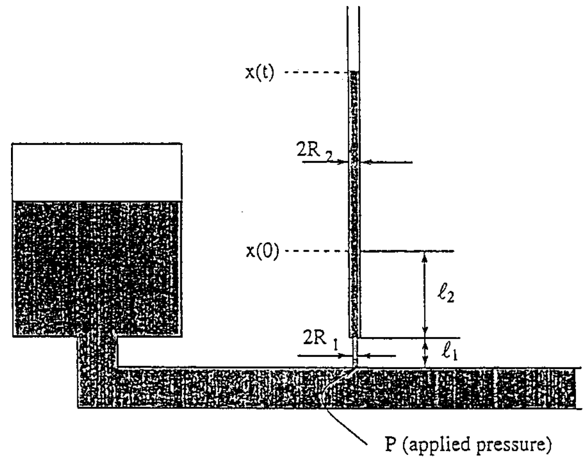

**Fig. 1 Schematic of experimental setup for manometry system**

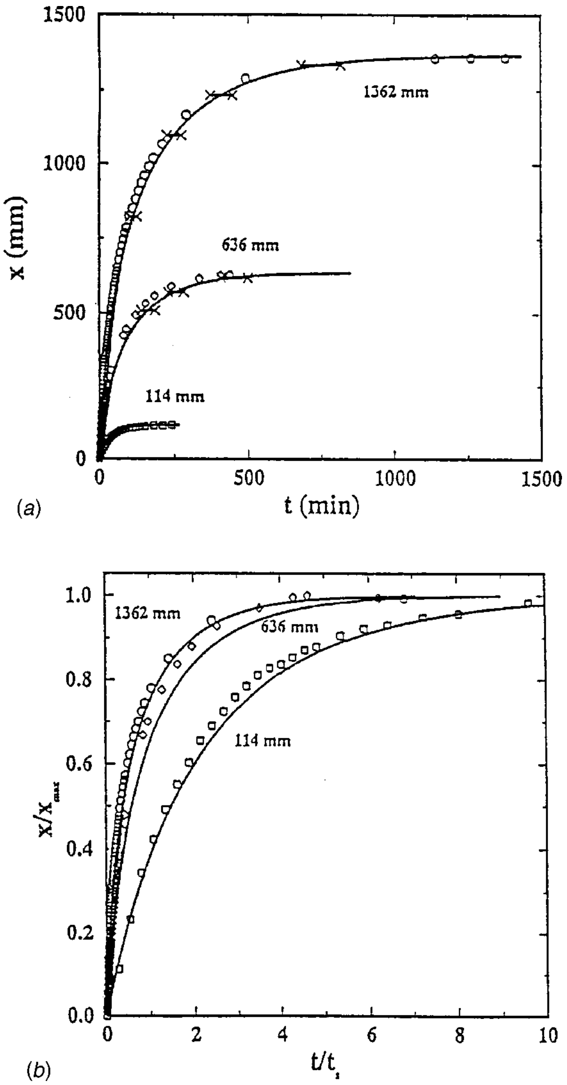

**Fig. 2 Height of the fluid as a function of time for different values of applied pressure shown in (*a*) dimensional and (*b*) nondimensional form**

though the output is usually read by a human operator, the possible errors and accuracy of measurements are comparable to transducer systems. The response (rise or fall) of a liquid column to the application of static pressure change requires a finite amount of time. Normally, for inclined and other manometers that have low viscosity liquids with specific gravity of the order unity, for static pressure applied of the order of several millimeters of water, the ''total'' rise time could be a few seconds. In contrast with that, for viscoelastic fluids that are highly viscous, such as those considered here, with viscosities approaching tens of Pa.s, the rise time could approach several hours.

The prediction of this rise time is very useful when one plans experiments where the pressure measurements are important. In this paper, we describe a method of predicting this rise time for applied pressures that are steady and time-dependent. Comparisons of the predictions with experimental measurements for various types of applied pressures and various geometries are presented. The experimental apparatus for manometry system consists of a PVC tank approximately 300 mm in diameter and 450 mm in height connected to a horizontal pipe 12.7 mm in diameter and 0.62 m long, as shown in Fig. 1. We refer to this horizontal pipe as the flow pipe. Small holes are drilled at various locations in this pipe so that vertical tubes of radius $R_2 = 3.2$ mm can be utilized to measure the change in pressure at the flow pipe wall due to a pressure change in the storage tank. Vertical tubes are connected to these holes by smaller tubes of radius $R_1 = 2.3$ mm and length $\ell_1$. The height of the fluid in the vertical tube is measured as a function of time within an accuracy of 1 mm.

Initially the fluid in the vertical tube is at height $\ell_2$. We denote the difference between the height of the fluid column at time $t$ and the initial height $\ell_2$ by $x(t)$. The maximum value of $x$ designated as $x_{\max}$ is the indication of static pressure $P$ applied to the tank, at time $t=0$, as measured in the flow pipe (see Fig. 1). Experimental data corresponding to the height of the fluid as a function of time was recorded and is displayed in Fig. 2 for three different applied pressures. Figure 2(*a*) presents the results in dimensional form while Fig. 2(*b*) presents the same results in nondimensional form. As shown in the figures, for the highly viscous fluid used in these experiments, rise times are extremely long even for low pressures. The solid lines in the figure correspond to the analytic prediction described below.

In the analytic description used here, we neglect surface tension, inertial, elastic, and compressible effects. A rough comparison shows that for the tubes and fluid used in this experiment, surface tension forces are negligible compared to gravity and pressure forces. The relative importance of elastic and inertial forces compared to the viscous forces is determined by Deborah and Reynolds numbers that are given by $\mathrm{De} = \lambda_1(\dot{\gamma})u/R$ and $\mathrm{Re} = 2\rho uR/\eta_0(\dot{\gamma})$. Here $\lambda_1(\dot{\gamma})$ is the shear-rate dependent Oldroyd relaxation time of the fluid, $\dot{\gamma}$ is the shear rate, $u$ is the fluid velocity, $R$ is the radius of the tube, $\rho$ ($=890$ kg/m$^3$) is the density, and $\eta_0(\dot{\gamma})$ is the total shear viscosity of the fluid with the zero shear rate value of $\lim_{\dot{\gamma}\to 0} \eta_0(\dot{\gamma}) = 48$ Pa.s. The relaxation time $\lambda_l$ is defined as [4], $\lambda_1(\dot{\gamma}) = N_1(\dot{\gamma})/(2\eta_p(\dot{\gamma})\dot{\gamma}^2)$, where $N_1$ is the first normal stress difference and $\eta_p(\dot{\gamma})$ is the polymeric contribution to the total viscosity. We define the Deborah number in terms of the zero-shear-rate value of the relaxation time ($\lim_{\dot{\gamma}\to 0} \lambda_1(\dot{\gamma})$) which is about 2 s for the test fluid used in the present experiments at $T = 23.5°$C.

The maximum values of the Deborah and Reynolds numbers at the very early stage of the fluid rise are $\mathrm{De} = 0.05$ and $\mathrm{Re} = 0.003$ for the largest pressure change considered here. These small values of De and Re justify neglecting the elastic and inertial forces in the analysis described below. The effect of temperature is not considered since all experiments were performed at nearly constant room temperature.

We model the rise of the fluid as a fully developed incompressible Poiseuille flow in tubes. When the operating pressure is high such as in polymer melt processing compressible effects may need to be considered by including bulk modulus in the model. We denote the pressure drop in the tube of radius $R_1$ and length $\ell_1$ (see Fig. 1) as $\Delta P_l$ and the pressure drop in the longer tube of radius $R_2$ as $\Delta P_2$. At any given instant, the sum of the two pressure drops equals the difference between the applied static pressure $\rho g x_{\max}$ and the hydrostatic head $\rho g x(t)$, i.e.,

$$\Delta P_1 + \Delta P_2 = \rho g (x_{\max} - x(t)). \tag{1}$$

These pressure drops are related to the flow velocities $u_1$ and $u_2$ in the short and longer tubes by

$$\Delta P_1 = \frac{8\eta_0 u_1 \ell_1}{R_1^2}, \quad \Delta P_2 = \frac{8\eta_0 u_2(\ell_2 + x)}{R_2^2}. \tag{2}$$

Using the continuity equation and noting that under the present assumptions the rate of change of $x$ must equal the velocity $u_2$, we obtain

$$u_1 R_1^2 = u_2 R_2^2 = \frac{dx}{dt} R_2^2. \tag{3}$$

We can express the pressure drops in terms of $dx/dt$. Substitution of these expressions into (1) produces the following differential equation for the determination of $x(t)$

$$\frac{8\eta_0}{\rho g R_2^2}\left(\ell_1 \frac{R_2^4}{R_1^4} + \ell_2 + x\right)\frac{dx}{dt} = x_{\max} - x. \tag{4}$$

The solution of this equation, with the initial condition $x = 0$ at time $t = 0$, is

$$\frac{t}{t_s} = -X - (1 + A_1)\ln(1 - X), \tag{5}$$

where $X = x/x_{\max}$, the nondimensional parameter $A_1 = (\ell_1(R_2/R_1)^4 + \ell_2)/x_{\max}$, and the time scale $t_S$ is given by $t_S = 8\eta_0 x_{\max}/(\rho g R_2^2)$. As mentioned earlier, the solid lines in Fig. 2(*a*) and 2(*b*) are obtained using Eq. (5), and the measured data are represented by various symbols.

For an applied pressure of about 13.5 kPa, it is seen that it takes approximately 24 hours for the column height to approach its final value (≈1362 mm). For lower pressures the final height is reached at shorter times but still considerable amount of time is needed. The experimental measurements agree very well with the model used here. Having verified the validity of our analytical prediction, we now consider the utility of such an approach for time-dependent pressure measurements in the main flow pipe. Is it possible to predict this pressure (or equivalently $x_{\max}$) by observing the rise of the fluid in the manometer for a relatively short time; thus avoiding a long wait? We assume that the geometric parameter $(\ell_1(R_2/R_1)^4 + \ell_2)$ is known. Inspection of Eq. (5) reveals that two observations $x_1$ and $x_2$ of the fluid column height at times $t_1$ and $t_2$ are sufficient to predict $t_s$ and $x_{\max}$. Theoretically speaking, these observations can be done at any two times $t_1$ and $t_2$. However, to minimize errors, the larger $t_1$ and $t_2$ are, the better the prediction will be. This issue is illustrated in Fig. 3 where we plot the relative error between the predicted and actual $x_{\max}$ versus $(t_2 - t_1)/t_s$ for three values of $t_1$ (5, 10, and 20 min). The time $t_2$ is varied between $t_1$ and $t_s$. Here $t_s$ is estimated using the first two measurements. As can be seen from the figure, for the worst case of $t_1 = 5$ min and $t_2 = 8$ min the error in predicting $x_{\max}$ is less than 10 percent. This error decreases significantly as $t_2 - t_1$ is increased, reducing to less than 1 percent as $(t_2 - t_1)/t_s$ goes beyond 0.5. In order to give a clearer understanding of the effect of the parameters on the rise time we introduce $t_{\text{rise}}$, the time required for $x$ to reach 99 percent of $x_{\max}$. We then obtain from Eq. (5) $t_{\text{rise}} = t_s(4.605 A_1 + 3.615)$. As expected, lower $t_s$ and $A_1$ result in decreased rise times.

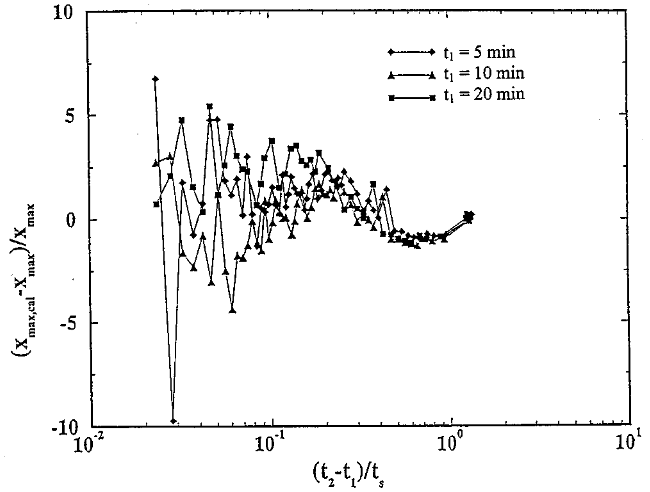

**Fig. 3 Relative error between the predicted and measured $x_{\max}$ as a function of $(t_2 - t_1)/t_s$ for three different values of $t_1$**

Another way of accelerating the rise of the fluid would be to overload the vertical tube, i.e., to start at an increased $\ell_2$ which does not correspond to an equilibrium pressure in the main flow pipe. Hence, when the pressure increase $P$ is applied to the main conduit, the fluid is already way ahead in the vertical tube closer to the corresponding $x_{\max}$. From an analytical point of view this requires the solution of the differential Eq. (4) with an altered initial condition $x(0) \neq 0$. The pressure measurements discussed so far deal with a step increase in pressure that is applied to stationary fluid. It is worth noting that a similar description of the problem is also valid when the fluid is flowing through the main flow pipe. In fact, as we shall see later, similar arguments and modeling are valid even when the applied pressure is time-dependent. In all such cases it is preferable to have a low rise time and a small measurement time.

**2.2 Rise Time in Fluid-Filled Transducer Systems.** In this section, we describe a method of pressure measurement (Fig. 4) which utilizes a system consisting of a transducer combined with a fluid filled short pipe (pipes for differential pressure measurements). In the present experiments the transducer used in Validyne DP 15 with 0.5 percent of full-scale accuracy. The pressure transducer results reported here are of 1 percent or better accuracy. The pressure transducer is connected to the main flow pipe wall with pressure taps and tubing. The output of the transducer is connected to an A/D board with 12 bit resolution in a 80486 PC to provide time dependent pressure measurements.

Electronic pressure measurement such as described above is more suitable for capturing time dependent pressure fluctuations. We develop an analytical model for this system using arguments similar to the ones presented in Section 2.1. The geometric dimensions of the system, such as the length $\ell_1$ and diameter $D_1$ of the tube connecting the transducer to the main flow pipe, the length $\ell_2$ and diameter $D_2$ of the transducer chamber are shown in Fig. 4. The transducer reading consists of an estimate of $P$, the pressure directly applied to the transducer diaphragm by the fluid. We would like to relate the pressure $P$ to the pressure $P_a$ at the bottom of the connecting tube, which is the relevant pressure. A change in $P_a$ is reflected by a change in $P$ with some time delay due to the high viscosity of the fluid as explained earlier. We model the flow in the tubes and derive an analytic prediction of this delay.

The transducer/pipe combination system for pressure measurements is filled with the flowing fluid, and the back of the membrane is vented into the atmosphere. The diaphragm deflection $\ell_v$ is small and is linearly related to the pressure $P$ applied by the fluid on the membrane. The volume change $V$ in the cavity due to the deformation of circular membrane of diameter $D_2$ into a spherical shell with a deflection $\ell_v$ is given by

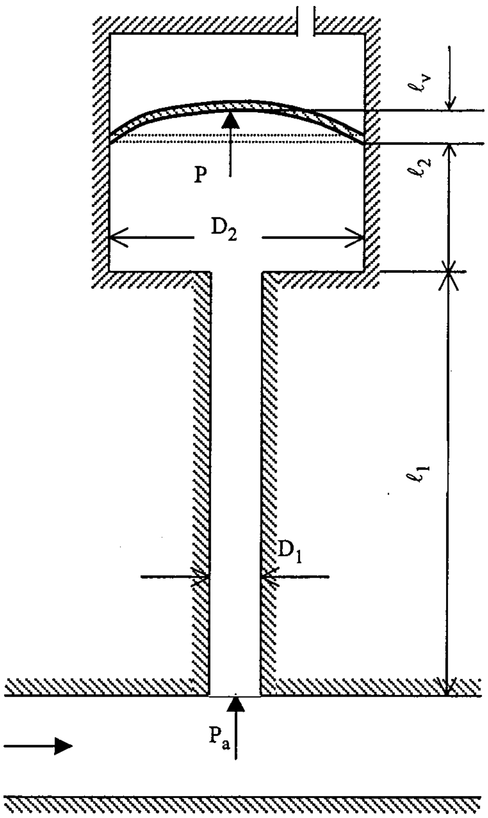

**Fig. 4 Schematic of fluid-filled transducer/pipe system**

$$\frac{V}{\pi(D_2/2)^2}=\frac{\ell_v}{2}\left[1+\frac{4}{3}\left(\frac{\ell_v}{D_2}\right)^2\right]. \tag{6}$$

The continuity equation for the incompressible fluid in the pipe-transducer system implies that

$$\frac{\pi D_1^2}{4}u=\frac{dV}{dt}, \tag{7}$$

which in view of (6) and for small $\ell_v/D_2$ gives

$$u=\frac{1}{2}\left(\frac{D_2}{D_1}\right)^2\frac{d\ell_v}{dt}. \tag{8}$$

Since $\ell_v$ is linearly related to $P$, say with diaphragm constant $k$, $P=k\ell_v$, we can write

$$u=\frac{1}{2k}\left(\frac{D_2}{D_1}\right)^2\frac{dP}{dt}. \tag{9}$$

The length of the transducer chamber ($\ell_2$) is small compared to the length of the connecting tube ($\ell_1$) and the diameter of the chamber ($D_2$) is large compared to that ($D_1$) of the connecting tube. Consequently, we can neglect the viscous pressure drop due to flow in the transducer chamber and write

$$P_a-P=\frac{32\eta_0\ell_1}{D_1^2}u, \tag{10}$$

where we use the fully-developed flow approximation neglecting gravity, inertia and elastic effects, and $\eta_0$ is the total viscosity of the fluid. Combining Eqs. (9) and (10), and with the delay time constant $T_s$ given by $T_s=16\eta_0\ell_1 D_2^2/kD_1^4$, we write

$$T_s\frac{dP}{dt}+P=P_a. \tag{11}$$

We note that the time scale, $T_s$, of this system is different from the time scale, $t_s$, of the manometry system. We also note that some device details not considered in the present modeling (such as swelling and deformation of the connecting tube, hardening of the transducer membrane, etc.) may introduce additional but small errors in the time scale $T_s$, but most likely leave the nature of Eq. (11) unaltered. In view of the above complexities, we evaluate $T_s$ from experimental observations rather than from its definition.

We now consider the general case of a time dependent pressure $P_a(t)$ and obtain the solution of the differential Eq. (11) with the initial condition $P=P_0$ at $t=t_0$ as

$$P=P_0\exp[(t_0-t)/T_s]+\int_{\tau=t_0}^{t}\frac{P_a(\tau)}{T_s}\exp[(\tau-t)/T_s]d\tau. \tag{12}$$

For the case of constant $P_a$, one obtains

$$\frac{P}{P_a}=1+\left(\frac{P_0}{P_a}-1\right)\exp[(t_0-t)/T_s]. \tag{13}$$

We consider the following experiment for the verification of the prediction derived above. With the exit valve of the main flow pipe closed, compressed air was used to apply a known pressure increase $P_a$ to the fluid in the tank connected to the flow pipe, at a known time ($t_0$). This air pressure increase in the tank induces a fluid pressure increase $P_a$ at the pressure tap position of the main flow pipe, which in turn causes the output of the transducer to start increasing. Initially, at the time of application of the pressure increase, the reading of the transducer is $P=P_0=0$. The magnitude of the applied pressure $P_a$ is checked by an independent measurement of the air pressure in the tank. These two pressure readings, $P$ and $P_a$, are recorded simultaneously after the initiation of the pressure increase and shown in Fig. 5(*a*) as a function of time. In Fig. 5(*b*), we show the analytical prediction (solid line) obtained from Eq. (13) using the condition $P_0=0$. The relationship turns out to be

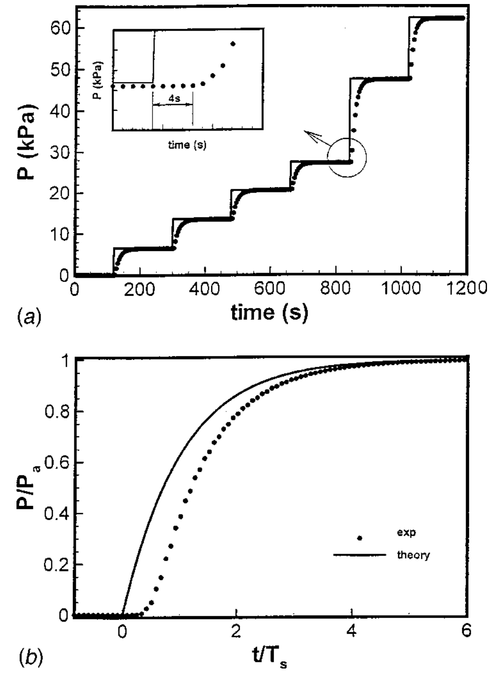

**Fig. 5 Pressure readings for multiple-step-sequence experiments: (*a*) Multiple-step increases applied (shown with solid line) and pressure readings by transducer/pipe system (shown with closed symbol), (*b*) the comparison between the results of experimental and theoretical model**

$$\frac{P}{P_a} = 1 - \exp(-t/T_s). \qquad (14)$$

The measured values lag behind the analytical prediction initially. The discrepancy between the analytical and experimental results is dramatically reduced if the experimental results are shifted in time so that the initial time of the disturbance is matched for analytical and experimental results. Such a time shift is justified considering that we start measuring time from the instant the pressure is increased at the holding tank, and since it takes a finite amount of time for the disturbance to reach the point in the main flow pipe where the pressure tap is located. This time shift is quite often negligible for low viscosity fluids but not for fluids of high viscosity used here. This issue is considered in more detail in Section 3.3.

We now consider more complex pressure variations corresponding to square wave pulses with various periods for $P(t)$. Figures 6(*a*)–(*c*) illustrate these results. In Fig. 6(*a*) a square wave of low frequency, $t_p = 6t_r$, is illustrated. Here $t_p$ is the period of the pressure variation (of $P(t)$) and $t_r$ is the time required by the experimental apparatus (for the transducer) to record a pressure equal to 99 percent of a step increase of the pressure. From Eq. (14) we can obtain $t_r = 4.605T_s$. This result combined with a measured $T_s = 11.9 \pm 1$ s for the experimental apparatus used, provides a value for $t_r = 54.8 \pm 4.6$ seconds. From Fig. 6(*a*) we see that when the frequency of $P(t)$ is low ($t_p = 6t_r$), the transducer is capable of capturing the pressure wave measuring its amplitude accurately. Figure 6(*b*) illustrates the results for $t_p = t_r$. As $t_p$ drops below $2t_r$ the transducer does not have a chance to record the full amplitude of the wave with the situation getting progressively worse for increased frequencies.

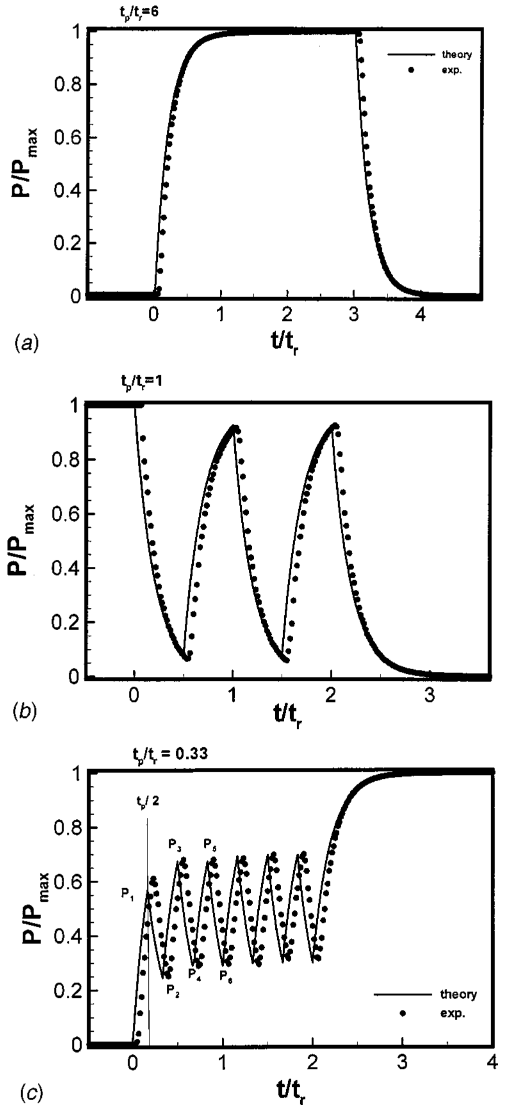

**Fig. 6 Pressure variations of square wave pulse with periods $t_p/t_r$ of (*a*) 6, (*b*) 1, and (*c*) 0.33**

The analytical model described earlier is valid for all frequency pressure pulses considered here and it can be used to predict the final amplitudes based on readings corresponding to pressures earlier in the cycle. To develop and illustrate this approach, consider Fig. 6(*c*) which depicts the transducer response for a square wave with period $t_p = t_r/3$. We use $P_1, P_3, P_5, \ldots$ to denote the maximum pressures recorded during the experiment and $P_2, P_4, P_6, \ldots$ for the minimum pressures. Using the procedure indicated below our model can predict this data.

As was indicated earlier, the solution of the differential equation governing the response is given by Eq. (13) for a constant applied pressure $P_a$. For $P_a = 0$ we have

$$P = P_0 \exp[(t_0 - t)/T_s]. \qquad (15)$$

The first maximum response $P_1$ occurs when the source pressure is switched from $P_a = P_{\max}$ to $P_a = 0$, at time $t = t_p/2$. Using the fact that at time $t = 0$, $P = 0$, from (13) we obtain

$$\frac{P_1}{P_{\max}} = 1 - Z, \qquad (16)$$

where $Z = \exp(-t_p/2T_s)$, and we note that its value varies between zero (for $t_p/T_s \to \infty$) and unity (for $t_p/T_s \to 0$). Specifically for the case shown on Fig. 6(*c*), we have $Z = 0.464$. It can be easily shown that using Eqs. (13) and (15) we obtain at times $t = t_p$, $t = 3t_p/2$, $t = 2t_p$, etc. the expression

$$\frac{P_2}{P_{\max}} = Z(1-Z), \quad \frac{P_3}{P_1} = \frac{P_4}{P_2} = 1 + Z^2$$

and so on for

$$\frac{P_{2n+1}}{P_1} = \frac{P_{2n+2}}{P_2} = 1 + Z^2 + \ldots + Z^{2n} \qquad (17)$$

In the limit of $n \to \infty$, Eqs. (17) predict

$$\lim_{n\to\infty} \frac{P_{2n+1}}{P_{\max}} = \frac{1-Z}{1-Z^2} = \frac{1}{1+Z}$$

and

$$\lim_{n\to\infty} \frac{P_{2n+2}}{P_{\max}} = \frac{Z(1-Z)}{1-Z^2} = \frac{Z}{1+Z} \qquad (18)$$

Clearly, as $Z$ tends to unity (vanishingly small period), the limiting values of $P_{2n+1}$ and $P_{2n+2}$ are equal to $P_{\max}/2$. Again, using Eqs. (13) and (15), we obtain the response $P/P_{\max}$ for all values of time as

$$\frac{P}{P_{\max}}=\begin{cases} 1+\left(\dfrac{P_{2n}}{P_{\max}}-1\right)\exp[(nt_p-t)/T_s] & \text{for } nt_p<t<(n+1/2)t_p \\ \dfrac{P_{2n+1}}{P_{\max}}\exp[((n+1/2)t_p-t)/T_s] & \text{for } (n+1/2)t_p<t<(n+1)t_p \end{cases} \tag{19}$$

with $n=0,1,2,\ldots\ldots$ and $P_0=0$. The comparison between measurements and predictions shown in Fig. 6 clearly brings out the utility and merit of the analysis described above.

The technique described here was used to measure instantaneous static pressure (or normal force) at the wall in inertialess viscoelastic flow of PIB Boger fluid through a 4:1 contraction geometry (Yesilata et al. [1,2]) and viscoelastic flow in a planar square cavity (Kim et al. [3]). Differential pressure measurements between two points were made in these experiments by connecting each end (port) of the transducer to the base of small holes at the wall, ensuring that geometric parameters (i.e., diameter, length) of the connections are nearly the same for both ports. Such measurements in viscoelastic flow systems provide information about temporal structure of flows that are otherwise very difficult to detect.

## 3 Systematic Disturbances in Pressure Measurements

**3.1 Hole-Pressure Effect.** In viscoelastic flows, hole-pressure effects may occur when the pressure or normal stress at points on the wall is determined by attaching manometers or pressure transducers to the base of a small hole at the wall. As described by Joseph [12], the presence of the hole disturbs the flow and introduces errors in the measured pressure due to inertial and normal stress effects. The disturbances resulting from inertial effects can be minimized if the hole size is very small. However, Broadbent et al. [11] has reported that it is not sufficient to use small holes to eliminate the disturbances arising from fluid elasticity. Joseph [12] suggested a critical diameter, $d_c$, $d_c=(\lambda_1\eta/\rho)$, and argued that disturbances due to inertia dominate when $d>d_c$ and disturbances due to normal stress dominate when $d<d_c$. For the test fluid used in the present experiments, $d_c\cong 195$ mm and the diameter of holes used, $d=2.3$ mm at all locations. Here $d\ll d_c$, and contributions from inertia are negligible.

The elastic contribution to the pressure is explained by the fact that the extra elastic normal stress along the curved streamlines near the hole tries to lift the fluid out of the hole, as a weight on a sagging chain (Joseph [12]). Since the fluid is not lifted out of the hole, the tension on the chain is balanced by the difference in the pressure. Higastani and Pritchard [19] proposed a simple relation between the hole-pressure effect and the primary normal stress at a circular hole over a flat surface, and is similar to that proposed by Tanner and Pipkin [8]. Elastic contribution to the pressure is given by (Bird et al. [4])

$$P-P_1=\frac{1}{3}\int_0^{\tau_w}\frac{N_1(\dot\gamma)-N_2(\dot\gamma)}{\tau_{12}(\dot\gamma)}\,d\tau_{12}, \tag{20}$$

where $N_1$, $N_2$ are first and second normal stress differences, $\tau_{12}$ is the shear stress, P is the undisturbed pressure in the tube, $P_1$ is the pressure measured at the hole, and $\dot\gamma$ is the undisturbed shear rate with no hole. Equation (20) suggests that the hole pressure effect is independent of the size and the shape of the hole. This is experimentally verified by Pritchard [20] in the range of 0.3–7 non-dimensional hole sizes.

Several investigators have used Eq. (20) to determine rheological properties of fluids by measuring the extra pressure caused by the presence of a hole over a flat surface (Malkus et al. [21], Lodge and De Vargas [10], Lodge [13,14], Lodge et al. [22]). A slit-die rheometer with transverse slot was used in these studies since it is a simple geometry and it matches with the theory of Higastani and Pritchard [19] and Tanner and Pipkin [8]. Townsend [23] also has investigated the hole pressure effect in pressure driven flows in slit geometry. The results of Townsend's numerical simulations agree well with the prediction by the theory developed by Tanner and Pipkin [8]. More recently, Malkus et al. [21] investigated the validity of the theories outlined in Eq. (20) by performing numerical simulations for Maxwell and Johnson and Segalman fluids (Johnson and Segalman [24]), and showed that these approximate theories have a wide range of applicability.

The primary goal here is not to detect the hole-pressure effect or to characterize the rheological properties of the test fluid. On the contrary, the objective here is to determine the influence of these disturbances, if any, on the pressure measurements conducted to study the structure of flow. In order to do this we have conducted experiments with flow through a circular pipe. Direct measurement of hole-pressure effect was not possible due to the curved surface of the conduit/pipe. Instead, we compared pressure measured at the wall using a pressure tap with predictions of the pressure drop in pipe flow. For sufficiently low flow rates, Oldroyd-B rate equation can model the fully developed flow of PIB-Boger fluid in a pipe. Oldroyd-B constitutive model predicts a constant (shear rate independent) viscosity and first normal stress difference in a pure shear flow (Bird et al. [4]). Rheological characterization of the fluid used here (Shiang et al. [18]) indicates that the viscometric properties of the fluid are nearly constant for values of shear rate $\dot\gamma<8\ \mathrm{s}^{-1}$. For the low Reynolds number (inertialess) pipe flow of Oldroyd-B fluid, equation equations governing mass and momentum conservation are $\nabla\cdot\mathbf{u}=0$ and $\nabla\cdot\tau-\nabla P=0$, where $\nabla$ is the nabla operator in polar coordinates, $\mathbf{u}$ is the velocity vector and $P$ is the pressure. The total extra stress $\tau$ is decomposed as $\tau=S+\eta_s\dot\gamma$, where $\dot\gamma=(\nabla\mathbf{u}+(\nabla\mathbf{u})^T)$ is the rate of strain tensor and $(\cdot)^T$ denotes transpose. The polymeric contribution $S$ to the extra stress tensor $\tau$ is given by the Oldroyd-B model (Bird et al. [4]) as

$$S+\lambda_1\left[\frac{DS}{Dt}-(\nabla\mathbf{u})^T\cdot S-S\cdot\nabla\mathbf{u}\right]=\eta_p\dot\gamma. \tag{21}$$

The solution to the conservation of mass and momentum equation with Eq. (21) for fully developed axisymmetric pipe flow of Oldroyd fluid is

$$u_z(r)=2U\left[1-\left(\frac{r}{R}\right)^2\right],\quad P-P_0=\frac{8\eta_0 U}{R^2}z,\quad S_{rz}=\eta_P\frac{\partial u_z}{\partial r},$$

$$S_{zz}=2\lambda_1 S_{rz}\frac{\partial u_z}{\partial r},\quad S_{rr}=S_{r\theta}=S_{\theta\theta}=S_{z\theta}=0. \tag{22}$$

Here $U$ is the average velocity in the pipe of radius $R$. $\lambda_1$ and $\eta_p$ are respectively the zero-shear-rate Oldroyd relaxation time and polymeric contribution to the total viscosity. For this flow system, Eq. (20) and Eq. (22) imply that

$$P-P_1=\frac{1}{3}\int_0^{\tau_w}\frac{S_{zz}(\dot\gamma)}{\tau_{rz}(\dot\gamma)}\,d\tau_{rz}=\frac{1}{3}\lambda_1\eta_p\left(\frac{\partial u_z}{\partial r}\right)^2_{\text{wall}}=\frac{16}{3}\lambda_1\eta_P\left(\frac{U}{R}\right)^2. \tag{23}$$

Comparison between measured and calculated pressure indicates that there is no discernible hole-pressure effect, as shown in Fig. 7. We use Eq. (23) to predict the hole-pressure effect despite the fact that this model was developed for holes over a flat surface. We compare our pressure measurement against the calcu-

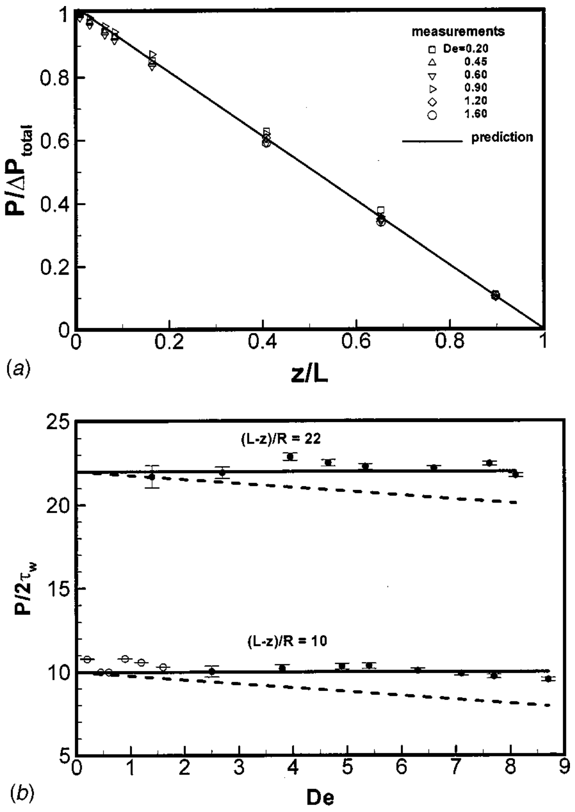

**Fig. 7 (*a*) Axial pressure distribution in inertialess circular pipe flow of a PIB/PB/C14 polymer solution at different values of flow rate (or De). (*b*) Pressure at two axial locations depicted as a function of De in creeping pipe flow of PIB Boger fluid. The predictions by Oldroyd-B model are shown by solid lines without the hole pressure effect and by dashed lines with the hole pressure effect. Open symbols denote measurements using standing fluid columns (manometry) and solid symbols denote measurements using transducers.**

lated pressure with (solid line in Fig. 7) and without (dashed line in Fig. 7) the pressure hole effect given by Eq. (23). The measured pressure data (up to De=9) agree well with calculated pressure that did not include hole pressure effect. This indicates that measurements in viscoelastic flow of typical polymeric solutions with recessed transducer system can be made without significant contribution from hole-pressure disturbances. Similar results have been reported by Lodge and De Vargas [10]. They have indicated that typical contribution of hole-pressure effect ($P_h/P$) ranges from 0.01–0.001 for the flow of polymer melts in a slit-die rheometry. This range appears to be below the accuracy range of most transducers (from 0.1 to 1 percent of full scale) used in practical applications. Lodge and De Vargas [10] have claimed to detect the relatively small hole-pressure errors. Their objective was the measurement of the normal stress difference of the polymeric fluids.

**3.2 Instabilities in Cavity Flow.** The pressure measuring system used in the present experiments consists of transducers combined with fluid filled pipes. The pressure transducers are connected to the base of a small hole in the wall of flow system with pressure taps and tubing. Hence the pressure measuring system includes the viscoelastic flow of a highly viscous and elastic fluid past a deep cavity. Such viscoelastic recirculating flows have been examined by Cochrane et al. [25]. For flow rates above the critical value, the inertialess viscoelastic flow past a cavity is subject to elastic instabilities (Pakdel and McKinley [15], Kim et al. [3]), which can lead to time-dependent pressure variations. These elastically driven flow instabilities in the cavity flow might cause systematic disturbances to pressure measurements.

The critical value of the Deborah number for the onset of the elastic flow instability in the inertialess cavity flow of PIB based Boger fluid is reported to be about 0.35 (for aspect ratios unity or greater). Pressure measurements were conducted in pipe flow for flow rates up to De=4.5 (De=4.5 for the pipe flow corresponds to De≅27 for the cavity flow in the pressure measuring system), but the pressure traces did not indicate any dependence in time. The pressure measurements in the main flow appear not to be influenced by possible disturbances in the cavity flow.

**3.3 Time Lag of the Pressure Wave.** Another possible systematic error in pressure measurements in the flow of polymeric fluid is due to the slow propagation speed of the disturbances in viscoelastic materials. Kazakia and Rivlin [16] and Yoo and Joseph [17] showed that the shear wave speed or the speed of vorticity waves for Maxwell fluid is given by $c=(\eta_0/\lambda_1\rho)$, where $\eta_0$ and $\lambda_1$ are zero shear rate total viscosity and relaxation time, respectively, and $\rho$ is the density of the polymeric material. The predictions of $c$ provide a good description for the experimentally determined wave speed in several polymeric systems including M1 Boger fluid (Hu et al. [26]).

The systematic error due to the time lag in our pipe flow experimental system (described in Section 2) can be estimated with $t_c=\ell_1/c=(\ell_1^2\lambda_1\rho/\eta_0)^{1/2}$, where $\ell_1\cong 1$ m is the total distance between where the pressure input is applied to where it is measured. According to this equation a lag time of approximately $t_c=6$ s is predicted for pressure information to be transmitted from tank to the transducer. Results of our static experiments (see Fig. 2(*a*)) indicate that the time lag is about 4 s in the pressure measurement. The discrepancy between the predicted and measured time lag is not surprising. The experimental setup and measurements involve wave propagation in an elastic material in a three-dimensional domain with nonrigid boundaries.

## 4 Conclusions

Experimental measurements and theoretical modeling of the dynamic response of pressure measurement systems, which include transducers connected to a hole (pressure tap) in the wall of a flow system, have been performed. Disturbances such as hole-pressure effects, instabilities for flow past a deep cavity, and time lag of pressure waves that could impede pressure measurements in highly viscous and elastic fluids have been carefully examined.

Instabilities due to flow past a deep cavity (pressure tap), and hole-pressure effects have been shown to be unobtrusive in making desired fluid pressure measurements in pipe flow for a highly elastic (and viscous) PIB Boger fluid. The time lag of the pressure wave due to the slow speed of sound in such fluids can be significant, but can be estimated well.

The primary conclusion of this work is that pressure measurements in flows of highly viscous and elastic fluids can be successfully made when proper care is taken. Temporal and spatial structures of complex unsteady viscoelastic flows can be characterized using dynamic pressure measurements. Quite often, such pressure measurements can identify flow features much better than other techniques.

A step change in time of applied pressure manifests itself as an exponential change in measured pressure with a time constant that is a function of system geometry, and fluid properties. This is also true with the use of manometers for pressure measurement. For dynamic pressure measurements, the response time ($t_r$) of the system is also a function of system as well as fluid properties, and can be evaluated using the procedures given in this work. To achieve accurate dynamic pressure measurements, the response time of the system must be smaller than the period of the pressure perturbation.

## Acknowledgment

We are grateful for the support provided for one of the authors (B.Y.) by the Harran University, Turkey to complete this work.

## Nomenclature

$A_1$ = expressed in Eq. (5)
$D_1$ = diameter of the tube
$D_2$ = diameter of the spherical membrane
$d_c$ = critical diameter
De = Deborah number, dimensionless flow rate
$k$ = diaphragm constant
$N_1$ = first normal stress difference
$N_2$ = second normal stress difference
$P$ = pressure
$P_a$ = applied pressure
$R$ = radius of the tube
Re = Reynolds number
$S$ = polymeric contribution to the total extra stress
$t$ = time
$t_s$ = time constant
$T_s$ = time constant
$t_p$ = period
$t_r$ = response time
$u$ = fluid velocity in the tube
$U$ = average velocity (Eq. (16))
$V$ = volume change in cavity
$Z$ = defined in Eq. (11)
$x$ = axial position
$X$ = non-dimensional axial position
$\dot{\gamma}$ = shear rate
$\Delta P$ = pressure drop
$\eta_0$ = total viscosity of the fluid
$\eta_P$ = polymeric contribution to the total viscosity
$\eta_S$ = solvent contribution to the total viscosity
$\lambda_1$ = relaxation time
$\rho$ = fluid density
$\tau$ = total extra stress
$\tau_{12}$ = shear stress
$\ell_1$ = length of the tube
$\ell_2$ = length of the tube
$\ell_v$ = diaphragm deflection

### Subscripts

1, 2 = tube 1 and 2
max = maximum value

## References

[1] Yesilata, B., Öztekin, A., and Neti, S., 1999, ''Instabilities in Viscoelastic Flow through an Axisymmetric Sudden Contraction,'' J. Non-Newtonian Fluid Mech., **85**, p. 35.

[2] Yesilata, B., Öztekin, A., and Neti, S., 2000, ''Nonisothermal Viscoelastic Flow through an Axisymmetric Sudden Contraction,'' J. Non-Newtonian Fluid Mech., **89**, p. 133.

[3] Kim, J., Öztekin, A., and Neti, S., 2000, ''Instabilities in Viscoelastic Flow Past a Cavity,'' J. Non-Newtonian Fluid Mech., **90**, p. 261.

[4] Bird, R. B., Armstrong, R. C., and Hassager, O., 1987, *Dynamics of Polymeric Liquids, Volume 1: Fluid Mechanics*, 2nd ed. Wiley Interscience, New York.

[5] Walters, K., 1975, *Rheometry*, Chapman and Hall, London.

[6] Hatzikiriakos, G. H., and Dealy, J. M., 1994, ''Start-Up Pressure Transients in a Capillary Rheometer,'' Polym. Eng. Sci., **34**, p. 493.

[7] Dealy, J. M., 1995, ''On the Significance of Pressure Relaxations in Capillary or Slit Flow,'' Rheol. Acta, **34**, p. 115.

[8] Tanner, R., and Pipkin, A., 1969, ''Intrinsic Errors in Pressure-Hole Measurements,'' Trans. Soc. Rheol., **14**, p. 471.

[9] Macosco, C. W., 1994, *Rheology: Principles, Measurements and Applications*, VCH Publishers, New York.

[10] Lodge, A. S., and De Vargas, L., 1983, ''Positive Hole-Pressures and Negative Exit Pressure Generated by Molten Low-Density Polyethlene Flowing through a Slit Die,'' Rheol. Acta, **22**, p. 151.

[11] Broadbent, J. M., Kay, A., Lodge, A. S., and Vale, D. G., 1968, ''Possible Systematic Error in the Measurement of Normal Stress Differences in Polymer Solutions in Steady Shear Flow,'' Nature (London), **217**, p. 55.

[12] Joseph, D. D., 1990, *Fluid Dynamics of Viscoelastic Liquids*, Springer-Verlag, Berlin.

[13] Lodge, A. S., 1985, ''Low-Shear-Rate Rheometry and Polymer Quality Control,'' Chem. Eng. Commun., **32**, p. 1.

[14] Lodge, A. S., 1989, ''An Attempt To Measure the First Normal-Stress Difference $N_1$ in Shear Flow for a Polyisobutylene/Decalin Solution at High Shear Rates,'' J. Rheol., **33**, p. 821.

[15] Pakdel, P., and McKinley, G. H., 1998, ''Cavity Flows of Elastic Liquids: Purely Elastic Instabilities,'' Phys. Fluids, **10**, p. 1058.

[16] Kazakia, J. Y., and Rivlin, R. S., 1981, ''Run-Up and Spin-Up in a Viscoelastic Fluid,'' Rheol. Acta, **20**, p. 111.

[17] Yoo, Y. L., and Joseph, D. D., 1985, ''Hyperbolicity and Change of Type in the Flow of Viscoelastic Fluids through Channels,'' J. Non-Newtonian Fluid Mech., **19**, p. 15.

[18] Shiang, A. H., Lin, J. C., Öztekin, A., and Rockwell, D., 1997, ''Viscoelastic Flow Around a Confined Cylinder: Measurements Using High-Image-Density Particle Image Velocimetry,'' J. Non-Newtonian Fluid Mech., **73**, p. 29.

[19] Higastani, K., and Pritchard, W. G., 1972, ''A Kinematic Calculation of Intrinsic Errors in Pressure Measurements Made with Holes,'' Trans. Soc. Rheol., **16**, p. 687.

[20] Pritchard, W. G., 1970, ''The Measurements of Normal Stresses by Means of Liquid-filled Holes in a Surface,'' Rheol. Acta, **9**, p. 200.

[21] Malkus, D. S., Pritchard, W. G., and Yao, M., 1992, ''The Hole-Pressure Effect and Viscometry,'' Rheol. Acta, **31**, p. 521.

[22] Lodge, A. S., Pritchard, W. G., and Scott, L. R., 1991, ''The Hole-Pressure Problem,'' IMA J. Appl. Math., **46**, p. 39.

[23] Townsend, P., 1980, ''A Computer Model of Hole-pressure Measurement in Poiseuille Flow of Visco-elastic Liquids,'' Rheol. Acta, **19**, p. 1.

[24] Johnson, M. W., and Segalman, D., 1977, ''A Model for Viscoelastic Behavior Which Allows Non-Affine Deformation,'' J. Non-Newtonian Fluid Mech., **2**, p. 255.

[25] Cochrane, T., Walters, K., and Webster, M. F., 1981, ''On Newtonian and Non-Newtonian Flow in Complex Geometries,'' Philos. Trans. R. Soc. London, Ser. A, **301**, p. 163.

[26] Hu, H. H., Riccius, O., Chen, K. P., Arney, M., and Joseph, D. D., 1990, ''Climbing Constant, Second Order Correction of Trouton's Viscosity, Wave Speed and Delayed Die Swell for M1,'' J. Non-Newtonian Fluid Mech., **35**, p. 287.

Journal of Fluids Engineering

Technical Briefs

# A Method of Correlating Fully Developed Turbulent Friction in Triangular Ducts

**S. F. Nan**
Associate Professor

**M. Dou**
Lecturer

Department of Chemical Engineering,
Zhejiang University, Hangzhou, 310027,
The People's Republic of China

*Fanning factors in isosceles-triangular ducts are examined. Data obtained in the literature were examined for deviations from the smooth circular tube line. It was found that the constant C in a form of the Blasius equation* $4f\,Re^{0.25}=C$ *decreases as the apex angle does within the extent of experiments, and has 20 percent low deviation at 4 degree. For the apex angles greater than 60 degree, it was found that the constant C decreases as the apex angle increases. It is thus concluded that the hydraulic diameter is not the proper length dimension to use in the Reynolds number to insure similarity between the circular and triangular ducts. Instead, if an area equivalent round diameter is used in the Reynolds number, the deviations from the smooth circular tube line is within ~6 percent. By using this area equivalent round diameter, it is demonstrated that circular tube methods may be readily applied to triangular ducts eliminating large errors in estimation of friction factors.* [S0098-2202(00)00503-4]

## Introduction

It has been common practice in the fields of fluid mechanics to utilize the hydraulic or equivalent diameter in predicting turbulent pressure drop along duct lengths having noncircular cross section. But there is often great deviation from the circular tube line by using the hydraulic diameter in the Reynolds number, and therefore many authors have suggested various modifying methods to predict friction factors. In case of rectangular ducts, for example, Jones [1] uses a ''laminar equivalent diameter'' to form the Reynolds number, which is in turn used in any circular tube correlation for friction factors. And in case of annuli, Brighton and Jones [2] modify the constant $C$ in the Blasius equation on the basis of the experimental data.

Carlson and Irvine [3] and Schiller [4] had done experimental research on fully developed pressure drop in triangular shaped ducts. Their experimental data have deviation from the smooth circular tube line. Carlson and Irvine noted that the circular-tube correlation, with the hydraulic diameter, predicts values some 20 percent high for a 4-degree apex angle, and 5 percent high at a 38.8-degree apex angle. And they also noted that the calculation method of Deissler and Taylor [5] underestimates the friction factor by almost as much as the hydraulic diameter rule overestimates it for the 12 and 22.3 degree ducts.

There was little experimental data for apex angles greater than 60 degree in literature. And until now there is no proper correlation for isosceles triangular ducts reported. Therefore, the purpose of the investigation reported here was to obtain friction factors for isothermal, fully developed, laminar, and turbulent flow in smooth isosceles triangular ducts having apex angles that varied from 100 to 147 degrees. Moreover, an area equivalent round diameter is proposed to use in the Reynolds number.

## Apparatus

The sketch of the experimental procedure used to obtain pressure drop data is illustrated in Fig. 1 and Fig. 2. In the setup used, water was pumped from the water pool into the elevated tank that

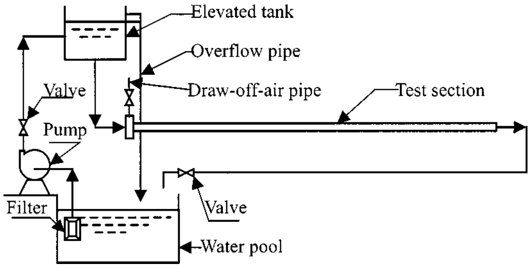

Fig. 1 Sketch of the experimental procedure

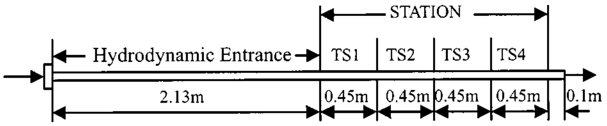

Fig. 2 Sketch of the positions of the pressure holes distributing over the test sections (TS)

Table 1 Dimensions of experimental ducts

| | | | | |
|---|---|---|---|---|
| Apex angle, deg. | 99.5 | 114.7 | 127.9 | 147.1 |
| Hydraulic diam., $\mathrm{m}\times10^3$ | 10.63 | 8.631 | 6.815 | 4.252 |
| Hydrodynamic entrance length, hydraulic diam. | 200.4 | 246.8 | 312.5 | 500.9 |
| Individual test section length, hydraulic diam. | 42.3 | 52.1 | 66.0 | 105.8 |

---

Contributed by the Fluids Engineering Division of THE AMERICAN SOCIETY OF MECHANICAL ENGINEERS. Manuscript received by the Fluids Engineering Division December 25, 1999; revised manuscript received February 7, 2000. Associate Technical Editor: M. Hajj.

had an overflow pipe to maintain a fixed water level, then flowed through a duct and past an abrupt entrance and into the hydrodynamic entrance section where it became fully developed. It then entered the test section where the pressure drop readings were made, which consisted of four identical test sections in series. These multiple sections served to check on the reproducibility of the measurements and to insure that the flow was fully developed. After leaving the test section, the water flowed through a duct and back to the water pool. The flow rates were determined by measuring the volume of water during a known time interval. The pertinent dimensions of the duct are listed in Table 1 for the various apex angles investigated.

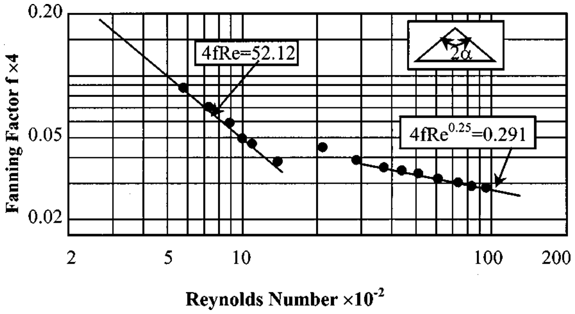

**Fig. 3** **Fanning factor versus Reynolds number $2\alpha$=99.5 deg**

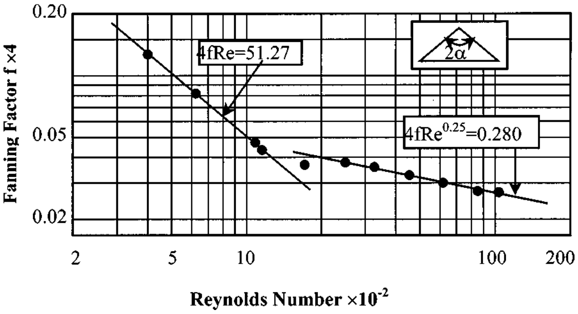

**Fig. 4** **Fanning factor versus Reynolds number $2\alpha$=114.7 deg**

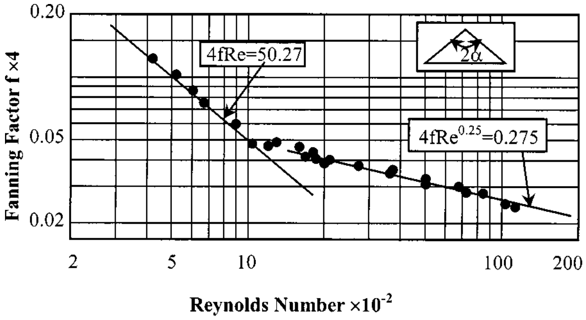

**Fig. 5** **Fanning factor versus Reynolds number $2\alpha$=127.9 deg**

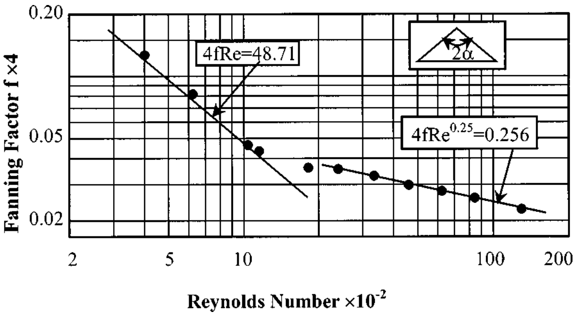

**Fig. 6** **Fanning factor versus Reynolds number $2\alpha$=147.1 deg**

**Presentation of Results.** The experimental data are presented in the form of Fanning factor against Reynolds number. These two quantities are defined as follows

$$f=\frac{d_e}{2Lu^2}\frac{\Delta P}{\rho} \tag{1}$$

and

$$\mathrm{Re}=\frac{d_e u \rho}{\mu} \tag{2}$$

where $P$ is pressure, $\rho$ is the density of the fluid, $f$ is Fanning factor, $L$ is the pipe length, $d_e$ is the hydraulic diameter, $u$ is the average velocity in flow direction, Re is Reynolds number, $\mu$ is the dynamic density of the fluid.

For each duct angle, Fanning factors were measured in the laminar, transitional, and turbulent regimes. Figures 3, 4, 5, and 6 show the experimental Fanning factors for apex angles of 99.5, 114.7, 127.9, and 147.1 degrees, respectively.

## Area Equivalent Round Diameter and Modified Reynolds Number

It is known that if the curve $4f\,\mathrm{Re}=64$ is extended from laminar into turbulent regime, we will obtain the value of Fanning factor that is much smaller than the turbulent one at the same Reynolds number. A peculiarity of turbulent flow in a triangular duct is that where there are very acute corner angles the thickness of the viscous sublayer can become large relative to the distance between adjacent wall surfaces. This leads to what is sometimes described as coexisting laminar and turbulent flow in the duct. The shear stress then tends to be very much lower in the acute-angle corners. So considering this configuration effect on Fanning factor, we suggest an area equivalent round diameter be used in Reynolds number. An area equivalent round diameter may be defined as

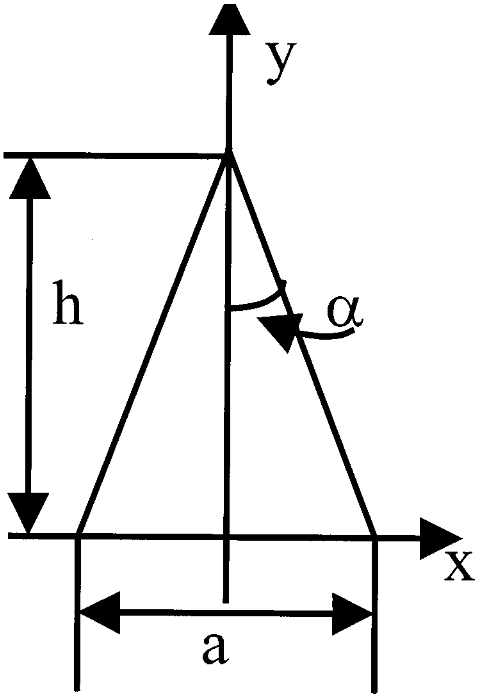

**Fig. 7** **As isosceles-triangular duct**

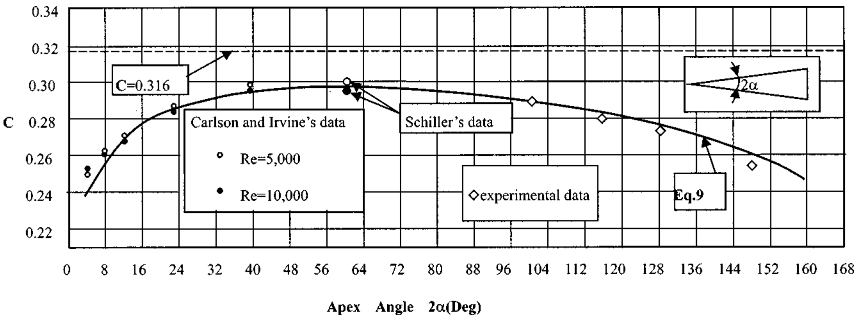

**Fig. 8 Comparison between Eq. (4), Eq. (5), the Blasius equation, and experimental data**

$$d_{Se}=\frac{4\times S}{P_S}=\sqrt{\frac{4S}{\pi}} \tag{3}$$

where $S$ is the cross-sectional area of fluid flow, shown in Fig. 7, $S=ha/2=\pi d_{Se}^2/4$, and $P_S$ is the perimeter of a circle whose area is equal to $S$, $P_S=\pi d_{Se}$.

According to the geometric relation shown in Fig. 7, we have

$$h=\frac{a}{2tg\,\alpha} \tag{4}$$

so

$$d_{Se}=\frac{a}{\sqrt{\pi tg\,\alpha}} \tag{5}$$

$$P_S=\pi d_{Se}=a\sqrt{\frac{\pi}{tg\,\alpha}} \tag{6}$$

The modified Reynolds number may be defined as

$$\mathrm{Re}^*=\frac{d_{Se}u\rho}{\mu} \tag{7}$$

The relation between Re* and Re is

$$\mathrm{Re}^*=\frac{d_{Se}u\rho}{\mu}=\frac{\frac{4S}{P_S}\cdot u\rho}{\mu}=\frac{\frac{4S}{P}\cdot\frac{P}{P_S}\cdot u\rho}{\mu}=\mathrm{Re}\cdot\frac{P}{P_S}=k\,\mathrm{Re} \tag{8}$$

where $P$ is the perimeter of the isosceles triangle, $P=a(1+1/\sin\alpha)$; and $k=P/P_s=(1+1/\sin\alpha)\sqrt{tg\,\alpha/\pi}$, only related to half of the apex angle.

If Re* is substituted for Re in the Blasius equation, we have

$$4f(\mathrm{Re}^*)^{0.25}=0.316 \tag{9}$$

or

$$4f\,\mathrm{Re}^{0.25}=0.316k^{-0.25}=C \tag{10}$$

Figure 8 shows a comparison between Eq. (9) and the experimental results of Carlson and Irvine, Schiller, and the triangular ducts having apex angles of 99.5, 114.7, 127.9, and 147.1 degrees, respectively.

## Discussion and Conclusion

It has been shown in Fig. 8 that the use of an area equivalent round diameter to calculate a modified Reynolds number yields excellent agreement between Eq. (9) and the experimental data. For the 4.01 and 7.96 degree ducts, Eq. (9) underestimates the friction factors, but the deviation from the experimental data is within ~6 percent. For the 114.7, 127.9, and 147.1 degree ducts, Eq. (9) overestimates the friction factors, and the deviation from the experimental data is within 2.5 percent.

## References

[1] Jones, Jr., O. C., 1976, ''An Improvement in the Calculation of Turbulent Friction in Rectangular Ducts,'' ASME J. Fluids Eng., **98**, pp. 173–181.
[2] Brighton, J. A., and Jones, J. B., 1964, ''Fully Developed Turbulent Flow in Annuli,'' ASME J. Basic Eng., **86**, pp. 835–844.
[3] Carlson, L. W., and Irvine, T. F., 1961, ''Fully Developed Pressure Drop in Triangular Shaped Ducts,'' ASME J. Heat Transfer, **83**, pp. 441–444.
[4] Schiller, L., 1923, ''Über den Strömungswiderstand von Rohren verschiedenen Querschnitts and Rauhigkeitsgrades,'' Z. Angew. Math. Mech., **3**, pp. 2–13.
[5] Deissler, R. G., and Taylor, M. F., 1958, ''Analysis of Turbulent Flow and Heat Transfer in Non-Circular Passages,'' NACA Technology Note 4384, Sept.

---

# Numerical Properties of the Discrete Gas Cavity Model for Transients

**Jim C. P. Liou**
Professor, Department of Civil Engineering, University of Idaho, Moscow, ID 83844-1022

*Wylie's discrete gas cavity model offers a simple way to simulate transients in liquids with a small amount of free gas, and to model vaporous and gaseous cavitations. It uses a constant and gas-free wave speed to avoid interpolations and a weighting factor to control numerical oscillations. The model has an intriguing ability to capture features associated with pressure-dependent wave speeds. This paper describes a von Neumann analysis on this model, shows why the need for the weighting factor and how to select it, and explains why the model exhibits variable wave speed features. [S0098-2202(00)00703-3]*

## Introduction

When a small amount of free gas is distributed in the liquid contained in a pipeline, the flow can be regarded as homogeneous. The gas makes the wave speed pressure dependant. This dependency causes difficulties with the widely used method of characteristics with specified time intervals. One way to deal with the variable wave speed is to use interpolation (Wylie [1]). Alternatively, Provoost and Wylie [2] introduced a discrete gas cavity model in which the free gas is lumped at computational sections and the liquid between sections is gas-free. As a result, the wave speed is constant and interpolations are no longer needed.

---

Contributed by the Fluids Engineering Division of THE AMERICAN SOCIETY OF MECHANICAL ENGINEERS. Manuscript received by the Fluids Engineering Division February 5, 1999; revised manuscript received April 3, 2000. Associate Technical Editor: M. Sommerfeld.

This model uses a weighting factor to control numerical oscillations. Although a heuristic guideline for choosing this factor has been given (Wylie and Streeter [3]), no numerical analysis of this model has been performed. This paper presents such an analysis.

## Discrete Gas Cavity Model

This study neglects the frictional resistance to flow. Between computational sections, the transient motion of the liquid is modeled by the conventional waterhammer equations (Wylie and Streeter [3]). At computational sections, the equation of state for the gas and the continuity equation for the gas volume apply. This is explained in terms of Fig. 1 where a computational grid with two spatial computational reaches $\Delta x$, one time step $\Delta t$, and three computational sections are shown. The free gas in each half of a $\Delta x$ is lumped at of the nearest computational section. The liquid in the reaches is gas-free and has a constant bulk modulus and mass density. There are four variables at each section: piezometric head $H$, gas volume $V$, flow entering the section $U$, and flow leaving the section $Q$.

In the method of characteristics, the two compatibility equations relating the head and flows at grid points $(j-1,n)$, $(j,n+1)$, and $(j+1,n)$ are (Wylie and Streeter [3])

$$H_j^{n+1}=H_{j-1}^n+BQ_{j-1}^n-BU_j^{n+1} \tag{1}$$

$$H_j^{n+1}=H_{j+1}^n-BU_{j+1}^n+BQ_j^{n+1} \tag{2}$$

in which $B=a/gA$, $a=$gas-free wave speed, $g=$gravitational acceleration, $A=$pipe cross-sectional area, $\Delta x=$length of a computational reach, and $D=$diameter. Equations (1) and (2) are valid only along the $C+$ characteristic defined by $\Delta x/\Delta t=a$ and the $C-$ characteristic defined by $\Delta x/\Delta t=-a$, on the distance $x$ versus time $t$ plane. A Courant number of unity, based on the gas-free wave speed, is implied in Fig. 1.

An isothermal volume versus head relationship is assumed at a gas cavity

$$V_j^{n+1}=\frac{C_3}{H_j^{n+1}-Z-H_v} \tag{3}$$

in which the constant $C_3$ can be computed from (Wylie and Streeter [3])

$$C_3=\frac{P_0\alpha_0\Delta xA}{\rho g} \tag{4}$$

where $P_0=$a reference absolute pressure, $\alpha_0=$void ratio at $P_0$, $\rho=$liquid mass density, $Z=$elevation of the pipe, and $H_v=$gauge vapor pressure head of the liquid. $H^*-Z-H_v$ is the absolute partial pressure head of the free gas. The isothermal gas behavior is assumed because the distributed free gas before lumping is visualized as very small bubbles.

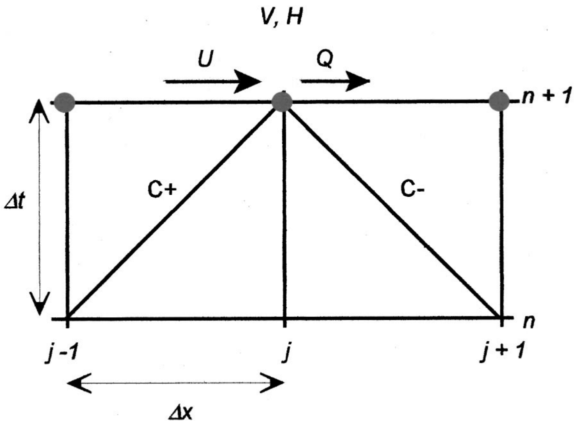

**Fig. 1 The computational grid and variable definitions**

The increase of the gas volume at a section over a time step is equated to the net liquid outflow integrated over the time step. A weighting factor $\psi$ is used in this integration (see Eq. (5)). By expressing the liquid flows and the gas volume in terms of head, a quadratic equation results which enables an explicit solution for the head and subsequently all the unknowns. The solution is unstable when $\psi<0.5$, stable but contains oscillations when $\psi=0.5$, and stable but damped when $\psi>0.5$ (Wylie [4]).

## Linearization

The gas volume versus absolute gas partial pressure head hyperbola (Eq. (3)) can be represented locally around a head $H^*$ by a straight line. With this linearization, the gas continuity equation is approximated locally as

$$\frac{-C_3}{(H^*-Z-H_v)^2}\,\frac{H_j^{n+1}-H_j^n}{\Delta t}=\psi(Q_j^{n+1}-U_j^{n+1})+(1-\psi)(Q_j^n-U_j^n) \tag{5}$$

Equations (1), (2), and (5) form a linear system from which $H_j^{n+1}$, $U_j^{n+1}$, and $Q_j^{n+1}$ can be solved. The properties of this numerical scheme are analyzed next.

## von Neumann Analysis and Results

The solutions to Eqs. (1), (2), and (5) can be expressed by a discrete Fourier series. Consider one typical term in the series and let

$$H_j^n=h\,\exp(i(\beta n\Delta t+\sigma j\Delta x)),U_j^n=u\,\exp(i(\beta n\Delta t+\sigma j\Delta x)),\quad Q_j^n=q\,\exp(i(\beta n\Delta t+\sigma j\Delta x)) \tag{6}$$

where $h$, $u$, and $q$ are unknown constants, $\beta$ is an unknown variable, $\sigma=2\pi/\lambda$ with $\lambda=$wave length of a sinusoid, and $i=\sqrt{-1}$. Substituting Eq. (6) into Eqs. (1), (2), and (5) results in a linear system of homogeneous equations. For non-trivial solutions of $h$, $u$, and $q$, the determinant of the coefficient matrix of the linear system of equations must be zero. This condition yields the following equation for $\exp(i\beta\Delta t)$

$$2(C_1\exp(i\beta\Delta t)+C_2)(\exp(i\beta\Delta t)-\exp(i\sigma\Delta x))(\exp(i\beta\Delta t)-\exp(-i\sigma\Delta x))+B(\exp(i\beta\Delta t)-1)(\exp(i2\beta\Delta t)-1)=0 \tag{7}$$

where $C_1=\psi(H^*-Z-H_v)\rho g/aP_0\alpha_0A$ and $C_2=C_1(1-\psi)/\psi$. The three roots of this equation cannot be expressed analytically. However, they can be evaluated numerically. Results show that root 1 has a zero argument and roots 2 and 3 are conjugate to each other. The roots depend on the absolute partial gas pressure head, the amount of free gas, the mass density and the gas-free wave speed of the liquid, and the extent of discretization as represented by $\sigma\Delta x$ (explained later). The area $A$ in $C_1$, $C_2$, and $B$ can be factored out so that the roots do not depend on it.

Let $N$ be the number of computational reaches with a length of $\Delta x$ such that $N\Delta x=$pipe length $L$. Let $M$ be the number of $\Delta x$'s within one $\lambda$. The $\sigma\Delta x$ in Eq. (7) can be expressed as

$$\sigma\Delta x=\frac{2\pi}{\lambda}\frac{L}{N}=\frac{2\pi}{M\Delta x}\Delta x=\frac{2\pi}{M} \tag{8}$$

Thus the effects of wave length and the extent of numerical discretization can be represented simply by $M$. A plot of $\exp(-Im\beta\Delta t)$ against $M$, called an amplitude portrait (Cunge et al. [5]), displays the behaviour of the amplification and the damping of the numerical scheme over ranges of wave length and the extent of discretization.

The ratio $|\mathrm{Re}\,\beta|/\sigma$ represents the propagation speed of a sinusoid. Divide this propagation speed, herein called the numerical wave speed, by the physical wave speed of the gas-free liquid to obtain

$$\frac{\frac{|\mathrm{Re}\,\beta|}{\sigma}}{a}=\frac{|\mathrm{Re}\,\beta\Delta t|}{\sigma a\Delta t}=\frac{|\mathrm{Re}\,\beta\Delta t|}{\sigma\Delta x}=|\mathrm{Re}\,\beta\Delta t|\frac{M}{2\pi} \tag{9}$$

This wave speed ratio is plotted against $M$ to obtain the phase portrait of the numerical scheme. Spurious oscillations occur when the ratio deviates from unity.

## Example

The example problem in Wylie [1] and Provos and Wylie [3] was used. It is a frictionless horizontal pipe with $L=3000\,\mathrm{m}$, $D=0.61\,\mathrm{m}$, $\rho=992\,\mathrm{kg/m^3}$, $a=981.4\,\mathrm{m/s}$, $Z=10.3\,\mathrm{m}$, and $\alpha_0=0.002$ at $P_0=101325\,\mathrm{Pa}$. Initially it has a steady flow of 0.89 $\mathrm{m^3/s}$ and a head of 60 m at both ends. The outlet head is kept constant. Starting at $t=0$ s, the inlet head is lowered to 58 m in 0.204 s and then kept at that level. The volume versus absolute head relationship is linearized at $H^*=59\,\mathrm{m}$.

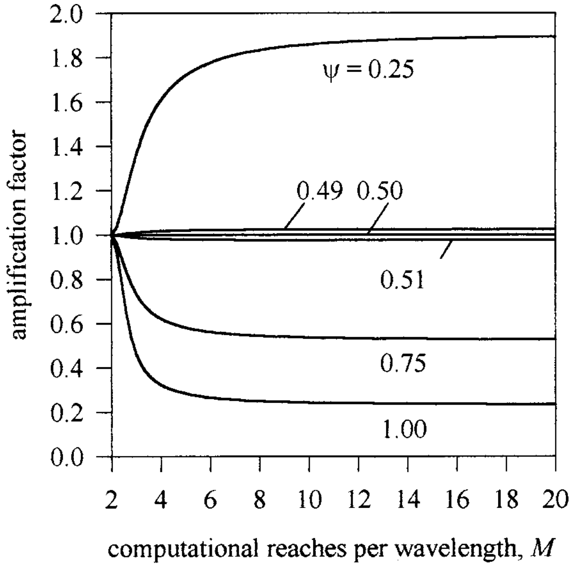

Fig. 2 The amplitude portrait using the first root

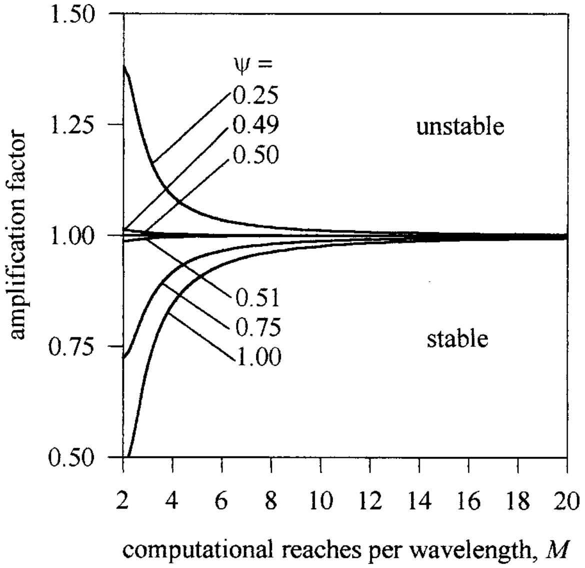

Fig. 3 The amplitude portrait using the conjugate roots 2 and 3

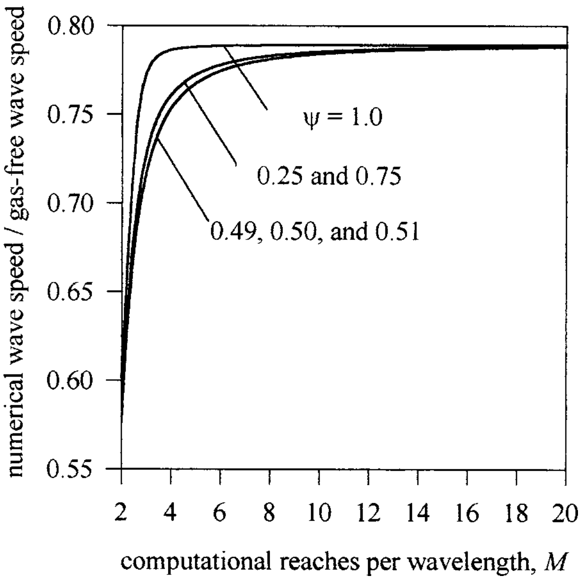

Fig. 4 The phase portrait using the conjugate roots 2 and 3

The amplitude portrait using the root with zero argument is shown in Fig. 2. It is seen that $\psi=0.5$ produces an amplification factor of 1.0 for all $M$. Curves with $\psi<0.5$ lie in the unstable region and curves with $\psi>0.5$ lie in the stable region. For all curves with $\psi\geqslant 0.5$, their damping increases as $M$ increases and eventually reach their own asymptotes.

Numerical evaluations of the root with zero argument show that $\mathrm{Re}\,\beta\Delta t=\pi$ for all $\psi$ values. Therefore, the phase portrait is simply a straight line with an intercept of zero and a slope of 0.5. Numerical waves always lead the physical wave for any $M$ greater than 2. This lead causes spurious oscillations which will be damped out when a $\psi\geqslant 0.5$ is used.

The amplitude portrait using the conjugate roots is shown in Fig. 3. Like the first root, a $\psi$ of 0.5 yields an amplification factor of unity for all $M$. Curves with $\psi<0.5$ lie in the unstable region and curves with $\psi>0.5$ lie in the stable region. Unlike the first root, all curve converges to unity as $M$ increases. Thus the numerical damping per time step is less when more computational reaches are used.

The phase portrait using the conjugate roots is shown in Fig. 4. For all $\psi$ values, the numerical wave speed lags behind the physical wave speed. As $M$ increases, the lag becomes smaller and all curves approach a common asymptote.

## The Numerical Wave Speed at Large *M*

Following the derivations of Wylie and Streeter [3], the physical wave speed of a low void fraction gas-liquid mixture can be expressed as

$$a'=\frac{a}{\sqrt{1+\frac{P_0\alpha_0 a^2}{\rho g^2(H^*-Z-H_v)^2}}} \tag{10}$$

in which $a'=$the wave speed of the mixture. For the example, $a'/a=0.7892$.

The phase portrait in Fig. 4 shows that, for the solution component associated with the conjugate roots, the wave speed ratios also approach an asymptote of 0.7892 (evaluated at $M=30$). This is not a coincidence. Evaluations of the limiting value and $a'/a$ are made for ranges of absolute partial pressure head and amount of free gas. The results are shown in Fig. 5. The $a'/a$ dots fall on the curves of the limiting value for all the conditions tested. Therefore, when $M$ is sufficiently large, the numerical wave speed

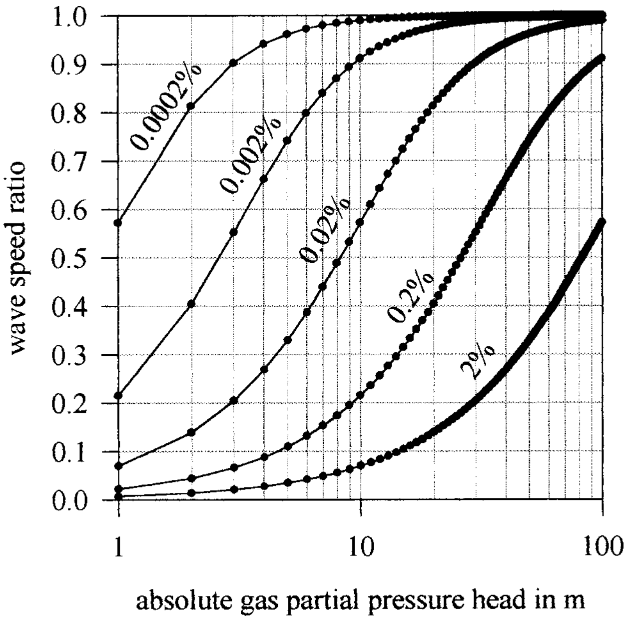

**Fig. 5 Wave speed ratios. Numerical wave speed/gas-free wave speed (dots), mixture wave speed/gas-free wave speed (lines)**

equals the wave speed of the gas-liquid mixture. This is why the discrete gas cavity model can capture the steepening of a positive pressure wave and the spreading of a negative pressure wave.

## Extending to Nonlinear Problems

For large-amplitude transients, the nonlinear gas volume versus pressure behavior must be modeled correctly. This can be accomplished by iterations. Iterations use the fact that only the slope of the gas volume versus pressure head hyperbola affects the solution. The hyperbola can be tracked by adjusting this slope using the mean pressure head between two consecutive time steps. In the solution process, the local unknown $H^*$ in Eq. (5) is first set to the known $H_j^n$. A trial $H_j^{n+1}$ is computed. $H^*$ is then updated by the average of $H_j^n$ and the trial $H_j^{n+1}$ for the next iteration. This process is repeated until $H_j^{n+1}$ converges.

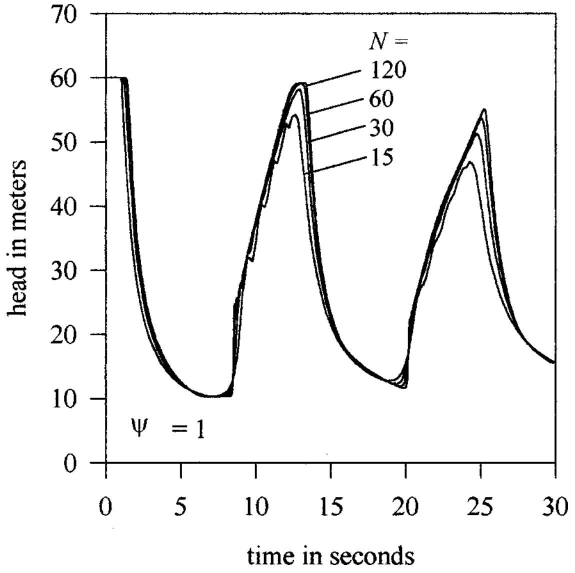

**Fig. 6 Computed large-amplitude transient head 1200 m from the inlet**

Large amplitude transients where the inlet pressure head was lowered to 10.3 m (the pipe elevation) linearly in 0.204 seconds were computed by this procedure using $\psi=1$. The results are shown in Fig. 6. The traces reflect the spreading of the negative pressure wave propagating toward downstream, and the subsequent steepening of the positive pressure wave reflected from the constant and higher head at the downstream end. The gas volume versus pressure head hyperbola was closely tracked by the iteration process.

## Summary and Conclusions

The discrete gas cavity model of Wylie [4] was linearized by approximating the volume versus pressure head hyperbola locally with a straight line. This resulted in a linear finite difference scheme on which a von Neumann analysis was carried out. Through iterations, the linearized scheme converges to the original model. Thus, the numerical stability and phase properties of the linear scheme are expected to indicate those of the original model.

The results show that the numerical wave speeds lead the physical wave speed in one of the solution components irrespective of the value of the weighting factor $\psi$. The effect this phase error, however, can be damped out by using a $\psi$ greater than 0.5.

For the remaining solution components, the numerical wave speeds lag behind the physical wave speed. This phase error decreases and eventually disappears as more computational reaches are used. This vanishing phase error enables the discrete gas cavity model to exhibit the pressure-dependent wave speed of a low void ratio gas-liquid mixture.

A $\psi$ approaching unity should be used because (1) it offers greater damping to reduce the numerical dispersion in the solution component associated with the first root, (2) it produces less phase error in the solution components associated with the conjugate roots, and (3) although the numerical damping in the solution components associated with the conjugate roots is greater, the damping can always be reduced by using a larger $M$.

We noted that, although a larger $M$ yields a more accurate numerical solution, one should not use an $M$ so large that the gas volume becomes significant relative to the liquid volume between two adjacent computational sections. This limitation of the discrete gas cavity model has previously been pointed out by Wylie and Streeter [3].

## Acknowledgment

The author would like to thank Professor E. B. Wylie of the University of Michigan for the many discussions on the discrete gas cavity model. This study was conducted while the author was a visiting professor at the International Institute for Infrastructural, Hydraulic and Environmental Engineering, Delft, The Netherlands.

## References

[1] Wylie, E. B., 1980, ''Free Air in Liquid Transient Flow,'' *Proceedings of the Third International Conference on Pressure Surges*, Paper B1, pp. 27–42, BHRA Fluids Engineering, Canterbuy, U.K., Mar.

[2] Provoost, G. A., and Wylie, E. B., 1981, ''Discrete Gas Model to Represent Distributed Free Gas in Liquids,'' *Fifth International Symposium on Column Separation*, Obernach, Germany, Sept. 8 pp.

[3] Wylie, E. B., and Streeter, V. L., 1993, *Fluid Transients in Systems*, Prentice-Hall, Englewood Cliffs, NJ, pp. 38–39, 184–187.

[4] Wylie, E. B., 1984, ''Simulation of Vaporous and Gaseous Cavitation,'' ASME J. Fluids Eng., **106**, Sept., pp. 307–311.

[5] Cunge, J. A., Holly, Jr., F. M., and Verwey, A., 1980, *Practical Aspects of Computational River Hydraulics*, Pitman, London, U.K., pp. 80–89.

Journal of Fluids Engineering

# Erratum

# Erratum: ''Large Eddy Simulation of Flow Past a Square Cylinder: Comparison of Different Subgrid Scale Models'' [ASME J. Fluids Eng., 122, No. 1, pp. 39–47]

A. Sohanker, L. Davidson, and C. Norberg

---

In the above paper, Eq. (4) was printed incorrectly. The correct equation appears below:

Equation (4) on p. 40 should read:

$$\begin{aligned}\widehat{P}_{k_{sgs}}-\frac{1}{\Delta}\widehat{C_*^k k_{sgs}^{3/2}}=P_K-\frac{1}{\widehat{\Delta}}C_*^k K^{3/2}\Rightarrow(C_*^k)^{n+1}\\ =\left(P_K-\widehat{P}_{k_{sgs}}+\frac{1}{\Delta}\widehat{(C_*^k)^n k_{sgs}^{3/2}}\right)\frac{\widehat{\Delta}}{K^{3/2}}.\end{aligned} \tag{4}$$